DETERMINING THE STRESS REGIME WITHIN A VOLCANIC EDIFICE FROM IGNEOUS INTRUSIONS AND DEFORMATION MEASUREMENTS

by

Michael Patrick Poland

A Dissertation Presented in Partial Fulfillment
of the Requirements for the Degree
Doctor of Philosophy

ARIZONA STATE UNIVERSITY

December 2001

DETERMINING THE STRESS REGIME WITHIN A VOLCANIC EDIFICE FROM IGNEOUS INTRUSIONS AND DEFORMATION MEASUREMENTS

by

Michael Patrick Poland

has been approved

November 2001

APPROVED:

_____, Chair

_____

_____

_____

_____

Supervisory Committee

ACCEPTED:

_____

Department Chair

_____

Dean, Graduate College

ABSTRACT

Understanding the controls on the stress regime within a volcanic edifice is important when considering the likely locations and characteristics of future eruptive activity. In most volcanoes, magmatic dikes, which align with the most compressive stress in the crust, are oriented radially to the center of the edifice due to outward compression from a pressurized magma body. However, eruptive fissures at many basaltic shields are circumferential on the upper flanks and radial on the lower flanks. An explanation for the contrasting orientations is downsagging caused by loading from dense subvolcanic intrusions. As a test of the proposed model, deformation measurements were collected from a shield volcano with radial and circumferential eruptive vents, and the process of dike emplacement was studied using exposures at an eroded stratovolcano.

Leveling measurements at Medicine Lake volcano, in northern California, indicate approximately ~8 mm/yr subsidence maximized at the summit, decaying symmetrically on the flanks, and remaining relatively constant on a decadal time scale. Regional Global Positioning System surveys reveal a spatially complex field of volcano-tectonic deformation, including tectonic shear east of Medicine Lake and subsidence of the volcano. The deformation is fit equally well by a deflating volume source at depth and a dense subvolcanic load; however, the loading model is preferred due to the lack of a physical mechanism for volume loss at the modeled depth.

Analysis of ~20 silicic radial dikes at the eroded Summer Coon volcano, in southern Colorado, suggests that radially oriented rhyolite, rhyodacite, and quartz latite intrusions have segmented geometries, require high driving pressures, and follow paths that are inclined near the center of the volcano and become sub-horizontal with increasing radial distance. Based on the geometry of the intrusions, eruptions from radial dikes are most likely to occur near the base of a volcanic cone and eruption volume is

probably greatest from lower elevation vents. No circumferential dikes were observed at Summer Coon, possibly because the density contrast between solidified silicic intrusions and the host volcano is greater for felsic systems than for mafic.

ACKNOWLEDGEMENTS

Funding for my research came from a number of sources. For three years, my salary was paid by a National Defense Science and Engineering Graduate Fellowship. Jon Fink also generously supported my salary for 1 year and helped to finance much of my field work. Additional funding for field studies was provided by the SCION Natural Science Association, the Arizona State University chapter of the Sigma Xi Scientific Research Society, the Geological Society of America, the Colorado Scientific Society, and the Associated Students of Arizona State University.

I am indebted to my dissertation committee, consisting of Ed Garnero, Steve Reynolds, Ramon Arrowsmith, and Stan Williams, for their reviews and willingness to discuss various aspects of my research. I am especially grateful to my advisor, Jon Fink, for taking time away from his duties as the Vice Provost for Research to guide my education. I am proud to have been one of his students.

My work at Medicine Lake volcano would not have succeeded without the support and advice of Roland Bürgmann (University of California, Berkeley) and Dan Dzurisin (US Geological Survey). I cannot underscore the importance of their contributions to this document and my career. Paleomagnetic sampling equipment was supplied by Ken Verosub (University of California, Davis) and John Geissman (University of New Mexico). Analysis of samples from Summer Coon volcano was supervised by Dr. Lisa Tauxe and her staff and students (Scripps Institute of Oceanography), who I thank for their time and for allowing me to use their paleomagnetism laboratory. Dennis Geist and Bill Chadwick provided me with the opportunity to visit the Galapagos Islands, where I was able to make first-hand observations relevant to this work. Simon Peacock and Tom Sharp involved me in a variety of activities related to the department and university that enhanced my

educational experience at Arizona State University, and the Department of Geological Sciences staff (particularly Cammy Cecil, Chris Skiba, Joan Bahmonde, and Sue Selkirk) provided much needed support. John Braun and Matt D'alessio assissted with GPS data processing. Comments and advice from Andrea Borgia, Barry Cameron, Kurt Roggensack, Rick Wessels, and Mike Ramsey were helpful and much appreciated. I would also like to thank Lisa Koenig for the many hours she spent discussing various topics with me.

Were it not for the friendship of so many classmates and colleagues I would not have completed my studies at Arizona State University. I would like to acknowledge Sharolyn Anderson, Jill Welter, Crystal Levine, Cayle Lisenbee, Emily Taylor, Sarah Robinson, Beth Stone, Jill Best, Kevin Williams, Tracey Carpenter, Jeri Young, Patricio Figuredo, Steve Holloway, Gail Morrissey, Robin Paarlberg, Paul Niles, Andria Skaff, Tim Glotch, Deanne Rogers, Amy Knudson, Courtneay Dowrick, and Josh Bandfield. For three years I shared an office with Aaron Lyman (who also assisted me in the field) and Chris Eisinger, and I benefitted from their advice and insights. My heartfelt gratitude goes to Scott Nowicki, Merry Nowicki, Kaatje Kraft, Mike Kraft, Wendy Kennedy, and Ken Voglesonger for the many years that they supported my efforts.

Finally, I owe my greatest thanks to the four most important people in my life. My sister Amanda, and my parents, Barbara and Jim, have supported my quest to earn my "union card" at every turn, providing everything from a sympathetic ear to a mini van to their own valuable time helping with my field work (on more occasions than I can count). Chantelle Lucas supported me in the field enough times that she probably could have earned a M.S. in geology herself, and she has been the source of my inspiration for the past 5 years.

TABLE OF CONTENTS

LIST OF TABLES

LIST OF FIGURES

PREFACE

The work contained in this dissertation is the result of field work and data processing conducted between August 1997 and December 2001. However, I also relied heavily on data that was collected by other people and software provided to me by various individuals.

The three main projects I completed for this dissertation are given in Chapters 2, 3, and 4. Chapter 2 details leveling surveys conducted at Medicine Lake volcano. The chapter is an exact reproduction of a manuscript that was submitted to the *Journal of Geophysical Research* on August 3, 2001. Dan Dzurisin (US Geological Survey) is the first author, followed by myself and Roland Bürgmann (University of California, Berkeley). Dzurisin collected and processed all of the leveling measurements and wrote the first half of the paper. I was responsible for modeling the data and writing the second half of the manuscript (which was later modified by Dzurisin so that both pieces fit together). The modeling software I used was originally written by Bürgmann and Paul Segall (Stanford University), although I modified the code to fit my purposes.

Chapter 3 describes the results of three GPS surveys at Medicine Lake volcano. Data from 1990 was collected by the US Geological Survey and generously shared by the staff of the Cascades Volcano Observatory (Dzurisin, Elliot Endo, and Gene Iwatsubo). I organized and financed the 1996 campaign while an undergraduate student at the University of California, Davis, under the guidance of Bürgmann. Some of the modeling described in the chapter also uses the aforementioned code of Bürgmann and Segall.

Finally, Chapter 4 is an analysis of radial dike emplacement at Summer Coon volcano. The research builds on mapping conducted by William Moats (M.S., Arizona State University, 1990), and most of the models and conclusions in the chapter are based

on dike geometry data that he collected. Data processing software used in the paleomag sample analysis was developed by Lisa Tauxe (Scripps Institute of Oceanography).

I am hopeful that in addition to Chapter 2, three manuscripts will be submitted to various journals based on this work. Chapter 3 will be revised and submitted to the *Journal of Geophysical Research* with myself, Bürgmann, Dzurisin, and Fink as authors. I am optimistic that 2 journal articles will result from Chapter 4. I plan to submit the paleomagnetic results as a paper by myself, Tauxe, and Fink to *Geology*. The bulk of the chapter (mostly geologic descriptions and inferences) will be submitted to the *Geological Society of America Bulletin* by myself, Fink, and perhaps Moats.

1. Downsagging as a mechanism for the formation of circumferentially-oriented intrusions at large basaltic volcanoes

Abstract. In a volcano where the only source of stress heterogeneity is a pressurized magma chamber, radial diking is the common form of intrusive activity. However, at some volcanoes, typified by the basaltic shields of the western Galapagos Islands, dikes inferred from eruptive fissures trend both circumferentially and radially with respect to the summit of the edifice. The bimodal intrusion geometry suggests that at least two distinct stress regimes occur within the host volcano. Although several mechanisms have been proposed, none can account for the occurrence of both circumferential and radial dikes at all of the observed locations. Downsagging due to loading by dense subvolcanic intrusions has been invoked to explain the formation of normal fault calderas on basaltic volcanoes [*Walker,* 1988]. The mechanism may also create a stress field supporting circumferential dike intrusion near the summit and radial diking on the flanks of a volcano. Mafic intrusions have a higher density contrast with the country rock and are more likely to cause downsagging than felsic intrusions, which have lower densities. The model may be evaluated by deformation measurements at relatively inactive basaltic shields (high levels of magmatic activity may obscure downsagging) and insights into the emplacement of both radial and circumferential dikes from eroded volcanoes.

1.1 Introduction

Dike intrusion is a common form of igneous activity in volcanic environments and can represent a significant danger when magma approaches the surface. Hazard mitigation efforts at active volcanoes would benefit from knowledge of areas that are most prone to dike injection, and to the orientations of such intrusions. Simple models of the stress field within a volcano due to a pressurized magma chamber at depth (e.g. the problem of a

pressurized hole in an infinite homogenous elastic plate as presented by *Odé* [1957]) predict radial dike emplacement. In the absence of preexisting fractures, a dike will intrude parallel to the most compressive stress in the crust (σ_1), and perpendicular to the least compressive stress (σ_3) [*Stevens*, 1911; *Anderson*, 1938; *Delaney et al.*, 1986]. Radial contraction caused by the pressurized source results in radially oriented local σ_1 and similarly oriented dikes. Silicic volcanic systems typified by stratovolcanoes are commonly associated with radial dike swarms, as demonstrated by *Nakamura* [1977]. Similarly, eroded silicic volcanoes are often the focus of a radial dike swarm, for instance the Spanish Peaks [*Ode*, 1957] and Summer Coon volcano [*Lipman*, 1968] in southern Colorado.

Dikes and eruptive fissures with orientations that are circumferential to the center of a volcano have also been mapped both in eroded and active volcanic settings. Sets of inclined intrusive sheets and ring-dikes in Scotland and Iceland have orientations that are concentric about a common origin [e.g. *Gautneb et al.*, 1989; *Walker*, 1993]. Similarly, the mafic shields of the western Galapagos islands are characterized by radial eruptive fissures on their lower flanks in addition to higher-elevation fissures that are circumferential to the summits. The eruptive fissures probably reflect the trends of feeder dikes, implying that radial and concentric dikes coexist on the Galapagos volcanoes [*McBirney and Williams*, 1969; *Simkin*, 1972; *Chadwick and Howard*, 1991]. Similar patterns of eruptive fissures have also been observed at other locations, including extraterrestrial volcanoes on Mars and Venus. Circumferential dike swarms occur in a stress regime with σ_1 that is concentric to the center of the volcano, whereas radial dikes occur where σ_1 is radially oriented. Therefore, two different stress regimes are implied to have been present within volcanoes that host both concentric and radial intrusions. Unfortunately, no existing models can satisfactorily explain the occurrence of the two stress fields within a single volcano.

Here, I present a model of a mafic volcanic edifice in which the stress field is controlled by two sources. A pressurized, subvolcanic magma chamber favors radial dike intrusion, while downsagging of the edifice due to loading by subvolcanic intrusions (probably high-density igneous material) causes circumferential extension, and hence circumferential dike injection. The downsagging element of the model builds on an earlier idea developed by *Walker* [1984; 1987; 1988] for the formation of caldera complexes on basaltic shields. Both stress fields are clearly manifested in the Galapagos due to the lack of additional sources of stress (e.g. the growth of a neighboring volcanic edifice, deviatoric regional stress, etc.). In contrast to mafic shields, stratovolcanoes are characterized by low-density silicic magmas. An intrusive complex composed of crystallized silicic magmas would be less likely to cause downsagging because of the smaller density contrast between silicic intrusives and country rock. Therefore, stresses favoring concentric dikes would be absent and the major source of stress within a stratovolcano is a pressurized magma chamber that promotes radial dike intrusion. The model does not apply to the formation of large silicic calderas due to the evacuation of a large magma chamber (e.g. Valles Caldera, New Mexico [*Smith and Bailey*, 1968], and Crater Lake, Oregon [*Bacon*, 1983]).

Data that can be used to evaluate the proposed model include deformation measurements from shield volcanoes that display circumferential eruptive fissures (with or without radial vents), and maps of dike morphology and geometry in eroded volcanoes. High deformation rates due to magmatic activity characterize many active shield volcanoes, including Hawaii [*Owen et al.*, 1995] and the Galapagos [*Amelung et al.*, 2000], and would tend to overprint existing signals from downsagging. Therefore Medicine Lake volcano, a dormant shield located in northern California, was chosen as the site for deformation studies. Dike emplacement is investigated at the eroded Summer Coon volcano in southern Colorado. Although no circumferential dikes occur at Summer Coon,

a nearly perfect swarm of mafic and silicic radial dikes are exposed. Results form Summer Coon may be applied to similar intrusive swarms, providing constraints on the proposed model for radial and circumferential dike intrusion within a single volcanic edifice.

1.2 Previous Work

The process of dike intrusion in a volcano is controlled by 1) magmatic overpressure, 2) the material properties of the country rock, and 3) the stress field acting in the edifice. A dike will propagate when its driving pressure exceeds the forces that oppose dilation (e.g. the horizontal stress in the crust acting perpendicular to the dike, the tensile strength of the host rock, etc.) [*Anderson*, 1938; *Gudmundsson*, 1998]. After opening, a dike's orientation is controlled by the stress regimes acting in the volcano and generated by the dike itself, and by the mean stress [*Koenig and Pollard*, 1998]. As a result, dike trends may be used to infer the nature of the stress field at the time of intrusion [*Stevens*, 1911; *Delaney et al.*, 1986; *Pollard*, 1987; *Delaney and Gartner*, 1997]. Further insights into the stress field within a volcano can come from theoretical, analytical, numerical, and analog modeling, and several such investigations are described below.

1.2.1 Theoretical and Analytical Models

An excellent example of a theoretical model of the interaction between a dike and a regional stress field is given by *Nakamura* [1977] and *Nakamura et al.* [1977], who notes that dikes with proximal radial trends will change orientations to align with the regional stress field as the move away from the center of the source volcano. In convergent plate boundary settings, σ_1 is usually directed perpendicular to the axis of the volcanic arc. As a result, radial dikes will tend to assume arc-perpendicular trends that are aligned with the

regional stress field upon leaving the vicinity of the magma chamber (Figure 1.1) [*Nakamura*, 1977]. *Nakamura et al.* [1977] presents evidence from volcanoes in the Aleutians of dikes (inferred from surface eruptive vents) which deviate from radial trends in order to parallel the regional σ_1 stress. The transition from a stress field dominated by the magma chamber to one dominated by regional stresses is dependent on the difference between the regional σ_1 and σ_3, and the magnitude of the magma pressure. High differential regional stress or low magma pressure will result in a transition zone that is closer to the magma chamber.

If additional sources of stress occur within or near a volcano (beyond a pressurized chamber or regional stresses), dike orientations will reflect the regions of dominance of the different stress fields. *Ode* [1957] noted that radial dikes to the west of the Spanish Peaks in Colorado were deflected away from the Sangre de Cristo mountain range. To model the dike pattern and associated stress field, *Ode* [1957] analyzed the problem of a two-dimensional plate with a pressurized hole. In the absence of heterogeneity, the resulting stress pattern would be radially compressive, resulting in a radial pattern of cracks. In order to account for the deflection of intrusions near the Sangre de Cristo mountains, *Ode* [1957] included a rigid block to the west of the pressurized hole to simulate the mechanical barrier of the range. The resulting principal stress directions were a good approximation of the observed dike swarm geometry. The model was later improved by contributions from *Muller and Pollard* [1977] and *Muller* [1986].

1.2.2 Numerical Models

Sources of stress beyond regional tectonism also influence dike intrusion within a volcanic edifice, and may be modeled using numerical techniques. *Dieterich and Decker* [1975] explored the effects of differing magma chamber geometries (spheres, sills, dikes,

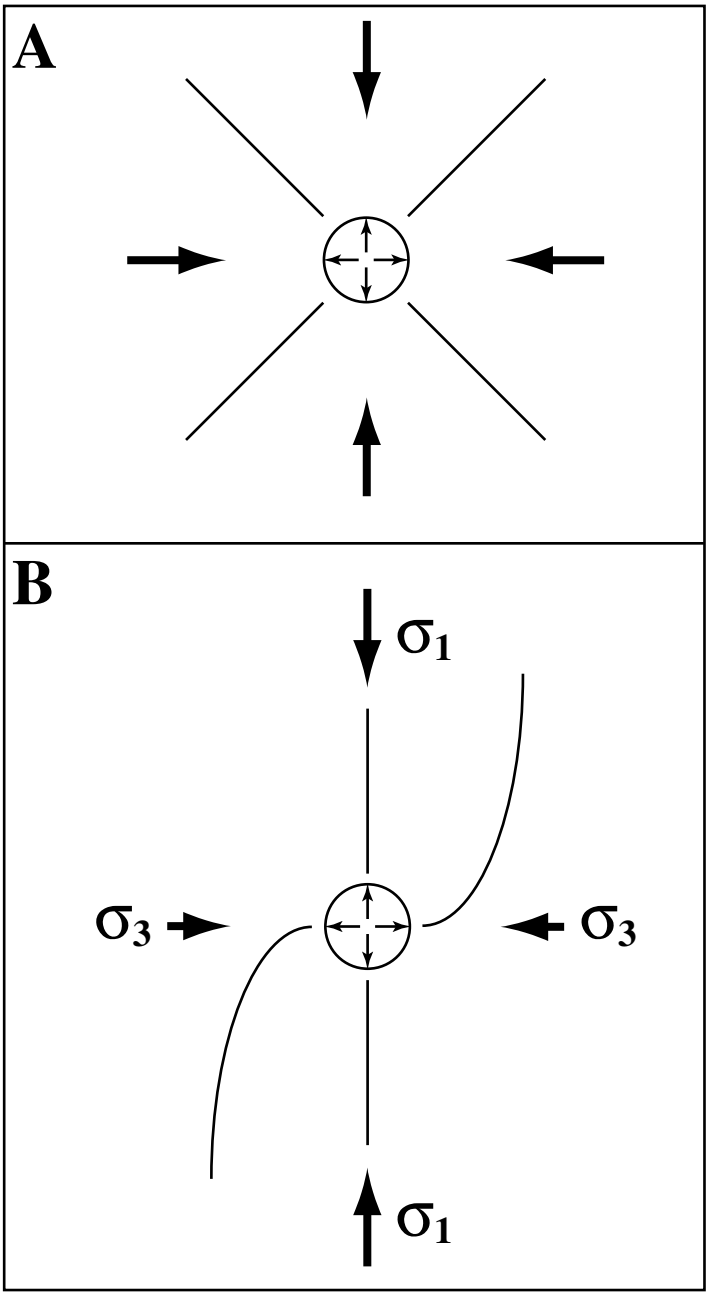

Figure 1.1. Predicted dike trajectories due to a positively pressurized magma chamber in differing regional stress fields. (a) In a isotropic regional stress field ($\sigma_1 = \sigma_3$), dikes intruded from a pressurized magma source will be perfectly radial. (b) Under anisotropic regional stress ($\sigma_1 > \sigma_3$), dikes that initiate with orientations that are radial to a pressurized magma source will deflect into orientations parallel with σ_1. Adapted from *Nakamura* [1977].

plugs, etc.) on surface deformation using the finite element approach with application to Kilauea volcano, Hawaii. Deformation has also been modeled using forward numerical methods by *Cayol and Cornet* [1998], who simulated surface displacements during an eruptive episode at Piton de la Fournaise volcano on Reunion Island using a three-dimensional boundary element model. *Chevallier and Verwoerd* [1988] base their finite element approximation on a geological model of an ocean island volcano (based on field studies of active and eroded hotspot volcanoes), and found that the shape of the magma chamber is a dominant control on the stress distribution of the edifice. They later modified their numerical simulations to account for the temperature distribution in a volcano due to conductive and convective cooling of the magma chamber and associated conduit [*Chevallier and Verwoerd*, 1990]. The incorporation of temperature dependent parameters illustrates the use of non-elastic rheologies in finite element models, which is an advantage over other methods.

A significant problem in modeling the stresses within a volcano is accounting for gravitational forces within the edifice. Most models treat volcanoes as instantaneously emplaced loads and do not account for the growth of the edifice over time. *McGovern and Solomon* [1993; 1998] present finite element models of large extraterrestrial volcanoes and account for gravitational forces by allowing for incremental volcano growth. Layers are added to the volcano on a time scale defined by the viscoelastic properties of the model mantle. As a result, stresses and deformation due to both elastic and viscoelastic processes may be studied.

1.2.3 Analog Models

Additional insights into the stress field within a volcano may be gained through the use of analog experiments. The work of *Fiske and Jackson* [1972] exemplifies the utility

of analog methods for modeling dike intrusion. They molded gelatin into ridge-shapes and injected colored water into the mold interiors to simulate dike intrusion, finding that the water "dikes" propagated along paths that paralleled the ridge crest regardless of ridge shape. By analogy with the models, *Fiske and Jackson* [1972] concluded that Hawaiian volcanoes that grew against preexisting topography will have rift zones that mimic the elongated shape of the preexisting edifice. For example, the orientations of Kilauea's rift zones are controlled by the shape of neighboring Mauna Loa volcano, while Mauna Loa's rift zones are in turn influenced by the shape of the adjacent and older Mauna Kea volcano. Additional studies of dike propagation utilizing gelatin models have been published by *Hyndman and Alt* [1987] and *Takada* [1990; 1994].

Scaled analog models are designed to accurately reflect the geometry, kinematics, and dynamics of a natural system. *Merle and Borgia* [1996] use a sand cone that sits atop stratified sand and silicone layers, simulating the effect of a weak substrate on the gravitational spreading of a volcanic edifice. Similar techniques have been used to model deformation preceeding the 1980 eruption of Mt. St. Helens [*Donnadieu and Merle*, 1998; *Donnadieu et al.*, 2001]. Scaled or unscaled, analog methods are useful for indicating stress conditions through fracture and deformation patterns observed on the surface and in the interiors of the model volcanoes.

1.3 Circumferential Dikes and Their Formation

Before beginning a discussion of the origin of circumferential dikes, it is necessary to distinguish such dikes from other similar intrusive forms. *Anderson* [1936] defines intrusions that "incline inwards towards a common center" as cone sheets, however other authors [e.g. *Harker*, 1904; *Gautneb et al.*, 1989] use the phrase "inclined sheets" to describe similar intrusions, and the terms are generally interchangeable. Cone sheets are

associated with magma injection into centrally inclined fractures that form when magma pressure in a subsurface chamber is high [*Anderson*, 1936; *Robson and Barr*, 1964]. However, there is considerable disagreement on the mode of cone sheet fracture, with some authors advocating shear failure [e.g. *Robson and Barr*, 1964; *Phillips*, 1974; *Chevallier and Verwoerd*, 1988; *Chevallier and Verwoerd*, 1990] and others invoking extensional fracturing [e.g. *Anderson*, 1936; *Roberts*, 1970; *Koide and Bhattacharji*, 1975]. Measurements of the dilation vector for inclined sheets in the Cuillins volcano, Scotland [*Walker*, 1993], Hafnarfjall volcano, Iceland [*Gautneb et al.*, 1989], and Reykjadalur volcano, Iceland [*Gautneb and Gudmundsson*, 1992] suggest opening without shear, implying cone sheets injected into extensional fractures. *Walker* [1993] prefers the term "centrally inclined sheet" because the term does not imply an association with either extensional or shear fractures, and because the conical form of an intrusive sheet swarm is evident from the entire complex of intrusions, rather than from an individual sheet. Excellent exposures of cone sheets occur in the eroded Tertiary volcanics of Scotland (for instance, the centers of Mull and Cuillin Hills [*Richey*, 1932; *Walker*, 1993] and Iceland [e.g. *Gautneb et al.*, 1989; *Gautneb and Gudmundsson*, 1992].

In contrast, a ring dike tends to have a "more or less vertical" dip and forms an arc that covers a much greater circumference of a circle than a cone sheet [*Anderson*, 1936]. Ring dike complexes can be several kilometers in diameter and are usually associated with caldera complexes [*Anderson*, 1936]. As with cone sheets, no clear consensus exists as to whether ring dikes intrude extensional or shear fractures. *Smith and Bailey* [1968] suggest that intrusions into the collapse fracture (or "ring fracture") at the silicic Valles caldera, New Mexico, led to surface eruptions along an arcuate trend. The extrusions probably overlie a more complete ring dike at depth. Ring dike intrusion usually occurs after caldera collapse and is approximately concurrent with resurgent doming [*Smith and Bailey*, 1968].

Inferred dikes that circumscribe the summit calderas of Medicine Lake and Newberry volcanoes in the Cascade arc have also been cited as examples of incomplete ring dikes [*Anderson*, 1941; *Heiken*, 1978; *MacLeod and Sherrod*, 1988; *Zucca and Evans*, 1992]. However, later work by *Donnelly-Nolan* [1988] suggests that Medicine Lake caldera did not collapse catastrophically and that eruptions on opposite sides of the caldera are not related.

Because dikes on active volcanoes can only be inferred from aligned fracture systems or eruptive vents [*Fink and Pollard*, 1983; *Fink*, 1985], the subsurface geometries of the intrusions are not known. The names "cone sheet" and "ring dike" imply a specific geometry and genetic origin, which cannot be confirmed from surface features alone. Instead, the term "circumferential dike" as used by *Banfield et al.* [1956] and *McBirney and Williams* [1969] to describe inferred intrusions at the western Galapagos shields is preferable because no geometric or genetic relationships are assumed.

Circumferential dikes are best represented on the shield volcanoes of the western Galapagos Islands, including Fernandina volcano on the island of the same name, and Cerro Azul, Sierra Negra, Alcedo, Darwin, and Wolf volcanoes on the island of Isabela (Figure 1.2). Both radial and circumferential eruptive fissures coexist on all six volcanoes, with radial fissures low on the flanks and circumferential fissures closer to the summits [*Chadwick and Howard*, 1991]. Varying fissure orientations indicate the presence of two different stress fields on the volcanoes: 1) radial tension near the summit, and 2) radial compression on the flanks [*Chadwick and Howard*, 1991]. Few eruptive vents occur between the two stress regimes, probably because the transition zone inhibits dike propagation [*McGuire and Pullen*, 1989; *Rowland*, 1996]. Two categories of western Galapagos volcanoes are distinguished by several authors, including *Nordlie* [1973], *Mouginis-Mark et al.* [1996], and *Munro and Rowland* [1996]. Wolf, Cerro Azul, and

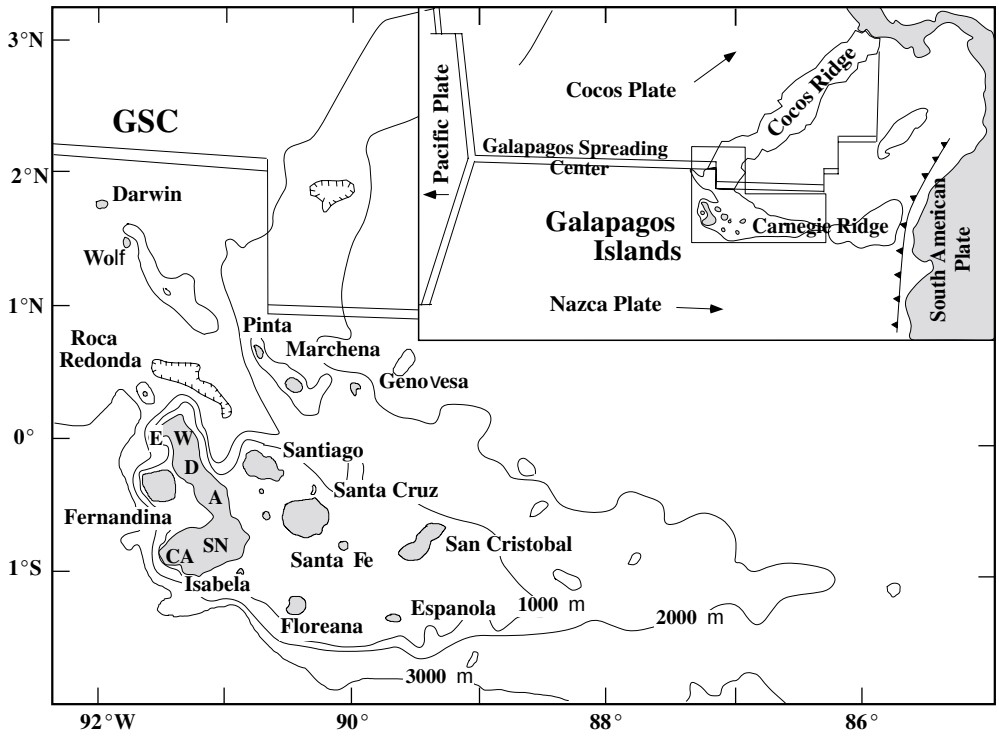

Figure 1.2. Location map and tectonic setting of the Galapagos archipelago. The islands are located south of the Galapagos Spreading Center (GSC) on the Nazca Plate. Fernandina volcano occupies the island of the same name. The volcanoes of Isabela Island are Ecuador (E), Wolf (W), Darwin (D), Alcedo (A), Sierra Negra (SN), and Cerro Azul (CA). Ecuador volcano has been substantially eroded and is not discussed in the text. The inset shows the regional tectonic setting, including plate boundaries (parallel lines are divergent, single lines are transforms, and the line with teeth is convergent with the teeth on the side of the downgoing slab). Plate motions are relative to the South American Plate. After *Naumann and Geist* [2000].

Fernandina (type 1) have calderas with large depth-to-diameter ratios and a well-developed pattern of circumferential eruptive fissures, whereas the calderas of Sierra Negra, Darwin, and Alcedo (type 2) have low depth-to-diameter ratios and the volcanoes host a poorly developed complex of circumferential eruptive fissures (Figures 1.3 and 1.4). Type 1 volcanoes also tend to have steeper flanks than type 2 volcanoes [*Munro and Rowland*, 1996].

Radial and circumferential eruptive fissures also coexist at volcanoes outside the Galapagos archipelago, including Medicine Lake, California [*Donnelly-Nolan et al.*, 1990], Newberry Crater, Oregon, [*MacLeod et al.*, 1995], Suswa, Kenya [*Johnson*, 1969], Askja, Iceland [*Gudmundsson*, 1998], and several other locations worldwide. In regions where the regional deviatoric stress is high (for instance, Askja and Medicine Lake volcanoes, which are both located in extensional tectonic settings), radial dikes will align with the tectonic orientation of σ_1 upon leaving the source magma chamber. The pattern of eruptive fissures on such volcanoes would manifest as circumferential near the summit and tectonically aligned on the flanks, the latter oriented along the regional σ_1 direction. In addition, many seamounts share characteristics with the Galapagos shields, including deep calderas, steep flanks, and circumferential eruptive fissures [*Simkin*, 1972; *Lonsdale and Spiess*, 1979; *Batiza et al.*, 1984; *Fornari and Ryan*, 1984]. Circumferential eruptive fissures have also been noted on a variety of extraterrestrial volcanoes [e.g. *Montesi*, in press].

Circumferential and radial eruptive fissures coexist on volcanoes in all tectonic settings (plate interiors, divergent boundaries, and convergent boundaries). As a result, models explaining the origin of such fissure patterns must not rely on an exclusively tectonic mechanism and should instead consider the morphology and structural development of the host volcanoes. One common characteristic of circumferential fissures

Figure 1.3. Morphology and eruptive fissures of Fernandina volcano, Galapagos Islands. (a) Photograph showing a profile of Fernandina volcano. Note the "overturned soup plate" profile described by *McBirney and Williams* [1969], with the broad summit bench, steep flanks, and broad, gently sloping apron. (b) Map of eruptive fissures on Fernandina volcano after *Chadwick and Howard* [1991]. Fernandina belongs to a classification of Galapagos volcanoes with steep flanks, deep calderas, and an evolved pattern of circumferential eruptive fissures. Similar volcanoes are Wolf and Cerro Azul on the Island of Isabela (Figure 1.2).

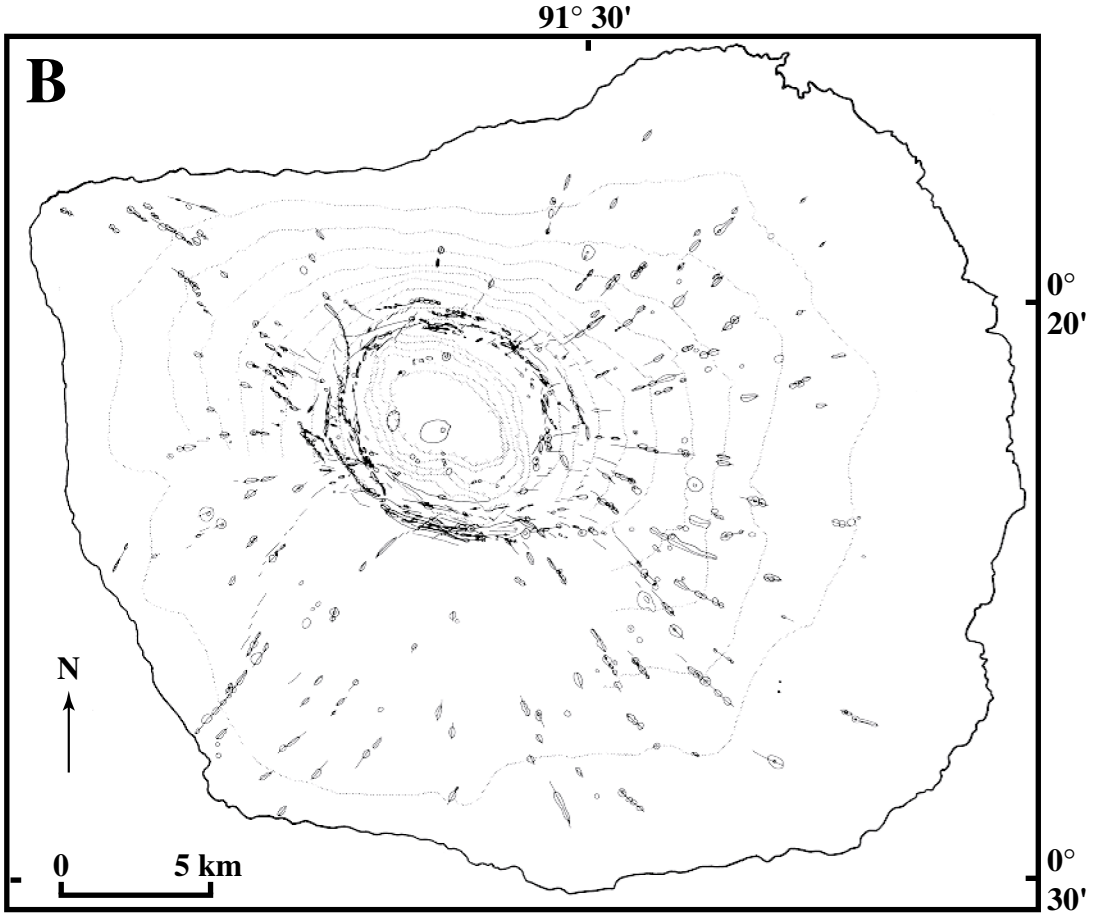

Figure 1.3. (Cont.)

Figure 1.4. Morphology and eruptive fissures of Alcedo volcano, Isabela Island, Galapagos archipelago. (a) Photograph showing a profile of Alcedo volcano. The "overturned soup plate" profile described by *McBirney and Williams* [1969] is not as pronounced on Alcedo as it is on Fernandina (Figure 1.3) due to the shallow slope of Alcedo's flanks. (b) Map of eruptive fissures on Alcedo volcano after *Chadwick and Howard* [1991]. Alcedo volcano belongs to a classification of Galapagos shields with gently sloping flanks, shallow calderas, and a poorly-developed system of circumferential eruptive fissures. Similar volcanoes are Darwin and Sierra Negra, also on the Island of Isabela (Figure 1.2).

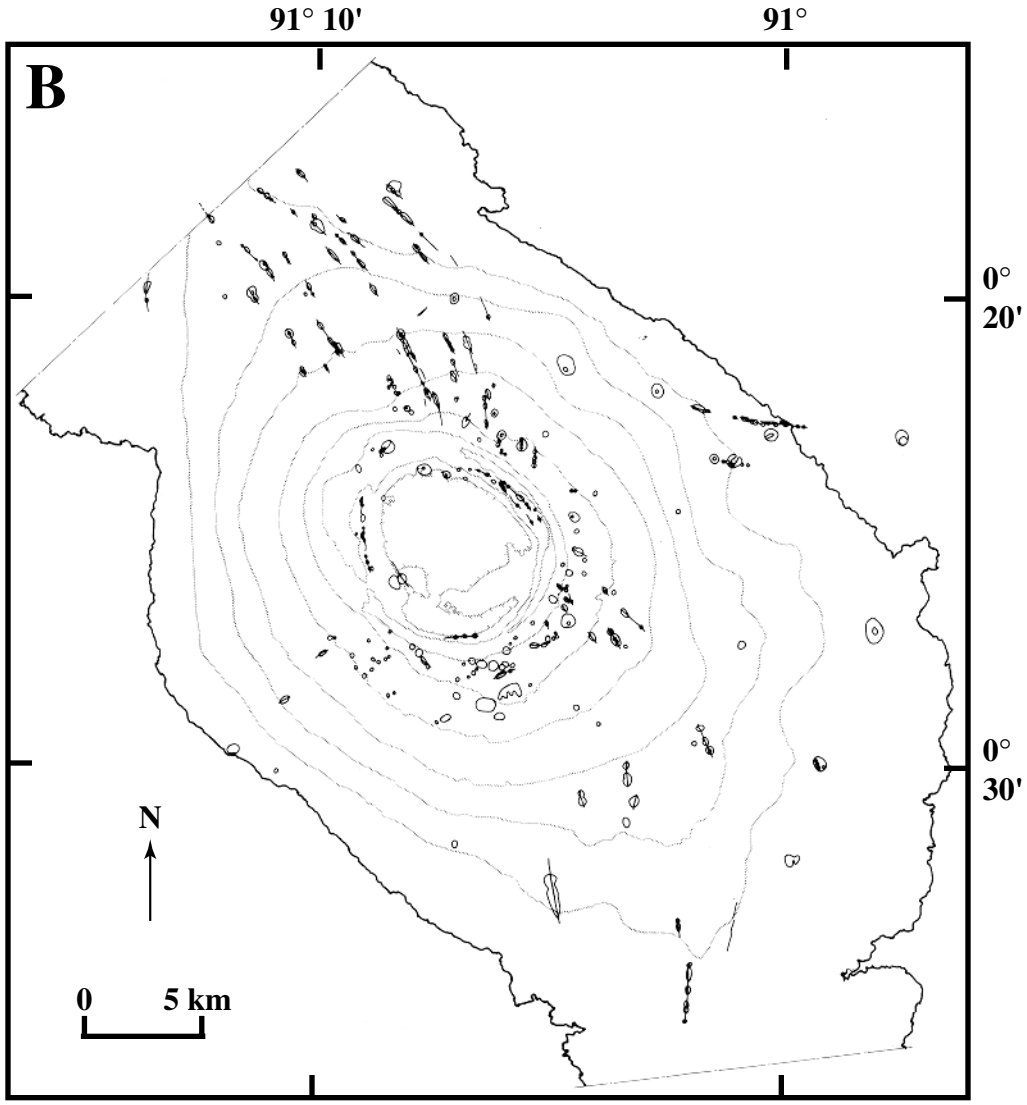

Figure 1.4. (Cont.)

is their occurrence on large mafic shields. Stratovolcanoes are dominated by radial dikes (e.g. the Spanish Peaks in Colorado [*Ode*, 1957]) that do not erupt from circumferentially oriented fissures. Proposals for the origin of circumferential eruptive fissures are described below and include: 1) dike intrusion into a circular ridge, 2) dike intrusion into caldera faults, 3) stress reorientation due to topographic barriers, 4) volcanic spreading, 5) surface loading, 6) underplating and 7) magma chamber pressurization.

1.3.1 Dike Intrusion Into a Circular Ridge

As reviewed earlier, *Fiske and Jackson* [1972] used gelatin models to show that gravitational stresses in a linear topographic ridge will cause a dike to propagate along a path parallel to the ridge axis. *Simkin* [1972; 1984] suggests that the circumferential feeder systems of the western Galapagos shields are formed in a similar manner. Initial volcanic activity builds a circular ridge at the summit of the volcano, possibly due to the development of a summit caldera. The circular ridge behaves analogously to the linear ridge of *Fiske and Jackson* [1972], causing dike intrusion to follow the ridge axis, resulting in the formation of circumferential eruptive fissures (Figure 1.5). Gravitational stress within a ridge promotes lateral dike propagation [*Fiske and Jackson*, 1972; *Simkin*, 1972], therefore eruptions would be expected at the lowest elevations of a circular ridge. Eruptions would continue to build the ridge, creating a positive feedback mechanism and resulting in the characteristic uniform summit platform elevations and steep flanks of the Galapagos volcanoes.

Chadwick and Howard [1991] argue that continued dike intrusion into a circular ridge would eventually alter the stress field, influencing the trends of intrusions. Repeated intrusions into Hawaiian rift zones are sustained by faulting on the flanks of the volcanoes, however little faulting has been mapped on the flanks of the Galapagos volcanoes.

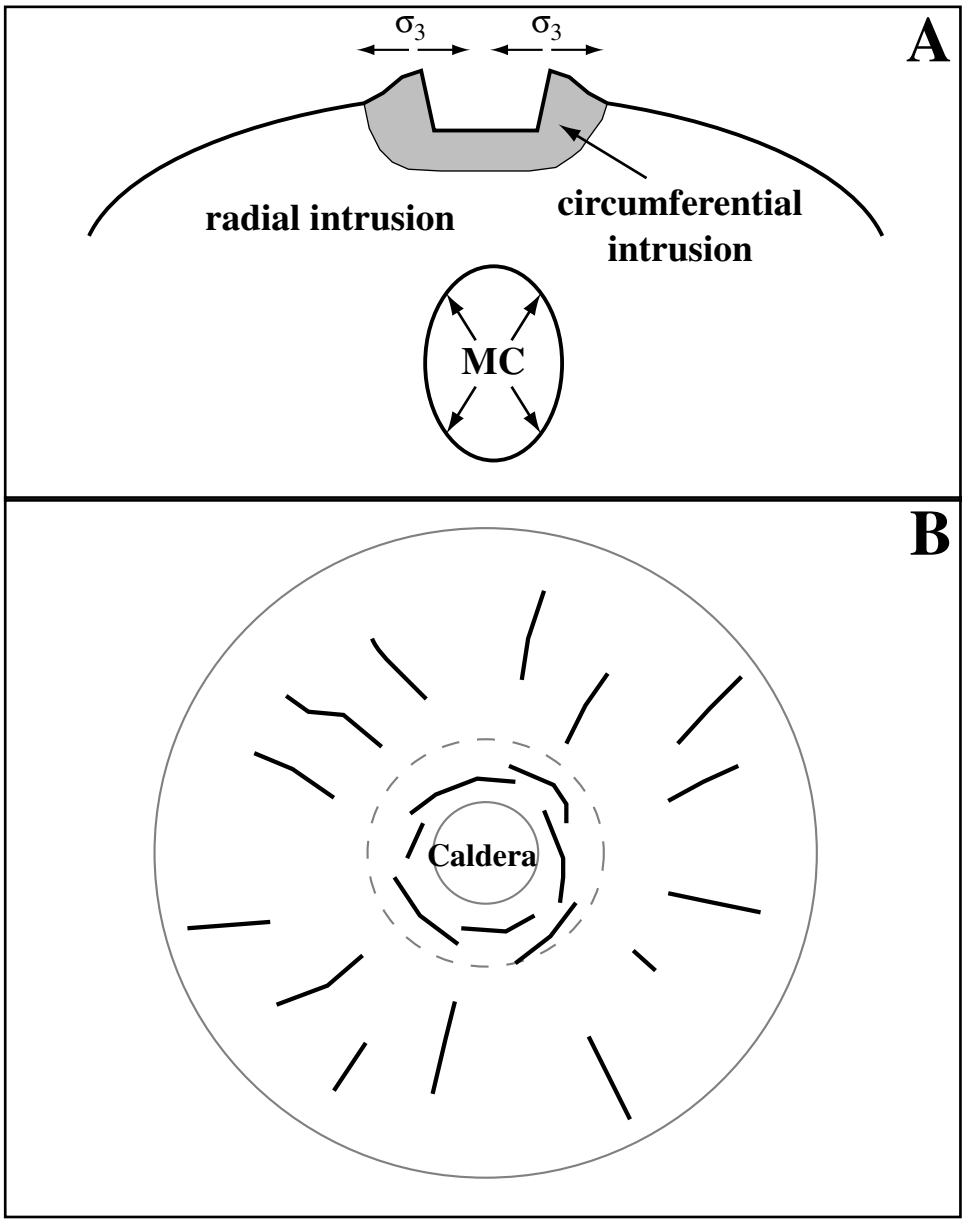

Figure 1.5. Circumferential dike intrusion due to a circular topographic ridge. *Fiske and Jackson* [1972] show that intrusions will follow the axis of a ridge due to the gravitational relaxation of higher topography. By analogy, *Simkin* [1972; 1984] proposes that the circular summit platform of the Galapagos shields acts as a ridge that controls dike orientations. Away from the caldera region, intrusions are radially oriented due to stresses associated with the pressurized magma chamber (MC). (a) Schematic profile of a Galapagos shield volcano showing dikes intruding the ridge-like summit platform, with the least compressive stress (σ_3, arrows) perpendicular to the topography. (b) Plan view of expected dike pattern (heavy lines) on the same volcano with the circular summit ridge outlined by a dashed line.

Therefore, intrusion into a circular ridge cannot explain the persistence of circumferential dike intrusion. The island volcano Marchena in the Galapagos offers additional evidence contradicting the model of *Simkin* [1972]. Marchena is characterized by a 5 x 7 km caldera that has been almost completely infilled by lava flows [*Vicenzi et al.*, 1990]. Young circumferential eruptive fissures exist yet no significant circular ridge is evident [*Vicenzi et al.*, 1990; *Chadwick and Howard*, 1991], suggesting that dike intrusion into a circular ridge does not dominate the development of the observed circumferential and radial eruptive fissure pattern.

1.3.2 Intrusion Along Caldera Faults

Magma may invade and dilate an existing crack if the fracture is favorably oriented with respect to the principal stress regime in the crust [*Delaney et al.*, 1986; *Delaney and Gartner*, 1997]. On occasion, magma has followed caldera-related fractures while rising towards the surface (Figure 1.6). As described earlier, ring dikes are probably the result of magmatic intrusion into ring-fracture systems related to collapse, usually associated with silicic calderas [e.g. *Smith and Bailey*, 1968]. However caldera-related extensional faults may also be dilated by basaltic magma, as exemplified by the 1921-1923 eruptions at Askja, Iceland, which seem to have erupted along the collapse faults of the 1875 caldera-forming eruption [*Thorarinsson and Sigvaldason*, 1962]. In addition, the seven eruptions that followed the 1968 caldera collapse at Fernandina volcano occurred within or around the caldera, possibly on the caldera bounding faults [*Chadwick et al.*, 1991]. The association of circumferential eruptive fissures and calderas at many basaltic volcanoes suggests that caldera fractures can control dike orientations.

Most evidence from the shield volcanoes of the western Galapagos does not favor circumferential dike intrusion into preexisting caldera-related ring fractures.

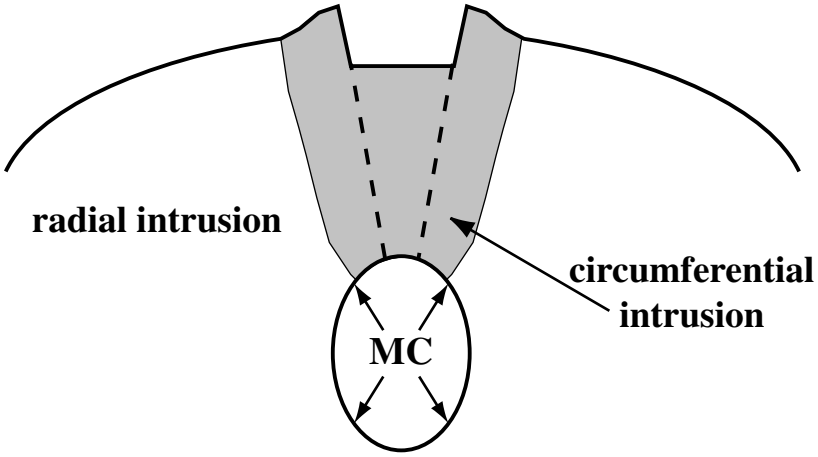

Figure 1.6. Schematic profile of a basaltic shield with caldera ring fractures (dotted lines) that may be used as paths for magma ascent. Eruptions along ring-dikes are well documented at many volcanoes, including the silicic Valles caldera in New Mexico [*Smith and Bailey,* 1968] and basaltic Askja shield, in Iceland [*Thorarinsson and Sigvaldason,* 1962]. Repeated magmatic intrusion along caldera fracture systems would result in a pattern of circumferential eruptive fissures centered within and around the caldera walls. MC = magma chamber.

Circumferential eruptive fissures are found at distances of up to 1.5 km from caldera rims, well removed from normal faults associated with caldera collapse [*Chadwick and Howard*, 1991]. In addition, *Chadwick and Howard* [1991] did not observe vertical offsets along circumferential eruptive fissures or between layers that are in contact with dikes exposed in the walls of Fernandina caldera, and noted that many circumferential fissures cross-cut caldera normal faults. The presence of calderas, circumferential dikes, and other tensional structures (e.g. grabens and tensional cracks) near the summits of the Galapagos shields indicates radial tension, thus preexisting fractures are not required to explain circumferential dike intrusion [*Chadwick and Howard*, 1991].

1.3.3 Stress Reorientation Due To a Topographic Wall

Munro and Rowland [1996] suggested that circumferential dikes of the western Galapagos volcanoes formed due to a reorientation of the local stress field near the rims of the summit calderas. The caldera of Fernandina volcano reaches 1 km in height, therefore a significant gravitational stress, with σ_1 parallel and σ_3 perpendicular to the to the caldera rim, would dominate the rim area. Any dike propagating into this region would tend to reorient itself to become parallel with the caldera walls (Figure 1.7). This mechanism of dike reorientation was originally proposed by *McGuire and Pullen* [1989] to explain the deflection of radial dikes at Mt. Etna volcano. The Valle del Bove, a 7 km long topographic depression with a 1 km high headwall [*McGuire and Pullen*, 1989; *Borgia et al.*, 1992], is located on the eastern flank of Mt. Etna. Dikes that propagate radially away and eastward from the summit of the volcano should intercept the Valle del Bove. However, several historical intrusions have deviated from radial orientations and assume trends that parallel the Valle del Bove rim, probably due to local stress reorientation caused by the gravitational instability of the unbuttressed scarp.

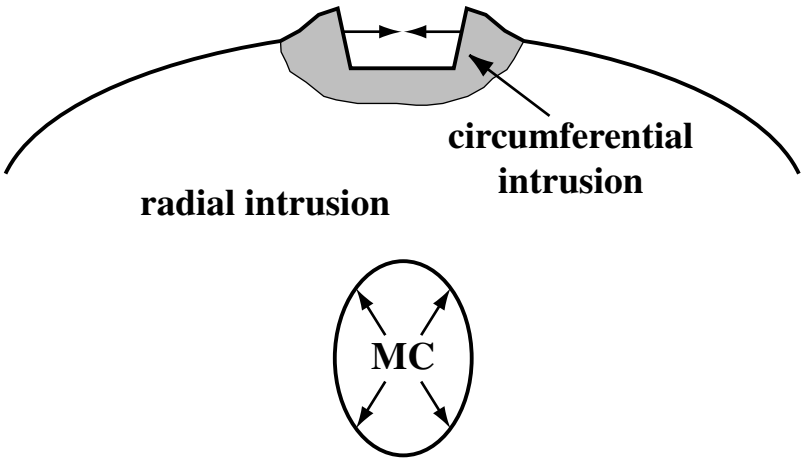

Figure 1.7. Schematic profile of circumferential dike intrusion due to stress reorientation in the vicinity of a topographic barrier. *McGuire and Pullen* [1989] map dikes at Mt. Etna, Sicily, that deviate from radial trends to parallel the headwall of a large landslide scarp (the Valle del Bove). They propose that local stress reorientations due to gravitational instability of the unbuttressed scarp cause the observed dike propagation paths. *Munro and Rowland* [1996] extend the model to the Galapagos volcanoes, where gravitational relaxation of the unbuttressed caldera walls (indicated by arrows) may affect the local stress regime.

Applying the model of *McGuire and Pullen* [1989] for stress reorientation due to a topographic wall to the western Galapagos volcanoes helps explain the correlation between caldera depth and circumferential fissure development [*Munro and Rowland*, 1996; *Rowland*, 1996]. Galapagos calderas are gravitationally unstable, as indicated by the collapse of a portion of the caldera wall on Fernandina in 1988 [*Chadwick et al.*, 1991]. However, on some Galapagos volcanoes the caldera rims are little more than minor ridges that reach heights of 100 meters above both the caldera floor and summit platform of the volcano (Figure 1.8). Assuming that the gravitational instability is directly proportional to topographic relief (which needs to be tested by future modeling - see Chapter 5), such a small caldera wall seems incapable of reorienting an igneous intrusion. In addition, a dike propagating upwards from depth into a rotating stress field would probably break into segments that individually reorient themselves [*Pollard*, 1987]. Thus, individual segments would be circumferential to the caldera but the overall trend of the system of segments would be radial. Eruptive fissures on the Galapagos are characterized by en echelon segments, however the orientations of both the individual segments and the eruptive fissure taken as a whole are more circumferential than radial (Figure 1.3B) [*Chadwick and Howard*, 1991]. Gravitational stresses related to the caldera rim must exist due to the great depth and instability of some Galapagos calderas, but probably only affect intrusions that propagate laterally towards the calderas from the lower flanks. *Chadwick and Howard* [1991] and *Chadwick and Dieterich* [1995] cite an eruptive fissure on Fernandina that is circumferential near the summit of the volcano and becomes radial with distance from the caldera (Figure 1.3B). The dike feeding the fissure was probably radial to the summit and propagated up the flank of the volcano where it encountered the reoriented stress field of the caldera rim and transitioned from a radial to a circumferential trend.

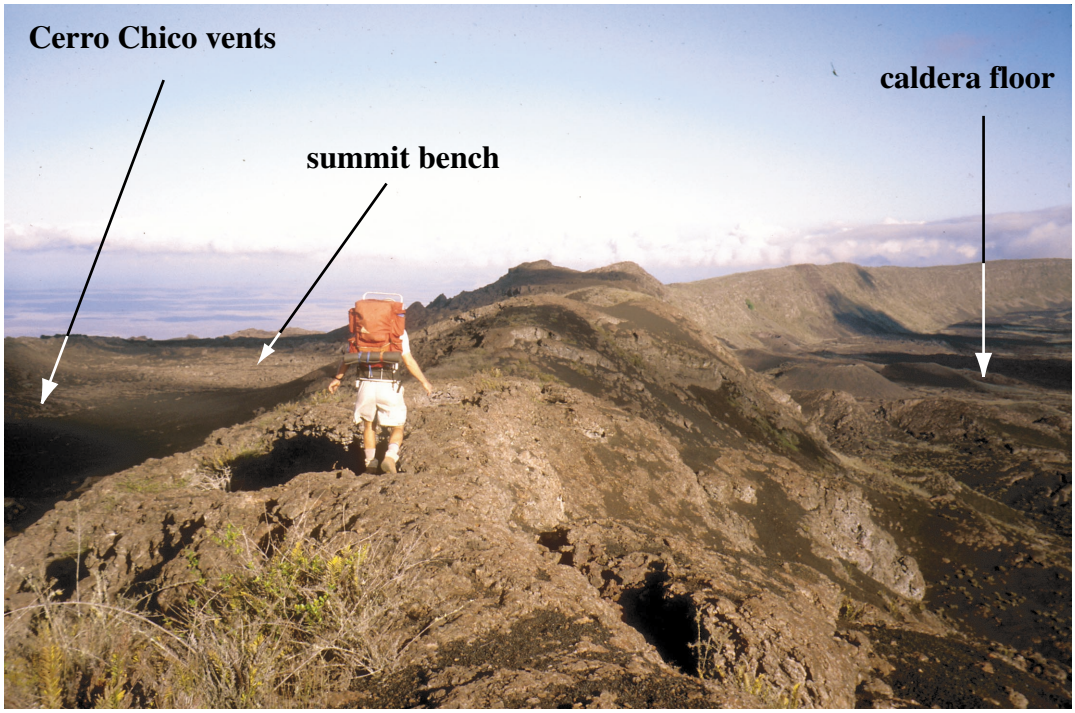

Figure 1.8. Photograph along the caldera rim of Sierra Negra. The caldera is to the right, while the summit bench of the volcano is to the left. The caldera rim is essentially a ridge that is 100 meters above both the caldera and summit bench. The most recent circumferential fissure eruption occurred in 1979 from the Cerro Chico vents located to the left of the photo. Based on the minor size of the ridge in this location, it is unlikely that relaxation of the caldera wall creates a stress field sufficient to induce circumferential dike injection, as proposed by *Munro and Rowland* [1996].

1.3.4 Volcanic Spreading

Borgia [1994] presents a model of gravitational spreading for large volcanoes which sit on weak substrates. The weak basement allows a massive, unbuttressed edifice to spread under gravity, causing summit extension and basal contraction (Figure 1.9). Numerous spreading features, consistent with this model, have been documented on the south and east flanks of Mt. Etna volcano, in Sicily, as well as many other volcanoes around the world [*Borgia et al.*, 1992; *Borgia*, 1994]. Analog experiments by *Merle and Borgia* [1996] demonstrate extension at the summit of a spreading volcano and thrusting near the base of the edifice.

Borgia [1994] and other authors do not consider the effects of spreading on dike intrusion within an edifice. However, it is clear from surface deformation on spreading volcanoes (e.g. Mount Etna [*Borgia et al.*, 1992], the Central Costa Rica volcanic range [*Borgia et al.*, 1990], Maderas volcano, Nicaragua [*van Wyk de Vries and Borgia*, 1996]) that the model favors a stress field compatible with circumferential dike intrusion near the summit and radial diking on the lower flanks [*Montesi*, in press]. However, circumferential eruptive fissures have not been documented on spreading volcanoes. In fact, radial dike intrusion has been inferred from aligned fractures and eruptive vents in the summit region of Mt .Etna. Additionally, spreading is apparently not a significant process in some Galapagos volcanoes. For instance, Sierra Negra volcano, which is buttressed on several sides, sits on a shallow submarine platform (Figure 1.2) and has both circumferential and radial eruptive fissures. Although volcanic spreading would introduce a stress field suitable for the formation of both circumferential and radial dikes, the process does not appear to influence dike intrusion at the Galapagos volcanoes.

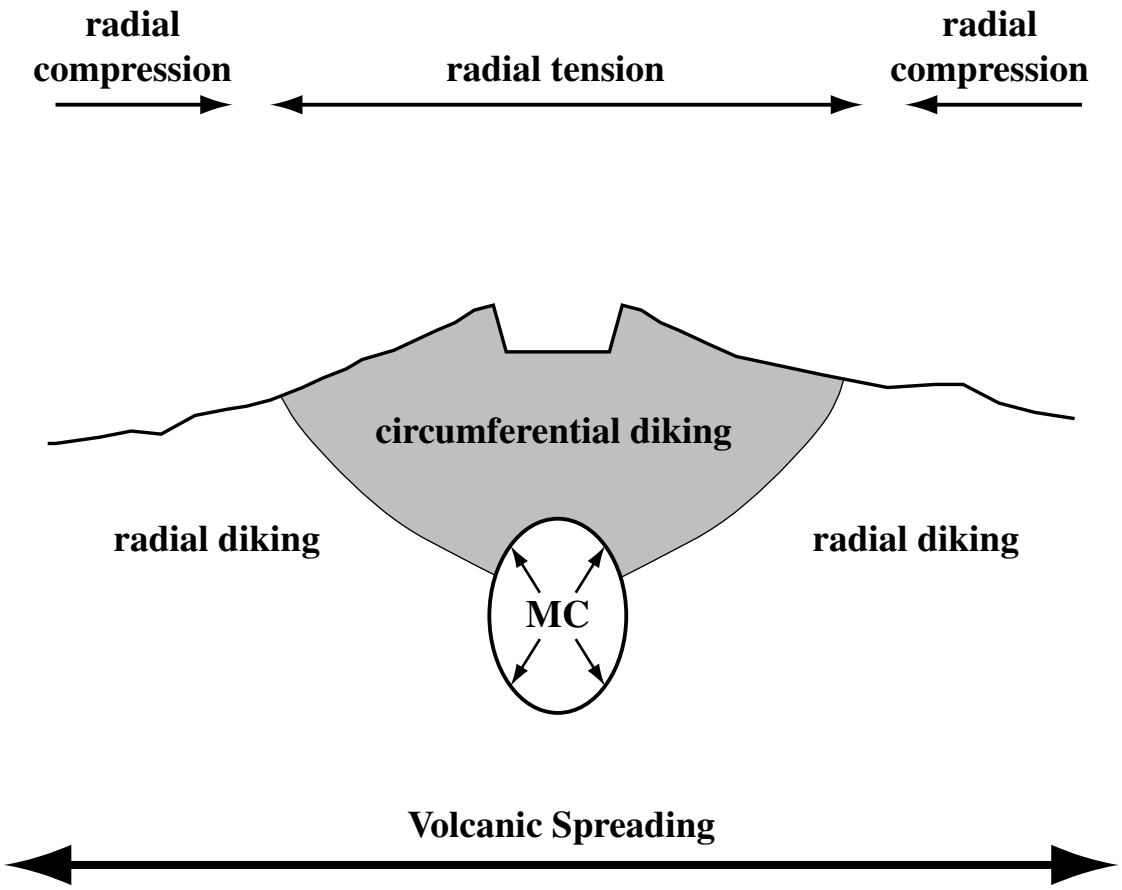

Figure 1.9. Schematic profile of circumferential dike intrusion due to spreading of a volcanic edifice. According to *Borgia* [1994], volcanoes will spread gravitationally under certain conditions, which causes radial extension on the upper flanks and compression on the lower flanks. The stress field associated with spreading is ideal for circumferential dike intrusion in the summit region of a volcano, while radial diking is favored at lower elevations on the edifice. MC = magma chamber.

1.3.5 Surface Loading

Chadwick and Dieterich [1995] used homogenous, elastic finite element models with varying boundary conditions to model stresses within a Galapagos-like shield volcano. They considered several origins for the observed pattern of diking and inferred stress orientations, including: 1) magma chamber depth, 2) magma chamber geometry (shaped as a sphere, oblate spheroid, prolate spheroid, or teardrop), 3) magma chamber pressurization, 4) surface loading from volcano growth, and 5) dike emplacement. Gravitational stresses were not considered due to the difficulty in modeling the growth of a volcanic edifice through time (see *McGovern and Solomon* [1993] for a finite element formulation for modeling volcano growth). Results suggested that the magma chamber was probably diapir-shaped because caldera collapse would flatten the roof of a chamber, allowing circumferential dikes to nucleate in the upper-outside corners. However, a diapir-shaped chamber alone is not enough to propagate a circumferential dike to the surface. An increase or decrease in the magma chamber pressure also does not create a stress field suitable for both radial and circumferential dike emplacement.

Combined with a teardrop-shaped pressurized magma chamber, surface loading from the base of the caldera wall outward creates a stress field that encourages circumferential and radial dike emplacement in a model Galapagos volcano (Figure 1.10) [*Chadwick and Dieterich*, 1995]. Surface loading is a result of lava flow emplacement, which has also been cited as a possible cause for near surface stress-field changes at Mt. Etna [*Murray*, 1988]. Similarly, *Montesi* [in press] suggests that burial of the flanks is a mechanism for the emplacement of a concentric dike swarm on Pavonis Mons volcano, Mars. *Chadwick and Dieterich* [1995] further show that the intrusion of a circumferential dike generates a stress field that favors radial dike emplacement, which in turn promotes further circumferential diking, creating a positive feedback mechanism. As a result, a

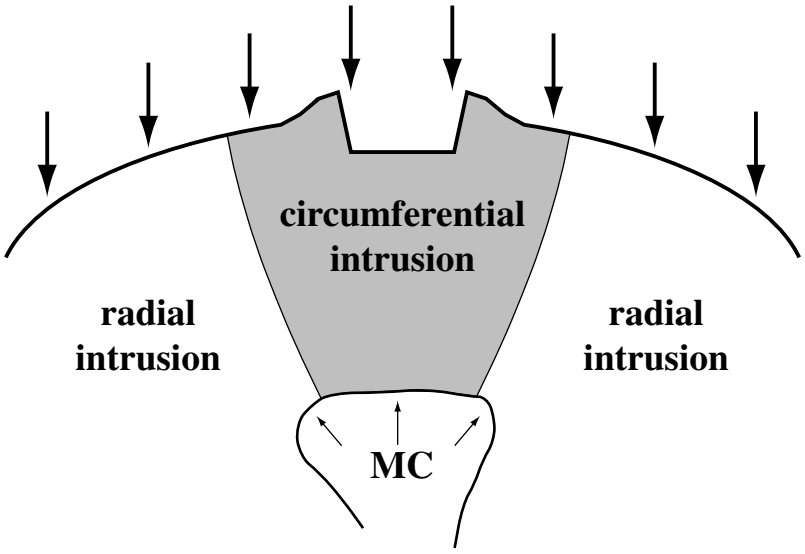

Figure 1.10. Schematic profile of a volcano that is loaded on its surface, perhaps by recently emplaced lava flows or burial of the flanks. Finite element models of *Chadwick and Dieterich* [1995] suggest that surface loading from the base of the caldera outward plus overpressure in a teardrop-shaped magma chamber (MC) creates a stress field suitable for circumferential dike intrusion near the summit and radial diking on the flanks. The model agrees with observations of *Murray* [1988] at Mt. Etna, Sicily, that recently emplaced lava flows cause near-surface changes in the local stress regime.

stress field favoring radial and circumferential dike emplacement can be sustained in the long term. Caldera collapse and flank faulting probably act to accommodate the volume of material added to Galapagos volcanoes by intrusions. Unfortunately, *Chadwick and Dieterich* [1995] cannot show how the stress field permitting concurrent circumferential and radial intrusions was initially established, but only how the pattern of dike intrusion may be sustained over time.

1.3.6 Underplating

Crustal underplating has been suggested as a mechanism for concentric dike emplacement on Mars and Venus [*McGovern and Solomon,* 1998; *McGovern et al.*, 1999; *Montesi*, in press]. Uplift occurs when buoyant material underplates a volcanic edifice, causing radial extension and promoting circumferential diking (Figure 1.11) [*Montesi,* in press]. Underplating is often the result of a mantle plume, and has been identified in Hawaii [*Watts et al.,* 1985] and other locations on Earth. *McGovern and Solomon* [1998] use the finite element method to model stresses and deformation due to underplating of a volcanic structure by a buoyant material. Their results confirm uplift due to underplating and suggest the process as a possible mechanism for the formation of concentric morphological features on Venusian volcanoes.

Underplating is an unlikely mechanism for the intrusion of circumferential dikes at terrestrial mafic shields. Uplift from underplating requires the emplacement of a large volume of buoyant material beneath the volcanic edifice, usually inferred to be partially melted mantle entrained by a deep-seated plume [*Montesi*, in press]. To extend the underplating model to the Galapagos and other volcanoes would require that each edifice be underlain by a significant amount of partially melted mantle. The Galapagos and other hotspots are thought to be the result of a single plume [*Naumann and Geist,* 2000],

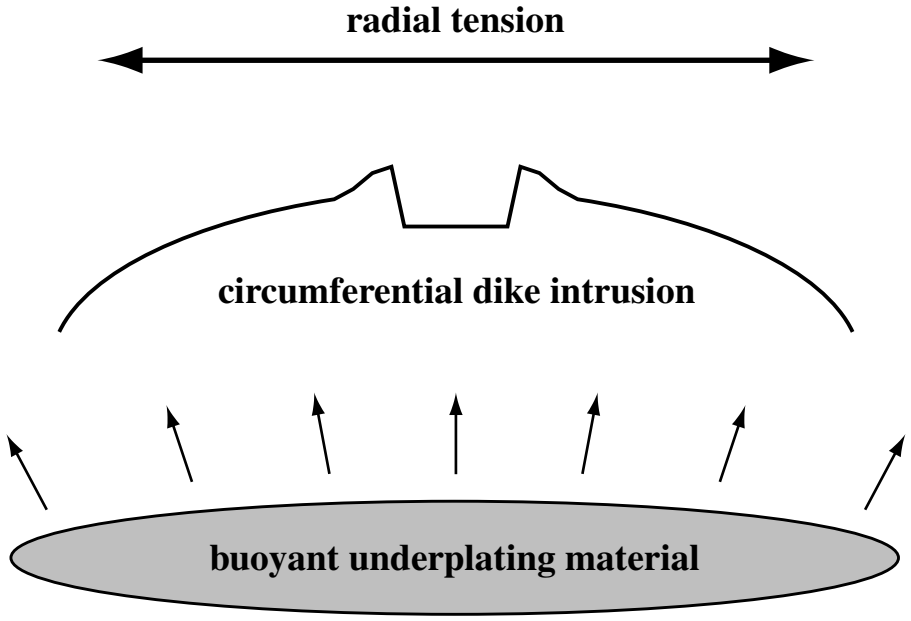

Figure 1.11. Schematic profile of a volcanic edifice that has been underplated by buoyant material. In most cases, the buoyant material is thought to be related to a mantle plume [*Montesi,* in press]. Buoyant underplating causes uplift and radial extension in the volcanic edifice above, creating a stress field suitable for circumferential dike emplacement.

therefore underplating of individual volcanoes in the archipelago is unlikely. Additionally, uplift due to underplating does not explain the occurrence of radial dikes in the Galapagos volcanoes, as the mechanism predicts radial tension (hence circumferential dike intrusion) above the buoyant region [*McGovern et al.*, 1999].

1.3.7 Magma Chamber Pressurization

If circumferential dikes observed at the western Galapagos volcanoes are equated with the inclined sheet swarms exposed in Iceland and Scotland [e.g. *Gautneb et al.*, 1989; *Walker*, 1993], a pressurized magma chamber may be the source of the associated stress field (Figure 1.12). *Anderson* [1936] suggests that centrally inclined sheet swarms (which he terms "cone sheets") formed due to intrusion along extensional fractures above a highly pressurized magma chamber. Although later work has debated the mode of failure (shear versus tensile), most investigators concur that positive magma pressure is necessary to produce centrally inclined sheets [e.g. *Billings*, 1943; *Robson and Barr*, 1964; *Phillips*, 1974]. Boundary element models by *Gudmundsson* [1998] of spherical and sill-like magma chambers subjected to internal pressurization in an elastic half space suggest inclined sheet intrusion with dips decreasing away from the magma chamber, consistent with field observations from eroded Icelandic volcanoes [*Gautneb et al.*, 1989; *Gautneb and Gudmundsson*, 1992; *Gudmundsson*, 1995].

Nordlie [1973] proposed that the steep upper slopes typical of the western Galapagos volcanoes may develop by doming due to inflation of a subsurface magma chamber. To test the hypothesis, *Cullen et al.* [1987] employed the boundary element technique to model volcano morphology. By varying the magma chamber geometry (narrow versus wide) and ratio of host rock stiffness to chamber pressurization, *Cullen et al.* [1987] were able to reproduce the entire spectrum of observed Galapagos

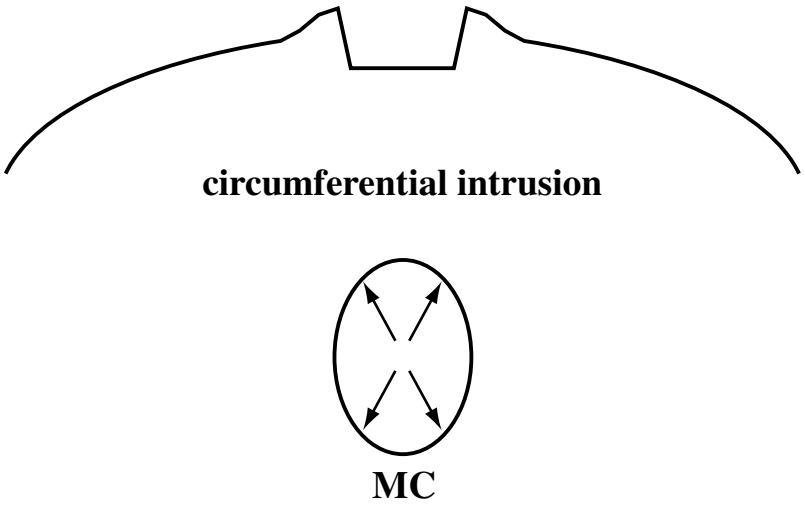

Figure 1.12. Schematic profile of circumferential dike intrusion due to pressurization in a subvolcanic magma chamber (MC). Boundary element models by *Gudmundsson* [1998] of pressurized magma chambers suggest that inclined sheet intrusion along a path circumferential to the center of the volcano is favored. The same conceptual model has also been invoked to explain concentric dike swarms on Venus [*Rogers and Zuber,* 1998].

morphologies. Steep-sided volcanoes with deep calderas (Fernandina, Cerro Azul, and Wolf) are modeled as having narrow chambers with low ratios of host rock stiffness to magma pressure, while broader volcanoes with deeper calderas (Darwin, Alcedo, Sierra Negra) may be approximated using wide magma chambers and high ratios of stiffness to pressure. Similarly, positive magma pressure in a sheet-like chamber has been proposed as the mechanism for inferred concentric eruptive fissures at the Venusian volcano Tepev Mons, which is morphologically similar to the western Galapagos shields [*Rogers and Zuber*, 1998].

A pressurized magma chamber may explain both the unique morphology of the Galapagos volcanoes and the presence of circumferential dikes. However, numerical models of pressurized chambers [e.g. *Gudmundsson*, 1998] only produce a stress field favoring circumferential dike intrusion. As *Chadwick and Dieterich* [1995] note, any model proposing an explanation of the observed intrusive pattern at the Galapagos must account for both circumferential and radial dikes.

1.4 Circumferential Dike Intrusion Due to Downsagging

Walker [1984] noted several differences between silicic calderas (e.g. Valles caldera and Crater Lake) and calderas that characterize the summits of basaltic shield volcanoes (e.g. Kilauea). The formation of a silicic caldera generally coincides with a major eruption, the volume of which is roughly equal to the volume of caldera subsidence. For instance, *Bacon* [1983] found that the total volume of eruptive products during the ~7000 yr. BP eruption of Crater Lake, Oregon, was equivalent to the total volume of the collapse. Caldera subsidence typically occurs on a cylindrical ring-fault that may act as a path for later magmatic activity (e.g. Valles Caldera as described by *Smith and Bailey* [1968]). Basaltic calderas, on the other hand, usually lack ring fracture systems, have broader areas

of subsidence, and co-collapse eruptions tend to be of lower volume than the subsidence. *Simkin and Howard* [1970] found the 1968 caldera collapse at Fernandina volcano to be 1-2 km^3, however the total volume of erupted products was only ~0.2 km^3. Of course, calderas at basaltic volcanoes may still form by collapse of the magma chamber roof, as illustrated by the 1875 eruption of Askja in Iceland. A total collapse volume of ~2 km^3 was accompanied by only 0.5 km^3 of erupted products, however the remaining volume could easily be accounted for by a dike of reasonable dimensions extending from the caldera to the site of a co-collapse flank extrusion [*Sigurdsson and Sparks*, 1978].

Calderas at the summits of basaltic shields also tend to grow incrementally instead of during a single event. The total 1000 meter depth of Fernandina caldera most likely formed by a series of small collapses, for instance, a 300 meter downdrop during the 1968 eruption [*Simkin and Howard*, 1970]. Subsidence of basaltic calderas occurs in a funnel-like zone, which causes a gradual inward slope near the summit and inward centripetal dip of originally horizontal strata (Figure 1.13) [*Walker*, 1984]. *Walker* [1984] documents inward centripetally dipping ignimbrite surfaces at several calderas, including Taupo and Rotorua, New Zealand, and Bolsena, Italy. Lava flows at the eroded Koolau volcano on the island of Oahu, Hawaii, have centripetal dips that increase with decreasing proximity to the caldera, suggesting a funnel-like structure [*Walker*, 1988], as do lava flows of the eroded Hafnarfjall volcano in Iceland [*Gautneb et al.*, 1989]. In addition, *Walker* [1988] notes that the subsidence profile of Kilauea volcano approximates a stepped funnel.

Numerous mafic volcanoes, including Kilauea and Mauna Loa on the island of Hawaii, the eroded Waianae and Koolau volcanoes on Oahu, and the active Katla central volcano in Iceland, are characterized by positive gravity anomalies that indicate dense intrusive complexes at relatively shallow depths [*Strange et al.*, 1965; *Walker*, 1988; *Zbinden and Sinton*, 1988; *Gudmundsson et al.*, 1994]. *Walker* [1987; 1988] proposes

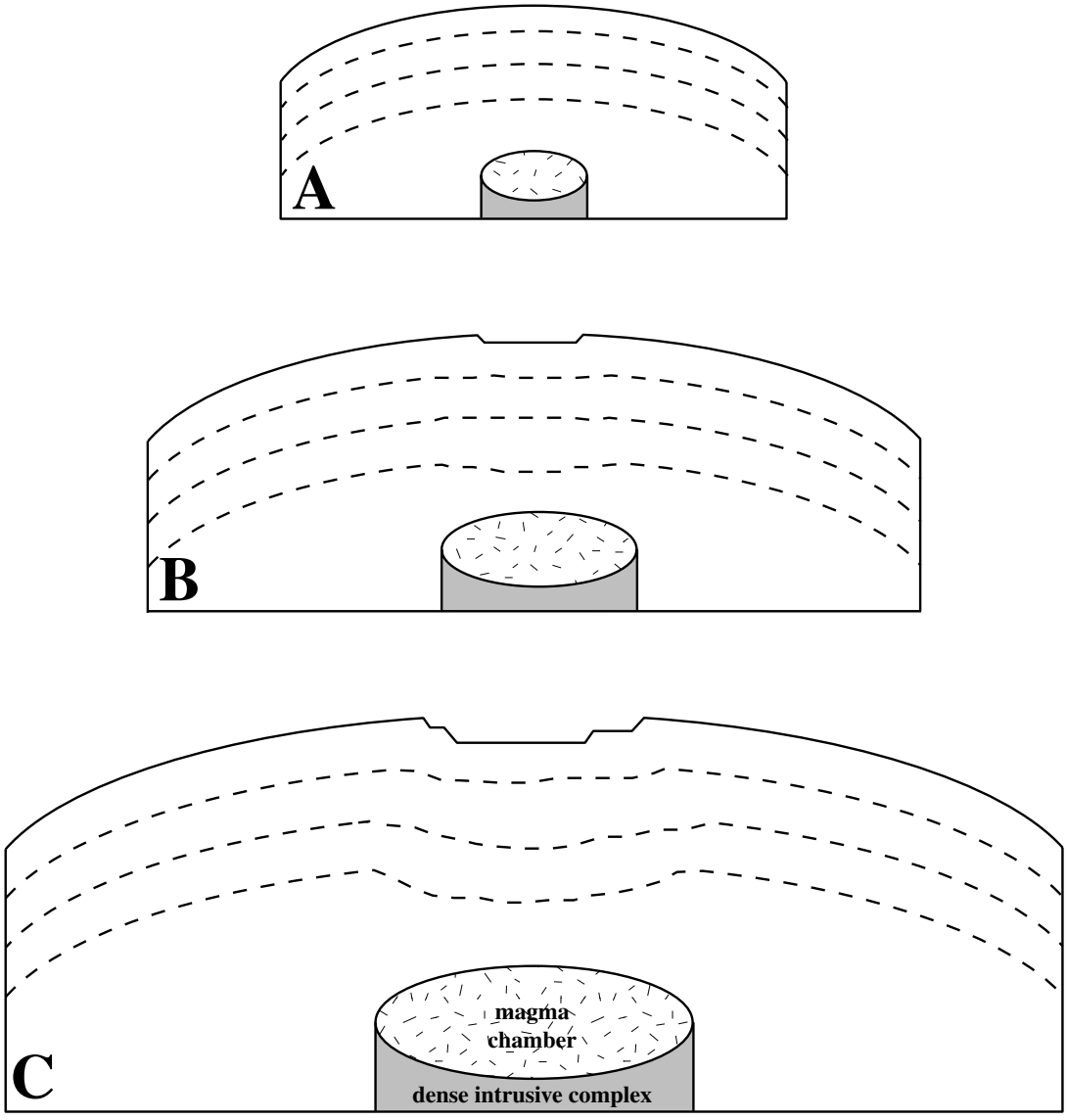

Figure 1.13. Schematic diagram illustrating downsagging of a large basaltic volcano through time. (a) Early in the history of a mafic shield volcano, the intrusive complex is small and does not cause significant downsagging. At this stage, a modern analog is Loihi seamount, off the coast of the island of Hawaii. (b) As the volcano and associated dense intrusive complex grow, a small caldera develops at the summit and lavas around the summit region begin to dip towards the caldera (especially older lavas buried by more recent eruptions, depicted by dashed lines). Kilauea is an example of a volcano in this stage. (c) Late in it's life, a large mafic shield will host a complex caldera and experience significant downsagging due to the large intrusive complex at depth, similar to Mauna Loa volcano. Modified from *Walker* [1988].

that dense, subvolcanic intrusions are the mechanism for funnel-like caldera subsidence at basaltic volcanoes. High-intensity (>40%) regions of mafic intrusions may even be a normal component of large mafic shield volcanoes [*Walker*, 1993]. Because intrusive complexes are concentrated under the summits of basaltic shields, caldera subsidence is restricted to the summit and upper flanks of the host volcano. The model was applied to the Galapagos by *Munro and Rowland* [1996], who propose that the shapes of magma chambers and associated intrusive complexes control caldera morphology. *Walker* [1984; 1988] predicts that much of the subsided volume is consumed, and subsidence may be locally enhanced by thermally weakened crust (e.g. from heat generated by a mantle plume).

Dike intensity at basaltic volcanoes should be highest at the center of the edifice, where the intrusive complex is focused. However, dikes are rare in the caldera of Koolau volcano, possibly due to subsidence of the dike complex beneath the present erosional level (funnel-like subsidence would reach a maximum at the center of the caldera) [*Walker*, 1987]. In contrast, *Zbinden and Sinton* [1988] found the greatest concentration of dikes exposed in the caldera of Waianae volcano, adjacent to Koolau on Oahu. The discrepancy may be due to the differing age of Koolau and Waianae. Because Waianae is older, the edifice may have reached an erosional level, deeper than that of Koolau, at which sub-caldera dikes are exposed. *Clague and Denlinger* [1994] demonstrate that olivine cumulates exist below Kilauea volcano and suggest that the dense mass drives outward deformation on the unbuttressed south flank of the edifice. They find that Hawaiian volcanoes are composed of 14% olivine cumulates concentrated at 4-9 km depth beneath the summit. The density contrast due to a cumulate mass at depth could drive the downsagging model of *Walker* [1987; 1988].

1.4.1 Circumferential Diking and Caldera Collapse from Downsagging

I propose that subvolcanic loading due to dense intrusions induces radial tension near the summit of a volcano, promoting caldera collapse and circumferential diking (Figure 1.14). Radial dikes at the same volcano form when positive pressure in a subvolcanic magma chamber causes radial compressive stress in the surrounding rock. Simple models of an elastic plate with a pressurized hole (i.e. a magma chamber) show that radial contraction around the hole will cause radial dike intrusion [e.g. *Ode,* 1957]. When a volcanic edifice overlies the magma chamber, radial dike emplacement is also favored because σ_1 will be perpendicular to contour lines due to gravitational relaxation of the cone, as is observed at Mt. Etna [*McGuire and Pullen*, 1989]. In the absence of a pressurized chamber, *Walker* [1984; 1987; 1988] suggests that subvolcanic loading due to dense intrusions will cause summit extension and downsagging, resulting in caldera collapse. The stress field in a volcanic edifice that contains both a dense intrusive complex and a pressurized magma chamber will be radially tensile in the summit region (inducing caldera collapse and circumferential diking) and radially compressive on the flanks (accommodating radial dike intrusion). A circumferential drainage pattern centered on Mt. St. Helens suggests subsidence due to loading of a large (15-20 km diameter) intrusive complex identified by gravity data [*Williams et al.*, 1987]. A similar pattern around Mt. Hood, Oregon, may also be attributed to subvolcanic loading [*Williams et al.*, 1987]. Katla volcano, in Iceland, is characterized by a dense body (inferred to be an intrusive complex) underlying a sub-solidus magma chamber [*Gudmundsson et al.*, 1994]. Downsagging due to the dense intrusions should favor circumferential dike injection, which is suggested in seismic profiles of Katla by *Gudmundsson et al.* [1994] that show dense conical regions extending to the surface from either side of the magma chamber.

Figure 1.14. Preferred model of the stress regime and pattern of dike injection at a large mafic volcano where subvolcanic loading by intrusions and a positively pressurized magma chamber are the primary sources of stress. The schematic plan view shows stress orientations near the summit and on the lower flanks, as well as possible dike orientations (heavy lines). Downsagging caused by a dense intrusive complex at depth causes radial extension around the summit area, resulting in the formation of a caldera and the intrusion of circumferential dikes (see cross section). Positive pressure from the magma chamber causes radial compression and radial dike intrusion on the lower flanks of the edifice. In the transition between radial extension and compression ("transition zone"), the stress field is not well defined, and few eruptions occur from dikes that have components of both radial and circumferential trends.

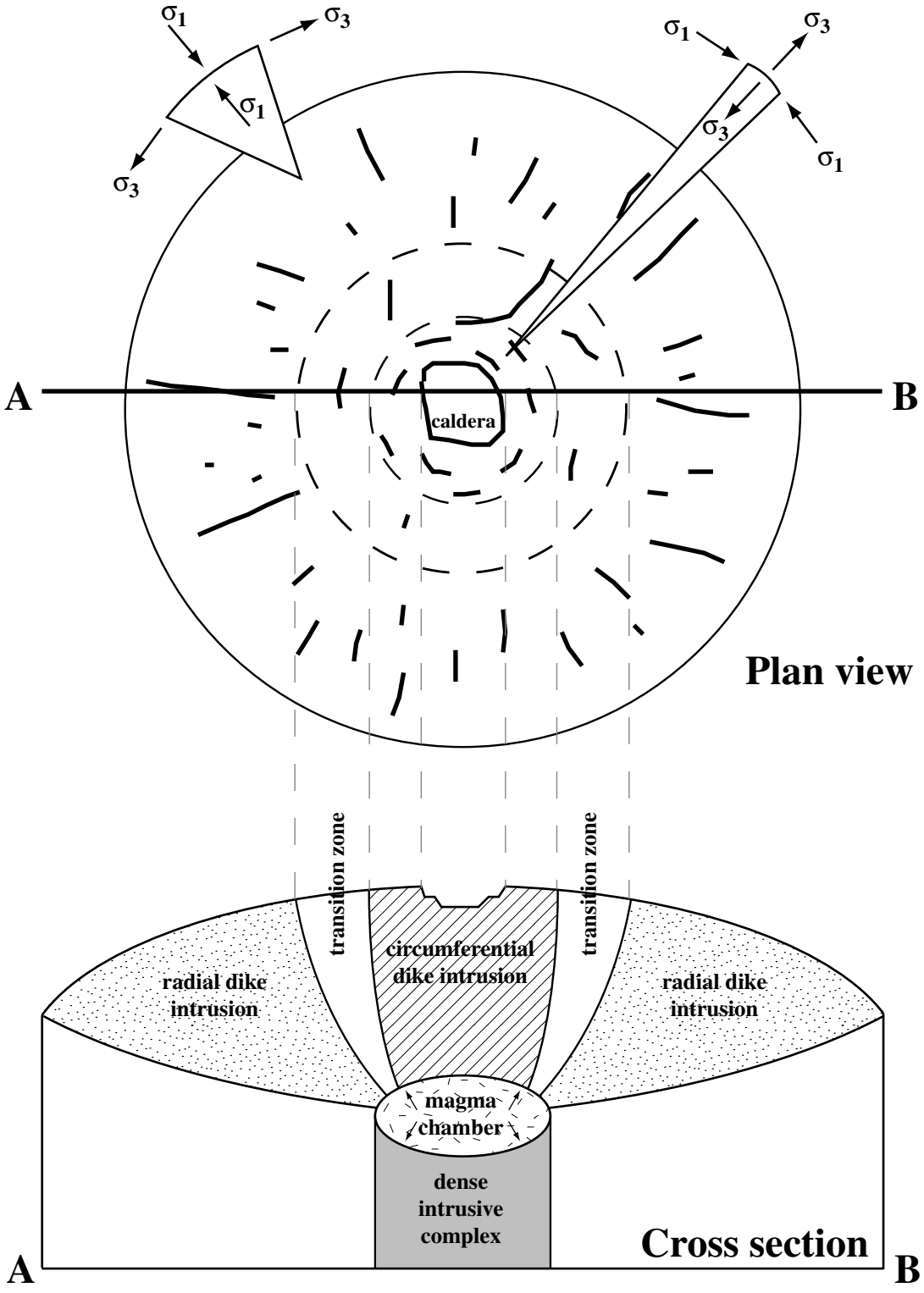
σ1
σ3
σ1
σ3
σ1
σ3
σ3
σ1
A
B
caldera
Plan view
transition zone
transition zone
radial dike intrusion
circumferential dike intrusion
radial dike intrusion
magma chamber
dense intrusive complex
Cross section
A
B

Crustal extension may be accommodated by dike emplacement, normal faulting, or a combination of the two processes [*Lachenbruch and Sass*, 1978; *Bursik and Sieh*, 1989; *Parsons and Thompson*, 1993]. As a result, both circumferential dike intrusion and caldera collapse may occur in response to radial summit tension at large basaltic volcanoes. At Sierra Negra volcano in the Galapagos, the southwestern half of the caldera is characterized by a complex system of faults that are absent to the northeast, giving the depression a "trapdoor" morphology [*Reynolds et al.*, 1995]. Deformation measurements by *Amelung et al.* [2000] indicate normal faulting in the southern portion of the caldera between 1997 and 1998. In contrast, the most recent circumferential eruption at Sierra Negra occurred northeast of the caldera from the Cerro Chico vents in 1979 [*Reynolds et al.*, 1995]. Circumferential eruptions have occurred most often to the north of the Sierra Negra caldera [*Chadwick and Howard*, 1991; *Reynolds et al.*, 1995], suggesting that radial summit extension is accommodated by faulting in the southwest half of the caldera and dike intrusion in the northeast.

1.4.2 Circumferential and Radial Intrusions on Mafic and Silicic Volcanoes

The volcanoes of the western Galapagos are unique because the pattern of circumferential and radial eruptive fissures is clearly displayed. As noted earlier, circumferential eruptive fissures occur at many mafic volcanoes worldwide, however local and regional stress heterogeneities (for instance, tectonic forces and topographic instabilities) often prevent the formation of purely radial dikes. Galapagos volcanoes have nearly isotropic regional stress fields due to 1) their intraplate tectonic setting [*Simkin*, 1984], and 2) the nearly contemporaneous growth of the western Galapagos shields [*Reynolds et al.*, 1995]. As a result, radial dikes do not deviate from their trends over long

distances [*Olson and Pollard*, 1991]. Hawaiian volcanoes do not display complete sets of radial dikes because gravitational stresses from preexisting volcanoes control the stress field within younger volcanoes [*Fiske and Jackson*, 1972]. Therefore, dikes that would be radial in an isotropic stress field are confined to the rift zones of Hawaiian volcanoes. Similarly in Iceland, the divergent boundary between the North American and Eurasian plates produces a highly deviatoric stress field resulting in east-west extension [*Gudmundsson*, 2000]. Intrusions that initiate with radial orientations from a magma chamber rapidly conform to ~N-S trends that are aligned with the regional stresses. Medicine Lake volcano, in northern California, sits on the edge of the Basin and Range E-W extensional province, and eruptive fissures around the caldera have circumferential orientations while flank eruptions trend ~N-S [*Donnelly-Nolan et al.*, 1990] due to the high differential in the regional principal stress magnitudes. Eruptive fissures that are concentric about a summit caldera are relatively common at large basaltic volcanoes; only the combined pattern of circumferential and perfectly radial fissures observed at the Galapagos volcanoes is rare.

In contrast, circumferential eruptive fissures are not well documented at silicic volcanoes (excluding ring-fault or ring-dike eruptions from silicic caldera systems). Stratovolcanoes are characterized by radial eruptive vents that align with the regional stress field with distance from the edifice, as demonstrated by *Nakamura et al.* [1977] in the Aleutian arc. Radial diking has also been documented at eroded silicic systems, including the Summer Coon stratovolcano [*Lipman*, 1968] and the Spanish Peaks [*Ode*, 1957] in southern Colorado. The absence of a differential regional stress field at Summer Coon results in an almost perfect radial pattern [*Mertzman*, 1971], whereas dikes at the Spanish Peaks are deflected into non-radial trends by an anisotropic stress regime [*Ode*, 1957]. The density contrast between the intrusive complex and edifice of a silicic volcano is minor. As

a result, summit extension due to subvolcanic loading is not a significant process, and downsag calderas and concentric dike swarms do not form. Large, dense intrusive complexes do underlie some composite volcanoes at shallow depths (for instance Mt. St. Helens [*Williams et al.*, 1987] in the Cascade Range), however the loading effects are regional (due to the great lateral extent of the complexes) and not restricted to the summit of the volcanic edifice [*Williams et al.*, 1987].

1.5 Evidence for Downsagging

Two types of data are important when considering a subvolcanic loading mechanism for the origin of circumferential eruptive fissures at large mafic volcanoes: 1) surface deformation, and 2) magma flow within dikes that feed the eruptive fissures. Deformation of large mafic shield volcanoes is characterized by flank faulting and magmatic excursions caused by inflation and deflation of a magma source, and dike emplacement [e.g. *Owen et al.*, 1995; *Owen et al.*, 2000]. *Jónsson et al.* [1999] and *Amelung et al.* [2000] present surface deformation data from the western Galapagos volcanoes derived from radar interferometry over a time period spanning 1992-1999. Fernandina and Cerro Azul volcanoes erupted during the interval between radar observations and show signs of coeruptive deformation. In addition, uplift was detected at Sierra Negra (240 cm), Wolf (9 cm), Darwin (22 cm), and Alcedo (>90 cm) volcanoes. *Amelung et al.* [2000] relate the deformation to inflation of summit magma chambers at shallow depths. The considerable magmatic deformation occurring at the western Galapagos shields masks potential subsidence due to subvolcanic loading. If downsagging due to the presence of a dense subvolcanic intrusive complex is a common process at large mafic volcanoes, such deformation will be best observed at a relatively inactive basaltic center.

Few measurements of magma flow have been made for centrally inclined intrusions. *Herrero-Bervera et al.* [2001] measured the magma flow in cone sheets at the Isle of Skye, Scotland, using Anisotropy of Magnetic Susceptibility (AMS) and found that sub-horizontal flow characterized ~50% of the intrusions. Many other flow direction studies using AMS and other geological flow indicators have been conducted on individual dikes and intrusive swarms [e.g. *Baer and Reches*, 1987; *Shelley*, 1988; *Philpotts and Asher*, 1994; *Baer*, 1995]. However, few investigations sample along the length of a single dike, preferring instead only 1-2 sites per intrusion. *Staudigel et al.* [1992] note that magma flow in an intrusion is likely to be complex, therefore multiple measurements along the length of an intrusion are necessary to characterize magma flow and emplacement. An analysis of magma flow at a radial dike swarm would help constrain the intrusion style of such dikes, and establish a basis for future measurements of inclined sheet swarms.

1.5.1 Deformation of a Volcano With Circumferential Eruptive Fissures

Medicine Lake volcano, a basaltic shield in northern California, is an excellent site for analysis of deformation due to downsagging. The volcano is characterized by both circumferential and radial dikes (the latter are aligned N-S due to E-W tectonic extension) and last erupted ~900 years BP [*Donnelly-Nolan et al.*, 1990]. Geophysical studies have also identified a dense intrusive complex beneath the summit of the volcano [*Finn and Williams*, 1982; *Zucca et al.*, 1986; *Fuis et al.*, 1987]. Although a small magma chamber is thought to exist at depth [*Evans and Zucca*, 1988], the lack of recent eruptions and doming deformation [*Dzurisin et al.*, 1991] suggest that the chamber is not highly pressurized. As a result, the stress field within the edifice (without considering the tectonic stress regime) should be controlled by the dense intrusive complex.

Leveling measurements conducted in 1954 and 1989 indicate ~8 mm/yr of subsidence at the summit of Medicine Lake volcano, decaying symmetrically on the flanks [*Dzurisin et al.*, 1991]. The shape of the subsidence at Medicine Lake resembles a funnel (Figure 1.15), similar to that hypothesized by *Walker* [1984; 1987; 1988] for subsidence due to downsagging (Figure 1.13). Chapter 2 is an analysis of three separate leveling datasets collected from Medicine Lake. Although the data may be approximated by a model incorporating volume loss at depth, several additional subsidence mechanisms may contribute to the observed deformation. Horizontal displacements from GPS data are presented in Chapter 3 and used to constrain the subsidence mechanism of Medicine Lake. The best fitting model incorporates a dense intrusive complex at depth beneath the volcano that causes vertical downsagging and the observed horizontal deformation.

1.5.2 Magma Flow in a Volcanic Edifice

Summer Coon volcano in southern Colorado is an eroded composite cone characterized by a radial dike swarm that is composed of hundreds of thin mafic dikes and about 20 large silicic dikes. The exposure provides an ideal setting for studying radial dike emplacement. *Moats* [1990] compiled a database of geometric measurements for 13 of the silicic dikes, including dike segmentation and thickness along the lengths of the intrusions. Chapter 4 builds on *Moats'* [1990] work, suggesting a mechanism for dike segmentation, analyzing dike driving pressures based on the measured thickness distributions, and determining magma flow directions using AMS at several locations along two of the silicic dikes. Results suggest sub-horizontal flow of magma within the volcanic edifice with isolated patches of steeply inclined flow. Driving pressures were probably influenced by decreasing burial depths along the intrusions with increasing radial distance from the center of the volcano (due to the surface slope of the cone).

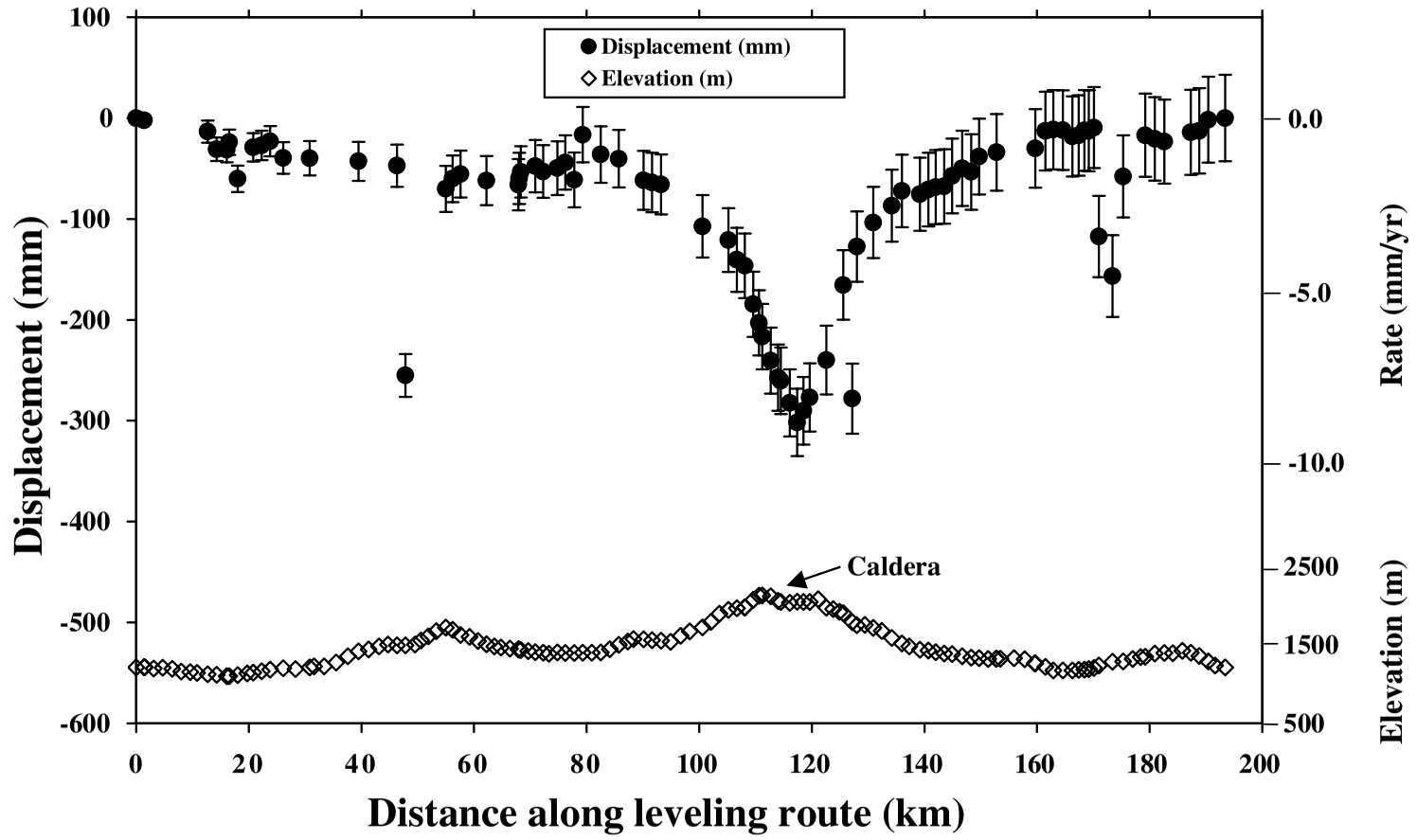

Figure 1.15. Vertical displacements from leveling measurements across the summit and flanks of Medicine Lake volcano, northern California. Displacements with error bars (described in Chapter 2) are shown in the upper portion of the plot, while topography (diamonds) is at the bottom. The vast majority of subsidence at Medicine Lake occurs within 25 km of the caldera [*Dzurisin et al.,* 1991], which suggests downsagging as a possible subsidence mechanism. Inward dipping lava flows or other deposits have not been documented, but may exist if downsagging is occurring. After *Dzurisin et al.* [in review].

1.6 Conclusions

I propose that the stress field within a basaltic shield volcano located in a region of isotropic tectonic stress is controlled by 1) a pressurized magma source, and 2) a dense subvolcanic intrusive complex underlying the summit region. Magma overpressure in a subsurface chamber will create a stress field where σ_1 is radial to the center of the volcano, and will result in the emplacement of radially oriented intrusions. A dense intrusive complex will induce a circumferentially oriented σ_1 in the center of the volcano, promoting caldera collapse and circumferential diking (Figures 1.6 and 1.7). Intrusions at silicic volcanoes (e.g. composite cones) do not have a high density contrast with respect to the rocks of the volcano, therefore subvolcanic loading by an intrusive complex does not significantly influence the stress field within the edifice. As a result, the stress regime is dominated by a pressurized magma chamber and radial dike emplacement is expected. Volcanic edifice stresses may be further modified by tectonic forces, which cause radial dikes to deflect into orientations parallel to the tectonic σ_1 direction, and by other local heterogeneities, including varying material properties or topographic irregularities [e.g. *McGuire and Pullen*, 1989].

The proposed model may be tested by measuring deformation at a large mafic volcano that is not experiencing magmatic unrest. Without stresses generated by a pressurized magma source, downsagging deformation due to dense subvolcanic intrusions may be quantified. The volcanoes of the western Galapagos Islands are magmatically active [*Amelung et al.*, 2000], therefore Medicine Lake volcano in northern California (which erupted approximately 900 years BP [*Donnelly-Nolan et al.*, 1990]) is chosen for deformation study. Chapters 2 and 3 describe leveling and GPS measurements collected at Medicine Lake and present models of the deformation mechanisms. In addition, the geometry of and magma flow within igneous dikes of the eroded Summer Coon volcano,

in Colorado, are analyzed. Dike emplacement within a volcanic edifice is not well understood, but is an important indicator of the stress regime within an edifice. A set of almost perfectly radial dikes are exposed by erosion at Summer Coon, providing a setting where dike emplacement within a silicic stratovolcano with few sources of stress (e.g. minor deviatoric tectonic stress) may be studied. Chapter 4 describes progress in understanding dike emplacement at stratovolcanoes based on research conducted at Summer Coon. Finally, future directions for research into the stress field within a volcanic edifice are discussed in Chapter 5.

NOTE: This chapter was submitted to the Journal of Geophysical Research as a manuscript authored by Dzurisin, Poland, and Bürgmann on August 3, 2001. The work is part of a larger project that I initiated in 1996 to addresses the mechanism of deformation at Medicine Lake volcano. The research was done in collaboration with Dzurisin, who collected leveling data from Medicine Lake in 1954, 1989, 1990, and 1999. The paper presented below is based on the leveling measurements; I contributed the modeling and analysis sections of the paper and discussed the implications of the models on the deformation source at Medicine Lake. Dzurisin combined my models and his data analysis into a single paper and submitted the article. A second paper, based primarily on GPS measurements at Medicine Lake, will be derived from Chapter 3 and authored by Poland, Bürgmann, Dzurisin, and Fink.

2. Steady subsidence of Medicine Lake volcano, northern California, revealed by repeated leveling surveys

Abstract. Leveling surveys of a 193 km circuit across Medicine Lake volcano in 1954 and 1989 showed that the summit area subsided as much as 302 ± 30 mm (average rate = -8.6 ± 0.9 mm/yr) with respect to a datum point near Bartle, California, 40 km to the southwest. This result corrects an error in the earlier analysis of the same data by *Dzurisin et al*. [1991], who reported the subsidence rate as -11.1 ± 1.2 mm/yr. The subsidence pattern extends across the entire volcanic edifice, which has a surface area of nearly 2000 km^2 and a volume of at least 600 km^3. In addition, localized vertical offsets by as much as 20 cm occurred at two sites near the periphery of the volcano: 1) subsidence of one benchmark located in the epicentral area of the 1978 Stephens Pass earthquake swarm about 30 km southwest of the summit, and 2) subsidence of three adjacent benchmarks about 30 km south-southeast of the summit, amidst a group of Quaternary north-trending normal faults. Surveys of an east-west traverse across Lava Beds National Monument on the north flank of Medicine Lake volcano in 1990 and of a 23 km traverse across the volcano's summit area in 1999 confirmed that subsidence continued at essentially the same rate during 1989-99 as 1954-89. The localized offsets are modeled as normal-slip dislocations, consistent in one case with the focal mechanisms and distribution of hypocenters for the Stephens Pass earthquake swarm, and in the other with the orientations

of nearby faults. Edifice-wide subsidence is modeled as deflation of a Mogi-type source located 10 km beneath the southern part of the summit caldera, which decreased in volume by 0.1129 ± 0.0046 km^3 from 1954 to 1989. The source locations, depths, and average deflation rates modeled from the 1954-89 circuit (-0.0032 ± 0.0001 km^3/yr), 1989-99 summit traverse (-0.0028 ± 0.0002 km^3/yr), and all of datasets combined (-0.0031 ± 0.0001 km^3/yr) are identical within two standard deviations. A horizontal rectangular dislocation model used to approximate a sill source fits the data equally well with somewhat smaller source-volume changes. Although deflation of a Mogi or sill source fits the leveling data very well, we suspect that the main physical mechanisms responsible for subsidence and faulting are: 1) gravitational loading of thermally weakened crust by the mass of the volcano and associated intrusive rocks, and 2) thinning of locally weakened crust due to Basin and Range extension. This hypothesis is being tested for consistency with results from GPS surveys conducted in 1990, 1996, and 1999. The next eruption of Medicine Lake volcano will likely be preceded by changes in the long-term deformation pattern as a result of magmatic intrusions into the upper crust. Such intrusions might be aseismic until they reach relatively cold, brittle rocks within ~5 km of the surface. Continued geodetic surveillance by leveling, GPS, or SAR interferometry offers an opportunity for early detection of intrusions, which could lead to better long-term eruption forecasting.

2.1 Geologic Setting and Eruptive History

The Medicine Lake region in northern California is a locus of magmatic, tectonic, and hydrothermal activity that combines to cause widespread and spatially complex crustal deformation along the boundary between the Cascade volcanic arc to the west and the Basin and Range tectonic province to the east. Medicine Lake volcano (MLV), an active

Pleistocene-Holocene shield volcano, is located about 50 km east-northeast of Mount Shasta between the towns of Tulelake, Bartle, and Tennant (Figures 2.1 and 2.2). MLV lavas cover nearly 2000 km^2 and their volume is at least 600 km^3, making MLV the largest volcano by volume in the Cascade Range [*Donnelly-Nolan*, 1988].

The broad MLV shield with its 7 x 12 km, 0.3-km-deep summit caldera (where the body of water called Medicine Lake is located) comprises mainly basalt and andesite lavas, but several late Holocene eruptions produced dominantly rhyolite lavas. During a few-hundred-year interval starting about 10,600 radiocarbon years ago (~12,900 calibrated radiocarbon years), eight eruptions produced 5.3 km^3 of basaltic and basaltic-andesite lavas. That episode was followed by a hiatus of ~6000 years that ended with a small andesitic eruption about 4300 radiocarbon years ago. During the most recent eruptive episode between 3000 and 900 radiocarbon years ago, eight eruptions produced approximately 2.5 km^3 of lavas that are predominantly rhyolite but range in composition through dacite and andesite to basalt [*Donnelly-Nolan et al.*, 1990].

Eruptive activity at MLV is driven by basaltic intrusions that are facilitated by crustal extension in the western Basin and Range province. Vents are typically aligned within 30º of N, parallel or sub-parallel to major faults that trend dominantly NNW to N [*Donnelly-Nolan et al.*, 1990]. This pattern of faults and vents is generally consistent with the orientation of maximum principal stress in the region [*Zoback and Zoback*, 1989; *Zoback*, 1992], although extension directions determined from geodetic surveys are generally more westerly (see next section). Evidence for a large, dense, mostly basaltic intrusive complex beneath the volcano includes: 1) a positive Bouguer gravity anomaly in the upper few kilometers of the crust [*Finn and Williams*, 1982]; 2) a corresponding zone

Figure 2.1. Leveling traverses (dark lines) near Medicine Lake volcano. Dots along the traverses represent benchmarks with corresponding labels. The circuit across the volcano (Bartle-Hambone-MLV-Tennant-Bartle) was measured in 1954 and 1989; the segment across the summit caldera between benchmarks 47M and J502 was measured in 1988 and 1999. The west-east traverse from A13 near Mount Shasta to OVERPASS was measured entirely in 1954 and partly in 1990 (see Figure 2.3). Datum point H197 is located near Bartle. Benchmarks mentioned in the text, shown in red here, are also shown in Figure 2.3. Contour interval for the generalized topography is 200 m. Longitude is expressed as degrees east of the Prime Meridian.

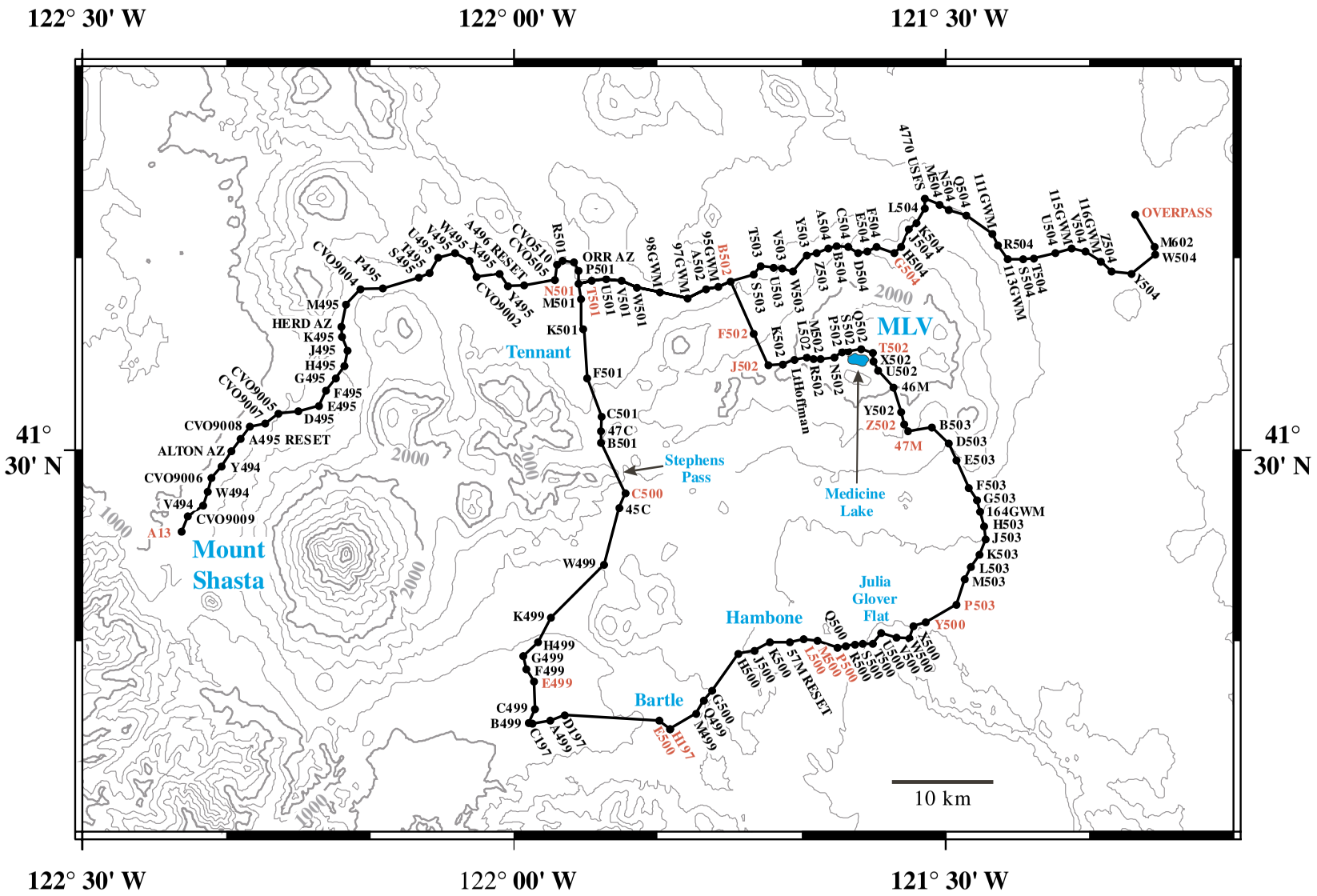
122° 30' W
122° 00' W
121° 30' W
41° 30' N
Mount Shasta
Tennant
MLV
Medicine Lake
Stephens Pass
Julia Glover Flat
Hambone
Bartle
LitHoffman
OVERPASS
ALTON AZ
HERD AZ
ORR AZ
A496 RESET
A495 RESET
47M RESET
111GWM
113GWM
115GWM
116GWM
164GWM
95GWM
97GWM
98GWM
4770 USFS
2000
1000
10 km

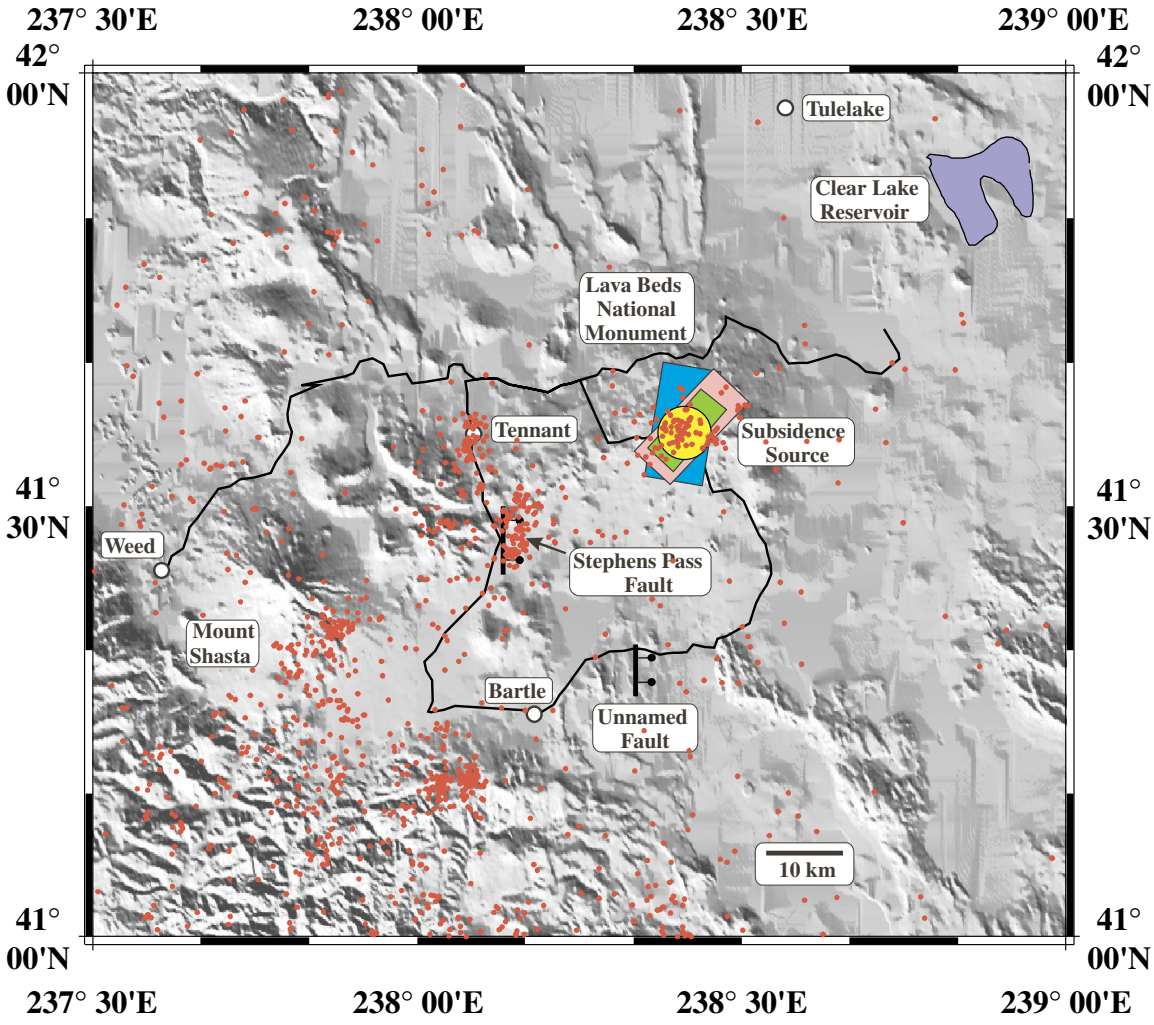

Figure 2.2. Leveling routes near Medicine Lake volcano (solid lines) and best-fit deformation sources discussed in the text. The Stephens Pass fault and an unnamed fault (bars on downthrown sides) are modeled from the 1954-89 displacements of nearby benchmarks as normal-slip dislocations on east-dipping faults (Table 2.2). The Mogi source (yellow circle) is located beneath the south part of Medicine Lake caldera. The model sills (rectangles) are based on displacements measured from 1954 to 1989 (pink), 1989 to 1999 (blue), and all data combined (green). Red dots represent earthquake epicenters for the period 1909-99 from the University of California Berkeley Seismographic Stations catalog. Longitude is expressed as degrees east of the Prime Meridian.

of anomalously high compressional wave velocity inferred from active seismic tomography [*Evans and Zucca*, 1988]; and 3) a much larger zone of high compressional wave velocity that extends through the crust into the upper mantle, inferred from teleseismic tomography [*Ritter and Evans*, 1997]. The active high-resolution tomography study also revealed a low-velocity, high attenuation (low-Q) region from ~2 km to 6 km beneath the summit caldera, which *Evans and Zucca* [1988] interpreted as a small silicic magma reservoir.

Based on her geologic and petrologic study of the volcano and guided by the geophysical results, *Donnelly-Nolan* [1988] proposed that primitive, low-K_2O, high-Al basalt—a dominant rock type at MLV—is parental to other, more silicic MLV lavas through fractional crystallization, assimilation of crustal material, and magma mixing. Her preferred model for the magmatic plumbing system includes numerous dikes, sills, and small bodies of mostly basaltic magma distributed throughout the crust beneath the volcano. In the upper crust beneath the summit area, she envisions several small, differentiated magma bodies that are represented by the low-velocity, low-Q region imaged by active seismic tomography. She cites the dominant N-S orientation of ground cracks and vent alignments as evidence for tectonic influence on both the location and style of volcanism.

2.2 Regional Deformation and Seismicity

There is abundant geodetic evidence for contemporary crustal extension throughout the Basin and Range, although the details are poorly understood in the vicinity of MLV. For example, *Dixon et al*. [1995] used very long baseline interferometry (VLBI) and satellite laser ranging (SLR) to measure integrated Basin and Range deformation (i.e., relative motion between the Sierra Nevada block and stable North America) at latitudes between ~ 35ºN and 41ºN (MLV is located at ~ 41.6 ºN). Their result, 12.1 ± 1.2 mm/yr

oriented N38ºW±5º, agrees with an earlier VLBI estimate (11 ± 1 mm/yr oriented N28ºW±3º) by *Argus and Gordon* [1991], and with an estimate based primarily on Holocene geological data (9.2 ± 2.6 mm/yr oriented N64ºW±9º) by *Minster and Jordan* [1987]. *Bennett et al*. [1998] analyzed 13.5 months of data starting in July 1996 from 18 continuous GPS stations spanning the northern Basin and Range province between 39°N and 41°N, from the Sierra Nevada in California to the Rocky Mountains in Utah. The integrated deformation across the province corresponds to northwestward motion of the Sierra Nevada at 11 ± 2 mm/yr. *Thatcher et al*. [1999], who surveyed a dense east-west GPS traverse across the Basin and Range between 38ºN and 40ºN in 1992, 1996, and 1998, obtained essentially the same result. They showed that the Sierra Nevada block is moving 12.5 ± 1.5 mm/yr N52ºW relative to stable North America, and that deformation is strongly concentrated in the westernmost ~200 km and easternmost ~100 km of the 800 km traverse. Deformation in the western Basin and Range province includes a dominant, right-lateral component associated with the eastern California shear zone-Walker Lane belt. The continuation and distribution of the eastern California shear zone deformation north of 41°N and its interaction with Cascadian backarc tectonics are not well understood [*Blakely et al.*, 1997; *Dixon et al.*, 2000; *Miller et al.*, 2001]. This includes the aforementioned discrepancy between dominantly NNW to N fault orientations in the MLV region and NW extension in the broader Basin and Range.

The USGS Volcano Hazards Program established a network of GPS stations in the vicinity of Mount Shasta and MLV in 1990. Several stations were added when the network was re-measured in 1996 and 1999. The 23-station network extends from the Klamath Mountains eastward to the western part of the Basin and Range, i.e., between 237°E and 239°E at latitudes of 41.2°N to 41.7°N (see Figure 2.9 for station locations). Preliminary analysis of the 1990, 1996, and 1999 data indicates that displacements are consistent with

the effects of Basin and Range deformation plus subsidence centered at MLV [*Poland et al.*, 2000].

Numerous young normal faults and sporadic seismicity in the MLV region suggest present-day Basin and Range related shear [*Blakely et al.*, 1997]. Seismic records collected by the University of California Berkeley Seismographic Stations starting in 1909 show no earthquakes in the MLV region prior to 1950, but sparse instrumental coverage during that period means that events smaller than *M* 4 probably would not have been located [*Bolt and Miller*, 1975]. Since stations were added in the 1950s and 1980, earthquakes have been located throughout the region but mostly west of MLV (Figure 2.2).

Three notable earthquake swarms have been recorded near MLV. The first, in August 1978, was centered about 15 km south of Tennant and 5 km south of Stephens Pass, approximately midway between MLV and Mount Shasta (hereafter called the 1978 Stephens Pass swarm). The largest event in the sequence (*M* 4.6 on August 1) was followed by hundreds of aftershocks during the next two weeks. Open fissures across Stephens Pass Road, 5 km south of Stephens Pass, were reported on August 14. Subsequent fieldwork documented a north trending, 2-km-long, 75-m-wide zone of tensional fractures, grabens, and collapse depressions. Vertical displacements were as large as 1 m in the grabens and 1.5 m in the depressions. Benchmark C500 is located within the ground breakage zone and apparently moved downward ~20 cm as a result of the swarm (see Section 2.3.3). The 8-km-long aftershock zone dips eastward from the surface breaks to about 4 km depth. Focal mechanisms suggest east-west extension on a north-striking fault, consistent with the regional fault pattern [*Cramer*, 1978; *Bennett et al.*, 1979]. We modeled this fault as a rectangular dislocation that intersects the surface just west of C500 (see Section 2.4).

Another swarm of shallow earthquakes occurred during January–February 1981 almost directly beneath Tennant (hereafter called the 1981 Tennant swarm). The largest event (M 4.1) occurred on January 9 and was followed by 11 $M \geq 3.0$ events within the next 24 hours. Activity declined sporadically over the next several weeks. No surface breaks were reported and no offsets are apparent in the 1954-89 or 1954-90 displacement profiles where they cross the epicentral zone (see Sections 2.3.3 and 2.3.4).

The only earthquake swarm recorded beneath MLV itself occurred in 1988-89 beneath the summit caldera. More than 80 events per hour were recorded during the swarm's peak on September 29, 1988, including the largest of the sequence (M 4.1). Sporadic flurries of smaller events ($M \leq 3.1$) occurred throughout the rest of 1988 and 1989. The 1988-89 earthquakes were all shallow, mostly within 2 km of the surface [*Walter and Dzurisin*, 1989]. *Dzurisin et al*. [1991] attributed the 1988-89 Medicine Lake swarm to subsidence-induced bending and episodic fracturing of cold, brittle rocks mostly within the MLV edifice.

2.3 Leveling Results

2.3.1 Error Estimates

Leveling procedures, standard corrections to leveling data, and expected accuracy of various types of leveling surveys are described by *Schomaker and Berry* [1981], *Balazs and Young* [1982], *Vanicek et al*. [1980], and the *Federal Geodetic Control Committee* [1984]. *Strange* [1980b; 1980a] and *Stein* [1981] discussed possible sources of systematic leveling error and its management. *Arnadottir et al*. [1991] emphasized the importance of appropriately treating correlated errors in leveling measurements when modeling these data. All of the MLV leveling surveys described here were conducted in accordance with

established procedures, and all appropriate corrections were applied to the data [*Dzurisin et al.,* 1991].

Throughout this paper, error estimates include both a length-dependent term to account for random surveying error [*Vanicek et al.,* 1980] and a time-dependent term to account for vertical benchmark instability [*Wyatt,* 1989]. In the first case, the standard deviation of a vertical displacement measured by comparison of two leveling surveys is given by

$$\sigma(L) = \left(\beta_1^{\,2} + \beta_2^{\,2}\right)^{1/2} \cdot L^{1/2} \tag{2.1}$$

where β_1 and β_2, in units of mm/km$^{1/2}$, are constants for each order, class, and vintage of leveling and L is the distance along the traverse. The appropriate values of β are 0.7 mm/km$^{1/2}$ for contemporary first-order, class II surveys (including the 1988, 1989, 1990, and 1999 surveys described here) and 3 mm/km$^{1/2}$ for second-order, class II surveys conducted during 1917-1955 (including the 1954 survey described here) [*Vanicek et al.,* 1980]. Thus, the 1-sigma uncertainty in displacements from random surveying error is 3.1 mm/km$^{1/2}$ $\cdot$ L (km)$^{1/2}$ for comparisons involving the 1954 survey and any subsequent survey, and 1.0 mm/km$^{1/2}$ $\cdot$ L (km)$^{1/2}$ for comparisons involving any two subsequent surveys.

Benchmark instability, which accumulates with time rather than distance, is another source of uncertainty in leveling results. *Wyatt* [1989] observed cumulative long-period vertical motions of benchmarks at Piñon Flat Observatory, California, of order 0.5 mm/yr and concluded (p. 1663): "The form of the vertical displacement power spectrum suggests that, in the analysis of field observations, including an error term dependent on time (its square root or a slightly higher power) should improve estimates of true ground deformation." *Pollitz et al*. [1998] adopted this approach in their analysis of leveling data

showing postseismic relaxation following the 1989 Loma Prieta earthquake. Accordingly, we included the following term in our error estimates throughout this paper

$$\sigma(t) = \alpha t^{1/2} \tag{2.2}$$

where α = 0.5 mm/yr$^{1/2}$. For the 35-year interval between the 1954 and 1989 surveys, for example, this term contributes ± 3.0 mm to the uncertainty in displacements and 0.1 mm/yr to the uncertainty in displacement rates. For the 10-year interval from 1989 to 1999, the corresponding values are ± 1.6 mm and 0.2 mm/yr. *Langbein and Johnson* [1997] showed that α = 1-2 mm/yr$^{1/2}$ is appropriate for horizontal benchmark instability at Piñon Flat Observatory. We chose the smaller value because it pertains to vertical motion, which is more directly relevant to leveling. For modeling purposes, inclusion of a non-length dependent term is important so closely spaced benchmarks do not receive undue weight. In summary, the net uncertainty in vertical displacements is given by

$$\sigma(L,t) = \sigma(L) + \sigma(t) \tag{2.3}$$

and the uncertainty in annual displacement rates is given by

$$\sigma(L,t,N) = \frac{\sigma(L,t)}{N} \tag{2.4}$$

where N is the number of years between surveys.

2.3.2 Earlier Results

An extensive leveling survey near MLV was conducted in 1954 by the National Geodetic Survey (NGS) using second-order, class II procedures. The 1954 survey included a 193 km circuit across the summit area of MLV by way of Bartle, Medicine Lake, Stephens Pass, and Tennant, plus a 148 km, east-west traverse between Weed and

California Highway 139 through Lava Beds National Monument (LBNM, Figures 2.1 - 2.3). An 18.5 km segment between T501 and B502 was common to both surveys.

The U.S. Geological Survey (USGS) re-measured the MLV circuit in 1989 and the LBNM traverse in 1990 using first-order, class II procedures. These surveys were prompted by results of smaller surveys across the summit caldera in August 1988 and October 1988, a period that included the peak of the 1988-89 Medicine Lake earthquake swarm. Comparisons showed that benchmark T502 near the center of the caldera subsided -167.2 ± 10.8 mm from 1954 to August 1988 at an average rate of -4.9 ± 0.3 mm/yr and -8.3 ± 3.5 mm from August 1988 to October 1988, both with respect to J502 near Little Glass Mountain [*Dzurisin et al.*, 1991]. In both cases, the subsidence pattern extended beyond the ends of the summit traverse (J502 and 47M), so the entire MLV circuit was re-measured in 1989 for comparison to the 1954 survey. The resulting discovery of volcano-wide subsidence led the USGS to re-measure the LBNM traverse in 1990 and the summit traverse in 1999 (Figure 2.3).

Dzurisin et al. [1991] compared results of the 1954, 1988, and 1989 surveys and concluded that the summit area of MLV subsided at an average rate of -11.1 ± 1.2 mm/yr during 1954-89. We have discovered an error in that analysis that we correct in this paper. The volcano-wide pattern of subsidence centered in the summit caldera is mostly unchanged, but some offsets in the 1954-89 displacement profile that were attributed to faulting are now recognized as mistakes in the earlier analysis. In addition, we present results of the 1990 and 1999 leveling surveys, which reveal the 1954-90 deformation pattern on the north flank of MLV and confirm ongoing, steady subsidence centered in the summit area during 1989-99, respectively.

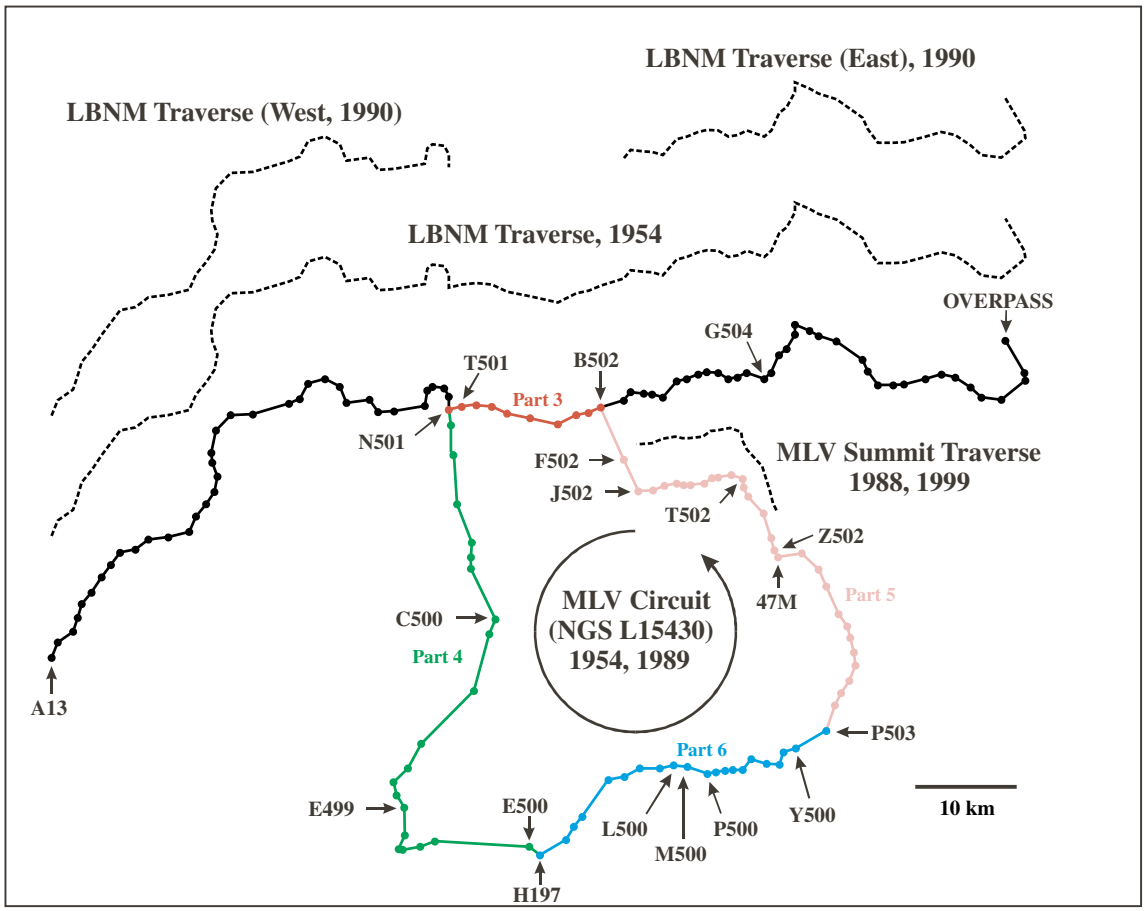

Figure 2.3. Leveling routes near Medicine Lake volcano and survey dates. The 1954 survey was conducted by the National Geodetic Survey using second-order, class II procedures. The 1988, 1989, 1990, and 1999 surveys were conducted by the USGS Volcano Hazards Program using first-order, class II procedures. Benchmarks mentioned in the text are labeled. The MLV circuit comprises NGS line L15430, parts 3 (red), 4 (green), 5 (pink), and 6 (blue).

2.3.3 MLV Circuit, Corrected Results for 1954-89

During our analysis of the 1999 leveling results, we discovered several spurious offsets in the 1954 data set used by *Dzurisin et al*. [1991] for comparison to the 1989 survey. The MLV circuit comprises NGS line number L15430, parts 3-6 (Figure 2.3). *Dzurisin et al*. [1991] failed to recognize that different reference elevations were used for each part of the line, which has the effect of introducing offsets in the elevation data where adjacent parts come together. We identified and removed these offsets by noting that, at each junction between parts, at least one benchmark was common to both parts. Setting the elevations of common marks equal in both parts and making the corresponding adjustments to other benchmark elevations allowed us to remove the following offsets from the 1954 data set (counterclockwise around the circuit starting near Bartle): +0.08781 m from part 6 to part 5 (between Y500 and P503), +0.00438 m from part 5 to part 4 (between F502 and B502), and -0.08829 m from part 4 to part 3 (between T501 and N501). Note that the net offset around the circuit is only +0.0039 m (+3.9 mm). This partly explains why *Dzurisin et al*. [1991] failed to recognize the offsets: one was relatively small (+4.4 mm from part 5 to part 4), and the other two were nearly equal in magnitude but opposite in sign. As a result, the net offset around the entire circuit was negligible and differencing with the 1989 data produced a displacement profile that returned to near zero in the vicinity of datum point H197. Another factor that played a role is that the two large offsets occurred in places where recent faulting seemed plausible: 1) near the epicentral area of the 1981 Tennant earthquake swarm, and 2) near a group of young normal faults about 30 km south-southeast of the summit.

The corrected elevation-change profile shown in Figure 2.4 was produced by subtracting the elevations relative to H197 determined by the 1954 survey (with offsets removed) from those determined by the 1989 survey, and plotting the resulting

Figure 2.4. Vertical displacements and average displacement rates relative to datum point H197 near Bartle (left and right scales, respectively) obtained by comparing results of leveling surveys in 1954 and 1989 (top, circles), plus topography (bottom, diamonds), along a 193 km circuit across Medicine Lake volcano and Stephens Pass by way of Bartle, Hambone, Medicine Lake volcano, and Tennant (MLV circuit). Distance is measured counterclockwise along the leveling circuit starting at benchmark E499, which appears at both the left and right ends of the circuit. Error bars represent one standard deviation and include the effects of distance-dependent surveying error and time-dependent benchmark instability (see text). The distance-dependent term ($3.1\ \mathrm{mm/km^{1/2}} \cdot L\ (\mathrm{km})^{1/2}$) accounts for random surveying error and pertains to the difference between a second-order, class II survey (1954) and a first-order, class II survey (1989), as given by *Vanicek et al*. [1980], calculated using the distance measured counterclockwise along the leveling route from H197. The time-dependent term ($0.5\ \mathrm{mm/yr^{1/2}} \cdot t$ (yr) accounts for benchmark vertical instability caused primarily by weathering of the ground [*Wyatt*, 1989]. Benchmarks between B502 and T501 are common to the MLV circuit and the LBNM traverse (see Figure 2.3). Anomalous movement of Z502 was probably caused by human disturbance, whereas the movements of C500, P500, M500, and L500 are attributed to faulting. Subsidence by a maximum of -302 ± 30 mm relative to H197, which corresponds to an average rate of -8.6 ± 0.9 mm/yr, is centered in the summit caldera (T502) and extends across the entire volcano. For consistency with *Dzurisin et al*. [1991], H197 was used as the datum point for calculating displacements and length-dependent errors. E499 was a more convenient choice for modeling purposes. Displacements and displacement rates shown in Figures 2.7 and 2.8 are relative to E499, not H197 as here.

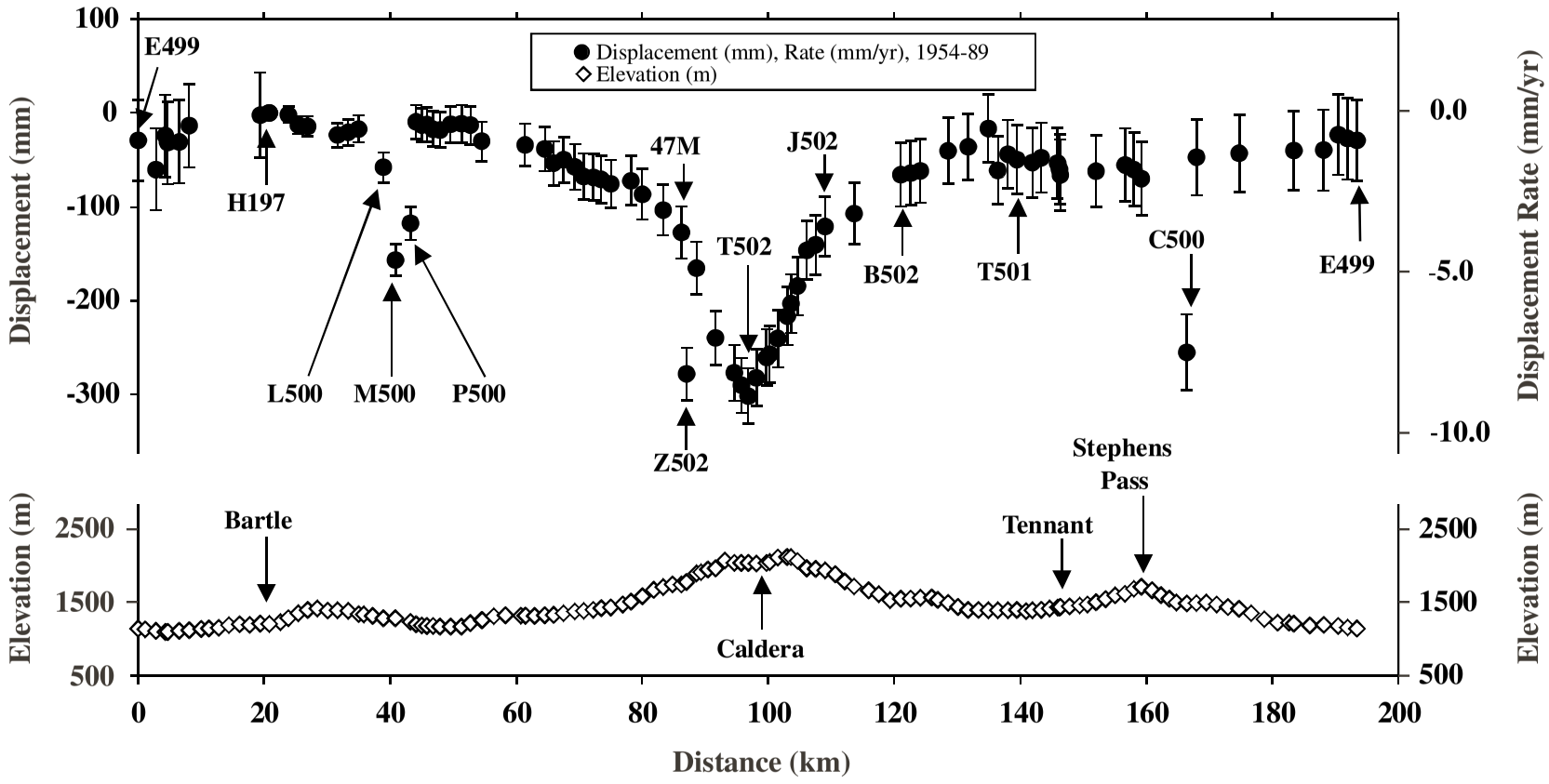
Displacement (mm), Rate (mm/yr), 1954-89
Elevation (m)
Displacement (mm)
Displacement Rate (mm/yr)
Elevation (m)
Distance (km)
E499
H197
L500
M500
P500
47M
Z502
T502
J502
B502
T501
C500
E499
Bartle
Caldera
Tennant
Stephens Pass
100
0
-100
-200
-300
0.0
-5.0
-10.0
2500
1500
500
0
20
40
60
80
100
120
140
160
180
200

displacements as a function of distance measured counterclockwise around the circuit from E499. H197 was used as the datum point for consistency with *Dzurisin et al*. [1991], while E499 was more convenient as a starting point for modeling. Error bars in Figure 2.4 represent one standard deviation from both length-dependent and time-dependent error sources, as discussed above.

Figure 2.4 is similar to Figure 5 of *Dzurisin et al*. [1991], except that the offsets described above do not appear in Figure 2.4 of the current paper because they were removed from the 1954 data set, and distances along the leveling route are measured from different benchmarks (H197 and E499). Several features are apparent in Figure 2.4: 1) T502 subsided 302 ± 30 mm with respect to H197 at an average rate of -8.6 ± 0.9 mm/yr from 1954 to 1989; 2) subsidence extended across the entire volcano, not just its summit caldera (compare the displacement profile with the elevation profile); 3) localized displacements occurred at C500 ~ 7 km south-southeast of Stephens Pass; at Z502 ~10 km south-southeast of Medicine Lake; and at P500, M500, and L500 between Hambone and Julia Glover Flat, ~20 km ENE of Bartle; and 4) the displacement and elevation profiles are inversely related across the volcano but not across Stephens Pass.

In most cases, anomalous movement of a single benchmark like that which occurred at C500 and Z502 can reasonably be attributed to benchmark instability and ignored. This is probably true for Z502, which is located in a concrete post near a road intersection and thus is susceptible to disturbance by logging equipment or other vehicles. C500 is also set in a concrete post, but it is located within the epicentral area of the 1978 Stephens Pass earthquake swarm, very close to the fissures that opened across Stephens Pass Road during the swarm. For this reason, we suspect that the anomalous movement of C500 was caused by the earthquakes rather than by cultural disturbance. Ground shaking might have induced the movement, but we modeled it with a fault dislocation that is

consistent with the distribution of hypocenters and their focal mechanisms (see Section 2.4). We also suspect that the anomalous movements of P500, M500, and L500 were caused by post-1954 movement along faults that form the west side of a large north-trending graben in the area. The southern 25 km of the Giant Crater lava field, which erupted from the south flank of MLV during a brief span of time about 10,500 ^{14}C yr B.P., was confined within the graben and is responsible for the present-day morphology of Julia Glover Flat [*Donnelly-Nolan et al.*, 1991]. No unusual seismicity has been recorded in the vicinity of the graben faults (Figure 2.2). On the other hand, Quaternary offsets of beds across the faults and their youthful morphologies are permissive of the idea that they have been active since the 1954 leveling survey, probably sometime before the 1978 Stephens Pass earthquake swarm. We modeled the movements of P500, M500, and L500 with a dislocation near the west side of the graben, although the lack of recorded seismicity in the area leaves open the possibility that the movements were caused by benchmark instability rather than faulting.

The apparent inverse relationship between displacement and elevation along part of the leveling circuit suggests the possibility of systematic, slope dependent error in one or both of the surveys [*Stein*, 1981]. *Dzurisin et al*. [1991, Appendix] addressed this issue in detail and concluded that slope-dependent error accounts for no more than one third of the 1954-89 subsidence. This result is not affected by the offset problem mentioned above. Nevertheless, resolution of this nagging issue was a primary motivation for the 1999 survey. Limited resources precluded measuring the entire circuit in 1999. Instead, the 23-km-long summit traverse (Figure 2.3) was selected for resurveying because nearly half of the 1954-89 subsidence occurred along this segment, which represents only 12% of the circuit. Also, because a likely source of slope-dependent error is rod-scale error, we used different rods for the 1989 and 1999 surveys. In fact, different levels and rods were used

for all three surveys (1954, 1989, and 1999), so the only common element that could cause uncorrected systematic error is slope-dependent refraction. Refraction corrections based on air temperature measurements made at two heights above the ground at every setup were applied to the 1989 and 1999 data, so the likelihood that uncorrected refraction error accounts for essentially the same result from 1954 to 1989 and from 1989 to 1999 is very small (see Section 2.3.5).

2.3.4 LBNM Traverse, 1954-90

Because the MLV circuit does not cross the northeast half of the volcano, it was unclear from the 1954-89 results whether the subsidence pattern is radially symmetric or perhaps elongate in a north-south direction, parallel to the regional faulting direction. The 1990 survey crossed the north flank of the volcano and thus helps to resolve this issue. Maximum subsidence along the traverse (-139 ± 36 mm with respect to H197, or -3.9 ± 1.0 mm/yr) occurs at G504, 10 km north-northeast of T502 (Figure 2.5). To convert the relative displacement measured between A13 at Weed and G504 to a displacement with respect to H197, we used the 1989 result for B502, which was included in all three surveys. Accordingly, the uncertainties listed above were calculated using the shortest distance along the leveling route from H197 to G504 by way of B502, even though the 1990 survey did not include H197. The 1954-90 LBNM displacement profile is smooth, with no evidence for surface faulting during that period. Its shape is consistent with a radially symmetric pattern of subsidence centered inside the caldera near T502 (see Section 2.4).

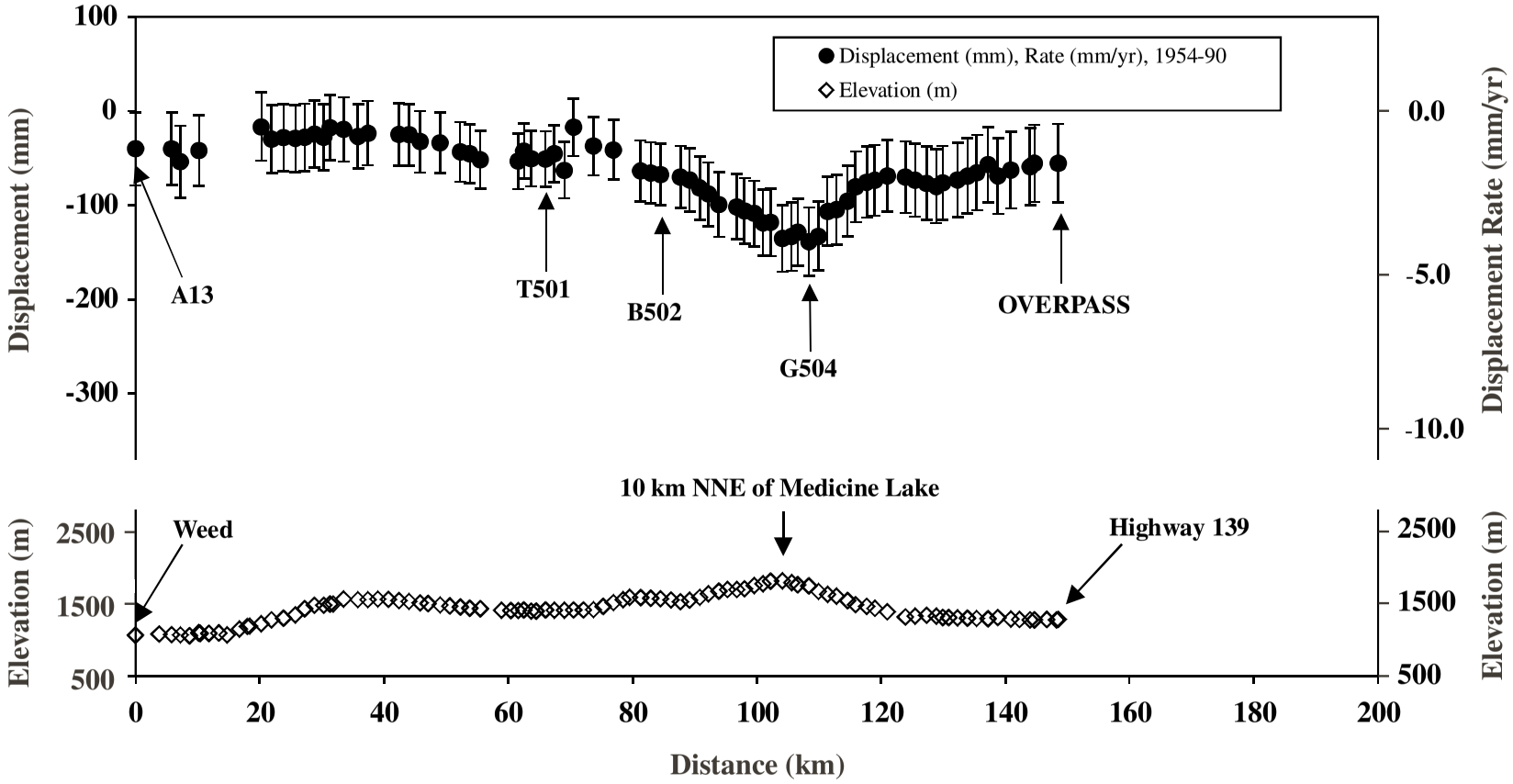

Figure 2.5. Vertical displacements and average displacement rates relative to datum point H197 near Bartle (left and right scales, respectively) from 1954 to 1990 (top, circles), plus topography (bottom, diamonds), along a 148 km east-west leveling traverse between Weed and California Highway 139 through Lava Beds National Monument (LBNM traverse). The segment between T501 and B502 is common to the MLV circuit and the LBNM traverse (see Figure 2.3). Maximum subsidence relative to H197, -139 ± 36 mm (-3.9 ± 1.0 mm/yr) at G504, was calculated using the 1954-89 displacement of B502 relative to H197 (see Figure 2.4).

2.3.5 MLV Summit Traverse, 1989-99

Based on the shapes of the MLV circuit and the 1954-89 displacement profile (Figures 2.3 and 2.4), we elected to re-measure the dogleg-shaped segment of the MLV circuit between J502 and 47M, which crosses the southwest part of the summit caldera, in July 1999. Figure 2.6 shows the vertical displacements relative to 47M measured along this summit traverse from 1989 to 1999, and also the displacements predicted by linear extrapolation of the 1954-89 results. To the extent that these results agree with one another, subsidence in the summit area from 1989 to 1999 was a steady continuation of the pattern observed from 1954 to 1989. In fact, the two displacement profiles are identical within two standard deviations at all of the benchmarks except Z502. Recall that Z502 moved anomalously during 1954-89, which accounts for its unusual position along the predicted profile in Figure 2.6. The measured displacement of Z502 during 1989-99 is consistent with the pattern of nearby benchmarks, which suggests that Z502 behaved normally during that period. We conclude from Figure 2.6 that the average rate and pattern of subsidence in the summit area were virtually identical during 1954-89 and 1989-99, and therefore that subsidence is a relatively steady process over decadal time scales. Over time scales of ~2 months to 1 year that span most of the 1988-89 Medicine Lake earthquake swarm, the subsidence rate might have been roughly a factor of two higher (see Section 2.3.2 and *Dzurisin et al*. [1991, p. 16,325]).

2.4 Modeling Results

Dzurisin et al. [1991] modeled the 1954-89 leveling circuit by inverting the data to fit either one or two point sources of volume change in an elastic half-space [*Mogi*, 1958]. They modeled two datasets separately: 1) all of the data, including those benchmarks

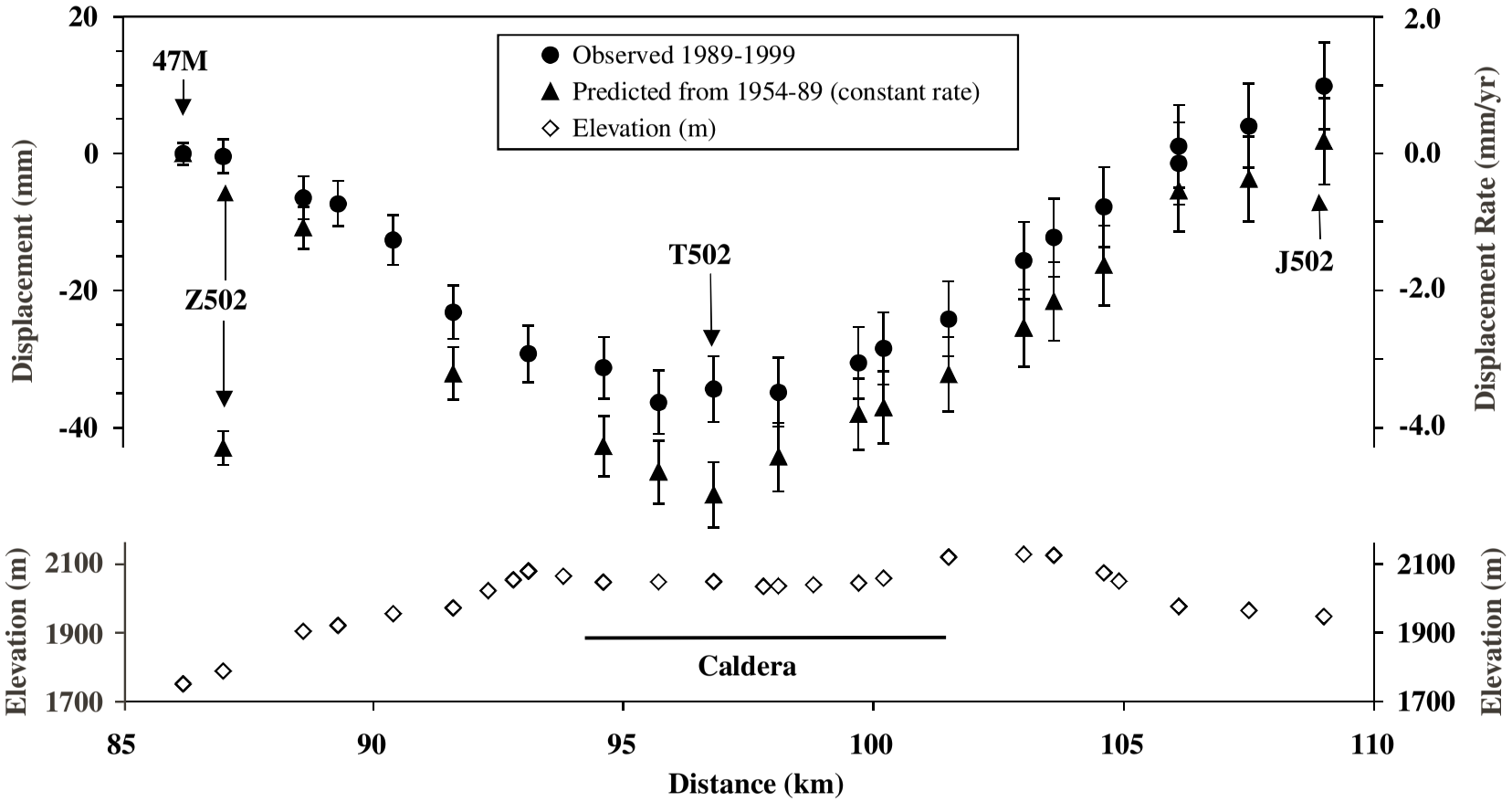

Figure 2.6. Measured and predicted vertical displacements and displacement rates relative to 47M for the period from 1989 to 1999 (top, circles and triangles, respectively), plus topography (bottom), along a 23 km leveling traverse across the summit area of Medicine Lake volcano. Distance is measured counterclockwise around the MLV circuit from H197 (same as Figure 2.4). Except for Z502, which moved anomalously during 1954-89 and is therefore discounted, all benchmarks were observed to subside at the predicted rate within two standard deviations in the measurements. Therefore, subsidence of MLV has been a relatively steady process over at least the past 5 decades and probably longer.

affected by faulting or analysis errors described above, and 2) data from only those benchmarks located within 25 km of T502, none of which were affected by faulting or errors. In the first case, the best- fitting Mogi source was located 15 km under the summit caldera and represented a volume decrease of 0.550 km^3. A slightly better fit was obtained by including two Mogi sources under the caldera, one at 15 km depth with a volume decrease of 0.450 km^3, and the other at 4 km depth with a volume decrease of 0.007 km^3. When only the data from within 25 km of T502 were considered, the best-fitting Mogi source was located 9 km beneath the caldera and represented a volume decrease of 0.140 km^3 (0.004 km^3/yr). In hindsight, this third model is the only appropriate one, because the others were affected by spurious offsets in the data that made it appear that the entire volcano was downfaulted 5-10 cm relative to the surrounding plateau. As a result, the first and second models significantly overestimated the source-volume decrease.

For this study, we modeled the corrected 1954-89 displacements using the inversion technique described by *Arnadottir et al*. [1992] and demonstrated in *Arnadottir and Segall* [1994] and *Bürgmann et al*. [1997]. For deformation sources, we used a point source of volume change [*Mogi*, 1958] and rectangular dislocations with uniform slip and opening (i.e., "model faults") [*Okada*, 1985], both in a homogeneous, isotropic, elastic half-space. Dislocations were used to simulate the effects of faults (slip $\neq 0$), dikes (opening $\neq 0$), and sills (dip = 0, opening $\neq 0$). The inversion technique minimizes the weighted residual sum of squares, $r^T \cdot \sum^{-1} \cdot r$, to determine the best-fitting source location and parameters; i.e., volume change for a Mogi source; length, width, strike, dip, opening, and slip for a dislocation source (r is the residual vector between modeled and measured elevation changes at each benchmark, r^T represents the transpose of the residual vector, and $\sum^{-1}$ represents the inverse of the data covariance matrix). The approach assumes that

measured elevation changes contain correlated errors [*Arnadottir et al.*, 1992], which are accounted for by weighting the misfit using the inverse of the covariance matrix.

To account for broad downwarping centered in the caldera and the two occurrences of known or suspected surface faulting mentioned earlier (near Stephens Pass and the Giant Crater lava field), we first modeled the 1954-89 displacements using a Mogi source and two dislocations. All of the benchmarks were included except Z502, which was apparently disturbed during that interval. Next, we inverted the 1954-89 and 1989-99 displacement-rate data separately using Mogi and sill sources to determine the best-fitting sources for each interval. Finally, we inverted all of the data (1954-89 MLV circuit, 1989-99 MLV summit traverse, and 1954-90 LBNM traverse) simultaneously to obtain the best-fitting Mogi and sill sources overall.

2.4.1 1954-89 Displacements

Three deformation features are apparent in the 1954-89 displacement data (Figures 2.4, 2.7 top): 1) a symmetrical subsidence bowl centered at T502 near the summit of MLV, 2) an offset near C500 on the west flank of the volcano, and 3) offsets near L500, M500, and P500 near Julia Glover Flat (see Figure 2.1), about 20 km east-northeast of Bartle. Two additional faults suggested by *Dzurisin et al.* [1991] are artifacts that were removed from the corrected dataset. Displacement of C500 probably occurred during the 1978 Stephens Pass earthquake swarm, because the mark is located within the epicentral zone on the downthrown (east) side of surface cracks that formed during the swarm and all nearby marks are west of the cracks. On the other hand, no earthquakes have been recorded in the vicinity of L500, M500, or P500 (Figure 2.2). *Dzurisin et al.* [1991] suggested that the displacements measured there were caused by an unrecorded faulting episode sometime

Figure 2.7. Vertical displacements for the MLV ciruit 1954-89 and MLV summit traverse 1989-99. (a) Vertical displacements and displacement rates (left and right scales, respectively) relative to E499 and best-fit model curves for the Medicine Lake circuit, 1954-89. Note that a different datum point (H197) was used for Figures 2.4 and 2.5. Deformation sources include a Mogi source at 10 km depth (solid curve) or a sill at 11 km depth (dashed curve) beneath the summit caldera, plus two normal faults near the periphery of the volcano. Source parameters are given in Tables 2.1 and 2.2. (b) Vertical displacements and displacement rates relative to 47M compared to best-fit Mogi (solid curve) and sill (dashed curve) sources for the Medicine Lake summit traverse, 1989-99. Slight irregularities in the lines representing the model fits reflect changes in direction along the leveling route with respect to the source location.

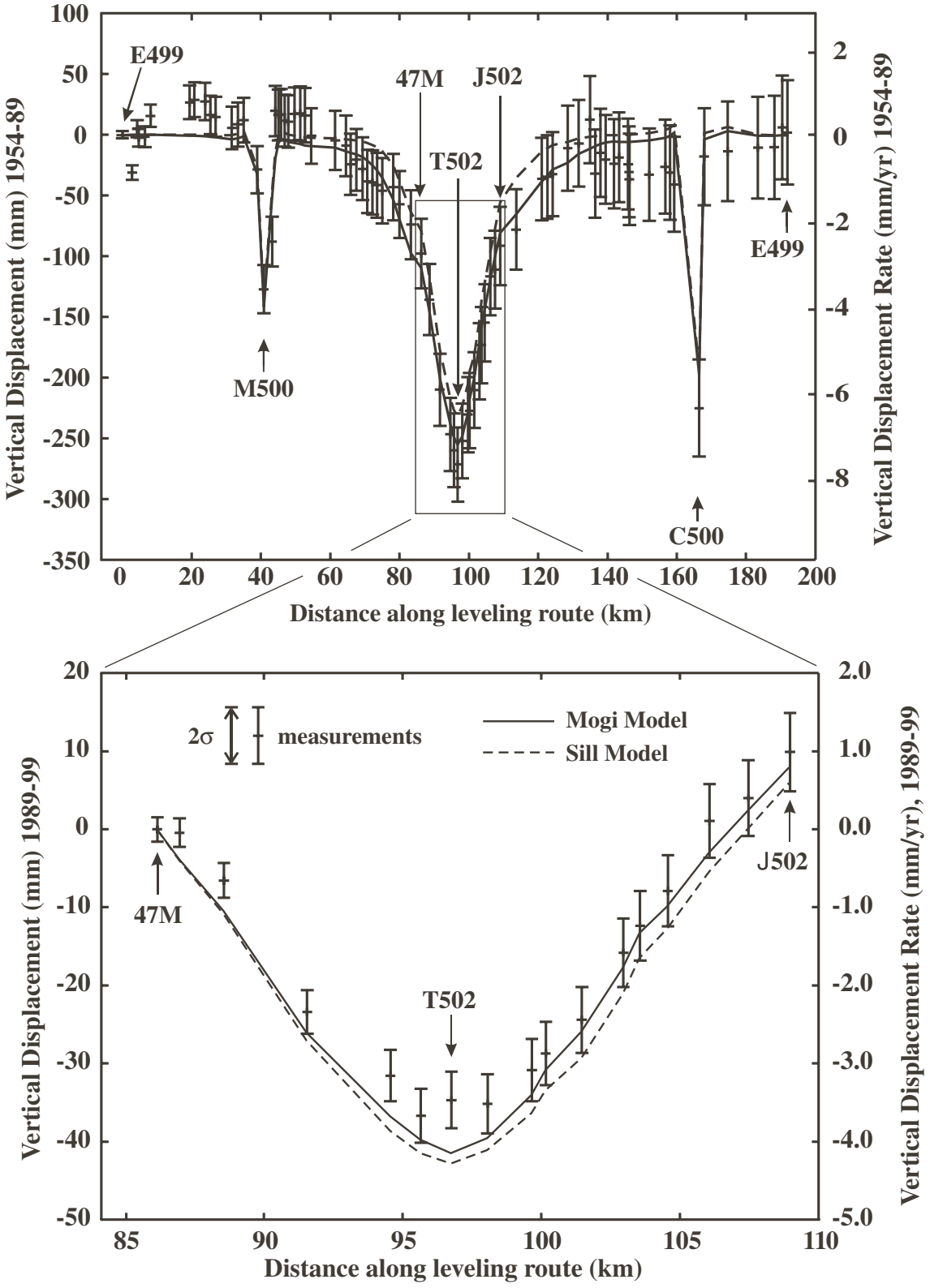
E499
47M
J502
T502
M500
C500
E499
Vertical Displacement (mm) 1954-89
Vertical Displacement Rate (mm/yr) 1954-89
Distance along leveling route (km)
2σ
measurements
Mogi Model
Sill Model
47M
T502
J502
Vertical Displacement (mm) 1989-99
Vertical Displacement Rate (mm/yr), 1989-99
Distance along leveling route (km)

between 1954 and 1989, probably before the 1978 Stephens Pass swarm at a time when the seismic network was relatively sparse.

To account for the observed subsidence and faulting, we inverted the 1954-89 displacement data for one Mogi source and two dipping dislocations (Figure 2.7 top, solid line; Tables 2.1, 2.2). The best fitting Mogi source is located 10 km beneath the southern part of the caldera floor and represents a volume decrease of 0.1129 ± 0.0046 km^3, corresponding to a mean volumetric loss rate of 0.0032 ± 0.0001 km^3/yr. We modeled the displacement of C500 with an east-dipping dislocation that intersects the surface west of C500 but east of other nearby benchmarks (informally called the Stephens Pass fault). The model fault parameters (dip = 38°E, normal slip component = 0.90 ± 0.02 m) are generally consistent with both the distribution of 1981 hypocenters and the pattern of surface cracks, which suggest 1-1.5 m of dip-slip displacement on a N-S striking fault that dips 35-45°E [*Bennett et al.*, 1979]. Similarly, we modeled the displacements of L500, M500, and P500 as 0.41 ± 0.02 m of dip-slip movement on a normal fault dipping 45°E (unnamed fault in Figure 2.2, Table 2.2). The model fault is located near a mapped east-dipping fault that forms the west side of a N-S-trending graben between Hambone and Julia Glover Flat, about 20 km ENE of Bartle. The graben served as a channel for the Giant Crater lava field, which was emplaced during eruptions from the south flank of MLV about 10,500 ^{14}C yr B.P. [*Donnelly-Nolan et al.*, 1990; 1991].

A model that includes a sill as the subsidence source and two dipping dislocations to approximate the faults (Figure 2.7, top, dotted line) fits the data only slightly better than the Mogi model described above (Tables 2.1 and 2.2). The sill is located at nearly the same depth as the Mogi source (9.7 km and 10.0 km, respectively), but requires nearly 1/3 less volume change to produce the same surface deformation.

Table 2.1. Modeling results for MLV subsidence source. WRSS = weighted residual sum of squares, N-P = degrees of freedom. The sill model consistently yields smaller source-volume changes than the Mogi model, but for either model the 1954-89 and 1954-99 volume-change rates are identical within one standard deviation. The 1989-99 rates derived from the much shorter summit traverse are somewhat lower than the 1954-89 and 1954-99 rates, but still within two standard deviations for the Mogi source. Apparently, subsidence has been relatively steady for several decades.

Dataset Modeled	Source Type	Latitude (°N)	Longitude (°E)	Depth (km)	Length (km)	Width (km)	Dip (deg)	Strike (deg)	Opening (m/yr)	Source-Volume Change (km^3)	Source-Volume-Change Rate (km^3/yr)	WRSS	WRSS/(N-P
1954-89 MLV Circuit	Mogi	41.590	238.420	10.0	-	-	-	-	-	-0.1129 ± 0.0046	-0.0032 ± 0.0001	506.4	6.58
	Sill	41.660-41.525	238.461-238.333	9.7	14.8	6.3	0	221	-0.0229 ± 0.0009	-0.0739 ± 0.0030	-0.0021 ± 0.0001	497.30	6.46
1989-99 Summit Traverse	Mogi	41.590	238.420	10.0	-	-	-	-	-	-0.0280 ± 0.0017	-0.0028 ± 0.0002	10.03	0.63
	Sill	41.666-41.523	238.464-238.339	7.7	14.9	7.7	0	189	-0.0112 ± 0.0010	-0.0128 ± 0.0011	-0.0013 ± 0.0001	9.43	0.59
1954-99 All	Mogi	41.590	238.420	10.0	-	-	-	-	-	-0.1116 ± 0.0041	-0.0031 ± 0.0001	2836.92	18.31
	Sill	41.566-41.637	238.441-238.590	11.0	10.3	4,4	0	221	-0.0446 ± 0.0014	-0.0903 ± 0.0028	-0.0020 ± 0.0001	2840.08	18.33

Table 2.2. Modeling results for Stephens Pass and unnamed fault sources.

Fault	Latitude at center (°N)	Longitude at center (°E)	Depth at center (km)	(km)	Width (km)	Dip (deg)	Strike (deg)	Slip (m)
Stephens Pass	41.50-41.42	238.16	2	8.9	2.5	38E	0	-0.90 ± 0.02
Unnamed	41.34-41.28	238.27	3	6.7	4.2	45E	0	-0.41 ± 0.02

2.4.2 1954-89 and 1989-99 Displacement Rates

The 1999 survey did not include H197, which was used as the datum point for the 1954 and 1989 surveys, so the 1954-89 and 1989-99 displacement data are not directly comparable. Nonetheless, we can model the shapes of the two displacement fields to invert for comparable source parameters. Our inversion of the 1989-99 data using a Mogi source (Figure 2.7, bottom, solid line) produced the same source location and a similar average rate of source-volume loss as our Mogi inversion of the 1954-89 data (-0.0028 ± 0.0002 km^3/yr and -0.0032 ± 0.0001 km^3/yr, respectively; see Table 2.1). On the other hand, sill models yield significantly different rates of volume loss for the two time periods (-0.0024 ± 0.0001 km^3/yr for 1954-89 versus -0.0013 ± 0.0001 km^3/yr for 1989-99; Figure 2.7, bottom, dotted line). The sill derived from the 1989-99 displacement data is larger in area and shallower than that derived from the 1954-89 data (Figure 2.2, Table 2.1). However, the 1989-99 sill model is based on fewer data points (17 benchmarks) and is therefore less well constrained than the 1954-89 sill model. We prefer the simpler and more self-consistent Mogi model for both time periods.

We conclude that the subsidence source was stable from 1954 to 1999 and all three of the leveling datasets (1954-89 MLV circuit; 1954-90 LBNM traverse, which was not considered separately in the models; and 1989-99 MLV summit traverse) can be combined to constrain a single model that applies equally well to the entire 45-year period spanned by the surveys. We acknowledge that the combined dataset is temporally very sparse and therefore the subsidence rate as a function of time is not well constrained.

2.4.3 Combined Datasets: 1954-89, 1989-99, and 1954-90

The inversion technique attempts to fit the slope of the elevation change between adjacent benchmarks (i.e., tilt) rather than the displacement of each benchmark relative to a datum point, so multiple datasets with different datum points can be combined in a single model. For modeling purposes, we split the 1954-90 LBNM traverse into two datasets with different datum points, because part of the traverse (between T501 in the west to B502 in the east) was not measured in 1990, as described earlier. Thus, the global inversion included four datasets: 1) 1954-89 MLV circuit, 2) 1989-99 MLV summit traverse, 3) 1954-90 LBNM traverse (west side), and 4) 1954-90 LBNM traverse (east side). This approach gives appropriately greater weight to 17 summit-area benchmarks that were surveyed three times (1954, 1989, 1999) relative to others that were measured only twice.

As with the individual datasets, we inverted the combined dataset for both Mogi and sill sources. The best-fit Mogi source is located under the south part of the caldera at a depth of 10 km. It has a slightly lower reduced χ^2 than the best-fit sill, which is also located under the south caldera at a depth of 11.7 km (Figure 2.8, Table 2.1). The volume loss rates of the two best-fit sources are 0.0030 ± 0.0001 km^3/yr and 0.0023 ± 0.0001 km^3/yr, respectively. Consistent with our experience modeling the 1954-89 separately, we found that including two or more Mogi or sill sources in the global inversion did not significantly improve the model fit to the data.

2.5 Discussion

Possible mechanisms for volcano-wide subsidence at MLV include: 1) deflation of a Mogi or sill source as discussed above, 2) gravitational loading of the lithosphere by the MLV edifice and associated dense intrusive rocks, and 3) crustal thinning as a result of

Figure 2.8. Displacement rate data and best-fit model profiles for: (a) the 1954-89 MLV circuit relative to E499, (b) the 1989-99 MLV summit traverse relative to 47M, (c) the western part of the 1954-90 LVNM traverse relative to A13, and (d) the eastern part of the 1954-90 LVNM traverse relative to OVERPASS. Solid and dashed lines represent best-fit Mogi and sill sources, respectively. Error bars (1 sigma) include the combined effects of random surveying error, calculated using the distance measured counterclockwise around the circuit from E499 [*Vanicek et al*., 1980], and benchmark instability, which is assumed to be 0.5 mm/yr$^{1/2}$ · t (yr) [*Wyatt*, 1989]. Irregularities in the lines representing the model fits, which are especially evident in (d), are caused by changes in direction along the leveling route with respect to the source location.

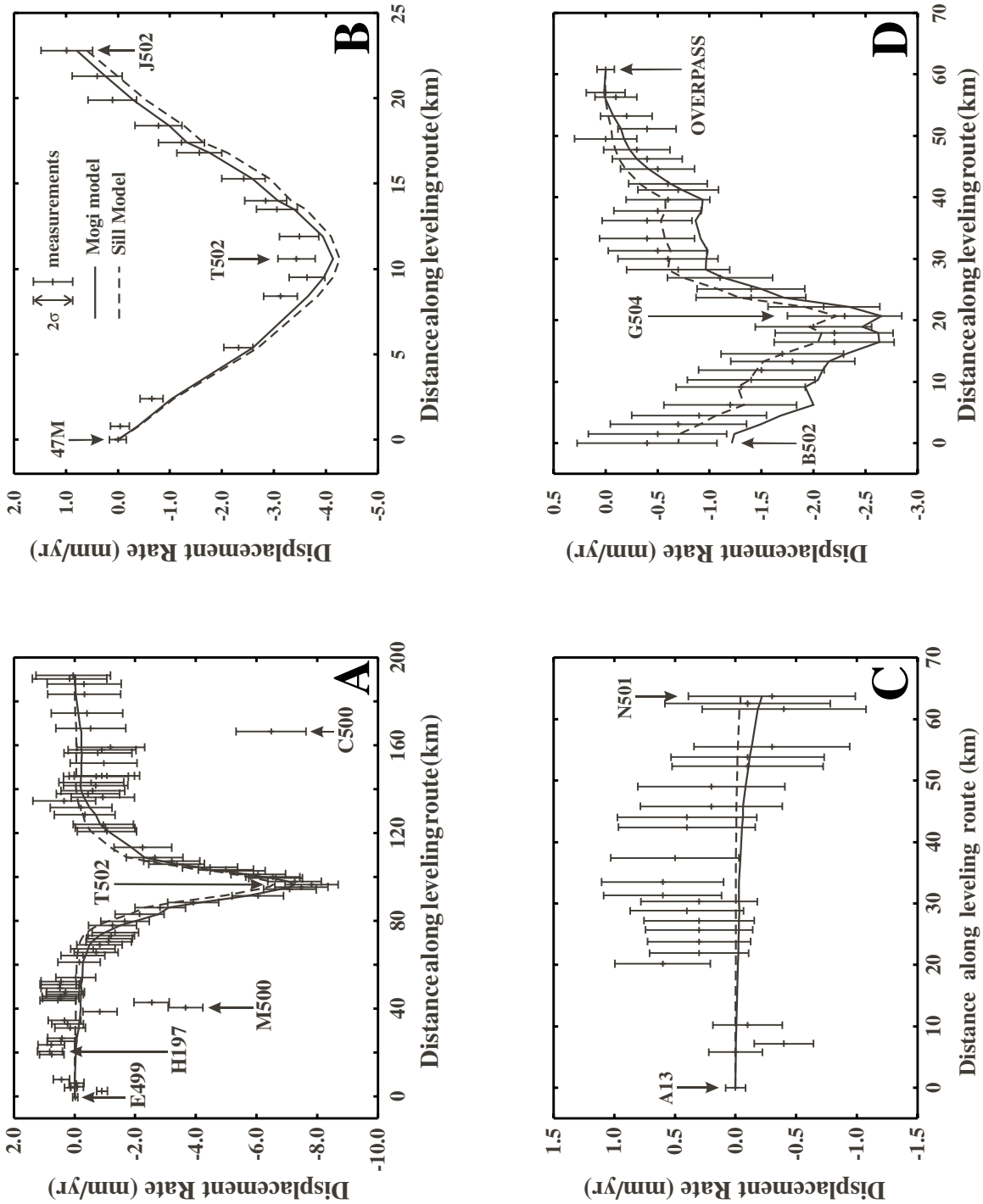
A
B
C
D
Displacement Rate (mm/yr)
Distance along leveling route (km)
measurements
Mogi model
Sill Model
47M
T502
J502
E499
H197
M500
C500
N501
A13
G504
B502
OVERPASS

Basin and Range extension. In the first case, deflation might be caused by loss of magma or volatiles from the source or by contraction of the source owing to cooling and crystallization. Our modeling shows that point sources of volume change (Mogi sources) and horizontal, rectangular uniform dilation sources (sills) fit the leveling data equally well, presumably because the source is too deep (~10 km) for its geometry to be constrained by vertical surface displacements alone. A common characteristic of all best-fit models is that sills require less subsurface volume change than Mogi sources to produce the same amount of vertical surface displacement, a relationship that was previously noted by *Delaney and McTigue* [1994] in their analysis of deformation at Kilauea volcano in Hawaii. *Dieterich and Decker* [1975] used finite element modeling to analyze the surface effects of various sources, including sills and Mogi sources, and concluded that vertical displacement data alone are not sufficient to constrain the depth, volume/pressure change, and geometry of the deformation source(s). With this in mind, the USGS Cascades Volcano Observatory (CVO) established a network of GPS stations in the MLV – Mount Shasta region in July 1990 to measure three-dimensional surface displacements. The network has since been expanded and re-measured twice [*Poland et al.*, 2000].

We used the best-fitting Mogi and sill sources from this study to predict horizontal displacement rates at benchmarks included in the MLV – Mount Shasta network. The sources produce similar vertical displacement rates, but significantly different horizontal rates at some locations (Figure 2.9). Both produce horizontal velocity vectors that generally point toward the summit, reach a maximum near the caldera rim, and decrease both inward and outward from there. However, at some sites the Mogi source predicts horizontal velocities that are several times larger than those predicted by the sill source. This is because the magnitudes of vertical and horizontal forces produced by a Mogi source are equal, whereas horizontal forces produced by a sill are much smaller than the

Figure 2.9. Predicted horizontal displacement rates at existing survey-mode GPS stations based on the best-fitting Mogi source (red arrows) and sill (black arrows). Results of repeated GPS surveys [*Poland et al*., 2000] should help to distinguish between these two source geometries or, if the subsidence mechanism is other than deflation, between other proposed mechanisms (*e.g*., gravitational loading and crustal extension). Longitude is expressed as degrees east of the Prime Meridian.

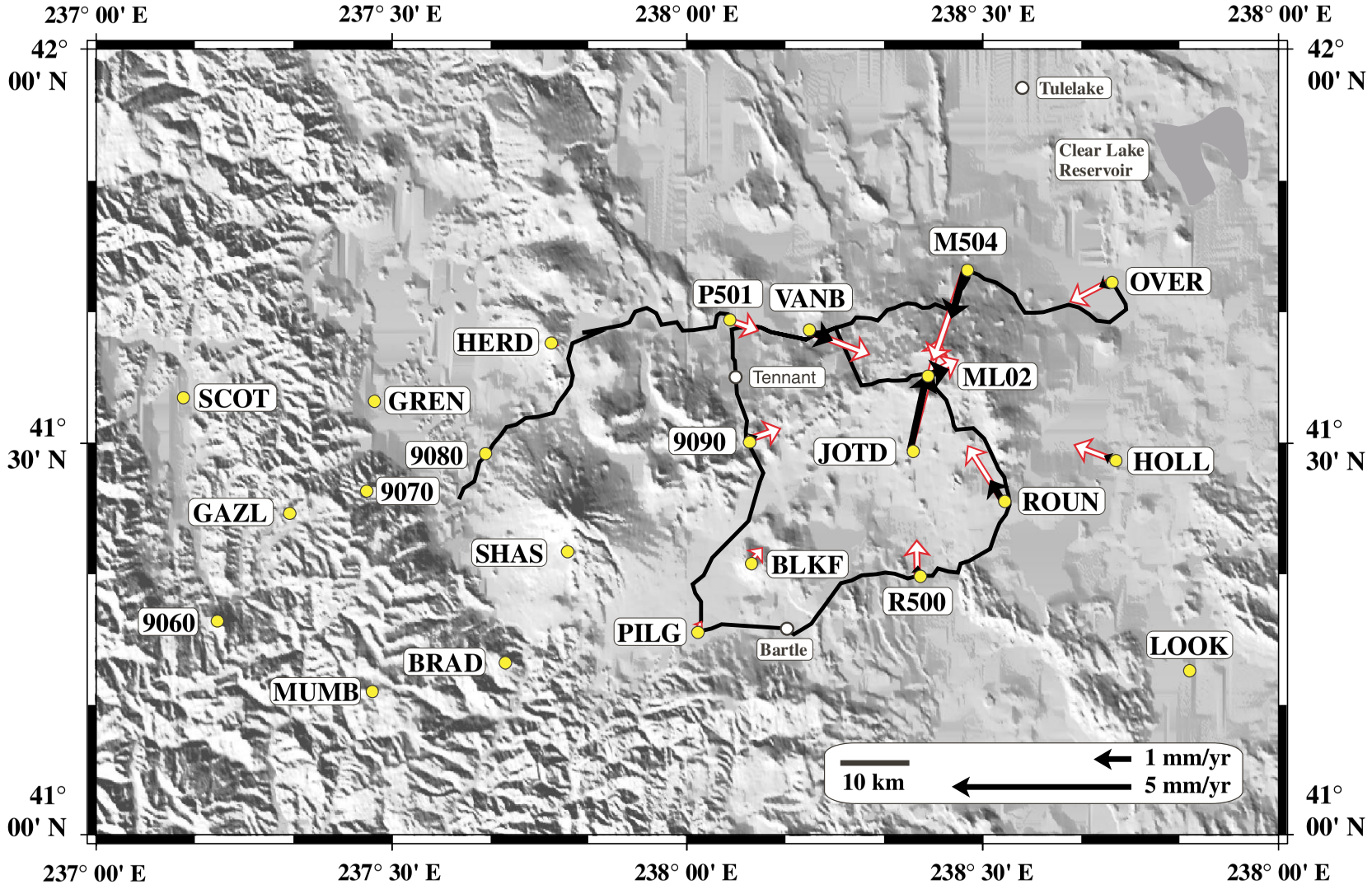
237° 00' E
237° 30' E
238° 00' E
238° 30' E
238° 00' E
42° 00' N
41° 30' N
41° 00' N
Tulelake
Clear Lake Reservoir
M504
OVER
P501
VANB
HERD
Tennant
ML02
SCOT
GREN
9090
JOTD
HOLL
9080
9070
ROUN
GAZL
SHAS
BLKF
R500
9060
PILG
Bartle
LOOK
BRAD
MUMB
10 km
1 mm/yr
5 mm/yr

corresponding vertical forces. As a result, the surface volume change exceeds the source volume change for a Mogi source, but for a sill these two volumes are essentially equal (i.e., a Mogi source produces host-rock dilatation but a sill source does not) [*Delaney and McTigue*, 1994]. As a consequence of this difference, repeated GPS surveys should be capable of distinguishing between a Mogi and sill source at MLV [*Poland et al.*, 2000].

Even though volume loss or depressurization of a Mogi or sill source produces a very good fit to the leveling data, other subsidence mechanisms could produce similar surface deformation patterns. For example, *Dzurisin et al*. [1991] proposed: 1) gravitational loading of thermally weakened crust by the mass of the volcano and associated intrusive rocks, and 2) thinning of locally weakened crust due to Basin and Range extension. The MLV edifice is too young (500-600 ka) [*Donnelly-Nolan*, 1988] to be gravitationally compensated so loading almost surely contributes to contemporary subsidence. Likewise, Basin and Range extension is known to be occurring at MLV, so resulting subsidence of thermally weakened crust (by repeated magmatic intrusions) is to be expected.

Leveling results suggest that the subsidence rate at MLV has been essentially constant for nearly five decades (based on measurements in 1954, 1988, 1989, 1990, and 1999 only), which raises the question of how far into the past the current rate should be extrapolated. For example, a constant subsidence rate of 8.6 ± 0.8 mm/yr would produce 8.6 ± 0.8 m of subsidence in 1,000 years and 860 ± 80 m of subsidence in 100,000 years. The most recent eruption at MLV occurred about 900 ^{14}C yr B.P. [*Donnelly-Nolan et al.*, 1990], so extrapolation over an interval at least that long seems reasonable. *Dzurisin et al*. [1991] reviewed the evidence for long-term subsidence of MLV from 8 drill holes, 5 of which penetrated the entire volcanic pile. They concluded that the crust beneath MLV has been downwarped ~500 m relative to the surrounding plateau, at least partly as a result of

loading by the edifice and a dense, subvolcanic intrusive complex. If we consider just the portion of subsidence that occurs inside the caldera (i.e., T502 relative to 47M), the average subsidence rate is 3.4 ± 0.4 mm/yr and the corresponding amounts of subsidence are 3.4 ± 0.4 m in 1,000 years and 340 ± 40 m in 100,000 years.

The current rate would have produced 500 m of subsidence in only ~60,000 years, approximately 10% of the time span of the volcano. It is highly unlikely that all of the subsidence would occur in the last 10% of the volcano's history, especially given that there is no obvious increase in eruptive productivity. Thus, the current rate of subsidence must be anomalous and either the subsidence rate has increased through time, the subsidence process has been episodic, or subsidence has been counterbalanced by uplift associated with intrusions.

Another likely mechanism for subsidence at MLV is crustal thinning as a result of tectonic extension across the Basin and Range province. *Dzurisin et al.* [1991] envisioned a situation akin to a "hole in a plate" in which the hole represents a cylindrical zone of hot and mechanically weak crust beneath the volcano. As the plate extends, the weak zone is expected to thin and further subside under gravity. The mechanism remains viable and will be tested by modeling. The availability of a second mechanism to account for subsidence might seem to exacerbate the dilemma described above, but not necessarily. The relatively high rate of contemporary subsidence could be a relatively recent phenomenon, i.e., a delayed response of the lithosphere to the increasing load imposed by the growing MLV edifice plus intrusive complex. For example, changes in the subsurface temperature distribution caused by intrusions or eruptions could lead to time-varying viscous strength of the crust. In this scenario, crustal extension could be responsible for a relatively minor amount of subsidence throughout the entire 500-600 ka lifespan of MLV, while

gravitational loading by the mature volcanic system has only recently become the dominant mechanism and is largely responsible for the high contemporary subsidence rate.

Alternatively, crustal extension might be the dominant cause of subsidence and the extension rate might have increased recently. In this scenario, gravitational loading produced a relatively minor, steady amount of subsidence as the volcano grew, while the crustal extension rate increased to produce the relatively high contemporary subsidence rate. Thus, the current anomalous subsidence rate could be explained by an unusually high crustal extension rate in the MLV region during Holocene time. Regardless of the subsidence mechanism, the historical rate of subsidence is clearly greater than the average rate over the lifespan of the volcano.

The next eruption of Medicine Lake volcano will likely be preceded by changes in the long-term deformation pattern as a result of magmatic intrusions into the upper crust. Such intrusions might be aseismic until they reach relatively cold, brittle rocks within ~5 km of the surface [*Hill*, 1993]. Continued geodetic surveillance by leveling, GPS, and SAR interferometry offers an opportunity for early detection of intrusions, which could lead to better long-term eruption forecasting. More sophisticated modeling of existing and future geodetic data could help to resolve several issues, including the time history and mechanism(s) of subsidence.

3. Crustal deformation in NE California: constraints on the subsidence mechanism of Medicine Lake volcano and the geometry of the northern Walker Lane

Abstract. Leveling surveys spanning 50 years at Medicine Lake volcano in northeastern California have revealed bowl-shaped subsidence centered on the summit of the volcano and reaching a maximum of 8.6 ± 0.9 mm/yr [*Dzurisin et al.*, in review]. *Dzurisin et al.* [1991] proposed several possible subsidence mechanisms, including: 1) magma withdrawal from a subsurface reservoir, 2) thermal contraction due to cooling and crystallization of magma at depth, 3) loading by the volcano and dense subvolcanic intrusions, and 4) crustal thinning due to lithospheric extension. GPS campaigns in 1990, 1996, and 1999 reveal horizontal displacements towards the summit of Medicine Lake as well as a significant component of right-lateral motion east of the volcano. The shearing is approximated by a NW-trending dextral shear zone slipping at a rate of ~6 mm/yr, and suggests the northward continuation of the right-lateral Walker Lane belt into northeastern California and southern Oregon. Displacements towards the caldera are caused by the subsidence, which is best approximated by a Mogi or sill source of volume loss at depth or a model of loading by subvolcanic intrusions. Geophysical studies identify a dense, seismically fast body at shallow depths under Medicine Lake caldera, but no magma apparently exists at depths required by the volume loss models (10 km), therefore downsagging due to dense intrusions is the preferred model.

3.1 Introduction

Medicine Lake Volcano (MLV) is a Quaternary-Holocene shield located on the Modoc Plateau in northern California, 50 km east-northeast of Mt. Shasta volcano (Figure 3.1) [*Donnelly-Nolan*, 1988]. The edifice is situated east of the axis of Cascade volcanism and on the western edge of the Basin and Range extensional province [*Dzurisin et al.*,

Figure 3.1. Shaded relief map of the Pacific northwest United States showing tectonic provinces. Cascade volcanoes are denoted by triangles. Abbreviations are as follows: Newberry volcano (N), Medicine Lake volcano (MLV), Mt. Shasta (S), Cape Mendecino (CME), San Andreas fault zone (SAF), Walker Lane - Eastern California Shear Zone (WL / ECSZ). The Basin and Range is dominated by E-W extension, although the western margin of the province (the Walker Lane / Eastern California Shear Zone) is characterized by dextral shear, accommodating NW translation of the rigid Sierra Nevada block, which lies between the WL / ECSZ and SAF systems. The Cascade volcanic arc results from subduction of the Juan de Fuca plate (which extends from Cape Mendecino to northern Washington) under the North American Plate. South of Cape Mendecino, the plate boundary is composed of right-lateral strike slip faults of the San Andreas system. MLV is located where several of the tectonic provinces intersect. Inset outlines the area of Figure 3.2.

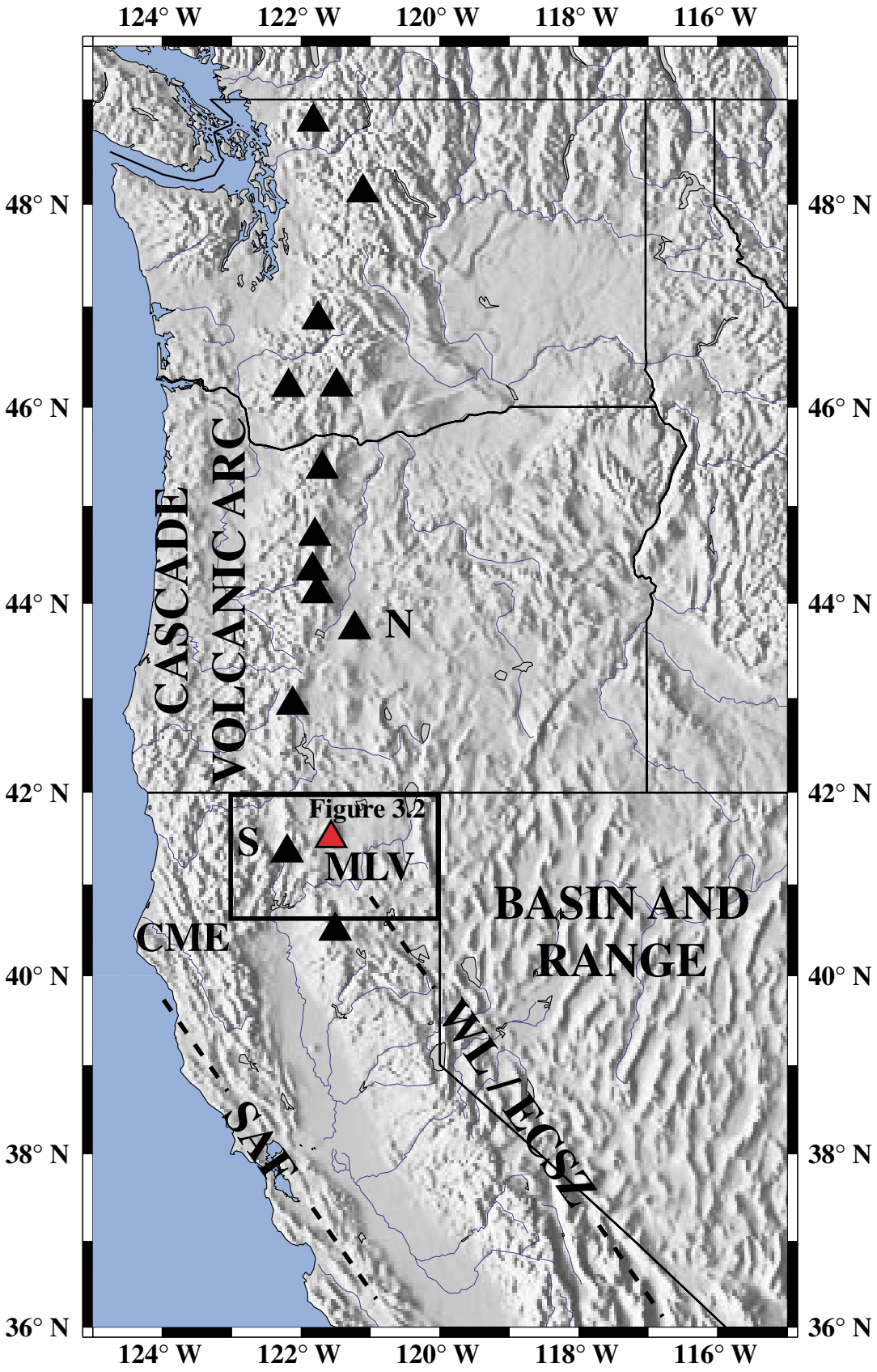
124° W
122° W
120° W
118° W
116° W
48° N
46° N
44° N
42° N
40° N
38° N
36° N
CASCADE VOLCANIC ARC
N
Figure 3.2
S
MLV
CME
BASIN AND RANGE
WL / ECSZ
SAF

1991], making the volcano an ideal natural laboratory for volcano-tectonic investigations. Leveling surveys in 1954 and 1989 indicate subsidence at MLV, with the greatest deformation at the summit and decaying symmetrically on the flanks of the edifice [*Dzurisin et al.*, 1991]. The subsidence may be caused by a variety of mechanisms, none of which can be distinguished by vertical deformation data alone. Additional leveling data presented by *Dzurisin et al.* [in review] further characterizes the physical and temporal characteristics of the subsidence but does not constrain the deformation source. In 1990, a 23-station GPS network was installed in the Medicine Lake - Mt. Shasta area by the US Geological Survey to measure horizontal displacements in the region [*Yamashita and Wieprecht*, 1995]. The network was reoccupied and expanded in 1996 and 1999, and results from the surveys are presented below. In addition, observations from leveling and GPS are compared to displacements predicted by various possible subsidence sources in order to determine the mechanisms controlling deformation at MLV.

3.2 Volcanology and Petrology of MLV

Medicine Lake is the largest volcano by volume in the Cascade Range, with lavas covering 2000 km^2 with a volume of 750 km^3 [*Donnelly-Nolan and Nolan*, 1986; *Dzurisin et al.*, 1991]. The volcano rises 1200 m above the Modoc Plateau, reaching an elevation of 2376 m [*Donnelly-Nolan and Nolan*, 1986], and has a 7x12 km caldera elongate about an east-west axis occupies the summit region (Figure 3.2). Because a major eruption has not been related to the formation of the caldera, *Donnelly-Nolan* [1988] suggests that the depression is a collapse structure that formed due to numerous extrusions of mafic lava early in the volcano's history, perhaps similar to Kilauea caldera in Hawaii. The geological characteristics of MLV were initially documented by *Peacock* [1931] and *Powers* [1932], and the volcano was later mapped and described in detail by *Anderson* [1941]. Since that

Figure 3.2. Shaded relief map of the Medicine Lake / Mt. Shasta region showing Quaternary faults, recent seismicity, and geodetic networks. (a) Blue lines are faults that have ruptured in the Quaternary, and magenta have ruptured in the Holocene. The Likely Fault, which shows right-lateral displacement [*Jennings*, 1994], is green. Red dots are earthquakes that have occurred in the region between 1954 and 1999. The leveling lines of *Dzurisin et al.* [in review] are noted by black lines. GPS stations are labeled by 4-character ID and noted by yellow triangles. The locations of normal faults modeled by *Dzurisin et al.* [in review] are shown near sites R500 and 9090 (ball on downdropped side). The focal mechanism is from the 1978 Stephens Pass earthquake swarm and suggests a normal faulting event with a component of dextral slip [*Patton and Zandt*, 1991]. Mt. Shasta is the topographic high located immediately north of the "SHAS" station, while the inset, which outlines part (b) of the figure, approximately outlines MLV. (b) Close-up of seismicity, GPS stations, leveling lines, and topography in the summit region of MLV. The caldera is outlined by a dashed ellipse. Focal mechanisms are from a shallow earthquake swarm that occurred in 1988/1989 and indicate both reverse and normal events with strike-slip components.

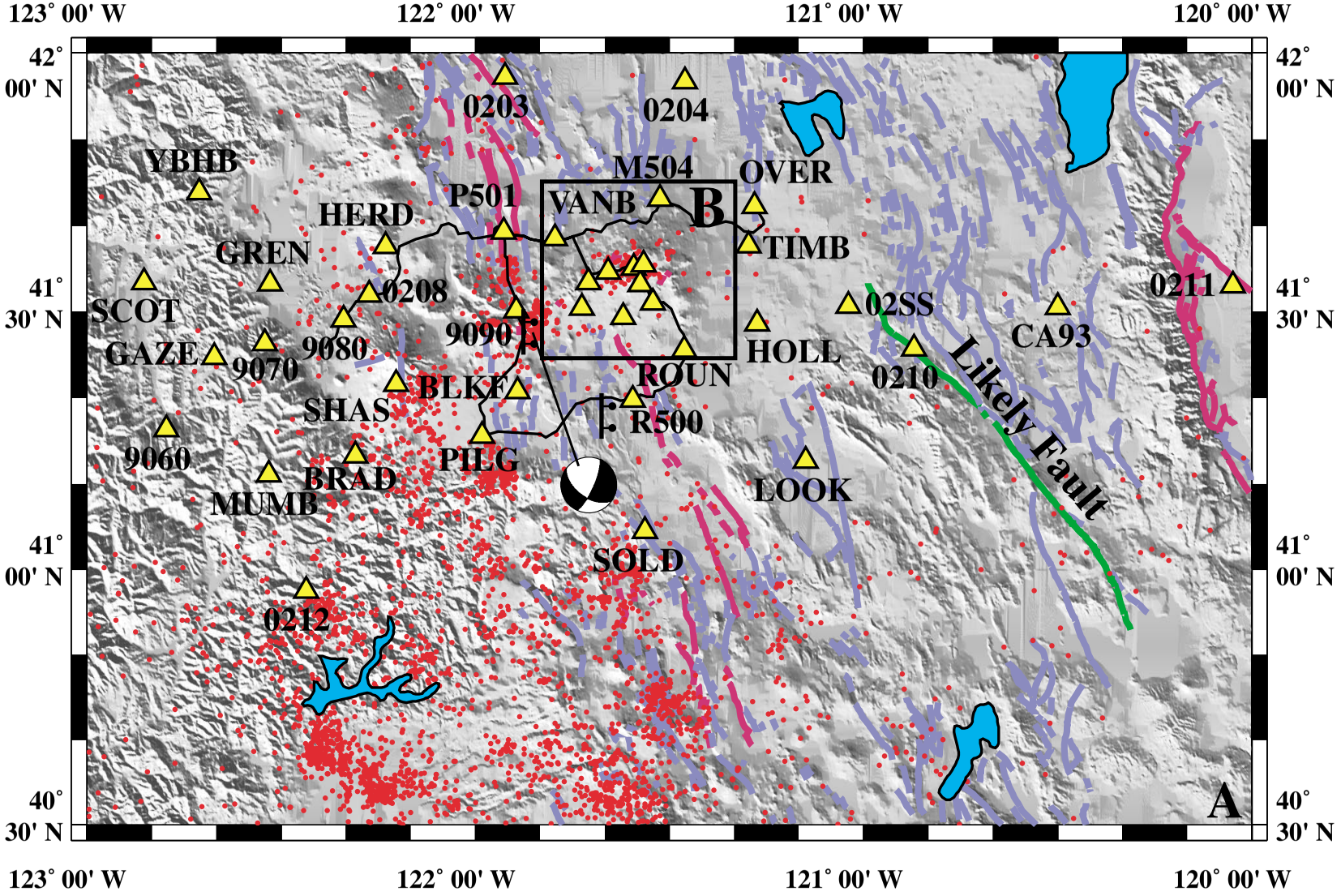
123° 00' W
122° 00' W
121° 00' W
120° 00' W
42° 00' N
41° 30' N
41° 00' N
40° 30' N
0203
0204
YBHB
M504
OVER
P501
VANB
B
HERD
TIMB
GREN
0208
0211
SCOT
02SS
CA93
9090
9080
GAZE
9070
HOLL
0210
ROUN
BLKF
SHAS
R500
9060
PILG
BRAD
LOOK
MUMB
SOLD
0212
Likely Fault
A

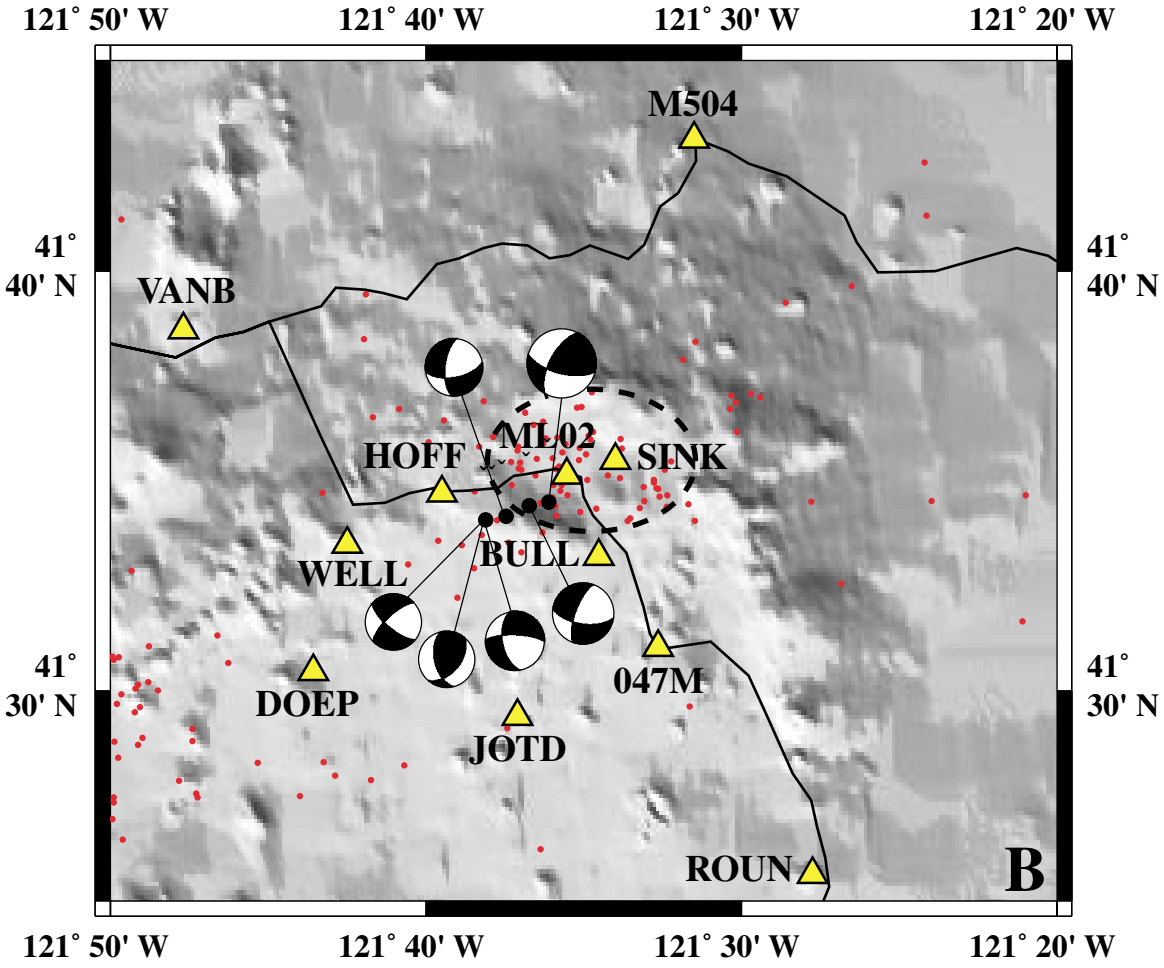

Figure 3.2. (Cont.)

time, new mapping and geochemical studies by Julie Donnelly-Nolan of the U.S. Geological Survey [e.g. *Donnelly-Nolan et al.,* 1990] and co-workers has led to greater understanding of the volcanic and petrologic history of MLV.

Primitive tholeiitic high-alumina basalt derived from a depleted mantle source was the first lava to be erupted in the Medicine Lake region at about 1 Ma, and is recognized as the parental magma for MLV eruptive products [*Grove et al.,* 1982; *Donnelly-Nolan,* 1988; *Donnelly-Nolan et al.,* 1991]. The Medicine Lake shield is composed of calc-alkaline basalts and basaltic andesites, with a small volume of silicic lavas near the summit [*Donnelly-Nolan,* 1988]. Calc-alkaline lavas are produced by fractional crystallization of high-alumina basalt, assimilation of silicic crust by high alumina basalt, and magma mixing [*Gerlach and Grove,* 1982; *Grove et al.,* 1982; *Grove and M,* 1986; *Grove et al.,* 1988; *Donnelly-Nolan et al.,* 1991]. Several lava flows at MLV are compositionally zoned, including the Giant Crater flow which began with the extrusion of differentiated products and terminated after the eruption of high-alumina basalt. To explain the evolution of the Giant Crater eruption, *Donnelly-Nolan et al.* [1991] conclude that extension at Medicine Lake facilitates the rise of mantle-derived magmas which differentiate in the upper crust.

In the past 11,000 years, 17 eruptions have occurred at MLV with compositions ranging from basalt to rhyolite [*Condie and Hayslip,* 1975; *Donnelly-Nolan et al.,* 1990]. The most recent eruption occurred ~1000 years ago at Glass Mountain on the eastern edge of the caldera. About 1 km^3 of rhyolite and dacite were erupted from numerous aligned vents forming a steep sided lava flow and several coalescing domes. Aligned eruptive vents and rhyolite domes also occur west of the caldera, forming during the Little Glass Mountain eruption at 1000 years BP [*Donnelly-Nolan et al.,* 1990]. *Fink and Pollard* [1983] interpret the alignment of eruptive vents and associated fractures as evidence of a subsurface feeder dike.

3.3 Subsurface Geology of MLV

Models of the magmatic system at MLV have been proposed by *Heiken* [1978], *Eichelberger* [1981], and *Donnelly-Nolan* [1988]. The chemical similarity of silicic lavas on opposite sides of the caldera leads *Heiken* [1978] to infer that a small silicic reservoir exists at depth. *Eichelberger* [1981] suggests that a large silicic magma chamber underplated by mafic magmas is responsible for the recent rhyolitic eruptions. Finally, *Donnelly-Nolan* [1988] concludes that many small magma bodies are present at depth along with solidifued intrusions of varying compositions. In an extensional setting, like that of MLV, central magma chambers are unlikely to form because tectonic extension favors a system including numerous dikes, sills, and other small intrusive bodies.

Geophysical studies of the volcano support *Donnelly-Nolan's* [1988] interpretation. On the basis of gravity anomalies, *Finn and Williams* [1982] infer a dense (0.41 g/cm^3 greater than surrounding rocks), cone-shaped body extending from depths of 1.5 km to 4 km below MLV caldera. The upper surface of the cone has a diameter of 9 km, while the lower surface is 20 x 36 km elongated in an east-west direction (the direction of crustal extension). *Fuis et al.* [1987] and *Zucca et al.* [1986] identify a dense feature at 1-2 km depth under the caldera from seismic refraction data, and *Stanley* [1990] analyzes magnetotelluric and refraction data to image the same body, which is characterized by high resistivity and high seismic velocity. Seismic tomography of the crust beneath MLV by *Ritter and Evans* [1997] also shows a high-velocity anomaly in the upper crust (0-10 km depth) under the caldera. All four studies interpret the dense, resistive, seismically fast body as a solidified intrusive complex, similar to that imaged at Newberry volcano, in central Oregon (Figure 3.1) [*Stauber et al.*, 1988; *Zucca and Evans*, 1992].

Additionally, *Evans and Zucca* [1988] report a low velocity body beneath the dense intrusive complex that they interpret as a small (10 km^3) silicic magma chamber. *Chiarabba*

et al. [1995] analyze the same dataset using a different technique and identify similar characteristics, including a cone-shaped high-velocity body at 1-3 km depth beneath the caldera underlain by a low-velocity body at 3-5 km depth. No geophysical studies have identified a large (100 km^3) silicic magma chamber, however, a small, hot intrusion (possibly still molten) and a dense solidified intrusive complex apparently do exist at depth beneath MLV caldera. Newberry volcano also hosts a shallow, possibly active magma body [*Achauer et al.*, 1988; *MacLeod and Sherrod*, 1988] and is analogous to MLV in both tectonic setting (back arc) and volcanic style (bimodal shield).

3.4 Tectonic Setting and Recent Seismicity

MLV is located at the intersection of three tectonic provinces: the Basin and Range extensional terrane, the Cascadia subduction zone, and the possible northward continuation of the Eastern California Shear Zone (ECSZ) - Walker Lane belt of dextral shear. Deformation and seismicity in the MLV region are a consequence of the interactions between the three terranes, in addition to local volcanic sources. Clearly, the overlap of tectonism and volcanism makes MLV an ideal setting for studies of volcano-tectonic interactions.

3.4.1 Basin and Range

Numerous geologic and geodetic studies have characterized extension in the Basin and Range province of the western Unites States. Deformation in the last 10 Ma has resulted in the formation of regularly spaced mountain ranges and basins, implying uniform crustal strain [*Bennett and Davis*, 1998; *Wernicke et al.*, 2000]. However, current seismicity is concentrated in three bands in the Basin and Range: the intermountain seismic

belt along the Wasatch Fault in Utah, the Central Nevada Seismic Zone, and the western margin of the province in western Nevada and eastern California [*Wernicke et al.*, 2000]. Space geodetic studies indicate that deformation is localized around the seismically active zones, with east-west extension in the east evolving into right lateral shear in the west [*Dixon et al.*, 1995b; *Bennett et al.*, 1998; *Bennett et al.*, 1999; *Thatcher et al.*, 1999]. Of the GPS transects that cross the Basin and Range, only the Northern Basin and Range continuous GPS network [*Bennett et al.*, 1998] at 39˚ - 41˚ approaches the latitude of MLV (41.6˚). None of the networks reach the western longitude of MLV (121.6˚ W).

Clear evidence for extensional tectonism at MLV is manifested as N-S and NW-SE striking normal faults, which are located both north and south of the volcano and presumably exist under the volcanic pile (Figure 3.2) [*Donnelly-Nolan*, 1988; *Blakely et al.*, 1997]. In addition, three episodes of seismicity have been documented in the MLV region (Figure 3.2A). The first occurred in 1978 near Stephens Pass, located between MLV and Mt. Shasta. All earthquakes were shallow and occurred on a north-trending fault zone with an eastward dip, similar to other normal faults in the region. Vertical displacements measured along the fault zone were 1-1.5 meters [*Bennett et al.*, 1979]. A focal mechanism recorded during the largest event of the swarm by *Patton and Zandt* [1991] (M_L=4.6, 8/1/78) indicates normal motion with a component of right-lateral slip (Figure 3.2A). Another swarm of shallow events was recorded 10 km north of Stephens Pass in 1981 near the town of Tennant, again along a north-trending fault. Ground breakage was not observed in the area following the Tennant earthquakes [*Dzurisin et al.*, 1991]. In September 1988, seismic activity commenced under the caldera of MLV. The earthquakes were low magnitude, short-period, within 4 km of the surface, and continued throughout 1989. Focal mechanisms from the swarm (obtained from the Northern California Earthquake Data Center (NCEDC) at the University of California, Berkeley)

indicate mixed first motions and fault planes, with both dip-slip and strike-slip displacement (Figure 3.2B). One long-period earthquake was recorded at 15 km depth in December 1989, and may be evidence of magma movement within the crust [*Dzurisin et al.*, 1991]. An additional faulting event approximately 30 km south of Medicine Lake caldera is suggested by leveling data collected by *Dzurisin et al.* [1991]. No records of significant seismic activity in the region exist prior to the 1978 earthquakes, however seismic stations were sparse in the region before 1980 and an episode of normal faulting could have gone undetected [*Dzurisin et al.*, 1991; *Dzurisin et al.*, in review].

3.4.2 Eastern California Shear Zone - Walker Lane

In addition to extension, right-lateral displacement may be occurring in the MLV region due to NW translation of the coherent Sierra Nevada block [*Wells et al.*, 1998]. Dextral shear is well-documented along the southeastern margin of the mountain range, but ambiguous to the north.. *Dokka and Travis* [1990a] propose the existence of the Eastern California Shear Zone (ECSZ) as an explanation for vertical-axis rotations and strike-slip faulting south of the Garlock Fault in the Mojave Desert of southeastern California. Later authors extend the ECSZ north of the Garlock fault into Owens Valley [e.g. *Dixon et al.*, 1995a; *Reheis and Dixon*, 1996]. The ECSZ is made of up multiple NW-trending strike-slip faults that are connected by a series of smaller NE-striking faults [*Reheis and Dixon*, 1996]. Up to 65 km of dextral shear has been documented on the ECSZ, and geological studies suggest that the boundary accommodates 9-23% of Pacific-North America plate motion [*Dokka and Travis*, 1990b; *Dokka and Travis*, 1990a]. Estimates based on GPS data by *Miller et al.* [2001a] suggest that the ECSZ may account for up to 28-29% of motion between the two plates.

Geodetic studies have documented approximately 12 mm/yr of right-lateral strike-slip displacement on the ECSZ [*Sauber et al.*, 1994; *Dixon et al.*, 2000]. North of Owens Valley, the ECSZ becomes the Walker Lane, although the structural characteristics of the deforming zone do not vary significantly. The Walker Lane has been mapped as far north as the Honey Lake fault zone in eastern California at 40˚ latitude [*Stewart*, 1988]. *Dixon et al.* [2000] use GPS measurements to infer a displacement rate of 8 ± 3 mm/yr at that latitude distributed on the Honey Lake and Mohawk Valley fault zones, which agrees with estimates obtained by *Thatcher et al.* [1999] for the region. GPS data of *Miller et al.* [2001b] suggest displacements of 11 ± 0.8 mm/yr east of the Sierra Nevada block in the same region directed at an azimuth of 311° along an interpreted northward extension of the ECSZ - Walker Lane system. The GPS measurements are in agreement with VLBI data from *Argus and Gordon* [1991], who find NW motion of the Sierra Nevada block at 11 ± 1 mm/yr.

Limited geodetic measurements have been attempted north of 40˚ latitude in California, therefore the extent of Walker Lane - ECSZ deformation is not well known. However, numerous NW-trending dextral faults have been mapped in northeast California and southern Oregon, including the Likely Fault, the Mt. McLaughlin fault zone, the Eugene-Denio fault zone, and the Brothers Fault zone [*Pease*, 1969; *Wright*, 1976; *Roberts*, 1985; *Page et al.*, 1993; *Pezzopane and Weldon II*, 1993]. All four faults have significant right-lateral displacement components and are arranged in a right-stepping en echelon pattern north of the Honey Lake fault zone (Figure 3.3) [*Page et al.*, 1993]. An analysis of Quaternary faults by *Blakely et al.* [1997] suggests that fault orientations are probably controlled by preexisting basement structure and material heterogeneities within the lithosphere. Faults trend north-south in the warm, weak crustal blocks that surround the southern Cascade volcanoes (including Mt. Shatsa and MLV), while in relatively

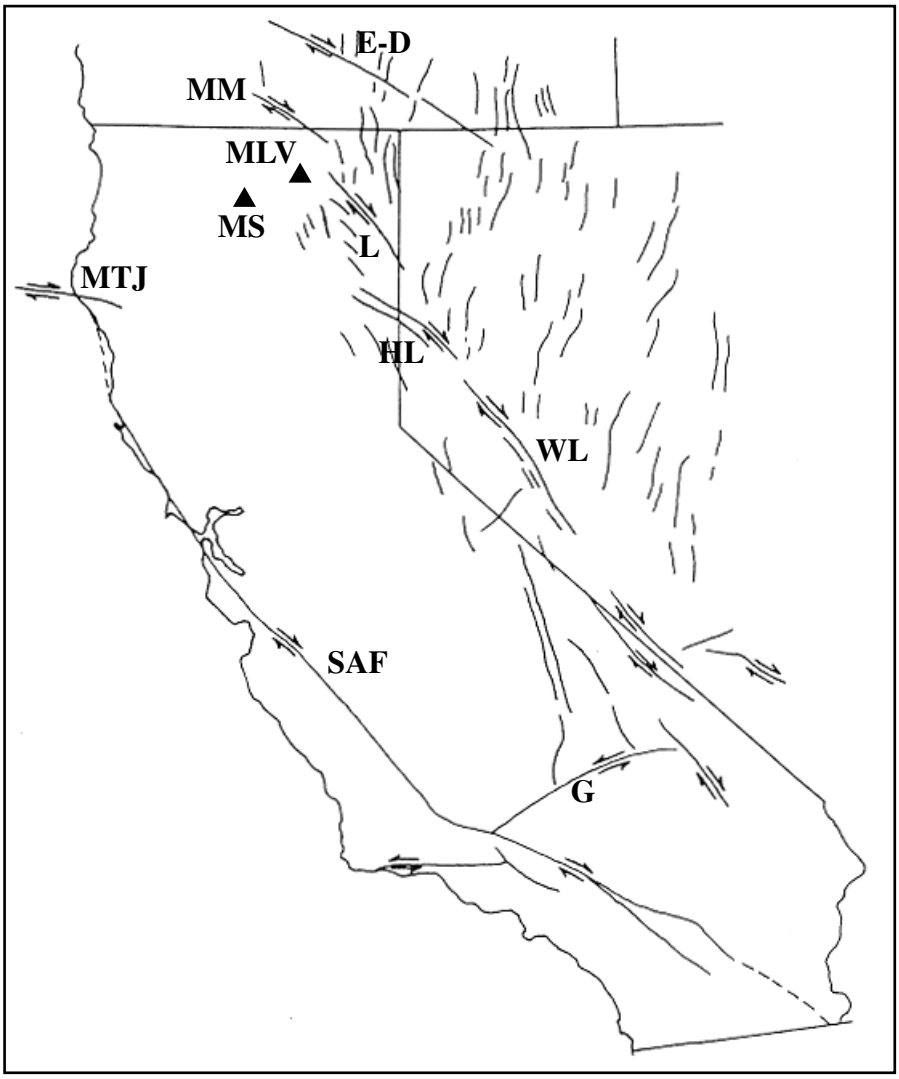

Figure 3.3. Major faults and fault zones in California, Oregon, and Nevada. Labeled features are: (SAF) San Andreas Fault, (MTJ) Mendecine Triple Junction, (E-D) Eugene-Denio fault zone, (MM) Mount McLaughlin fault zone, (L) Likely fault, (HL) Honey Lake fault, (WL) Walker Lane, (G) Garlock Fault, (MLV) Medicine Lake volcano, (MS) Mount Shasta volcano. Note the echelon arrangement of dextral faults and fault zones extending north from the Garlock fault into southern Oregon. The Brothers fault zone, north of the Eugene-Denio fault zone, is not shown. Modified from *Hannah* [1977].

amagmatic regions between volcanic centers they are NW-SE. Dextral shear is concentrated on the NW-striking faults and extends from Lassen Peak into the Klammath mountains of southern Oregon [*Blakely et al.*, 1997]. *Pezzopane and Weldon* [1993] further suggest that shear in eastern California may extend through central Oregon and into Washington before rejoining the Pacific-North America plate boundary. Alternatively, *Miller et al.* [2001b] note that approximately half the strain budget of the ECSZ - Walker Lane system is lost in the vicinity of the Klamath Mountains in southern Oregon. Regardless, northeastern California and southern Oregon are clearly locations of dextral shear [*Blakely et al.*, 1997]. The Likely Fault is approximately 50 km east of MLV [*Fuis et al.*, 1987; *Jennings*, 1994], suggesting that dextral deformation associated with the ECSZ - Walker Lane system may be measurable by the MLV-Mt. Shasta GPS network.

3.4.3 Cascadia Subduction Zone

A third source of tectonic deformation in the MLV region is the Cascadia subduction zone, where the Juan de Fuca plate thrust beneath the North American plate. GPS measurements of deformation in Oregon indicate that the main thrust fault is locked, causing contraction along an east-west axis [*McCaffery et al.*, 2000; *Murray and Lisowski*, 2000; *Savage et al.*, 2000]. Dislocation models based on geodetic and other data suggest that the region of zero slip on the megathrust is largely offshore, with a width of 30-40 km [*Flück et al.*, 1997; *McCaffery et al.*, 2000; *Savage et al.*, 2000]. Deformation due to plate locking is measurable up to 150 km inland in the Cascadia forearc [*Savage et al.*, 2000]. For comparison, the westernmost station in the MLV GPS network is ~200 km from the deformation front. *Miller et al.* [2001b] note that no residual velocity from strain associated with the subduction zone is detected at a GPS station ~80 km west of MLV. As a result,

trench-perpendicular motion due to locking of the subduction megathrust probably is not a major source of deformation in the MLV GPS network.

A major component of arc-parallel displacement is superimposed on the contraction throughout Oregon, causing rotation of the Cascadia forearc [*Wells et al.*, 1998; *McCaffery et al.*, 2000; *Savage et al.*, 2000]. *Wells et al.* [1998] propose that coastal Oregon is rotating clockwise about a vertical axis relative to stable North America due to northwest translation of the rigid Sierra Nevada block (described above). The boundary between the Sierra Nevada and coastal Oregon blocks is located by *Wells et al.* [1998] in the Klamath Mountains in southern Oregon. Both *McCaffery et al.* [2000] and *Blakeley et al.* [1997] suggest that Oregon block rotation may extend into northern California, which includes the MLV - Mt. Shasta area.

3.5 Deformation and Associated Mechanisms

Dzurisin et al. [1991] present results for a 193 km-long leveling circuit that crosses the summit and flanks of MLV and was measured in 1954 and 1989 (Figure 3.2). They detect a maximum of 11.1 +/- 1.2 mm/yr of subsidence at the summit of the edifice, which decays rapidly and symmetrically on the flanks. The subsidence rate was later amended by *Dzurisin et al.* [in review] to 8.6 ± 0.9 mm/yr to account for artifacts in the data not previously recognized (see Chapter 2 for a more thorough description). In addition to the subsidence, two faulting events are recognized in the leveling circuit. The 1978 Stephen's Pass earthquake swarm is clearly documented by the displacement of a single benchmark on the down-dropped (east) side of the surface rupture and inferred fault. Additional faulting is suggested by anomalous displacements of three benchmarks approximately 30 km south of MLV caldera, although no earthquakes have been detected in the region (see

section 3.4.1). Both regions of inferred faulting were modeled by *Dzurisin et al.* [in review] as dip-slip dislocations approximating east-dipping normal faults.

At least four mechanisms can explain subsidence of MLV measured by leveling: 1) volume loss due to magma withdrawal (Figure 3.4A), 2) volume loss due to thermal contraction of a cooling and crystallizing magma body at depth (Figure 3.4A), 3) flexure from the volcanic load on the crust (Figure 3.4B), and 4) thinning and subsidence due to Basin and Range extension (Figure 3.4C) [*Dzurisin et al.*, 1991]. *Dzurisin et al.* [1991; in review] favor a model including crustal thinning due to Basin and Range extension coupled with loading by the volcano and subvolcanic intrusions, both facilitated by heat-induced weakening of the crust. The role of subvolcanic intrusions in the loading process follows the proposal of *Walker* [1987; 1988] that dense intrusions emplaced at depth below mafic volcanoes drive caldera formation through downsagging deformation. *Walker* [1984] cited the centripetal dips (e.g. inclined towards the summit of the volcano) of eruptive units at several volcanoes (including Bolsena, Italy, Koolau, Oahu (Hawaii), and Taupo, New Zealand) as evidence of subsidence from downsagging due to dense intrusions that are inferred from gravity data. Geophysical studies of MLV (described in section 3.3) suggest that a dense body exists at shallow depths below the caldera, supporting the possibility of downsagging as a subsidence mechanism. Unfortunately, the mechanisms proposed by *Dzurisin et al.* [1991] are indistinguishable based on vertical deformation data alone, and horizontal displacements from GPS are necessary to assess the models.

3.6 GPS Data and Results

In July 1990, the USGS Cascades Volcano Observatory established a network of 23 GPS stations over a broad area in northern California, which includes Medicine Lake and Mt. Shasta volcanoes (Figure 3.2) [*Dzurisin et al.*, 1991; *Yamashita and Wieprecht,*

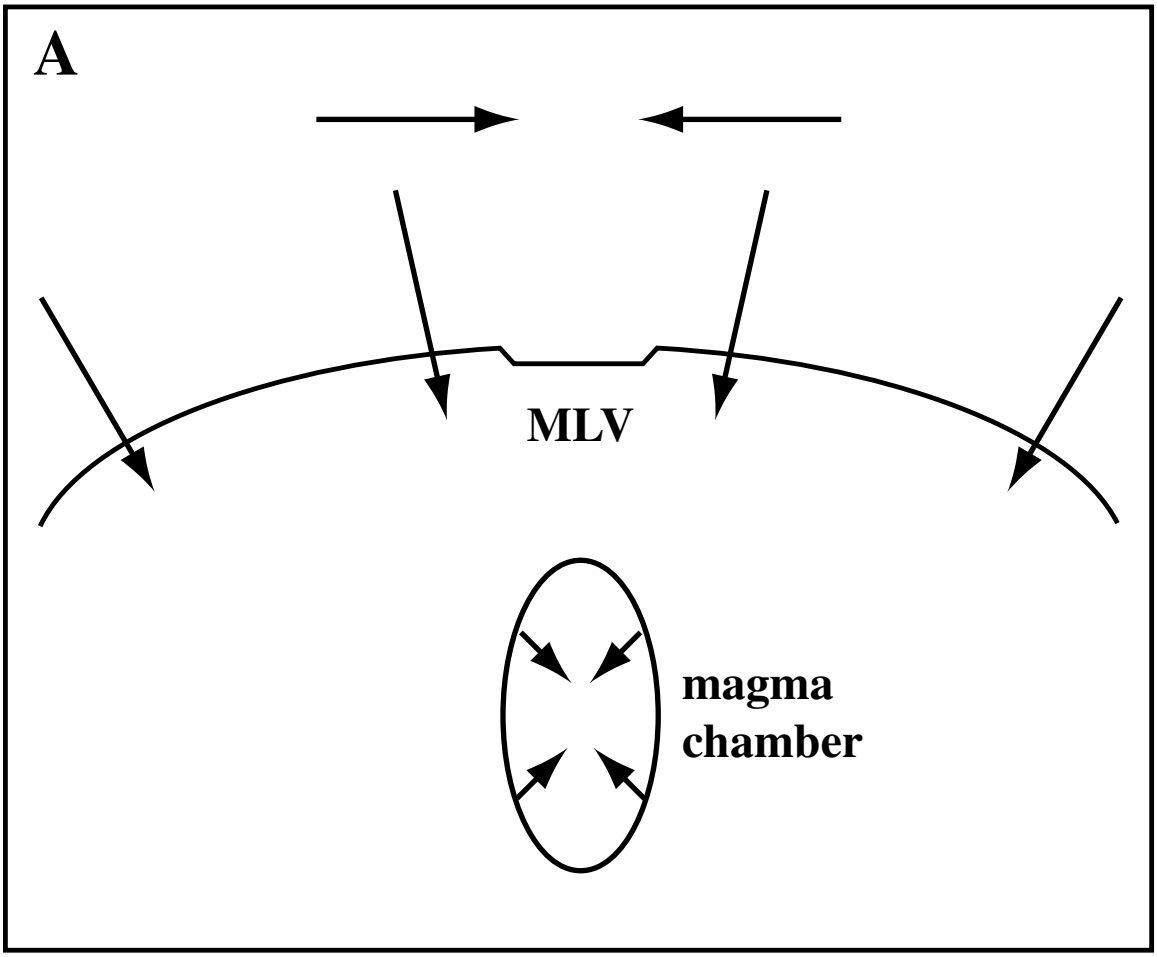

Figure 3.4. Schematic cross sections through Medicine Lake volcano (MLV) illustrating the possible subsidence mechanisms of *Dzurisin et al.* [1991]. (a) Volume loss at depth beneath the volcano will cause radial deflation of the edifice, including subsidence maximized at the center of the volcano and horizontal displacements that are radially towards the summit of MLV. Possible causes of deflation include magma withdrawal from a subsurface chamber, or volumetric contraction of magma due to cooling and crystallization. (b) The load of the volcano and associated dense subvolcanic intrusions on the crust may cause subsidence, as has been show at many other volcanoes (for instance, Hawaii as described by *Walcott* [1970]. Horizontal deformation due to loading would be radially toward the summit of MLV. (c) If the crust beneath MLV has been thermally weakened by intrusions, Basin and Range extension (manifested by east-west lengthening across MLV) may cause local subsidence of the edifice.

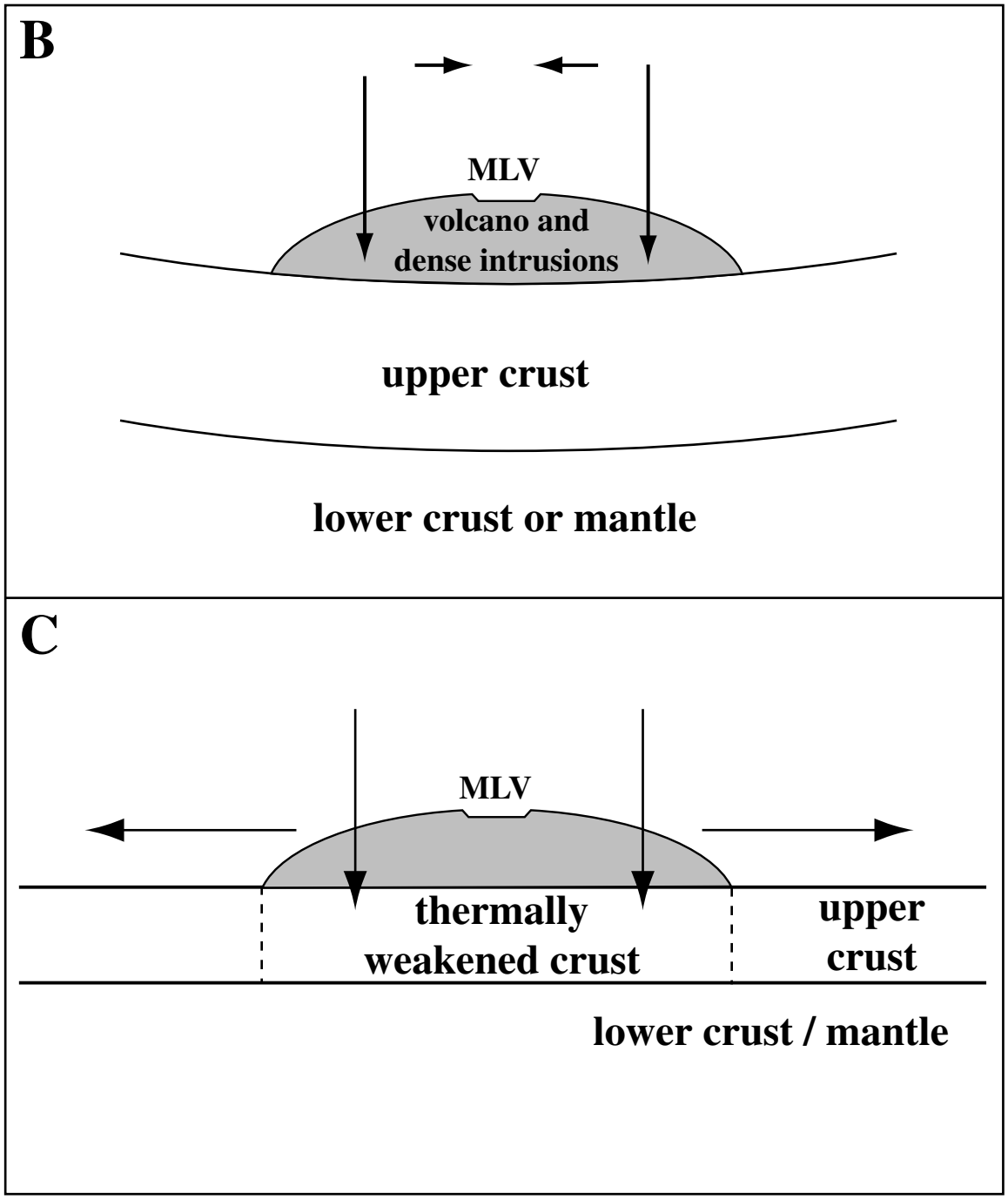

Figure 3.4. (Cont.)

1995]. All stations, with one exception, were occupied for two consecutive days for eight hours each with a TI 4000 receiver. Station P501 was occupied each day of the campaign. Between 1990 and 1996, two stations were destroyed: SHAS, located high on the south flank of Mt. Shasta and LAKE, positioned in MLV caldera. During a second campaign in 1996, both sites were reestablished, three additional sites were installed near Medicine Lake (BULL, DOEP, and TIMB), and two sites of the California Department of Transportation High Precision Geodetic Network (HPGN) were occupied (0208 and 0212). Four sites that are located far from MLV and Mt. Shasta were not surveyed in 1996 (9060, SCOT, GREN, and LOOK). During the 1996 campaign, all stations were occupied for at least 8 hours on three consecutive days with Trimble 4000 SSE and SSi receivers and corresponding 4000 SSE and choke ring antennae.

The same equipment and techniques were used for a third survey of 35 benchmarks in August 1999. Again, three sites located at great distances from MLV and Mt. Shasta were not occupied (9060, GREN, and GAZE), and one site had been destroyed sometime between 1990 and 1999 (LOOK). Six additional HPGN sites were occupied (0203, 0204, 0210, 0211, 02SS, and CA93), and five new sites were established (HOFF, SINK, SOLD, WELL, 047M). A summary of GPS sites and years occupied is given in Table 3.1, and site locations are shown in Figure 3.2.

GPS data were processed in the ITRF97 reference frame using version 4.2 of the Bernese Processing Engine [*Beutler et al.*, 1987] following the procedures described in *Bürgmann et al.* [1997]. Station velocities were calculated for 24 local stations and are shown relative to site MUMB, located on the western edge of the network, in Figure 3.5 (site velocities are given in Table 3.1). GPS data from the Bay Area Regional Deformation (BARD) [*Murray and Segall*, in press] and Northern Basin And Range (NBAR) [*Bennett et al.*, 1998] networks, as well as permanent sites of the International GPS Service (IGS),

Table 3.1. Locations, years occupied, and site velocities for stations in the Medicine Lake - Mt. Shasta GPS network, northern California. All velocities are relative to Mumbo, which is held fixed.

Station Name	ID	Occupation Years			Lat. (° N)	Long. (° W)
		1990	1996	1999		
047M	047M			X	41.555	121.562
Arnica Sink	SINK			X	41.592	121.567
Black Fox	BLKF	X	X	X	41.347	121.891
Bullseye Lake	BULL		X	X	41.554	121.576
CVO 9060	9060	X			41.272	122.795
CVO 9070	9070	X	X	X	41.440	122.541
CVO 9080	9080	X	X	X	41.486	122.340
CVO 9090	9090	X	X	X	41.503	121.894
CVO ML02	ML02		X	X	41.586	121.592
Doe Peak	DOEP		X	X	41.508	121.726
Gazelle	GAZE	X	X		41.413	122.673
Greneda	GREN	X			41.555	122.529
Herd Peak	HERD	X	X	X	41.628	122.232
Hollenbeck	HOLL	X	X	X	41.478	121.274
HPGN 0203	0203			X	41.954	121.923
HPGN 0204	0204			X	41.945	121.459
HPGN 0208	0208		X	X	41.533	122.274
HPGN 0210	0210			X	41.430	120.871
HPGN 0211	0211			X	41.551	120.019
HPGN 0212	0212		X	X	40.958	122.435
HPGN 02SS	02SS			X	41.512	121.039
HPGN CA93	CA93			X	41.510	120.501
Jot Dean	JOTD	X	X	X	41.490	121.618
Lake	LAKE	X	**DESTROYED**		41.586	121.592
Little Mt. Hoffman	HOFF			X	41.579	121.658
Lookout	LOOK	X	**DESTROYED**		41.211	121.150
M504	M504	X	X	X	41.719	121.525
Mt. Bradley	BRAD	X	X	X	41.222	122.309
Mumbo	MUMB	X	X	X	41.184	122.533
Overpass	OVER	X	X	X	41.705	121.281
P501	P501	X	X	X	41.656	121.926
Pilgrim	PILG	X	X	X	41.260	121.982
Pumice Stone Well	WELL			X	41.558	121.708
R500	R500	X	X	X	41.330	121.606
Round Mountain	ROUN	X	X	X	41.427	121.462
Scott Valley	SCOT	X		X	41.558	122.854
Shasta (original)	SHAS	X	**DESTROYED**		41.361	122.203
Shasta (UCD Reset)	SHAS		X	X	41.361	122.203
Soldier Mountain	SOLD			X	41.074	121.563
Timber Mountain	TIMB		X	X	41.629	121.296
Van Bremmer	VANB	X	X	X	41.643	121.795
TOTAL SURVEYED:		**23**	**24**	**35**		

Table 3.1. (Cont.)

Station Name	station velocity (mm/yr)				Correl.
	E vel.	E σ	N vel.	N σ	
047M					
Arnica Sink					
Black Fox	3.37	0.49	-0.22	0.56	-0.04778
Bullseye Lake	0.52	0.62	-0.46	0.78	-0.04002
CVO 9060					
CVO 9070	2.10	0.37	0.48	0.40	-0.02377
CVO 9080	2.25	0.48	0.30	0.51	-0.05068
CVO 9090	1.18	0.44	-0.38	0.50	-0.00304
CVO ML02	1.59	1.05	-2.94	1.30	-0.00734
Doe Peak	3.85	0.52	0.85	0.66	0.00594
Gazelle	3.34	1.36	1.32	1.26	-0.01846
Greneda					
Herd Peak	2.53	0.43	-0.62	0.51	-0.01214
Hollenbeck	1.56	0.49	-1.24	0.56	-0.01217
HPGN 0203					
HPGN 0204					
HPGN 0208					
HPGN 0210					
HPGN 0211					
HPGN 0212	3.20	1.29	-1.45	1.60	-0.12793
HPGN 02SS					
HPGN CA93					
Jot Dean	2.25	0.54	0.66	0.54	-0.07007
Lake					
Little Mt. Hoffman					
Lookout					
M504	1.40	0.60	-2.79	0.60	-0.00152
Mt. Bradley	0.68	0.41	0.12	0.48	-0.01565
Mumbo	**REFERENCE STATION**				
Overpass	1.50	0.60	-2.66	0.72	-0.09395
P501	3.10	0.41	0.23	0.45	-0.01352
Pilgrim	1.53	0.48	-0.93	0.53	-0.07369
Pumice Stone Well					
R500	-1.42	0.58	-0.22	0.66	-0.10174
Round Mountain	1.07	0.48	-0.27	0.53	-0.01336
Scott Valley	3.58	0.86	0.65	0.82	-0.04110
Shasta (original)					
Shasta (UCD Reset)	2.26	1.26	-3.27	1.30	-0.20991
Soldier Mountain					
Timber Mountain	2.58	0.49	-2.91	0.60	-0.06032
Van Bremmer	4.11	0.43	-0.18	0.49	-0.01046

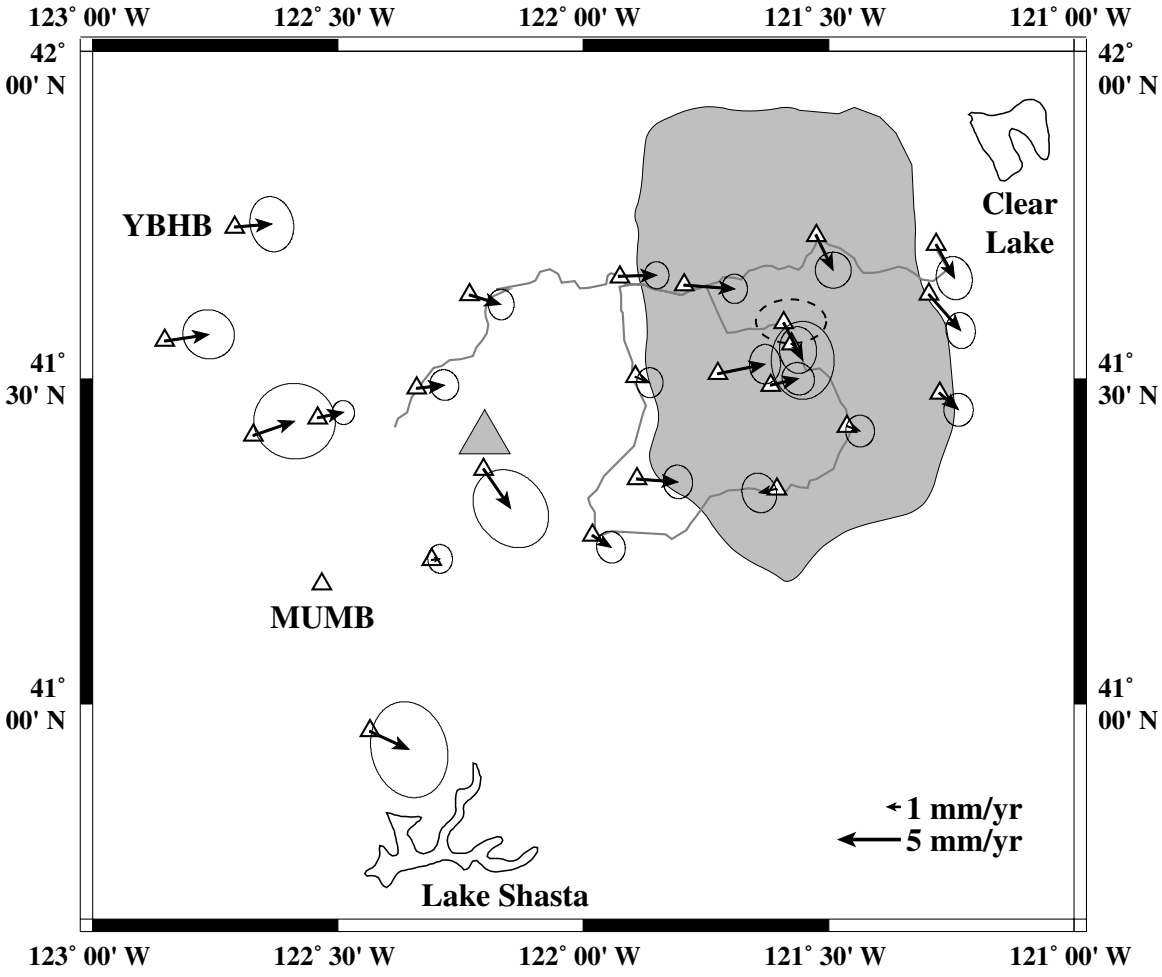

Figure 3.5. Velocity map of GPS stations in the Medicine Lake region occupied in 1990, 1996, and 1999. Mt. Shasta is indicated by a gray triangle. The approximate aerial extent of MLV is shaded gray, and the caldera outline is dashed. Leveling lines occupied by *Dzurisin et al.* [in review] are represented by gray lines. Station velocities are shown with respect to MUMB, which is held fixed. Individual site designations are given in Figure 3.2. Error ellipses denote 2-sigma confidence values. A complete listing of local site velocities and associated confidence intervals is given in Table 3.1. Site YBHB is a BARD station and not part of the local network.

were included when processing the 1996 and 1999 data (see Table 3.2 for a listing of regional sites, velocities, and years occupied). Calculated velocities, displayed relative to MUMB in Figure 3.6, agree with previously published results for the same networks [e.g. *Bennett et al.*, 1998; *Bennett et al.*, 1999; *Wernicke et al.*, 2000; *Murray and Segall*, in press]. Only three fiducial sites (Mojave, Richmond, and Westford) were available when processing the 1990 data, and were not used in subsequent campaigns. Data from 1996 and 1999 were processed using five fiducial sites (ALGO, GOLD, QUIN, VNDP, and YELL) that were constrained to within 1 cm of ITRF97 locations and velocities.

High uncertainty in many of the local stations is influenced by error associated with the 1990 campaign. Precise International GPS Service (IGS) orbits do not exist for the span covered by the 1990 survey, therefore less accurate broadcast orbits were used. Additionally, poor constellation geometries and short occupation times decreased the accuracy of the campaign. The 1996 and 1999 surveys benefit from precise IGS orbits, increased occupation times, and an improved satellite constellation. Despite the apparent high uncertainty of some sites, significant trends are clearly expressed in time series baselines between sites (Figure 3.7). Uncertainty in the vertical component of deformation is greater than the measured velocities for almost all stations occupied, and is therefore not used in the present analysis.

A profile of the east and north velocity components along an east-west transect across the network highlights anomalous station velocities (Figure 3.8). The east component of most stations is distinctly positive across the network with the exception of site R500, which has a westward velocity that suggests contraction between R500 and BLKF (to the west). A possible explanation for the shortening is given below (section 3.7.1). In addition, 6 of the 24 sites have significant negative north velocity components, whereas most of the stations have little or no northward velocity. The discrepancy at

Table 3.2. Locations, years occupied, and site velocities (relative to local site MUMB) for regional and fiducial GPS stations. GPS sites at Algonquin, Goldstone, Quincy, Vandenberg, and Yellowknife were fixed to within 1 cm of their ITRF97 positions and velocities during processing of 1996 and 1999 data. Fiducial data from Mojave, Richmond, and Westford were used during processing of data collected in 1990 (not shown).

Station Name	ID	Occup. Years		Long.	Lat.	velocities and error (mm/yr)				Correl.
		1996	1999	(° W)	(° N)	E vel.	E σ	N vel.	N σ	
Algonquin	ALGO	X	X	78.071	45.956	6.30	2.04	1.42	0.75	0.57480
Briones	BRIB	X	X	122.152	37.919	-7.43	0.37	10.34	0.45	-0.02724
Columbia	CMBB	X	X	120.386	38.034	-3.05	0.36	2.58	0.45	-0.04235
Cape Mendecino	CME1		X	124.396	40.442	0.72	0.81	27.97	0.93	-0.03013
Farallon Islands	FARB	X	X	123.000	37.697	-19.29	0.37	30.80	0.46	-0.01803
Garlic	GARL	X	X	119.355	40.417	0.97	0.36	-3.62	0.44	-0.03034
Goldstone	GOLD	X	X	116.889	35.425	1.80	0.40	0.97	0.47	-0.14902
Hopland	HOPB	X	X	123.074	38.995	-10.45	0.36	14.85	0.44	-0.00225
Quincy	QUIN	X	X	120.944	39.975	-3.30	0.40	1.28	0.46	-0.02124
Shinn	SHIN	X	X	120.225	40.592	-0.13	0.37	-2.35	0.44	-0.02538
Tungsten	TUNG	X	X	118.257	40.403	1.45	0.37	-4.58	0.44	-0.05342
Vandenberg	VNDP	X	X	120.616	34.556	-23.33	0.37	28.44	0.50	-0.03414
Yreka	YBHB		X	122.711	41.732	3.05	0.74	0.28	0.93	-0.10332
Yellowknife	YELL	X	X	114.480	62.481	3.72	0.38	-4.26	0.70	0.14987
TOTAL SURVEYED		**12**	**14**							

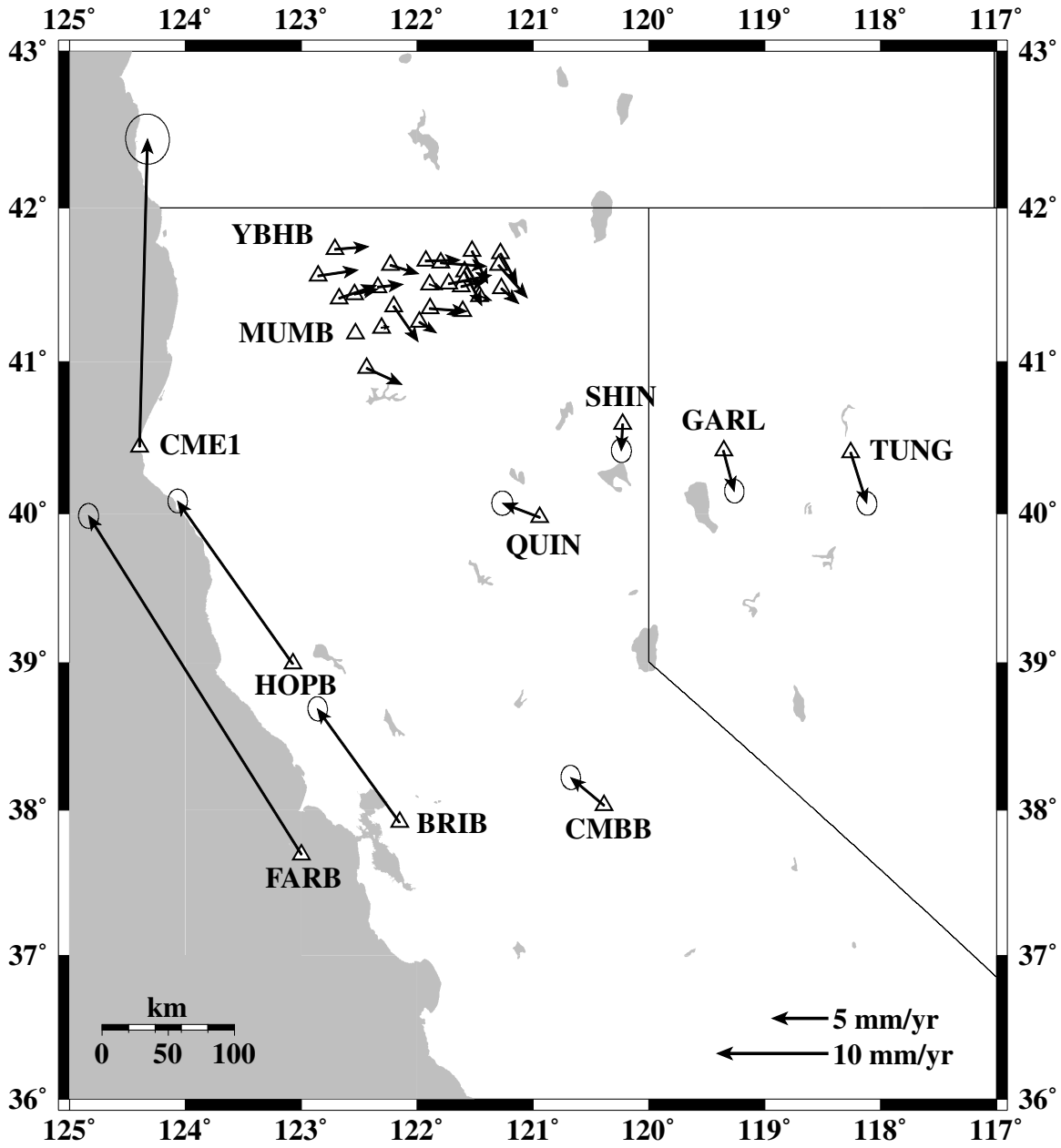

Figure 3.6. Local and regional GPS station velocities. Latitude is given in degrees north, and longitude in degrees west. All velocities are relative to MUMB. Error ellipses show 2-sigma confidence intervals and are ommitted from local stations for clarity (see Figure 3.5 for local station velocities). QUIN is an IGS station, while SHIN, GARL, and TUNG are part of the NBAR network [*Bennett et al.,* 1998]. All other sites shown are part of the BARD network [*Murray and Segall,* in press]. Regional site velocities (given in Table 3.2) agree with velocities for the same sites published by other authors [e.g. *Bennet et al.,* 1998; *Murray and Segall,* in press].

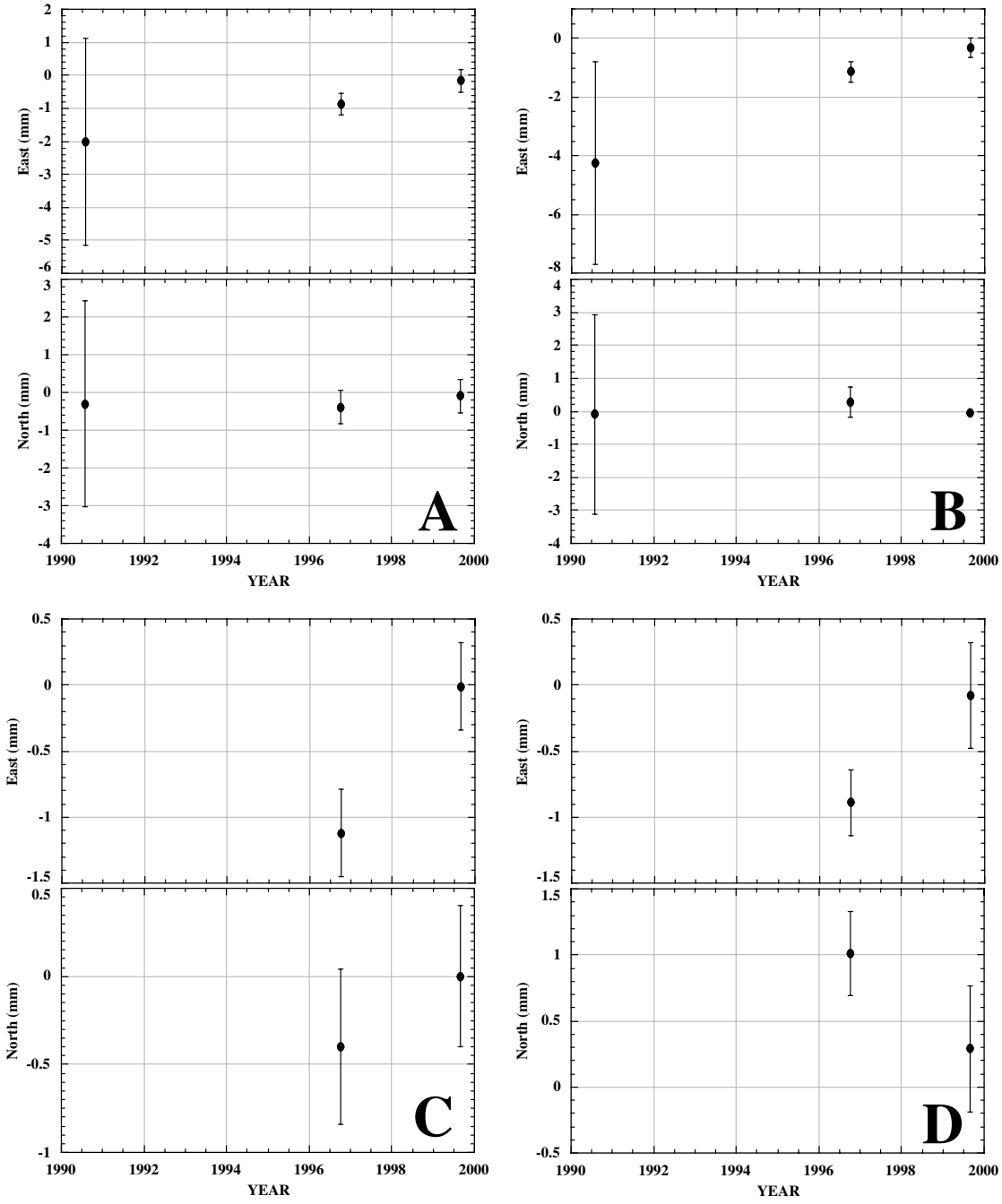

Figure 3.7. Time evolution of four local baselines in the Medicine Lake GPS network. (a) MUMB - P501 (b) MUMB - VANB (c) MUMB - DOEP (d) MUMB - TIMB. Because no sites continuously recorded data during all 3 surveys, site positions were averaged to obtain a single coordinate for each campaign, which are shown above. Uncertainties are based on RMS error from individual occupations of each site.

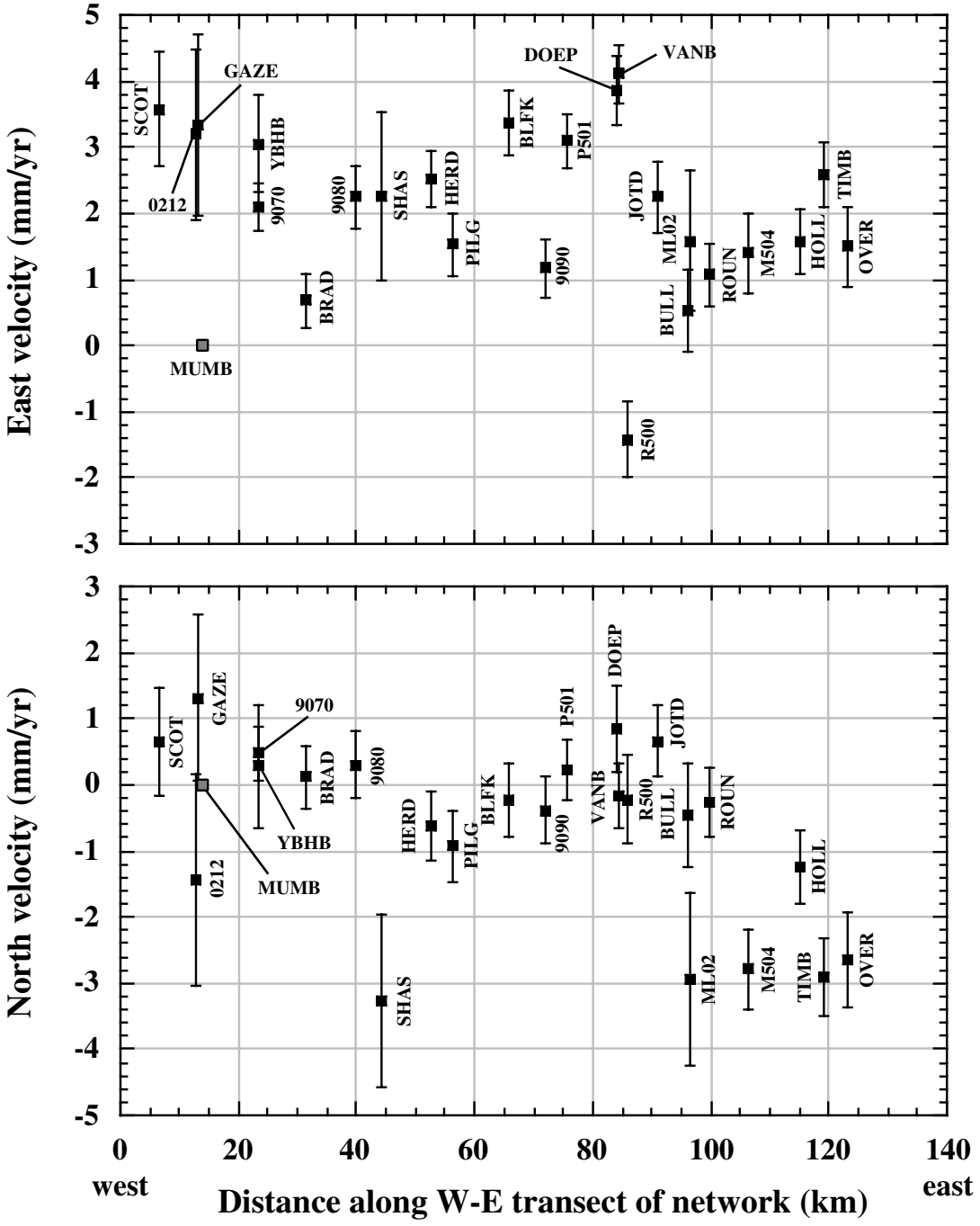

Figure 3.8. East and west velocity components of local sites in the Medicine Lake GPS network with distance along an E-W transect of northern California. Velocities are relative to MUMB (shaded gray) which is held fixed. Several anomalous displacements are apparent (including the east component of R500 and the north components of SHAS, ML02, M504, TIMB, HOLL, and OVER) and are discussed in the text.

SHAS may be related to a local deformation source associated with the Mt. Shasta volcanic system (the benchmark is only ~3 km from the summit of the volcano. Clearly, additional data is necessary to characterize deformation around the Cascade stratovolcano, and recent GPS surveys by Dr. Susan Owen (University of Southern California) may help to isolate deformation restricted to Mt. Shasta. The displacement of ML02, near the center of MLV caldera, is probably influenced by subsidence of the volcano. Finally, sites M504, HOLL, TIMB, and OVER seem to be affected by dextral shear on a northward extension of the Walker Lane - ECSZ system, which *Miller et al.* [2001b] and others suggest traverses northeastern California.

3.7 Modeling and Discussion

Models of crustal deformation around MLV must address several possible source mechanisms (described in section 3.5). As a result, a variety of analysis techniques are required. Analytical methods are useful for modeling crustal flexure due to the load of a volcanic edifice on the crust [e.g. *Brotchie and Silvester*, 1969; *Brotchie*, 1971] as well as transient deformation due to faulting [e.g. *Wernicke et al.*, 2000]. Crustal displacements due to magma chambers and faults are approximated by Mogi sources of volume change [*Mogi*, 1958] and rectangular dislocations with uniform slip [*Okada*, 1985] in an elastic half space. Finally, numerical modeling (finite and boundary element methods) is a versatile technique for investigating problems that involve complex geometries or loading conditions (for instance, downsagging due to subvolcanic intrusions). The methods have been successfully applied to crustal deformation problems in volcanic regions by several authors [e.g. *Dieterich and Decker*, 1975; *Cayol and Cornet*, 1998]. Because most of the models presented below are of axisymmetric problems, it is useful to display the measured crustal displacements with radial distance from the summit of MLV. Figure 3.9 plots

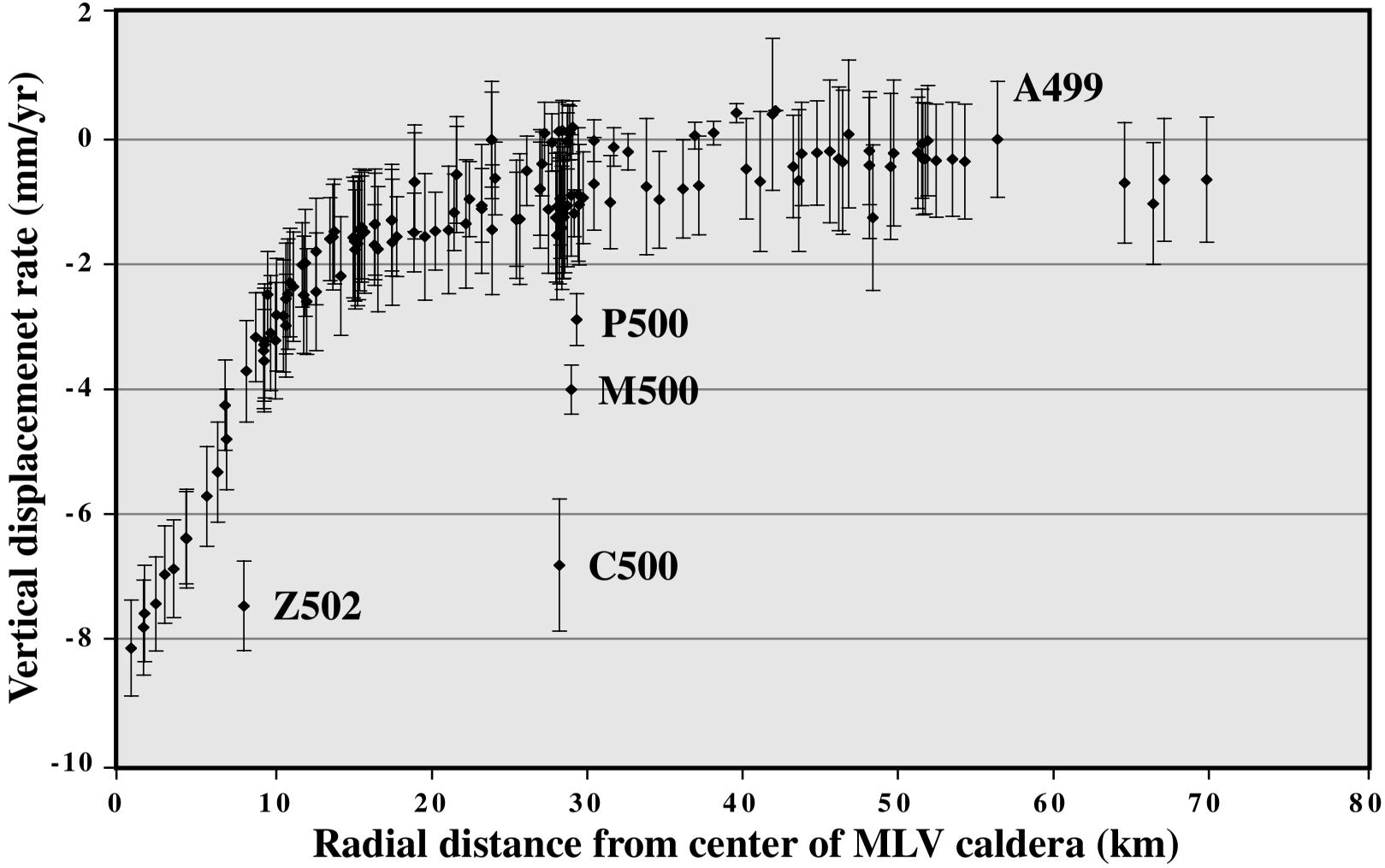

Figure 3.9. Plot of vertical displacements from leveling with radial distance from MLV (latitude 41.59, longitude -121.58). All displacements and 2-sigma error bars are relative to A499,which is held fixed. Benchmark Z502 was likely disturbed by logging activity, and marks C500, M500, and P500 were probably displaced by faulting [*Dzurisin et al.,* in review].

vertical displacements from leveling against distance from MLV, and Figure 3.10 is the same for the horizontal component of deformation that is radial to MLV as determined from GPS.

3.7.1 Anomalous Velocity of Site R500

The horizontal velocity site R500 is not consistent with nearby stations in the GPS network and shows a significant component of shortening (4-5 mm/yr) relative to the neighboring site BLKF. Analysis of data from R500, which was occupied in 1990, 1996, and 1999, suggests that the velocity of the station is not a product of high scatter or other sources of error. Normal faults are abundant around MLV and recent seismicity suggests crustal extension in the region, therefore the contraction associated with R500 is unexpected.

A possible explanation for the anomalous velocity at R500 is the viscous response of the lower crust / upper mantle to perturbation caused by a normal fauting event [*Wernicke et al.*, 2000]. Contractional strain transients in extensional tectonic settings have previously been modeled using a layered, one-dimensional approximation of the crust that consists of an elastic upper plate (upper crust) overlying a viscous lower plate (lower crust or mantle), both on top of a rigid substrate (Figure 3.11, inset). During a normal fault earthquake, elastic strain is released in the upper plate, causing a perturbation in the lower crust / mantle [*Wernicke et al.*, 2000]. As a result, a contractional wave is created which moves away from the fault plane and decreases in magnitude with time. The model, derived by *Elsasser* [1969] and *Bott and Dean* [1973], can be quantitatively expressed as:

$$V_h = \frac{U_o}{t\sqrt{\pi}} \frac{x}{2\sqrt{\kappa t}} e^{-x^2/4\kappa t} \qquad (3.1)$$

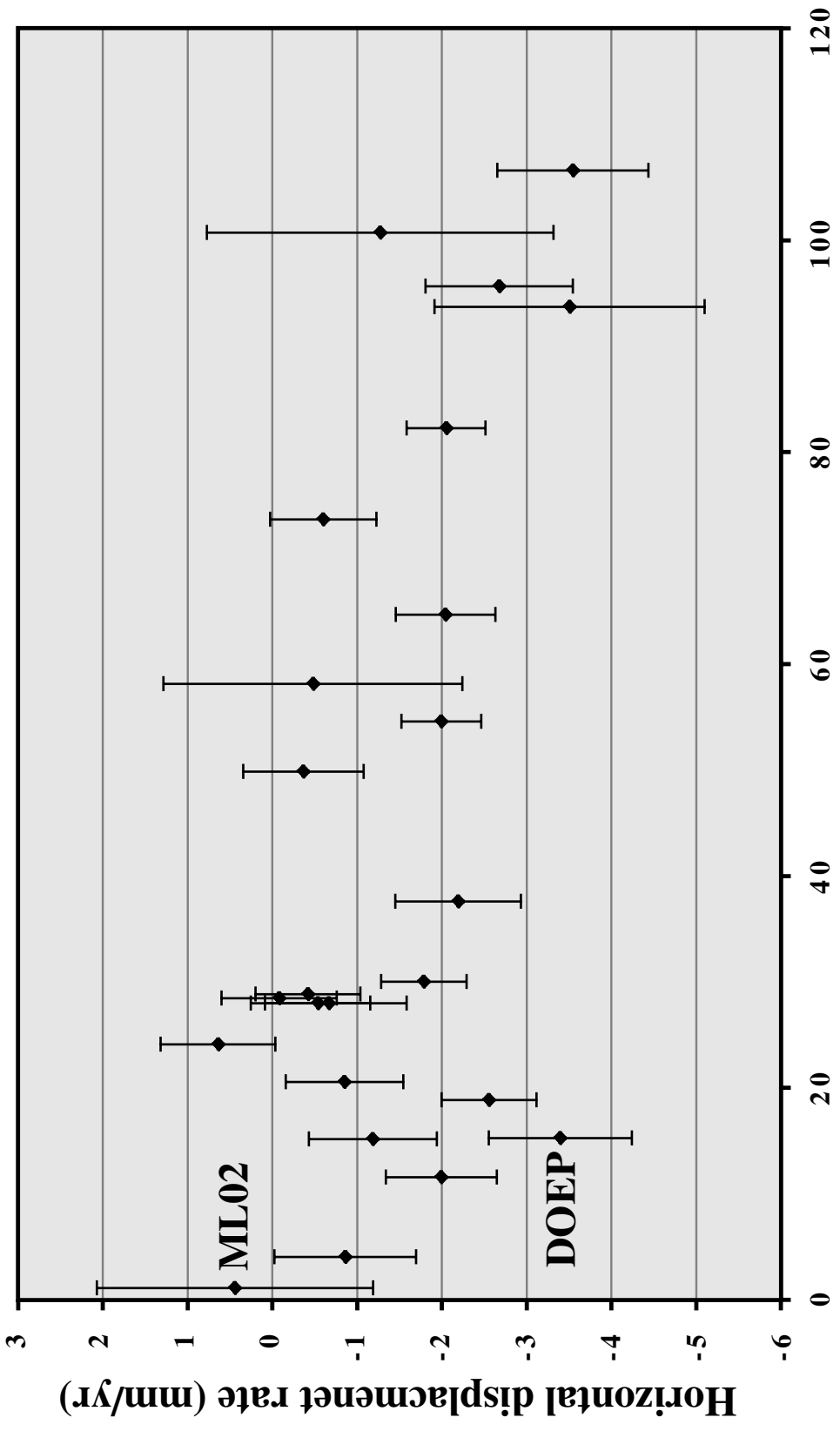

Figure 3.10. Plot of the radial component of horizontal displacements from GPS with radial distance from MLV (latitude 41.59, longitude -121.58). Deformation due to dextral shearing east of MLV has been subtracted from the dataset (see text). All displacements and error are relative to MUMB, which is held fixed. Negative displacements are towards MLV caldera.

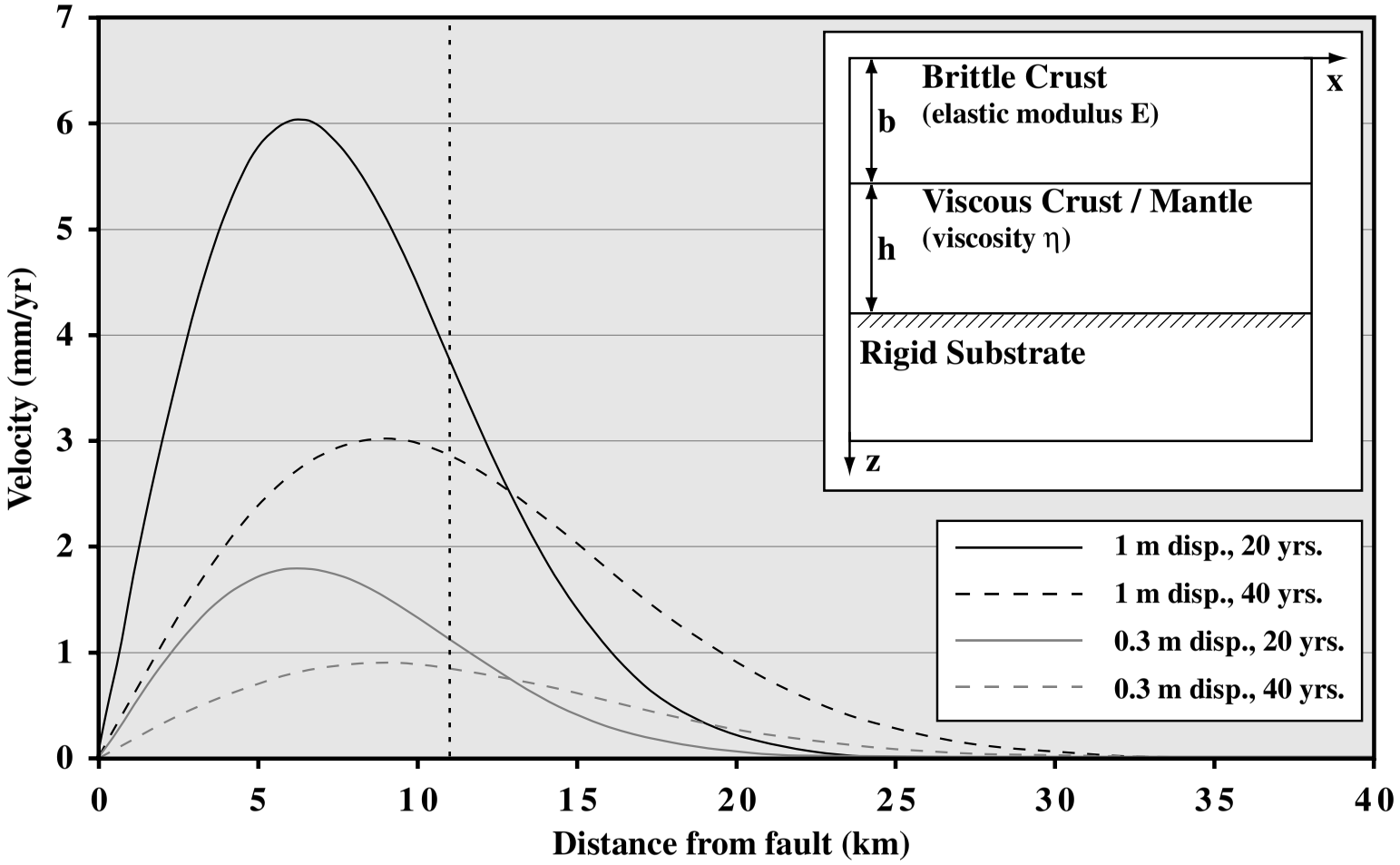

Figure 3.11. Horizontal surface velocities at 20 and 40 years following normal fault displacments of 1 and 0.3 m, predicted by a model including brittle crust overlying a viscous upper crust / mantle. Velocities are perpendicular to the trend of the fault. Positive slopes indicate extension and negative suggest shortening. Dotted line at ~11 km is the distance from the fault modeled by *Dzurisin et al.* [in review] to GPS site R500. Inset shows model geometry (variables are defined in the text).

where U_o is the 1/2 the horizontal dilation caused by the faulting, x is the horizontal distance from the fault, t is time, and κ is the diffusivity ($\kappa = Ebh/\eta$ where b is the thickness of the elastic upper plate with elastic modulus E, and h is the thickness of the viscous lower plate with viscosity η).

Foulger et al. [1992; 1996] applied the model to explain transient strains near Krafla volcano in northern Iceland. Krafla was the site of repeated episodes of dike intrusion between 1975 and 1984, resulting in several meters of widening [*Foulger et al.*, 1992]. GPS surveys in 1987 and 1990 revealed continued widening at a rate far greater than that of background plate spreading. The horizontal displacements from GPS are best explained by the viscous response of the lower plate in a layered model 11 years after dike intrusion. *Wernicke* [2000] applied the same model to an anomalous GPS velocity from the Basin and Range province. A GPS site in central Nevada showed shortening at ~2 mm/yr, which should cause thrust faulting within a few thousand years. A normal faulting event that occurred 60 km away with a horizontal dilation of 4 meters in about the year 1900 may explain the measured strain transient using the model described by equation 3.1 [*Wernicke et al.*, 2000].

Dzurisin et al. [in review] modeled leveling data from MLV and found evidence for normal faulting approximately 11 km to the west of R500. The best fitting dislocation included a fault with a dip of 45 degrees to the east and a displacement of 0.41 ±0.02 m. The event must have occurred between 1954 and 1989 (the years between the leveling survey), however no seismicity that suggests surface faulting was recorded in the region during the time span [*Dzurisin et al.*, in review]. Seismic monitoring in the area was sparse between 1954 and 1980, therefore earthquake swarms that occurred during that time period may gone undetected [*Dzurisin et al.*, 1991]. The displacement of the model fault of *Dzurisin et al.* [in review] would cause ~0.3 m of horizontal dilation. MLV lies on the

western edge of the Basin and Range, therefore elastic and viscous plate thicknesses of 15 km each, and a lower plate viscosity of 5×10^{19}, are assumed (consistent with values from the Basin and Range [*Wernicke et al.*, 2000]). The crust in the MLV region is probably weaker than other regions due to higher heat flow from magmatic intrusions, therefore a relatively low elastic modulus of 7×10^{9} is used.

The horizontal velocities predicted by the layered crustal model due to 0.3 m of horizontal dilation at 20 and 40 years before the GPS measurements (averaged to 1995) are shown in Figure 3.11. Both models predict shortening at a distance of ~11 km (as indicated by negative slopes). However, the magnitude of the contraction is far less than observed. A horizontal dilation of at least 1 meter, 20 years prior to the GPS measurements (Figure 3.11), is required to cause the measured shortening (a greater horizontal displacement more than 20 years prior would also fit the data). Despite the sparse seismic monitoring prior to ~1980, an earthquake with 1 meter of horizontal dilation would have a significant magnitude ($M > 6.0$) and should have been detected [*E. Garnero*, personal communication]. The difference between the predicted fault displacement of *Dzurisin et al.* [in review] and that required by the viscous response model is probably due to the simplicity of both the models and the lack of geologic data to constrain the faulting event. Future GPS occupations should indicate a gradual decrease in the magnitude of contraction between R500 and BLKF as the transient strain dissipates (assuming the contraction is due to a past earthquake). Additional modeling of such data may be used to estimate the rheological conditions of the crust and mantle in northeastern California, as well as to constrain the timing of the probable fault slip. Similar transient strain may also be occurring near sites of confirmed normal faulting in 1978 (Stephens Pass earthquake swarm) and 1981 (Tennant earthquake swarm). Although the GPS data do not indicate anomalous horizontal displacements near the faults, it is important to note that deformation

due to past faulting may be influencing deformation around MLV and should be considered as a subject of future research.

3.7.2 Shear from the Walker Lane / ECSZ System

In the eastern portions of the GPS network, horizontal displacements are a function of both deformation related to MLV (which is manifested vertically as subsidence) and dextral shear, probably resulting from aseismic creep on faults related to a northern extension of the Walker Lane - ECSZ system. Models of deformation at MLV must therefore explain both the tectonic shear and the subsidence. To account for the shear, GPS data collected in this study and leveling data collected by *Dzurisin et al.* [in review] are inverted for a strike-slip dislocation that is constrained to have a 90° dip and is several thousand kilometers long and deep (to minimize edge effects). The best fitting dislocation trends approximately N45W at a distance of 50 km east of MLV with a right-lateral displacement of about 6 ± 1 mm/yr (model parameters and results are given in Tables 3.3 and 3.4, respectively). The residual velocity field (Figure 3.12) shows little shear outside 95% confidence east of MLV and illustrates the effects of MLV subsidence on GPS stations that surround the caldera (note station velocities that are radially toward the summit caldera).

The modeled slip rate for the Walker Lake - ECSZ system east of MLV agrees with existing models of dextral shear in northeastern California. Generally, modeled right-lateral displacements decrease with distance northward from the Mojave Desert in eastern California [*Sauber et al.*, 1994; *Dixon et al.*, 1995b; *Dixon et al.*, 2000; *Miller et al.*, 2001a; *Oldow et al.*, 2001], reaching 8 ± 3 mm/yr in the vicinity of the Honey Lake fault zone [*Dixon et al.*, 2000], ~120 km south of MLV (Figure 3.3). The modeled dislocation east of MLV is along strike with the Likely Fault, one of several NW-striking dextral faults

Table 3.3. Dislocation and Mogi source geometries for inversions of GPS and leveling data. Inversion results are given in Table 3.4. Dip is degrees from horizontal.

Model Parameter	Lat. (°N)	Long. (°E)	Depth (km)	Length (km)	Width (km)	Dip (deg)	Strike (deg)
Dislocation (Fault)	49.800-32.400	225.900-248.900	3050.0	2500.0	3000.0	90	315
Mogi	41.590	238.420	10.0	-	-	-	-
Dislocation (Sill)	41.566-41.637	238.441-238.590	11.0	10.3	4.4	0	221

Table 3.4. Modeling results for MLV deformation. WRSS = weighted residual sum of squares, N-P = degrees of freedom. GPS and leveling data are inverted for 1) a right-lateral dislocation east of MLV only, 2) a right-lateral dislocation east of MLV and the best-fitting Mogi source of *Dzurisin et al.* [in review], and 3) a right-lateral dislocation east of MLV and the best-fitting sill source of *Dzurisin et al.* [in review]. The best-fitting model (characterized by the lowest WRSS/(N-P)) includes a right-lateral dislocation east of MLV and a Mogi source beneath the volcano.

Model	Fault Slip (mm/yr)	Vol. Change (km3)	WRSS	WRSS/(N-P)
Dextral Shear Only	5.5 ±0.7 (right lateral)	-	4410.91	19.34
Dextral Shear & Mogi Source	6.2 ± 0.7 (right lateral)	-0.0030 ± 0.0001	3371.72	14.85
Dextral Shear & Sill Source	5.6 ± 0.7 (right lateral)	-0.0020 ± 0.0001	3395.38	14.96

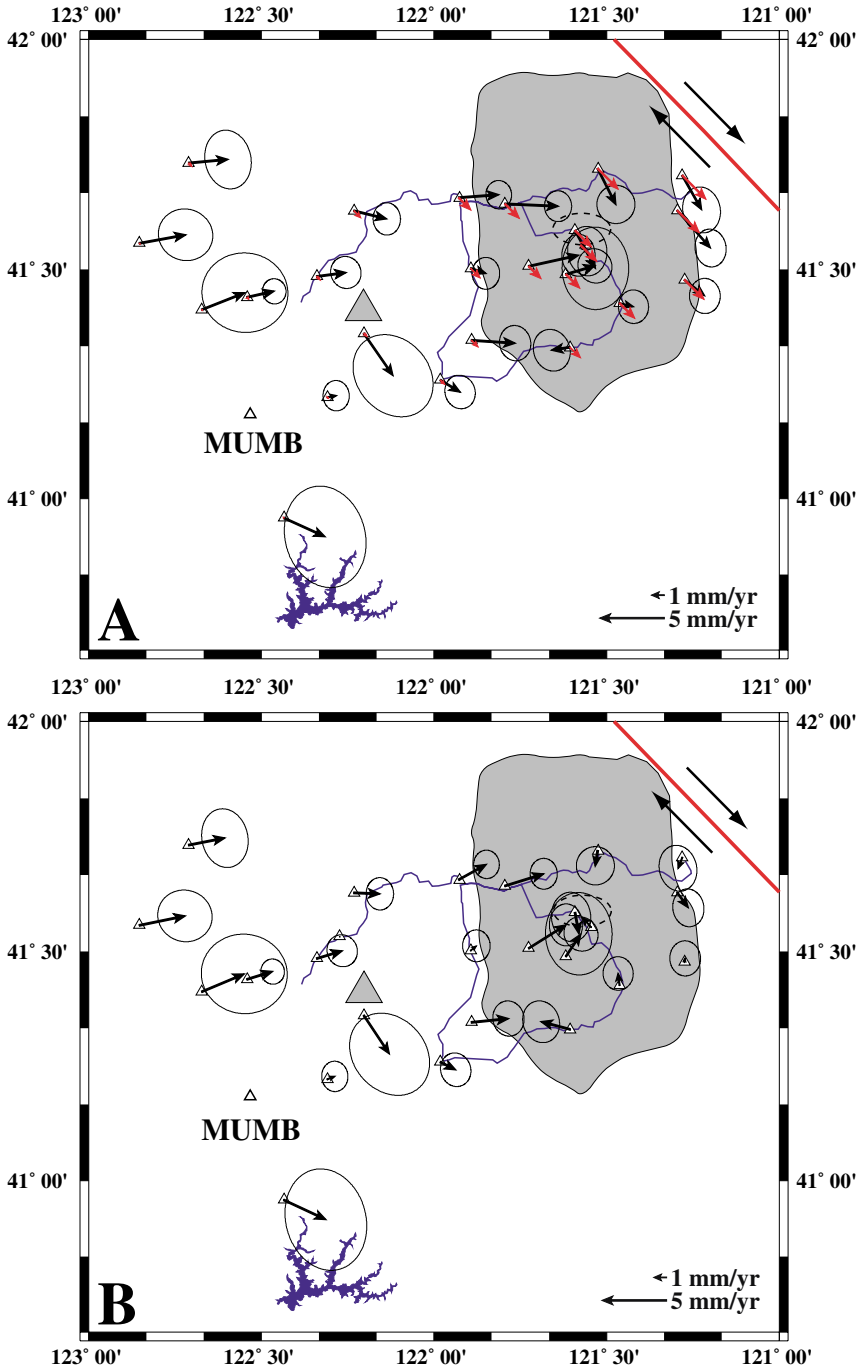

Figure 3.12. Model of GPS site velocities that includes a right-lateral dislocation east of MLV. Longitude is in degrees west and latitude in degrees north. The aerial extent of MLV is shaded gray, and MLV caldera is outlined by a dashed line. Mt. Shasta is shown as a gray triangle, and the dislocation is represented by a red line. MLV-area leveling lines are shown in blue. All velocities are relative to MUMB. (a) Observed (black arrows with 2-sigma error ellipses) and modeled (red arrows) site velocities. (b) Residual velocities (observed minus modeled).

between Lassen Peak and Newbery volcano in Oregon [e.g. *Hannah*, 1977; *Pezzopane and Weldon II*, 1993]. Based on geologic evidence, several workers have noted that right-lateral shear is occurring in NE California [e.g. *Pease*, 1969; *Lawrence*, 1976; *Wright*, 1976; *Hannah*, 1977; *Roberts and Grose*, 1984; *Roberts*, 1985; *Bryant*, 1991; *Page et al.*, 1993; *Pezzopane and Weldon II*, 1993]. Limited geodetic data collected from previous studies from the region agrees with the geologic studies [e.g. *Miller et al.*, 2001b]. However, *Potter* [1988] finds no evidence for dextral displacements on the northern portion of the Likely fault. GPS stations established in 1999 transect the northern tip of the fault, therefore future campaigns are necessary to model the contribution of the fault to lateral shearing in NE California. Regardless, preliminary models presented above suggest that dextral shearing is an important process in NE California, and that the Likely fault is a probable surficial manifestation of the deformation.

3.7.3 Volume Loss at Depth

Volume loss from a source at depth below MLV caldera (Figure 3.4A) is modeled by both a sill (approximated as an opening dislocation with a dip of 0°) and a Mogi point source of volume change. The best fitting sill and Mogi source geometries of *Dzurisin et al.* [in review], in addition to the dextral dislocation described above, are used in an inversion of both GPS and leveling data. Model parameters are given in Table 3.3, while results are listed in Table 3.4. The best-fitting Mogi source (Figure 3.13) has a volume change of -0.0030 ± 0.0001, while the best-fitting sill source (Figure 3.14) has a volume change of -0.0020 ± 0.0001, essentially the same as the model sill and Mogi of *Dzurisin et al.* [in review]. Both models fit the leveling data of *Dzurisin et al.* [in review] equally well (Figure 3.15), but overall the Mogi model has a slightly better fit to the combined GPS and leveling datasets (Table 3.4). GPS measured displacements in the vicinity of MLV caldera

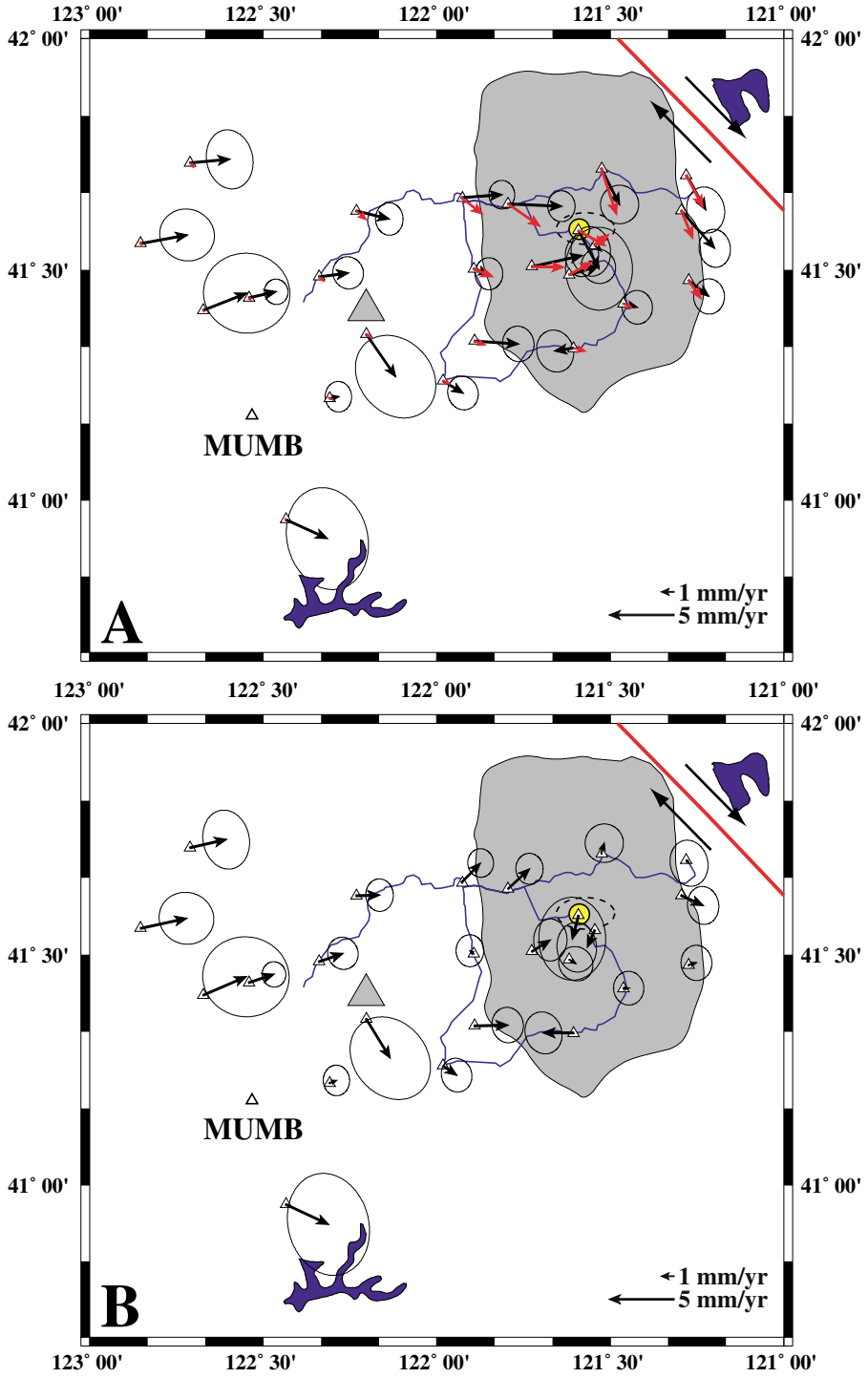

Figure 3.13. Model of GPS site velocities including a right-lateral fault east of MLV and a Mogi source of volume loss (yellow circle) at 10 km depth beneath MLV caldera. Latitude is in degrees north and longitude in degrees west. See Figure 3.5 for other symbol definitions. (a) Observed (black arrows with 2-sigma error ellipses) and modeled (red arrows) site velocities. (b) Residual site velocities.

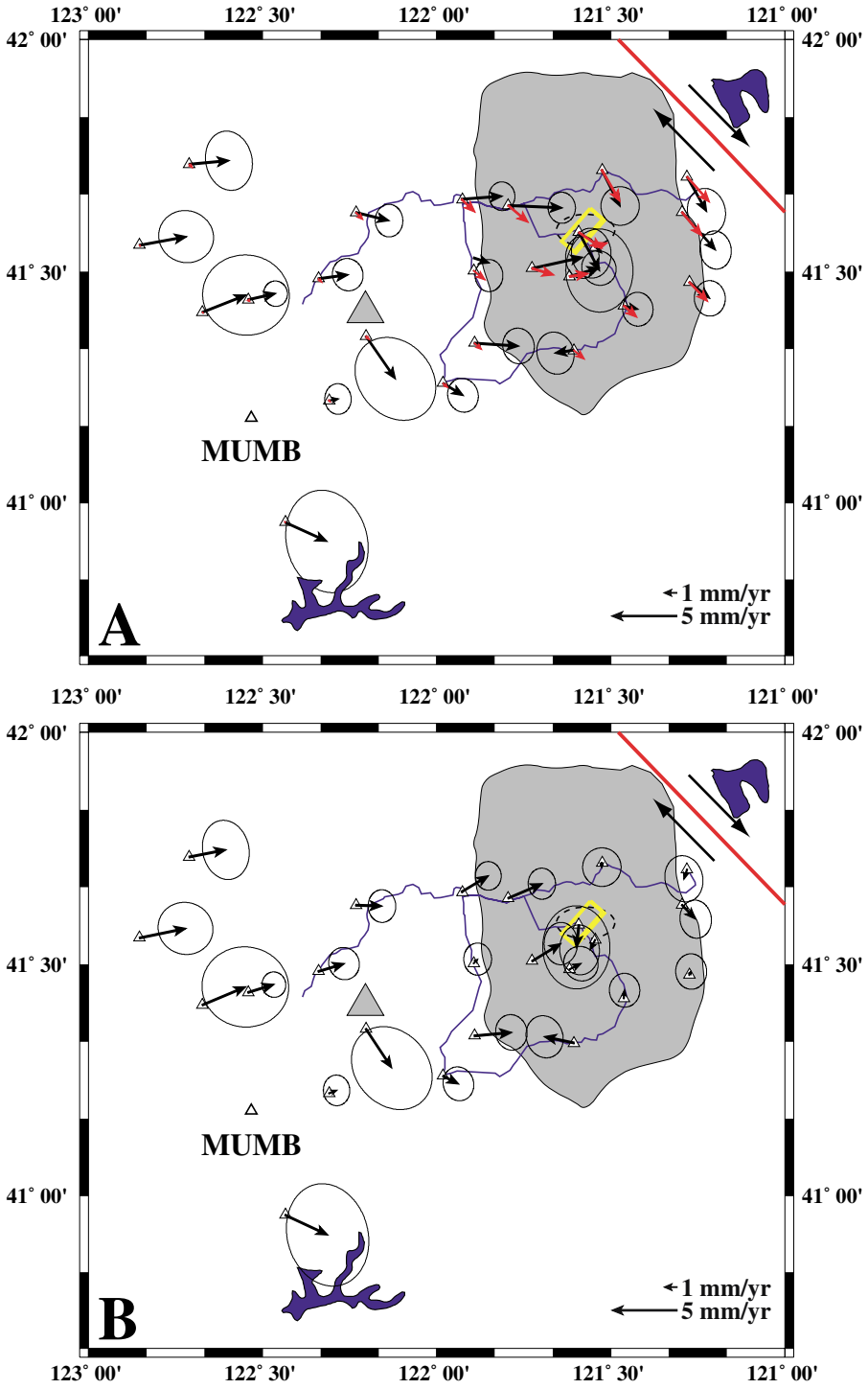

Figure 3.14. Model of GPS site velocities that includes a right-lateral fault east of MLV and a deflating sill (yellow box) at 11 km depth beneath MLV caldera. Latitude is in degrees north and longitude in degrees west. See Figure 3.5 for other symbol definitions. (a) Observed (black errors with 2-sigma error elllipses) and modeled (red arrows) site velocities. (b) Residual site velocities.

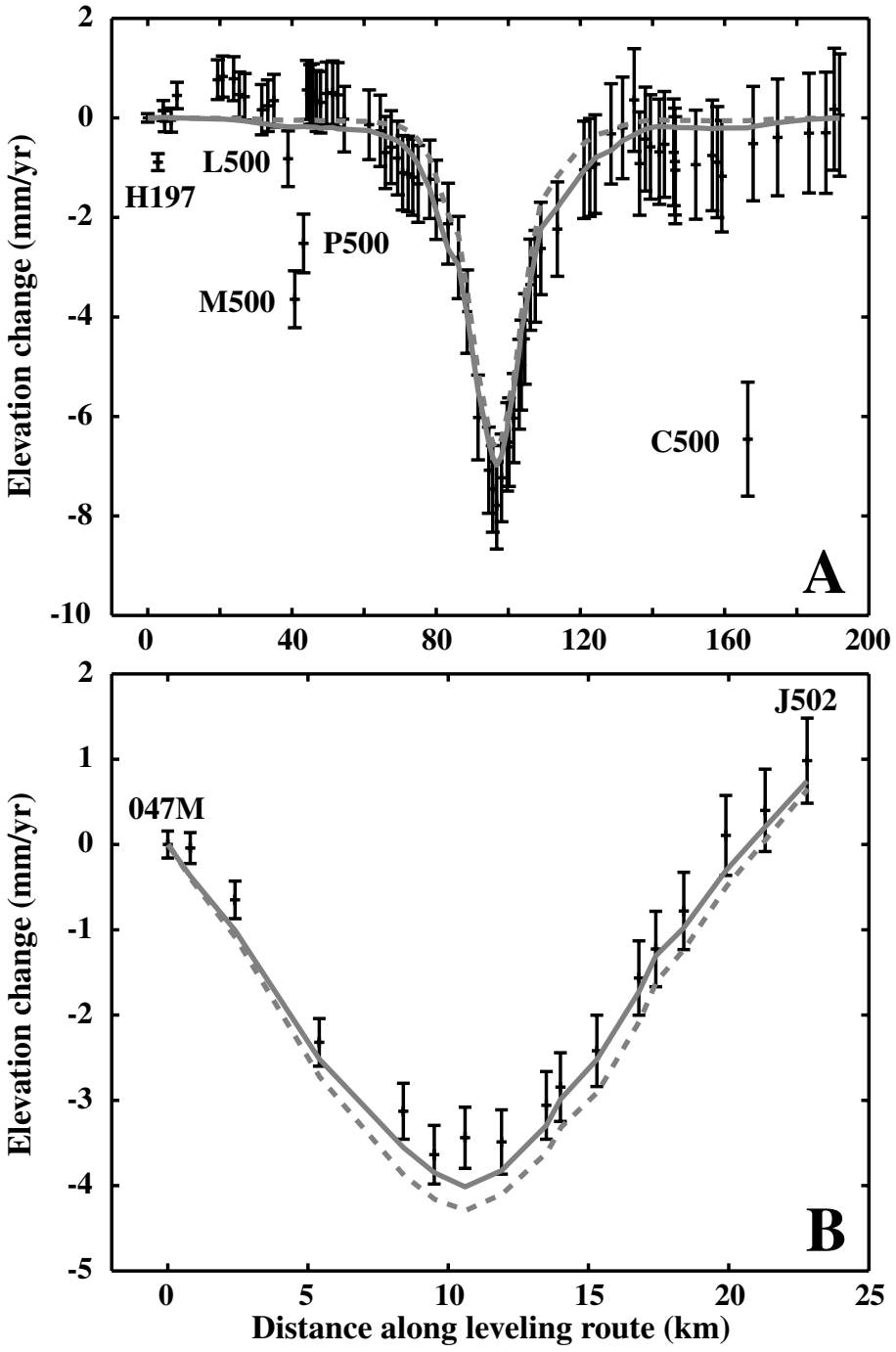

Figure 3.15. Profiles of vertical displacements from leveling data with best fitting Mogi (solid line) and sill (dashed line) models. Data is from *Dzurisin et al.* [in review]. Benchmarks are labeled and shown in map view in Figure 2.1. (a) 1954-1989 leveling circuit (displacements of C500, M500, P500, and L500 was probably caused by unmodeled faulting). (b) 1989-1999 summit portion of leveling circuit. (c) 1954-1990 western portion of leveling traverse. (d) 1954-1990 eastern portion of leveling traverse.

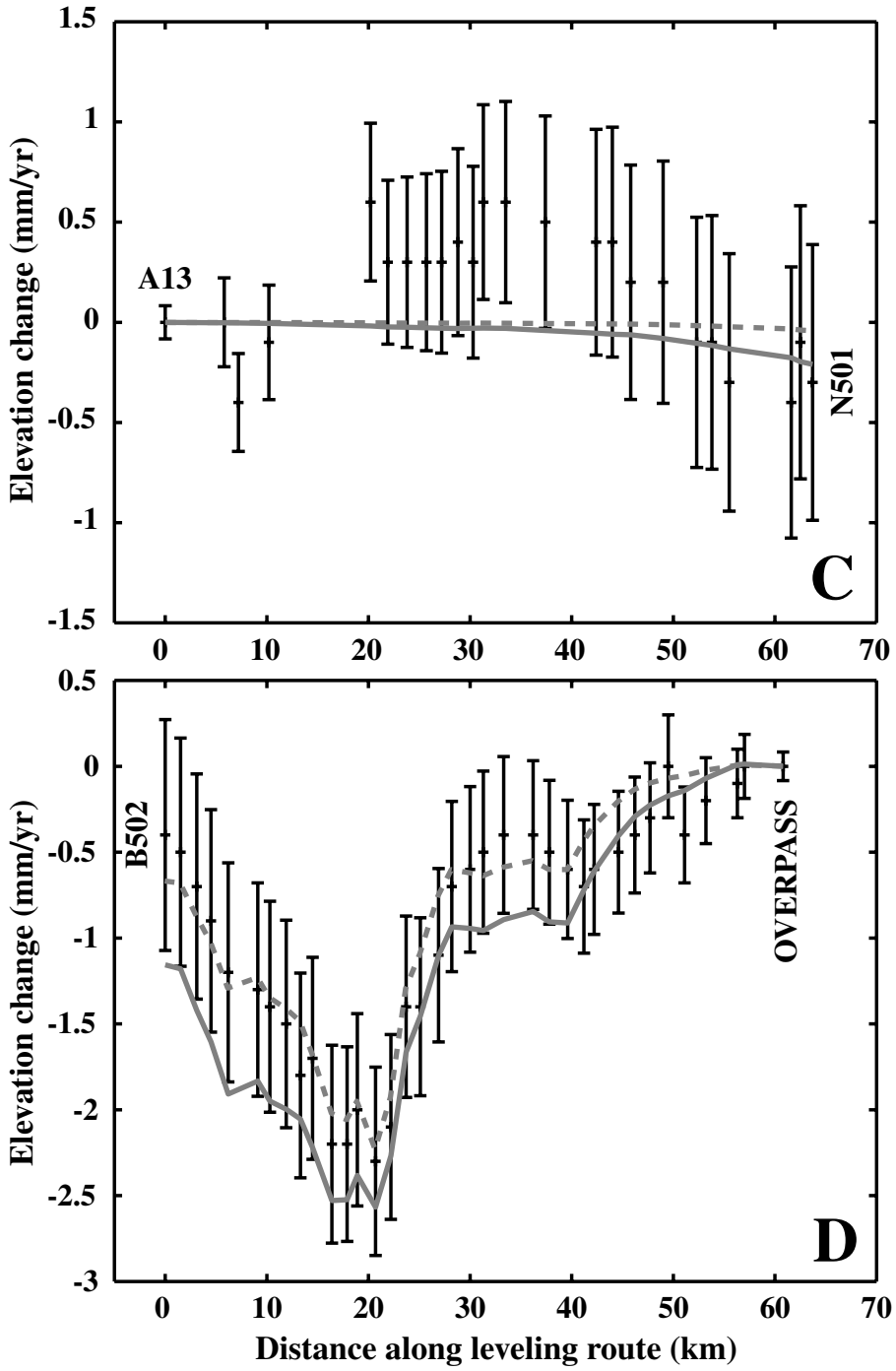

Figure 3.15. (Cont.)

are not well approximated by either model, though volume loss at depth does seem to account for some of the observed deformation (see residual velocity plots in Figures 3.13 and 3.14). Below, two possible causes of volume loss at depth are evaluated in further detail based on model results.

3.7.3.1 Magma Withdrawal. Previous studies of volcanic subsidence have found that magma withdrawal from a shallow chamber is accurately modeled by a Mogi source of volume loss. After the 1991 eruption of Hekla volcano in Iceland, displacements radially towards the summit of the volcano were measured by GPS [*Sigmundsson et al.*, 1992]. *Sigmundsson et al.* [1992] interpret the signal as resulting from deflation of a subvolcanic magma chamber due to the expulsion of magma during the eruption. Similar measurements and interpretations have also been made in Hawaii [e.g. *Delaney and McTigue*, 1994].

Volume loss from a subsurface chamber is probably not a result of a past eruption at MLV. The most recent eruptive event was the extrusion of ~1 km^3 of rhyolite lava from Glass Mountain approximately 1000 years B.P. [*Donnelly-Nolan et al.*, 1990]. Elastic models, including those presented above, cannot account for deformation that is time-dependent. However, even in a model including a viscoelastic shell around a deflating magma chamber [*Newman et al.*, 2001], the high subsidence rate cannot be explained by volume loss during the most recent eruption [*T. Dixon*, personal communication]. In addition, geophysical surveys of the volcanic basement have not detected any active or recently active magma bodies at the 10 km depth required by the models. As a result, a model that relies on draining of a shallow magma chamber into a deeper reservoir is not supported, and magma withdrawal is probably not the primary cause of subsidence at MLV.

3.7.3.2 Cooling and Crystallization of Magma. Cooling and crystallization of a magma body will lead to thermal contraction and net volume loss [*Fournier*, 1989]. At the surface, the volume loss will be manifested by subsidence similar to that observed at MLV [*Dzurisin et al.*, 1991]. Several authors have suggested thermal contraction as a subsidence mechanism at recently active volcanoes. Deformation of Krafla volcano, Iceland, has been measured by SAR interferometry and shows subsidence with a rate that is decreasing with time. *Sigmundsson et al.* [1997] model the subsidence as volume loss from a Mogi source at 3 km depth. Krafla's last eruptive episode was 1975-1984, and cooling of the magma chamber associated with the event is a likely explanation for the deformation [*Sigmundsson et al.*, 1997]. Similarly, deflation of Askja volcano, also in Iceland, has also been attributed to thermal contraction of a recently active magma body [*Sturkell and Sigmundsson*, 2000]. Askja last erupted in 1961, and leveling measurements conducted since 1983 combined with GPS data from 1993 and 1998 indicate subsidence that is decreasing with time. *Sturkell and Sigmundsson* [2000] find that the best fit to the displacements is a Mogi source of volume loss at a depth of 2.8 km, which agrees with previous models of Askja deflation based on other datasets. Clearly, thermal contraction may be accurately modeled by deflating Mogi sources.

Fournier [1989] notes that crystallization of 0.2 km^3 of rhyolitic magma causes a volume contraction of 0.014 km^3, assuming that the aqueous-rich magmatic fluids escape to a shallow hydrothermal system during cooling of the pluton. Based on models of volume loss at MLV (Table 3.4), volume contractions of 0.0020 km^3/yr (sill) and 0.0030 km^3/yr (Mogi) may be caused by the crystallization of 0.0286 km^3/yr and 0.0429 km^3/yr of magma, respectively. In comparison, the predicted volume of crystallization at Krafla is between 0.013 km^3/yr (1992-1993) and 0.005 km^3/yr (1993-1995) [*Sigmundsson et al.*, 1997], and at Askja averages 0.0156 km^3/yr between 1983 and 1998 [*Sturkell and*

Sigmundsson, 2000]. Although the predicted crystallization volume at MLV compares favorably with volumes determined for Krafla and Askja, a much lower volume is expected at MLV because of the longer time since the most recent eruption. Additionally, no change in the rate of subsidence is measured by leveling that spans two separate time periods (1954-1898 and 1989-1999) [*Dzurisin et al.*, in review], and there is no evidence of a crystallizing intrusion at ~10 km depth beneath MLV (as predicted by the sill and Mogi models). The only possibly molten rock siggested by geophysical data lies at approximately 3-5 km depth [*Chiarabba et al.*, 1995]). For the reasons listed above, thermal contraction due to cooling of a subvolcanic magma body is not a likely source of subsidence at MLV.

3.7.4 Crustal Flexure

As stated earlier, MLV is the largest volcano by volume in the Cascade volcanic arc (up to 750 km^3) [*Dzurisin et al.*, 1991]. The surface load of MLV will undoubtedly cause flexure of the underlying crust (Figure 3.4B), and indeed, at least 500 meters of flexure-related subsidence has been recognized from drill cores that have penetrated the basement beneath MLV [*Dzurisin et al.*, 1991]. Surface loading has been cited as an important deformation mechanism at other large basaltic shields, especially ocean island volcanoes and seamounts. Flexure of the oceanic lithosphere under the load of the Hawaiian island chain is evident from morphological features including the Hawaiian Deep and Arch that surround the archipelago [*Walcott*, 1970]. The topographic low adjacent to the load and topographic high (also known as the "peripheral bulge") at a distance from the load is characteristic of flexure due to loading [*Turcotte and Schubert*, 1982, p. 125]. Similar features have been recognized and modeled as due to surface loads by many other authors [e.g. *Watts et al.*, 1975]. Active subsidence of the Hawaiian islands has been documented

and attributed to surface loading by *Moore* [1971], and is a viable subsidence mechanism at MLV.

Simple analytical models of elastic crustal flexure due to surface loads include both two-dimensional and axisymmetric solutions. *Turcotte and Scubert* [1982, p. 104-133] give a two-dimensional solution for flexure of the lithosphere due to a line load on the crust (for example, a linear mountain range or island chain). In contrast, *Brotchie and Silvester* [1969] and *Brotchie* [1971] present an axisymmetric solution for a load on the surface of a spherical, liquid filled shell. The thickness of the shell is the crustal thickness, while the radius of the sphere corresponds to the planetary radius. The liquid enclosed by the shell approximates a viscous mantle, which may be used to model instantaneous elastic and/or time-dependent viscous deformation due to the application or removal of surface loads [*Brotchie and Silvester*, 1969]. Similar analytical and numerical solutions have been successfully applied to assess the flexural parameters of the lithosphere underlying extraterrestrial volcanoes, including those on the Moon [*Solomon and Head*, 1980; *Comer et al.*, 1985], Mars [*Melosh*, 1978; *Thurbur and Toksöz*, 1978], and Venus [*McGovern and Solomon*, 1997].

Crustal loading at MLV is clearly an axisymmetric process due to the uniform bowl-shaped subsidence determined from leveling benchmarks on all quadrants of the volcano (Figure 3.9). As a result, the elastic solution presented by *Brotchie and Silvester* [1969] and described in detail below is the most appropriate solution for modeling the observed deformation.

When the load is approximated by a point source, the deflection of the lithosphere (w) with distance (x) from the applied load is given by:

$$w = \frac{PL^2}{2\pi D}\,\mathrm{kei}\left(\frac{x}{L}\right) \tag{3.2}$$

in which the P is the magnitude of the load (mass times the gravitational constant), D is the flexural stiffness, L is the radius of relative stiffness. The flexural stiffness is defined as:

$$D = \frac{ET^3}{12\left(1-\nu^2\right)} \tag{3.3}$$

where E is elastic modulus, T is the thickness of the lithosphere, and ν is Poisson's ratio. The radius of relative stiffness is calculated by:

$$L = \sqrt[4]{\frac{D}{\left(\frac{ET}{R^2}+\gamma\right)}} \tag{3.4}$$

where R is the radius of the shell and γ is the density of the mantle times the gravitational constant. In addition to point sources, surface loads may be modeled by cylinders of height H and radius A. The solution for loading by a cylinder has two parts which determine vertical displacements inside and outside the radius of the load [*Brotchie*, 1971]. The deflection (w_i) of the lithosphere within the radius is:

$$w_i = \frac{\rho H}{\gamma + \frac{ET}{R^2}}\left(\left(\frac{A}{L}\right)\mathrm{ker}(A/L)\mathrm{ber}(x/L) - \left(\frac{A}{L}\right)\mathrm{kei}(A/L)\mathrm{bei}(x/L) + 1\right) \tag{3.5}$$

The deflection (w_o) outside the radius of the cylinder is:

$$w_o = \frac{\rho H}{\gamma + \frac{ET}{R^2}}\left(\left(\frac{A}{L}\right)\mathrm{ber}(A/L)\mathrm{ker}(x/L) - \left(\frac{A}{L}\right)\mathrm{bei}(A/L)\mathrm{kei}(x/L)\right) \tag{3.6}$$

where ρ is the density of the loading cylinder. In all of the above equations (3.2-3.6), ber, bei, ker, and kei are Bessel-Kelvin functions of zero order [*Brotchie*, 1971].

At MLV, seismic studies suggest a crustal thickness of ~37 km [*Zucca et al.*, 1986], while gravity evidence indicates a bulk density of up to 2400 kg/m^3 [*Finn and*

Williams, 1982]. The mass of MLV may be approximated by a cylinder of radius 25 km and height 400 m, which simulates the 2000 m^2 area and 750 km^3 volume of the volcano [*Dzurisin et al.*, 1991]. The radius of the earth is taken as 6350 km, while mantle density is assumed to be 3370 kg/m^3 [*Brotchie*, 1971]. Typical values for the elastic modulus and Poisson's Ratio of basalt, as specified by *Turcotte and Schubert* [1982, p. 432], are 7.0 x 10^{10} and 0.25, respectively. Parameters and results from all loading models are given in Table 3.5. The "Standard" model curve in Figure 3.16 shows the shape of the vertical deformation expected from point load with a magnitude equal to the mass of the MLV edifice (all models are normalized to compare curve shapes, because no time-dependent deformation rates are assumed). Subsidence is greatest directly under the point load and decreases with radial distance, transitioning to uplift at ~220 km and reaching a maximum at ~270 km from the applied load. Strengthening (increasing the elastic modulus) or thickening the lithosphere causes the region of maximum uplift to move further away from the applied load, while weakening (decreasing the elastic modulus) or thinning the crust causes the vertical deflection profile to narrow (Figure 3.16).

Treating the load as an axisymmetric cylinder (dashed curve in Figure 3.17) narrows the zone of subsidence predicted by the "standard" model, with uplift beginning at ~100 km and peaking ~150 from the center of the load. A volcano may also be represented by a set of stacked concentric cylinders, which better simulates the morphology and distribution of mass of an edifice. Because the solution is elastic, the deformation is calculated by combining the deflections caused by the individual cylinders [*Comer et al.*, 1985]. However, while stacked cylinder models do best approximate the slope of the observed displacements from leveling, the zone of subsidence is still much broader than observed (dotted curve in Figure 3.17). A stacked cylinder model that fits the measured vertical deformation would require either an elastic modulus several orders of magnitude

Table 3.5. Parameters (elastic modulus and crustal thickness) are results for models of crustal flexure due to point and cylindrical loads. Model curves are plotted in Figures 3.16 and 3.17. The column "Distance to max. uplift" gives the radial horizontal distance from the center of the applied load to the point of maximum uplift on the "arch" at distance from the load. The "Cylindrical" model consists of a cylinder 400 m high and 25 km in radius (approximating the dimensions of MLV) on the crust. All other models are based on surface deflections due to a point load.

Model	Young's Modulus	Crustal Thickness	Maximum Deflection	Maximum Uplift	Distance to max. uplift
Standard	7×10^{10}	37 km	482 m	6.9 m	270 km
Weak	1×10^{7}	37 km	40396 m	567 m	30 km
Strong	1×10^{13}	37 km	35 m	0.5 m	890 km
Thick	7×10^{10}	50 km	280 m	4 m	360 km
Thin	7×10^{10}	20 km	1111 m	15.8 m	180 km
Cylindrical	7×10^{10}	37 km	202 m	5.8 m	150 km

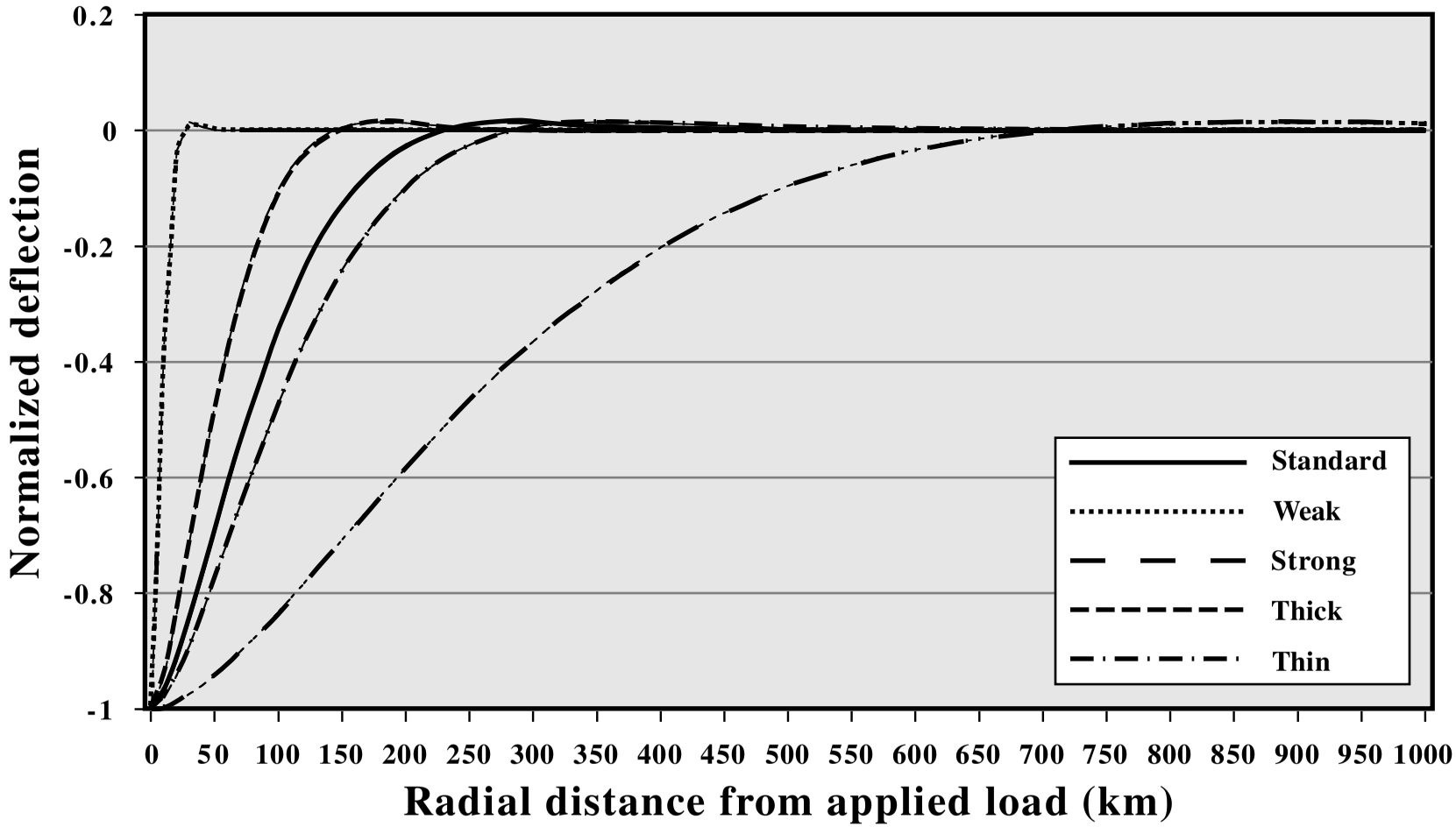

Figure 3.16. Profiles of vertical displacement with radial distance predicted by axisymmetric elastic flexure models. The "standard" model is based on data from MLV, while other models test the effects of varying Young's Modulus ("weak" and "strong") and crustal thickness ("thick" and "thin") on the displacement profiles. Specific model parameters are given in Table 3.5.

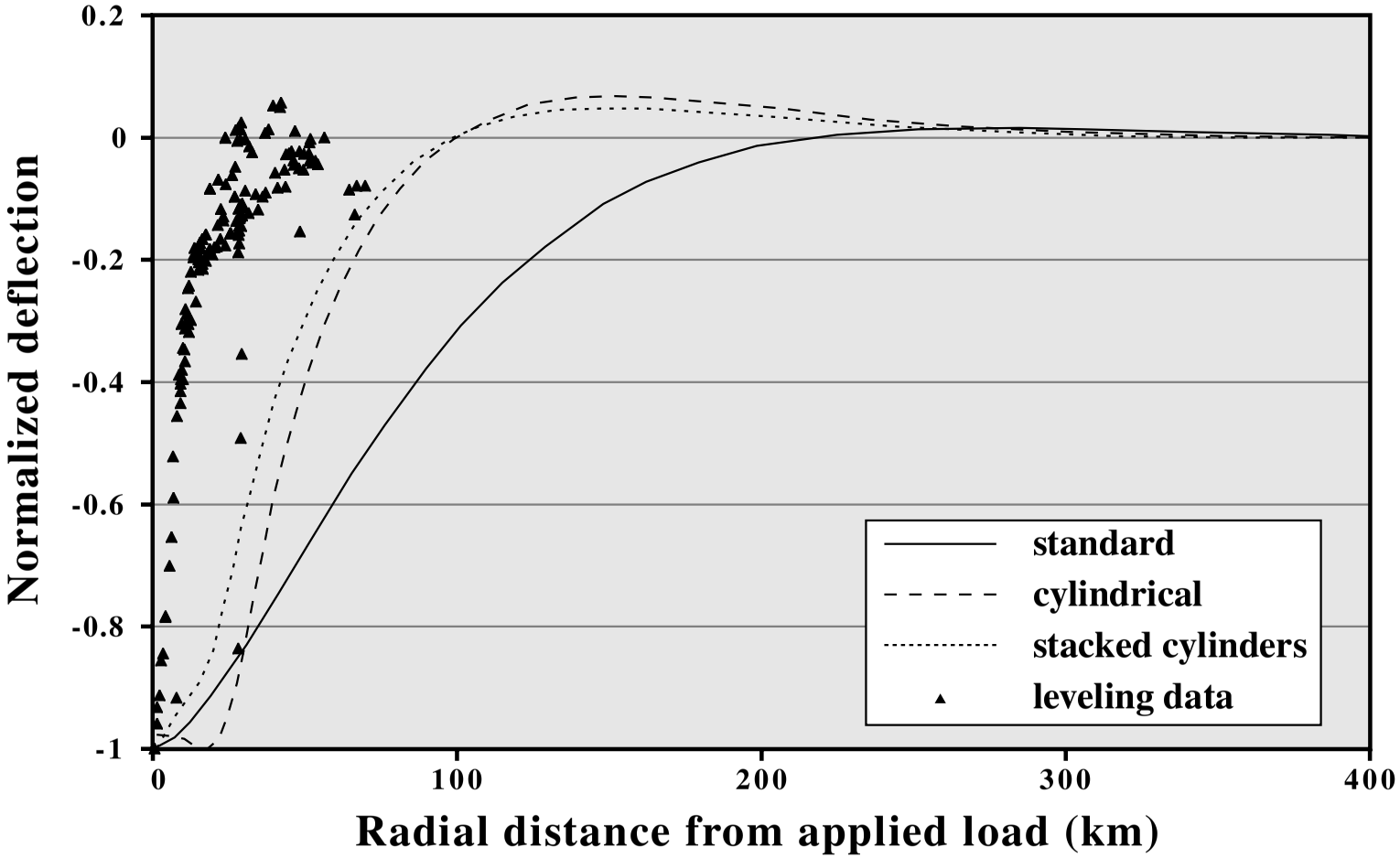

Figure 3.17. Profile of vertical displacements measured from leveling and predicted by elastic flexure models assuming point and cylindrical loads. Displacements are normalized by the maximum subsidence. Parameters for the "standard" and "cylindrical" models are given in Table 3.5. The "stacked cylinders" model uses similar parameters as "cylindrical," but approximates the laod as a set of 4 concentric stacked cylinders (see text). The leveling data is a compilation of all marks described by *Dzurisin et al.* [in review] with radial distance from MLV caldera (see Figure 3.9). Error bars are omitted for

lower than expected (e.g. 1 x 10^7) or an unreasonably thin lithosphere (~20 km). Although geological evidence suggests thermally weakened crust in the MLV region [*Dzurisin et al.*, 1991; *Blakely et al.*, 1997], the weakening required by flexure models is much greater than the elastic modulus for weakened crust in other regions [*Ryan and Sammis,* 1981].

In addition, the subsidence rate a MLV cannot be easily reconciled with a mechanism of flexure due to surface loading. The total loading-related downwarp of MLV inferred from drill cores is 500 meters [*Dzurisin et al.*, 1991]. At the maximum rate of vertical deformation (-8.6 ± 0.9 mm/yr), 500 meters of subsidence would occur in just over 58,000 years [*Dzurisin et al.*, in review]. The maximum age of MLV is 1 Ma [*Donnelly-Nolan et al.*, 1990], and the volcano reached its current configuration by about 150,000 years BP [*Dzurisin et al.*, 1991], both of which are several times longer than necessary to recover the measured subsidence at the current rate. The discrepancy suggests that the current deformation is not solely the result of the emplacement of a volcanic load on the lithosphere on or before 150,000 years BP. Further research, perhaps including deformation measurements far from MLV where flexural uplift may be occurring, is required to further assess the contribution of surface loading to the current deformation, however crustal flexure does not seem ot be the dominant subsidence mechanism at MLV.

3.7.5 Crustal Extension

East-west crustal extension is obviously occurring in northeastern California, based on focal mechanisms from recent earthquakes and the presence of numerous north-striking normal faults (Figure 3.2). *Dzurisin et al.* [1991] suggest that extension of heat-weakened crust could cause the subsidence observed at MLV (Figure 3.4C). If the crust under MLV is mechanically weaker than the surrounding lithosphere, crustal thinning and subsidence due to tectonic extension may be concentrated at the volcano [*Dzurisin et al.*, 1991]. The

opposite process has been modeled by *Meertens and Levine* [1985], who use the finite element method to characterize uplift as a consequence of tectonic shortening of weak crust at Yellowstone caldera, Wyoming. Mechanical weakening of the lithosphere at Yellowstone is caused by elevated temperatures [*Meertens and Levine,* 1985]. Drill holes confirm similar temperature conditions at MLV, suggesting that the crust underlying the volcano has been weakened by heat associated with intrusive activity [*Dzurisin et al.*, 1991].

The ANSYS finite element software is used to evaluate the deformation caused by crustal extension in weakened lithosphere. A simple two dimensional plane strain model consisting of a homogenous elastic block with elastic modulus E and Poisson's ratio ν is stretched along the horizontal axis (Figure 3.18), and the surface deformation is computed. The left side of the model is fixed in the horizontal direction, while the right side is displaced by an arbitrary amount. The bottom of the model space is fixed in the vertical direction. The elastic modulus, magnitude of extension, and geometry of the weak inclusion are varied to determine the effects of the various parameters on the surface deformation of the half space. Model parameters and results are given in Figure 3.19 and Table 3.6. Because the model is elastic, all displacements are instantaneous. For purposes of modeling deformation with respect to time, viscous or viscoelastic rheologies must be incorporated into the model [e.g. *Newman et al.*, 2001]. However, comparing the shapes of the predicted and measured crustal displacements is useful for evaluating various deformation source mechanisms. In a homogenous elastic block, the vertical and horizontal displacements caused by extension are constant over the length of the model (A in Figure 3.19 and Table 3.6). However, when a portion of crust along the fixed axis is weakened by decreasing the magnitude of the elastic modulus, both extension and subsidence are concentrated in the weakened zone. The magnitude of the subsidence is

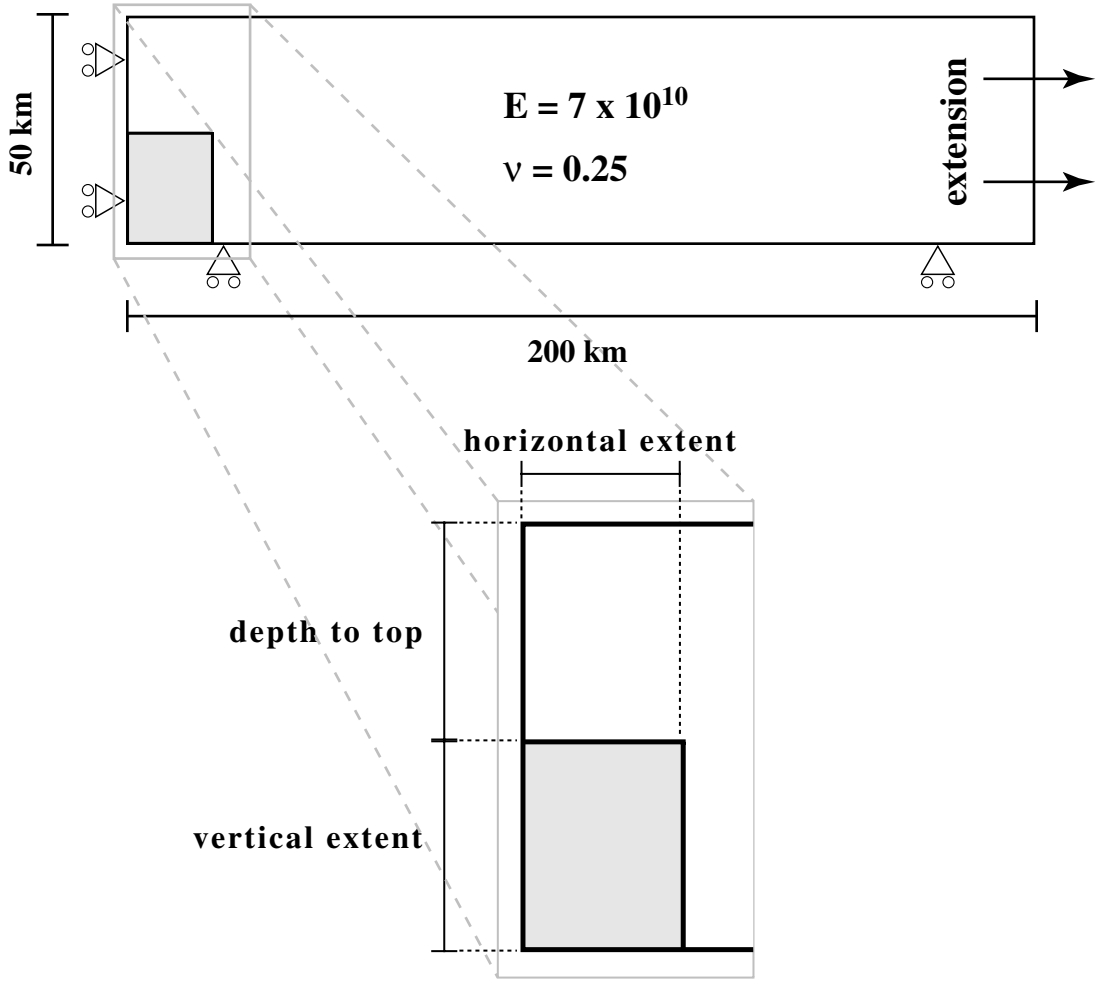

Figure 3.18. Schematic diagram showing boundary conditions and parameters for a finite element model of an elastic half space under tension. The left side of the model is fixed in the horizontal direction, and the bottom in the vertical direction. Plane strain is assumed. The right side of the model is displaced by some percentage of the initial model length (which is 200 km). The material properties that define the half space are the elastic modulus (E) and Poisson's ratio (ν). A weak zone (distinguished by a value of E less than that of the half space), meant to simulate the conditions of crustal material weakened by the thermal effects of repeated igneous intrusion, is located along the left side of the model. Inset shows the horizontal extent, vertical extent, and depth to top of the weakness, which distinguish the various models (see Table 3.6). As an example, the geometry of model C is shown, where the shaded area is the region of lower elastic modulus. Model results are given in Figure 3.19.

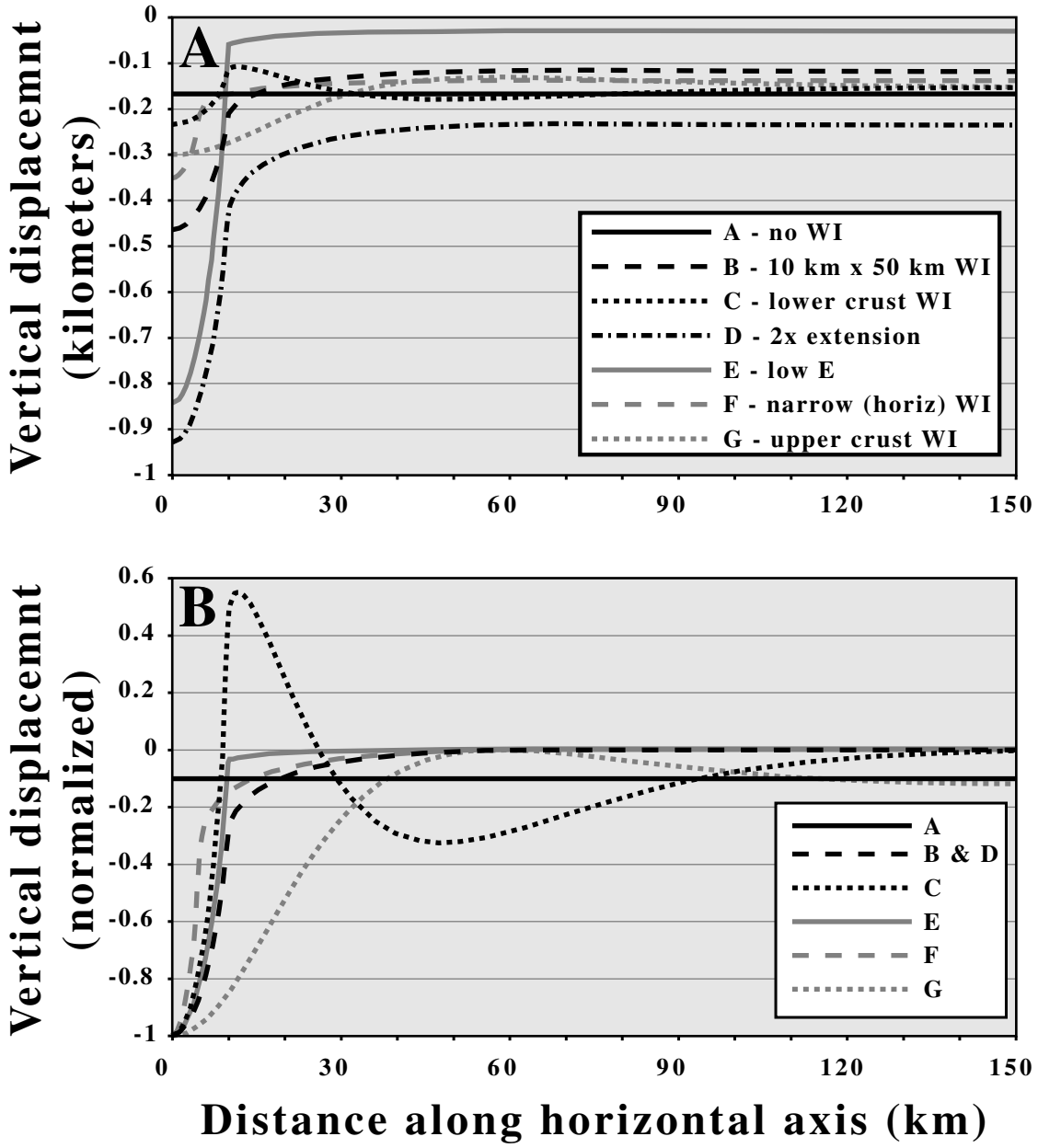

Figure 3.19. Predicted deformation for finite element models of a crustal block that is undergoing extension. Individual parameters and results for Models A-G are given in Table 3.6, and model parameters are defined in Figure 3.18. (a) Predicted vertical displacements with distance along the horizontal axis of the model. (b) Predicted vertical displacements normalized to compare deformation profiles. (c) Predicted horizontal displacements. WI = weak inclusion.

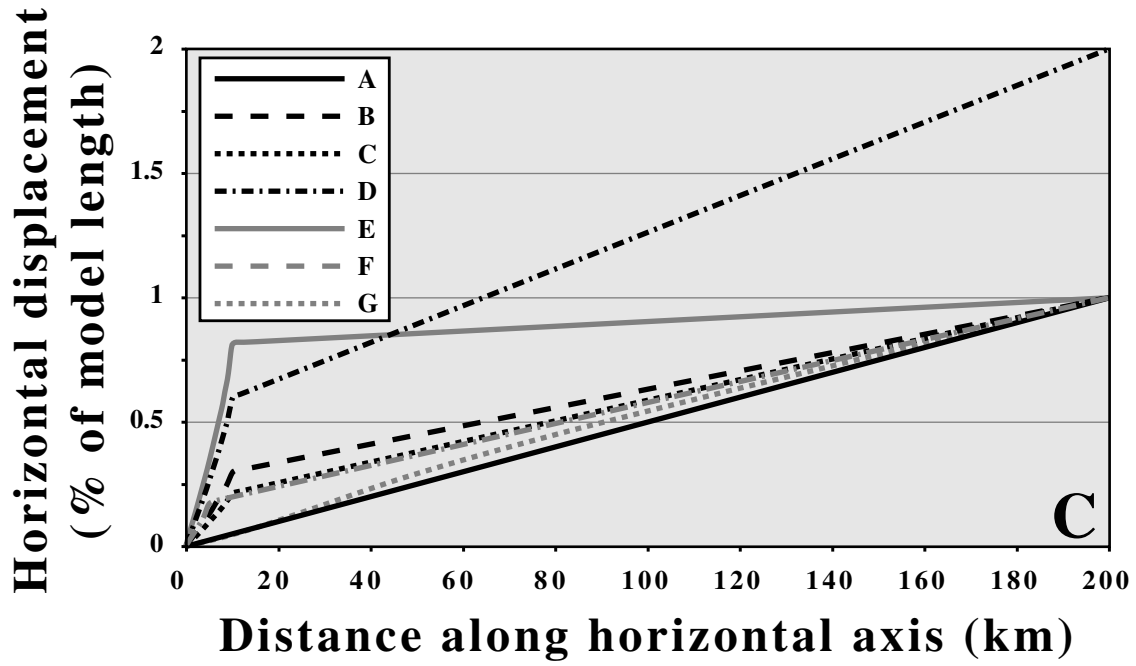

Figure 3.19. (Cont.)

Table 3.6. Model parameters and results for finite element models of an extending elastic half space with a weak inclusion. Plots of model curves are shown in Figure 3.19. The extension magnitude is given as a percentage of the initial model length (200 km). See Figure 3.18 for a graphical representation of the model parameters.

Model	elastic modulus	depth to top	vertical extent	horizontal extent	extension magnitude	maximum subsidence
A	-	-	-	-	1%	166.7 m
B	7.00E+09	0 km	50 km	10 km	1%	463.9 m
C	7.00E+09	25 km	25 km	10 km	1%	233.5 m
D	7.00E+09	0 km	50 km	10 km	2%	927.8 m
E	7.00E+08	0 km	50 km	10 km	1%	843.0 m
F	7.00E+09	0 km	50 km	5 km	1%	351.9 m
G	7.00E+09	0 km	25 km	10 km	1%	299.8 m

controlled by: 1) the amount of extension (Model D) and 2) the difference in the strength (elastic modulus) between the normal and weakened crust (Model E) (Figure 3.19A). In contrast, the shape of the subsidence curve is function of the weakened crustal geometry (Figure 3.19B). A narrow weakened region (Model F), or a weakened region that does not extend through the entire thickness of the crust (Models C and G), surface deformation that has a different profile than a weak zone that has a greater horizontal or vertical extent (Model B). In all cases where a weakened region exists in the model, the horizontal strain is greatest in the weakened material (Figure 3.19C).

Despite the simplicity of the model, the results do allow for a rough test of the crustal extension hypothesis of *Dzurisin et al.* [1991]. The subsidence with radial distance at MLV (Figure 3.9) resembles the shape of the vertical deformation predicted by a model that includes an extending crustal block with a weakened region extending through the thickness of the crust (Model B in Figure 3.19B). However, the GPS data are not well approximated by the extensional model. Strain should be highest in the region of weakened crust, but GPS results clearly do not indicate any variations in crustal strain across the volcano (Figures 3.5 and 3.8). Although extension is certainly occurring, tectonic stretching of weakened crust is probably not the dominant subsidence mechanism at MLV.

3.7.6 Downsagging Due to Dense Intrusions

The preferred MLV subsidence mechanism of *Dzurisin et al.* [1991] is extension of heat-weakened lithosphere and loading by the volcano and subvolcanic intrusions. As shown above, extension does not seem to be a major factor controlling subsidence and surface loading probably does not cause all of the measured vertical displacement, therefore loading by a buried intrusive complex may be an important source of crustal deformation at

MLV. The mechanism is essentially the same as that of *Walker* [1987; 1988] for the formation of calderas at the summits of mafic shield volcanoes (see Chapter 1). *Walker* [1987; 1988] proposes that funnel-like subsidence occurs at the summits of large basaltic volcanoes (e.g. Kilauea and Mauna Loa in Hawaii) due to downsagging caused by dense intrusions at depth. Vertical deformation predicted by *Walker's* [1987; 1988] conceptual model resembles the radially symmetric subsidence at MLV (Figure 3.9). In addition, geophysical evidence from gravity [*Finn and Williams*, 1982], magnetics [*Stanley et al.*, 1990], and seismic studies [*Zucca et al.*, 1986; *Fuis et al.*, 1987; *Ritter and Evans*, 1997] suggest the presence of dense solidified intrusions at ~1-4 km below the summit of MLV which may drive downsagging deformation.

The finite element method is again employed to determine surface displacements due to a buried dense inclusion. The model is composed of an axisymmetric elastic half space of elastic modulus E, Poisson's ratio ν, and density ρ (Figure 3.20). Both sides of the crustal block are fixed in the horizontal direction, and the bottom is fixed in the vertical. Loads are applied in two steps: 1) a gravitational acceleration of 9.8 m/s^2 is applied to the homogenous half space, and 2) the density of an arbitrary region along the axis of symmetry is changed to simulate the emplacement of a dense intrusive complex. The resulting deformation includes subsidence above the dense region and radial horizontal displacements towards the axis of symmetry (and the center of the dense inclusion). Model parameters and results are shown in Figure 3.21 and Table 3.7. Model H reflects realistic MLV parameters (with the exception of topography), with an intrusive complex that is at 3 km depth and has dimensions of 3 km deep by 6 km wide. Increasing the horizontal extent of the intrusive complex (Model K) broadens and increases the magnitude of both the vertical (Figure 3.21A) and horizontal (Figure 3.21C) deformation. Variations in the vertical extent (Model J) or density (Model I) of the inclusion affect the magnitude of the

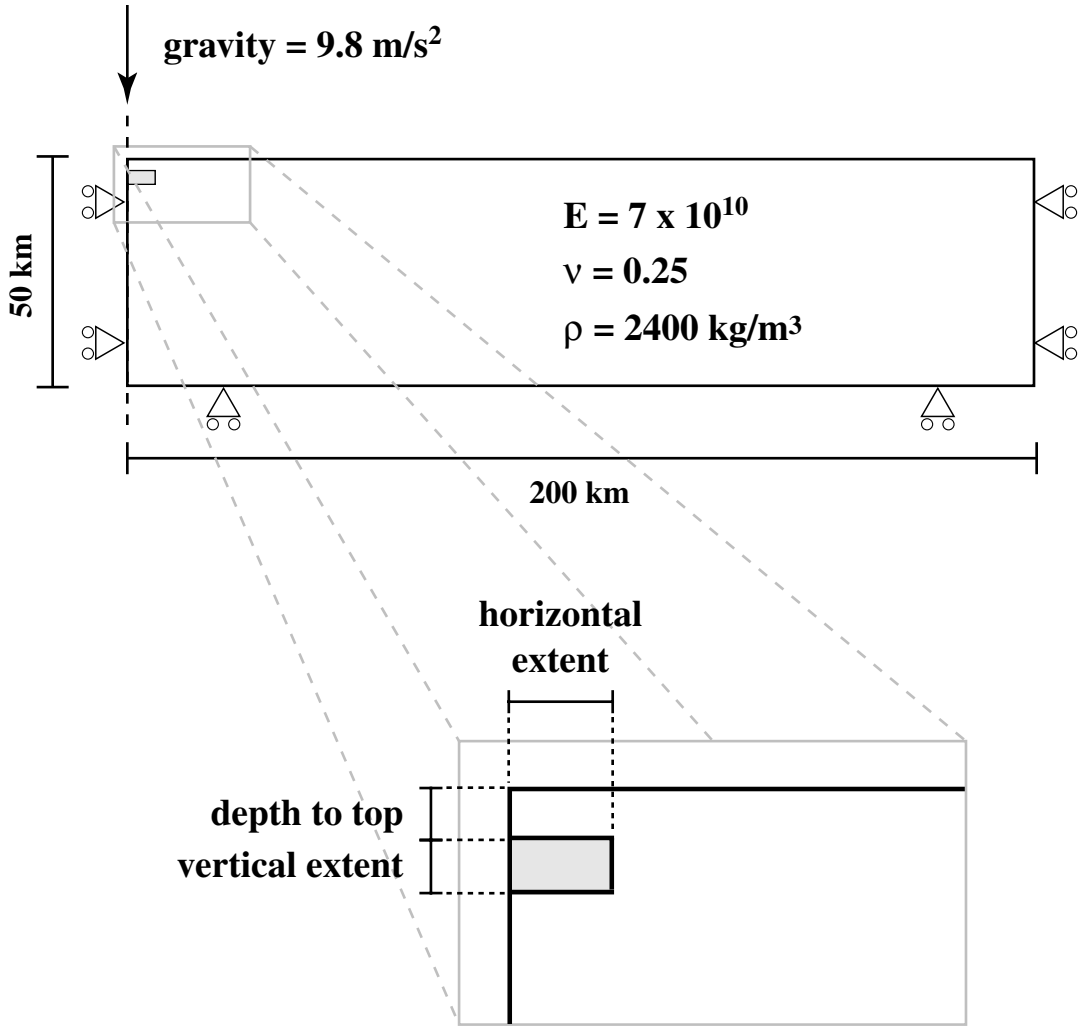

Figure 3.20. Schematic diagram showing boundary conditions and parameters for an axisymmetric finite element model of an elastic half space containing a dense inclusion (axis of symmetry is the dashed line at the left of the model). The left and right sides of the model are fixed in the horizontal direction and the bottom in the vertical direction, and a gravitational acceleration of 9.8 m/s^2 is applied. The material properties that define the half space are the elastic modulus (E), Poisson's ratio (ν), and density (ρ). A block of higher density, representing a solidified intrusive complex, occurs within the elastic half space along the axis of symmetry. The model consists of two load steps: 1) application of gravity to the homogenous elastic half space, and 2) changing the density of a selected region within the model to approximate the emplacement of the intrusive complex. Inset shows the horizontal extent, vertical extent, and depth to top of the dense inclusion, which distinguish the various models (see Table 3.7). As an example, the geometry of model H is shown, where the shaded area is the region of higher density. Model results are given in Figure 3.21.

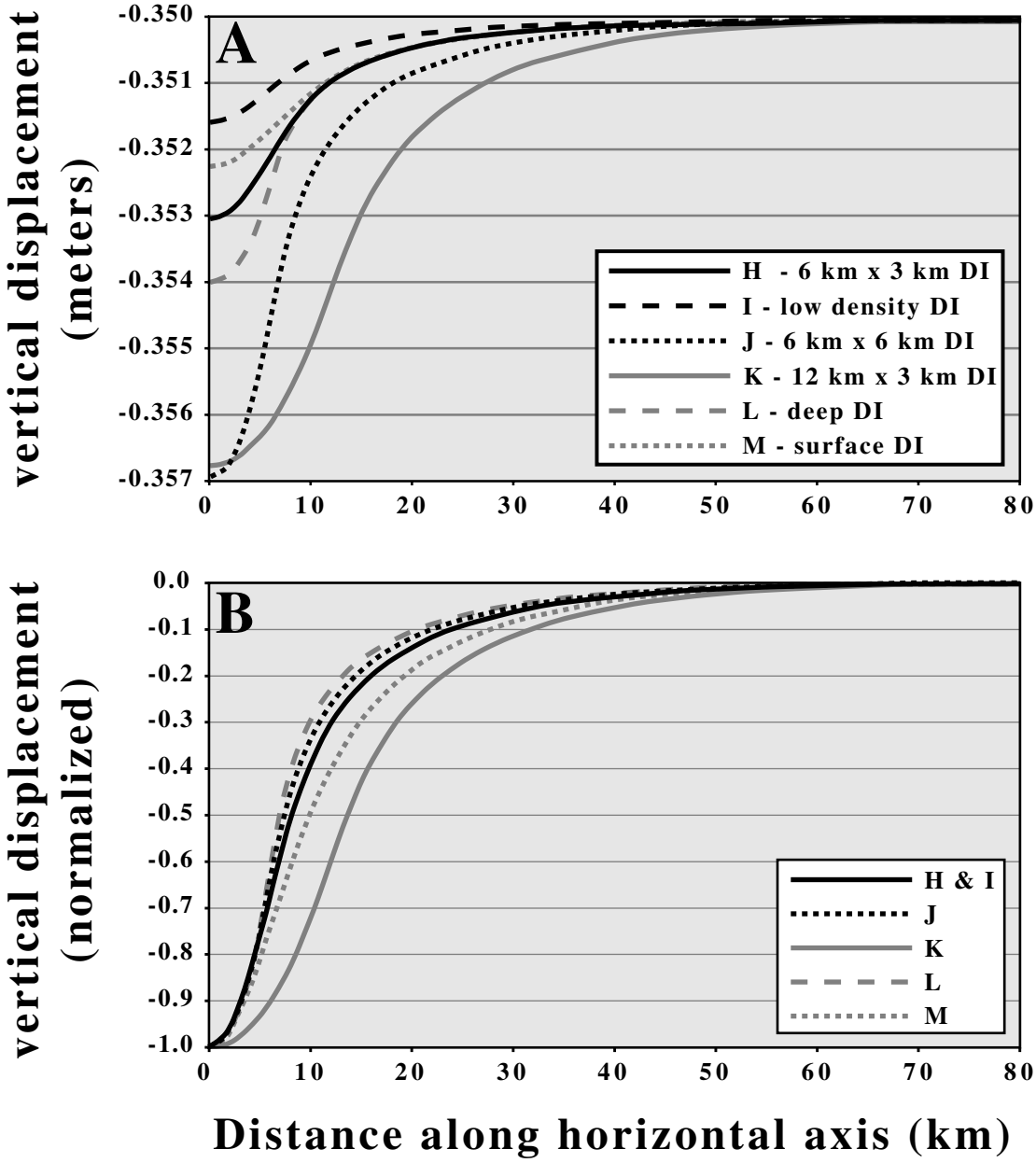

Figure 3.21. Predicted deformation for finite element models of a crustal block containing a dense inclusion. Individual parameters and results for Models H-M are given in Table 3.7, and model parameters are defined in Figure 3.20. (a) Predicted vertical displacements with distance along the horizontal axis of the model. (b) Predicted vertical displacements normalized to compare deformation profiles. (c) Predicted horizontal displacements. DI = dense inclusion.

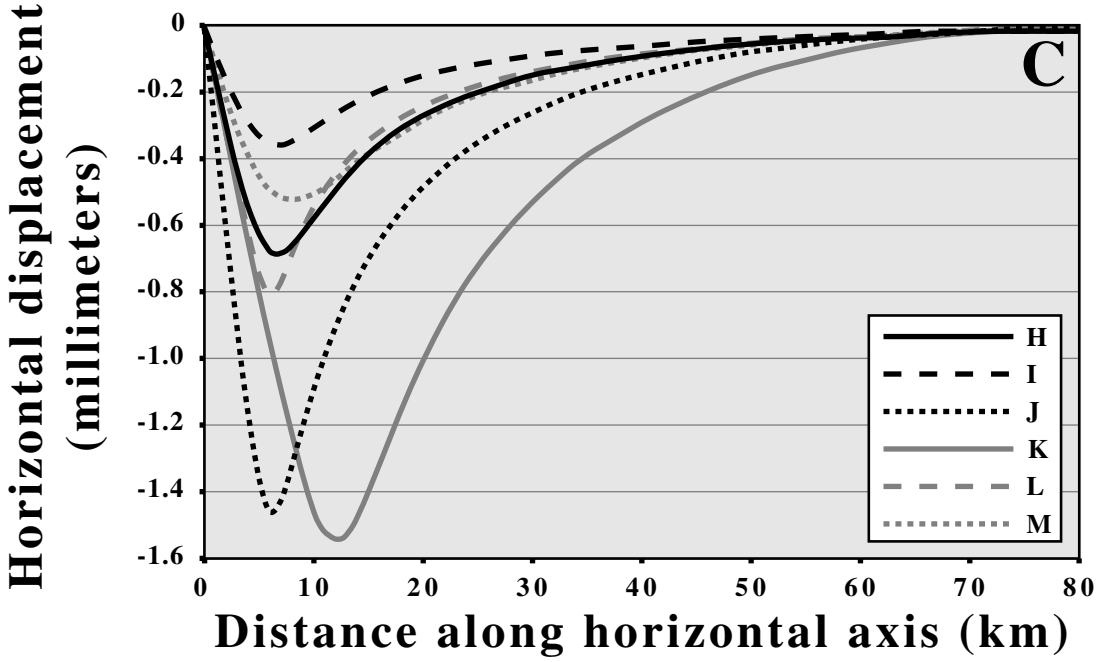

Figure 3.21. (Cont.)

Table 3.7. Model parameters and results for finite element models of an elastic half space containing a dense inclusion. Plots of model curves are shown in Figure 3.21. The "dist. to max. inward disp." is the radial distance along the top of the model from the axis of symmetry to the point of maximum radial displacement towards the center (left side) of the model. See Figure 3.20 for a graphical representation of the model parameters.

Model	Depth to top	horizontal extent	vertical extent	density (kg/m^3)	maximum subsidence	max. inward disp.	dist. to max. inward disp.
H	3 km	6 km	3 km	3400	0.3530 m	0.685 mm	7 km
I	3 km	6 km	3 km	2900	0.3515 m	0.354 mm	7 km
J	3 km	6 km	6 km	3400	0.3563 m	1.470 mm	6 km
K	3 km	12 km	3 km	3400	0.3568 m	1.560 mm	12 km
L	6 km	6 km	3 km	3400	0.3540 m	0.814 mm	6 km
M	0 km	6 km	3 km	3400	0.3522 m	0.528 mm	8 km

deformation but do not significantly alter the shape of the vertical (Figure 3.21B) or horizontal displacements. Finally, a shallow inclusion (Model M) has lower magnitudes of vertical and horizontal deformation and influences a narrower horizontal region of the crust than a deeper inclusion of the same size (Model L).

Again, although the model is simple and does not include such components as topography, the results suggest that loading by dense subvolcanic intrusions is a good approximation for both the vertical and horizontal displacements measured by leveling and GPS. A comparison of the predicted (Model H) and observed (GPS and leveling) displacements is given by the solid curve in Figure 3.22, where both the model and data have been normalized (to compare the shapes of the deformation profiles) and plotted with radial distance from MLV. In the leveling data, benchmark D495 is held fixed, because it is far from MLV caldera and is not likely to have been affected by subsidence. Because GPS data are influenced by several additional deformation sources (for instance, rotation of the Cascadia forearc), the data are normalized by setting the minimum and maximum displacements to -1 and 0, respectively. GPS displacements are corrected for dextral shear east of MLV (see section 3.7.2) and the only the deformation component radial to MLV at each site is shown. The subvolcanic loading model approximates the shape leveling data, however the maximum inward horizontal displacement of the model is several kilometers closer to MLV than the GPS measurements indicate (~15 km for GPS vs. ~7 km for model). In the models, the dense intrusive complex takes the rather simple form of a cylinder. Gravity data from *Finn and Williams* [1982] suggests that the geometry of the dense intrusive complex is more complicated, resembling a cone elongated in an east-west direction rather than a cylinder centered under the summit of MLV. Variations in the three-dimensional shape of the dense inclusion will have a effect on the geometry of the resulting deformation field. For instance, a dense inclusion with an elongated E-W axis should

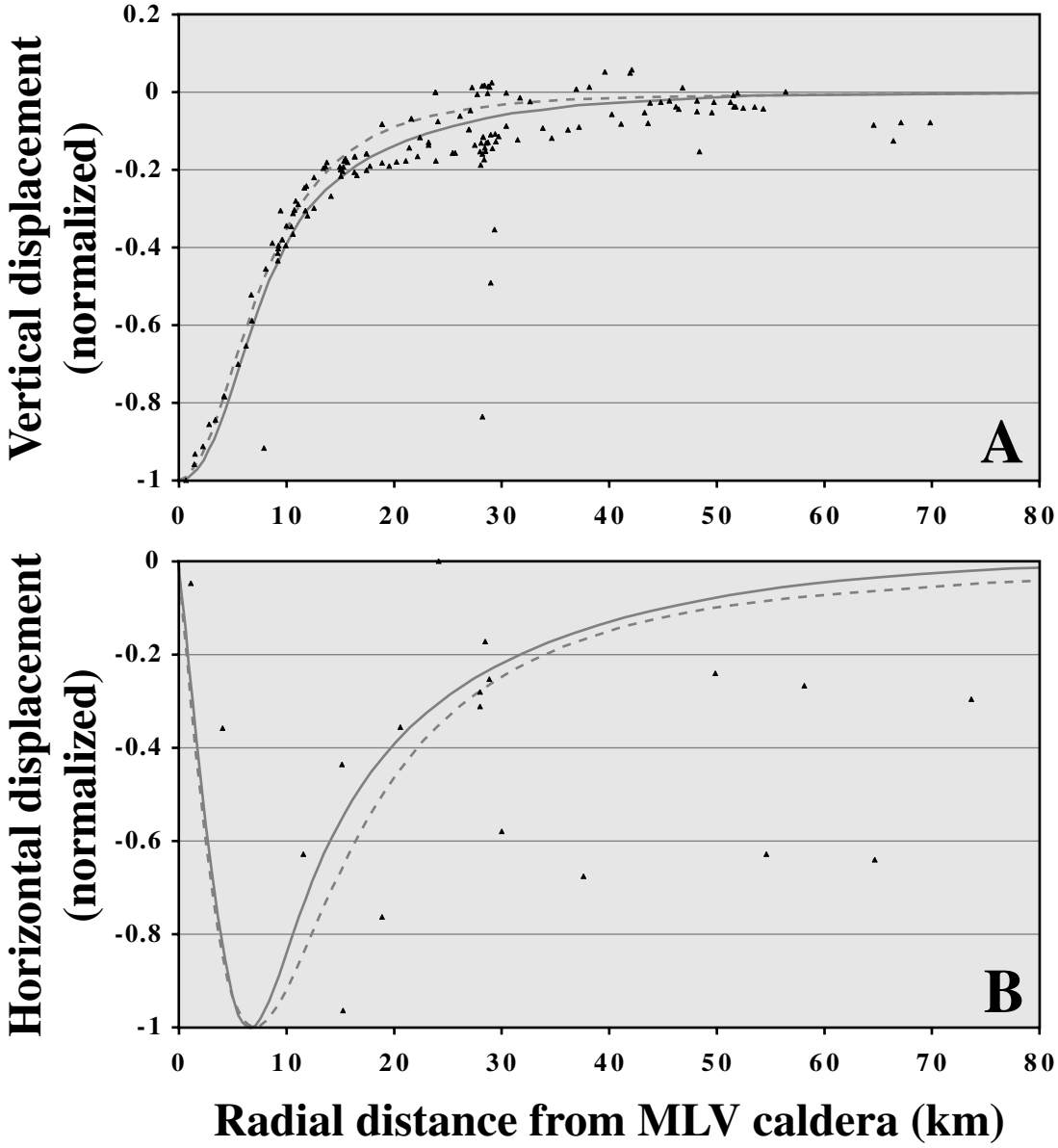

Figure 3.22. Comparison of subvolcanic loading (Model H, solid curve) and Mogi (dashed curve) models to observed vertical and horizontal displacements (triangles) from leveling and GPS, respectively. (a) Predicted and observed vertical displacements. (b) Predicted and observed horizontal displacements. Data and models are normalized to their maximum displacements to facilitate comparison of profile shapes. Error bars are omitted for clarity, but are shown in Figures 3.9 (leveling) and 3.10 (GPS).

cause surface deformation that has a greater extent in the E-W direction than N-S (see Models H and K in Figure 3.21). The discrepancy between observed and predicted horizontal deformation may be caused by the complex morphology of the intrusive complex.

Both the vertical and horizontal deformation profiles predicted by the subvolcanic loading model resemble the displacements predicted by the 10 km deep Mogi source of *Dzurisin et al.* [in review] (dashed line in Figure 3.22). Despite the similarity, loading by dense intrusions is the preferred mechanism. As noted above (section 3.7.3), no mechanical or material heterogeneity has been recognized by geophysical methods at ~10 km depth below MLV, with the exception of a single long period (magmatic) earthquake at 15 km depth in 1989. In contrast, a dense subvolcanic intrusive complex at shallow depths has been well-characterized by a variety of geophysical measurements (Figure 3.23). Subsidence due to dense intrusions has been recognized at numerous other mafic, and often extinct, volcanoes [*Walker*, 1984; 1987; 1988]. Repeated magmatic activity over the ~1 Ma lifetime of MLV should be sufficient for the development of a subvolcnic intrusive complex. Because the volcano has not erupted for ~1000 years, magmatic activity is minor and should not obscure deformation due to downsagging. Although both the Mogi and subvolcanic loading models seem to fit the measured deformation equally well, the abundant geologic, geodetic, and geophysical evidence favors a mechanism of downsagging due to dense intrusions.

3.8 Conclusions and Future Work

Leveling surveys at MLV indicate bowl-like subsidence centered on the summit of the volcano. *Dzurisin et al.* [1991] propose that the subsidence may be caused by a combination of several mechanisms, including volume loss at depth, loading by the

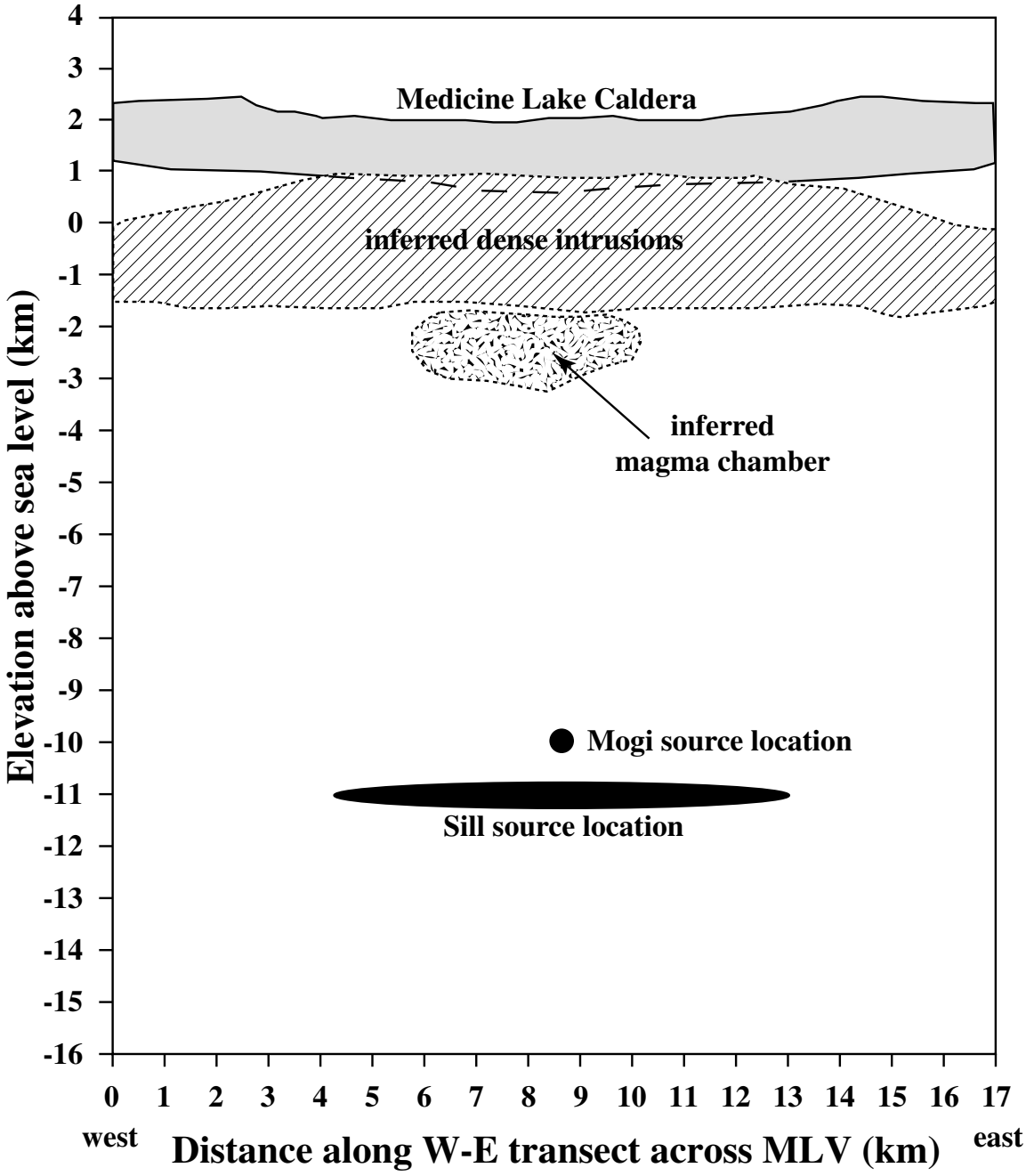

Figure 3.23. W-E cross section through MLV with no vertical exaggeration, and showing subsurface geology (inferred from geophysical measurements) and volume loss model sources. Note that the bottom of the volcanic pile (dashed where it overlaps with the inferred intrusive complex) is deflected, possibly due to crustal flexure from the load of the volcanic edifice. Although the volume loss models (Mogi and sill sources) and subvolcanic loading model (Model H) fit the shape of the deformation equally well, the only inferred magma body is several kilometers shallower than the models. Therefore, subvolcanic loading by dense intrusions is the preferred subsidence mechanism at MLV.

volcano and dense subvolcanic intrusions, and extension of heat-weakened crust. All three mechanisms would produce similar vertical displacements, therefore horizontal deformation measurements are necessary to isolate the deformation source. GPS data collected in the MLV - Mt. Shasta region in 1990, 1996, and 1999 reveal several anomalous features, most notably shearing east of MLV and displacements towards MLV caldera within a few kilometers of the volcano's summit.

Horizontal displacements east of MLV are best approximated by a dextral dislocation slipping at a rate of approximately 6 mm/yr. The model dislocation lies along strike with the Likely fault, a NE-trending right-lateral fault that may represent a northern extension of the Walker Lane - ECSZ system. The presence of dextral displacements suggests that shear associated with the NW translation of the rigid Sierra Nevada block is occurring at least as far north as MLV, and perhaps continues into southern Oregon.

A model of loading by dense subvolcanic intrusions is the preferred model for subsidence at MLV. Although models of volume loss at depth beneath the volcano fit the data equally well, geologic and geophysical evidence favor subsidence due to subvolcanic loading (Figure 3.23). The deformation is characteristic of downsagging due to dense intrusions at depth, which has been proposed to explain the inward tilting (towards the summit of the volcano) of originally outward-dipping (away form the summit of the volcano) deposits at several inactive mafic volcanoes (e.g. Koolau, Hawaii [*Walker*, 1987]). Sustained activity over 1 Ma at MLV should result in the formation of a complex of solidified intrusions below of the summit of the volcano, and subsidence occurs due to the density contrast between the intrusions and the MLV edifice. The process may be occurring at other active basaltic volcanoes, however magmatic activity would obscure any deformation due to downsagging.

That non-magmatic sources are necessary to explain deformation measured at MLV, a Holocene volcano, is an important result of the research. Most models of crustal deformation at active volcanoes rely on Mogi sources (to model volume changes due to magma bodies) and dislocations (approximating faults as well as volume changes in dikes and sills) to explain observed displacements. Although the deformation measured at MLV may be fit by a deflating Mogi source, a mechanism of volume loss at depth is not physically realistic. The finite element method allows for the evaluation of complex model geometries, and variable material and rheological conditions. The next step in the present work is to model displacement rates, which requires a viscous model component that would be best implemented in a finite element model

Additional deformation data, particularly from GPS, should be collected at MLV. The anomalous site velocity of a GPS station on the flank of Mt. Shasta volcano may indicate some as yet unrecognized activity there, but data is too sparse for a thorough assessment. In addition, transient strain from past earthquakes may be affecting displacements at one or more sites in the network. The strain should dissipate with time, which would be easily observed and modeled. Finally, GPS measurements of deformation east of MLV can be used to further constrain the source of dextral shearing. Sites established in 1999 traverse the Likely fault and extend from MLV to the California-Nevada border. Displacements east of the volcano will be useful for establishing a tectonic framework for the region, important when considering the effects of volcano-tectonic interaction.

Finally, GPS occupations should be initiated at Newberry volcano, in central Oregon. Newberry and MLV share numerous characteristics, including tectonic setting, volcanic history, morphology, and subsurface geology, yet recent work by *Dzurisin* [1999] suggests that Newberry is uplifting (by analogy with MLV, the volcano should be

subsiding). Measurements of the horizontal velocity field at Newberry volcano will aid with the evaluation of deformation mechanisms (as shown by the present research) and provide an additional example of volcanic deformation that may not be related to magma movement within the crust.

4. Patterns of magma flow and dike emplacement at the eroded Summer Coon stratovolcano, southern Colorado, and application to modern silicic volcanic centers

Abstract. Population centers tend to cluster around the bases of volcanoes, therefore distal flank eruptions can be the most hazardous. The emplacement mechanisms of radial dikes that commonly feed such eruptions are poorly understood. Hazard assessments of flank eruptions should be based on 1) the likely location of a flank vent, 2) the probable volume of an eruption, 3) the geometry of the vent or system of vents, and 4) the potential for detection of a flank intrusion prior to eruption. Summer Coon volcano, in southern Colorado, is ideal for studying intrusion emplacement because erosion has exposed a swarm of hundreds of mafic and ~ 20 silicic radial dikes. A model of radial dike emplacement based on observations of intrusion geometry and magma flow directions from Summer Coon suggests that magma flow is inclined near the center of a stratovolcano and subhorizontal on the flanks along the base of the cone. High driving pressures (~40 MPa) are required to propagate blade-shaped, high-silica dikes. As intrusions approach the surface of a volcano the dikes will thicken and the dike tops will break into echelon segments (as the magma intrudes fractures that formed in front of the propagating dike). The model suggests that the highest volume eruptions from radial dikes will occur low on the flanks of an edifice. Silicic dike emplacement should be accompanied by significant surface deformation and the eruptive vents will likely have an echelon geometry in plan view.

4.1 Introduction

In addition to eruptions from their summits, arc volcanoes commonly extrude magma from flank vents fed by subsurface dikes that have radial orientations [*Nakamura*, 1977]. Flank eruptions are relatively common during the lifetime of an average

stratovolcano, as indicated by the numerous cinder cones, fissures, and domes on volcanic flanks, and pose a significant hazard to population centers and infrastructure at the base of a volcano. The 1669 eruption of Mt. Etna illustrates the potential devastation due to an eruption away from the central conduit. During the episode, a vent opened 2500 m below and 15 km distant from the summit of the volcano and erupted almost 1 km^3 of magma. The ensuing lava flow partially buried the city of Catania on the Sicilian Coast, approximately 30 km away from the summit cone of Mt. Etna [*Corsaro et al.*, 1996]. Eruptive hazards may be increased at glaciated volcanoes where volcanic heating may initiate significant melting of ice and cause floods and lahars depending on the location of the vent. At Mt. Rainier, Washington, for example, an eruption high on the flank where glaciers are abundant would lead to significantly more meltwater production than the same event occurring lower on the flank where glaciers are absent.

Assessment of the potential hazard due to flank eruptions should be based on the following information: 1) vent location, 2) vent geometry (eruption from a single point versus a fissure, which may or may not be composed of distinct segments), 3) probable eruption volume and 4) potential for detection prior to eruption. The zones of potential flank activity may be constrained using principles developed by *Nakamura* [1977], who showed that dikes with initially radial orientations will curve to become parallel to the most compressive stress in the crust during emplacement. Stress orientations can be determined from the paths of previous intrusions, which may be inferred from vent and crack alignments at the surface [*Fink and Pollard*, 1983]. Regions with greater potential for dike intrusion may therefore be distinguished as zones of higher hazard due to flank eruptions. In contrast, data that can constrain the probable elevation, geometry, volume, and precursory activity of future flank eruptions are scarce.

The characteristics of a flank eruption from a radial dike depends on the path that the magma follows as it rises to the surface. End-member models categorize dike propagation as being either a vertical or horizontal process [*Rickwood*, 1990; *Baer and Reches*, 1991]. Unfortunately, little unambiguous evidence exists to support or refute either model for volcanoes in arc settings. *Nakamura* [1977] proposed that radial dikes are emplaced through the lateral flow of magma away from the central conduit of a volcano (Figure 4.1A). However, based on flow indicators found at the Spanish Peaks in Colorado, *Smith* [1987] concluded that radial dikes propagate up and away from a central location at depth (Figure 4.1B). Determination of magma flow in the continental-scale MacKenzie radial dike swarm in Canada suggests vertical magma transport near the center of the swarm evolving to lateral flow with distance from the source (Figure 4.1C) [*Ernst and Baragar*, 1992]. Gelatin models of *Hyndman and Alt* [1987] suggest that radial dikes spread both laterally and vertically within a volcanic edifice. *Gudmundsson* [1984] also favors a model of mixed vertical and horizontal flow, with the variability caused by differing layers in the crust and changes in host rock density.

Evidence from basaltic shield volcanoes, most notably those in Hawaii and Iceland, supports predominantly lateral transport of magma in dikes with isolated patches of vertical flow. Geodetic measurements in Hawaii indicate summit subsidence and rift inflation as magma is transported laterally from a chamber beneath the summit into flank rift zones [*Pollard et al.*, 1983]. *Fiske and Jackson* [1972] demonstrated lateral propagation of rift zone intrusions in Hawaii through analogy with gelatin models. Seismic evidence for horizontal magma migration during the 1977 rifting episode of Krafla volcano in Iceland is presented by *Brandsdottir and Einarrson* [1979]. *Sigurdsson and Sparks* [1978] review volcanological and geochemical evidence from Iceland and conclude that lateral magma transport over distances of 70 km is a common process. Also in Iceland, *Helgason and*

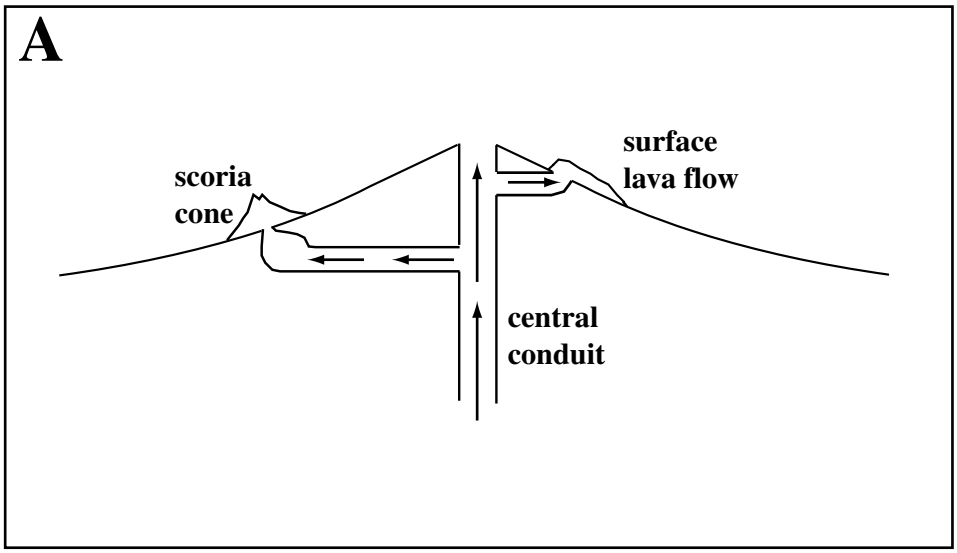

Figure 4.1. Generalized models of the possible form of radial dikes in arc volcanoes. Note that the magma chambers depicted are much larger than is realistic. (a) *Nakamura* [1977] infers lateral propagation of radial dikes away from the central conduit of a volcano. (b) Indicators of magma flow direction at the Spanish Peaks suggest upward and outward dike propagation from a source at depth beneath the volcano (either the deep portion of the central conduit of the top of the magma chamber), possibly in the form of fan-shaped or planar dikes (not represented), as proposed by *Smith* [1987]. (c) By analogy with continental-scale radial dike swarms [*Ernst and Baragar,* 1992], dikes that originate at depth below the volcano (from the magma chamber or central conduit) would have steep flow near the center of the volcano, transitioning to sub-horizontal with increasing radial distance. Eruptions from radial dikes may occur as scoria cones, surface lava flows, and lava domes. Arrows indicate probable magma paths.

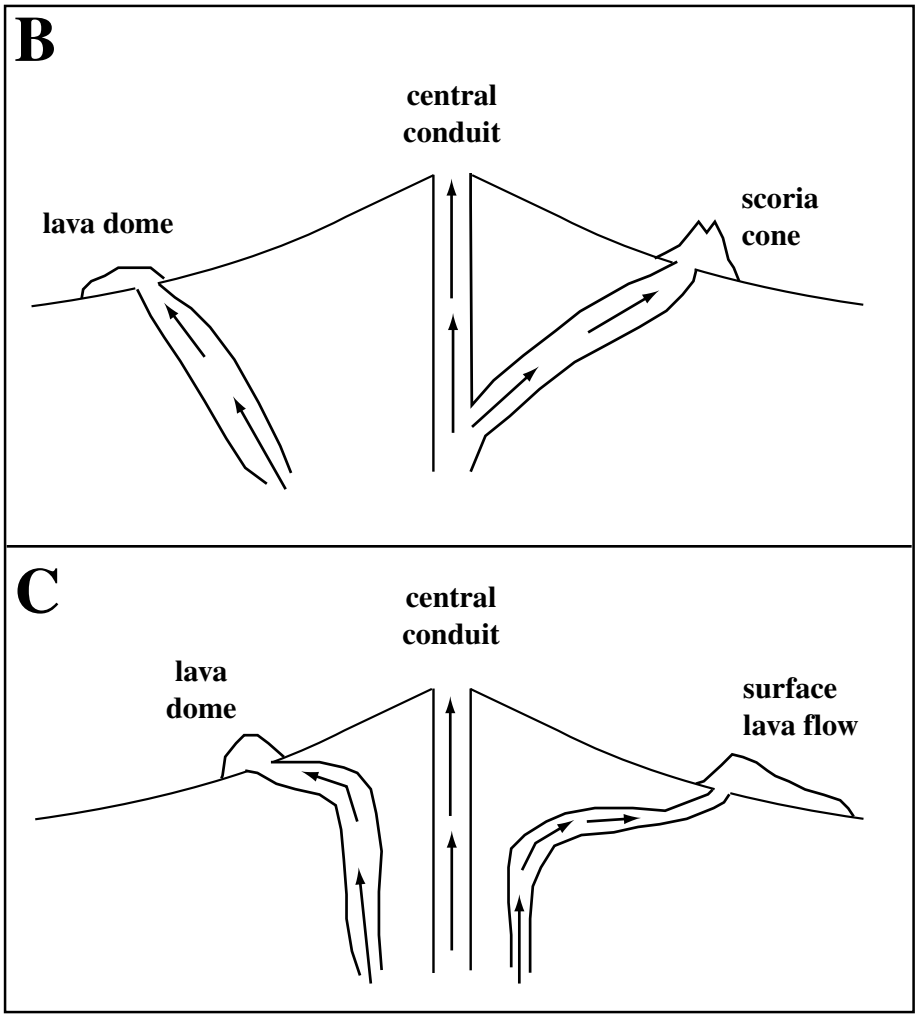

Figure 4.1. (Cont.)

Zentilli [1985] mapped a swarm of dikes that are vertically discontinuous yet extend laterally for tens of kilometers, leading them to conclude that magma flow was horizontal in the dikes. Finally, *Gudmundsson* [1987] noted that dikes in Iceland are typically denser than the felsic or heavily fragmented mafic rocks of central volcanoes, suggesting that magma will travel laterally away from the source chamber along zones of neutral buoyancy. Unfortunately, little information is available regarding magma transport through dikes in silicic volcanic systems, which are more explosive and pose greater hazards than eruptions from mafic shields.

In this chapter, I investigate the characteristics of stratovolcano flank eruptions by studying dike geometry and inferred magma flow at the eroded Summer Coon volcano in south-central Colorado. A set of hundreds of small basaltic andesite dikes and approximately 20 large silicic dikes are arranged in a radial pattern [*Lipman*, 1968]. Measurements of dike thickness are used to determine the driving pressures during emplacement, which can indicate the potential volume and likely elevation of a flank eruption. In addition, the probable geometry of an eruptive fissure at the surface is considered based on the geometry of stepping dike segments. Finally, anisotropy of magnetic susceptibility and examination of petrographic sections from two of the largest silicic dikes at Summer Coon are used to determine the flow direction of magma. The goal of the work is to gain a better understanding of dike emplacement in stratovolcanoes, which may be applied to future volcanic episodes in active arcs.

4.2 Geologic Background of Summer Coon Volcano

Summer Coon volcano is located approximately 10 km north of the town of Del Norte on the western edge of the San Luis Valley, which represents the northern extension

of the Rio Grande rift into Colorado (Figures 4.2, 4.3, and 4.4) [*Moats*, 1990]. The volcano is part of the San Juan volcanic field, a region covering 25,000 km^2 in southwest Colorado and northern New Mexico and containing many silicic calderas and stratovolcanoes [*Lipman et al.*, 1970]. Volcanic activity in the San Juan field, which consisted of intermediate composition lavas and breccias, commenced 35-40 Ma and reached a peak between 30 and 35 Ma, based on K-Ar dating by *Lipman et al.* [1970]. Later activity between 26.4 and 30 Ma was dominated by explosive ash-flow eruptions. *Lipman et al.* [1970] dated two dikes at Summer Coon, obtaining ages of 32.4 ± 1.3 and 34.4 ± 1.4 Ma. Volcanic deposits of Summer Coon uncomformably overlie a rhyodacite flow dated at 33.8 ± 1.6 Ma while younger ash flow tuffs around Summer Coon have dates that do not exceed 30 Ma. Therefore the growth and some erosion of the edifice must have occurred in the 4 million year time interval between 30 and 34 Ma. *Perry et al.* [1999] report nine 40Ar/39Ar dates ranging from 32.6 Ma to 33.9 Ma for the volcano. Seven of the dates are between 33.0 and 33.5 Ma, implying a duration of magmatic activity on the order of 100,000 to 200,000 years.

Erosion has destroyed much of the original Summer Coon edifice. Only the central intrusive stocks, radial dikes, and some outward dipping extrusive deposits (Figure 4.5) are preserved [*Lipman*, 1968; *Mertzman*, 1971; *Moats*, 1990]. A 1:48,000 geological map of the volcano prepared by *Lipman* [1976] shows the distribution of extrusive and intrusive units, including dikes. Dips of extrusive deposits vary around the volcano, with greater dips on the east flank than on the west. The asymmetric dip distribution suggests that the volcano may have been tilted sometime after the cessation of volcanic activity, probably due to the formation of the Rio Grande Rift to the east [*Lipman*, 1968; *Mertzman*, 1971; *Moats*, 1990]. Eruptive and intrusive units of Summer Coon range in composition from basaltic-andesite to rhyolite [*Lipman*, 1968; *Mertzman*, 1971]. Based on cross-cutting

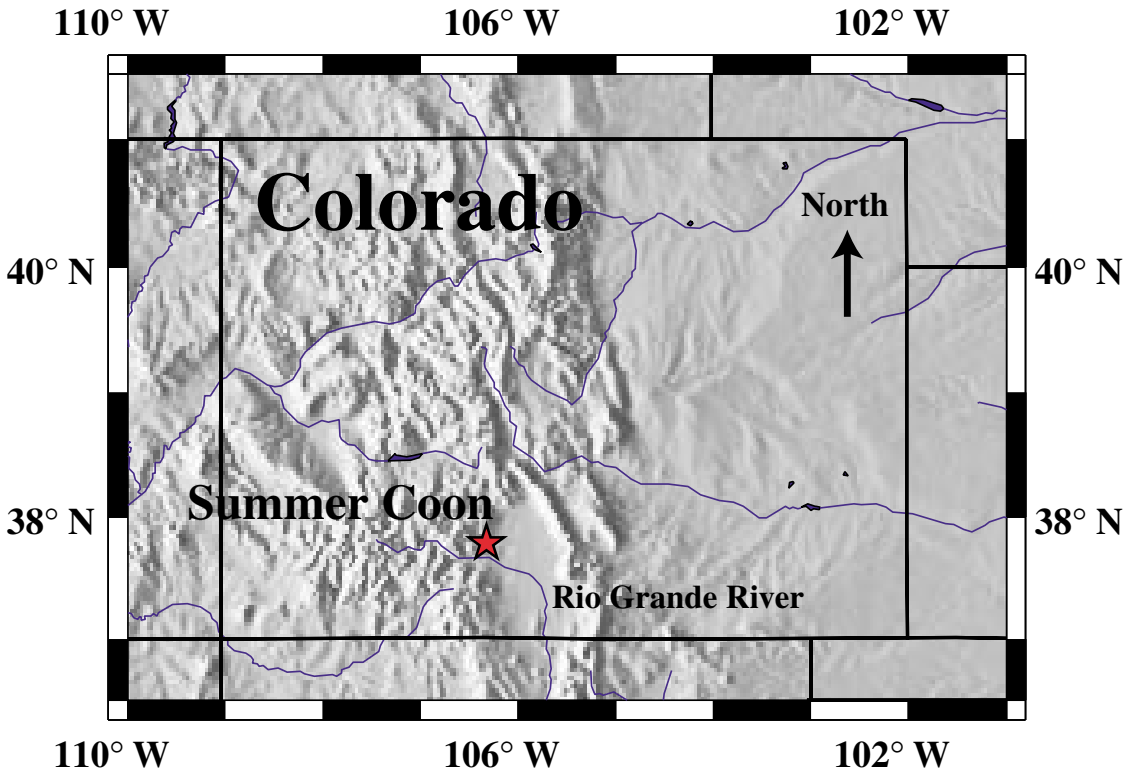

Figure 4.2. Shaded relief map showing the location of Summer Coon volcano. San Luis Valley, the northern extension of the Rio Grande Rift, is the depression immediately east of Summer Coon.

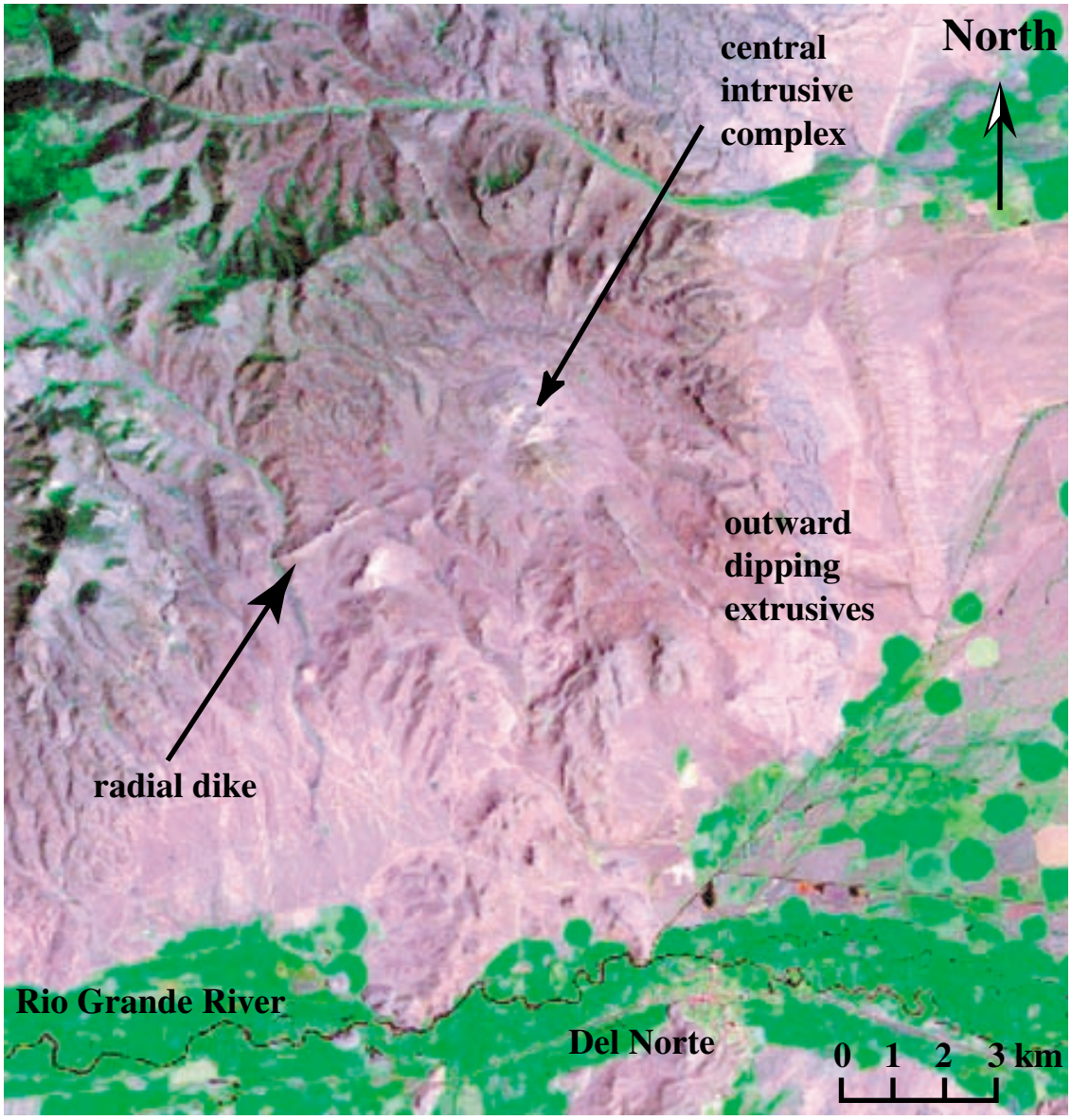

Figure 4.3. Landsat TM image of Summer Coon volcano (band combination 7-4-3). Green areas are vegetated and cluster along rivers, streams, and irrigated farms (circular features). Summer Coon is the elliptical shape in the center of the figure. The shape is a result of extrusive deposits that dip away from the center of the volcano. The intrusive complex is the light region at the center of the elliptical structure. Several large silicic dikes are visible extending radially away from the central intrusive complex and cutting through the dipping extrusives.

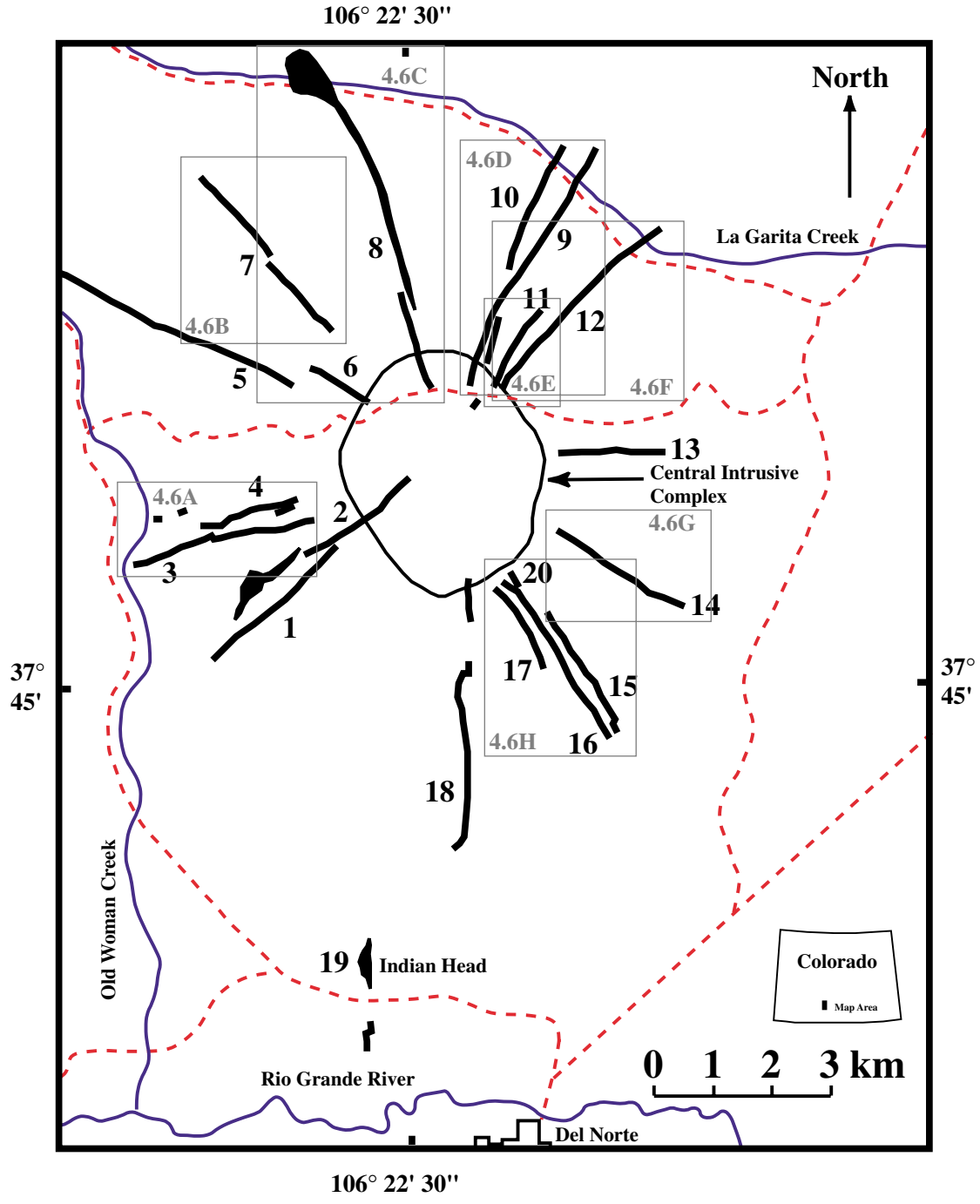

Figure 4.4. Sketch map of Summer Coon volcano, adapted from *Moats* [1990]. Numbered silicic dikes are discussed in the text. Dike traces are approximated. Red dashed lines are roads, and blue lines are rivers and streams. The locations of figures 4.6A-H are outlined. See Figure 4.6 for the detailed morphologies of individual dikes.

Figure 4.5. Dipping extrusive deposits located northeast of the central intrusive complex of Summer Coon volcano. The units, which are comprised mainly of andesitic breccia, dip down to the right (northeast), radially away from the center of Summer Coon. The white object in the middle ground is a house. View is to the northwest.

relationships between dikes and extrusive deposits and superposition of flank extrusives, *Lipman* [1968] divides the compositional evolution of the volcano into three stages: 1) early basaltic andesite, 2) middle rhyolite, and 3) late-stage dacite, which is consistent with the later interpretation of *Mertzman* [1971]. In contrast, *Perry et al.* [2001] favor a sequence including an early mafic phase dominated by basaltic andesite with minor amounts of rhyolite and dacite followed by a less voluminous dacite phase. *Zielinski and Lipman* [1976] examine trace elements from Summer Coon and conclude that the andesitic end member was formed by partial melting of a garnet-bearing source enriched in trace-elements, while more silicic rocks were derived from fractional crystallization of the andesite.

The most distinguishing characteristic of Summer Coon is the pattern of radial dikes that emanate from the center of the volcano. The dike swarm consists of hundreds of short (~200 m average outcrop length) and thin (~1 m average) basaltic andesite dikes with approximately 20 longer (~2-7 km) and thicker (~10-20 m) silicic dikes [*Lipman*, 1968; *Moats*, 1990; *Perry et al.*, 2001]. The mafic dikes are easily eroded and thus poorly exposed. In contrast, the silicic dikes form topographic walls that can exceed 30 m in height above the surrounding country [*Lipman*, 1968]. *Moats* [1990] mapped, in detail, the geometry of 13 silicic dikes, including measurements of thickness, azimuth, and segmentation. His maps, georeferenced to 1:24000-scale USGS topographic quadrangle maps, are shown in Figure 4.6A-H. Table 4.1 lists geometric statistics of all 20 silicic dikes at Summer Coon. The dikes generally do not deviate from radial orientations over large distances, suggesting that the regional differential stress was low at the time of dike emplacement [*Mertzman*, 1971; *Nakamura*, 1977]. *Olson and Pollard* [1991] show that fractures driven only by internal pressurization in an isotropic stress field will have an anastamosing geometry characterized by curving crack paths and intersections. At Summer

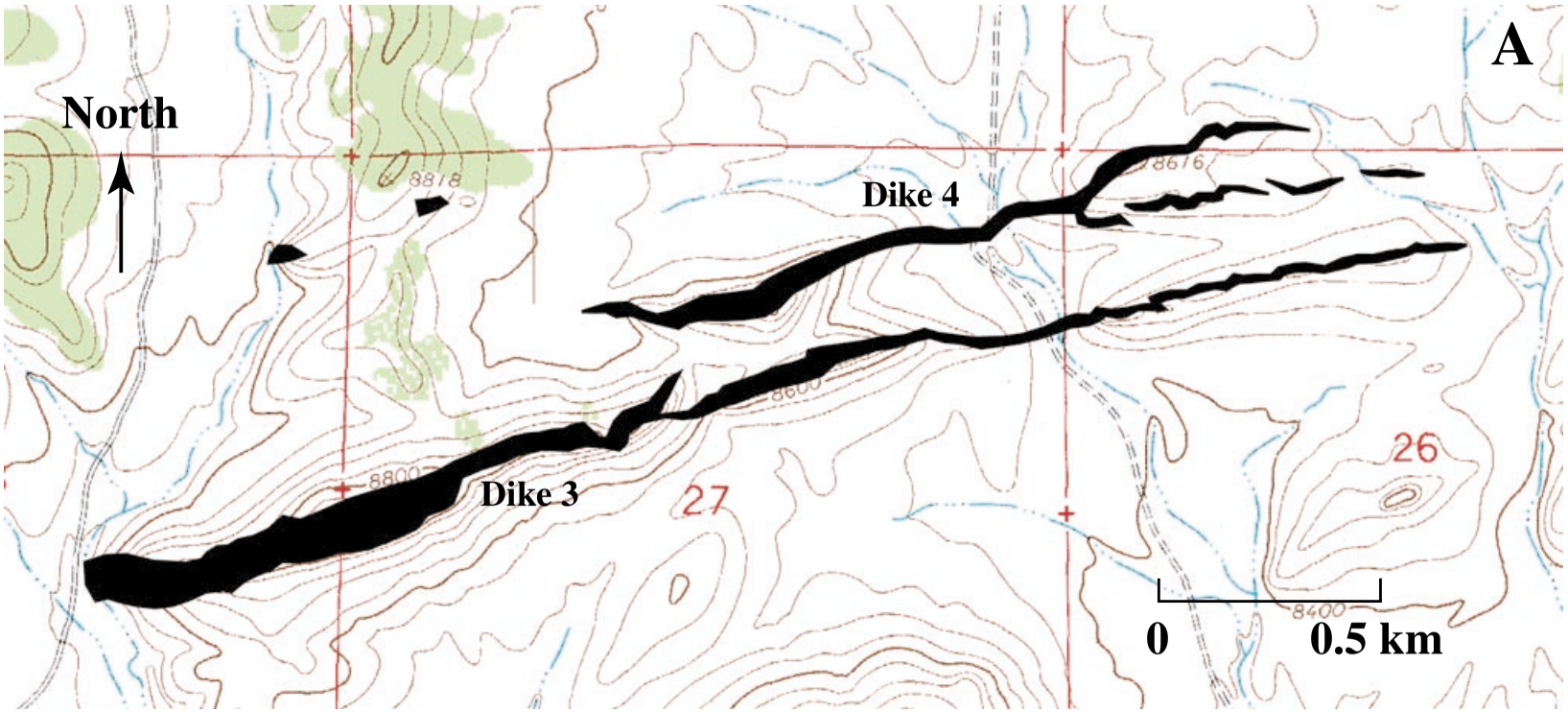

Figure 4.6. Geological maps of Summer Coon dikes georeferenced to 1:24,000 USGS topographic quadrangles. Maps were constructed by *Moats* [1990]. Dike numbers are from Figure 4.4. (a) Dikes 3 and 4. (b) Dike 7. (c) Dike 8. (d) Dikes 9 and 10. (e) Dike 11. (f) Dike 12. (g) Dike 14. (h) Dikes 15-17 and 20. Note that although several of the maps overlap, portions of dikes from overlapping regions are not shown. For example, Figures 4.6E (Dike 11) and 4.6F (Dike 12) overlap significantly, but because Dike 12 is not completely enclosed in the map from Figure 4.6E the intrusion is not shown. See Figure 4.4 for an index map showing locations of Figure 4.6A-H.

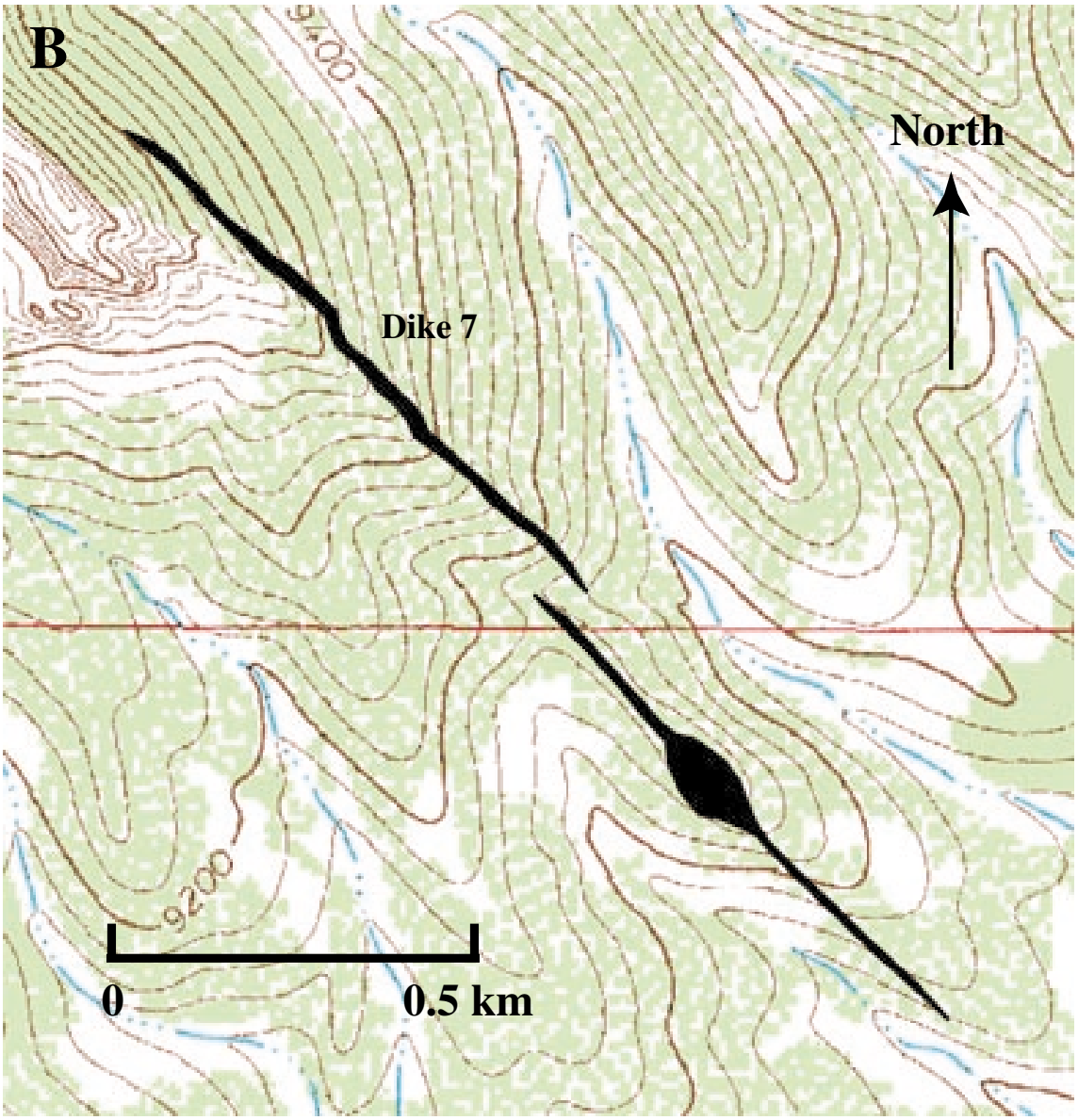

Figure 4.6. (Cont.)

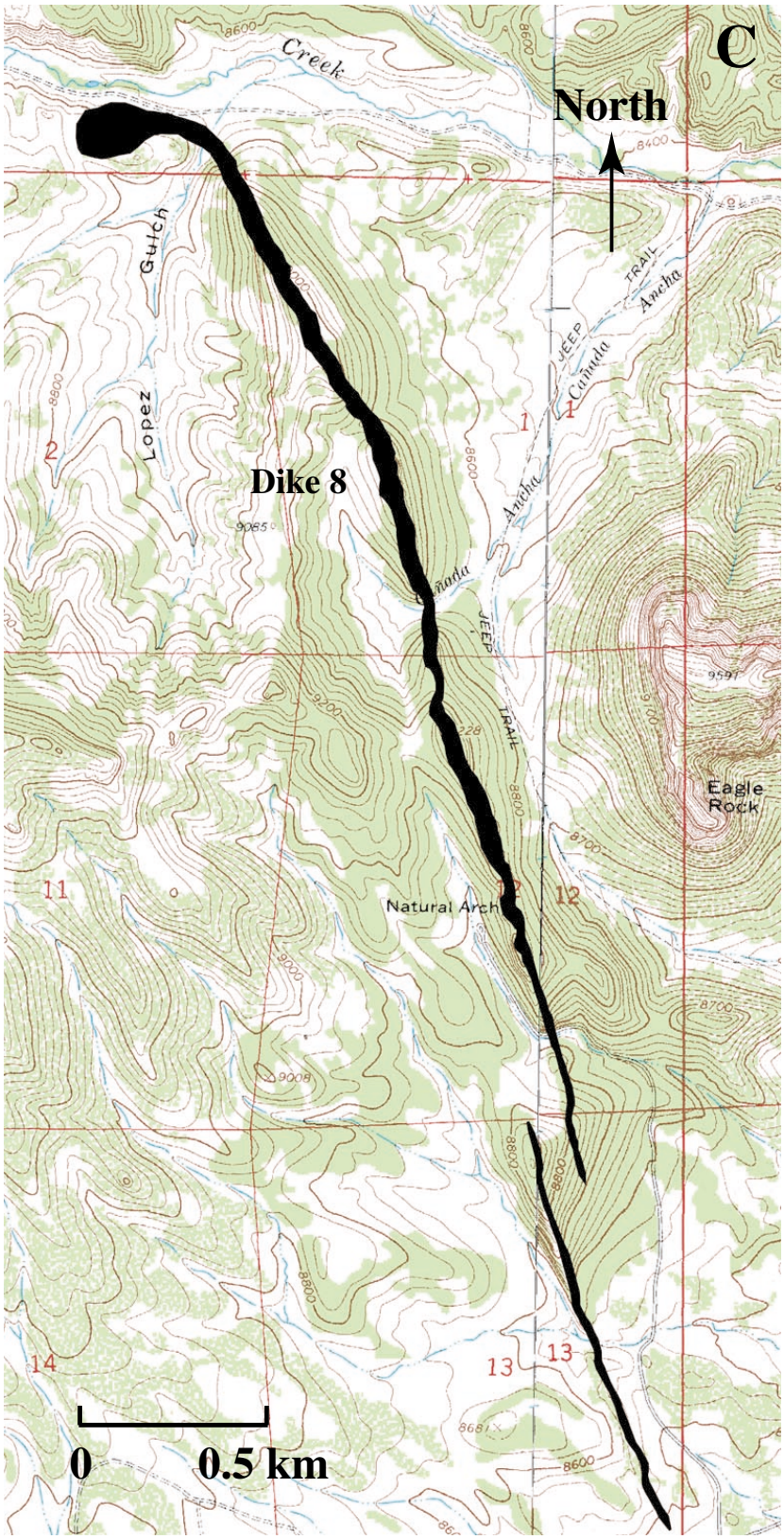

Figure 4.6. (Cont.)

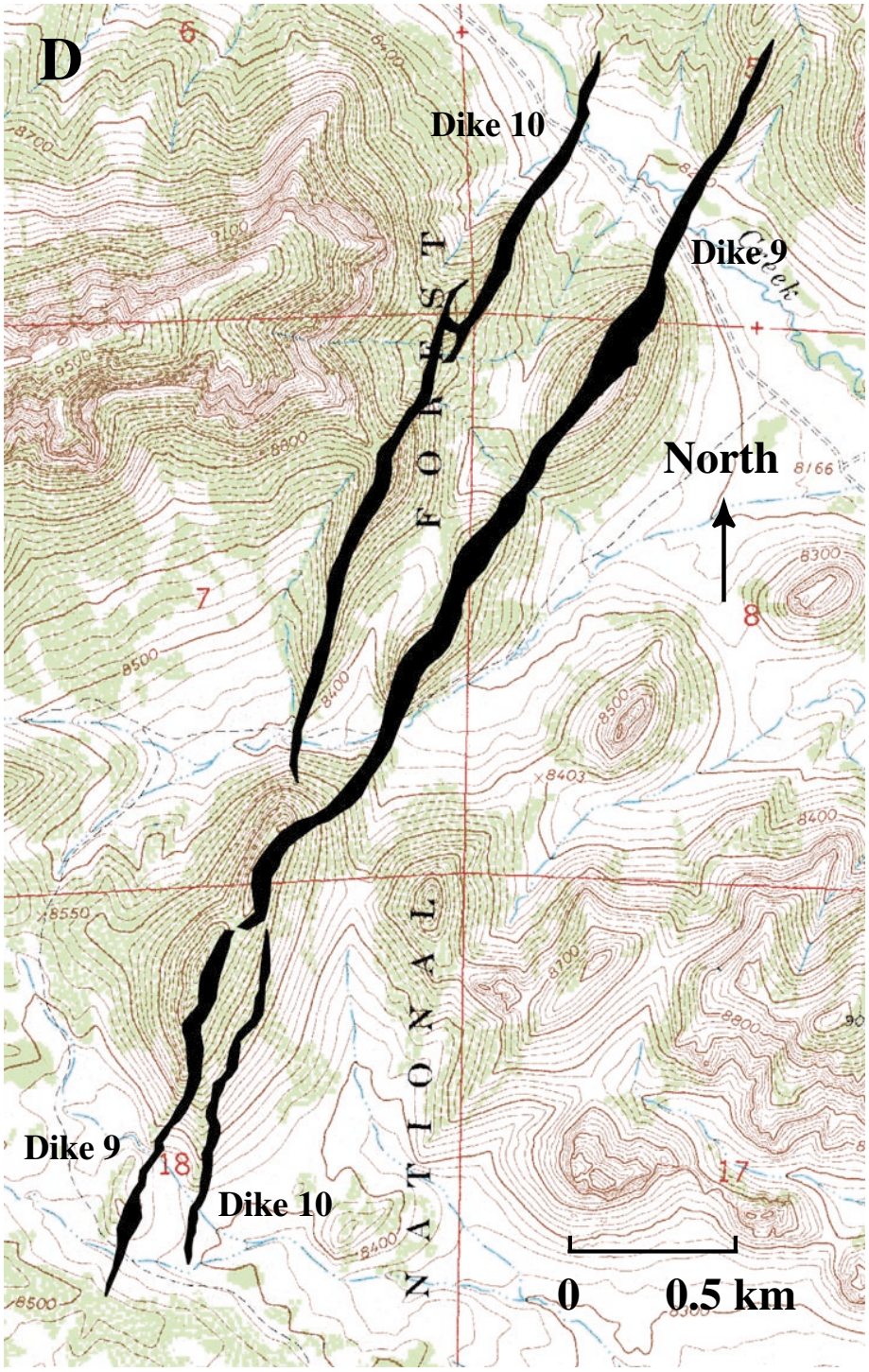

Figure 4.6. (Cont.)

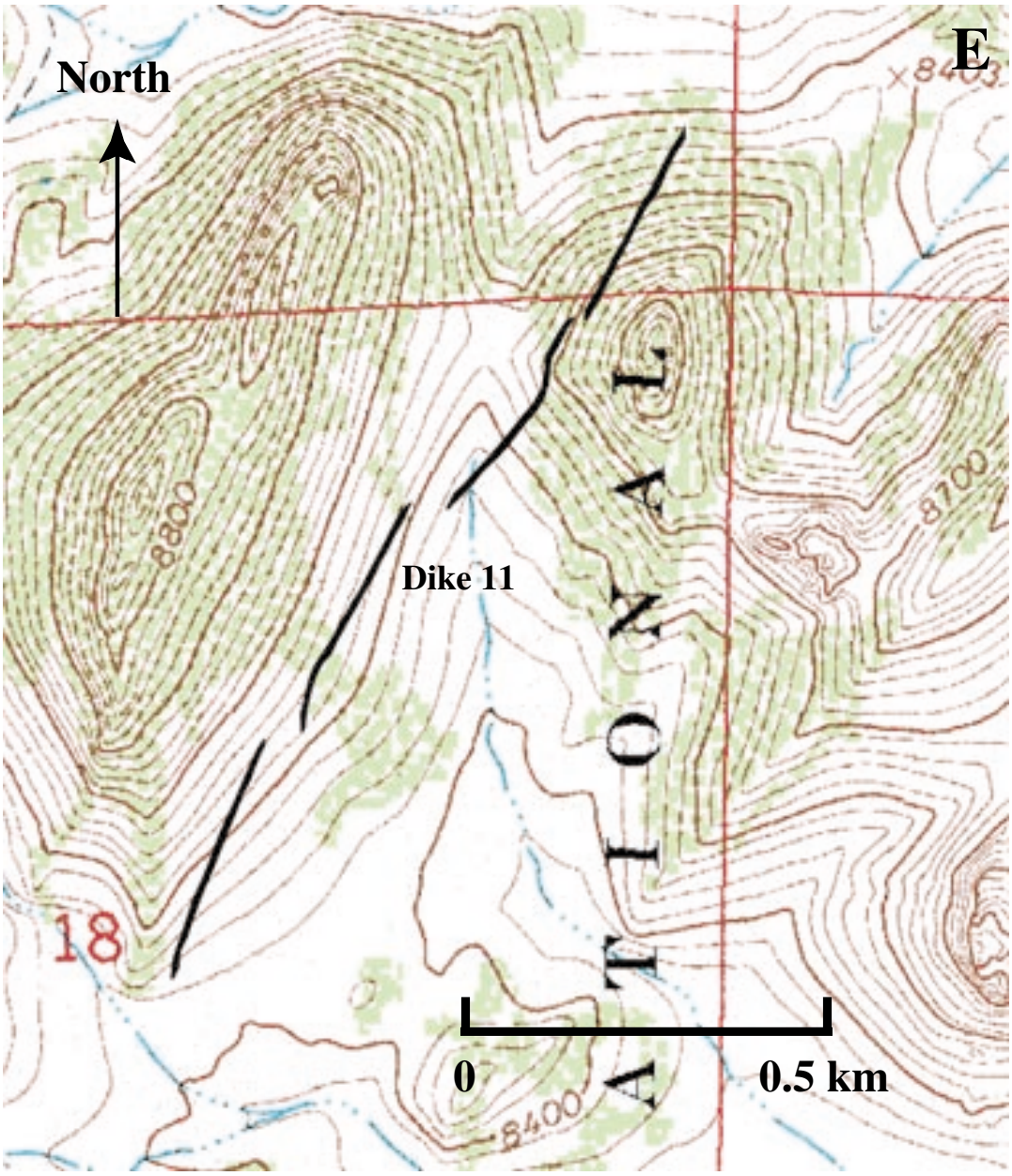

Figure 4.6. (Cont.)

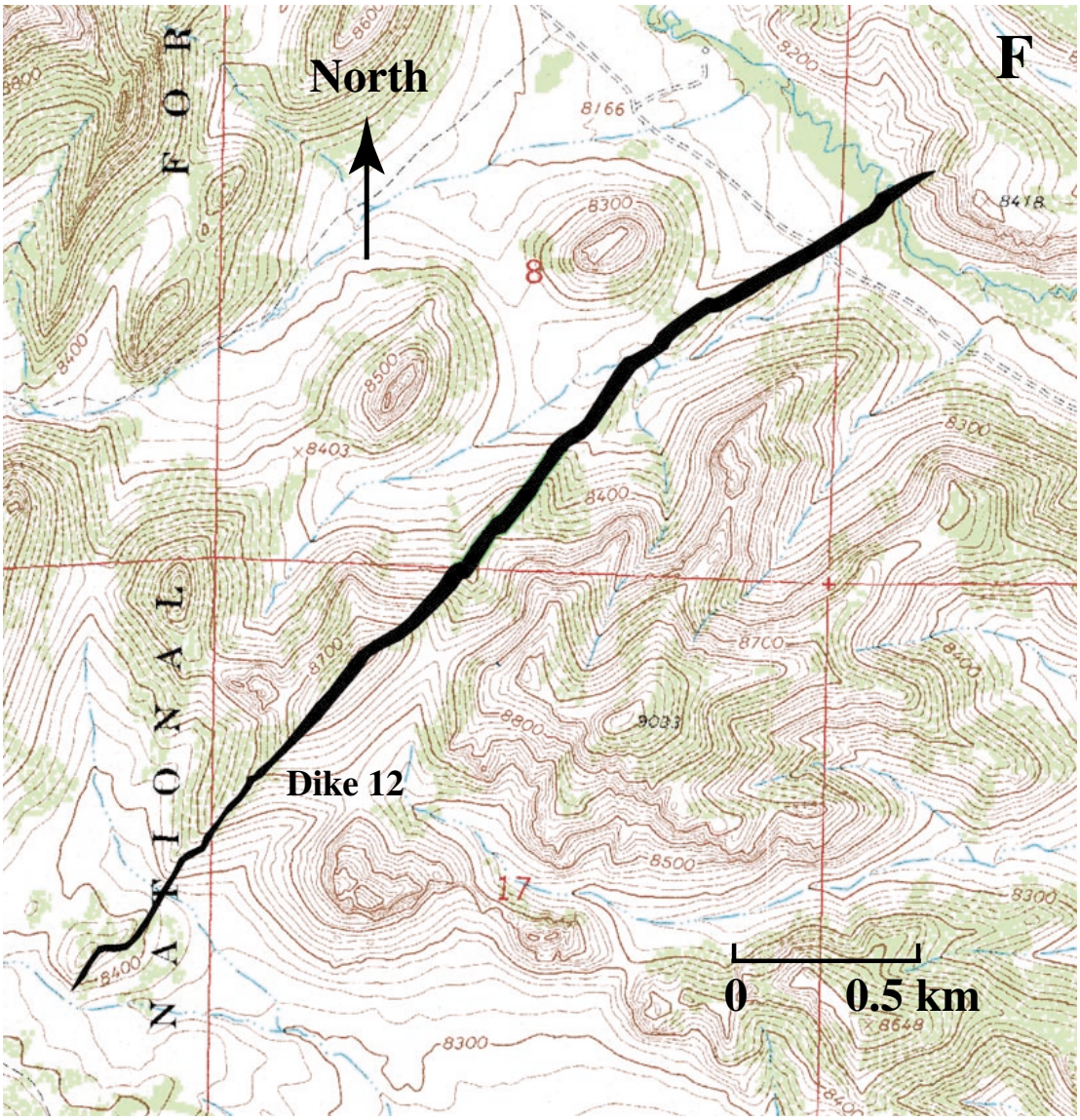

Figure 4.6. (Cont.)

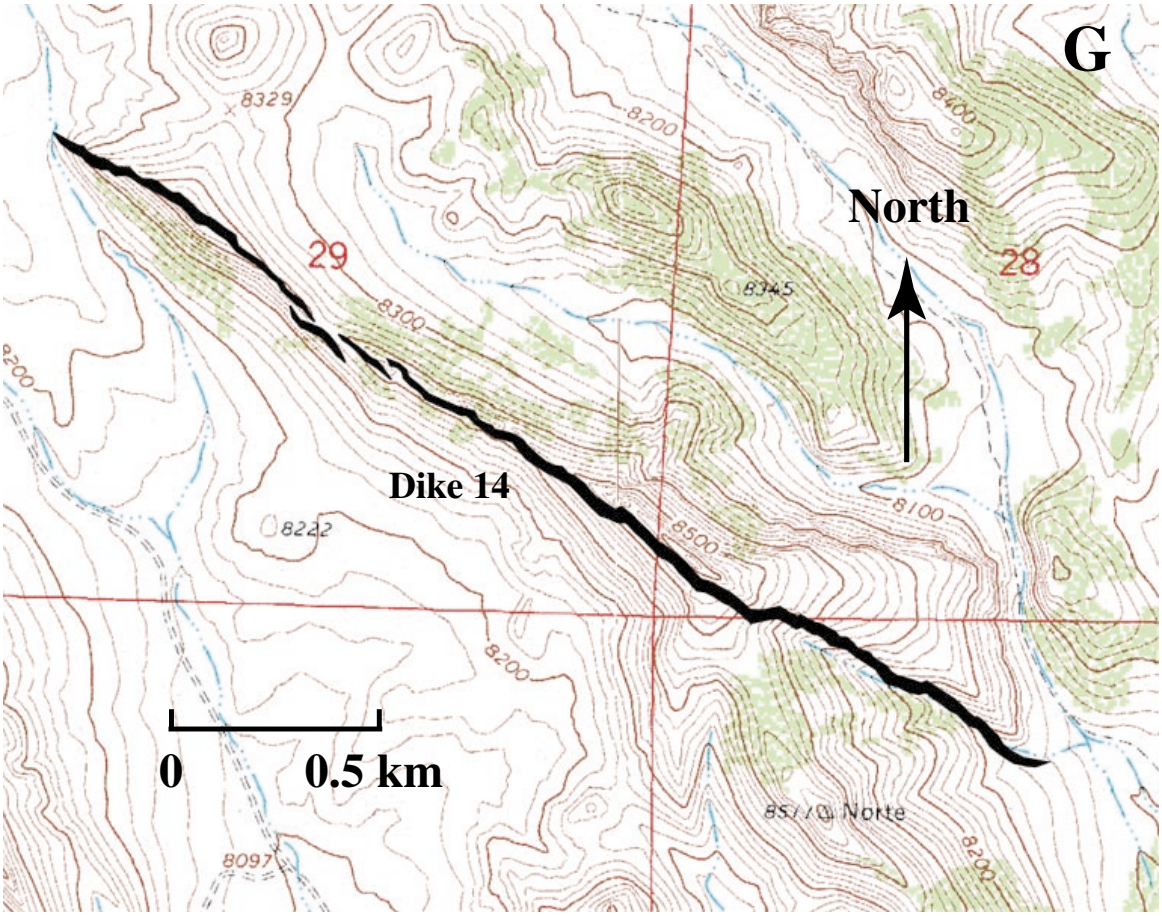

Figure 4.6. (Cont.)

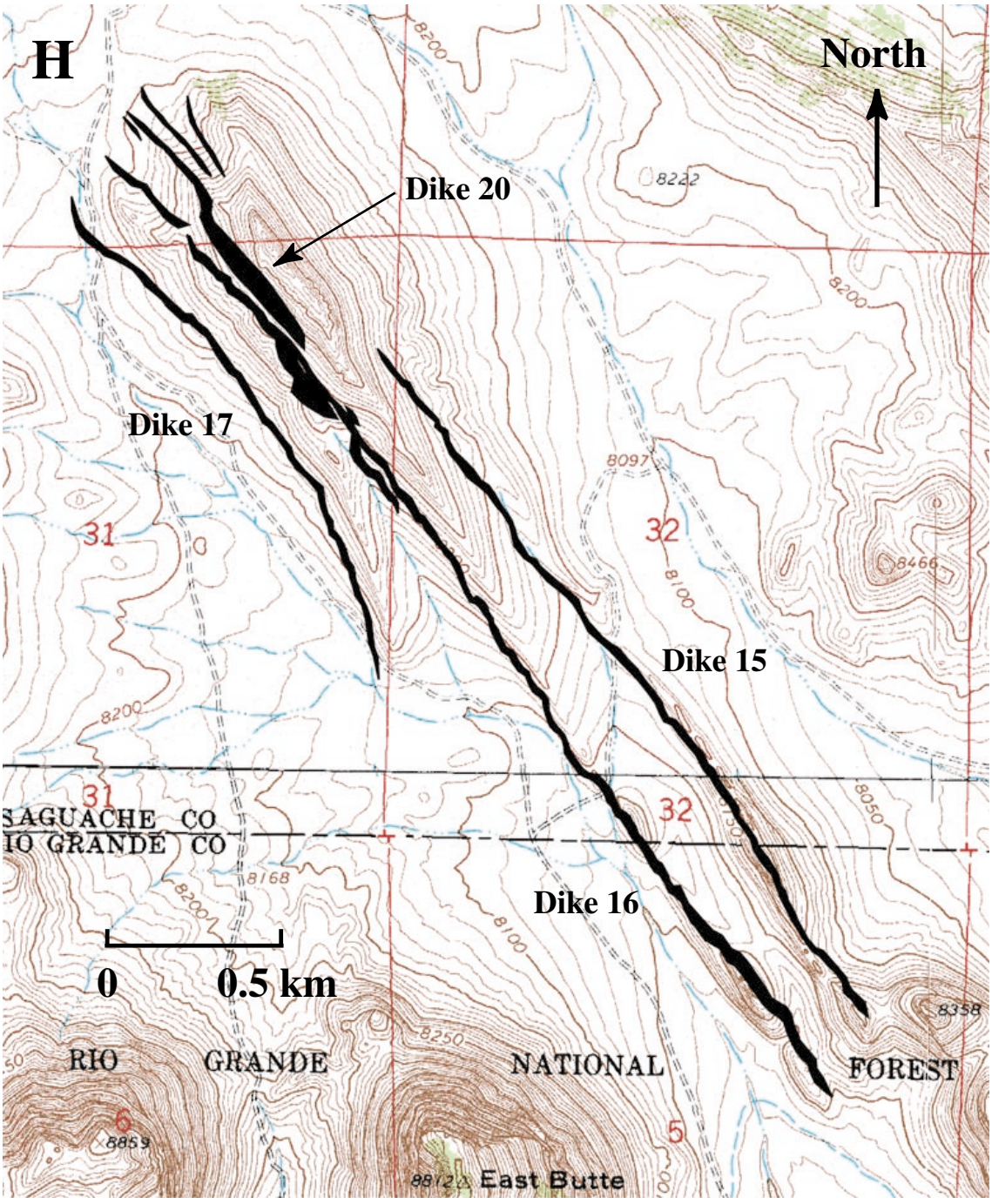

Figure 4.6. (Cont.)

Table 4.1. General characteristics of Summer Coon dikes (based on data from *Moats* [1990]). Azimuth is the average trend of the entire dike. The sense of offset is given for intrusions where one stepping direction clearly dominates the outcrop. Determinations were not made for dikes not mapped by *Moats* [1990].

Dike Number	Chemical Composition	Azimuth (degrees)	Outcrop Length (m)	Sense of Step
1	Rhyodacite	226	3027	unknown
2	Rhyolite	264	3147	unknown
3	Rhyodacite	258	3465	Left
4	Rhyodacite	255	1822	Left
5	Rhyodacite	301	1093	unknown
6	Rhyodacite	297	3313	unknown
7	Rhyodacite	316	1625	Right
8	Rhyodacite	343	5578	Right
9	Rhyodacite	29	4300	Mixed
10	Rhyodacite	17	3850	Right
11	Rhyolite	35	1350	Right
12	Rhyolite	43	3266	Right
13	Rhyodacite	90	3317	unknown
14	Rhyodacite	123	3005	Left
15	Quartz-latite	142	2330	Mixed
16	Quartz-latite	142	3350	Left
17	Quartz-latite	146	1648	Left
18	Rhyodacite	180	4744	unknown
19	Rhyodacite	182	901	unknown
20	Quartz-latite	142	1450	Mixed

Coon, Dikes 9 and 10, as well as Dikes 16 and 20, intersect, and curving dike trends are common (Figure 4.4), implying a homogenous horizontal stress field during intrusion.

Moats [1990] reconstructed the paleotopography of the volcanic cone by measuring the attitude of the contact between andesite breccias and silicic lavas around the volcano, then projecting the contact up-dip. The reconstruction gives minimum dimensions for the edifice, which reached approximately 4200 m in elevation with a basal diameter of 14.2 km. The cone rose at least 2200 m above the surrounding terrain, had a volume of 113 km^3, and was characterized by an average surface slope of 17 degrees (note that the measurements, with the exception of slope, are minimum values because they are based on the attitude of a contact near the top of, but still within, the volcanic pile). For comparison, Mt. Rainier volcano in Washington is 2200 m high, has a basal diameter of 17 km, and a volume of 140 km^3 [*Sherrod and Smith*, 1990; *Wood and Kienle*, 1990 p. 158]. The reconstruction of *Moats* [1990] can be used to determine the minimum burial depths along the lengths of the dikes, which is necessary to constrain the emplacement conditions of the intrusions. Much of the research described in this chapter makes use of field measurements by *Moats* [1990], which is one of the largest databases on dike geometry assembled for any one locality.

4.3 Dike Thickness

Variations in the thickness of an intrusion in cross-section can be used to calculate the driving pressure during emplacement, provided the material properties of the host rock are known or can be inferred. Assuming the host rock behaves as a homogenous, elastic solid, a uniformly pressurized dike should approximate the form of a symmetrical elliptical

crack [*Pollard and Muller*, 1976]. The thickness (t) of a dike as a function of distance can be related to driving pressure by the following expression:

$$t = 2\left(P_m - \sigma_3\right)\left(a^2 - x^2\right)^{1/2}\left(\frac{1-\upsilon}{\mu}\right) \tag{4.1}$$

where P_m is the magma pressure, σ_3 is the least compressive stress in the crust, a is the half-length of the dike, x is the distance along the dike from the dike center (i.e. $-a < x < a$), μ is the elastic modulus, and υ is Poisson's ratio [*Delaney and Pollard*, 1981]. The driving pressure is defined as $P_m - \sigma_3$ [*Reches and Fink*, 1988]. However, most intrusions that have been mapped in horizontal cross section are not elliptical, but have the form of an elongated teardrop [*Pollard and Muller*, 1976]. *Weertman* [1971] suggests that asymmetry of a fluid-filled crack is caused by a gradient in stress or pressure (termed an "effective stress gradient") along the fracture. Possible sources of an effective stress gradient in an igneous intrusion include 1) a gradient in regional stress along the dike, 2) variation in magma pressure along the dike, and 3) variation in material properties of the host rock along the dike [*Pollard and Muller*, 1976]. *Delaney and Pollard* [1981] relate dike thickness as a function of distance to a combination of uniform driving pressure plus an effective stress gradient, using the expression:

$$t = 2\left(P_m - \sigma_3\right)\left(a - x^2\right)^{1/2}\left(\frac{1-\upsilon}{\mu}\right) + \left(\Delta P_m - \Delta\sigma_3\right)x\left(a - x^2\right)^{1/2}\left(\frac{1-\upsilon}{\mu}\right) \tag{4.2}$$

where $(\Delta P_m - \Delta \sigma_3)$ is the effective stress gradient along the dike. *Pollard and Muller* [1976] mapped the thickness of the Walsen dike, part of the Spanish Peaks dike complex, and the Theater Canyon Sill, in the Henry Mountains of Utah, and found that a model including both a constant driving pressure and an effective stress gradient (equation 4.2) best approximates the measured distribution of intrusion thicknesses. They offer three

explanations for the source of the gradient that caused the asymmetry: 1) a sloping surface, which would cause the horizontal stress to vary, 2) stresses induced during the formation of nearby structures (for instance, a syncline or anticline), and 3) residual pressure from a subsurface magma chamber that is transmitted along the dike by magma that either flows or has a finite strength, and decreases in intensity with distance from the source.

4.3.1 Dike Thickness and Pressure Distribution at Summer Coon

At Summer Coon, nearly all of the silicic dikes have teardrop shapes with thicknesses that increase with distance from the central intrusive complex [*Moats*, 1990]. To gain a better understanding of the source of the asymmetric thickness distribution, a least squares linear inversion is used to determine 1) the uniform pressure that best fits the observed thickness distribution using equation 4.1, and 2) the combination of uniform pressure and effective stress gradient that best fits the observed thicknesses using equation 4.2. The source code for the inversion is given in Appendix A. Thickness data collected by *Moats* [1990] from 13 silicic dikes at Summer Coon are used in the inversion. A Poisson's Ratio (υ) of 0.25 and an elastic modulus (μ) of 4 GPa are used to characterize the elasticity of the host rock. Traditional laboratory estimates of the elastic modulus are often as high as 70 GPa. However the rocks of a pervasively fractured and altered volcanic edifice are likely to have much different elastic properties than laboratory samples. *Schultz* [1993] calculates an elastic modulus of 4-23 GPa for a volcanic edifice and *Rubin and Pollard* [1987] estimate 1-6 GPa for the upper few kilometers of Kilauea volcano in Hawaii. Both *Pollard* [1987] and *Schultz* [1993] find that a Poisson's Ratio of 0.25 is reasonable value for a rock mass at the scale of a km-long dike. Our estimates for the elastic parameters agree with both *Schultz* [1993] and *Pollard* [1987]. However, the

specific properties of Summer Coon rocks are not well-known and estimates of driving pressure and effective stress gradient are probably only valid at the order of magnitude scale. Despite uncertainty in the values of the elastic parameters, the calculated driving pressures for Summer Coon dikes will be directly comparable to one another because the dikes were emplaced in the same country rock [*Moats*, 1990].

Each dike is treated as a single crack, regardless of the number of segments. *Delaney and Pollard* [1981] analyzed a dike with 35 segments at Ship Rock, New Mexico, using models treating the intrusion as 35 individual cracks, 10 individual cracks, and a single crack. They found that the best fit was obtained using the single crack model, which probably gives a lower bound on the magnitude of the dike driving pressure. At Summer Coon, most dikes are characterized by 2-4 major segments and tens of minor segments. Models treating any individual dike as more than one crack do not produce a significantly better fit than single crack models.

Results of the modeling are given in Table 4.2, and the data and model curves for each dike are presented in Appendix B. Misfits are given as the sum of the squared residual (RSS) and RSS divided by degrees of freedom (denoted RSS/(N-P)). The latter statistics allow for comparison of the misfits of the constant pressure and effective stress gradient models by accounting for the decreased degrees of freedom in the effective stress gradient model (equation 4.2) due to the addition of a second model parameter. If any thickness data fall more than two standard deviations from the effective stress gradient model, the data points are removed, following the procedure of *Pollard and Muller* [1976]. The smoothing accounts for anomalous dike thicknesses from plugs that may have fed surface vents. The best-fitting model for a specific dike will have the lowest value for RSS/(N-P). For Dikes 3, 4, 7-12, 14, and 16 the effective stress gradient model fits the data better than the constant pressure model (although the improvement is marginal for

Table 4.2. Model results for inversions of dike thickness for 1) constant pressure, and 2) constant pressure plus a uniform pressure gradient. Pressure is given in Megapascals and the gradient has units of Megapascals per meter. RSS = residual sum of squares, N-P = degrees of freedom. The best-fitting model will have the lower value of RSS/(N-P). The "points omitted" column gives the number of measurements that were removed from the data because they fell more than 2 standard deviations from the modeled thickness (see text for a thorough explanation).

Dike	Constant pressure model			Constant pressure plus a gradient model				Points
Number	Pressure (MPa)	RSS	RSS/(N-P)	Pressure (MPa)	Gradient (MPa/m)	RSS	RSS/(N-P)	Omitted
3	34	2154.6	79.8	42	0.036	1032.1	39.7	3
4	97	1711.8	155.6	103	0.133	996.2	99.6	
7	31	188.0	14.5	32	0.044	130.9	10.9	3
8	39	7166.6	355.8	39	0.024	4199.9	221.0	
9	66	7356.4	367.8	69	0.037	4849.7	255.2	
10	36	1376.3	81.0	35	0.018	965.7	60.4	
11	19	18.3	1.7	18	0.031	7.9	0.8	
12	47	2564.4	116.6	54	0.057	496.9	23.7	
14	33	1137.9	54.2	34	0.013	1035.3	51.8	
15	36	347.2	28.9	36	0.011	335.4	30.5	
16	36	2164.8	120.3	35	0.017	1959.0	115.2	
17	47	159.8	13.3	47	-0.017	150.5	13.7	
20	142	3665.0	261.8	142	0.022	3657.1	281.3	

Dikes 14 and 16). The opposite is true for Dikes 15, 17, and 20. Error sources in the inversion include 1) incomplete exposure of the dike (dike ends may be concealed, which would yield an incorrect dike length and influence the results of the modeling) and 2) errors in the thickness measurements (which are not considered).

Moats [1990] notes that dikes 17 and 20 are relatively short and do not reach the outer flanks of the volcano (Figure 4.6H), implying that there is little variation in the effective stress gradient along these intrusions. As a result, the shorter dikes may be expected to better approximate an elliptical crack with a minor effective stress gradient (Table 4.2). Dike 15 is also poorly fit by the effective stress gradient model, however its proximal and distal ends are buried by alluvium [*Moats*, 1990]. If the concealed dike terminations taper down in thickness, both models would have improved fits. The minor decrease in the misfit of Dikes 14 and 16 by the effective stress gradient model may be explained if both dikes erupted to the surface at their distal ends [*Moats*, 1990]. An eruption would decrease the magma pressure in the intrusion, thereby causing the dike to close (i.e. decrease in thickness) along its length. The present thickness of a feeder-dike would not reflect the thickness distribution before eruption [*Hyndman and Alt*, 1987].

Driving pressures predicted by the model range from 18 to 142 MPa, averaging 51 MPa. For dikes that are better fit by the gradient model, the effective stress gradient varies between 0.018 - 0.133 MPa/m. In comparison, *Pollard and Muller* [1976] found driving pressures of 3.5 - 48 MPa for the Walsen Dike and 36 - 500 MPa for the Theater Canyon Sill, with effective stress gradients of 5.2×10^{-5} - 7.1×10^{-4} MPa/m and 0.084 - 1.2 MPa/m for the two intrusions, respectively. Both the sill and dike models of *Pollard and Muller* [1976] are relevant to models of Summer Coon dikes because sills and dikes both have the same tabular form (only the orientation of the form varies). Values from Summer Coon compare more favorably to those of the Theater Canyon sill. Both intrusions mapped

by *Pollard and Muller* [1976] have similar thicknesses (no more than 8 m in either case), however the Theater Canyon sill is much shorter (1 km) than the Walsen Dike (11.5 km). Summer Coon dike lengths fall between the two extremes but are much thicker, thus the modeled values of driving pressure and effective stress gradient fall between those of the Walsen dike and Theater Canyon sill, though closer to those of the sill.

Estimates of driving pressure within a dike are important when considering the conditions of dike emplacement. As noted by *Rubin* [1993] and other workers, long silicic dikes are not a common form of igneous intrusion, probably because the low temperature and high viscosity of rhyolitic magmas oppose rates of dike propagation that exceed the time necessary to freeze the dike magma. In contrast, basaltic dikes can propagate to great distances from their source regions, primarily due to their lower viscosity and therefore greater propagation rates. Analytical and theoretical modeling by *Rubin* [1993; 1995] suggests that an increase in magma viscosity by five orders of magnitude may be offset by an order of magnitude increase in magma source pressure. Analog and theoretical models of *McLeod and Tait* [1999] also support the requirement of high source overpressure for rhyolite dike propagation. *Rubin* [1993] further shows that for a rhyolite dike with a viscosity of 10^5 - 10^8 Pa·s, a source overpressure of 16 - 63 MPa or a temperature gradient less than 1°C per meter is required for dike propagation. Shallow magma reservoirs are probably associated with high thermal gradients due to the cold temperatures in the upper crust, therefore a low temperature gradient does not seem likely [*Rubin*, 1995]. Driving pressures for Summer Coon dikes are well above *Rubin's* [1993] lower bound, thus it seems that significant overpressure is a necessary constraint for silicic dike propagation.

4.3.2 Sources of Effective Stress Gradients at Summer Coon

There are no obvious explanations for the radial outward increase in effective stress gradient modeled in most Summer Coon silicic dikes. The near perfect radial form of the dikes suggests that regional stress was nearly isotropic, thus heterogeneity in regional stress is an unlikely source. In addition, *Moats* [1990] notes that all silicic dikes are either wholly or mostly emplaced in basaltic andesite breccia, so that the elastic parameters of the host rock should be relatively constant along the intrusions. An outward stress gradient is caused by pressure in a subvolcanic magma chamber, however stress gradients cannot be transmitted by a liquid (magma in a dike, in this case) unless the fluid has a finite yield strength or is flowing [*Pollard and Muller*, 1976]. As noted in section 4.5.4 below, Summer Coon dikes are characterized by a component of flow laterally away from the center of the volcano. Additionally, silicate liquids have strength, therefore the stress gradient due to magma chamber pressure may influence dike thickness. Because the effects of positive pressurization will decrease with radial distance from the chamber, the stress gradient will be negative, implying a decrease in transmitted stress along the length of the dike and favoring a teardrop shape that is thickest at the center of the volcano. As a result, the effective stress gradient that controls the observed increase in dike thickness with radial distance at Summer Coon must overcome the gradient imposed on the dike by a pressurized magma chamber. Rhyodacite, the most common composition for Summer Coon silicic dikes, has a relatively high yield strength (k) of 2.5 x 10^5 Pa [*Fink and Griffiths*, 1998], therefore the magma can support a stress gradient (defined here as Δp) from the magma chamber given by:

$$\Delta p \leq -2\frac{k}{t} \tag{4.3}$$

where t is the thickness of the magmatic conduit [*Pollard and Muller*, 1976]. Dike thicknesses at Summer Coon commonly vary between 10 m and 30 m, therefore the magma can support a pressure gradient of 0.01 to 0.03 MPa/m.

Horizontal stresses due to the surface slope of the volcano above a dike will oppose stress gradients from the magma chamber and cause the dike to thicken with radial distance from the source. *Moats* [1990] estimates a surface slope α of 17 degrees for Summer Coon. Under conditions of hydrostatic stress the maximum horizontal stress is proportional to the overburden height, therefore the horizontal stress gradient ΔS_y is related to the surface slope by:

$$\Delta S_y = \rho g \tan \alpha \qquad (4.4)$$

where ρ is the density of the host rock, and g is the acceleration due to gravity [*Obert and Duvall*, 1967, p. 495]. Assuming a density of 2800 kg/m^3 for the basaltic andesite breccia host [*Moats*, 1990] and a gravitational acceleration of 9.8 m/s^2, the maximum horizontal stress gradient due to the surface slope is 0.008 MPa/m. If the stress gradient caused by a pressurized magma chamber (equation 4.3) is greater than the horizontal stress gradient caused by a sloping surface (equation 4.4), the dike will be thickest near its source. The opposite is true if the horizontal stress gradient is larger than the pressure transmitted from the magma chamber. If the two values are equal, the dike should be elliptical in horizontal cross section, as if no stress gradients were acting on the intrusion. According to the above calculations, for dikes greater than 10 meters thick the effective stress gradients caused by a pressurized magma chamber will be slightly larger than the horizontal stress gradient caused by a surface slope, therefore an alternative source for the observed dike form must exist.

Two sources which may account for the observed dike thickening with radial distance from the center of Summer Coon are 1) the shallow depth of the dikes under the flanks of the edifice, and 2) varying elastic properties of the andesitic breccia with depth. Burial depth measurements by *Moats* [1990] show that many Summer Coon dikes terminated laterally within tens of meters of the surface, and plugs at the ends of several dikes suggest that the intrusions fed surface eruptions. Most models of crack propagation ignore the effects of a free surface close to the crack tip, treating the problem as a crack in an infinite elastic medium. *Pollard and Holzhausen* [1979] examined the effect of a free surface on a propagating fracture and found that the resistance to crack dilation decreases as an intrusion approaches the surface, resulting in dike thickening. A shallow dike propagating along a horizontal path under a sloping surface will become thicker downslope due to the decreasing depth from the ground surface to the dike top.

Although the host rock along the entire length of most Summer Coon dikes is relatively homogenous, the elastic properties of the rock are likely to vary with depth. Compaction due to the weight of overlying rock will tend to seal fractures and decrease pore space within the core of the edifice. However, rock near the surface has less overburden and is likely to host open fractures and less compressed material [*Rubin and Pollard,* 1987]. *Bürgmann et al.* [1994] use boundary element models to demonstrate that strike slip faults passing through regions of lower elastic modulus will have higher slip in the weaker material. Faults that terminate in a region of lower elastic modulus will have a teardrop-shaped slip distribution. Extending the analysis to dilational fractures, a dike that propagates into a region of low elastic modulus will tend to thicken without a corresponding increase in driving pressure.

In summary, the distribution of dike thickness along a horizontal cross section is a function of several competing factors. If the magma in a dike is flowing or has a finite

yield strength, the intrusion will become thinner with radial distance from its source due to the decrease in magma chamber pressure transmitted through the dike. A dike will tend to thicken in response to 1) a surface slope above the dike where the intrusion is propagating in the downslope direction, 2) decreasing burial depth, and 3) a decrease in the elastic modulus of the host rock. At Summer Coon the observed outward thickening of most dikes is most likely caused by a combination of decreases in the burial depth and elastic modulus. Models of the effective stress gradient in a dike do not account for possibilities 2 and 3 above, and therefore may not be applicable unless the thickness distributions of each dike are modified to account for changes in burial depth and elastic properties of the host rock. With additional study, variations in dike thickness may aid in the reconstruction of surface topography and morphology. Assuming constant magma pressure in all directions, the horizontal cross section of a dike will be a function of burial depth, surface slope, and material properties. An approximation for the effect of surface slope on dike thickness already exists (equation 4.4), and future constraints for the effects of burial depth and material properties on dike thickness will allow for topographic reconstructions based on the morphologies of shallow intrusions.

In contrast to Summer Coon, thicknesses of the Spanish Peaks dikes decrease with increasing distance from the source [*Smith*, 1987]. The depth of exposure at Spanish Peaks is probably much greater than at Summer Coon, because no surfical deposits are preserved and the intrusive stocks of the Spanish Peaks extend several thousand feet above the surrounding dikes. Surface slope, the proximity of the free surface, and varying elastic properties of the host rock probably did not influence the thickness of these intrusions due to the depths at which the dikes currently exposed were emplaced. As a result the only significant influence on dike thickness is overpressure in the magma chamber (transmitted

along the dike by magma that flows or has a yield strength), and the dikes should thin with distance from their source.

4.3.3 Deformation and Potential Eruptive Volume from Radial Dikes

Because the radial dikes of Summer Coon thicken with increasing radial distance from the center of the volcano and eruption rates are proportional to conduit dimensions, a greater volume of magma is likely to erupt from the flank of the edifice than the summit. Observations of dike terminations at Summer Coon support the inference, as several long dikes at Summer Coon end in plugs that may have fed surface eruptions. The termination of Dike 2 is concealed by a large surficial rhyolite flow of similar composition, which is probably connected to the intrusion at depth [*Moats*, 1990]. In addition, the terminations of both Dikes 2 and 3 are characterized by thin intrusions that are radial to the primary dikes, suggesting that the terminations of the primary dikes acted like pressure sources analogous to a magma chamber (Figure 4.7). Only Dike 7 has a major plug far from its termination (Figure 4.6B). This plug may have fed a surface eruption high on the flank of Summer Coon, but its small size suggests that it transported a relatively minor volume of magma to the surface. Field observations and modeling results both suggest that the potential eruptive volume of magma is directly proportional to radial dike length. Large volume eruptions from summit vents are most likely fed by a central conduit that taps the magma chamber, rather than a radial dike.

Given the thicknesses of silicic dikes at Summer Coon, surface deformation above the intrusions was probably a significant precursor to eruptive activity. Elastic boundary element models (which are supported by field evidence) indicate that extensional strain maxima should be evenly spaced on either side of a vertical dike [*Pollard and Holzhausen*,

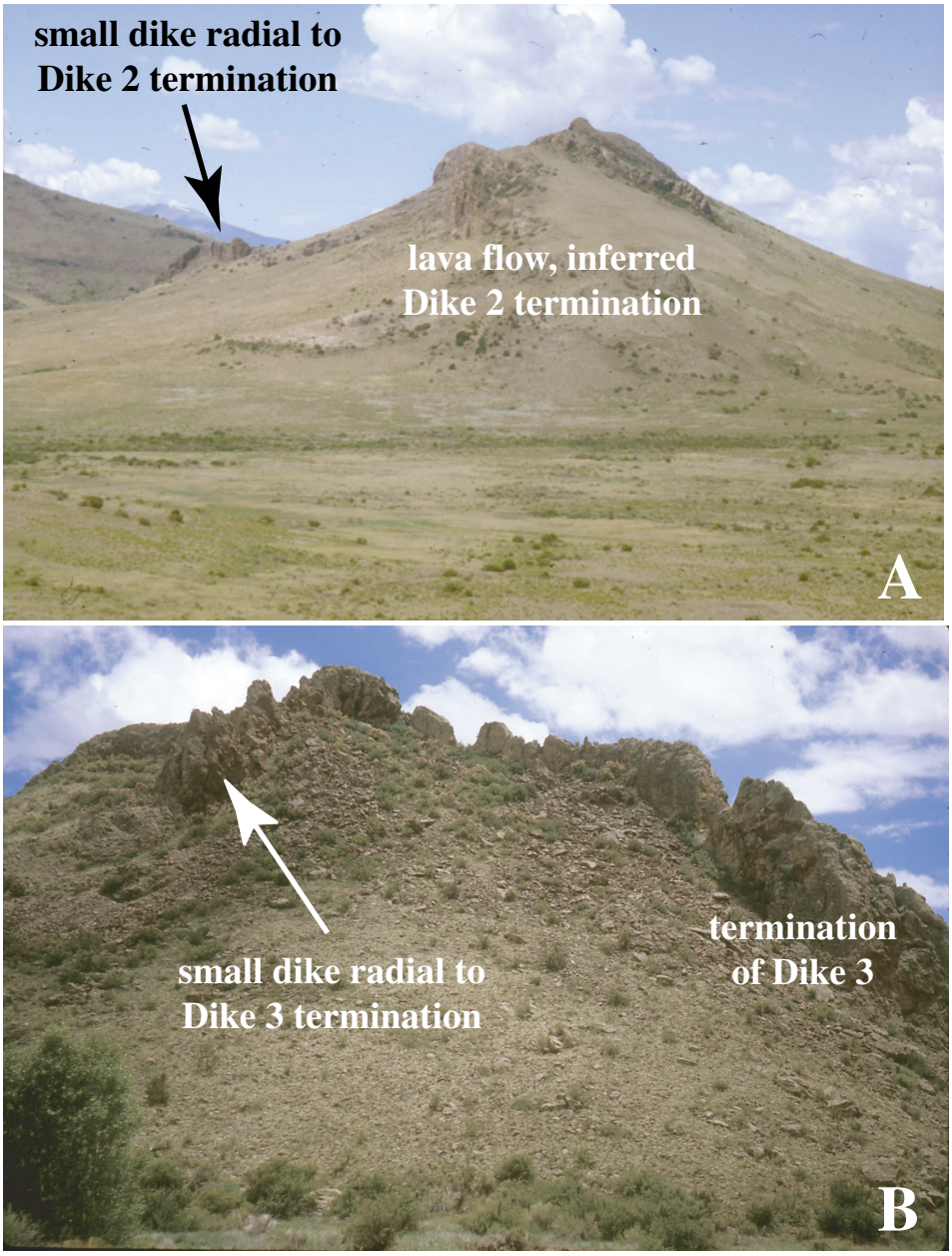

Figure 4.7. Examples of small intrusions that have orientations radial to the terminations of large Summer Coon radial dikes. (a) View looking west at a rhyolite lava flow overlying the termination of Dike 2 as seen from the central intrusive complex of Summer Coon. A small dike can be seen at the left, trending south away from the lava flow and the inferred termination of Dike 2. Hill is approximately 200 meters above the surrounding terrain. (b) Termination of Dike 3, where a small dike trends radially away from the main intrusion. View is to the east, and the ridge containing the dikes is approximately 75 meters high.

1979; *Pollard et al.*, 1983]. The spacing between the strain maxima is an indicator of the depth to the top of the dike [*Fink and Pollard*, 1983; *Pollard et al.*, 1983]. Through the use of analog models, *Mastin and Pollard* [1988] showed that increasing dilation of a dike held at a constant depth causes the surface deformation to evolve from a series of small extensional fractures to a complex graben bounded by dip-slip faults (the outermost fractures of the system correspond to the theoretical strain maxima). Therefore, a thick silicic radial dike that intrudes an arc volcano will likely manifest itself at the surface as a well-developed zone of parallel extensional fractures whose spacings decrease radially, possibly culminating in a graben.

4.4 Dike Segmentation

Moats [1990] recognizes three distinct generations of dike segmentation at Summer Coon, with each successive generation of smaller scale and superimposed on the preceding. The first generation is characterized by stepping segments that are en echelon and usually overlap, as exemplified by Dikes 7 and 8 (Figures 4.6B and 4.6C, respectively). These segments may or may not be connected by thin strands of igneous material (as is shown for Dikes 3 and 10 in Figures 4.6A and 4.6D). Second and third generation segments are sometimes en echelon and almost always coalesced, giving the dikes a jagged appearance in map view (for example, Dike 15 in Figure 4.8). Commonly, second and third generation segments have the appearance of igneous fingers with random geometries, similar to those described by *Pollard et al.* [1975], which are typically found at the periphery of igneous intrusions. For the present study, the second and third generations of segmentation are combined because the third generation is relatively rare. *Moats* [1990] documents third-generation segments on only two Summer Coon silicic

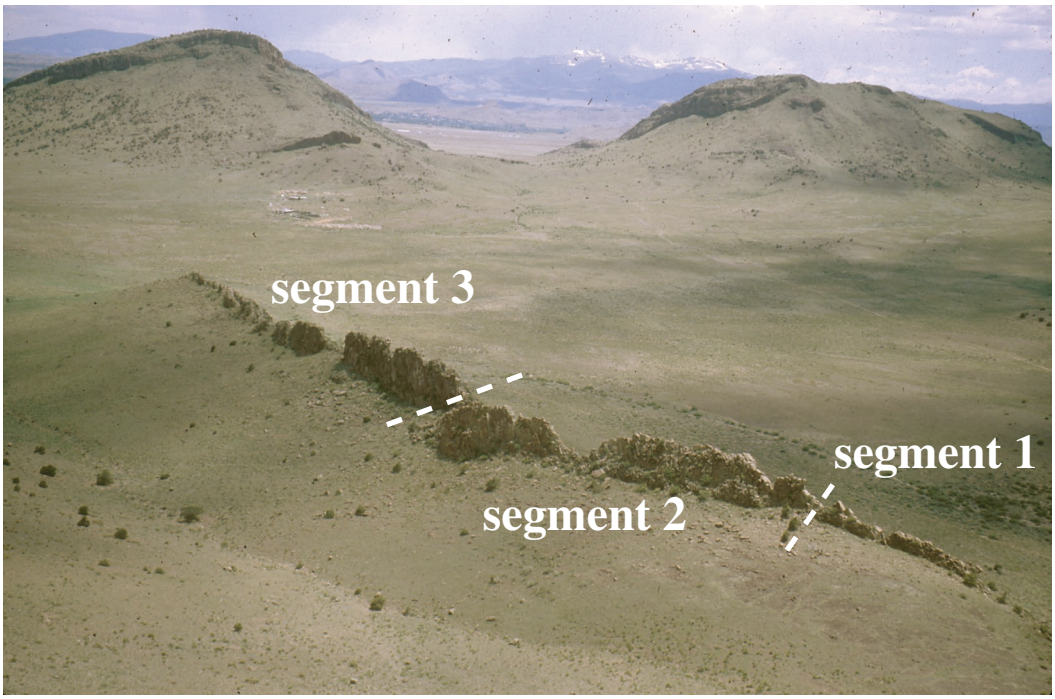

Figure 4.8. View of Dike 17 looking south from the ridge near Dikes 16 and 20. The 3 first generation segments mapped by *Moats* [1990] are labeled on the photograph. Note the many second-generation segments which are coalesced but distinct along the length of the intrusion. The exposed outcrop is approximately 1650 meters in length.

dikes), and the second and third generations are coalesced whereas first generation segments are distinct from each other. Segments are generally right-stepping in the northern hemisphere of Summer Coon and left-stepping in the south [*Moats*, 1990].

En echelon fractures have been noted at a variety of scales in many different materials. Small, centimeter-scale echelon fractures have been produced in glass by *Sommer* [1969]. At the meter scale, crevasses in glacial ice [*Meier*, 1960], crease structures in lava flows [*Anderson and Fink*, 1992], eruptive fissures [*Nakamura*, 1970], and ground cracks above unerupted dikes [*Fink and Pollard*, 1983; *Fink*, 1985] have echelon geometries. Finally, kilometer-scale echelon features include mid-ocean ridge segments [*Parson et al.*, 1993; *Abelson and Agnon*, 1997]. The mechanism of en echelon dike segmentation has been a subject of some debate [e.g. *Currie and Ferguson*, 1970; *Delaney and Pollard*, 1981; *Reches and Fink*, 1988]. Given the range of environments and scales at which en echelon fractures form, there is reason to believe that multiple mechanisms may influence the development of segmentation in dilatant cracks [*Pollard et al.*, 1982]. Depending on the formation mechanism, segmentation may be used as an indicator of dike propagation direction. *Pollard et al.* [1975] suggest that segment rotation about a vertical axis indicates vertical magma flow. However, *Currie and Ferguson* [1970] argue that magma flow is perpendicular to the axis of segmentation. Below, several proposals regarding dike segmentation are evaluated in light of observations from Summer Coon, where excellent along-strike exposures of silicic dikes and burial depth determinations by *Moats* [1990] provide constraints on the mechanism of segmentation.

4.4.1 Stress Rotation with Depth

In the absence of preexisting fractures or material heterogeneities, an igneous dike should propagate in a plane that is perpendicular to the least compressive stress in the crust, and parallel to the most compressive stress [*Stevens*, 1911; *Anderson*, 1938; *Nakamura*, 1977]. Therefore dikes are usually good indicators of the orientation of tectonic stress that existed at the time of emplacement [*Delaney et al.*, 1986]. If the orientations of the principal stresses change during dike intrusion, a component of shear is resolved onto the plane of the dike, causing the dike to change orientation to resume a trend that parallels the most compressive stress [*Pollard et al.*, 1975; *Pollard*, 1987]. Rotation of the least compressive stress about an axis parallel to the propagating edge of the dike will cause the intrusion to break into several smaller rotated en echelon segments that are individually perpendicular to the least compressive stress (Figure 4.9) [*Pollard*, 1987]. Sudden changes in stress orientations will produce kinked intrusions, whereas more gradual rotations lead to smoothly conforming intrusions [*Thomas and Pollard*, 1993; *Cooke and Pollard*, 1996]. *Sommer* [1969] demonstrates the formation of en echelon fractures due to stress rotation by applying a torque to a glass rod under axial tension. Fractures were initially perpendicular to the axis of the rod but separated into multiple echelon fractures during propagation, with a sense of step consistent with the moment of the applied torque. Multiple echelon crack formation is favored over rotation of the parent crack because less energy is required for echelon breakdown. Although an infinite number of small echelon fractures will minimize the energy necessary for fracture, the number of fractures is probably limited by host rock heterogeneity [*Pollard et al.*, 1982].

Stress rotation about a vertical axis has been used to explain the formation of numerous dikes with en echelon segments in map view, including those at Ship Rock,

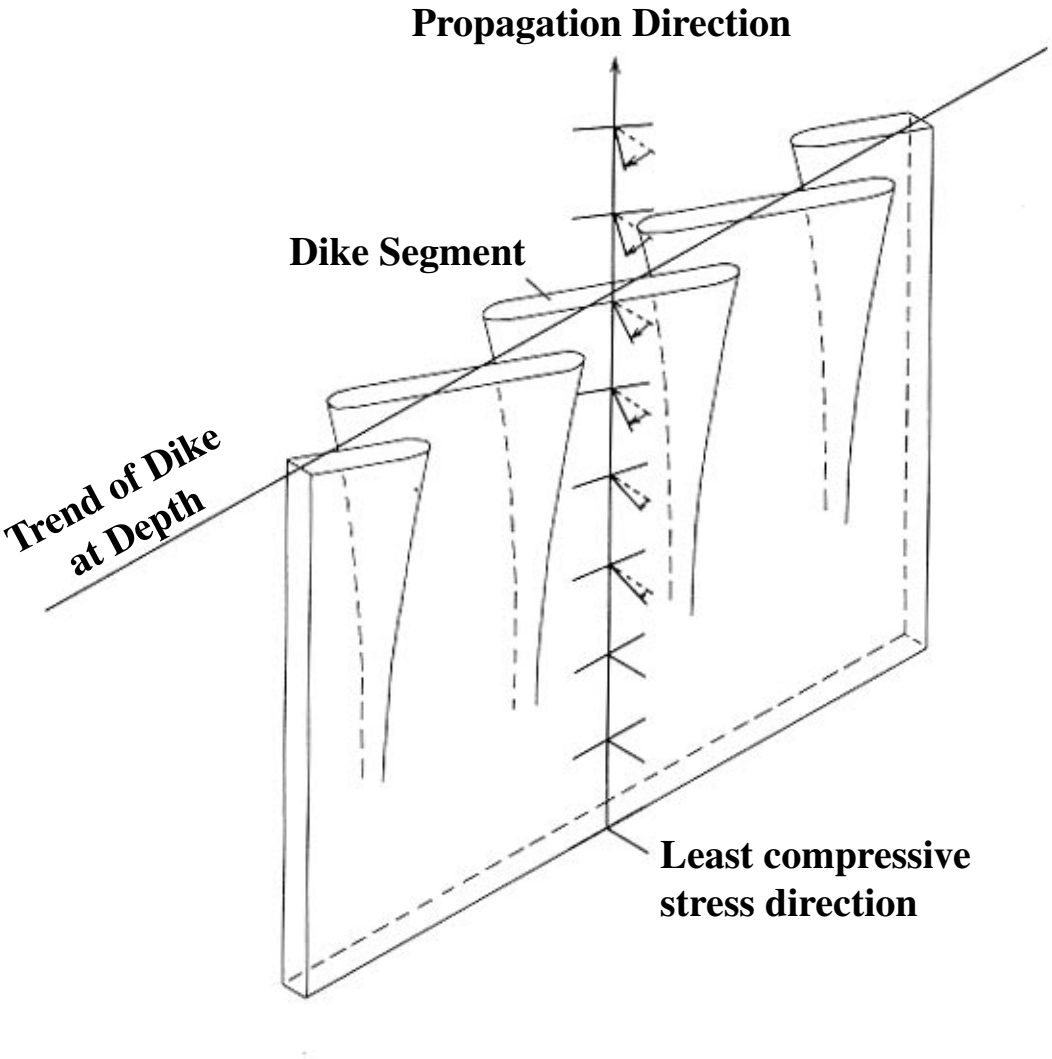

Figure 4.9. Diagram of dike segmentation due to rotation of the least compressive stress direction with depth. The intrusion is continuous at depth, but as it propagates upward the least compressive stress rotates about a vertical axis. Because dikes intrude parallel to the most compressive stress (perpendicular to the least compressive stress), the dike breaks into segments which rotate to align with the new stress field. Rotation of segments minimizes the energy necessary to fracture the rock and is mechanically more favorable than rotation of the dike as a whole [*Pollard et al.,* 1982]. After *Delaney and Pollard* [1981].

New Mexico [*Delaney and Pollard,* 1981] and at Spanish Peaks, Colorado [*Pollard et al.*, 1975]. The principle has also been applied to en echelon fissure eruptions in Hawaii [*Pollard et al.,* 1983]. The mechanism for stress rotation about a vertical axis is unclear. *McGarr* [1980] reports that the magnitude of maximum shear (defined as half the difference between the maximum and minimum principal stress) increases with depth. However there is little unambiguous evidence that the stress orientations change with depth in the crust. Changes in the stress regime along horizontal transects are common, and may be induced by variations in material properties or tectonic setting [e.g. *Prejean et al.*, 2000]. *Ode* [1957] and *Muller and Pollard* [1977] cite the asymmetry of the Spanish Peaks radial dike swarm as evidence that the Sangre de Cristo mountain range, located immediately west of the Spanish Peaks, acted as a rigid block during dike intrusion. The effect of the mountain range was to induce a change in the stress field, deflecting dikes from their radial trends. Similar relationships have been observed at Mount Etna volcano in Sicily, where historical dikes have curved away from the walls of the Valle del Bove landslide scarp [*McGuire and Pullen,* 1989]. If the change in stress orientation with horizontal distance is abrupt, a dike propagating from one stress regime into another may form echelon segments with a sense of rotation that is consistent with the shear imparted on the dike plane [*Thomas and Pollard,* 1993; *Cooke and Pollard,* 1996].

In a radial dike swarm, a horizontal change in stress orientation would occur where the influence of tectonic stresses becomes greater than the circumferential compression generated by the pressurized magma chamber. In such a case, segment rotation would be clockwise in two diagonally-opposing quadrants of the volcano and counter clockwise in the others [*Moats,* 1990]. At Summer Coon, the only indication of the principal stress orientation is a slight deviation from radial orientation near the north end of Dike 8, which curves to the west suggesting generally north-south least compressive stress and east-west

most compressive stress (Figure 4.6C). Therefore, segment rotation in the radial dikes at Summer Coon should be left-stepping (clockwise) in the NW and SE quadrants of the volcano, and right-stepping (counterclockwise) in the NE and SW (Figure 4.10). Dike rotation does not follow such a pattern at Summer Coon. Nearly all segments in the northern half of the volcano are right-stepping, while the southern half is dominated by left-stepping segments [*Moats*, 1990].

If segment rotation is a function of depth, the degree of rotation should increase with decreasing burial depth. *Pollard et al.* [1982] idealize echelon dikes as helicoidal fractures that are continuous along twisted surfaces, so that points on the dike at different burial depths will have varying degrees of twist. The proposal can be tested at Summer Coon, where burial depths along each dike and segment azimuths are well known. Figure 4.11 is a plot of segment rotation (defined as change in segment azimuth referenced to the azimuth of the first segment) vs. burial depth. Although a few individual dikes show general increases in segment rotation with decreasing burial depth, there is no overall correlation between the two variables. As a result, it appears unlikely that a rotation of the stress field with depth is a realistic mechanism for dike segmentation at Summer Coon.

4.4.2 Intrusion into Existing Fractures

If favorably oriented fractures are present in a magmatically active region, dikes may become segmented if they intrude the existing cracks. *Delaney and Gartner* [1997] mapped the geometry of several hundred mafic dikes on the western margin of the Colorado Plateau in Utah. They found no relationship between the strike, thickness, and length of the dikes, and noted that segmentation was random as opposed to classically en echelon [e.g. *Delaney and Pollard*, 1981]. Dike strike varied over 110 degrees, leading

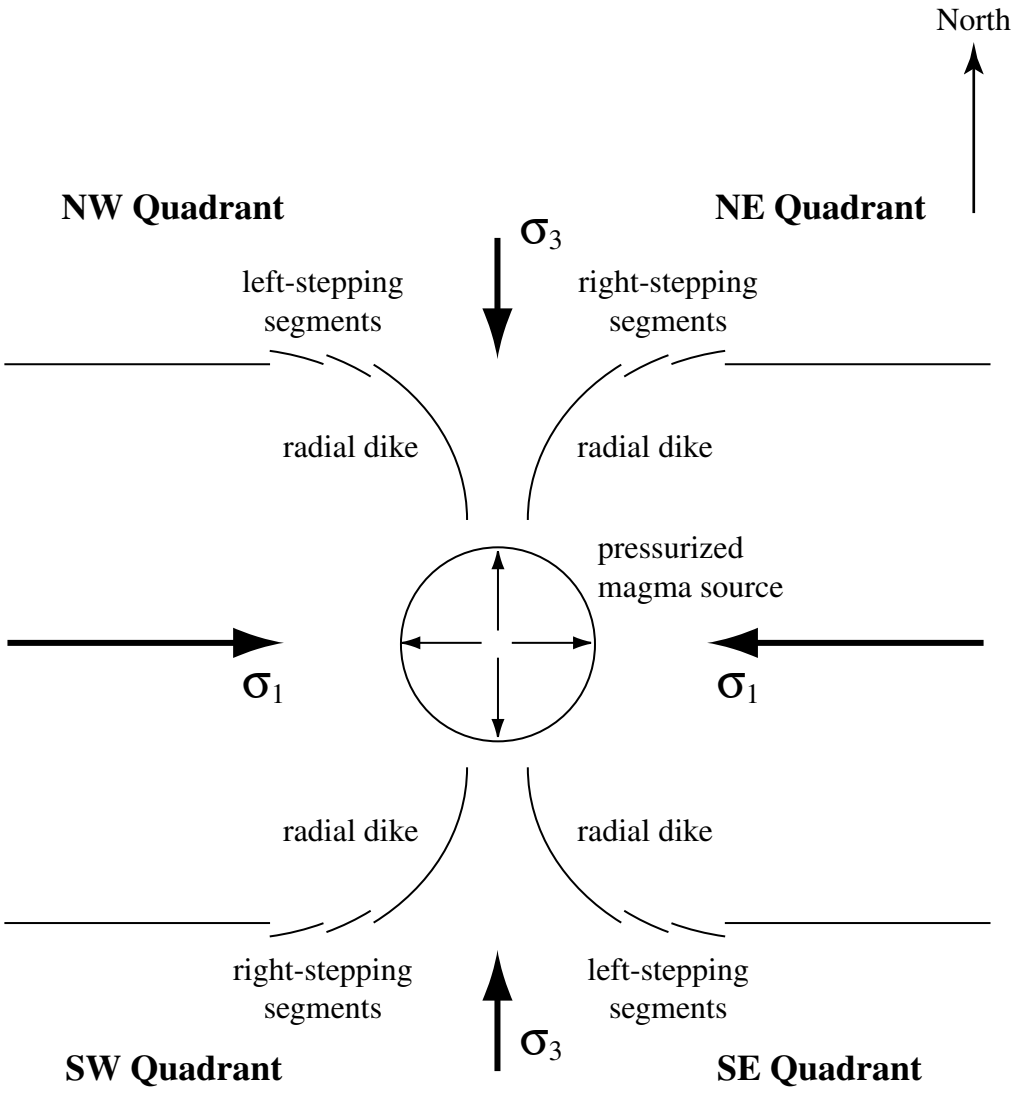

Figure 4.10. Predicted offset of en echelon dike segments for E-W directed most compressive stress (σ_1). The westward curvature of Dike 8 (located in the NW quadrant of the volcano) suggests that σ_1 is oriented E-W, and the least compressive stress (σ_3) is oriented N-S. Shear resolved onto radial dikes by the transition from radial compression (volcanic stress field) to E-W compression (tectonic stress field) should induce right-lateral echelon offsets in the NE and SW quadrants of the volcano, and left-lateral in the NW and SE. The predicted pattern of segmentation is not observed, therefore shear imparted by regional stresses is probably not the mechanism for en echelon segmentation at Summer Coon.

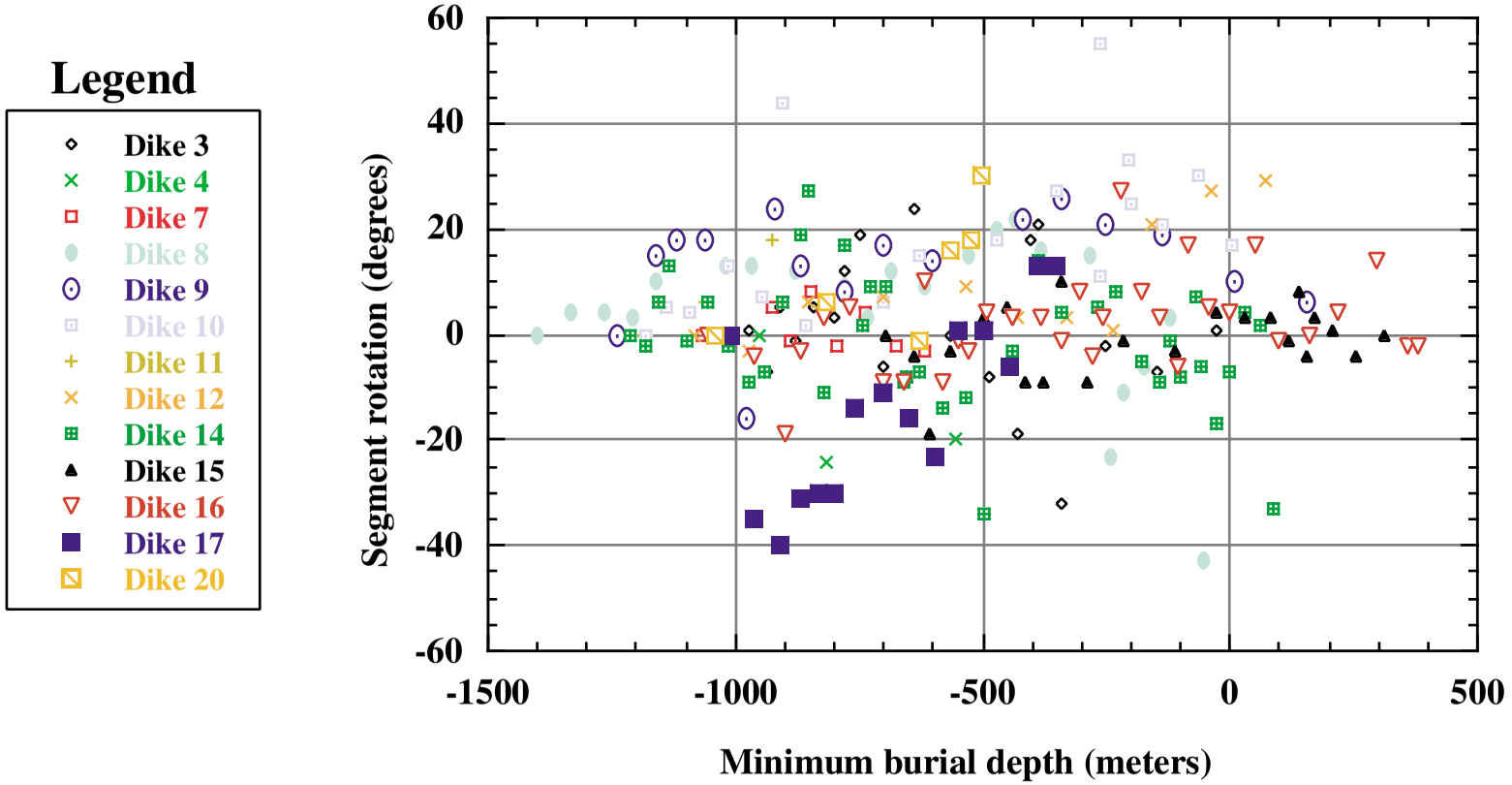

Figure 4.11. Plot of dike segment rotation versus burial depth. Rotation is calculated relative to the segment closest to the center of Summer Coon volcano for each dike. If the segmentation mechanism of *Pollard et al.* [1982] and other workers is occurring at Summer Coon, the magnitude of dike rotation (either positive or negative) should increase with decreasing burial depth. Although a relationship seems to exist for a few dikes (e.g. Dike 17) there is no overall correlation between segment rotation and burial depth. Rotation due to decreasing burial depth is probably not the dominant mechanism for dike segmentation at Summer Coon. Data from *Moats* [1990].

Delaney and Gartner [1997] to conclude that rotation of tectonic stress with depth could not account for dike segmentation, and that the intrusions most likely ascended through preexisting joints. Regional fracture systems may be invaded by magma if they are favorably oriented with respect to the principal stresses at the time of dike emplacement [*Delaney et al.*, 1986; *Delaney and Gartner*, 1997]. When deviatoric stress (the difference between the magnitudes of the maximum and minimum principal stresses) is low, pressurized magma may intrude joints with a range of different orientations (Figure 4.12). However, with increasing deviatoric stress the range of existing fractures that can be dilated decreases until the stress differential is large enough that dikes will only intrude self-generated fractures that are parallel to the most compressive stress in the crust [*Delaney and Gartner*, 1997]. Therefore dike segmentation may be caused by intrusion into existing joints only when the tectonic stresses are nearly equal in magnitude.

Baer and Beyth [1990] attribute dike segmentation of a doleritic dike in Har Timna, Israel, to previously existing structure. Thick segments of the dike are dilated perpendicular to the walls of the intrusion (based on piercing points on opposite margins) whereas thinner segments show oblique dilation, probably because the dike invaded an existing fracture oriented at an angle to the overall dilation direction (Figure 4.13). Therefore, dike thickness is a function of the magma pressurization and the dilation angle (essentially the angle of the existing fracture to the preferred dilation direction of the dike). Friction across the preexisting fracture must be low, otherwise oblique dilation is not possible and the dike will ignore the fracture and continue along an orientation parallel to the most compressive stress in the crust.

Based on field work in the dissected Tertiary volcanic sections of Iceland, *Gudmundsson* [1984] discusses two possible mechanisms for the formation of en echelon dikes due to intrusion into existing fractures. The tensile strength of the lava pile in Iceland

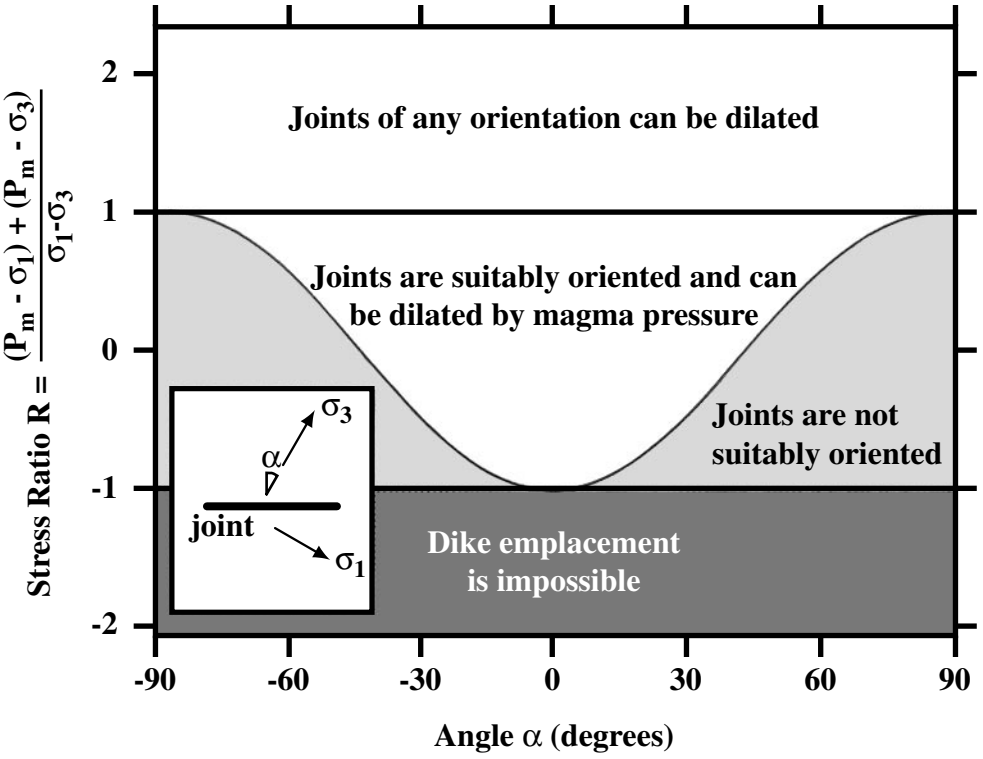

Figure 4.12. Graph showing the stress ratio (R) for a joint oriented at an angle (α) to the least compressive stress direction (σ_3). Magma pressure is P_m and the most compressive stress is noted by σ_1. Under conditions of isotropic stress ($\sigma_1 \approx \sigma_3$), joints with a wide range of azimuths may be dilated by pressurized magma (usually from a dike that has intersected the joint). High deviatoric stress ($\sigma_1 >> \sigma_3$) prevents magmatic intrusions from dilating joints that are oblique to the σ_1 direction. Inset shows a plan view of a joint oriented at an angle to the regional stress field, defined by σ_3 and σ_1. After *Delaney et al.* [1986].

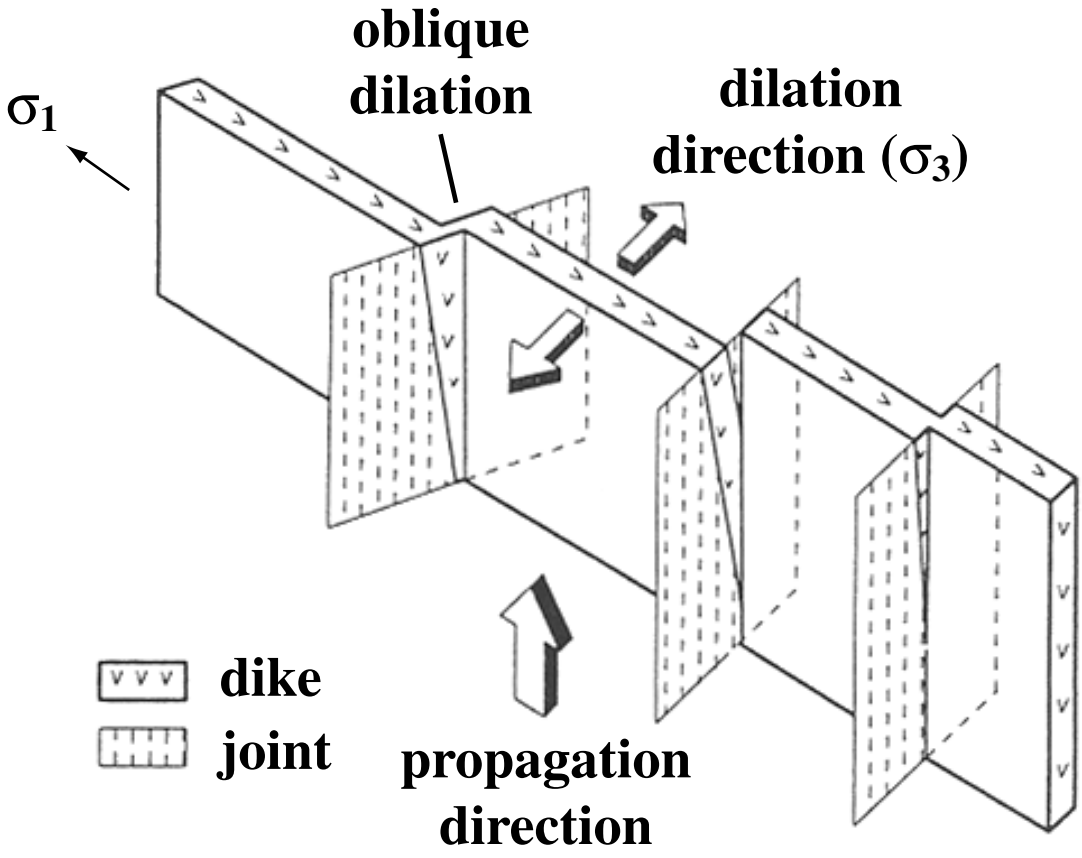

Figure 4.13. Three-dimensional schematic of en echelon dike segmentation due to oblique dilation of preexisting joints. The model dike intrudes parallel to the most compressive stress (σ_1) and dilates in the direction of the least compressive stress (σ_3). If the dike intersects a joint that is at an angle to the dilation direction (σ_3), the fracture is intruded and dilated obliquely. The resulting dike form is that of a segmented intrusion with echelon offsets. After *Baer and Beyth* [1990].

varies due to the presence of numerous columnar joints and other cooling-related fractures. A propagating dike will travel along a path that minimizes the resistance to opening, which is defined as the magnitude of the least compressive stress plus the tensile strength of the host rock. Therefore when a dike intersects a fracture, the tensile strength decreases and the dike is able to intrude the crack. The "radius of influence" [*Gudmundsson*, 1984] at the tip of a dike (i.e. size of the region that interacts with the dike) is a function of dike thickness, therefore steps due to variable tensile strength are usually not larger than the thickness of the dike. In some places, however, steps are much greater than the dike thickness, and the dike is completely discontinuous. *Gudmundsson* [1984] attributes such segmentation to decreasing magmatic overpressure. Loss of pressure causes the dike fracture to close along its length in places where the intrusion is not perpendicular to the least compressive stress in the crust, resulting in a dike with stepping segments (Figure 4.14).

Lipman [1968] originally proposed that the radial dikes of Summer Coon were emplaced into a radial fracture system that was created by doming of the host rock due to a pressurized magma chamber at depth. Later workers at Summer Coon have found no evidence for a systematic joint set in the region [*Mertzman*, 1971; *Moats*, 1990]. Subsequent investigations into dike propagation [e.g. *Delaney et al.*, 1986] demonstrates that dikes flow through self-induced fractures. As stated earlier, most Summer Coon segments in the northern half of the volcano are right stepping, while the southern half contains left-stepping segments. No fracture set that explains the observed segmentation pattern has been observed. In addition, most silicic dikes at Summer Coon intrude andesitic breccias that are free of systematic joints, unlike heavily fractured lava flows. Although dikes inevitably encountered and intruded some open or favorably oriented cracks

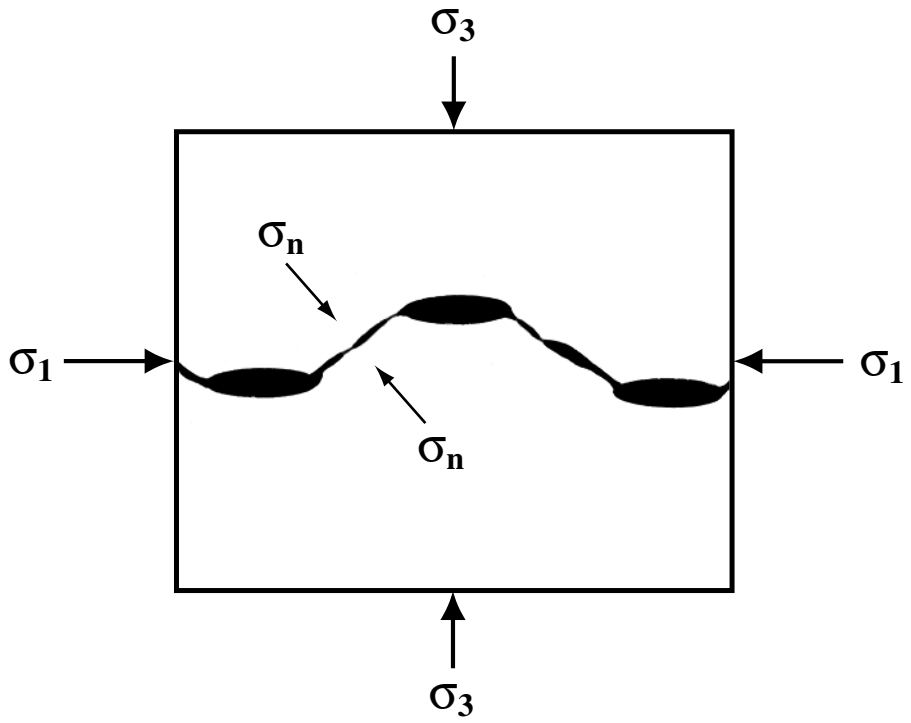

Figure 4.14. Map view of a dike that is discontinuous along its length, possibly due to decreasing magma pressure in the intrusion. The stress perpendicular to the offset segments is noted by σ_n. If magma pressure decreases, the walls of the dike that are not perpendicular to the least compressive stress (σ_3) will begin to close. Segments of the dike that are parallel to the most compressive stress (σ_1) and perpendicular to σ_3 will remain open, producing an offset geometry in horizontal section. Modified from *Gudmundsson* [1984].

during emplacement, it is unlikely that the overall pattern of segment steps at Summer Coon is a function of intrusion into preexisting fractures.

4.4.3 Changes in Host Rock Properties

A third mechanism for dike segmentation is based on variations in the material properties of the host rock intruded by a dike. *Baer* [1991] mapped the geometry of dikes in Makhtesh Ramon, Israel, which passed through two contrasting sedimentary formations. Dikes that intruded a unit of well-stratified dolomite and shale form thick (1-20 m) segments within distinct layers that may or may step or overlap. A sedimentary formation consisting of massive, porous sandstone with shale lenses contains dikes with smaller segments and numerous fingers. *Baer* [1990] concludes that in well-stratified and nonporous host rock, dike propagation and geometry will be influenced by the changing shear moduli of rocks in adjacent layers and by "in situ stresses" (differing ratios of vertical and horizontal stresses in various rock types). In the porous, massive sandstone, fluids that precede dike intrusion increase pore pressures and "fluidize" the host rock in front of the dike tip, giving rise to viscous fingering [see *Pollard et al.*, 1975].

Similar evidence was presented by *Gudmundsson* [1983; 1987] for dikes exposed in the Tertiary sections of Iceland. Where a dike passes from a coherent lava flow into a less consolidated scoria layer, the thickness and orientation of the dike changes, giving rise to stepping geometries (Figure 4.15). Applying the conclusions of *Baer* [1990] to the observations of *Gudmundsson* [1983; 1987] implies that the differing mechanical properties (e.g. shear modulus and porosity) of lava and scoria layers cause deviations in the shape and form of dikes that cross the lithologic contact. Mechanical heterogeneities may also be responsible for dike segmentation mapped in the eroded Koolau volcano on the

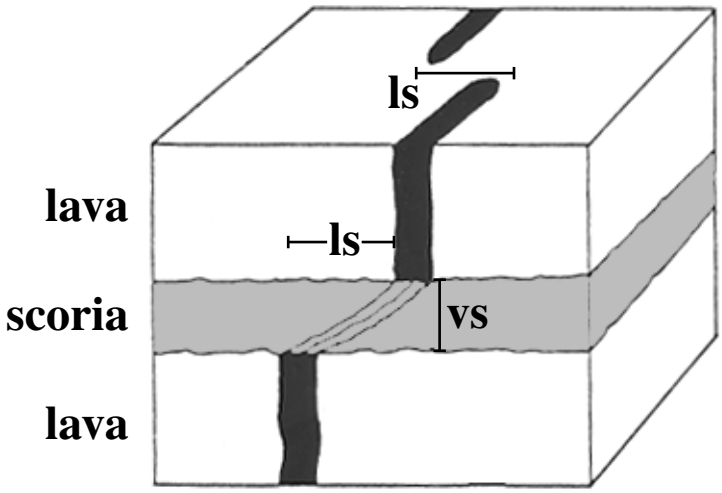

Figure 4.15. Schematic block diagram of a dike which is offset both laterally (ls) and vertically (vs). The offsets may occur as the dike propagates through a weakly consolidated scoria deposit between two lava flows. Variation in the material properties (e.g. Young's Modulus, Poisson's Ratio) between the two lithologies is a possible mechanism for the observed segmentation. Modified from *Gudmundsson* [1983].

Island of Oahu, Hawaii, where *Walker* [1987] attributes "sidesteps" to oblique dike trends across preexisting grains (for instance, an older solidified intrusion).

In addition to mechanical properties, changes in host rock rheology may contribute to dike segmentation. *Reches and Fink* [1988] examined the region surrounding the Inyo craters and domes in eastern California and concluded that as the rheology changed from ductile to brittle with decreasing depth, the mode of fracture changed from tensile to shear in response to relatively large upper crustal shear stresses. As a result, two conjugate shear fracture orientations were favored instead of one extensional fracture direction (Figure 4.16). Magma from the Inyo dike intruded one set of conjugate fractures resulting in the observed en echelon pattern of segmentation. The model is supported by the bimodal distribution of surface fractures in the vicinity of the dike. *Reches and Fink* [1988] further cite the distribution of fractures and eruptive fissure segments in Tarawera, New Zealand, and Little Glass Mountain, northern California, as sites where changing rheology may also have caused en echelon dike segmentation.

Variation in the material properties of the host rock is not a likely source for the observed dike steps at Summer Coon. Dikes are generally intruded into andesitic breccia, which is homogenous and isotropic at the kilometer scale of most Summer Coon dikes [*Moats*, 1990]. However, rheological conditions at the time of intrusion may have influenced dike geometry. If the segmentation mechanism of *Reches and Fink* [1988] is responsible for the dike geometry mapped at Summer Coon, the region surrounding the central intrusive complex would have been an area of ductile rheology during dike intrusion, changing to brittle with increasing distance. *Moats* [1990] found that chill zones thicknesses on dike margins were much thinner and less well-developed proximal to the central intrusive complex, indicating hot host rocks and perhaps ductile rheology. Distal ends of the dikes are characterized by thick glassy chilled margins, suggesting colder,

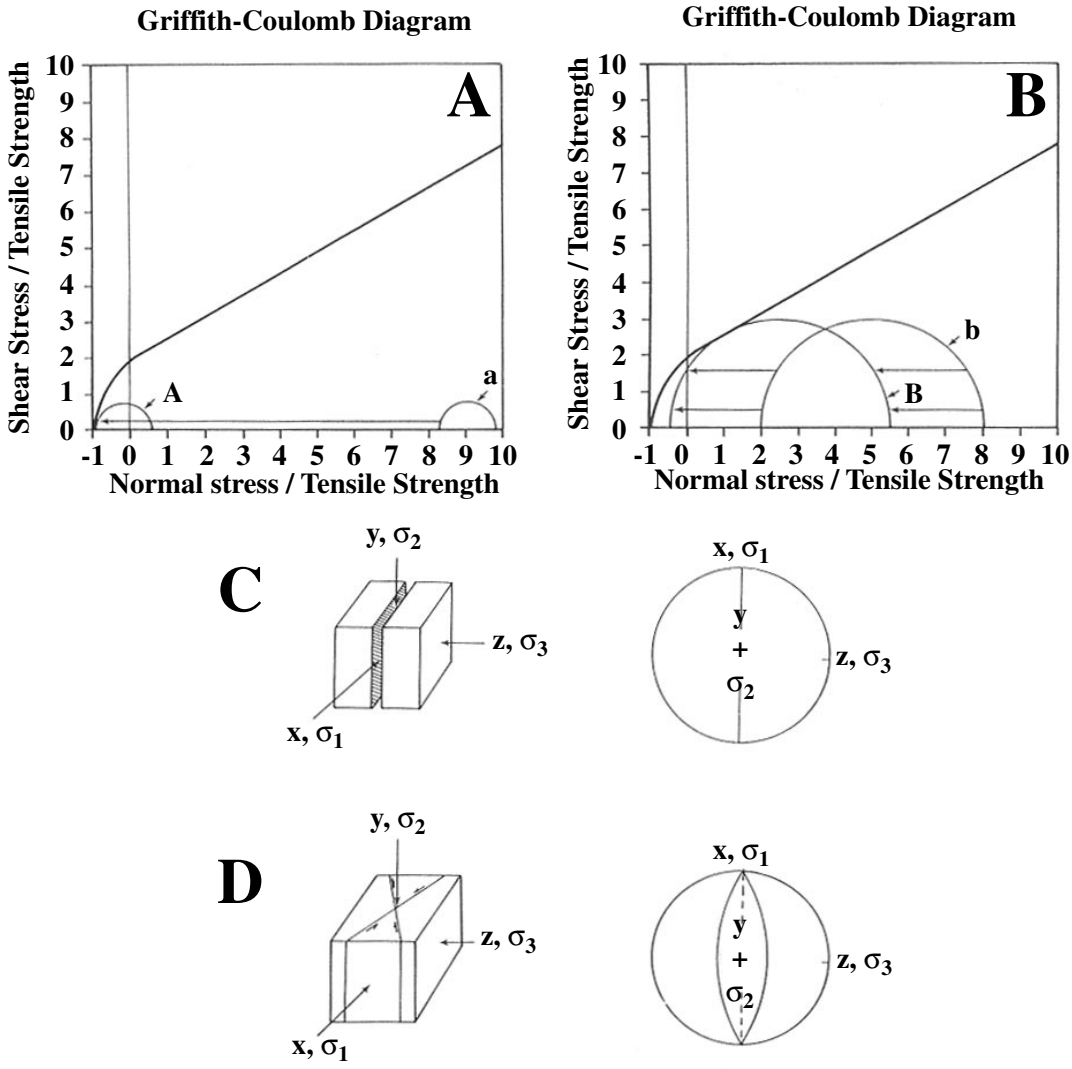

Figure 4.16. Schematic Mohr and block diagrams illustrating the mode of fracturing of the Inyo dike in eastern California due to changing rheological conditions. (a) At depths of ~10 km, where the country rock is ductile due to high heat from a magma source and cannot support shear stress, the state of stress is shown by circle a. Dike intrusion causes the circle to shift to location A, where tensile failure occurs. (b) At shallow depths (~3 km), crustal rocks are brittle and can support shear stress. As a result, the new state of stress is represented by circle b, which becomes circle B upon dike intrusion. The mode of failure is shear, and the magma in the dike will intrude fractures that are oblique to the extensional fractures described in (a). (c) Block diagram and stereographic projection of fracturing predicted in the ductile region of the crust (part (a)). (d) Block diagram and stereographic projection of fracturing predicted in the brittle region of the crust (part (b)). After *Reches and Fink* [1988].

brittle host rocks. However, the magnitude of segment rotation does not notably increase systematically with distance from the central intrusive complex, as predicted by the *Reches and Fink* [1988] model (Figure 4.17). In addition, there is no evidence for a bimodal distribution of fractures (one of which would include the plane of the dike), perhaps because joints are rare at Summer Coon and generally parallel the intrusions. Shear displacements could not be determined on the few joints that were observed, and the mode of fracturing for the intrusions themselves cannot be determined due to the lack of outcrop on either margin of most dikes. The application of the *Reches and Fink* [1988] rheology model to Summer Coon is uncertain based on the limited data available there.

4.4.4 Mechanical Interactions and Dike-Parallel Joints

Olson and Pollard [1991] present a model for the formation of en echelon cracks based on the mechanical interaction between fractures as determined by numerical modeling. Their proposed mechanism is as follows: 1) a rock mass is characterized by local stress concentrations due to randomly distributed heterogeneities (Figure 4.18A), 2) fractures initiated at these points will grow perpendicular to the most compressive stress, forming subparallel arrays (Figure 4.18B), 3) fluids fill the fractures (Figure 4.18C), and 4) the fractures lengthen and interact, favoring the growth of en echelon arrays over stacked and co-planar arrays (Figure 4.18D).

To understand how the model of *Olson and Pollard* [1991] may relate to en echelon dike emplacement, consider the findings of *Delaney et al.* [1986] regarding joints formed during intrusion. While mapping intrusions at three locations on the Colorado Plateau, *Delaney et al.* [1986] noted that most dikes are accompanied by a set of parallel joints, the spatial density of which decreases with distance from the intrusion. They conclude that

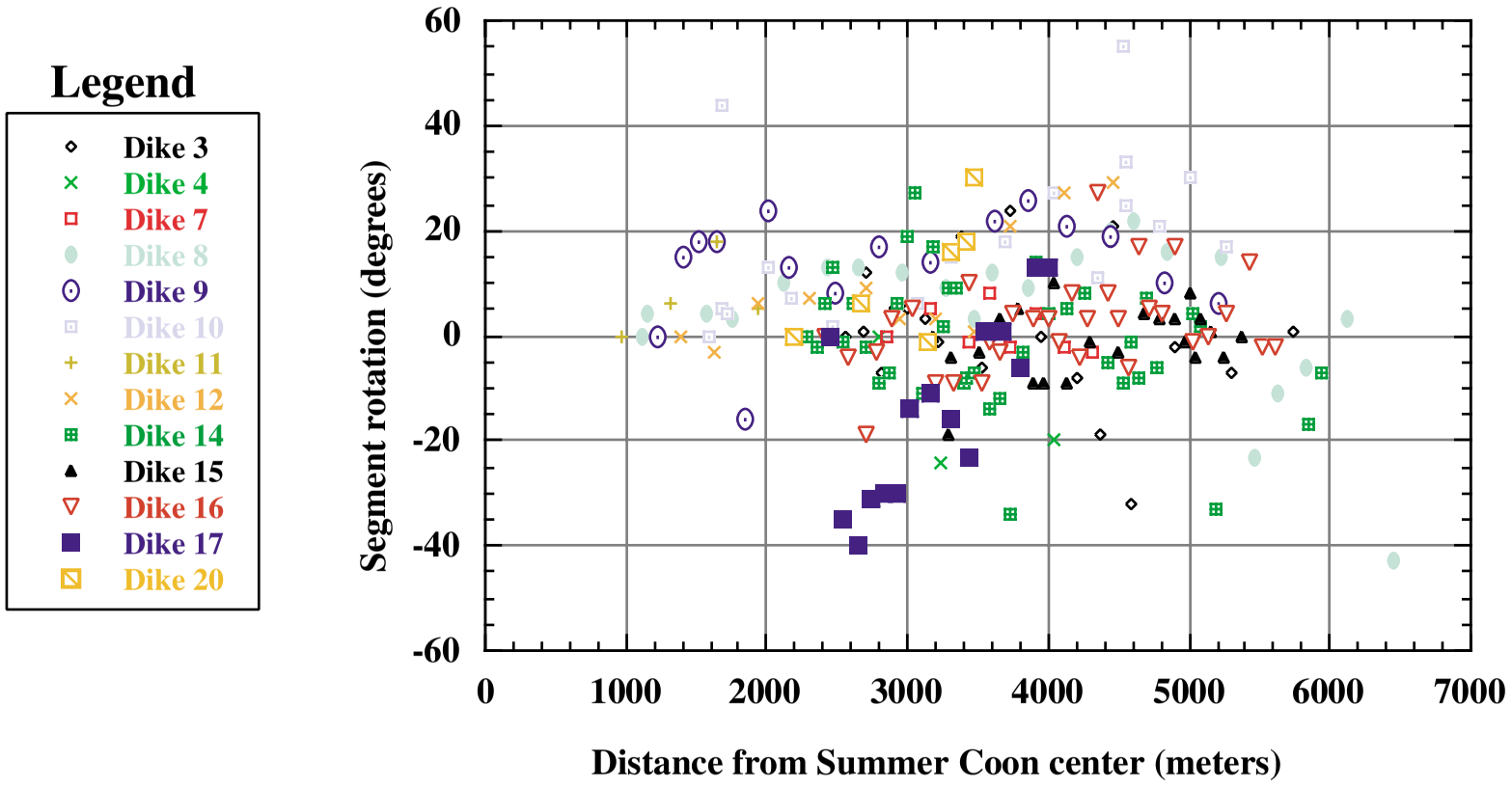

Figure 4.17. Plot of dike segment rotation with distance from the center of Summer Coon volcano. Rotations are calculated relative to the segment proximal to the center of the volcano for each dike. The mechanism of *Reches and Fink* [1988] predicts an increase in rotation with distance from the center of the volcano (as the country rock rheology changes from ductile to brittle). A correlation does exist for selected dikes (e.g. Dike 17) however there is no overall relationship between the two variables. A change in the rheological properties of the country rock is probably not the primary mechanism of dike segmentation at Summer Coon. Data from *Moats* [1990].

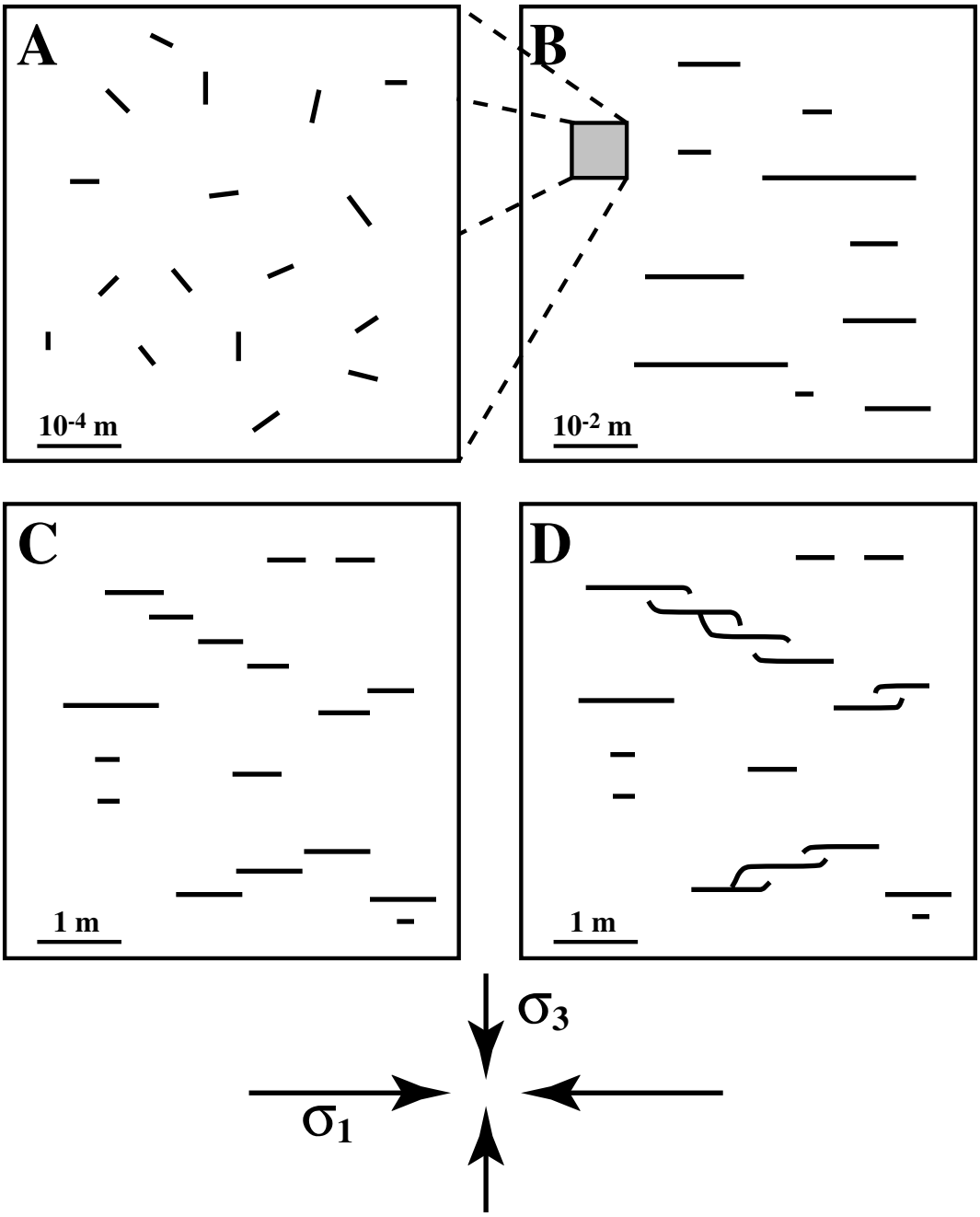

Figure 4.18. Model of echelon crack growth due to mechanical interactions between subparallel fractures. (a) A rock mass is characterized by randomly located and oriented flaws. (b) Flaws grow into cracks that align with the most compressive stress (σ_1) shown at the base of the figure. (c) Further crack growth is promoted by fluid intrusion, and the development of echelon arrays is favored over co-planar or stacked fractures. (d) Crack tips will interact when the overlap between echelon fractures reaches a critical value. Scales are schematic. Adapted from *Olson and Pollard* [1991].

because dike intrusion induces tension diagonally ahead of the propagation front, extensional fractures are likely to form parallel and on either side of the dike (Figure 4.19). Surface cracks mapped in Hawaii by *Pollard et al.* [1983] above recently emplaced dikes are analogous to the dike-parallel joints described by *Delaney et al.* [1986]. Joints that form close to the dike plane are sometimes invaded and dilated, introducing a step in the cross sectional form of the dike [*Delaney et al.*, 1986]. Based on the model of *Olson and Pollard* [1991], once a step forms (as magma intrudes a dike-parallel fracture), en echelon growth will be favored over co-planar development.

Delaney et al. [1986] derive a relationship between dike pressurization, regional stresses, and host rock properties to determine the distance (r_f) from the dike plane at which dike-parallel joints are expected to form:

$$r_f \leq \frac{1}{2} a \left[\frac{P_m - \sigma_3}{T + \sigma_3} \right]^2 \tag{4.5}$$

where a is the half-length of the dike, P_m is the magma pressure in the dike, T is the tensile strength of the host rock, and σ_3 is the least compressive horizontal stress in the crust. *Delaney et al.* [1986] apply this criterion to mafic dikes of the Colorado Plateau and find that typical values of tensile strength and least compressive stress yield realistic distances for dike-parallel joints given measured dike lengths and driving pressures inferred from the dike thickness.

By estimating the parameters in equation 4.5 for dikes at Summer Coon, the typical distance at which dike parallel joints will form may be calculated. The average length of the silicic dikes at Summer Coon is 3000 meters, yielding a half-length of 1500 m. *Delaney and Pollard* [1981] and *Delaney et al.* [1986] use a value of 24 MPa when considering the least compressive stress during emplacement of intrusions on the Colorado Plateau at

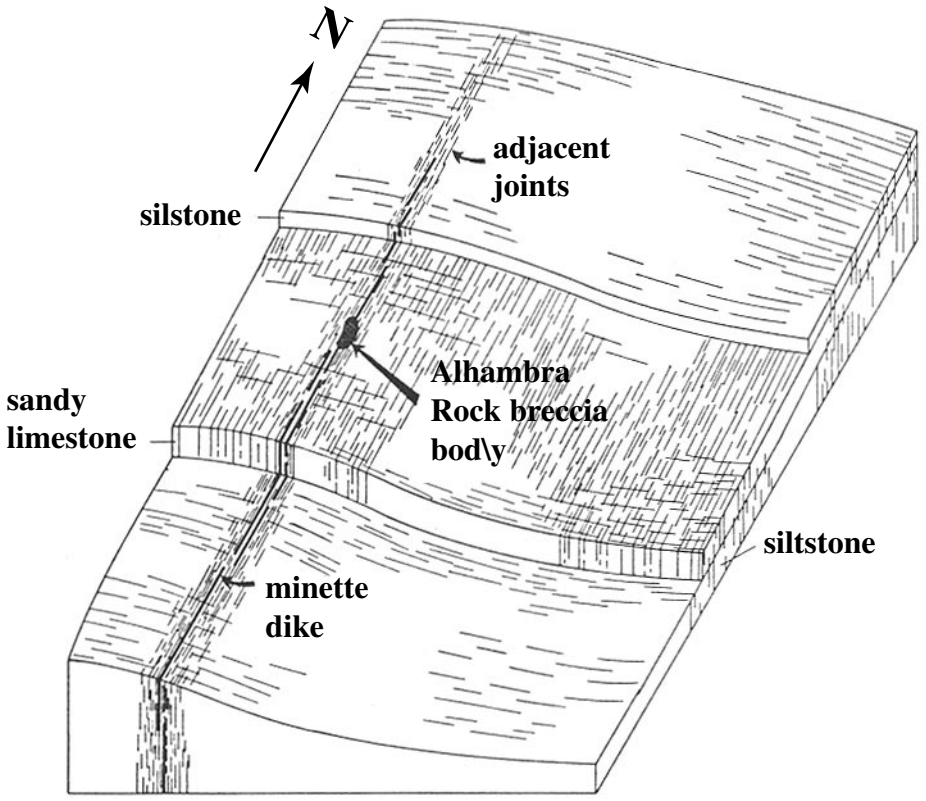

Figure 4.19. Schematic block diagram showing joints, strata, and a minette dike in the vicinity of Alhambra Rock, southern Utah. Vertical joints parallel and immediately adjacent to the minette dike occur in all lithologic units. The dike-parallel joints were most likely formed during emplacement of the intrusion. After *Delaney et al.* [1986].

approximately 30 Ma, which is within 200 miles and approximately the same age as Summer Coon. *Delaney et al.* [1986] also use tensile strength values of 1-10 MPa, although *Schultz* [1993] suggests that tensile strengths determined from laboratory samples are higher than those of in situ rock masses, which may be as low as 0.2 MPa. Finally, a lower bound for driving pressure ($P_m - \sigma_3$) in Summer Coon dikes, as determined in the analysis of dike thickness above, is taken as 20 MPa. Using these values, dike-parallel joints may form at distances of 250 to 500 meters from the dike (using tensile strength values of 10 and 0.2 MPa respectively). The greatest echelon step of a Summer Coon segment is in the southern portion of Dike 8, where a right-step of 150 meters occurs (Figure 4.6C). The distance clearly falls within the accepted bound for joint formation, therefore it is conceivable that the dike segment intruded and dilated a dike-parallel fracture at the front of the propagating dike tip. Once the initial step formed, mechanical interaction between dike segments would promote the development of echelon geometry with a consistent sense of stepping segments, as demonstrated by *Olson and Pollard* [1991]. Unfortunately, alluvial and colluvial cover of the ground surface adjacent to Summer Coon dikes does not allow for detailed mapping of joint patterns. However, field work by *Moats* [1990] and the author has confirmed the existence of dike-parallel joints, if not the spatial distribution.

4.4.5 Changes in Pressure Source Geometry with Depth

A unique characteristic of Summer Coon dike segments is the dominance of right-stepping segments in the northern hemisphere of the volcano, and left-stepping in the south (Table 4.1). Few models can account for the observed distribution of steps. *Smith* [1987] describes similar conditions at the Spanish Peaks, where most dike segments in the

southern quadrant of the swarm are left-stepping. Only dike segments located far from the origin of the swarm have the expected sense of step based on the regional stress regime at the time of dike emplacement. *Smith* [1987] attributes the consistent sense of step to a change in the position of the pressure source with depth (e.g. a kink or bend in a pressurized magmatic conduit), which modifies the radial stress field and forces dike segments to reorient with depth (Figure 4.20).

The model seems applicable to Summer Coon, as the observed segment stepping pattern would result if the dikes initiated from a source deeper and to the west of the current exposure of the central intrusive complex (analogous to the schematic in Figure 4.20). Although the dikes probably do connect with their associated source chambers at greater depths [*Mertzman*, 1971], there is no evidence favoring or contradicting a change in the position of the pressure source with depth. Additional work, possibly including subsurface geological characterizations based on geophysical data and numerical models of the subvolcanic stress field, is clearly necessary to assess the applicability of the model as initially proposed by *Smith* [1987].

4.4.6 Preferred Segmentation Mechanism at Summer Coon

Clearly, most proposed dike segmentation mechanisms cannot explain the observed geometry of intrusions at Summer Coon. Rotation of stresses with depth about a vertical axis predicts that dike rotation should increase with decreasing burial depth. Figure 4.11 demonstrates that no such relationship exists. Similarly, Figure 4.17 shows that there is no correlation between segment rotation and distance from the center of the volcano, which would be expected if rheological changes caused segment rotation. Because the dikes almost exclusively intrude andesitic breccia in the present exposures, variation in material

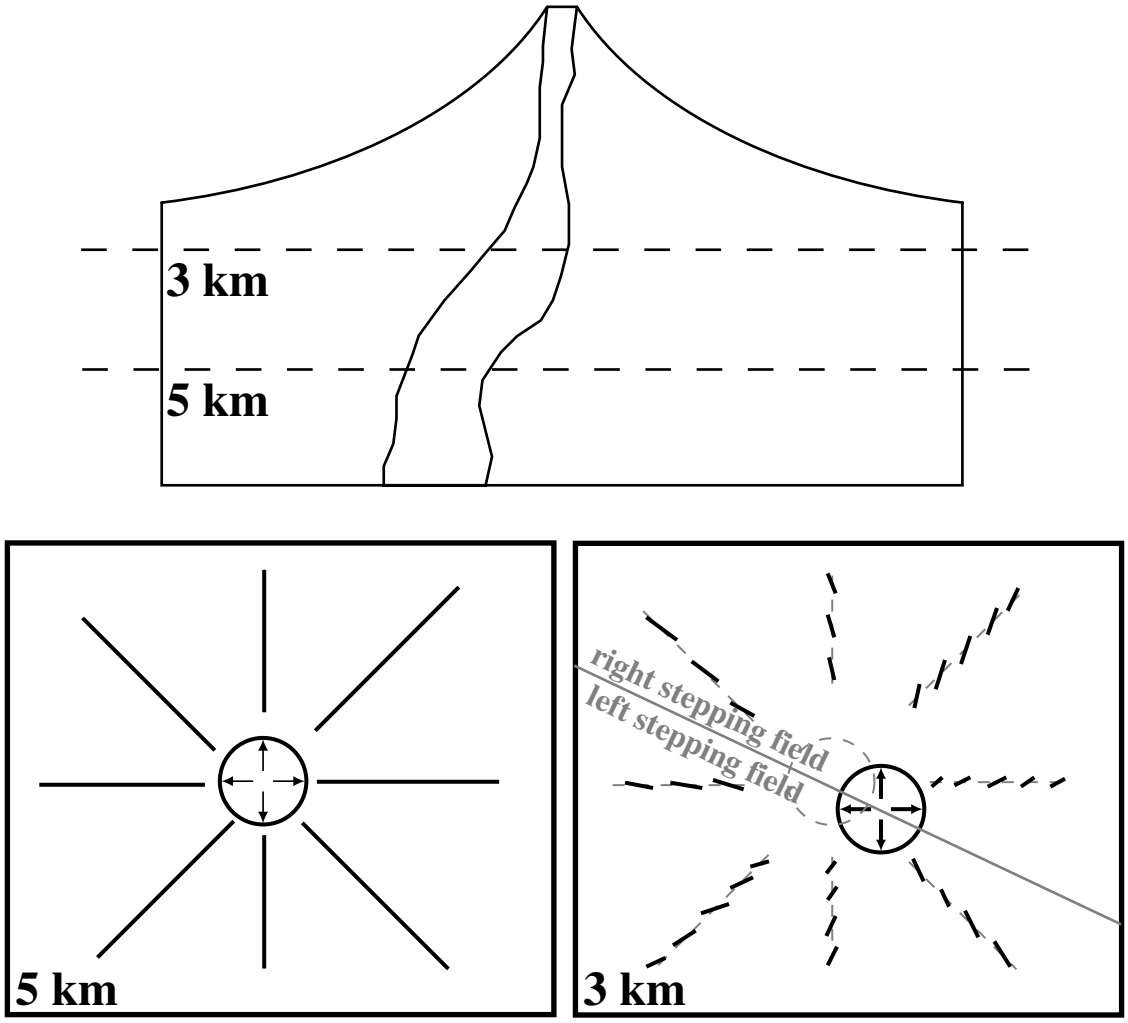

Figure 4.20. Schematic cross section and plan views at different depths through a volcano's conduit system illustrating the effect of a change in the location of a pressure source on dike geometry. The cross section (top) shows the changing position of the volcano's feeder system with depth. If a dike initiates at a depth of 5 km the intrusion will be radial to the pressurized conduit (bottom left plan view). However, at 3 km depth the change in the location of the pressure source alters the local stress field, causing the formation of offset segments that are individually radial to the new pressure source (bottom right plan view). Note that the segments are right-stepping in the northeast hemisphere and left stepping in the southwest hemisphere, similar to the form of radial dikes at Summer Coon. Based on a model presented by *Smith* [1987].

properties is not a probable cause for dike segmentation. Finally, field studies do not support the proposal that a radial fracture set exists and predates the volcanic activity at Summer Coon.

A model of magma intrusion into dike-parallel fractures and mechanical interactions between segments best explains the consistent sense of step within individual dikes, as well as the lack of distance and depth dependent segment rotation. The model assumes that a significant component of lateral magma migration occurs and causes mechanical interaction between echelon segments, which is supported by measurements of magma flow described below. However, the model does not account for the distribution of right-stepping segments in the northern half of Summer Coon and opposite steps in the south. A secondary stress field superimposed on the radial system is one potential explanation for the distribution of steps. The model of dike segmentation based on a change in the geometry of a pressure source with depth does explain the distribution of the sense of step (Figure 4.20). While no evidence exists to indicate a change in the geometry of the magmatic system with depth at Summer Coon, the possibility of a secondary stress source is a reasonable explanation for the right-stepping segments observed at Summer Coon. It is reasonable to predict that both models are applicable to a certain degree at Summer Coon, but future work, especially addressing the model of pressure source geometry with depth, is clearly necessary to assess the contributions of the two sources.

4.5 Flow Direction Analyses

When attempting to determine the flow direction of magma, one must be careful to distinguish indicators of magma flow direction from indicators of dike propagation direction. *Baer* [1995] identifies three stages of dike emplacement that can be recognized

by analysis of features on and near a solidified dike: 1) propagation of a dry fracture ahead of the magma-filled dike can be determined from the overall geometry of the dike, including offsets and steps, 2) initial intrusion of magma into the dry fracture is recorded by grooves, slickensides, and other strain indicators on the dike margin, and 3) magma flow within the dike is preserved in strained features and mineral alignments in the dike interior. *Pollard et al.* [1975] present detailed analyses of the geometry of two separate intrusions, a dike of the Spanish Peaks and a sill near the Highwood Mountains in central Montana. Based on fingering and segmentation on the margins of both intrusions, they conclude that dike propagation was parallel to the axes of the segmentation (i.e. horizontal in the sill and vertical in the dike). *Baer and Reches* [1987], *Baer and Beyth* [1990], and *Baer* [1991] agree with the interpretation of *Pollard et al.* [1975], however *Currie and Ferguson* [1970] conclude that flow was perpendicular to axes of fingers, and that stepping segments form due to explosive degassing of water-rich magmas.

Tweto [1951] describes several sills in central Colorado and noted features including drag folds, aligned minerals, and slickensides on sill margins and concludes that sill growth occurred via horizontal propagation of rod-shaped fingers of magma which expanded laterally and grew into tongue-shaped features which later coalesced. *Smith et al.* [1993] distrust phenocryst alignment because magma pressure in the molten part of the dike may cause crystals to flatten against the cooling margin of the dike. Instead, shear zones that form a bisector to conjugate fractures in the dike are used to indicate flow. The shear zones form as a solidifying dike experiences stretching along its axis and shortening perpendicular to the dike margin due to flow of magma. One of the two bisectors of the conjugate shears will be oriented parallel to the dike and indicates the axis of flow (Figure 4.21) [*Smith et al.*, 1993]. Applied to dikes in Japan, the technique suggests upward magma flow that is inclined to the surface approximately 60 degrees. *Coward* [1980]

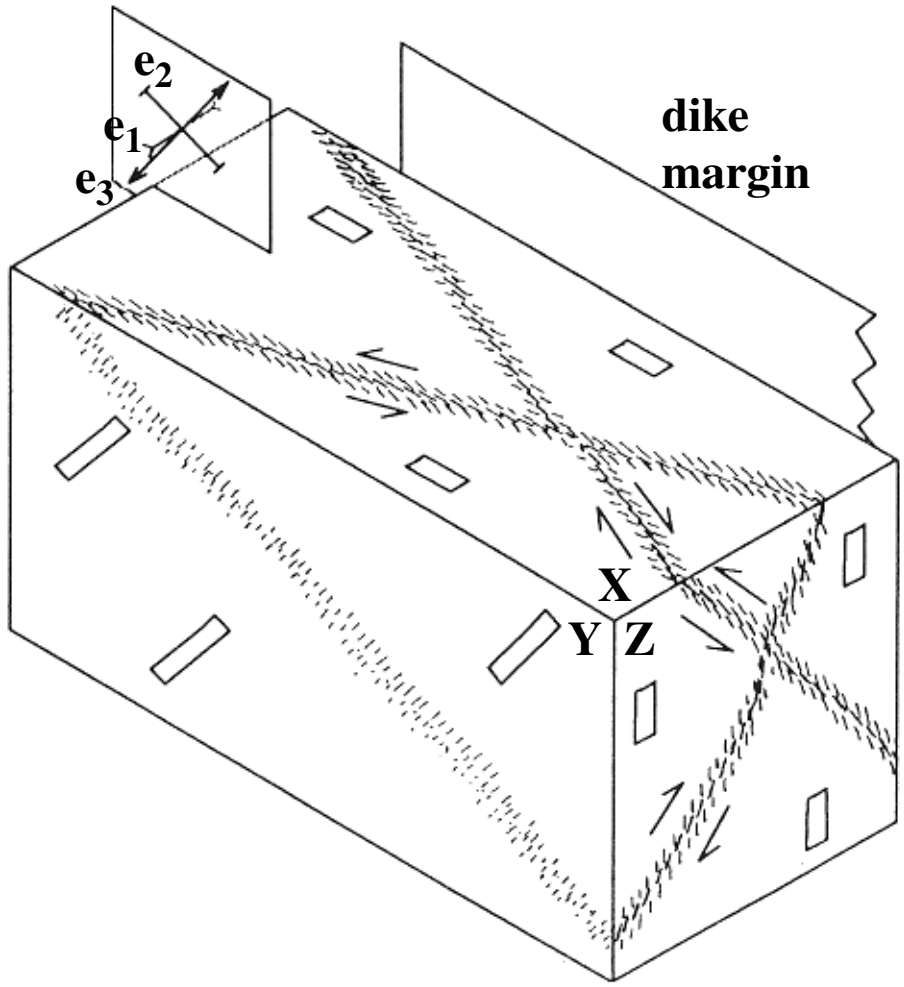

Figure 4.21. Schematic block diagram showing the relationship between conjugate shear zones and phenocryst alignment within an igneous intrusion. The perpendicular bisector of the shear planes contains the inferred shortening (e_1) and extending (e_3) strain axes. The intermediate strain axis is e_2. Magma flow and the long axes of phenocrysts (noted by rectangles) are parallel to the e_3 axis, while phenocryst flattening occurs in the e_1 direction. After *Smith et al.* [1993].

infers horizontal magma flow from strained vesicles in a dike located in western Namibia, southern Africa. The shapes of the vesicles indicate higher strain on the dike margins than in the interior, indicating extensional flow on the dike margin and compressional in the center.

4.5.1 Anisotropy of Magnetic Susceptibility to Determine Magma Flow

The orientations of magnetic minerals may also be used to infer magma flow within dikes. The induced magnetization in a mineral due to an applied magnetic field is a function of the mineral's magnetic susceptibility:

$$M_i = \chi_{ij} H_j \tag{4.6}$$

where M_i is the induced magnetization, H_j is the applied field, and χ_{ij} is the dimensionless magnetic susceptibility [*Tauxe*, 1998, p. 173]. The susceptibility can be a function of several variables including crystal shape, lattice structure, state of stress, etc., thus the susceptibility along the different axes of a magnetic mineral may vary. Anisotropy of magnetic susceptibility (AMS) with mineral shape may be used to indicate the underlying petrofabric in rock, and has been successfully applied to identifying strain patterns in metamorphic rocks [e.g. *Borradaile*, 1988], paleoflow in sedimentary rocks [e.g. *Rees*, 1961], and flow directions in lava flows [e.g. *Ellwood*, 1978], pyroclastic deposits [e.g. \ [*Ellwood*, 1982], and igneous dikes [e.g. *Knight and Walker*, 1988]. Within a dike, flowing magma will cause elongated particles to become imbricated against the dike margins (Figure 4.22). Because the axis of maximum susceptibility usually occurs along the long axis of a magnetic crystal, the orientation of the maximum susceptibility may be used to infer the direction of magma flow [*Knight and Walker*, 1988; *Tauxe et al.*, 1998].

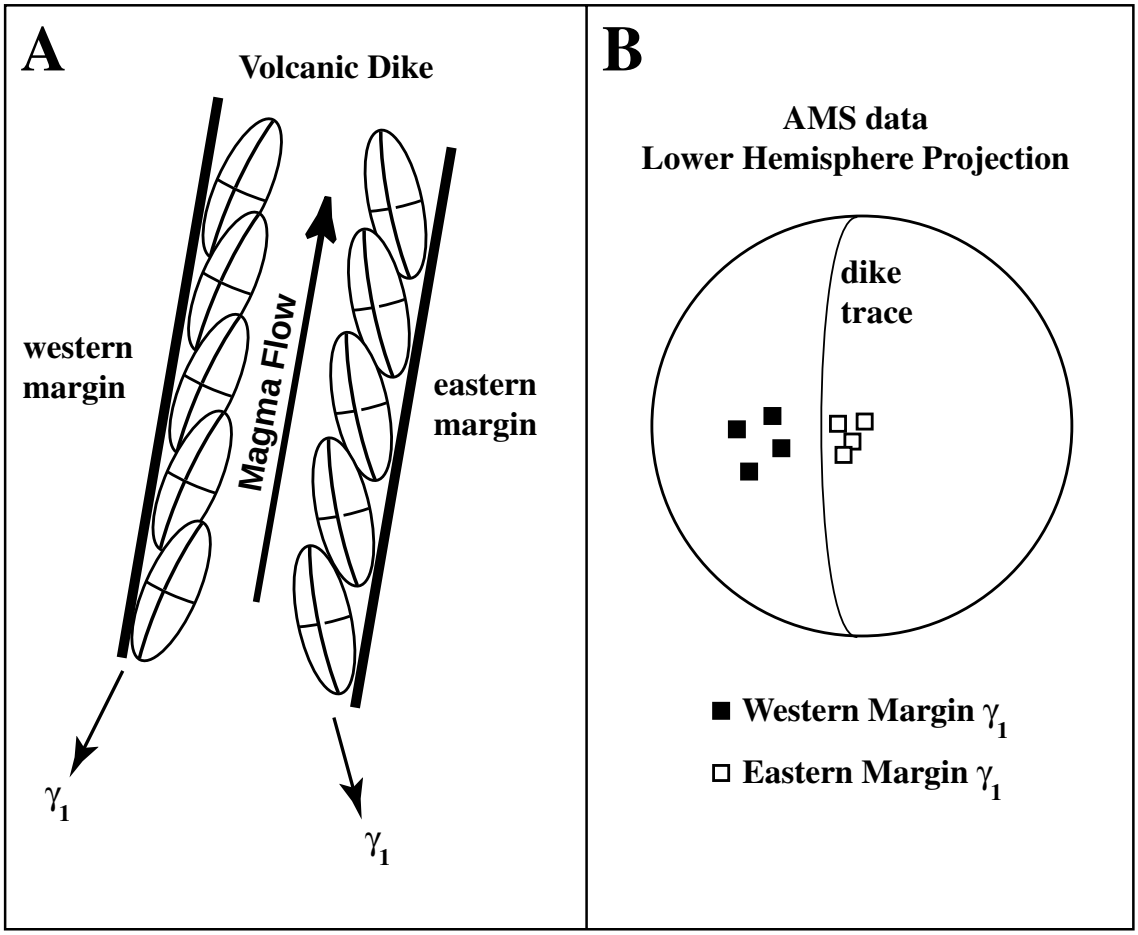

Figure 4.22. Schematic representation of phenocryst imbrication in a dike due to magma flow. (a) Phenocrysts will be imbricated against one another and the sides of the dike due to magma flowing within the intrusion. The orientations of the imbricated crystals indicates the direction of magma flow. (b) Lower hemisphere, equal area projection of the maximum eigenvectors (γ_1) from each margin of the dike. The γ_1 directions for the eastern margin plot on the eastern side of the dike while γ_1 directions for the western margin plot on the western side of the dike, suggesting subvertical flow. The actual flow direction falls on the plane of the dike between the western and eastern margin γ_1 directions. From *Knight and Walker* [1988].

Further, because flow causes imbrication of mineral grains, the maximum susceptibility axes should form a low angle to the plane of the dike (~10 - 30 degrees) and dip towards the source of magma flow, enabling a unique flow direction to be determined [*Knight and Walker,* 1988].

Statistical significance in magnitudes and orientations of the AMS ellipsoid axes must be demonstrated in order to confirm flow vectors. *Tauxe et al.* [1998] developed a statistical bootstrap for this purpose, and the following procedures are taken from their work. Because most AMS studies involve the collection of few (~5) samples per site, typical measurements of confidence are not appropriate and a bootstrap is necessary to define the 95% confidence intervals of the data. The parametric bootstrap described by *Tauxe et al.* [1998] assumes that data from a single margin of a dike are normally distributed and each measurement has an analytical uncertainty. A data point is chosen at random and a replacement point is selected from a normal distribution with the same mean and standard deviation as the original data point and uncertainty. The process of selecting replacement data is repeated for some number of times (for instance, 500), and the resulting paradata set reflects the underlying distribution of the original data, allowing calculation of accurate 95% confidence bounds (of the 500 paradata points, the 475 closest to the mean define the 95% confidence bound).

In equation 4.6, χ_{ij} is the susceptibility coefficient of a mineral in the i direction due to a magnetization along the j direction (i and j = 1 to 3, representing 3 axes), therefore χ_{ij} defines a tensor with 9 elements, 6 of which are independent (because $\chi_{ij} = \chi_{ji}$). One coordinate system exists where all off-diagonal terms of χ_{ij} are 0, which defines the shape of the AMS ellipsoid. The magnitudes and directions of the axes of the ellipsoid are the eigenvalues (τ_1 - maximum, τ_2 - intermediate, τ_3 - minimum) and eigenvectors (γ_1 - maximum, γ_2 - intermediate, γ_3 - minimum), of the susceptibility tensor χ_{ij}, respectively.

Several criteria must be met in order to determine a preferred flow direction in a dike using the statistical bootstrap: 1) Multiple samples must be collected from opposing margins of the same dike to confirm crystal imbrication, 2) τ_1 must be greater than τ_2 without overlap at the 95% confidence level for both sites, and 3) γ_1 values from the two sites must be distinguishable from both each other and the plane of the dike. At the 95% confidence level, if $\tau_1 = \tau_2 = \tau_3$, the AMS ellipsoid is spherical and no unique direction can be determined. If $\tau_1 = \tau_2 > \tau_3$, the AMS ellipsoid is oblate (disc-shaped), and again no direction can be determined. When $\tau_1 > \tau_2 = \tau_3$, the AMS ellipsoid is prolate, and since τ_1 is distinct from τ_2 and τ_3 a flow direction can be extracted. Flow can also be inferred in the case of $\tau_1 > \tau_2 > \tau_3$, when the AMS ellipsoid is triaxial. All four shapes and sample data are given in Figure 4.23. For triaxial distributions of eigenvectors, γ_1 should plot just off the plane of the dike (due to imbrication of the grains - see Figure 4.22) and γ_3 should be perpendicular to the dike plane, indicating a "normal" AMS fabric [*Tauxe et al.*, 1998]. *Rochette et al.* [1991] describe samples from the Oman ophiolite where γ_1 is more than 45 degrees from the dike plane (which they term a "reverse" fabric), and give possible reasons for the anomalous AMS results.

Several studies have used AMS to measure flow directions in igneous dikes since *Knight and Walker* [1988] proved the viability of the procedure. *Mushayandebvu et al.* [1995] infer subhorizontal magma flow from AMS studies of intrusions in Zimbabwe. Similarly, *Ernst* [1990] presents AMS results from two regional-scale dike swarms in Canada, showing upward and outward flow of magma. Despite the continued success of the technique, some authors warn against blind reliance on AMS results without supporting geological evidence of flow. *Smith et al.* [1993] suggest that flattening of magnetic phenocrysts against the dike margin due to pressure applied by molten material in the interior may give a false flow direction. *Philpotts and Asher* [1994] prefer structural

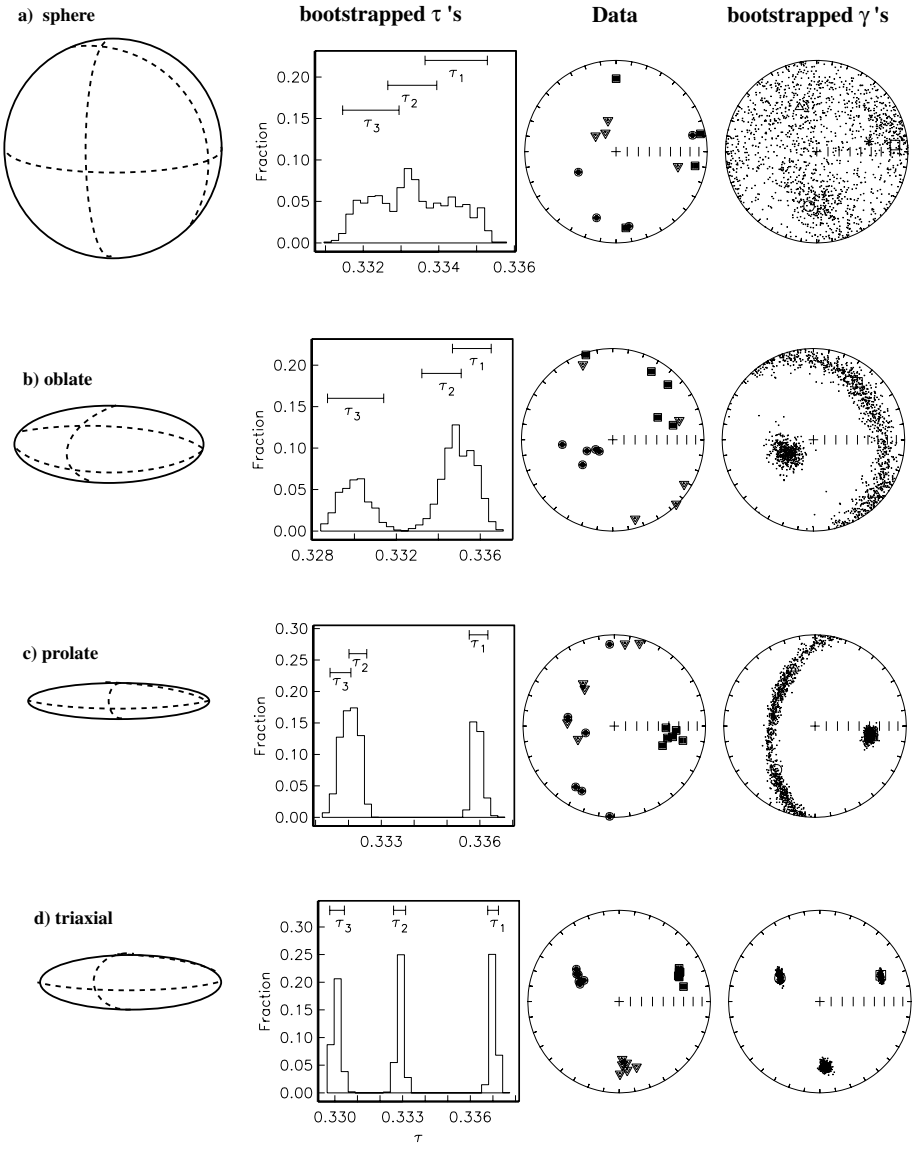

Figure 4.23. Possible shapes of the AMS ellipsoid with corresponding histograms of bootstrapped eigenvalues (τ's) and equal-area plots of data and bootstrapped eigenvectors (γ 's). The shapes on the left are the possible forms of the AMS ellipsoid: a) sphere ($\tau_1 = \tau_2 = \tau_3$), b) oblate ($\tau_1 = \tau_2 > \tau_3$), c) prolate ($\tau_1 > \tau_2 = \tau_3$), and d) triaxial ($\tau_1 > \tau_2 > \tau_3$). Immediately to the right are histograms of the bootstrapped eigenvalues shown with 95% confidence bounds. Lower hemisphere, equal-area projections of the data (γ_1 as squares, γ_2 as triangles, and γ_3 as circles) and bootstrapped eigenvectors (points) are shown to the right. A unique flow direction can be determined for prolate and triaxial ellipsoids, where the 95% confidence bounds of τ_1 are distinct from those of τ_2 and τ_3. Taken from *Tauxe et al.* [1998].

indicators of magma flow because AMS fabric forms upon dike solidification and may record back flow of magma. With careful analysis, both complications may be overcome. Phenocryst flattening will prevent grain imbrication, therefore the direction of maximum susceptibility will not be distinct from the dike plane. In addition, by collecting AMS samples from the chilled margin of the dike, only the initial direction of magma flow will be recorded. Back flow will only be measured in AMS samples taken from the dike interior [*Shelley*, 1988; *Tauxe et al.*, 1998].

4.5.2 Previous Studies of Magma Flow: Individual Dikes and Dike Swarms

Surprisingly few studies analyze flow at multiple locations along a single dike, or within or across en echelon dike segments. *Knight and Walker* [1988] collect AMS samples at one location for each dike, as do *Staudigel et al.* [1992]. However, *Staudigel et al.* [1992] note that one or two sampling locations are probably not sufficient to map complex flow patterns. In contrast, *Philpotts and Asher* [1994] determined flow directions at three different locations within one segment of the ~25 meter-thick Higganum dike in Connecticut. They collected samples from the dike margin and cut thin sections to better identify aligned phenocrysts, broken and sheared phenocrysts, compositional streaks, and other indicators. Based on their observations, magma flow in the segment was vertical in the center but upward and inclined to the north and south for the north and south terminations of the segment, respectively. *Philpotts and Asher* [1994] conclude that magma rises vertically in individual dike segments, accompanied by lateral flow and expansion of segment terminations. *Baer* [1995] collected samples from the margin of a dike in Makhtesh Ramon, Israel that is segmented in vertical section. Flow directions from

AMS agreed with those determined from the rock fabric and indicate subhorizontal flow in the center of the segment, which parallels the general flow direction for the region. Towards the segment ends flow is inclined in the direction of segment termination, and the transition from steep to horizontal flow occurred in some places over distances as small as 2 meters.

Two authors have studied flow at multiple locations per dike in several dikes of a radial swarm. *Smith* [1987] mapped flow lineations (aligned vesicles, scour marks, aligned pheoncrysts, etc.) in radial dikes of the Spanish Peaks and found subhorizontal to shallow-plunging magma flow, indicating outward and upward propagation of magma from depth. Magma flow in radial dikes of the eroded Lyttleton volcano in New Zealand was measured by *Shelley* [1988]. Based on the alignment of feldspar phenocrysts in the dikes (specifically the orientations of poles to the 010 faces of feldspar crystals [*Shelley*, 1985]) magma flow was in all locations away from the center of Lyttleton volcano, but was inclined in both the up and down directions along the lengths of the dikes. *Shelly* [1988] determined that randomly distributed components of vertical magma flow were superimposed on the dominant trend of subhorizontal magma transport away from the conduit of Lyttleton volcano. While not specifically addressing the patterns of magma flow at segment terminations, *Shelley* [1988] did note that flow was not uniform across a dike's cross section, suggesting magma drainback in the inner portion of the dike. *Delaney and Pollard* [1981] point out that drainback is commonly observed at the end of Hawaiian fissure eruptions and should be represented by textural and compositional differences in eroded dikes.

4.5.3 Sampling Strategy at Summer Coon and Paleomagnetic Analysis

Because macroscopic indicators of magma flow (e.g. grooves, slickensides, aligned vesicles, etc.) are rare, AMS measurements, accompanied by thin section analyses, are used to determine flow directions in Summer Coon dikes. Samples were collected from multiple sites along the lengths of two dikes. Dike 8 was sampled at 15 different locations (treating 8-10a and 8-10b as separate sites) over the southern portion of the intrusion (Figure 4.24), which includes an en echelon step of ~150 meters (Figure 4.25). Two pairs of sites (8-5 and 8-11; 8-12 and 8-13) were located on opposing dike margins. In addition, samples were collected from four sites (8-1 through 4) across the width of the dike where it is cut by a stream. Dike 3 was sampled in 18 locations (Figure 4.26), including 4 pairs of sites on opposing dike margins (3-4 and 3-5; 3-6 and 3-7; 3-11 and 3-12; 3-17 and 3-18). Samples were collected at the initiation of the dike (proximal to the central intrusive complex) for a distance of 1 km to the west, across a minor (~10 meters) echelon step (Figure 4.27), to a point where a stream cuts the dike. Additional samples were collected further west where a major step (~50 meters) is connected by a thin (~2 m) strand of magma (Figure 4.28).

The sampling strategy follows guidelines suggested by *Tauxe* [1998, p. 237-239]. All samples were drilled in situ using a portable, gasoline-powered, Pomeroy drill. Cores were oriented using a Brunton compass (a sun compass was not necessary due to the low magnetization of the dikes). At least five samples were obtained from most sites, however in some places only three or four useable cores could be extracted. The attitudes of joints near the sample sites were collected, though none of the joints mapped appear to be related to the flow directions described below.

Figure 4.24. Magma flow measured by anisotropy of magnetic susceptibility in Dike 8. The map view shows sample locations along the intrusion. At the same scale is a cross section of the dike showing a profile of the dike top and AMS results as arrows with 95% confidence bounds plotted as arcs at the arrow tips. The center of Summer Coon volcano is to the south. No flow directions were obtained from sites 8-6 and 8-9. Flow lineations for sites 8-1 through 4, which were collected from a vertical, perpendicular cross section of the dike (and therefore cannot be used to show absolute directions), are listed on the map as trend (all of which are along the dike in a northerly direction) and plunge. Flow may have been either to the north or south along the lineation. The wide range of flow inclinations across the face of the dike suggests that magma drainback in the dike occurred, or multiple pulses of magma were injected into the dike. Sites 8-7 and 8-14 yield anomalous subhorizontal flow directions towards the central intrusive complex. The measurement at site 8-14 may be in error due to a poor dike exposure, however the geometry of the dike at site 8-7 is well constrained and the flow direction appears real. Overall, flow directions vary widely along the dike. Magma flow on the northern segment of the major offset between sites 8-9 and 8-10 was steep, and petrographic analyses suggest subhorizontal flow on the southern segment tip (Figure 4.25). The flow pattern in the vicinity of the offset is similar to that observed at Dike 3 (Figure 4.26)

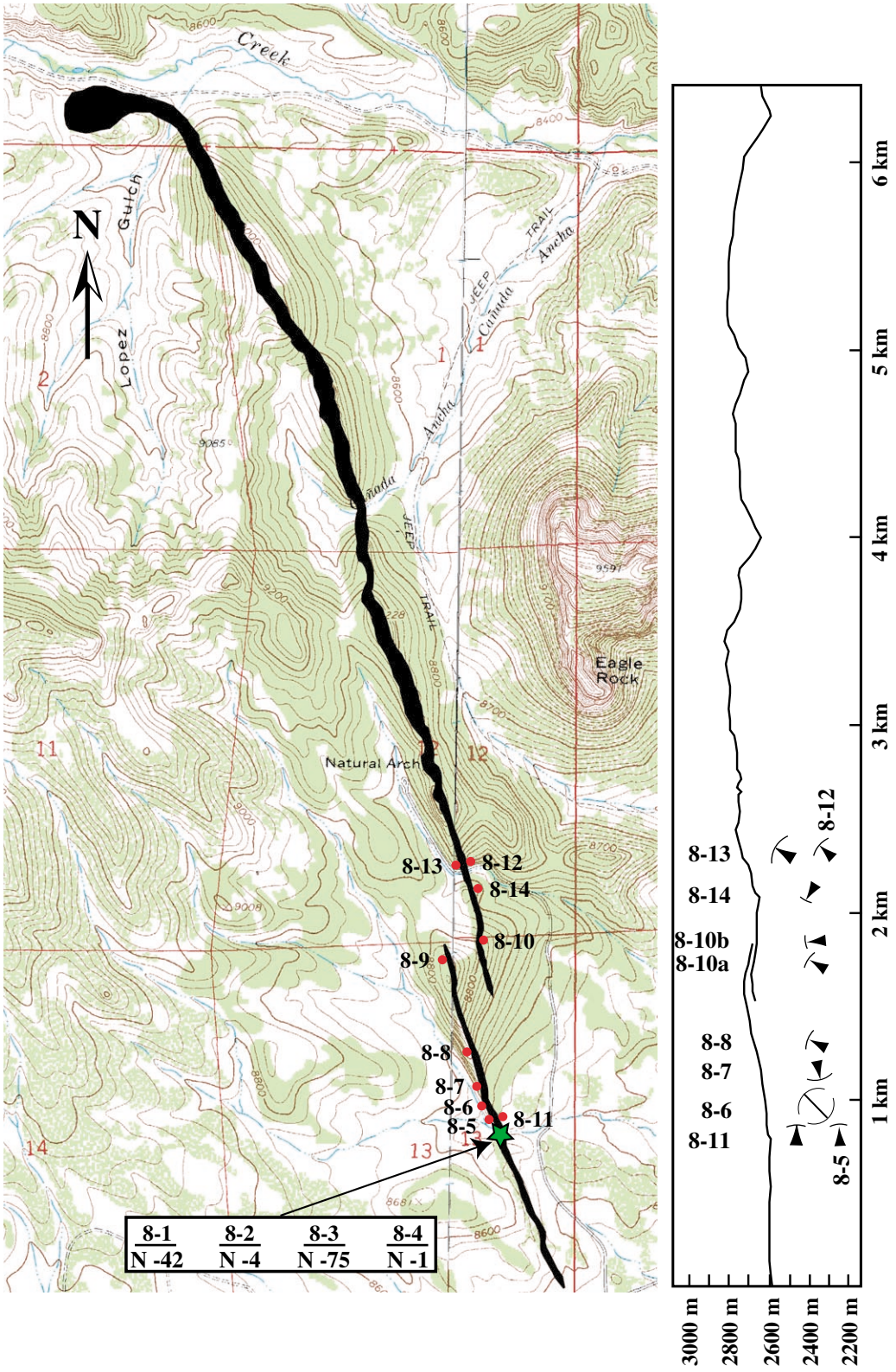
N
Lopez Gulch
Creek
Natural Arch
Eagle Rock
JEEP TRAIL
Cañada Ancha
8-13
8-12
8-14
8-10
8-9
8-8
8-7
8-6
8-5
8-11
8-1 N -42
8-2 N -4
8-3 N -75
8-4 N -1
3000 m
2800 m
2600 m
2400 m
2200 m
1 km
2 km
3 km
4 km
5 km
6 km
8-10b
8-10a

Figure 4.25. View south from the Natural Arch along Dike 8 of a major offset proximal to the central intrusive complex. The offset distance is approximately 150 meters. Drill sites 8-9 and 8-10 at the tips of the offset segments are indicated. The large rock mass at the lower left is the top of Dike 8.

Figure 4.26. Magma flow measured by anisotropy of magnetic susceptibility in Dike 3. The map view shows sample locations along the intrusion. At the same scale is a cross section of the dike showing a profile of the dike top and AMS results as arrows with 95% confidence bounds plotted as arcs at the arrow tips. The center of Summer Coon volcano is to the east. Dashed line between sites 3-8 and 3-9 denotes a small (~10 meter) offset in the dike (see Figure 4.27). No flow directions were obtained for samples 3-2 and 3-18. Magma flow in the segment proximal to the central intrusive complex is up and to the west at the segment initiation, becomes subhorizontal with increasing distance, and plunges shallowly down and to the west at the termination. The initiation of the next segment follows the same pattern. The measured flow suggests that magma intruded offset fractures that were formed at the front of the propagating dike. The segment offset in the area of sites 3-13 through 18 is the largest along the length of the dike, and the segment tips seem to propagate towards each other. A small strand of magma connects the segment (see Figure 4.28). Driving pressure in this portion of the dike, which is thicker than outcrops to the east, must have been high enough for the segment tips to propagate, which was not the case for the segment offset between sites 3-8 and 3-9.

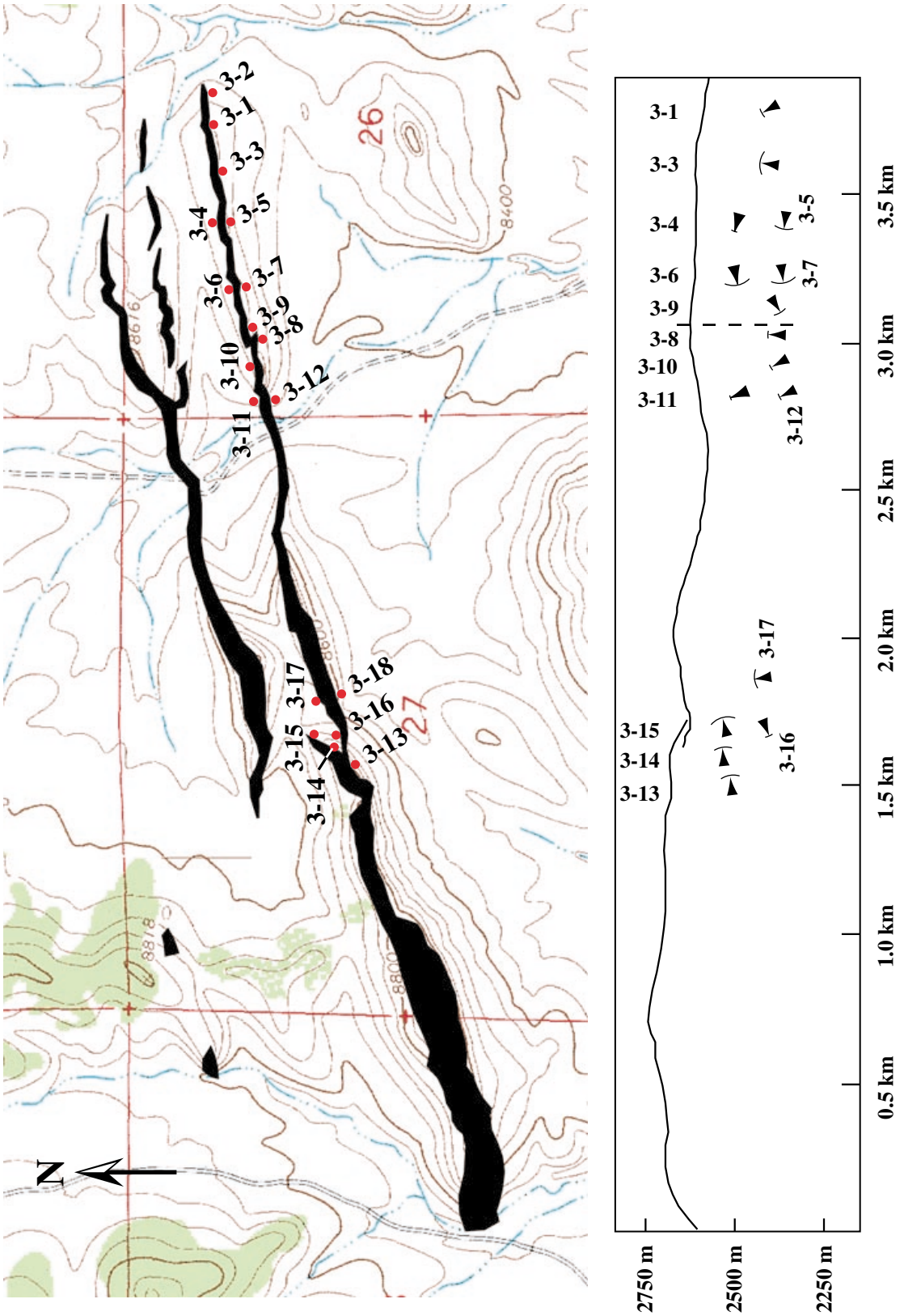
3-1
3-2
3-3
3-4
3-5
3-6
3-7
3-8
3-9
3-10
3-11
3-12
3-13
3-14
3-15
3-16
3-17
3-18
26
27
8400
8800
8818
N
0.5 km
1.0 km
1.5 km
2.0 km
2.5 km
3.0 km
3.5 km
2750 m
2500 m
2250 m

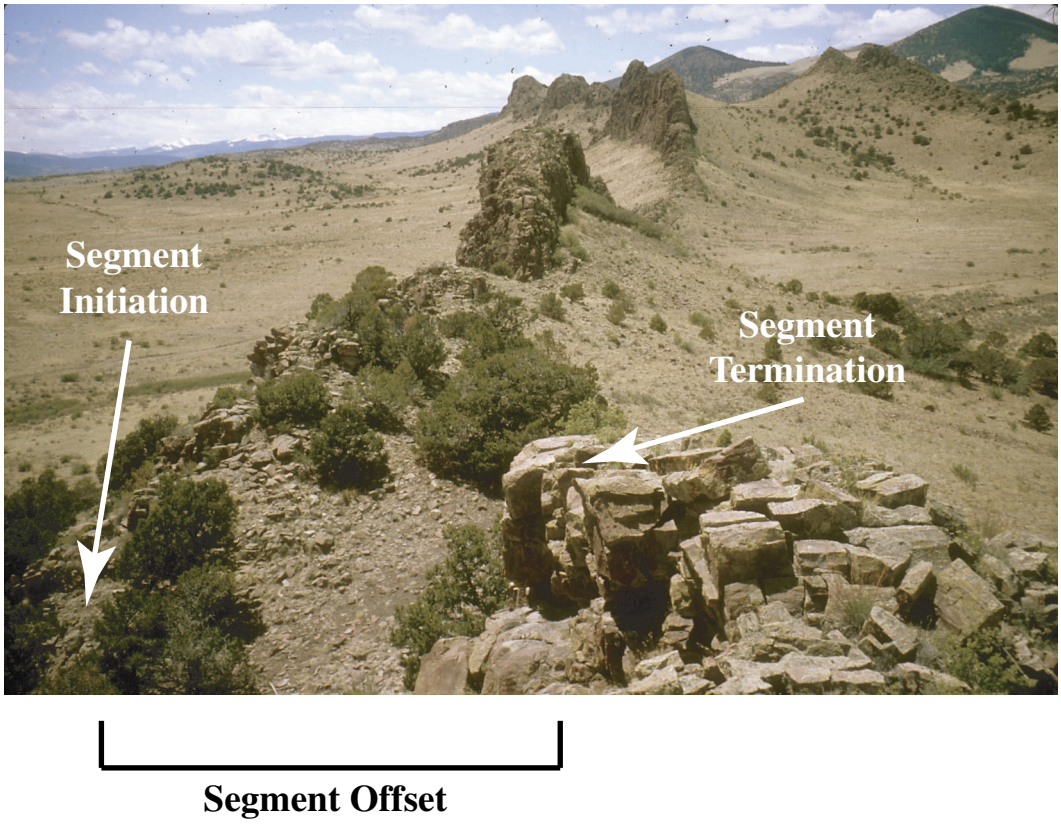

Figure 4.27. Minor segment offset in Dike 3 proximal to the central intrusive complex. View is to the west along Dike 3. One segment terminates in the foreground, while a new segment, offset by ~10 meters, begins at the bottom left. The two segments are not connected.

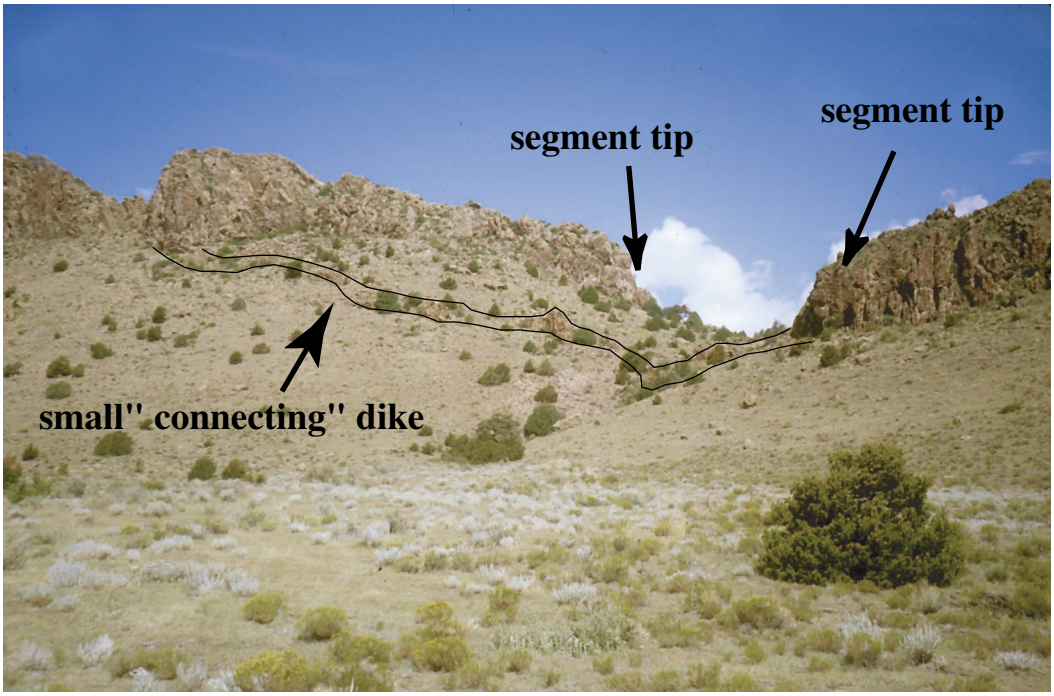

Figure 4.28. Major offset segment (~50 meters) that is connected by a thin strand of magma (outlined) in the distal portion of Dike 3. View is to the north, and the offset is perpendicular to the photograph. The top of the dike at the right is approximately 100 meters above the flat surface in the foreground. Note that the connecting strand does not link the segment tips, but rather trends from the segment tip on the right to a point in the interior of the segment on the left.

Each core was trimmed to 1" in length, and 5 cores yielded two 1" sections. The total number of cores after trimming, excluding samples that were not used in the analysis due to lost orienting lines or poor sample location (in the dike interior as opposed to the margin), was 165. The anisotropy of magnetic susceptibility of each core was measured in a KLY-2 Kappabridge susceptibility meter. Curie temperature measurements on a sample from each dike suggest that magnetite is the primary magnetic mineral in the dikes.

4.5.4 Results of AMS Analyses at Summer Coon

The anisotropy of samples from Summer Coon varies between 0.25% and 2.59%, using the method of *Tauxe* [1990] where the percent anisotropy is defined as $100(\tau_1 - \tau_3)$. A complete listing of the eigenvalues, eigenvectors, and magnetic characteristics of each sample is given in Appendix C. In addition, the AMS directions and associated bootstrapped confidence bounds are shown in graphical format for each site in Appendix D. A compilation of AMS data by sample site is provided in Table 4.3. At 2 sites (3-2 and 8-9), the maximum eigenvalues (τ_1) are not distinct from the intermediate eigenvalues (τ_2), therefore no flow direction or lineation can be determined. In addition, at 3 of the sites (3-13, 3-18, and 8-6), the parametric bootstrap cannot be applied because of high scatter in the data (see appropriate sites in Appendix D). The four sites collected across the width of Dike 8 (8-1 through 4), yield only flow lineations because they were collected from the dike interior and not the margin. All 24 remaining sites are characterized by the "normal" fabric of *Rochette et al.* [1991] and *Tauxe et al.* [1998], where the maximum eigenvectors (γ_1) are within 45 degrees of the dike plane (Figure 4.29), and the minimum eignevectors (γ_3) are perpendicular to the dike. In summary, of the 33 sites sampled, 24 have absolute

Table 4.3. AMS results from Summer Coon. The magnitudes of the maximum, intermediate, and minimum eigenvalues (τ_1, τ_2, and τ_3), directions of the eigenvalues (dec = declination and inc = inclination), and associated uncertainties (σ) are listed for each sample site as determined by the bootstrap method of *Tauxe et al.* [1998]. If τ_1 and τ_2 are distinct from each other and γ_1 is distinct from the plane of the dike, a unique flow direction can be determined. The dike attitude at each site is also listed, as well as the flow direction from AMS where determined (positive values indicate upward flow, OUT is radially away from the center of the volcano, and IN is radially towards the center of the volcano). If present, other indicators of magma flow at the sample sites (e.g. grooves, strained vesicles, etc.) are also noted.

Sample	No.	Maximum eigenvalue				Intermediate eigenvalue				Minimum eigenvalue			
Site	Samples	τ_1	σ	Dec	Inc	τ_2	σ	Dec	Inc	τ_3	σ	Dec	Inc
3-1	5	0.33779	0.00044	111.2	61.2	0.33512	0.00014	240.5	19.2	0.32709	0.00042	338.1	20.6
3-2	3	0.33618	0.00023	286.8	60.2	0.33459	0.00026	59.5	21.2	0.32923	0.00012	157.6	19.9
3-3	6	0.33707	0.00011	190.7	67.9	0.33341	0.00025	55.9	16.0	0.32952	0.00023	321.5	14.9
3-4	5	0.33781	0.00020	58.0	17.1	0.33400	0.00026	280.4	67.4	0.32818	0.00021	152.5	14.3
3-5	4	0.33600	0.00016	71.7	14.3	0.33413	0.00023	206.9	70.2	0.32988	0.00015	338.2	13.4
3-6	7	0.33573	0.00053	243.7	6.0	0.33247	0.00043	9.5	79.8	0.33180	0.00056	152.8	8.2
3-7	5	0.33677	0.00010	270.9	5.5	0.33367	0.00017	152.0	78.7	0.32955	0.00019	1.8	9.8
3-8	3	0.33825	0.00012	174.7	76.4	0.33237	0.00013	46.9	8.5	0.32938	0.00023	315.3	10.6
3-9	5	0.33610	0.00014	287.2	29.5	0.33381	0.00021	78.7	57.3	0.33009	0.00026	189.7	13.0
3-10	5	0.33803	0.00012	43.4	57.3	0.33388	0.00026	241.3	31.4	0.32808	0.00026	146.3	8.1
3-11	5	0.33733	0.00019	69.1	67.7	0.33319	0.00013	261.0	21.9	0.32948	0.00009	169.4	4.2
3-12	3	0.33758	0.00028	109.7	59.2	0.33308	0.00021	245.3	23.1	0.32935	0.00011	343.9	19.2
3-13	4	0.33512	0.00028	38.4	0.0	0.33363	0.00017	308.4	63.5	0.33125	0.00024	128.5	26.5
3-14	5	0.33585	0.00017	202.0	7.3	0.33348	0.00020	9.2	82.6	0.33066	0.00035	111.8	1.6
3-15	5	0.33652	0.00045	206.0	8.3	0.33354	0.00018	312.8	63.2	0.32994	0.00032	112.0	25.3
3-16	4	0.33708	0.00010	274.8	24.7	0.33382	0.00016	37.4	49.5	0.32910	0.00011	169.5	29.8
3-17	5	0.33500	0.00027	19.0	67.4	0.33355	0.00019	237.0	18.1	0.33144	0.00024	142.7	13.0
3-18	4	0.33526	0.00036	136.2	64.4	0.33452	0.00038	287.0	22.7	0.33022	0.00063	21.8	11.2
8-1	9	0.33665	0.00040	2.0	35.5	0.33414	0.00028	157.1	51.8	0.32921	0.00022	263.1	12.2
8-2	8	0.33576	0.00014	327.3	6.2	0.33394	0.00017	75.7	71.0	0.33029	0.00013	235.3	17.9
8-3	5	0.33782	0.00033	358.7	71.6	0.33411	0.00059	181.8	18.4	0.32807	0.00030	91.5	0.9
8-4	5	0.33839	0.00023	336.2	0.3	0.33421	0.00021	69.4	84.9	0.32739	0.00023	246.1	5.1
8-5	5	0.33603	0.00011	358.4	3.3	0.33406	0.00016	113.3	82.1	0.32991	0.00011	268.0	7.1
8-6	5	0.33579	0.00098	151.7	41.6	0.33470	0.00079	350.8	46.8	0.32951	0.00163	250.4	9.6
8-7	6	0.33605	0.00029	130.7	12.3	0.33368	0.00030	305.2	77.6	0.33027	0.00029	40.5	1.2
8-8	9	0.33824	0.00027	172.4	68.0	0.33349	0.00064	352.7	22.0	0.32827	0.00059	262.7	0.1
8-9	3	0.34182	0.00020	1.3	40.2	0.33626	0.00045	202.6	47.8	0.32192	0.00051	100.5	10.8
8-10a	3	0.33714	0.00061	194.4	57.6	0.33442	0.00035	14.6	32.4	0.32844	0.00027	284.5	0.1
8-10b	3	0.34034	0.00018	45.1	63.6	0.33448	0.00007	190.0	22.1	0.32517	0.00019	285.7	13.7
8-11	5	0.33797	0.00068	317.0	5.1	0.33399	0.00032	196.7	80.0	0.32804	0.00062	47.8	8.6
8-12	5	0.33673	0.00020	124.5	44.3	0.33402	0.00052	340.3	39.7	0.32925	0.00037	233.9	18.8
8-13	5	0.33810	0.00039	185.3	54.9	0.33376	0.00066	321.3	26.8	0.32813	0.00048	62.4	20.9
8-14	6	0.33906	0.00037	355.3	32.4	0.33366	0.00061	236.3	37.3	0.32727	0.00094	112.7	36.0

Table 4.3. (Cont.)

Sample Site	τ_1 and τ_2 distinct?	γ_1 distinct from dike?	Dike Attitude		AMS flow inclin. (positive is up)	other indicators?
			Dip Direct.	Dip		
3-1	Y	Y	349	75	56 OUT to 66 OUT	
3-2	**N**	**N**	349	84	**N/A**	
3-3	Y	Y	341	88	82 OUT to 68 IN	
3-4	Y	Y	335	84	13 OUT to 19 OUT	
3-5	Y	Y	335	84	-5 OUT to 19 OUT	grooves 18 OUT
3-6	Y	Y	340	87	-28 OUT to 4 OUT	
3-7	Y	Y	340	87	-23 OUT to 7 OUT	
3-8	Y	Y	0	80	84 OUT to 88 IN	
3-9	Y	Y	351	85	-40 OUT to -26 OUT	
3-10	Y	Y	342	80	58 OUT to 65 OUT	
3-11	Y	Y	170	86	65 OUT to 72 OUT	
3-12	Y	Y	170	86	60 OUT to 68 OUT	
3-13	Y	Y	337	83	**too scattered**	
3-14	Y	Y	316	83	-6 IN to 18 IN	
3-15	Y	Y	316	83	-3 IN to 31 IN	
3-16	Y	Y	6	75	-27 OUT to -18 OUT	
3-17	Y	Y	349	89	69 OUT to 85 IN	
3-18	Y	Y	349	89	**too scattered**	
8-1 (Lineation Only)	Y	**from dike interior**	64	88	-43 OUT to -42 OUT 42 IN to 43 IN	
8-2 (Lineation Only)	Y	**from dike interior**	64	88	-11 OUT to 2 OUT -2 IN TO 11 IN	
8-3 (Lineation Only)	Y	**from dike interior**	64	88	-85 OUT to '65 OUT 65 IN to 85 IN	
8-4 (Lineation Only)	Y	**from dike interior**	64	88	-5 OUT to 5 OUT -5 IN to 5 IN	
8-5	Y	Y	64	88	-8 OUT to 14 OUT	
8-6	Y	**N**	71	83	**too scattered**	
8-7	Y	Y	71	83	-27 IN to 5 IN	
8-8	Y	Y	71	83	51 OUT to 76 OUT	strained vesicles, lineation 72 OUT
8-9	**N**	Y	74	83	**N/A**	
8-10a	Y	Y	140	86	48 OUT to 70 OUT	
8-10b	Y	Y	62	86	79 IN to 90	
8-11	Y	Y	64	88	-10 OUT to 13 OUT	
8-12	Y	Y	60	85	33 OUT to 61 OUT	grooves, 70 OUT
8-13	Y	Y	60	85	39 OUT to 80 OUT	lineation, 64 OUT
8-14	Y	Y	270	78	25 IN to 39 IN	lineation, 45 OUT

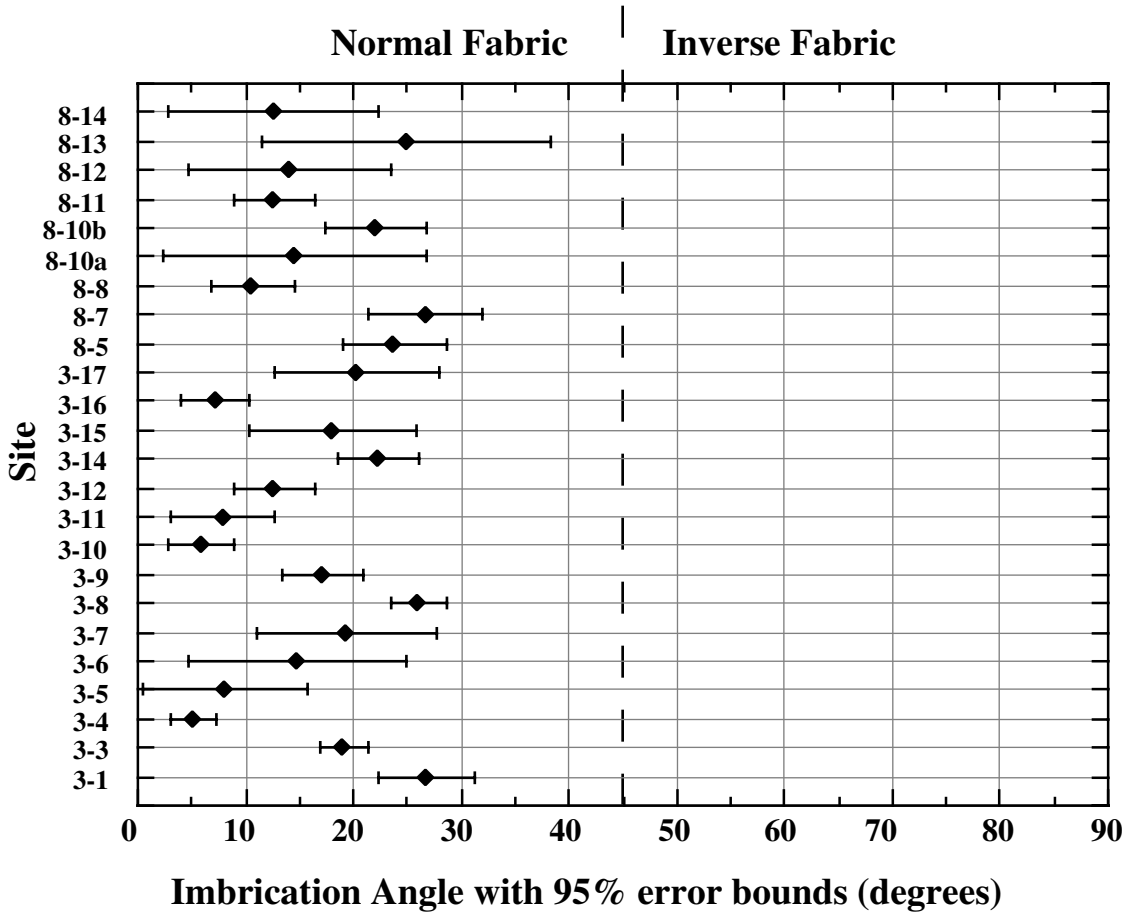

Figure 4.29. Imbrication (the angle between γ_1 and the dike plane) for AMS sites at Summer Coon. Sites that do not have τ_1 values that are distinguishable from τ_2 at the 95% confidence level (3-2 and 8-9), those where τ_1 is not distinct from the plane of the dike (3-2, 8-3, 8-4, and 8-6), and sites 8-1 through 4 (which were collected from the dike interior) are not included in the plot because they do not meet the criteria for determination of a unique flow direction. Of the remaining sites, none have imbrication angles that exceed 40 degrees at the 95% confidence level. *Tauxe et al.* [1998] suggest that an imbrication angle greater than 45 degrees indicates inverse fabric. Such sites are not suitable for flow direction determination. All sites in the plot above display "normal" fabric, and indicate unique flow directions.

flow directions, 4 have flow lineations, and no flow could be determined at the remaining 5 sites.

Tauxe et al. [1998] advocate sampling on both margins of a dike to confirm the flow direction, since γ_1 directions from each margin should fall off the plane of the dike by the same magnitude in opposite directions (Figure 4.22). Due to the nature of the dike outcrops at Summer Coon, opposing margins could only be sampled at 6 localities (12 sites). Five of the areas satisfied the criteria of *Tauxe et al.* [1998] for determining a unique flow direction, including γ_1 values from opposing margins that are distinct from the dike plane and from each other, as well as offset from the dike plane by the same magnitude (see Appendix E). Excessive scatter in site 3-18 does not allow the 3-17 / 3-18 pairing to be evaluated. Based on the success at the 5 localities, I treat sites with data from one dike margin as capable of isolating a unique flow direction when γ_1 is distinct from the dike plane.

The results of the AMS analyses indicate a complex pattern of flow that includes components of both vertical and horizontal magma migration. The flow profile of Dike 8 varies through more than 180° in an apparently random pattern (Figure 4.24). No flow direction could be determined at site 8-9, however petrographic observations of imbricated phenocrysts (see below) suggest subhorizontal magma flow (Figure 4.30). At sites 8-7 and 8-14, magma flow is back in the direction of the presumed source, the central intrusive complex at Summer Coon. *Shelley* [1988] finds no evidence for lateral flow towards the source of the Lyttleton radial dike swarm in New Zealand, and no such flow pattern is expected in a radial dike proximal to its pressurized source. By the method of *Tauxe et al.* [1998], an incorrect dike strike may result in a flow direction that is diametrically opposed to the true magma flow vector. The trend of the dike is difficult to determine at site 8-9, where the intrusion is extensively fractured. At site 8-7 the dike is well-exposed and its

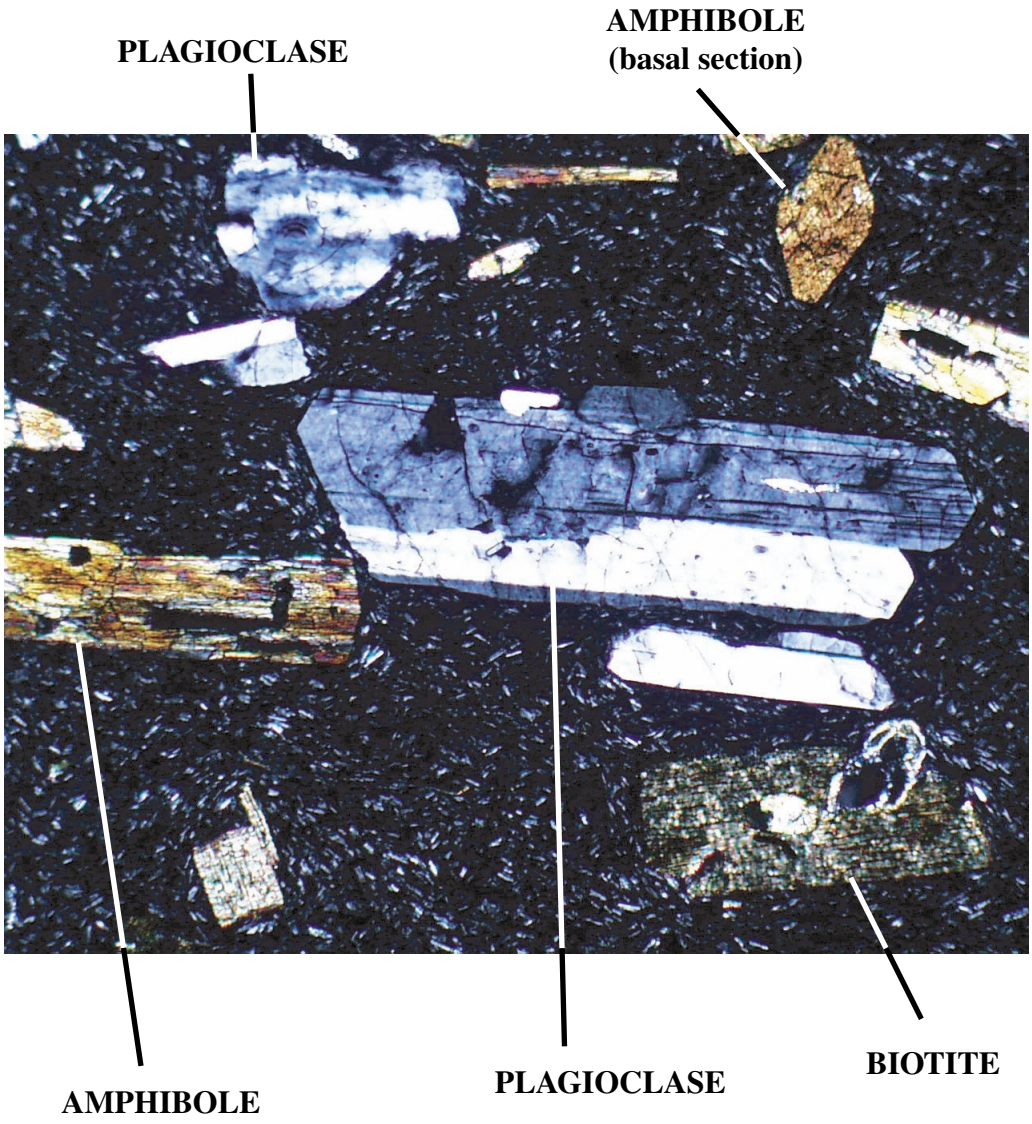

Figure 4.30. Thin section from sample 8-9C in cross polarized light showing magma flow (figure is oriented so that up corresponds to the vertical axis of the dike). The section was cut parallel to the γ_1 direction. Although AMS measurements of samples from site 8-9 cannot distinguish a flow direction (because τ_1 and τ_2 overlap at the 95% confidence level), thin sections clearly show aligned and imbricated phenocrysts that suggest subhorizontal magma flow. Other thin sections of samples from site 8-9 exhibit the same behavior. Field of view is 1.7 mm across.

measured strike is accurate, therefore the anomalous flow direction is probably real and may represent a local irregularity in magma flow. Unfortunately, AMS samples could not be collected from the distal 2/3 of Dike 8 due to the inaccessibility of the outcrops. A flow lineation from grooves on the dike margin at the natural arch (north of sites 8-12 and 8-13 in Figure 4.31) suggests flow inclined either upwards towards the north or downwards to the south. The overall pattern of magma flow in the sampled section of Dike 8 is mixed vertical and lateral magma flow with no apparent pattern.

Magma flow is more consistent along the length of Dike 3 (Figure 4.26). Although no flow vector or lineation could be determined for site 3-2, closest to the central intrusive complex, nearby sites suggest steeply inclined magma flow. The middle of the first segment is characterized by lateral outward flow, while magma flow dips shallowly downward in the distal end of the segment. At the initiation of the next segment at site 3-8, magma flow is once again steep and shallows with increasing radial distance from the segment tip. The pattern is similar to that observed near the proximal echelon step of Dike 8, where flow is steep at the initiation of the segment (site 8-10) and subhorizotal at segment terminations (site 8-9, inferred from thin section observations). The measured flow suggests that magma entered an offset fracture proximal to the central intrusive complex from a continuous dike at some depth below the current exposure, filled the crack, and flowed down and out of the fracture at its distal end. The fracture was most likely generated as an echelon crack at the propagating front of the dike and subsequently filled. The lack of extensive vertical flow in the middle and distal portion of the segments suggests that the dikes are not vertically extensive, but formed due to lateral flow with isolated pockets of subvertical flow (Figure 4.32).

Samples from the distal segments of Dike 3, at sites 3-13 through 3-18, suggest lateral growth of opposing segment tips towards each other. Magma flow at sites 3-13, 3-

Figure 4.31. Grooves suggesting magma flow in a vertical section of Dike 8 near the natural arch (see Figure 4.6H). North is to the left in the photograph. The grooves dip south, suggesting magma flow either up and to the north or down and to the south. A quarter, right center, provides a scale. Grooves indicating magma flow are rare at Summer Coon, and form when flowing magma is sheared against the country rock along the sides of the dike.

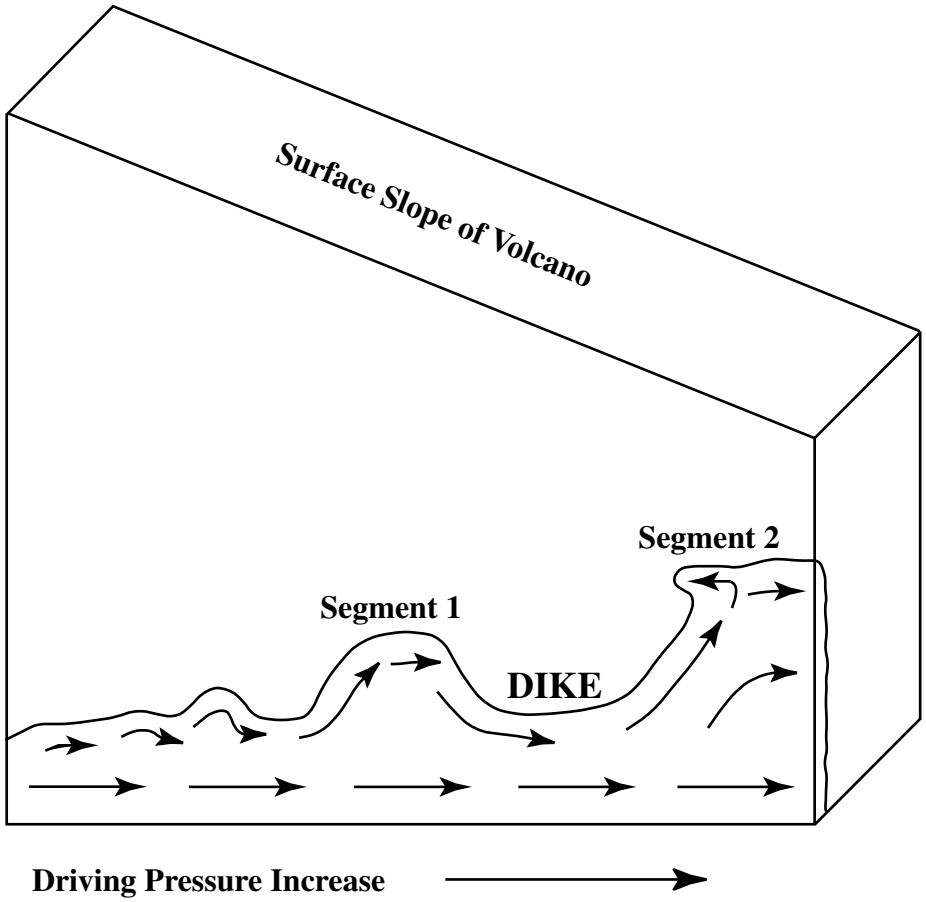

Figure 4.32. Schematic diagram of magma flow and intrusive form for a radial dike below the flank of a volcanic edifice based on observations from Summer Coon. The overall flow of magma is laterally away from the chamber. Isolated patches of inclined flow may occur when magma encounters fractures that formed in front of the propagating dike, resulting in en echelon segmentation. Proximal to the magma chamber, where the overburden thickness is greatest, the driving pressure in the dike will be low and the segment tips will not propagate outward, as suggested by flow measurements in segments proximal to the central intrusive complex in Dikes 3 and 8 and shown above as "Segment 1." As the dike approaches the surface, driving pressure in the dike will increase. As a result, the tips of echelon segments are likely to propagate, interacting with neighboring segment tips (not shown above) as inferred at the distal segment offset of Dike 3. Loosely based on Figure 9 from *Gudmundsson* [1984].

14, and 3-15 is horizontal to the east, while flow in the strand of magma that connects the echelon segments is subhorizontal to the west. The geometry of the segments in map view strongly resembles that predicted by mechanically interacting cracks as shown by *Olson and Pollard* [1991] and other authors. The segment tips probably propagated towards one another due to the higher pressure in the segments (as indicated by their great thicknesses). Lower pressures (and hence lower thicknesses) characterize all dikes proximal to the source region, therefore segments (for example, at sites 3-8 and 3-9) do not propagate towards each other. Observations of magma flow at segment tips supports the proposed dike segmentation mechanism for Summer Coon. Fractures offset from the main trend of the dike form above and in front of the dike tip and are subsequently intruded by magma that enters the fracture at a steep angle. When the fracture is filled, magma either exits the crack and returns to the continuous dike below if the magma pressure is lower than the rock fracture toughness, or propagates the fracture if the magma pressure is higher than the rock fracture toughness. The overall pattern of magma flow is subhorizontal and away from the source region (the central intrusive complex of the volcano), with isolated patches of subvertical flow where dike-induced fractures are intersected (Figure 4.32). Vertical flow is also inferred to have occurred under vents where magma may have erupted to the surface.

As demonstrated by *Shelley* [1988], magma flow is not constant across the width of a dike. Samples from sites 8-1 through 4 were collected along a cross section perpendicular to the strike of Dike 8. The measured magma flow can only be expressed as a lineation (because the samples were collected from the dike interior and not the margin) and indicate widely varying flow directions across the intrusion. The lineations trend parallel to the dike but are inclined downward and away from the central intrusive complex of Summer Coon at angles of -42°, -4°, -75°, and -1° from west to east across the dike's

width (Figure 4.24). The variations may be due to magma drainback following eruption [*Delaney and Pollard*, 1981; *Shelley*, 1988], however it is unlikely that the dike reached the surface based on the relatively thin dike width at the sample sites. An alternative explanation is that the dike was formed by multiple magma pulses from a pressurized source. *Gudmundsson* [1984] infers multiple magma pulses through the warm interiors of exposed Tertiary Icelandic dikes based on the presence of more than one "columnar row" in a cross section perpendicular to the dike strike. By analogy, the 1975-1984 rifting event at Krafla volcano in Iceland was likely due to the formation of a single dike via multiple magma pulses spread over the 10 year interval of the activity [*Gudmundsson*, 1995]. Although no jointing exists at sample sites 8-1 through 4, multiple columnar rows and cooling surfaces are exposed in sections north of sites 8-12 and 8-13 in Dike 8, and west of sites 3-11 and 3-12 in Dike 3 (Figure 4.33). Multiple magma pulses probably contributed to the growth of Summer Coon dikes, therefore flow directions obtained on dike interiors would reflect magma pulses after the initial dike emplacement. Samples from dike margins, where most sites were located, are more likely to record the initial magma flow in the intrusion.

4.5.6 Results of Petrographic Analyses at Summer Coon

Of the original 165 cores used in the AMS analysis, 116 samples were cut into thin sections for petrographic analysis. Fourteen of the cores were cut into 2 sections, parallel and perpendicular to the dike plane. The remaining 102 samples were sectioned parallel to the plane that includes the direction of magma flow as determined by AMS (i.e. the γ_1 direction), yielding a total of 130 thin sections. Both Dikes 3 and 8 are characterized by porphyrytic textures, with phenocrysts of 85% plagioclase and 15% biotite in Dike 3

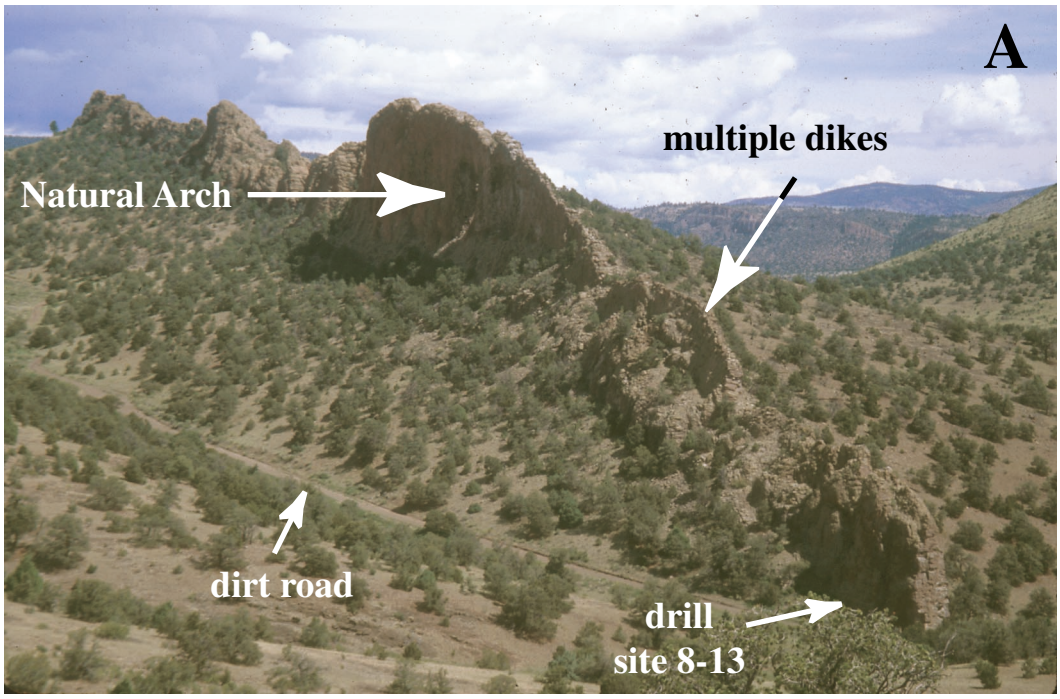

Figure 4.33. Evidence for multiple magma pulses in Summer Coon radial dikes. (a) View north along Dike 8. A Natural Arch is located in the tallest part of the dike, oblique to the photograph so it cannot be seen (although the sunlight that passes through the arch is apparent in the shadows below the intrusion). Along the dike below the segment containing the arch is a thicker area where the dike is composed of several parallel intrusions indicated by sets of columnar joints, probably injected by magma pulses that occurred at different times during the growth of Dike 8. Sample site 8-13 is indicated. The brown strip at the bottom of the small valley below the dike is a dirt road. (b) Eroded section showing the interior of Dike 3 near sample sites 3-11 and 3-12 (labeled) looking east. The vertical cross section exposes several cooling surfaces, most likely caused by multiple magma injections into the dike. The pulses intruded either between or along previously intruded and cooled magma, resulting in the observed interior structure. The exposed dike face is ~20 meters tall.

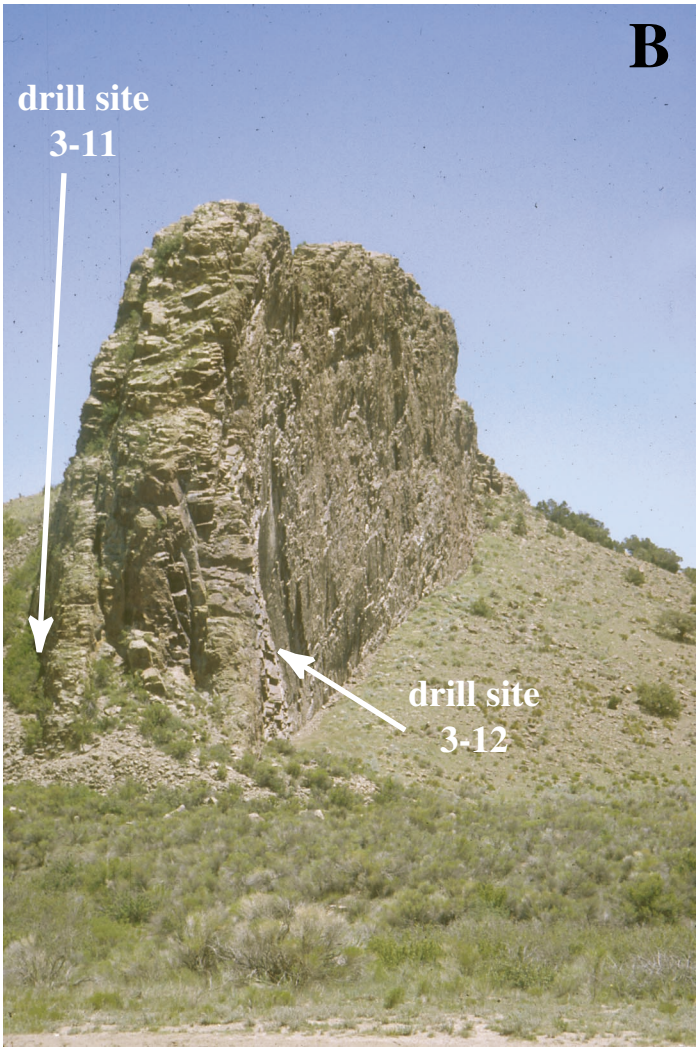

Figure 4.33. (Cont.)

(Figure 4.34) and 85% plagioclase, 10% amphibole, and 5% biotite in Dike 8 (Figure 4.35). Samples sectioned parallel to the γ_1 direction are dominated by the long axes of crystals, and alignment and/or imbrication of phenocrysts is common. In contrast, the 14 sections that were cut approximately perpendicular to the flow direction (perpendicular to the dike plane) contain abundant basal sections and blocky crystals. Alignments are most pronounced in relatively large phenocrysts with well-developed blade-like shapes. Grains with length-to-width ratios that approach 1 and small crystals tend to be randomly oriented (Figure 4.36). In some sections alignment due to magma flow appears to have been impeded by closely packed crystals, where phenocryst rotation was blocked by neighboring grains (Figure 4.36).

Alignments in individual thin sections commonly vary by 10-20 degrees, however the overall sense of flow can be estimated. Figure 4.37 gives several examples of flow in oriented sections, and compares the crystal alignments with values determined by AMS from Table 4.3. Qualitatively, flow alignments and imbrication from thin sections confirm the AMS measurements described above, supporting the application of the AMS method at Summer Coon.

4.6 Discussion

The configuration of the silicic dikes at Summer Coon in vertical section may be determined from the overall outcrop pattern, magma flow directions, and observed dike geometry. Erosion of the volcanic edifice has exposed rocks at the base of the volcano. The most proximal dike outcrops are within 1-2 km of the central intrusive complex, and most extend radially outward for several kilometers (Figure 4.4). Three models may explain the present pattern of silicic dike exposures: 1) all dikes originated at the same depth

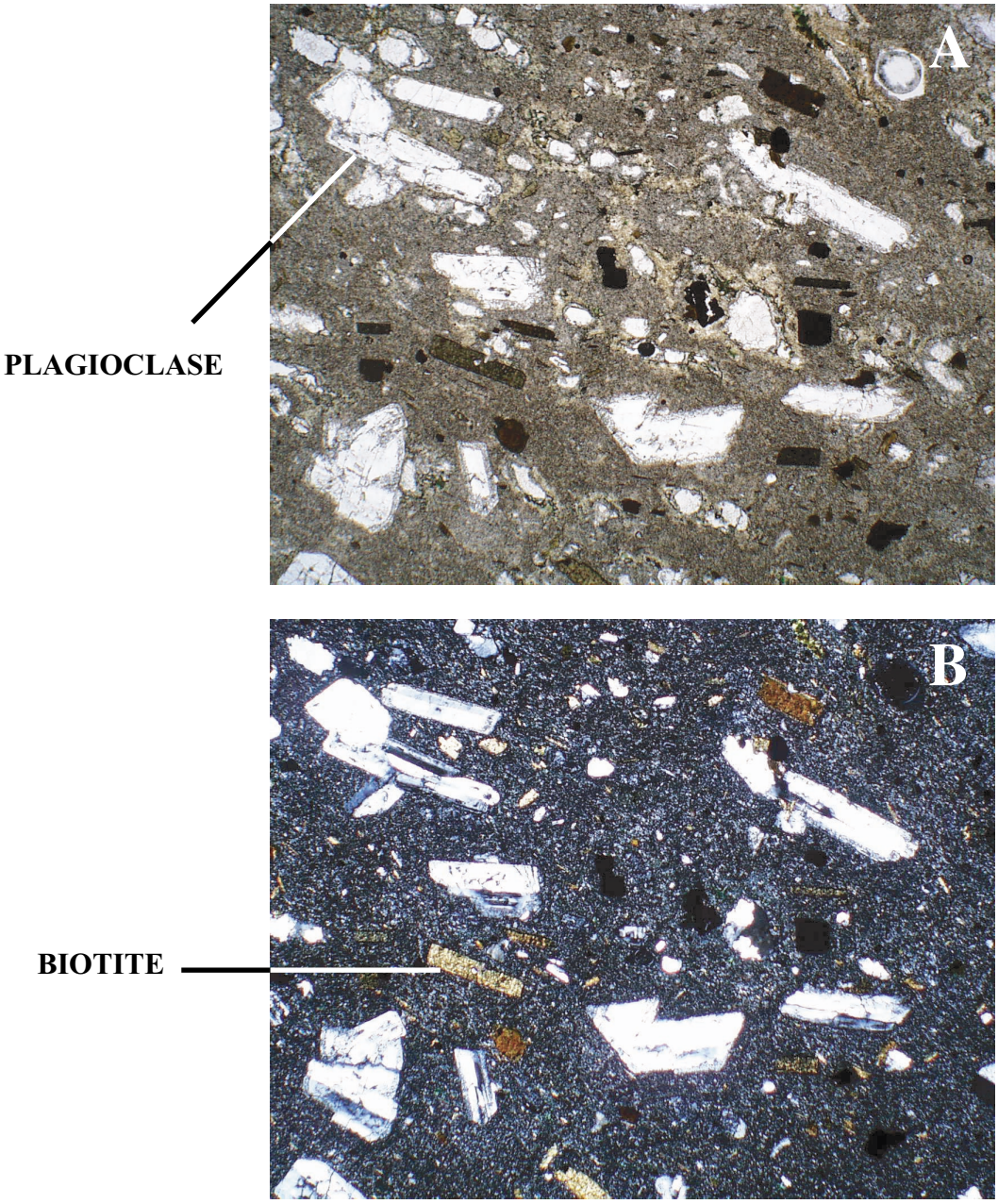

Figure 4.34. Thin section from sample 3-9B showing typical mineral assemblage and porphyritic texture of Dike 3. (a) Thin section under plane polarized light. (b) The same section under cross polarized light. Phenocrysts include plagioclase and biotite. Note the alignment of elongated minerals along an axis trending from the upper left to the lower right of the section. The field of view in both images is 4.2 mm.

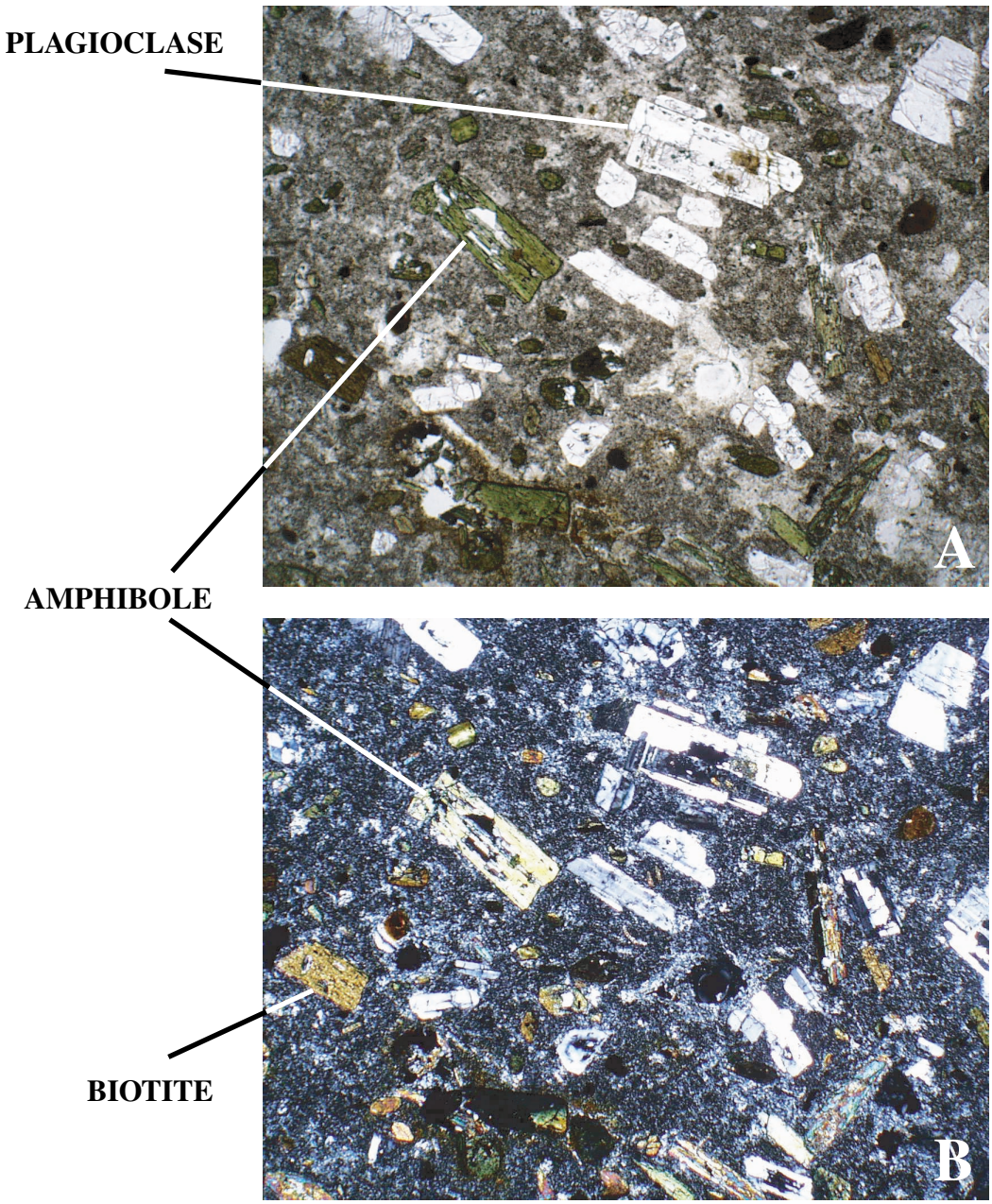

Figure 4.35. Thin section from sample 8-6A showing typical mineral assembledge and porphyritic texture of Dike 8. (a) Thin section under plane polarized light. (b) The same section under cross polarized light. Phenocrysts include plagioclase, amphibole, and biotite. The elongated minerals tend to follow an axis that trends from upper left to lower right in the section. The field of view in both images is 4.2 mm.

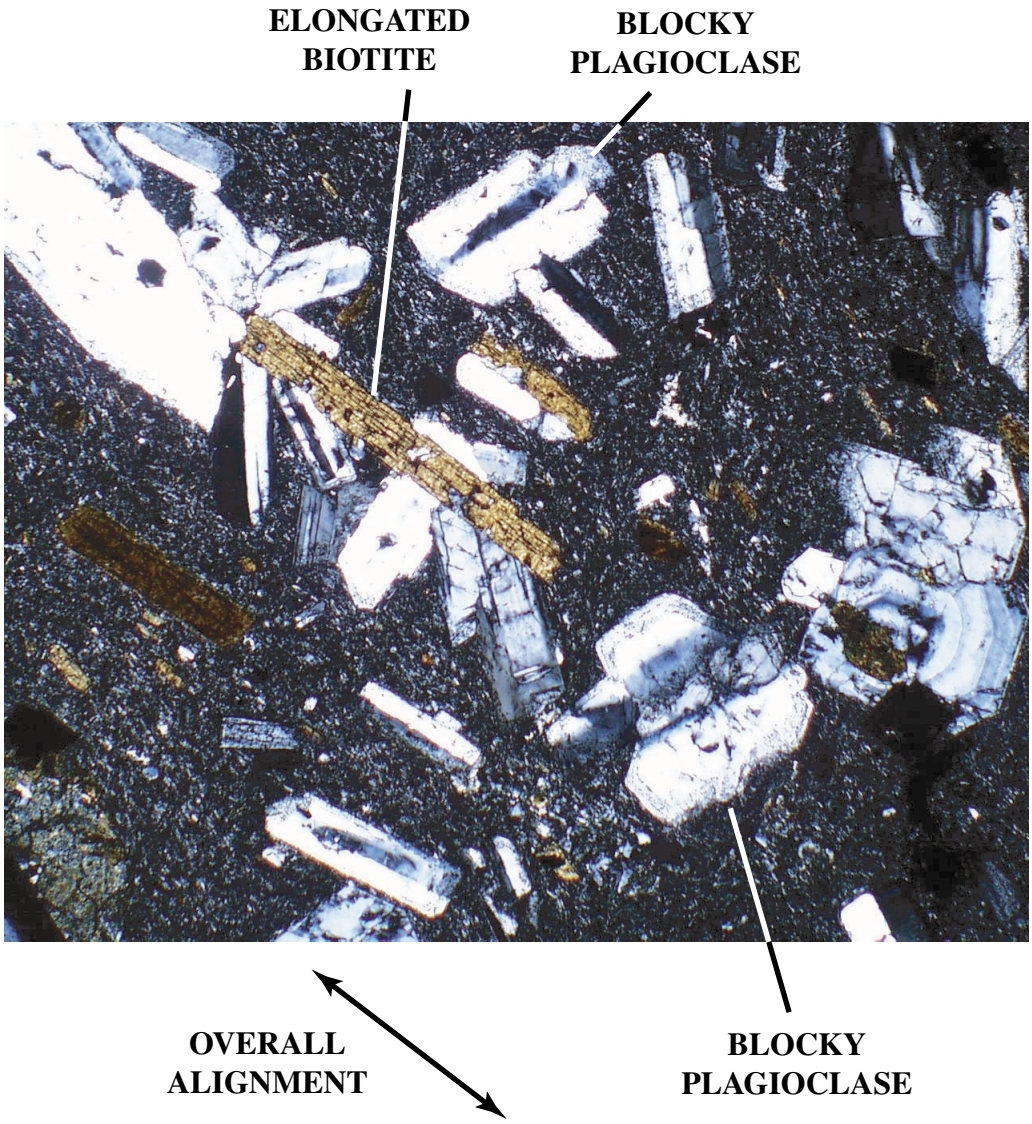

Figure 4.36. Thin section of sample 3-12A under cross polarized light. Field of view is 4.2 mm across. Light-colored plagioclase and brown biotite are surrounded by dark groundmass. Crystals with high length to width ratios (elongated) tend to align themselves preferentially due to magma flow along an axis trending from the upper left of the image to the lower right. Blocky phenocrysts with length to width ratios close to 1 are not commonly aligned because their long and short axes are not sufficiently different to be reoriented by magma flow. In addition, some elongated crystals appear to have been blocked from aligning with the flow direction by neighboring grains (particularly below the large labeled biotite phenocryst). Nevertheless, the overall alignment remains clear.

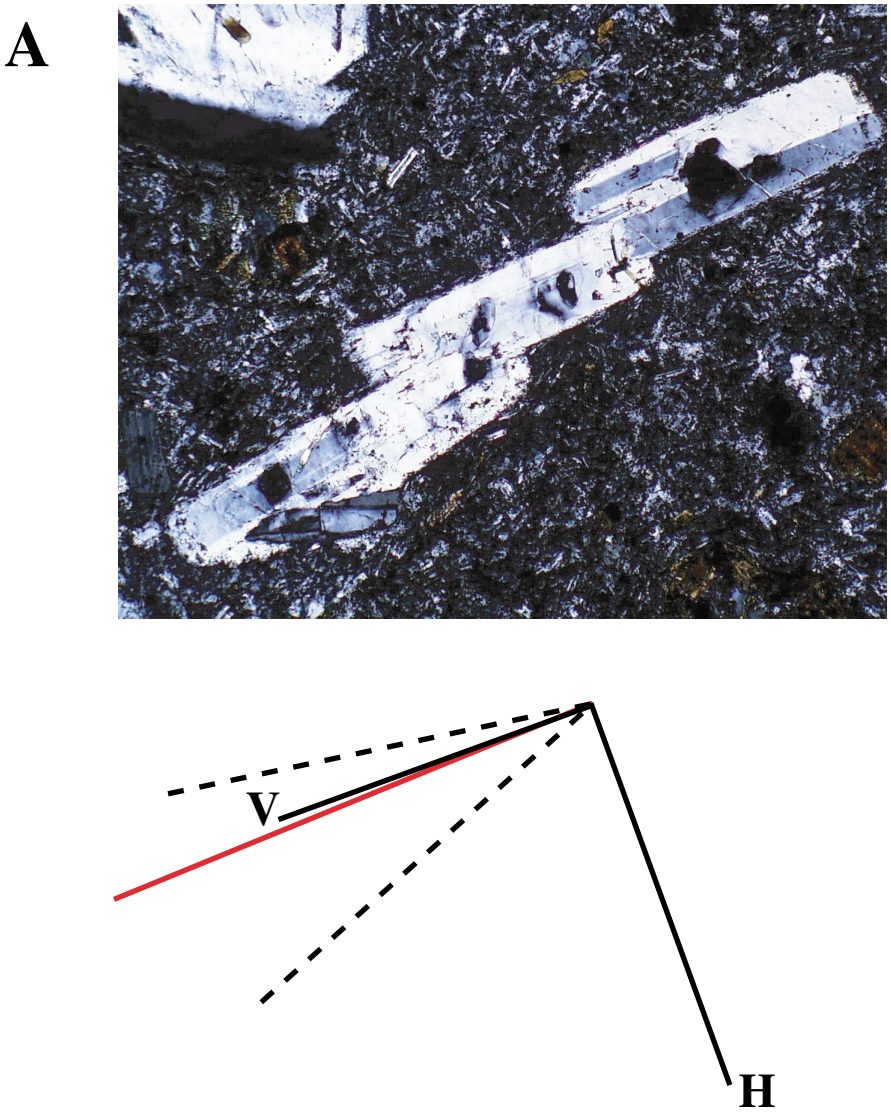

Figure 4.37. Oriented thin sections with aligned and/or imbricated phenocrysts and corresponding flow directions from AMS measurements. Below each image is a graph showing the horizontal (H) and vertical (V) axes of the thin section, which correspond to the horizontal and vertical axes of the dike. Dotted lines on the graph indicate the 95% confidence bounds of flow inclination from AMS while the red line is an estimate of the flow inclination based on mineral grain alignments and imbrication. Samples shown are: (a) 3-3E, cross polarized light, field of view = 1.7 mm, (b) 3-10E, plane polarized light, field of view = 4.2 mm, (c) 3-17D, plane polarized light, field of view = 4.2 mm, and (d) 8-13D, cross polarized light, field of view = 1.7 mm.

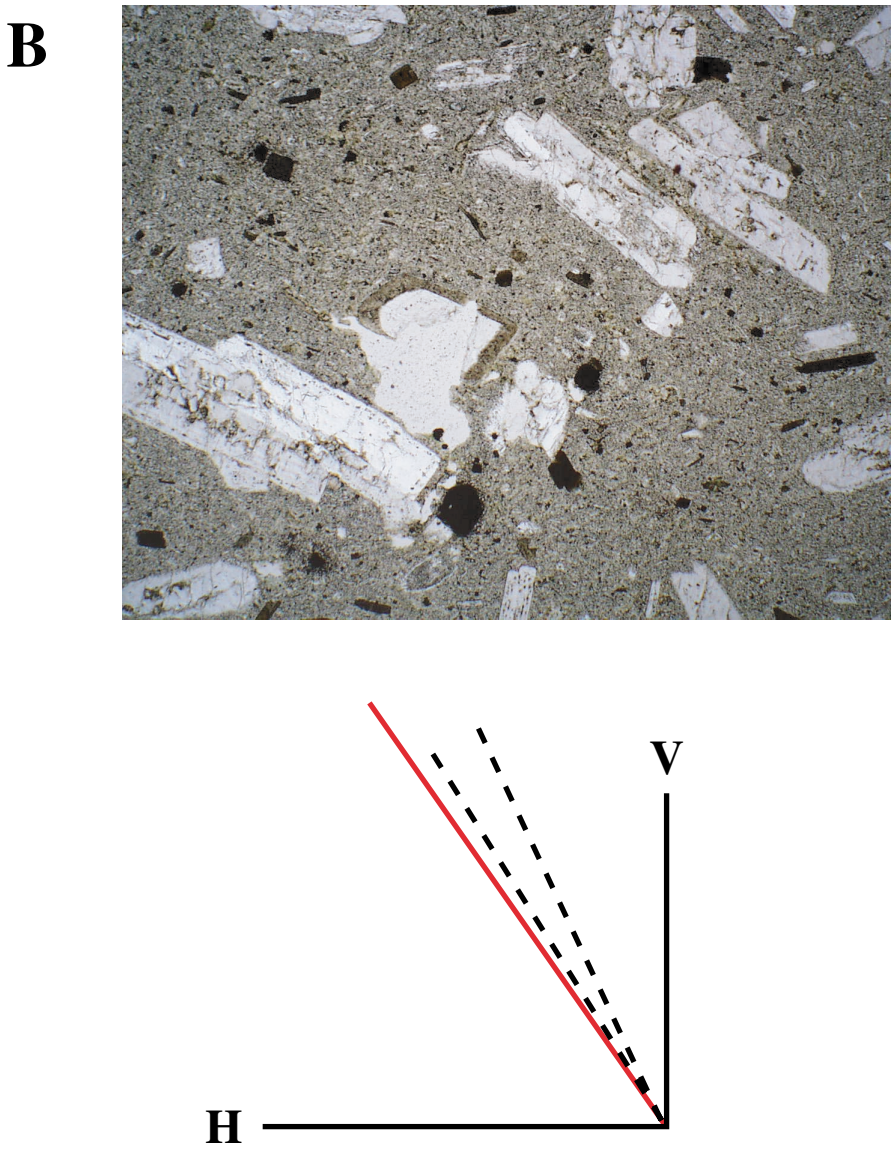

Figure 4.37. (Cont.)

C

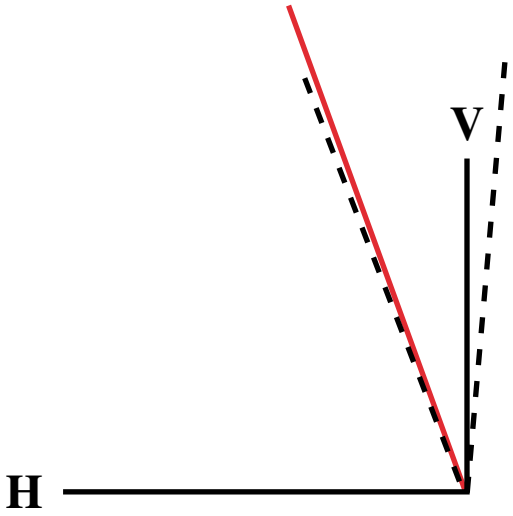

Figure 4.37. (Cont.)

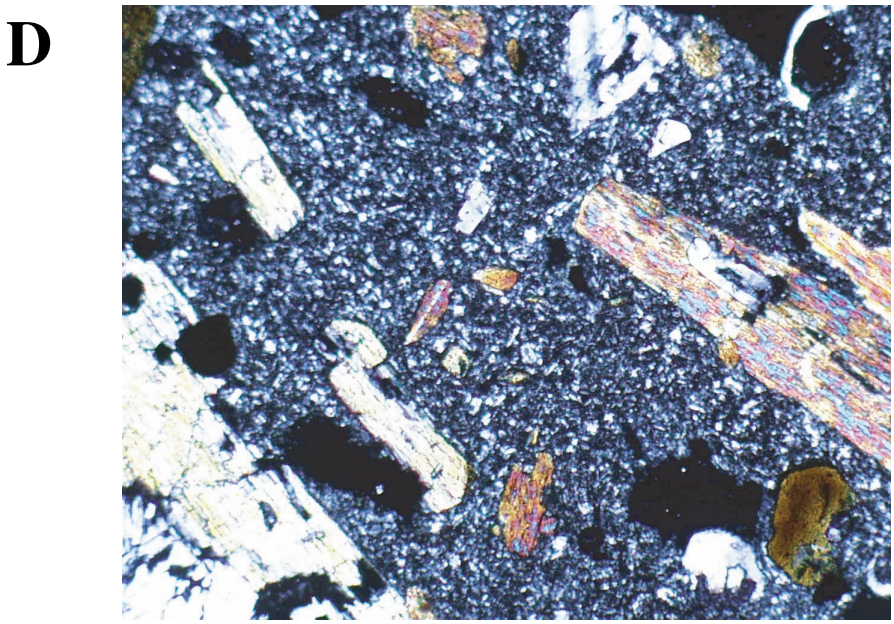

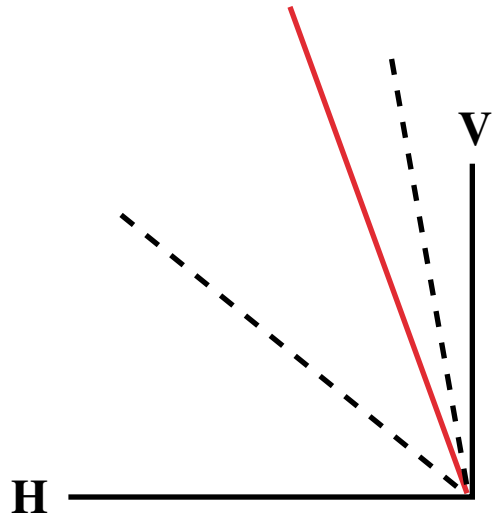

Figure 4.37. (Cont.)

from the central conduit and propagated along subhorizontal radial paths (Figure 4.38A), 2) the dikes are wide or fan shaped (in vertical cross section) and propagated obliquely (steeply) towards the surface from a source at depth (Figure 4.38B), and 3) the dikes originated from the top of a magma chamber or the base of the conduit and propagated upward until entering the volcanic edifice, when magma flow became subhorizontal (Figure 4.38C).

The first model assumes that dike exposures closest to the central intrusive complex have been eroded away and that magma flow along the lengths of all dikes was within a few degrees of horizontal, and is essentially the same as that of *Nakamura* [1977] (Figure 4.1A). However, magnetic surveys have confirmed the continuation of several dikes below the surface into the center of the volcano [*Mertzman*, 1971]. At least some of the dikes do seem to be connected with the central intrusive complex, but not at the depth predicted by the model.

The second explanation for the outcrop configuration at Summer Coon requires that magma flow be subvertical along the lengths of all dikes (if the intrusions are planar in vertical section) or subvertical proximal to the center of the volcano and shallowing with radial distance (if the dikes are fan-shaped). Three lines of evidence contradict the model. Most Summer Coon silicic dikes probably only erupted at isolated points along their lengths as suggested by plugs located near the terminations of several dikes. While erosion may have removed plugs that fed higher vents, the plugs would be manifested by a change in thickness of the present dike outcrop, which is not generally observed. A fan-shaped or planar dike would be more likely to erupt at several sites spread out over wide distances (Figure 4.38B). In addition, magma flow is often subhorizontal. Neither Dike 3 nor Dike 8 is dominated by vertical flow, suggesting that the dike forms do not approximate planes in cross section. Finally, the driving pressure distribution of dikes at Summer Coon does

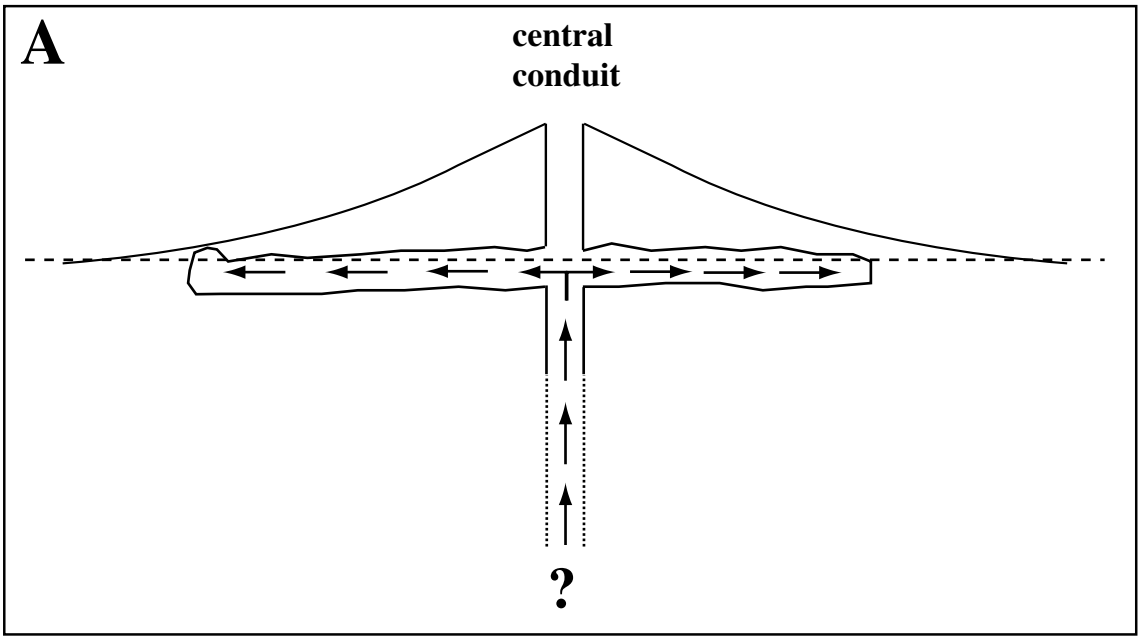

Figure 4.38. Possible schematic cross-sectional forms of radial dikes at Summer Coon based on outcrop geometry and magma flow directions. The dashed line is an approximation of the present erosional surface. The central intrusive complex is represented only as the central conduit, which has an uncertain configuration at depth. (a) A model favoring radial dikes that propagate horizontally from the central conduit is unlikely because no dikes can be traced into the central intrusive complex at the current level of exposure, and inclined flow, which is not predicted by the model, is observed. (b) Fan-shaped and planar dikes fit the observed outcrop pattern, but are not consistent with determinations of magma flow and driving pressure. (c) The preferred model consists of blade-like dikes that propagate upward to the base of the volcano, then follow sub-horizontal paths to the outer flanks of the edifice where eruptions are most likely to occur.

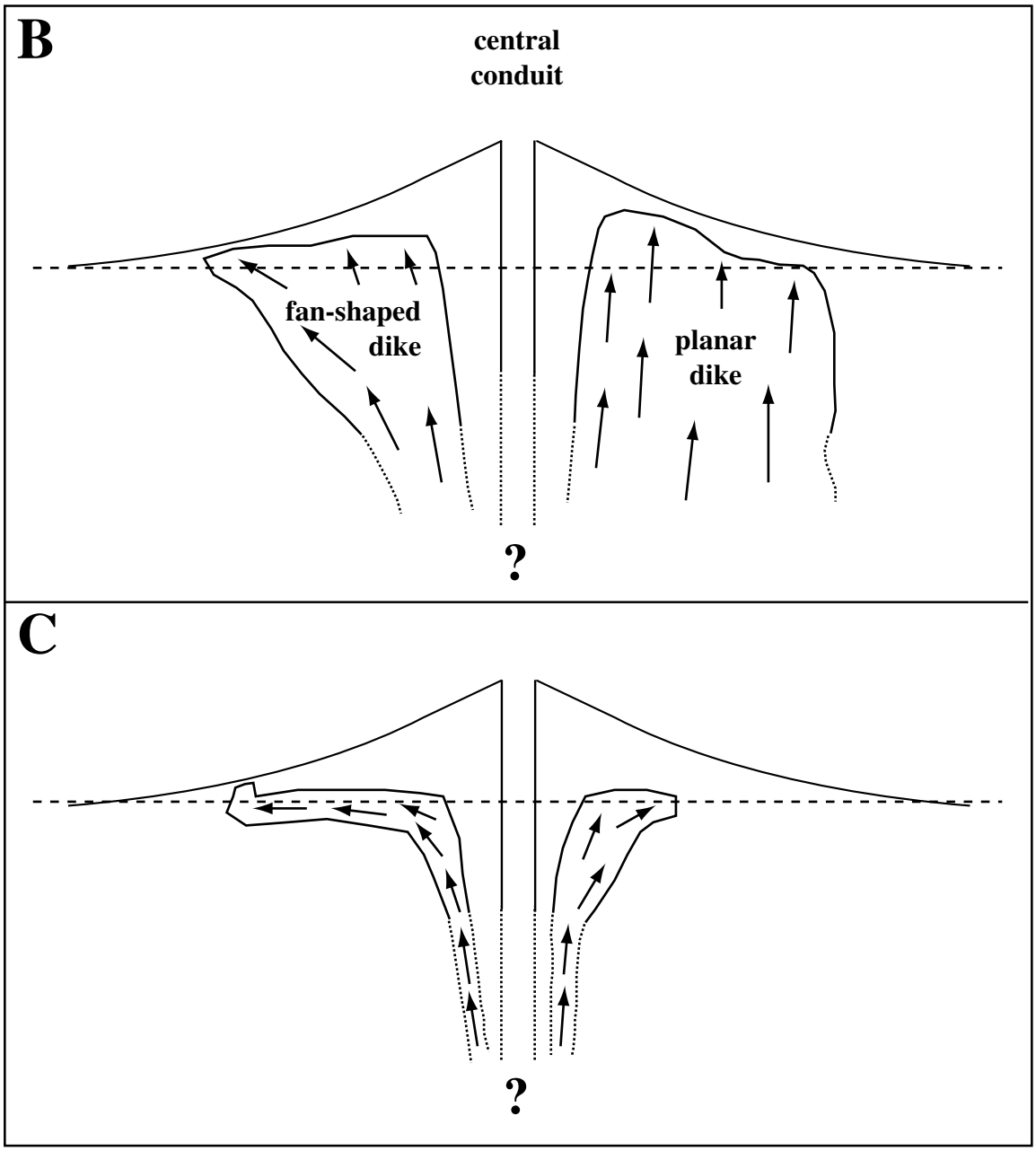

Figure 4.38. (Cont.)

not support fan-shaped dike geometry. If the cross-sectional area of a dike increases with radial distance, the total area of host rock that is in contact with the dike increases and the driving pressure should decrease. No decrease in calculated driving pressure is observed, and modeling indicates a positive stress gradient with increasing distance from the central intrusive complex along the lengths of most Summer Coon dikes.

The third possible configuration is the most consistent with observations of Summer Coon dikes. Magma flow is steeply inclined proximal to the center of the volcano and becomes subhorizontal with increasing radial distance, suggesting that the dikes propagated from depth into the volcanic cone before assuming lateral paths. The lack of dike outcrops near the central intrusive complex is therefore not a product of erosion, and dikes are assumed to connect with a source at depth, as suggested by the magnetic studies of *Mertzman* [1971]. *Rubin* [1995] also notes that high-viscosity magma will travel farther in blade-like dikes than fan or planar-shaped intrusions. Dikes with high height to length ratios are more susceptible to freezing, and are therefore unlikely to propagate far from their sources. The intrusions may have followed subhorizontal paths as they entered the volcanic cone because the contrast between low-density rocks of the edifice and higher density rocks of the basement creates a surface of neutral buoyancy for the ascending magma. As the dikes propagated laterally away from the volcano center, the burial depth and elastic strength of the rock decreased, causing the dikes to thicken and leading to eruptions on the lower flanks of the edifice. En echelon segmentation occurred along the tops of the intrusions as isolated patches of inclined flow entered recently formed dike-parallel fractures with trends offset from the axis of the dike. Viscous fingering is commonly observed at the peripheries of magmatic intrusions [*Pollard et al.*, 1975], and the numerous fingers and segments observed at Summer Coon (see, for example, Figure 4.8) suggest that the current exposures are at or near the original upward extents of the

dikes. As a result, magma flow measured along the exposed outcrops should be irregular and inclined, as is observed (see section 4.5.4). Lateral flow likely dominated below the current level of erosion. The model illustrated in Figure 4.38C is supported by the observations of *Parsons* [1939] of radial intrusions at the eroded Sunlight volcano, northwest Wyoming. Based on outcrop configurations and cross cutting relationships, *Parsons* [1939] speculates that magma flow was steeply inclined within ~800 meters of the center of Sunlight volcano, but lateral along the base of the edifice away from the central conduit.

Geologic evidence from the more deeply eroded radial dike swarm of the Spanish Peaks argues for planar or fan-shaped dikes. *Smith* [1987] notes that magma flow at all points along the dike lengths is inclined, which, when projected back to the source of the magma, suggests a planar shape for most intrusions. However, the deep exposures at the Spanish Peaks do not allow for determination of the behavior of the dikes upon entering a low-density volcanic structure. In addition, *Rubin* [1995] speculates that the Spanish Peaks dikes have a blade-like shape because of their great lengths. High-silica dikes are not often found > 10 km from their source regions, as observed at the Spanish Peaks, because the viscosity of rhyolitic magma opposes dike propagation and allows the magma to freeze [*Rubin*, 1995]. Blade-like forms tend to be the most efficient mechanism for transporting silicic magma over great distances because high source pressure, required for rhyolite dike propagation [*Rubin*, 1993], will be preserved in a dike with a low aspect ratio [*Rubin*, 1995]. Unfortunately, a direct comparison between Summer Coon and the Spanish Peaks cannot be attempted because of the differing depths of exposure and speculation regarding the three-dimensional geometry of the intrusions. However, excellent outcrops at both volcanic centers allow for testing of dike emplacement models

(theoretical, analytical, and numerical), and future research at both volcanic centers should address the problem of the preferred forms of igneous dikes.

4.7 Application to a Modern Stratovolcano

One possible modern analog to Summer Coon is South Sister, a recently active volcano in central Oregon. Almost 1 km^3 of magma erupted from aligned vents on the southwest, southeast, and northeast flanks of the volcano at 2000-2300 years BP in two separate episodes (Figure 4.39) [*Scott*, 1987]. Based on the synchronicity of eruptions, compositional similarity of eruptive products, and alignments of vents and ground cracks, *Scott* [1987] concludes that both eruptive episodes were fed by dikes. The older episode includes the Rock Mesa lava flow and a smaller set of domes on the southwest flank of the volcano termed the Rock Mesa ENE vents by *Scott* [1987]. Although the orientation of the feeder segment for the Rock Mesa lava flow is unknown, it is clearly distinct from the Rock Mesa ENE feeder because the Rock Mesa vent does not fall on the Rock Mesa ENE segment trend. The Rock Mesa ENE segment is radial to the summit of the South Sister, implying that the Rock Mesa dike is a radial intrusion composed of two segments, with the farther segment (that fed the Rock mesa lava flow) rotated with respect to the first. The younger Devil's Hill chain is composed of at least 16 lava domes on the southeast flank of the volcano fed from a dike with two distinct right-stepping segments. The four small domes of the Carver Lake chain are located northeast of the summit of South Sister and lie along strike with the overall trend of the Devils Hill domes. The Carver Lake domes also have the same composition and erupted at the same time as the Devils Hill lavas, and thus may have been fed by the same dike [*Scott*, 1987]. The orientation of the maximum

Figure 4.39. Sketch map of South Sister volcano showing Holocene silicic lava domes and inferred dike trends. Lava domes are shades of red, with glaciers in green and lakes in blue. Small dotted lines indicate inferred dike segment trends (the two segments of the Devils Hill chain are numbered). Inferred dike trends are based on vent locations (marked by 'X's on the Rock Mesa and Newberry lava flows) and surface deformation (ground cracks and grabens that are not shown). The Rock Mesa dome covers the vent area, therefore no structural features are evident and a dike segment trend cannot be inferred. Because the Rock Mesa vent does not fall on the trend of the inferred Rock Mesa ENE dike, two separate segments must have fed the Rock Mesa eruptive episode. The dike probably originated as an intrusion radial to the summit of South Sister. The Devils Hill vents may also have erupted from a radial dike which became segmented and rotated due to a tectonic ~N-S most compressive stress. An alternate interpretation is that the Devils Hill and Carver Lake vents erupted from a regional ~N-S regional dike indicated by a heavy dashed line. Adapted from *Scott* [1987].

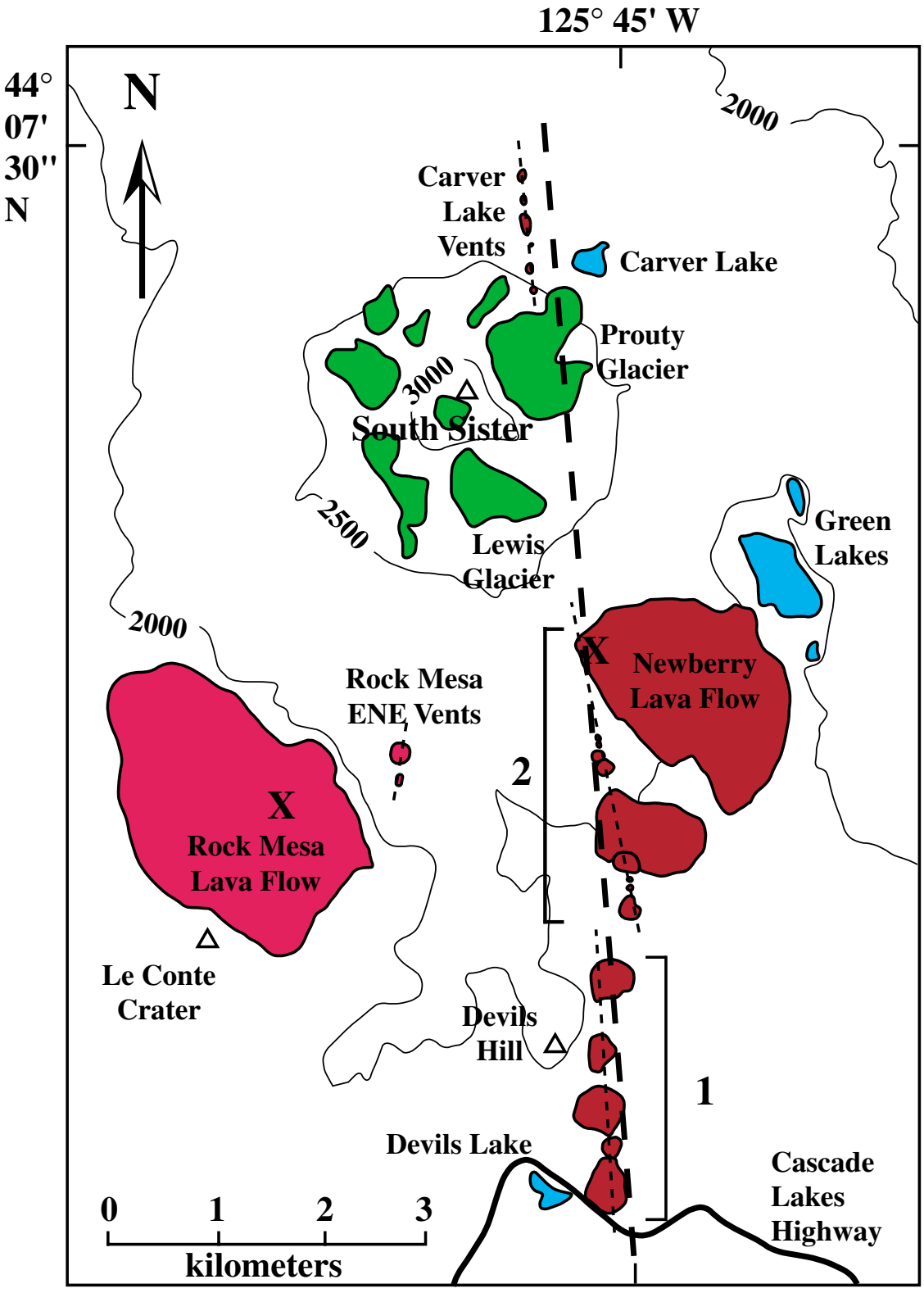
125° 45' W
44°
07'
30"
N
N
2000
Carver
Lake
Vents
Carver Lake
Prouty
Glacier
3000
South Sister
2500
Lewis
Glacier
Green
Lakes
2000
X
Newberry
Lava Flow
Rock Mesa
ENE Vents
2
X
Rock Mesa
Lava Flow
Le Conte
Crater
Devils
Hill
1
Devils Lake
Cascade
Lakes
Highway
0
1
2
3
kilometers

horizontal stress in the crust is roughly N-S in the region and apparently controls the orientation of the dikes at South Sister [*Zoback and Zoback*, 1980; *Scott*, 1987].

Scott [1987] considers two possibilities for the origin of the Holocene silicic dikes at South Sister: 1) the magma source is the central conduit of the volcano and the dikes propagate laterally away along radial orientations, curving to become N-S in response to the regional stress field, and 2) the magma source is beneath the southeastern flank of South Sister and is unrelated to a pressurized magma body beneath the volcano, so that the dikes are emplaced along a N-S trend that parallels the most compressive stress in the crust (the magma chamber does have a slight effect on the dike orientation near the summit). The first option is supported by radial trends of the Rock Mesa and Devils Hill dike segments that are proximal to the summit of South Sister Volcano. However, the Carver Lake vents are closest to the summit and the associated dike segment does not have a radial orientation. In contrast, the second possibility is supported by the lack of concurrent summit activity during the Rock Mesa and Devils Hill eruptions, suggesting that the central volcanic conduit was not active. The non-radial orientation of the Carver Lake vents is also explained by an origin unrelated to the South Sister conduit. *Scott* [1987] and other workers suggest that a large silicic chamber may underlie the south flank of the volcano, where the largest volume of silicic magma has erupted during the Holocene and where recent deformation has been documented by radar interferometry [*Wicks Jr. et al.*, in review].

Several comparisons may be made between South Sister and Summer Coon. At South Sister, both inferred Holocene dikes have en echelon segments that are several kilometers long. The segments are comparable to the first-generation segments in Summer Coon dikes. Eruptive vents are regularly spaced on the scale of hundreds of meters at South Sister and may represent second generation segmentation similar to that observed at

Summer Coon. The mechanism of segmentation is unclear at South Sister. The segment step of the Devils Hill chain is consistent with a N-S regional stress (which would induce right-stepping segments in the southeast quadrant of the volcano). Therefore a transition from a volcanic to tectonic stress field may explain the segmentation, assuming the dike originated at depth beneath the summit. The Rock Mesa dike, in the southwest quadrant of the volcano, also has right-stepping segments instead of the left-steps that the tectonic stress would impose on that quadrant of the volcano. The consistent sense of step at South Sister is analogous to the distribution of step into two hemispheres at Summer Coon. The pressure source modeled by *Wicks Jr. et al.* [in review] is west of the summit of South Sister, therefore the model of dike segmentation due to changes in the pressure source geometry with depth (Figure 4.20) may be applicable to South Sister. Clearly, dike segmentation at South Sister is not explained by the orientation of the regional stress regime.

The distribution of the erupted volume of the Devils Hill chain is not consistent with observations from Summer Coon. The majority of Summer Coon dikes thicken with increasing radial distance from the center of the volcano, therefore the largest volume of magma was available for eruption at the distal end of the dike. It follows that the largest volume eruptions should occur at the farthest distances from the summit of the volcano. The greatest extrusion of magma from the Devils Hill dike is the Newberry lava flow, which is the closest vent in the chain to the summit of South Sister [*Anderson and Fink*, 1992]. In contrast, the largest extrusion of lava from the Rock Mesa dike is farthest from the summit of South Sister, as expected.

Compositions of the eruptive periods are slightly different, with the earlier Rock Mesa extrusives slightly more silicic than the later Devils Hill and Carver Lake products [*Scott*, 1987]. The intriguing possibility exists that the Rock Mesa and Devils Hill dikes,

while compositionally similar, have two different sources. The distribution of erupted volume from the Rock Mesa dike is consistent with an origin as a radial dike emanating from beneath the summit of South Sister (no distinction between a shallow or deep source is possible). In contrast, the features of the Devils Hill / Carver Lake dike are best explained if the intrusion does not originate below the summit of South Sister, but instead has a source beneath the southeast flank of the volcano and is controlled by the N-S tectonic stress field. The presence of multiple eruptive sites suggests that the form of the Devils Hill / Carver Lake dike is probably that of a plane or fan in cross section (Figure 4.38B), unlike the expected blade-like form of a radial dike (Figure 4.38C). Modeling the Devils Hill dike as a regionally-controlled intrusion can explain both the anomalously large eruptive volume high on the flank of South Sister and the non-radial orientation of the Carver Lake vents, which lie along strike with the Devils Hill vents. Minor deviations from a N-S trend in the Devils Hill / Carver Lake dike may be due to the presence of a pressure source beneath the summit of South Sister, as suggested by *Scott* [1987].

Unfortunately, little evidence exists to favor either lateral or vertical transport of magma. Regardless of their origin from either tectonic or volcanic sources, magmas associated with the South Sister eruptive center can clearly reach distances of several kilometers where they may cause explosive eruptions. The Rock Mesa dike erupted a lava dome 6 km from the summit of South Sister, while lava from the Devils Hill eruptions was extruded at least 8 km away. Recent deformation studies by *Wicks Jr. et al.* [in review] suggest magmatic inflation beneath the west flank of South Sister. Such deformation may be precursory to shallow volcanic activity, including dike intrusion. The results of this study indicate that the hazard due to future eruptions of silicic magma fed by radial dikes at South Sister and other arc volcanoes extends to distances of as much as 10 km from the summit, where the largest volumes of magma may be likely to erupt.

4.8 Conclusions

Field measurements and observations of silicic radial dikes at Summer Coon have led to several conclusions regarding the emplacement of magmatic intrusions in stratovolcanoes:

1) Dike thicknesses increase with radial distance due to the combined effects of a) decreasing overburden due to the surface slope of the volcano, which causes a drop in both the vertical and horizontal stress, b) decreasing burial depth, and c) decreasing elastic modulus of fractured and poroushost rocks near the surface.
2) The greatest volume of magma is supplied to the farthest extent of radial dikes, therefore the most voluminous flank eruptions from intrusions will be around the base of a volcano, several kilometers from the summit. Radial dikes that reach the surface on the upper flanks of the volcano will typically initiate low-volume eruptions. Conversely, large eruptions near the summit may be fed by non-radial intrusions.
3) Silicic dikes will have a segmented geometry, possibly including multiple generations of stepping segments. The geometry of echelon steps is probably not controlled by the transition from volcanic to tectonic stress regimes, and the sense of step may be the same for the entire volcano regardless of the location or source of the dike.
4) Dikes propagate through a combination of vertical, oblique, and lateral flow. The overall pattern of magma flow can be characterized as subhorizontal in the volcanic cone with isolated patches of steeply inclined flow.
5) The active intrusion of a silicic radial dike will most likely be detectable by ground deformation studies. A dike on the same order of thickness as those at Summer Coon will generate significant surface cracks. The propagation of surface cracks away from the summit will indicate the subsurface location and propagation rate of the dike, which

may be used to forecast the behavior of the intrusion and potential for eruption. Deformation measurements using the Global Positioning System or radar interferometry are also necessary to distinguish between a long radial dike and a smaller, local intrusion.

Applying lessons from Summer Coon to inferred dike-fed rhyodacite domes on the flanks of South Sister volcano in central Oregon suggests that the larger of the two dikes may not be radial to the summit of the edifice. The Rock Mesa dike, which is probably radial, is segmented and has the greatest volume lava extrusion farthest from the summit of South Sister. The Devils Hill dike, which may not be radial, is also segmented and steps in the same sense as the Rock Mesa dike but has the largest volume of eruptive products in its center as opposed to its distal termination.

These conclusions are based on a detailed study of one eroded stratovolcano and should be tested at other locations. Eroded volcanoes with exposed radial dike swarms that may be targeted for additional work include West Elk Peak in central Colorado [*Gaskill et al.*, 1981] and Mt. Taylor in northern New Mexico [*Lipman et al.*, 1979].

5. Future directions for research regarding the stress regime within a volcanic edifice

Abstract. The geometry of igneous intrusions in a volcanic edifice is controlled by the state of stress within the volcano. A major source of stress heterogeneity in large basaltic shields is subvolcanic loading driven by dense solidified intrusions in the volcanic interior and basement. *Walker* [1984; 1987; 1988] has suggested that normal fault calderas at basaltic volcanoes may form by downsagging. In addition, the mechanism may create a stress field suitable for the intrusion of dikes with orientations that are circumferential to the center of the edifice on the upper flanks and radial on the lower flanks. Additional research to further assess the influence of downsagging on the stress regime within a volcano includes: 1) construction of a database of volcano characteristics and associated dike orientations, 2) numerical modeling of stress fields due to a) subvolcanic loading, and b) gravitational instabilities associated with topographic barriers, 3) initiation of deformation monitoring at Newberry volcano, an analog for Medicine Lake, and 4) field studies of the intrusive patterns and dike emplacement processes at eroded Icelandic volcanoes that host both radial and circumferential dikes. Taken together, these studies will advance the understanding of the stress regime within a volcanic edifice and lead to improved understanding of dike intrusion, applicable to volcanic hazard assessment and mitigation.

5.1 Introduction

Evidence presented in Chapters 2 and 3 suggests that downsagging deformation due to a dense subvolcanic intrusive complex may be occurring at Medicine Lake volcano (MLV) in northern California. The volcano hosts several dikes (inferred from surface vents) that are circumferentially oriented with respect to the caldera in the summit area. In contrast, flank intrusions are generally within a few degrees of north-south, an alignment

induced by east-west tectonic extension in the Basin and Range province. The pattern of eruptive fissures is similar to that observed on the shields of the western Galapagos, except that radial dikes at MLV are aligned by regional tectonic stresses upon leaving the magma chamber. The most recent volcanism at MLV occurred ~900 years ago [*Donnelly-Nolan et al.*, 1990], therefore non-magmatic crustal deformation, including downsagging, should be evident and unmodified by volcanic sources. However, additional deformation measurements at MLV and other volcanoes, and further modeling studies, are necessary to evaluate the proposed downsagging model (Chapter 1).

In addition, research into the process of dike emplacement should be continued. Work described at Summer Coon volcano in Chapter 4 indicates that radial dikes are the normal mode of intrusive activity at silicic stratovolcanoes. Downsagging does not appear to be a feature of silicic volcanoes due to the lack of a dense subvolcanic intrusive complex in such environments. As a result, radial dikes appear to propagate from depth at a steep angle until reaching the volcanic cone, where lateral propagation dominates. Similar studies at other eroded volcanoes will be valuable in mapping the stress field within the edifice nad testing the model dveloped from Summer Coon.

5.2 Future Research

The proposed model of the stress regime within a volcanic edifice may be evaluated by a variety of research projects. A database of eruptive fissure and fault orientations on the surfaces of different volcanoes would prove useful for testing the model and identifying volcanoes as sites for future research. Numerical models of stress within and deformation of a volcanic edifice are essential for characterizing expected patterns of dike intrusion and faulting due to the dynamic interaction of various volcanic processes (e.g. downsagging, magma chamber inflation, gravitational spreading, topographic effects, etc.). Deformation

measurements at volcanoes around the world are also important. As noted above, crustal displacements at Medicine Lake volcano may be explained by a combination of regional tectonism and downsagging due to a dense intrusive complex at depth. Additional GPS and radar interferometry measurements at similar volcanoes will test the applicability of the general structural model that is based on research at Medicine Lake. Finally, geological studies of intrusions at eroded volcanoes that display both radially and circumferentially oriented dikes (noting that radial intrusions may have been deflected by regional tectonism or other sources of stress) will further test the proposed model. Based on such work the model may be modified to describe general processes that occur at all volcanoes regardless of location (including extraterrestrial volcanoes) and geologic setting.

5.2.1 Database of Dike Orientations and Deformation

In the preceding chapters, a model for the structural development of a volcanic edifice is proposed. Unfortunately, the model is based on observations at few volcanoes, most notably the basaltic shields of the western Galapagos archipelago, Medicine Lake volcano, and the eroded Summer Coon composite cone. In order for the hypothesis to be developed into a generally applicable model, the deformation style and pattern of eruptive fissures at additional volcanoes must be documented.

A database that would prove useful for evaluating the proposed model should include for several volcanoes: 1) a description of the pattern of eruptive fissures and other surface faulting, 2) a description of deformation measurements that have been completed and the results, 3) the geologic setting of the edifice, 4) volcanology of the edifice (volcano morphology, eruptive history, composition of eruptive products, etc), and 5) geophysical evidence of the subvolcanic structure. Applying the proposed model to each volcano in the database will identify inadequacies and suggest ways in which the model may be amended

to explain the observations. After rigorous testing, the model may be applied to volcanoes that are not well studied, aiding hazard assessment and mitigation efforts.

5.2.2 Numerical Modeling of Subvolcanic Loading

Numerical modeling of the influence of a dense intrusive complex on the stress regime within a volcanic edifice is a vital research direction. The models of Medicine Lake volcano presented in Chapter 3 are the beginning of such work. Future efforts should focus on the effects of: 1) non-elastic rheologies, 2) different tectonic settings, 3) variations in magma chamber geometry and pressurization, 4) characteristics of the intrusive complex (density, geometry, position relative to magma chamber, etc.), and 5) morphology of the volcanic edifice. While a model assuming an elastic rheology is the easiest to implement, models incorporating viscoelastic rheologies tend to yield more realistic results [for instance, *Newman et al.*, 2001]. The tectonic setting of the volcano appears to influence the deformation style of the edifice. Subsidence at Medicine Lake is probably enhanced by Basin and Range extension, which causes crustal thinning under the volcano [*Dzurisin et al.*, 1991]. Deformation due to a pressurized magma source will probably overprint any downsagging due to a subvolcanic intrusive complex, as is proposed for volcanoes in the western Galapagos (Chapter 1). Therefore, models that investigate the dynamic interaction between magma chamber pressurization and downsagging are essential for interpreting deformation and structural patterns at active and dormant volcanoes. The physical characteristics of intrusive complexes are equally important, as varying sizes, locations, and densities will influence the stress regime within a volcanic edifice. Finally, knowledge of the surface morphology is essential for any realistic models of stress and deformation. *Cayol and Cornet* [1998] show that disregarding topography causes errors of 16-26% in

predicted displacements and 50% in magma pressure, while *McTigue and Segall* [1988] find errors of up to 40% in calculating the deformation source and depth.

Numerical models of the processes described above should focus on two outputs: stress orientations and magnitudes within the model volcano, and surface displacements. The most useful numerical analysis tool for such purposes is the finite element method (see *Bickford* [1990], for a thorough description). Finite element models are well suited to calculate stress and strain within two- and three-dimensional structures, and are capable of incorporating complex geometries and rheological conditions. Additional models, especially those that focus on fracture propagation within a volcanic cone, may consider the boundary element method (as described by *Crouch and Starfield* [1990]). Scaled analog models [e.g. *Merle and Borgia*, 1996] would be useful to test insights from numerical methods. Although analytical solutions do not have the complexity necessary to model the problems discussed above, such calculations are useful in benchmarking other numerical techniques.

5.2.3 Numerical Modeling of Topographic Barriers

In addition to modeling the stresses within an edifice, future research should investigate the stress field in the vicinity of a topographic barrier. *McGuire and Pullen* [1989] present compelling evidence that the 1000 meter high wall of the Valle del Bove landslide scarp at Mt. Etna, Italy, influences nearby magmatic intrusions. Historic dikes that propagated to the southeast along trends radial to the summit of the volcano and approached the Valle del Bove have deflected to parallel the wall, rather than erupting into the topographic depression (Figure 5.1). Dike azimuths have been attributed to a reorientation of the most compressive stress (σ_1) to parallel the scarp, which is supported by analog models of *McGuire and Pullen* [1989]. As noted in Chapter 1, *Munro and*

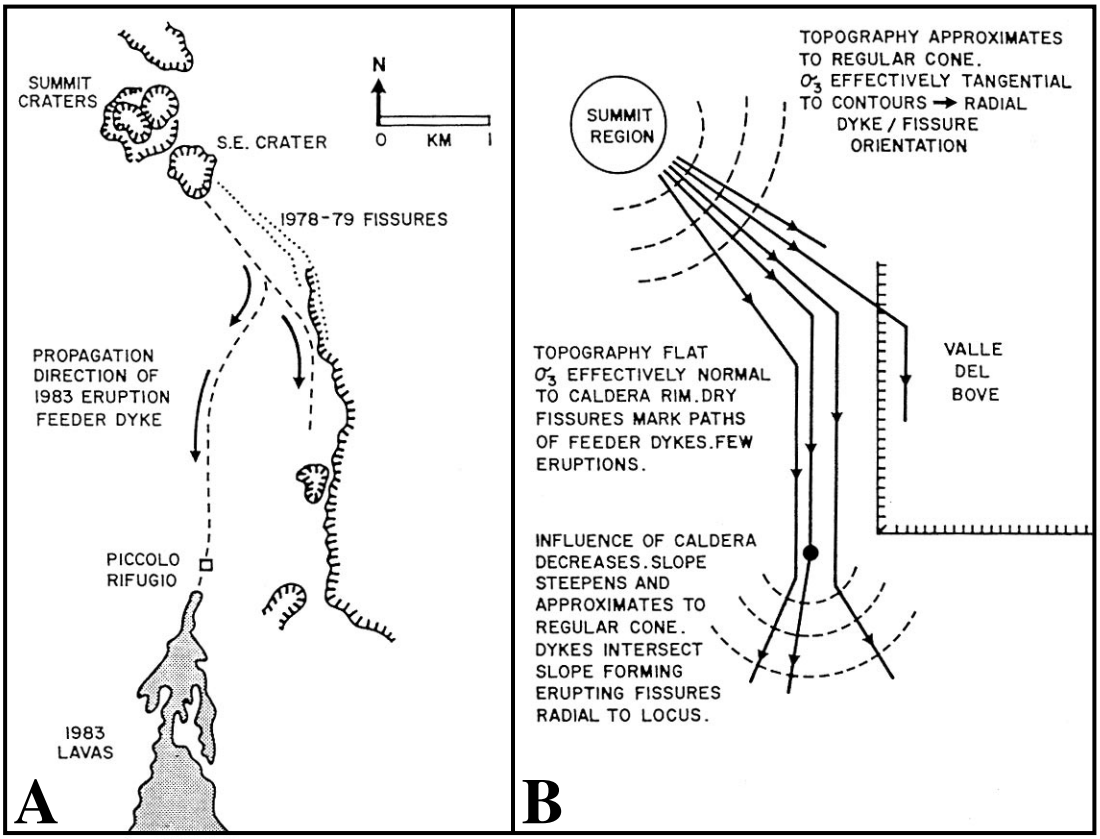

Figure 5.1. The effect of the Valle del Bove landslide scarp on dike propagation at Mt. Etna, Sicily, Italy. (a) Radial dikes that propagated southeast from the summit of Mt. Etna during the 1978-79 and 1983 eruptive episodes changed orientation as they approached the Valle del Bove. (b) A schematic of the Mt. Etna summit area illustrates the effects of gravitational stresses on dike propagation. Radial dikes are normal to topographic contour lines because of the gravitational relaxation of the volcanic cone. Intrusions become parallel to the Valle del Bove walls due to the gravitational instability (outward relaxation) of the 1000 meter scarp. Taken from *McGuire and Pullen* [1989].

Rowland [1996] suggested a similar mechanism for the formation of circumferential dikes at the volcanoes of the western Galapagos archipelago. *Tibaldi* [1996] has also invoked stress reorientation due to unbuttressed topography in his analysis of dikes exposed at Stromboli volcano, located in the Tyrrhenian Sea north of Sicily.

A primary motivation for the modeling is to determine the relationship between scarp geometry (height and slope), magma pressurization (both in a subvolcanic chamber and a propagating dike), and the resulting stress field. The results have important implications for the behavior of magmatic intrusions on volcanoes with irregular topographies, including Mt. Etna [*McGuire and Pullen*, 1989], Piton de la Fournaise in the Indian Ocean [*Cayol and Cornet*, 1998] and Kilauea and Mauna Loa in Hawaii [*Fiske and Jackson*, 1972]. Ground cracks above inferred intrusions at Mt. Etna suggest that the influence of the Valle del Bove wall may extend to a significant depth below the floor of the depression. Dikes that intruded during eruptive episodes in 1928 and 1979 followed radial orientations to the northeast of the summit of Mt. Etna, but then paralleled the inside wall of the Valle del Bove. After several hundred meters, the intrusions crossed the scarp and continued parallel to the outside of the depression for several hundred meters more [*M. Neri, pers. comm.*, 2000]. The dikes transected the Valle del Bove at an angle that is approximately 45° to the scarp. Numerous other prehistoric dikes mapped in the Valle del Bove walls by *Ferrari et al.* [1993], and presumeably pre-dating the formation of the depression, have similar orientations along both rims (Figure 5.2). The intriguing possibility exists that the interaction between the scarp walls and pressurized dikes causes intrusions to parallel the walls both inside and outside the Valle del Bove and causes the intrusion to cross the wall of the depression at a 45° angle. If true, many of the dikes exposed in the walls of the Valle del Bove intruded after the initial formation of the depression, which may have occurred several thousand years before the currently accepted

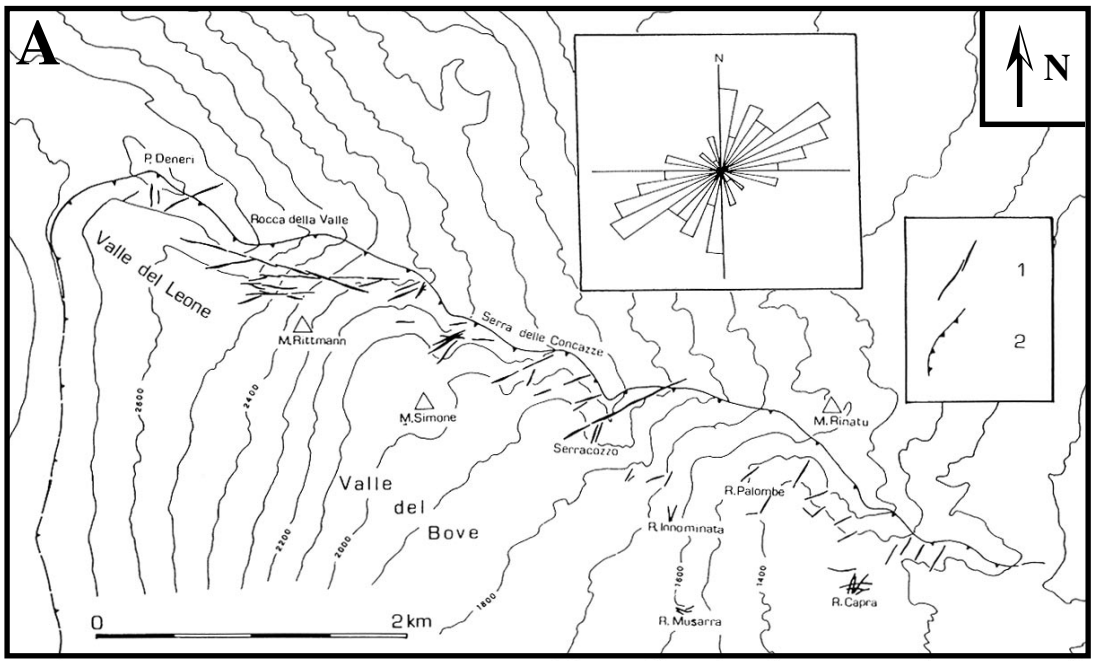

Figure 5.2. Dike orientations in the Valle del Bove landslide scarp on Mt. Etna. (a) Northern half of the Valle del Bove (1 = dikes, 2 = rim of the Valle del Bove). (b) Southern half of the Valle del Bove (1 = dikes, 2 = Valle del Bove rim, 3 = volcanic plug). The summit of Mt. Etna is directly west of the bottom of part (a) and top of part (b). Rose diagrams in both figures indicate the azimuthal distribution of dike strikes. Note that the vast majority of the dikes are oriented NE-SW in the northern half of the depression and NW-SE in the southern half. If the dikes were radial to the center of the volcano, dike strike would become E-W along both rims due to the increasing distance from the summit area. However, the observed regularity in strike raises the possibility that the Valle del Bove walls have been affecting dike propagation for several thousand years, much longer than the landslide scarp is thought to have existed. Additional modeling of interactions between topographic walls and stress is necessary to understand the orientations of dikes exposed in the Valle del Bove. After *Ferrari et al.* [1993].

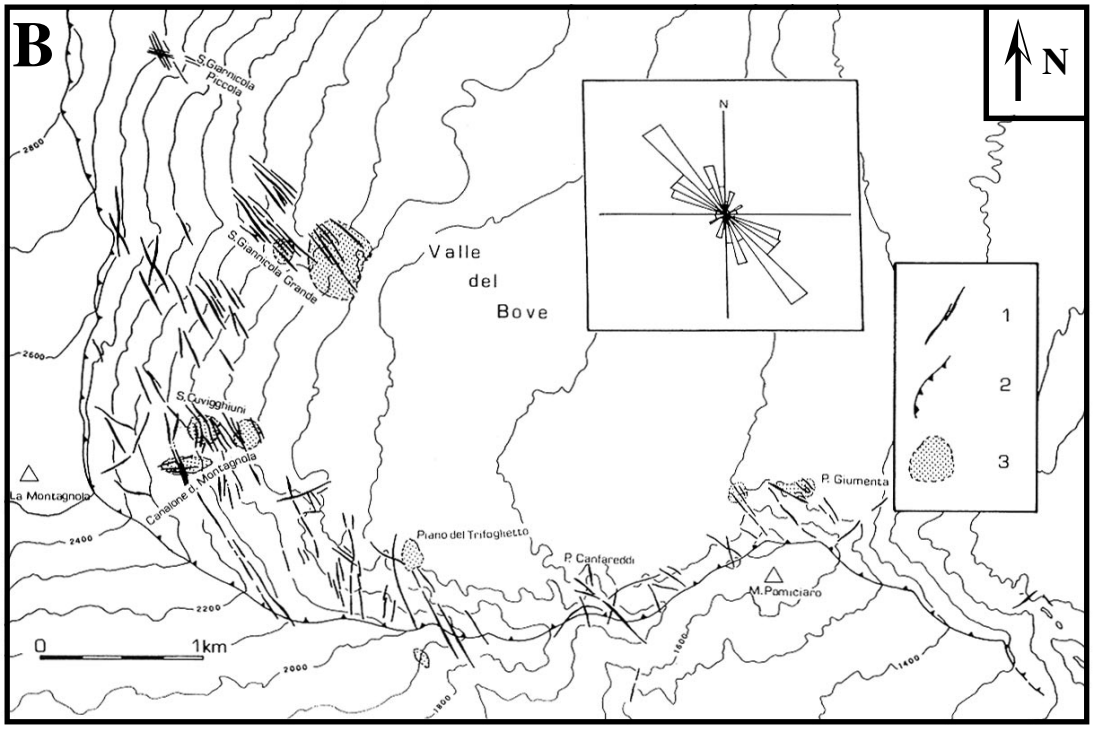

Figure 5.2. (Cont.)

15,000 to 40,000 years BP date range [*Calvari and Groppelli*, 1996]. Based on insights from Mt. Etna, models of the interaction between magmatic intrusions and surface topography are clearly important when classifying locations on a volcanic edifice of increased hazard due to eruption.

5.2.4 Deformation at Newberry Crater, Oregon

Deformation measurements of downsagging are important to evaluate the model proposed in Chapter 1. Displacements determined from GPS and leveling at Medicine Lake volcano in northern California suggest downsagging (see Chapters 2 and 3), however the model should be tested at other active volcanoes. An ideal location for further work is Newberry volcano, in central Oregon (Figure 3.1). Newberry is located east of the axis of Cascade volcanism on the western edge of the Basin and Range extensional province. The volcano is comparable in size, tectonic setting, composition, eruptive history, and morphology to Medicine Lake. Additional similarities include an inferred dense intrusive complex [*Fitterman*, 1988; *Gettings and Griscom*, 1988] and small magma chamber [*Achauer et al.*, 1988; *Fitterman*, 1988; *MacLeod and Sherrod*, 1988] below the summit, and abundant circumferential eruptive fissures around the Newberry caldera (Figure 5.3) [*MacLeod and Sherrod*, 1988; *Zucca and Evans*, 1992; *MacLeod et al.*, 1995].

The characteristics shared by Medicine Lake and Newberry have prompted many authors to treat the two volcanoes as analogs [e.g. *Donnelly-Nolan*, 1988; *Zucca and Evans*, 1992], however the deformation styles of the two volcanoes over the past ~60 years are clearly different. Tilted lake terraces in Newberry Caldera indicate an average uplift rate of 2-3 mm/yr over the last ~1800 years [*Jensen and Chitwood*, 1996]. *Dzurisin* [1999] compared leveling profiles across the summit and flanks of the volcano from 1931 and 1994 and found a maximum of 97 ± 22 mm of uplift in the caldera over the 63 year interval

Figure 5.3. Summit area of Newberry volcano, Oregon, from the geological map of *MacLeod et al.* [1995]. See the map reference for an explanation of symbols and geologic units. Note the many circumferential eruptive fissures (red lines) that occur to the north and east of the caldera rim (denoted by the dotted line). Numerous ~N-S eruptive fissures are present both north and south of the caldera, and may represent radial dikes that have been aligned by E-W extension. Circumferential intrusions may have initiated due to loading by dense intrusions which are known to underlie the summit [e.g. *Gettings and Griscom*, 1988]. However, recent deformation measurements indicate uplift in the caldera area of the volcano [*Jensen and Chitwood*, 1996; *Dzurisin*, 1999]. Downsagging deformation (Figure 1.13) similar to that proposed as an explanation for subsidence at Medicine Lake is not observed. Further deformation and modeling studies at Newberry volcano are necessary to constrain the sources of stress and deformation within the edifice.


NORTH
0
5 km
PAULINA LAKE
EAST LAKE
PAULINA CREEK
PAULINA CREEK FALLS
CE-NB-4
PHILLIPS 51
UNION 83-8
SF NC-01
SF 72-03
UNION 83-9
USGS N-2
USGS N-3
RDO-1
UNION 82-9
CE-NB-3
GEO N-1
Qc
Qyt
Qrpn?
Qd
Qypm
Qrd
Qru
Qrpn
Qsp
Qyb11
Qyc
Qyb12
Qpt
Qcw
Qr
Qbc
Qgs
Qyp
Qyo
Qru?
Qba
Qat
Qls
Qboa
Qbt
Qyrc
(Qyrc)
(Qru)
Qyrf
Qaf1
Qaf2
Qrps
Qyb13
Qyb14
Qyc?
Qyb15
Qer

relative to a site on the western flank. Additional surveys show that uplift did not occur between 1985 and 1994, suggesting that deformation is episodic and possibly related to magmatic intrusion. Subsidence similar to that observed at Medicine Lake is not occurring at Newberry volcano, and further measurements of horizontal and vertical displacements are essential for characterizing possible deformation mechanisms and assessing the applicability of the downsagging model proposed in Chapter 1.

5.2.5 Field Studies of Eroded Icelandic Central Volcanoes

In the proposed model (Chapter 1), the primary sources of stress in large basaltic volcanoes include a sub-volcanic intrusive complex and a pressurized magma chamber. The dense intrusive complex causes downsagging as predicted by *Walker* [1984; 1987; 1988] and radial extension near the summit of a volcano, while pressurization of the magma chamber causes radial contraction on the flanks. It follows that in a young basaltic volcano free of regional tectonic or other local effects, radial dikes should be the only intrusions represented because circumferential dikes can only form after the edifice has developed a dense intrusive complex. Therefore, radial dike intrusion should predate the initiation of downsagging and the emplacement of circumferential dikes. Any temporal relationships between the two styles of intrusion may be evaluated at eroded basaltic volcanoes.

Unfortunately, few locations with isotropic tectonic stress regimes exist. The eroded volcanoes of the Hawaiian Islands, including Waianae [*Zbinden and Sinton,* 1988] and Koolau [*Walker*, 1987], have stress fields that are largely controlled by preexisting volcanoes, and none of the Galapagos volcanoes have suffered sufficient erosion to expose their intrusive cores. Despite significant tectonic extension in Iceland [e.g. *Gudmundsson*, 2000], eroded central volcanoes exposed in the Tertiary volcanic pile may be useful for

testing the model proposed in Chapter 1. Most eroded Icelandic central volcanoes expose a set of centrally inclined sheets with shallow dips within 9 km of the center of the volcano [*Gautneb and Gudmundsson*, 1992], as well as steeply dipping dikes controlled by the regional stress field [*Gautneb et al.*, 1989; *Gautneb and Gudmundsson*, 1992; *Gudmundsson*, 1995; *Gudmundsson*, 1998; *Gudmundsson*, 2000], the latter of which are equivalent to radial dikes that have been deflected into orientations that parallel the tectonic σ_1 direction. According to the proposed model, N-S trending dikes (that initiate as radial intrusions) should dominate the early history of Icelandic volcanoes, followed by activity including a combination of centrally inclined sheets and N-S dikes.

A second field site is the eroded Sunlight volcano, in northwestern Wyoming. Both centrally inclined sheets and radial dikes are exposed by erosion [*Parsons*, 1939], similar to Summer Coon (Chapter 4). Cross-cutting relationships between centrally inclined sheets and steeply dipping dikes in eroded volcanoes will confirm the temporal relationship between inclined and radial intrusions, therefore further field studies are essential.

In addition, magma flow directions in the intrusions may also be measured using magnetic and other techniques, and compared with data collected from radial dikes at Summer Coon (Chapter 4). Observations from the two very different types of volcanoes (silicic composite cone vs. mafic shield) will suggest similarities and differences in the emplacement mechanisms of radial dikes, important for any model of the stress field within an edifice.

5.3 Conclusions

Deformation measurements at Medicine Lake volcano support the model of downsagging suggested by *Walker* [1984; 1987; 1988] and the proposed mechanism of

circumferential dike intrusion (Chapter 1). However, additional evidence is vital for testing models of the stress regime within a volcano. A database of eruptive fissures and dike orientations will provide numerous examples that may be used to assess numerical, theoretical, and analog models. Deformation measurements will indicate sources of stress heterogeneity within a volcano. Finally, field studies of eroded volcanoes, and particularly exposed magmatic intrusions, will allow for a direct inference of stress orientations within an edifice. When completed, the investigations described above will assist in the evaluation, modification, and application of the proposed and other models of the structural evolution of a volcanic edifice.

References

Abelson, M., and A. Agnon, Mechanics of oblique spreading and ridge segmentation, *Earth and Planetary Science Letters*, *148*, 405-421, 1997.

Achauer, U., J.R. Evans, and D. A. Stauberm, High-resolution seismic tomography of compressional wave velocity structure at Newberry volcano, Oregon Cascade Range, *Journal of Geophysical Research*, *93*, 10,135-10,147, 1988.

Amelung, F., S. Jónsson, H. Zebker, and P. Segall, Widespread uplift and 'trapdoor' faulting on Galápagos volcanoes observed with radar interferometry, *Nature*, *407*, 993-996, 2000.

Anderson, C.A., Volcanoes of the Medicine Lake highland, California, *University of California Publications in Geological Sciences*, *25*, 347-422, 1941.

Anderson, E.M., The dynamics of the formation of cone-sheets, ring-dykes, and caldron-subsidences, *Proceedings of the Royal Society of Edinburgh*, *56*, 128-157, 1936.

Anderson, E.M., The dynamics of sheet intrusion, *Proceedings of the Royal Society of Edinburgh*, *58*, 242-251, 1938.

Anderson, S.W., and J.H. Fink, Crease structures: Indicators of emplacement rates and surface stress regimes of lava flows, *Geological Society of America Bulletin*, *104*, 615-625, 1992.

Argus, D.F., and R. Gordon, Pacific-North American plate motion from Very Long Baseline Interferometry compared with motion inferred from magnetic anomalies, transform faults, and earthquake slip vectors, *Journal of Geophysical Research*, *95*, 17,315-17,324, 1991.

Arnadóttir, T., and P. Segall, The 1989 Loma Prieta earthquake imaged from inversion of geodetic data, *Journal of Geophysical Research*, *99*, 21,835-21,855, 1994.

Arnadottir, T., P. Segall, and P. Delaney, A fault model for the 1989 Kilauea south flank earthquake from leveling and seismic data, *Geophysical Research Letters*, *18*, 2217-2220, 1991.

Arnadottir, T., P. Segall, and M. Matthews, Resolving the discrepancy between geodetic and seismic fault models for the 1989 Loma Prieta, California, earthquake, *Bulletin of the Seismological Society of America*, *82*, 2248-2255, 1992.

Bacon, C.R., Eruptive history of Mount Mazama and Crater Lake Caldera, Cascade Range, USA, *Journal of Geophysical Research*, *18*, 57-115, 1983.

Baer, G., Mechanisms of dike propagation in layered rocks and in massive, porous sedimentary rocks, *Journal of Geophysical Research*, *96*, 11,911-11,929, 1991.

Baer, G., Fracture propagation and magma flow in segmented dykes: Field evidence and fabric analyses, Makhtesh, Israel, in *Physics and Chemistry of Dykes*, edited by G. Baer, and A. Heimann, pp. 125-140, A. A. Balkema, Rotterdam, 1995.

Baer, G., and M. Beyth, A mechanism of dyke segmentation in fractured host rock, in *Mafic Dykes and Emplacement Mechanisms*, edited by A.J. Parker, P.C. Rickwood, and D.H. Tucker, pp. 3-11, A. A. Balkema Publishers, Rotterdam, 1990.

Baer, G., and Z. Reches, Flow patterns of magma in dikes, Makhtesh Ramon, Israel, *Geology*, *15*, 569-572, 1987.

Baer, G., and Z. Reches, Mechanisms of emplacement and tectonic implications of the Ramon dike systems, Israel, *Journal of Geophysical Research*, *96*, 11,895-11,910, 1991.

Balazs, E.I., and G.M. Young, Corrections applied by the National Geodetic Survey to precise leveling observations, *Technical Memo NOS NGS 34*, National Oceanic and Atmospheric Administration, 12 pp., 1982.

Banfield, A.F., C.H. Behre Jr., and D. St. Clair, Geology of Isabela (Albemarle) Island, Archipelago de Colon (Galapagos), *Geological Society of American Bulletin*, *67*, 215-234, 1956.

Batiza, R., D.J. Fornari, D.A. Vanko, and P. Lonsdale, Craters, calderas, and hyaloclastites on young Pacific seamounts, *Journal of Geophysical Research, 89*, 8371-8390, 1984.

Bennett, J.H., R.W. Sherburne, C.H. Cramer, C.W. Chesterman, and R.H. Chapman, Stephens Pass earthquakes, Mount Shasta - August 1978, Siskiyou County, CA, *California Geology*, *32*, 27-34, 1979.

Bennett, R.A., and J.L. Davis, Integration of the Northern Basin and Range (NBAR) and Wasatch Front GPS networks for crustal deformation in and around the southern intermountain seismic belt, *Seismological Research Letters, 69*, 159, 1998.

Bennett, R.A., J.L. Davis, and B.P. Wernicke, Present-day pattern of Cordilleran deformation in the western United States, *Geology*, *27*, 371-374, 1999.

Bennett, R.A., B.P. Wernicke, and J.L. Davis, Continuous GPS measurements of contemporary deformation across the northern Basin and Range province, *Geophysical Research Letters, 25*, 563-566, 1998.

Beutler, G., I. Bauersima, W. Gurtner, M. Rothacher, and T. Schildknecht, Evaluation of the 1984 Alaska Global Positioning System campaign with the Bernese GPS software, *Journal of Geophysical Research, 92*, 1295-1303, 1987.

Bickford, W., *A first course in the finite element method*, 652 pp., Irwin, Boston, 1990.

Billings, M.P., Ring-dikes and their origin, *Transactions of the New York Academy of Sciences*, *5*, 131-144, 1943.

Blakely, R.J., R.L. Christiansen, M. Guffanti, R.E. Wells, N.J.M. Donnelly, L.J.P. Muffler, M.A. Clynne, and J.G. Smith, Gravity anomalies, Quaternary vents, and Quaternary faults in the southern Cascade Range, Oregon and California: Implications for arc and backarc evolution, *Journal of Geophysical Research, 102*, 22,513-22,527, 1997.

Bolt, B.A., and R.D. Miller, Catalogue of earthquakes in northern California and adjoining areas, 1 January 1910 - 31 December 1972, *Seismographic Stations Report*, University of California, Berkeley, 1975.

Borgia, A., Dynamic basis of volcanic spreading, *Journal of Geophysical Research, 99*, 17,791-17,804, 1994.

Borgia, A., J. Burr, W. Montero, L.D. Morales, and G.E. Alvarado, Fault propagation folds induced by gravitational failure and slumping of the central Costa Rica volcanic range; implications for large terrestrial and Martian volcanic edifices, *Journal fo Geophysical Research, 95*, 14,357-14,382, 1990.

Borgia, A., L. Ferrari, and G. Pasquare, Importance of gravitational spreading in the tectonic and volcanic evolution of Mount Etna, *Nature, 357*, 231-235, 1992.

Borradaile, G.J., Magnetic susceptibility, petrofabrics and strain, *Tectonophysics, 156*, 1-20, 1988.

Bott, M.H.P., and D.S. Dean, Stress diffusion from plate boundaries, *Nature, 243*, 339-341, 1973.

Brandsdóttir, B., and P. Einarsson, Seismic activity associated with the September 1977 deflation of the Krafla central volcano in northeastern Iceland, *Journal of Volcanology and Geothermal Research, 6*, 197-212, 1979.

Brotchie, J.F., Flexure of a liquid-filled spherical shell in a radial gravity field, *Modern Geology, 3*, 15-23, 1971.

Brotchie, J.F., and R. Silvester, On crustal flexure, *Journal of Geophysical Research, 74*, 5240-5252, 1969.

Bryant, W.A., Evaluation of fault activity in the Modoc Plateau region of northeastern California, *Abstracts with Programs - Geological Society of America, 23*, A140, 1991.

Bürgmann, R., D.D. Pollard, and S.J. Martel, Slip distribution on faults: Effects of stress gradients, inelastic deformation, heterogeneous host-rock stiffness, and fault interaction, *Journal of Structural Geology, 16*, 1675-1690, 1994.

Bürgmann, R., P. Segall, M. Lisowski, and J. Svarc, Postseismic strain following the 1989 Loma Prieta earthquake from GPS and leveling measurements, *Journal of Geophysical Research, 102*, 4933-4955, 1997.

Bursik, M., and K.E. Sieh, Range front faulting and volcanism in the Mono Basin, eastern California, *Journal of Geophysical Research*, *94*, 15,587-15,609, 1989.

Calvari, S., and G. Groppelli, Relevance of the Chiancone volcaniclastic deposit in the recent history of Etna Volcano (Italy), *Journal of Volcanology and Geothermal Research, 72*, 239-258, 1996.

Cayol, V., and F.H. Cornet, Three-dimensional modeling of the 1983-1984 eruption at Piton de la Fournaise Volcano, Réunion Island, *Journal of Geophysical Research, 103*, 18,025-18,037, 1998.

Chadwick, W.W., Jr., T. De Roy, and A. Carrasco, The September 1988 intracaldera avalanche and eruption at Fernandina Volcano, Galapagos Islands, *Bulletin of Volcanology, 53*, 276-286, 1991.

Chadwick, W.W., Jr., and J.H. Dieterich, Mechanical modeling of circumferential and radial dike intrusion on Galapagos volcanoes, *Journal of Volcanology and Geothermal Research*, *66*, 37-52, 1995.

Chadwick, W.W., Jr., and K.A. Howard, The pattern of circumferential and radial eruptive fissures on the volcanoes of Fernandina and Isabela islands, Galapagos, *Bulletin of Volcanology, 53*, 259-275, 1991.

Chevallier, L., and W.J. Verwoerd, A numerical model for the mechanical behavior of intraplate volcanoes, *Journal of Geophysical Research*, *93*, 4182-4198, 1988.

Chevallier, L., and W.J. Verwoerd, Influence of temperature on the distribution of stress and displacement in a volcano: A numerical approach, *Bulletin of Volcanology*, *52*, 413-425, 1990.

Chiarabba, C., A. Amato, and J.R. Evans, Variations on the NeHT high-resolution tomography method: A test of technique and results for Medicine Lake Volcano, northern California, *Journal of Geophysical Research*, *100*, 4035-4052, 1995.

Clague, D.A., and R.P. Denlinger, Role of olivine cumulates in destabilizing the flanks of Hawaiian volcanoes, *Bulletin of Volcanology*, *56*, 425-434, 1994.

Comer, R.P., S.C. Solomon, and J.W. Head, Thickness of the lithosphere from the tectonic response to volcanic loads, *Reviews of Geophysics, 23*, 61-92, 1985.

Condie, K.C., and D.L. Hayslip, Young bimodal volcanism at Medicine Lake volcanic center, northern California, *Geochimica et Cosmochimica Acta*, *39*, 1165-1178, 1975.

Cooke, M.L., and D.D. Pollard, Fracture propagation paths under mixed mode loading within rectangular blocks of polymethyl methacrylate, *Journal of Geophysical Research, 101*, 3387-3400, 1996.

Corsaro, R.A., R. Cristofolini, and L. Patanè, The 1669 eruption at Mount Etna: Chronology, petrology, and geochemistry, with inferences on the magma sources and ascent mechanisms, *Bulletin of Volcanology*, *58*, 348-358, 1996.

Coward, M.P., The analysis of flow profiles in a basaltic dyke using strained vesicles, *Geological Society of London*, *137*, 605-615, 1980.

Cramer, C.H., The Stephens Pass earthquake swarm of August 1978, east of Mount Shasta, California, *EOS, Transactions, American Geophysical Union*, *59*, 1130, 1978.

Crouch, S.L., and A.M. Starfield, *Boundary Element Methods in Solid Mechanics*, 322 pp., Unwin Hyman, London, 1990.

Cullen, A.B., A.R. McBirney, and R.D. Rogers, Structural controls on the morphology of Galapagos shields, *Journal of Volcanology and Geothermal Research*, *34*, 143-151, 1987.

Currie, K.L., and J. Ferguson, The mechanism of intrusion of lamprophyre dikes indicated by "offsetting" of dikes, *Tectonophysics*, *9*, 525-535, 1970.

Delaney, P.T., and A.E. Gartner, Physical processes of shallow mafic dike emplacement near the San Rafael Swell, Utah, *Geological Society of America Bulletin, 109*, 1177-1192, 1997.

Delaney, P.T., and D.F. McTigue, Volume of magma accumulation or withdrawal estimated from surface uplift or subsidence, with application to the 1960 collapse of Kilauea Volcano, *Bulletin of Volcanology, 56*, 417-424, 1994.

Delaney, P.T., and D.D. Pollard, Deformation of host rocks and flow of magma during growth of minette dikes and breccia bearing intrusions near Ship Rock, New Mexico, *USGS Professional Paper, 1202*, 61 pp., 1981.

Delaney, P.T., D.D. Pollard, J.I. Ziony, and E.H. McKee, Field relations between dikes and joints; emplacement processes and paleostress analysis, *Journal of Geophysical Research, 91*, 4920-4938, 1986.

Dieterich, J.H., and R.W. Decker, Finite element modeling of surface deformation associated with volcanism, *Journal of Geophysical Research, 80*, 4094-4102, 1975.

Dixon, T.H., F. Farina, A. Mao, F. Webb, M. Bursik, R. Stein, and G. Marshall, GPS monitoring data for active volcanoes available on Internet, *EOS, Transactions, American Geophysical Union, 76*, 2-3, 1995a.

Dixon, T.H., M. Miller, F. Farina, H. Wang, and D. Johnson, Present-day motions of the Sierra Nevada block and some tectonic implications for the Basin and Range province, North American Cordillera, *Tectonics*, *19*, 1-24, 2000.

Dixon, T.H., S. Robaudo, J. Lee, and M.C. Reheis, Constraints on present-day Basin and Range deformation from Space Geodesy, *Tectonics*, *14*, 755-772, 1995b.

Dokka, R.K., and C.J. Travis, Late Cenozoic strike-slip faulting in the Mojave Desert, California, *Tectonics*, *9*, 311-340, 1990a.

Dokka, R.K., and C.J. Travis, Role of the eastern California shear zone in accommodating Pacific-North American plate motion, *Geophysical Research Letters*, *17*, 1323-1326, 1990b.

Donnadieu, F., and O. Merle, Experiments on the indentation process during cryptodome intrusions: New insights into Mount St. Helens deformation, *Geology*, *26*, 79-82, 1998.

Donnadieu, F., O. Merle, and J.-C. Besson, Volcanic edifice stability during cryptodome intrusion, *Bulletin of Volcanology*, *63*, 61-72, 2001.

Donnelly-Nolan, J.M., A magmatic model of Medicine Lake Volcano, California, *Journal of Geophysical Research*, *93*, 4412-4420, 1988.

Donnelly-Nolan, J.M., D.E. Champion, T.L. Grove, M.B. Baker, J.E. Taggart, Jr., and P.E. Bruggman, The Giant Crater lava field; geology and geochemistry of a compositionally zoned, high-alumina basalt to basaltic andesite eruption at Medicine Lake Volcano, California, *Journal of Geophysical Research*, *96*, 21,843-21,863, 1991.

Donnelly-Nolan, J.M., D.E. Champion, C.D. Miller, T.L. Grove, and D.A. Trimble, Post-11,000-year volcanism at Medicine Lake Volcano, Cascade Range, Northern California, *Journal of Geophysical Research*, *95*, 19,693-19,704, 1990.

Donnelly-Nolan, J.M., and K.M. Nolan, Catastrophic flooding and eruption of ash-flow tuff at Medicine Lake Volcano, California, *Geology*, *14*, 875-878, 1986.

Dzurisin, D., Results of repeated leveling surveys at Newberry Volcano, Oregon, and near Lassen Peak Volcano, California, *Bulletin of Volcanology*, *61*, 83-91, 1999.

Dzurisin, D., J.M. Donnelly-Nolan, J.R. Evans, and S.R. Walter, Crustal subsidence, seismicity, and structure near Medicine Lake Volcano, California, *Journal of Geophysical Research, 96*, 16,319-16,333, 1991.

Dzurisin, D., M.P. Poland, and R. Bürgmann, Steady subsidence of Medicine Lake volcano, northern California, revealed by repeated leveling surveys, *submitted to the Journal of Geophysical Research on 8/3/01*, in review.

Eichelberger, J.C., Mechanism of magma mixing at Glass Mountain, Medicine Lake Highland volcano, California, in *Guide to Some Volcanic Terranes in Washington, Idaho, Oregon, and Northern Califonria*, edited by D.A. Johnston, and J.M. Donnelly-Nolan, pp. 183-189, US Geological Survey, Reston, VA, 1981.

Ellwood, B.B., Flow and emplacement direction determined for selected basaltic bodies using magnetic susceptibility anisotropy measurements, *Earth and Planetary Science Letters, 41*, 254-264, 1978.

Ellwood, B.B., Estimates of flow direction for calc-alkaline welded tuffs and paleomagnetic data reliability from anisotropy of magnetic susceptibility measurements: Central San Juan Mountains, southwest Colorado, *Earth and Planetary Science Letters, 59*, 303-314, 1982.

Elsasser, W.M., Convection and stress propagation in the upper mantle, in *The Application of Modern Physics to the Earth and Planetary Interiors*, edited by S.K. Runcorn, pp. 223-246, John Wiley, London, 1969.

Ernst, R.E., Magma flow directions in two mafic Proterozoic dyke swarms of the Canadian Shield: As estimated using anisotropy of magnetic susceptibility data, in *Mafic Dykes and Emplacement Mechanisms*, edited by A.J. Parker, P.C. Rickwood, and D.H. Tucker, pp. 231-235, A. A. Balkema Publishers, Rotterdam, 1990.

Ernst, R.E., and W.R.A. Baragar, Evidence from magnetic fabric for the flow pattern of magma in the MacKenzie giant radiating dyke swarm, *Nature, 356*, 511-513, 1992.

Evans, J.R., and J.J. Zucca, Active high-resolution seismic tomography of compressional wave velocity and attenuation structure at Medicine Lake Volcano, Northern

California Cascade Range, *Journal of Geophysical Research, 93*, 15,016-15,036, 1988.

Federal Geodetic Control Committee, Bossler, J.D. (chairman), *Standards and specifications for geodetic control networks*, Report, National Oceanic and Atmospheric Administration, 1984.

Ferrari, L., V.H. Garduno, and M. Neri, I dicchi della Valle del Bove, Etna: Un metodo per stimare le dilatazioni di un apparato vulcanico (in Itlaian), *Mem. Societa Geologica Italiana, 47*, 495-508, 1993.

Fink, J.H., Geometry of silicic dikes beneath the Inyo Domes, California, *Journal of Geophysical Research, 90*, 11,127-11,133, 1985.

Fink, J.H., and R.W. Griffiths, Morphology, eruption rates, and rheology of lava domes; insights from laboratory models, *Journal of Geophysical Research*, *103*, 527-545, 1998.

Fink, J.H., and D.D. Pollard, Structural evidence for dikes beneath silicic domes, Medicine Lake Highland Volcano, California, *Geology*, *11*, 458-461, 1983.

Finn, C., and D.L. Williams, Gravity evidence for a shallow intrusion under Medicine Lake Volcano, California, *Geology*, *10*, 503-507, 1982.

Fiske, R.S., and E.D. Jackson, Orientation and growth of Hawaiian volcanic rifts: the effect of regional structure and gravitational stresses, *Proceedings of the Royal Society of London, Series A, 329*, 299-326, 1972.

Fitterman, D.V., Overview of the structure and geothermal potential of Newberry Volcano, Oregon, *Journal of Geophysical Research, 93*, 10,059-10,066, 1988.

Flück, P., R.D. Hyndman, and K. Wang, Three-dimensional dislocation model for great earthquakes of the Cascadia subduction zone, *Journal of Geophysical Research, 102*, 20,539-20,550, 1997.

Fornari, D.J., and W.B.F. Ryan, The evolution of craters and calderas on young seamounts: insights from Sea Marc I and Sea Beam sonar surveys of a small seamount group near the axis of the East Pacific Rise at ~10°N, *Journal of Geophysical Research, 89*, 11,069-11,083, 1984.

Foulger, G.R., M.A. Hofton, and C. Voelksen, Viscoelastic modeling of post-diking anelastic deformation in north Iceland: A new epoch of GPS measurements, *EOS, Transactions, American Geophysical Union, 77*, F149, 1996.

Foulger, G.R., C.-H. Jahn, G. Seeber, P. Einarsson, B.R. Julian, and K. Heki, Post-rifting stress relaxation at the divergent plate boundary in Northeast Iceland, *Nature*, *358*, 488-490, 1992.

Fournier, R.O., Geochemistry and dynamics of the Yellowstone National Park hydrothermal system, *Annual Review of Earth and Planetary Sciences*, *17*, 13-53, 1989.

Fuis, G.S., J.J. Zucca, W.D. Mooney, and B. Milkereit, A geologic interpretation of seismic refraction results in northeastern California, *Geological Society of America Bulletin*, *98*, 53-65, 1987.

Gaskill, D.L., F.E. Mutschler, and B.L. Bartleson, West Elk volcanic field, Gunnison and Delta counties, Colorado, in *New Mexico Geological Society Guidebook, 32nd Field Conference, Western Slope Colorado*, edited by R.C. Epis, and J.F. Callender, pp. 305-316, New Mexico Geological Society, Socorro, 1981.

Gautneb, H., and A. Gudmundsson, Effect of local and regional stress fields on sheet emplacement in West Iceland, *Journal of Volcanology and Geothermal Research, 51*, 339-356, 1992.

Gautneb, H., A. Gudmundsson, and N. Oskarsson, Structure, petrochemistry and evolution of a sheet swarm in an Icelandic central volcano, *Geological Magazine*, *126*, 659-673, 1989.

Gerlach, D.C., and T.L. Grove, Petrology of Medicine Lake Highland volcanics: Characterization of endmembers of magma mixing, *Contributions to Mineralogy and Petrology*, *80*, 147-159, 1982.

Gettings, M.E., and A. Griscom, Gravity model studies of Newberry volcano, Oregon, *Journal of Geophysical Research*, *93*, 10,109-10,118, 1988.

Grove, T.L., D.C. Gerlach, and T.W. Sando, Origin of calc-alkaline series lavas at Medicine Lake Volcano by fractionation, assimilation and mixing, *Contributions to Mineralogy and Petrology*, *80*, 160-182, 1982.

Grove, T.L., R.J. Kinzler, M.B. Baker, D.-N.J. M, and C.E. Lesher, Assimilation of granite by basaltic magma at Burnt lava flow, Medicine Lake Volcano, Northern California; decoupling of heat and mass transfer, *Contributions to Mineralogy and Petrology*, *99*, 320-343, 1988.

Grove, T.L., and J.M. Donnelly-Nolan, The evolution of young silicic lavas at Medicine Lake Volcano, California; implications for the origin of compositional gaps in calc-alkaline series lavas, *Contributions to Mineralogy and Petrology*, *92*, 281-302, 1986.

Gudmundsson, A., Form and dimensions of dykes in eastern Iceland, *Tectonophysics*, *95*, 295-307, 1983.

Gudmundsson, A., Formation of dykes, feeder-dykes, and the intrusion of dykes from magma chambers, *Bulletin of Volcanology*, *47*, 537-550, 1984.

Gudmundsson, A., Lateral magma flow, caldera collapse, and a mechanism of large eruptions in Iceland, *Journal of Volcanology and Geothermal Research, 34*, 65-78, 1987.

Gudmundsson, A., The geometry and growth of dikes, in *Physics and Chemistry of Dykes*, edited by G. Baer, and A. Heimann, pp. 23-34, A. A. Balkema, Rotterdam, 1995a.

Gudmundsson, A., Infrastructure and mechanics of volcanic systems in Iceland, *Journal of Volcanology and Geothermal Research*, *64*, 1-22, 1995b.

Gudmundsson, A., Magma chambers modeled as cavities explain the formation of rift zone central volcanoes and their eruption and extrusion statistics, *Journal of Geophysical Research, 103*, 7401-7412, 1998.

Gudmundsson, A., Dynamics of volcanic systems in Iceland: example of tectonism and volcanism at juxtaposed hot spot and mid-ocean ridge systems, *Annual Review of Earth and Planetary Sciences, 28*, 107-140, 2000.

Gudmundsson, O., B. Brandsdottir, M. Menke, and G.E. Sigvaldason, The crustral magma chamber of the Katla volcano in south Iceland revealed by 2-D seismic undershooting, *Geophysical Journal International, 119*, 277-296, 1994.

Hannah, J.L., Tectonic setting of the Modoc region, northeastern California, *Short Contributions to California Geology; California Division of Mines and Geology, 129*, 35-39 pp., 1977.

Harker, A., The Tertiary igneous rocks of Skye, *Memoir of the Geological Survey of the United Kingdom*, 1904.

Heiken, G., Plinian-type eruptions in the Medicine Lake Highland, California, and the nature of the underlying magma, *Journal of Volcanology and Geothermal Research, 4*, 375-402, 1978.

Helgason, J., and M. Zentilli, Field characteristics of laterally emplaced dikes: anatomy of an exhumed miocene dike swarm in Reydarfjordur, eastern Iceland, *Tectonophysics, 115*, 247-274, 1985.

Herrero-Bervera, E., G.P.L. Walker, E. Cañon-Tapia, and M.O. Garcia, Magnetic fabric and inferred flow direction of dikes, conesheets and sill swarms, Isle of Skye, Scotland, *Journal of Volcanology and Geothermal Research, 106*, 195-210, 2001.

Hill, D.P., Temperatures at the base of the seismogenic crust beneath Long Valley caldera, California, and the Phlegraean Fields caldera, Italy, in *Volcanic Seismology*, edited by P. Gasparini, R. Scarpa, and K. Aki, pp. 432-461, Springer-Verlag, New York, 1993.

Hyndman, D.W., and D. Alt, Radial dikes, laccoliths, and gelatin models, *Journal of Geology*, *95*, 763-774, 1987.

Jennings, C.W., Fault activity map of California and adjacent areas with locations and ages of recent volcanic eruptions, *Division of Mines and Geology, Geologic Data Map No. 6*, 1:750,000, California Division of Mines and Geology, Sacramento, 1994.

Jensen, R.A., and L.A. Chitwood, Evidence for recent uplift of caldera floor, Newberry volcano, Oregon, *EOS, Transactions, American Geophysical Union*, *77*, F792, 1996.

Johnson, R.W., Volcanic geology of Mount Suswa, Kenya, *Philosophical Transactions of the Royal Society of London, Series A: Mathematical and Physical Sciences*, *265*, 383-412, 1969.

Jónsson, S., H. Zebker, P. Cervelli, P. Segall, H. Garbeil, P. Mouginis-Mark, and S. Rowland, A shallow-dipping dike fed the 1995 flank eruption at Fernandina volcano, Galápagos, observed by satellite radar interferometry, *Geophysical Research Letters*, *26*, 1077-1080, 1999.

Knight, M.D., and G.P.L. Walker, Magma flow directions in dikes of the Koolau Complex, Oahu, determined from magnetic fabric studies, *Journal of Geophysical Research*, *93*, 4301-4319, 1988.

Koenig, E., and D.D. Pollard, Mapping and modeling of radial fracture patterns on Venus, *Journal of Geophysical Research*, *103*, 15,183-15,202, 1998.

Koide, H., and S. Bhattacharji, Formation of fractures around magmatic intrusions and their role in ore localization, *Economic Geology*, *70*, 781-799, 1975.

Lachenbruch, A.H., and J.H. Sass, Models of an extending lithosphere and heat flow in the Basin and Range province, *Geological Society of America Memoir*, *152*, 209-250, 1978.

Langbein, J., and H. Johnson, Correlated errors in geodetic time series: Implications for time-dependent deformation, *Journal of Geophysical Research*, *102*, 591-603, 1997.

Lawrence, R.D., Strike-slip faulting terminates the Basin and Range province in Oregon, *Geological Society of America Bulletin*, *87*, 846-850, 1976.

Lipman, P.W., Geology of the Summer Coon volcanic center, eastern San Juan Mountains, Colorado, *Colorado School of Mines Quarterly*, *63*, 211-236, 1968.

Lipman, P.W., Geological map of the Del Norte area, eastern San Juan mountains, Colorado, *Miscellaneous Investigation Map, I-952*, 1:48,000, US Geological Survey, Reston VA, 1976.

Lipman, P.W., Geologic Map of the Mount Taylor Quadrangle, Valencia County, New Mexico, *Geologic Quadrangle Map, GQ-1523*, 1:24,000, US Geological Survey, Reston VA, 1979.

Lipman, P.W., T.A. Steven, and L.H. Mehnert, Volcanic history of the San Juan mountains, Colorado, as indicated by potassium-argon dating, *Geological Society of America Bulletin*, *81*, 2329-2352, 1970.

Lonsdale, P., and F.N. Spiess, A pair of young cratered volcanoes on the East Pacific Rise, *Journal of Geology*, *87*, 157-173, 1979.

MacLeod Jr., N.S., and D.R. Sherrod, Geologic evidence for a magma chamber beneath Newberry Volcano, Oregon, *Journal of Geophysical Research*, *93*, 10,067-10,079, 1988.

MacLeod Jr., N.S., D.R. Sherrod, L.A. Chitwood, and R.A. Jensen, Geologic Map of Newberry Volcano, Deschutes, Klamath, and Lake counties, Oregon, *Miscellaneous Investigations Map, I-2455*, 1:62,500 and 1:24,000, US Geological Survey , Reston VA, 1995.

Mastin, L.G., and D.D. Pollard, Surface deformation and shallow dike intrusion processes at Inyo Craters, Long Valley, California, *Journal of Geophysical Research*, *93*, 13,221-13,235, 1988.

McBirney, A.R., and H. Williams, Geology and Petrology of the Galapagos Islands, *Geological Society of America Memoir, 118*, 1-197, 1969.

McCaffery, R., M.D. Long, C. GOldfinger, P.C. Zwick, J.L. Nabelek, C.K. Johnson, and C. Smith, Rotation and plate locking at the southern Cascadia subduction zone, *Geophysical Research Letters, 27*, 3117-3120, 2000.

McGarr, A., Some constraints on levels of shear stress in the crust from observations and theory, *Journal of Geophysical Research, 85*, 6231-6238, 1980.

McGovern, P.J., and S.C. Solomon, State of stress, faulting, and eruption characteristics of large volcanoes on Mars, *Journal of Geophysical Research, 98*, 23,553-23,579, 1993.

McGovern, P.J., and S.C. Solomon, Filling of flexural moats around large volcanoes on Venus: implications for volcano structure and global magmatic flux, *Journal of Geophysical Research, 102*, 16,303-16,318, 1997.

McGovern, P.J., and S.C. Solomon, Growth of large volcanoes on Venus: Mechanical models and implications for structural evolution, *Journal of Geophysical Research, 103*, 11,071-11,101, 1998.

McGovern, P.J., S.C. Solomon, S.E. Faulkner, J.W. Head, D.E. Smith, and M.T. Zuber, Extension and volcanic loading at Alba Patera: Insights from MOLA observations and loading models, *Lunar and Planetary Science Conference, 10*, 1697, 1999.

McGuire, W.J., and A.D. Pullen, Location and orientation of eruptive fissures and feeder-dykes at Mount Etna; Influence of gravitational and regional tectonic stress regimes, *Journal of Volcanology and Geothermal Research, 38*, 325-344, 1989.

McLeod, P., and S. Tait, The growth of dykes from magma chambers, *Journal of Volcanology and Geothermal Research, 92*, 231-245, 1999.

McTigue, D.F., and P. Segall, Displacements and tilts from dip-slip faults and magma chambers beneath irregular surface topography, *Geophysical Research Letters, 15*, 601-604, 1988.

Meertens, C., and J. Levine, Compressive tectonic strain as a possible mechanism for long-term vertical deformation of the Yellowstone caldera, *EOS, Transactions, American Geophysical Union, 66*, 853, 1985.

Meier, M.F., Mode of flow of Saskatchewan Glacier Alberta, Canada, *US Geological Survey Professional Paper, 351*, 70 pp., 1960.

Melosh, H.J., The tectonics of mascon loading, *Proceedings of the Lunar and Planetary Conference, 9*, 3513-3525, 1978.

Merle, O., and A. Borgia, Scaled experiments of volcanic spreading, *Journal of Geophysical Research, 101*, 13,805-13,817, 1996.

Mertzman, S.A., The Summer Coon volcano, eastern San Juan mountains, Colorado, in *San Luis Basin Guidebook*, edited by H.L. James, pp. 265-272, New Mexico Geological Society, Socorro, New Mexico, 1971.

Miller, M.M., D.J. Johnson, T.H. Dixon, and R.K. Dokka, Refined kinematics of the Eastern California shear zone from GPS observations, 1993-1998, *Journal of Geophysical Research, 106*, 2245-2263, 2001a.

Miller, M.M., D.J. Johnson, C.M. Rubin, H. Dragert, K. Wang, A. Qamar, and C. Goldfinger, GPS-determination of along-strike variation in Cascadia margin kinematics: Implications for relative plate motion, subduction zone coupling, and permament deformation, *Tectonics, 20*, 161-176, 2001b.

Minister, J.B., and T.H. Jordon, Vector constraints on western US deformation from space geodesy, neotectonics, and plate motions, *Journal of Geophysical Research, 92*, 4798-4804, 1987.

Moats, W.P., Geometry and emplacement of silicic dikes at Summer Coon Volcano, Rio Grande and Saguache counties, Colorado, Masters thesis, Arizona State University, 1990.

Mogi, K., Relations between the eruptions of various volcanoes and the deformations of the ground surfaces around them, *Bulletin of the Earthquake Research Institute*, *36*, 99-134, 1958.

Montesi, L.G.J., Concentric dikes on the flanks of Pavonis Mons: Implications for the evolution of Martian shield volcanoes and mantle plumes, in *Locating Pre-Mesozoic Mantle Plumes*, edited by R.E. Ernst, and K.L. Buchan, in press.

Moore, J.G., Relationship between subsidence and volcanic load, Hawaii, *Bulletin of Volcanology*, *34*, 562-576, 1971.

Mouginis-Mark, P.J., S.K. Rowland, and H. Garbeil, Slopes of western Galapagos volcanoes from airborne interferometric radar, *Geophysical Research Letters*, *23*, 3767-3770, 1996.

Muller, O.H., Changing stresses during emplacement of the radial dike swarm at Spanish Peaks, Colorado, *Geology*, *14*, 157-159, 1986.

Muller, O.H., and D.D. Pollard, The stress state near Spanish Peaks, Colorado, determined from a dike pattern, *Pure and Applied Geophysics*, *115*, 69-86, 1977.

Munro, D.C., and S.K. Rowland, Caldera morphology in the western Galápagos and implications for volcano eruptive behavior and mechanisms of caldera formation, *Journal of Volcanology and Geothermal Research*, *72*, 85-100, 1996.

Murray, J.B., The influence of loading by lavas on the siting of volcanic eruption vents on Mt. Etna, *Journal of Volcanology and Geothermal Research*, *35*, 121-139, 1988.

Murray, M.H., and M. Lisowski, Strain accumulation along the Cascadia subduction zone, *Geophysical Research Letters*, *27*, 3631-3634, 2000.

Murray, M.H., and P. Segall, Modeling broadscale deformation in northern California and Nevada from plate motions and elastic strain accumulation, *Geophysical Research Letters*, in press.

Mushayandebvu, M.F., M.P. Bates, and D.L. Jones, Anisotropy of magnetic susceptibility results from the Mashonaland dolerite sills and dikes of northeast Zimbabwe, in *Physics and Chemistry of Dykes*, edited by G. Baer, and A. Heimann, pp. 151-161, A. A. Balkema, Rotterdam, 1995.

Nakamura, K., En echelon features of Icelandic ground fissures, *Acta Naturalia Islandica, 2*, 1-15, 1970.

Nakamura, K., Volcanoes as possible indicators of tectonic stress orientation; Principle and proposal, *Journal of Volcanology and Geothermal Research, 2*, 1-16, 1977.

Nakamura, K., K.H. Jacob, and J.N. Davies, Volcanoes as possible indicators of tectonic stress orientation; Aleutians and Alaska, *Pure and Applied Geophysics, 115*, 87-112, 1977.

Naumann, T., and D. Geist, Physical volcanology and structuyral development of Cerro Azul Volcano, Isabela Island, Galapagos: Implications for the development of Galapagos-type shield volcanoes, *Bulletin of Volcanology, 61*, 497-514, 2000.

Newman, A.V., T.H. Dixon, G.I. Ofoegbu, and J.E. Dixon, Geodetic and seismic constraints on recent activity at Long Valley Caldera, California: Evidence for viscoelastic rheology, *Journal of Volcanology and Geothermal Research, 105*, 183-206, 2001.

Nordlie, B.E., Morphology and structure of the western Galapagos volcanoes and a model for their origin, *Geological Society of America Bulletin, 84*, 2931-2955, 1973.

Obert, L., and W.I. Duvall, *Rock Mechanics and the Design of Structures in Rock*, 650 pp., John Wiley and Sons, New York, 1967.

Ode, H., Mechanical analysis of the dike pattern of the Spanish Peaks area, Colorado, *Geological Society of America Bulletin, 68*, 567-576, 1957.

Okada, Y., Surface deformation due to shear and tensile faults in a half-space, *Bulletin of the Seismological Society of America, 75*, 1135-1154, 1985.

Oldow, J.S., C.L.V. Aiken, J.L. Hare, J.F. Ferguson, and R.F. Hardyman, Active displacement transfer and differential block motion within the central Walker Lane, western Great Basin, *Geology*, *29*, 19-22, 2001.

Olson, J.E., and D.D. Pollard, The initiation and growth of en echelon veins, *Journal of Structural Geology*, *13*, 595-608, 1991.

Owen, S., P. Segall, J.T. Freymueller, A. Miklius, R.P. Denlinger, T. Arnadottir, M.K. Sako, and R. Bürgmann, Rapid deformation of the south flank of Kilauea Volcano, Hawaii, *Science*, *267*, 1328-1332, 1995.

Owen, S., P. Segall, M. Lisowski, A. Miklius, M. Murray, M. Bevis, and J. Foster, January 30, 1997 eruptive event on Kilauea Volcano, Hawaii, as monitored by continuous GPS, *Geophysical Research Letters*, *27*, 2757-2760, 2000.

Page, W.D., T.L. Sawyer, M.K. McLaren, W.U. Savage, and J. Wakabayashi, The Quaternary Tahoe-Medicine Lake Trough: The western margin of the Basin and Range transition, NE California, *Abstracts with Programs - Geological Society of America*, *25*, 131, 1993.

Parson, L.M., B.J. Murton, R.C. Searle, D. Booth, J. Evans, F. P., J. Keeton, A. Laughton, E. McAllister, N. Millard, L. Redbourne, I. Rouse, A. Shor, D. Smith, S. Spencer, C. Summerhayes, and C. Walker, En echelon axial volcanic ridges at the Reykjanes Ridge: a life cycle of volcanism and tectonics, *Earth and Planetary Science Letters*, *117*, 73-87, 1993.

Parsons, T., and G.A. Thompson, Does magmatism influence low-angle normal faulting?, *Geology*, *21*, 247-250, 1993.

Parsons, W.H., Volcanic centers of the Sunlight area Park County, Wyoming, *Journal of Geology*, *47*, 1-26, 1939.

Patton, H.J., and G. Zandt, Seismic moment tensors of western U.S. earthquakes and implications for the tectonic stress field, *Journal of Geophysical Research*, *96*, 18,245-18,259, 1991.

Peacock, M.A., The Modoc lava field, northern California, *Geographical Review*, *21*, 259-275, 1931.

Pease, R.W., Normal faulting and lateral shear in northeastern California, *Geological Society of America Bulletin*, *80*, 715-720, 1969.

Perry, F.V., G.A. Valentine, E.K. Desmarais, and G. WoldeGabriel, Probabilistic assessment of volcanic hazard to radioactive waste repositories in Japan: Intersection by a dike from a nearby composite volcano, *Geology*, *29*, 255-258, 2001.

Perry, F.V., G. Woldegabriel, G.A. Valentine, E.K. Desmaraus, G. Heiken, M. Heizler, M. Yamakawa, and K. Umeda, High-level radioactive waste disposal and volcanic hazard in Japan: A natural analog study of Summer Coon volcano, Colorado, *Abstracts with Programs - Geological Society of America*, *31*, A478, 1999.

Pezzopane, S.K., and R.J. Weldon II, Tectonic role of active faulting in central Oregon, *Tectonics*, *12*, 1140-1169, 1993.

Phillips, W.J., The dynamic emplacement of cone sheets, *Tectonophysics*, *24*, 69-84, 1974.

Philpotts, A.R., and P.M. Asher, Magmatic flow-direction indicators in a giant diabase feeder dike, Connecticut, *Geology*, *22*, 363-366, 1994.

Poland, M.P., D. Dzurisin, R. Bürgmann, E. Koenig, and J.H. Fink, Modeling deformation at Medicine Lake volcano in northern California using regional tectonic and local volcanic sources, *EOS, Transactions, American Geophysical Union*, *81*, F338, 2000.

Pollard, D.D., Elementary fracture mechanics applied to the structural interpretation of dykes, in *Mafic Dyke Swarms*, edited by H.C. Halls, and W.F. Fahrig, pp. 5-24, Geological Sassociation of Canada, Toronto, 1987.

Pollard, D.D., P.T. Delaney, W.A. Duffield, E.T. Endo, and A.T. Okamura, Surface deformation in volcanic rift zones, *Tectonophysics*, *94*, 541-584, 1983.

Pollard, D.D., and G. Holzhausen, On the mechanical interaction between a fluid-filled crack and the Earth's surface, *Tectonophysics, 53*, 27-57, 1979.

Pollard, D.D., and O.H. Muller, The effect of gradients in regional stress and magma pressure on the form of sheet intrusions in cross section, *Journal of Geophysical Research, 81*, 975-984, 1976.

Pollard, D.D., O.H. Muller, and D.R. Dockstader, The form and growth of fingered sheet intrusions, *Geological Society of America Bulletin, 86*, 351-363, 1975.

Pollard, D.D., P. Segall, and P.T. Delaney, Formation and interpretation of dilatant echelon cracks, *Geological Society of America Bulletin, 93*, 1291-1303, 1982.

Pollitz, F.F., R. Burgmann, and P. Segall, Joint estimation of aftersilp and postseismic relaxation following the 1989 Loma Prieta earthquake, *Journal of Geophysical Research, 103*, 26,975-26,992, 1998.

Potter, S.L., Geology of the northern portion of the Likely fault lineament, Modoc County, northeastern California, *Northwest Science, 62*, 84, 1988.

Powers, H.A., The lavas of the Modoc Lava-Bed quadrangle, California, *The American Mineralogist, 17*, 253-294, 1932.

Prejean, S.G., W.L. Ellsworth, F. Waldhauser, and M.D. Zoback, Earthquake relocations and stress inversions in the Long Valley Caldera, California, *EOS, Transactions, American Geophysical Union, 81*, F1323, 2000.

Reches, Z., and J. Fink, The mechanism of intrusion of the Inyo Dike, Long Valley Caldera, California, *Journal of Geophysical Research, 93*, 4321-4334, 1988.

Rees, A., The effect of water currents on the magnetic remanence and anisotropy of magnetic susceptibility of some sediments, *Geophysical Journal of the Royal Astronomical Society, 6*, 235-251, 1961.

Reheis, M.C., and T.H. Dixon, Kinematics of the Eastern California shear zone: Evidence for slip transfer from Owens and Saline Valley fault zones to Fish Lake Valley fault zone, *Geology*, *24*, 339-342, 1996.

Reynolds, R.W., D. Geist, and M.D. Kurz, Physical volcanology and structural development of Sierra Negra Volcano, Isabela Island, Galapagos Archipelago, *Geological Society of America Bulletin*, *107*, 1398-1410, 1995.

Richey, J.E., Tertiary ring structures in Britan, *Transactions of the Geological Society of Glasgow*, *19*, 42-140, 1932.

Rickwood, P.C., The anatomy of a dyke and the determination of propagation and magma flow directions, in *Mafic Dykes and Emplacement Mechanisms*, edited by A.J. Parker, P.C. Rickwood, and D.H. Tucker, pp. 81-100, A. A. Balkema Publishers, Rotterdam, 1990.

Ritter, J.R.R., and J.R. Evans, Deep structure of Medicine Lake volcano, California, *Tectonophysics*, *275*, 221-241, 1997.

Roberts, C.T., Cenozoic evolution of the northwestern Honey Lake Basin, Lassen County, California, *Colorado School of Mines Quarterly*, *80*, 1-64, 1985.

Roberts, C.T., and T.L. Grose, Structural boundary between the Sierra Nevada and Cascade provinces, northeastern California, *Abstracts with Programs - Geological Society of America*, *16*, 636, 1984.

Roberts, J.L., The intrusion of magma into brittle rocks, in *Mechanism of Igneous Intrusion*, edited by G. Newall, and N. Rast, pp. 287-338, Gallery Press, Liverpool, 1970.

Robson, G.R., and K.G. Barr, The effect of stress on faulting and minor intrusions in the vicinity of a magma body, *Bulletin of Volcanology*, *27*, 315-330, 1964.

Rochette, P., L. Jenatton, C. Dupuy, F. Boudier, and I. Reuber, Diabase dikes emplacement in the Oman Ophiolite: A magnetic fabric study with reference to geochemistry, in *Ophiolite genesis and evolution of the oceanic lithosphere*, edited by

T. Peters, A. Nicolas, and R.G. Coleman, pp. 55-82, Kluwer Academic Publishers, London, 1991.

Rogers, P.G., and M.T. Zuber, Tectonic evolution of Bell Region, Venus: Regional stress, lithospheric flexure, and edifice stresses, *Journal of Geophysical Research, 103*, 16,841-16,853, 1998.

Rowland, S.K., Slopes, lava flow volumes, and vent distributions on Volcán Fernandina, Galápagos Islands, *Journal of Geophysical Research, 101*, 27,657-27,672, 1996.

Rubin, A.M., On the thermal viability of dikes leaving magma chambers, *Geophysical Research Letters, 20*, 257-260, 1993.

Rubin, A.M., Getting granite dikes out of the source region, *Journal of Geophysical Research, 100*, 5911-5929, 1995.

Rubin, A.M., and D.D. Pollard, Origins of blade-like dikes in volcanic rift zones, in *Volcanism in Hawaii*, edited by R.W. Decker, T.L. Wright, and P.H. Stauffer, pp. 1449-1470, USGS Professional Paper 1350, 1987.

Ryan, M.P., and C.G. Sammis, The glass transition in basalt, *Journal of Geophysical Research, 86*, 9519-9535, 1981.

Sauber, J., W. Thatcher, S.C. Solomon, and M. Lisowski, Geodetic slip rate for the eastern California shear zone and the recurrence time of Mojave desert earthquakes, *Nature, 367*, 264-266, 1994.

Savage, J.C., J.L. Svarc, W.H. Prescott, and M.H. Murray, Deformation across the forearc od the Cascadia subduction zone at Cape Blanco, Oregon, *Journal of Geophysical Research, 105*, 3095-3102, 2000.

Schomaker, M.C., and R.M. Berry, *Geodetic leveling manual NOS NGS 3*, National Geodetic Survey, National Oceanic and Atmospheric Administration, Rockville MD, 1981.

Schultz, R.A., Brittle strength of basaltic rock masses with applications to Venus, *Journal of Geophysical Research*, *98*, 10,883-10,895, 1993.

Scott, W.E., Holocene rhyodacite eruptions on the flanks of South Sister volcano, Oregon, in *The Emplacement of Silicic Domes and Lava Flows*, edited by J.H. Fink, pp. 35-54, 1987.

Shelley, D., Determining paleo-flow directions from groundmass fabrics in the Lyttelton radial dykes, New Zealand, *Journal of Volcanology and Geothermal Research*, *25*, 69-79, 1985.

Shelley, D., Radial dikes of Lyttelton Volcano - their structure, form, and petrography, *New Zealand Journal of Geology and Geophysics*, *31*, 65-75, 1988.

Sherrod, D.R., and J.G. Smith, Quaternary extrusion rates of the Cascade Range, northwestern United States and southern British Columbia, *Journal of Geophysical Research*, *95*, 19,465-19,474, 1990.

Sigmundsson, F., P. Einarsson, and R. Bilham, Magma chamber deflation recorded by the global positioning system: the Hekla 1991 eruption, *Geophysical Research Letters*, *19*, 1483-1486, 1992.

Sigmundsson, F., H. Vadon, and D. Massonnet, Readjustment of the Krafla spreading segment to crustal rifting measured by satellite radar interferometry, *Geophysical Research Letters*, *24*, 1843-1846, 1997.

Sigurdsson, H., and R.S.J. Sparks, Rifting episode in North Iceland in 1874-1875 and the eruptions of Askja and Sveinagja, *Bulletin of Volcanology*, *41*, 149-167, 1978a.

Sigurdsson, H., and S.R.J. Sparks, Lateral magma flow within rifted Icelandic crust, *Nature*, *274*, 126-130, 1978b.

Simkin, T., Origin of some flat-topped volcanoes and guyots, *Geological Society of America Memoir*, *132*, 183-193, 1972.

Simkin, T., Geology of Galapagos Islands, in *Galapagos*, edited by R. Perry, pp. 15-41, Pergamon Press, New York, 1984.

Simkin, T., and K.A. Howard, Caldera Collapse in the Galápagos Islands, 1968, *Science, 169*, 429-437, 1970.

Smith, J.V., Y. Miyake, and S. Yamauchi, Flow directions and groundmass shear zones in dykes, Shimane Peninsula, Japan, *Geological Magazine*, *130*, 117-120, 1993.

Smith, R.L., and R.A. Bailey, Resurgent cauldrons, in *Studies in volcanology--A memoir in honor of Howel Williams.*, pp. 613-662, Geological Society of America (GSA), Boulder, CO, United States, 1968.

Smith, R.P., Dyke emplacement at Spanish Peaks, Colorado, in *Mafic Dyke Swarms*, edited by H.C. Halls, and W.F. Fahrig, pp. 47-54, Geological Association of Canada, Toronto, Canada, 1987.

Solomon, S.C., and J.W. Head, Lunar mascon basins: Lava filling, tectonics, and evolution of the lithosphere, *Reviews of Geophysics and Space Physics*, *18*, 107-141, 1980.

Sommer, E., Formation of fracture 'lances' in glass, *Engineering Fracture Mechanics*, *1*, 539-546, 1969.

Stanley, W.D., W.D. Mooney, and G.S. Fuis, Deep crustal structure of the Cascade Range and surrounding regions from seismic refraction and magentotelluric data, *Journal of Geophysical Research*, *95*, 19,419-19,438, 1990.

Stauber, D.A., S.M. Green, and H.M. Iyer, Three-dimensional P velocity structure of the crust below Newberry volcano, Oregon, *Journal of Geophysical Research*, *93*, 10,095-10,107, 1988.

Staudigel, H., J. Gee, L. Tauxe, and R.J. Varga, Shallow intrusive directions of sheeted dikes in the Troodos ophiolite: Anisotropy of magnetic susceptibility and structural data, *Geology*, *20*, 841-844, 1992.

Stein, R.S., Discrimination of tectonic displacement from slope-dependent errors in geodetic leveling from southern California, 1953-1977, in *Earthquake Prediction: An International Review*, edited by D.W. Simpson, and P.G. Richards, pp. 441-456, American Geophysical Union, Washington DC, 1981.

Stevens, B., The laws of intrusion, *Transactions of the American Institute of Mining Engineers*, 650-672, 1911.

Stewart, J.H., Tectonics of the Walker Lane belt, western Great Basin: Mesozoic and Cenozoic deformation in a zone of shear, in *Metamorphism and crustal evolution of the western United States*, edited by W.G. Ernst, pp. 683-713, Prentice Hall, New Jersey, 1988.

Strange, W.E., The effect of systematic errors on geodymanic analysis, in *Second International Symposium on Problems Related to the Redefinition of North American Vertical Geodetic Networks*, pp. 704-729, Canadian Institute of Surveying, Surveys and Mapping Branch, Ottawa, 1980a.

Strange, W.E., The impact of refraction corrections on leveling interpretations in California, *EOS, Transactions, American Geophysical Union*, *61*, 365, 1980b.

Strange, W.E., L.F. Machesky, and G.P. Woollard, A gravity survey of the island of Oahu, Hawaii, *Pacific Science*, *19*, 350-353, 1965.

Sturkell, E., and F. Sigmundsson, Continuous deflation of the Askja caldera, Iceland, during the 1983-1998 noneruptive period, *Journal of Geophysical Research*, *105*, 25,671-25,684, 2000.

Takada, A., Experimental study on propagation of liquid-filled crack in gelatin: shape and velocity structure in hydrostatic stress conditions, *Journal of Geophysical Research*, *95*, 8471-8481, 1990.

Takada, A., The influence of regional stress and magmatic input on styles of monogenetic and polygenetic volcanism, *Journal of Geophysical Research*, *99*, 13,563-13,573, 1994.

Tauxe, L., *Paleomagnetic Principles and Parctice*, 299 pp., Kluwer Academic Publishers, Dordrecht, The Netherlands, 1998.

Tauxe, L., C. Constable, L. Stokking, and C. Badgley, Use of anisotropy to determine the origin of characteristic remanence in the Siwalik Red Beds of northern Pakistan, *Journal of Geophysical Research*, *95*, 4391-4404, 1990.

Tauxe, L., J.S. Gee, and H. Staudigel, Flow directions in dikes from anisotropy of magnetic susceptibility data: The bootstrap way, *Journal of Geophysical Research*, *103*, 17,775-17,790, 1998.

Thatcher, W., G.R. Foulger, B.R. Julian, J. Svarc, E. Quilty, and G.W. Bawden, Present-day deformation across the Basin and Range province, western United States, *Science*, *283*, 1714-1718, 1999.

Thomas, A.L., and D.D. Pollard, The geometry of echelon fractures in rock: Implications from laboratory and numerical experiments, *Journal of Structural Geology*, *15*, 323-334, 1993.

Thorarinsson, S., and G.E. Sigvaldason, The eruption in Askja, 1961: A preliminary report, *American Journal of Science*, *260*, 641-651, 1962.

Thurbur, C.H., and M.N. Toksöz, Martian lithospheric thickness from elastic flexure theory, *Geophysical Research Letters*, *5*, 977-980, 1978.

Tibaldi, A., Mutual influence of dyking and collapses and Stromboli volcano, Italy, in *Volcano Instability on the Earth and Other Planets*, edited by W.J. McGuire, A.P. Jones, and J. Neuberg, Geological Society of London, London, 1996.

Turcotte, D.L., and G. Schubert, *Geodynamics: Applications of Continuum Physics to Geological Problems*, 450 pp., John Wiley and Sons, New York, 1982.

Tweto, O., Form and structure of sills near Pando, Colorado, *Geological Society of America Bulletin*, *62*, 507-532, 1951.

van Wyk de Vries, B., and A. Borgia, The role of basement in volcano deformation, in *Volcano Instability on the Earth and Other Planets*, edited by W.J. McGuire, A.P. Jones, and J. Newberg, pp. 95-110, Geological Society of London, London, 1996.

Vanicek, P., R.O. Castle, and E.I. Balazs, Geodetic leveling and its applications, *Reviews of Geophysics and Space Physics*, *18*, 505-524, 1980.

Vicenzi, E.P., A.R. McBirney, W.M. White, and M. Hamilton, The geology and geochemistry of Isla Marchena, Galapagos Archipelago: An ocean island adjacent to a mid-ocean ridge, *Journal of Volcanology and Geothermal Research*, *40*, 291-315, 1990.

Walcott, R.I., Felxure of the lithosphere at Hawaii, *Tectonophysics, 9*, 435-446, 1970.

Walker, G.P.L., Downsag calderas, ring faults, caldera sizes, and incremental caldera growth, *Journal of Geophysical Research*, *89*, 8407-8416, 1984.

Walker, G.P.L., The dike complex of Koolau volcano, Oahu: internal structure of a Hawaiian rift zone, in *Volcanism in Hawaii*, edited by R.W. Decker, T.L. Wright, and P.H. Stauffer, 961-993 pp., USGS Professional Paper 1350, 1987.

Walker, G.P.L., Three Hawaiian calderas: An origin through loading by shallow intrusions?, *Journal of Geophysical Research*, *93*, 14,773-14,784, 1988.

Walker, G.P.L., Re-evaluation of inclined intrusive sheets and dykes in the Cuillins volcano, Isle of Skye, in *Magmatic Processes and Plate Tectonics*, edited by H.M. Prichard, T. Alabaster, N.B.W. Harris, and C.R. Neary, pp. 489-497, Geological Society of London, London, 1993.

Walter, S., and D. Dzurisin, The Spetember, 1988 earthquake swarm at Medicine Lake volcano, northern California, *EOS, Transactions, American Geophysical Union*, *70*, 1189-1190, 1989.

Watts, A.B., J.R. Cochran, and G. Selzer, Gravity anomalies and flexure of the lithosphere: A three-dimensional study of the Great Meteor Seamount, Northeast Atlantic, *Journal of Geophysical Research*, *80*, 1391-1398, 1975.

Watts, A.B., U.S. ten Brink, P. Buhl, and T.M. Brocher, A multichannel seismic study of the lithospheric flexure across the Hawaii-Emperor seamount chain, *Nature*, *315*, 105-111, 1985.

Weertman, J., Theory of water-filled crevasses in glaciers applied to vertical magma transport beneath oceanic ridges, *Journal of Geophysical Research*, *76*, 1171-1183, 1971.

Wells, R.E., C.S. Weaver, and R.J. Blakely, Fore-arc migration in Cascadia and its neotectonic significance, *Geology*, *26*, 759-762, 1998.

Wernicke, B., A.M. Friedrich, M.A. Nieme, R.A. Bennett, and J.L. Davis, Dynamics of plate boundary fault systems from Basin and Range Geodetic Network (BARGEN) and geologic data, *GSA Today*, *10*, 1-7, 2000.

Wicks Jr., C.W., D. Dzurisin, S. Ingebritsen, W. Thjatcher, Z. Lu, and J. Iverson, Magmatic activity beneath the quiescent Three Sisters volcanic center, central Oregon Cascade Range, USA, *Geophysical Research Letters*, in review.

Williams, D.L., G. Abrams, C. Finn, D. Dzurisin, D.J. Johnson, and R. Denlinger, Evidence from gravity data for an intrusive complex beneath Mount St. Helens, *Journal of Geophysical Research*, *92*, 10,207-10,222, 1987.

Wood, C.A., and J. Kienle, *Volcanoes of North America*, 354 pp., Cambridge University Press, New York, 1990.

Wright, L., Late Cenozoic fault patterns and stress fields in the Great Basin and westward displacement of the Sierra Nevada block, *Geology*, *4*, 489-494, 1976.

Wyatt, F.K., Displacement of surface monuments: Vertical motion, *Journal of Geophysical Research*, *94*, 1655-1664, 1989.

Yamashita, K.M., and D.E. Wieprecht, Bench mark descriptions and photographs for Global Positioning System (GPS) stations in the vicinity of Mt. Shasta and Medicine Lake, California, *Open-File Report - U. S. Geological Survey*, *95-811*, 27 pp., 1995.

Zbinden, E.A., and J.M. Sinton, Dikes and Petrology of Waianae Volcano, Oahu, *Journal of Geophysical Research*, *93*, 14,856-14,866, 1988.

Zielinski, R.A., and P.W. Lipman, Trace-element variations at Summer Coon volcano, San Juan Mountains, Colorado, and the origin of continental-interior andesite, *Geological Society of America Bulletin*, *87*, 1477-1485, 1976.

Zoback, M.L., First- and second-order patterns of stress in the lithosphere: The world stress map project, *Journal of Geophysical Research, 97*, 11,703-11,728, 1992.

Zoback, M.L., and M. Zoback, State of stress in the conterminous United States, *Journal of Geophysical Research*, *85*, 6113-6156, 1980.

Zoback, M.L., and M.D. Zoback, Tectonic stress field of the continental United States, *Geological Society of America Memoir*, *172*, 523-572, 1989.

Zucca, J.J., and J.R. Evans, Active high-resolution compressional wave attenuation tomography at Newberry Volcano, central Cascade Range, *Journal of Geophysical Research, 97*, 11,047-11,055, 1992.

Zucca, J.J., G.S. Fuis, B. Milkereit, W.D. Mooney, and R.D. Catchings, Crustal structure of northeastern California, *Journal of Geophysical Research, 91*, 7359-7382, 1986.

APPENDIX A

MATLAB CODE FOR INVERTING MEASURED DIKE THICKNESSES TO DETERMINE DRIVING PRESSURES AND PRESSURE GRADIENTS

thick_invert.m

```
% Script to invert dike thicknesses for driving pressure
% Inverts for both a constant pressure only and a constant pressure combined with a
% pressure gradient

% Input file should consist of two columns, the first is distance along dike, and the
second
% is thickness

filename = input('Enter the name of the file containing the data: ','s');
filename = filename(1,:);

eval(['fopen ',filename]);
fid = ans;

if ans == -1
   disp('Could not read file'); disp(filename);
else

% Read thickness data file

% DATA FORMAT IS
% [Distance along dike; Dike thickness]

% Output:
%      t          = vector of thicknesses
%      dist       = vector of distances

   [A, count] = fscanf(fid, '%g %g', [2, inf]);
   nobs = count/2;

   A = A';
   dist = A(1:nobs,1);
   t = A(1:nobs,2);
end
```

```
% Read in the user-defined constant parameters

dike_length = input('Enter the length of the dike (in meters): ');
half_length = dike_length/2;
poisson = input('Enter the value for Poissons Ratio: ');
young = input('Enter the value for Youngs modulus (in Pascals): ');

% Calculate distances assuming middle of dike is at x = 0

dist_adjusted = dist - half_length;

% Invert for constant driving pressure

d = t;

for i = 1:nobs
   G(i) = 2*half_length*((1-poisson)/young)*(1-(dist_adjusted(i)/half_length)^2)^0.5;
end

G = G';

pressure_const = inv(G'*G)*G'*d;

% Calculate the curve misfit (sum of squares) for the constant pressure model

for j = 1:nobs
   const_thick(j) = 2*pressure_const*half_length*((1-poisson)/young)*...
      (1-(dist_adjusted(j)/half_length)^2)^0.5;
   error_const(j) = (const_thick(j) - t(j))^2;
end

RSS_const = sum(error_const);

% Invert for constant pressure plus pressure gradient
```

```
clear G;

for k = 1:nobs
   G(k,1) = 2*half_length*((1-poisson)/young)*(1-(dist_adjusted(k)/half_length)^2)^0.5;
   G(k,2) = half_length*dist_adjusted(k)*((1-poisson)/young)*...
      (1-(dist_adjusted(k)/half_length)^2)^0.5;
end

pressure_grad = inv(G'*G)*G'*d;

% Calculate the curve misfit (sum of squares) for the pressure gradient model

for m = 1:nobs
   grad_thick(m) = 2*half_length*pressure_grad(1)*((1-poisson)/young)*...
      (1-(dist_adjusted(m)/half_length)^2)^0.5 +...
      half_length*dist_adjusted(m)*pressure_grad(2)*((1-poisson)/young)*...
      (1-(dist_adjusted(m)/half_length)^2)^0.5;
   error_grad(m) = (grad_thick(m) - t(m))^2;
end

RSS_grad = sum(error_grad);

% Calculate thickness-to-width ratios

av_thick = sum(t)/nobs;
tw_ratio = (av_thick / dike_length) * 1000;

% Plot data, constant pressure model, and pressure gradient model

xmax = dike_length + 100;

figure
plot(dist,t,'b*')
axis([-100 xmax -inf inf])
hold on
```

```
temp = linspace(0,dike_length,100);
temp = temp - half_length;
for n = 1:100
   const_thick_temp(n) = 2*pressure_const*half_length*((1-poisson)/young)*...
      (1-(temp(n)/half_length)^2)^0.5;
   grad_thick_temp(n) = 2*half_length*pressure_grad(1)*((1-poisson)/young)*...
      (1-(temp(n)/half_length)^2)^0.5 +...
   half_length*temp(n)*pressure_grad(2)*((1-poisson)/young)*...
      (1-(temp(n)/half_length)^2)^0.5;
end
temp = temp + half_length;

plot(temp,const_thick_temp,'r-')
plot(temp,grad_thick_temp,'g:')
xlabel('Distance along dike strike (m)')
ylabel('Thickness (m)')
title('Observed vs. Predicted Dike Thickness')
legend('observed thicknesses','constant pressure model','pressure gradient model',2)
hold off

% Determine if any points fall two standard deviations away from the model

[two_std_dev,misfit] = deviation(t,grad_thick,nobs);
for z = 1:nobs
   if misfit(z) > two_std_dev
      disp(sprintf('WARNING: Measurement > than 2 standard deviations from the ....
      gradient model, should be removed: %g' ,z))
   end
end

% Calculate some of the standard statistics needed for the error analysis

mean = sum(t)/nobs;
variance = (std(t))^2;
RSS_const_dof = RSS_const/(nobs-1);
RSS_grad_dof = RSS_grad/(nobs-2);
```

```
% Display pressures and errors for constant and gradient pressures

disp(' ')
disp(' ')
disp(' ')
disp(' ')
disp(sprintf('Results of inversion for: %s' ,filename))
disp(' ')
disp('THICKNESS-TO-LENGTH RATIO')
disp('_____')
disp(' ')
disp(sprintf('T/W ratio (x 10 E-3): %g' ,tw_ratio))
disp(' ')
disp(' ')
disp('CONSTANT PRESSURE MODEL')
disp('_____')
disp(' ')
disp(sprintf('Driving pressure: %g' ,pressure_const))
disp(sprintf('Residual Sum of Squares: %g' ,RSS_const))
disp(sprintf('RSS/(N-P): %g' ,RSS_const_dof))
disp(' ')
disp(' ')
disp('PRESSURE GRADIENT MODEL')
disp('_____')
disp(' ')
disp(sprintf('Driving Pressure: %g' ,pressure_grad(1)))
disp(sprintf('Pressure gadient: %g' ,pressure_grad(2)))
disp(sprintf('Residual Sum of Squares: %g' ,RSS_grad))
disp(sprintf('RSS/(N-P): %g' ,RSS_grad_dof))
disp(' ')
disp(' ')
disp(' ')
disp(' ')
disp('Done')
```

deviation.m

```
function [two_std_dev,misfit] = deviation(t,grad_thick,nobs)

% function to calculate the value of two standard deviations from the model,
% as well as the misfit of each data point

t=t';
misfit = abs(t-grad_thick);
mean = (sum(misfit))/nobs;
dev = 0;
for z = 1:nobs
   dev_temp(z) = (grad_thick(z)-mean)^2;
   dev = dev_temp(z) + dev;
end
std_dev = sqrt(dev/nobs);
two_std_dev = 2*std_dev;
```

APPENDIX B

PLOTS OF OBSERVED AND MODELED THICKNESSES FOR 13 DIKES AT SUMMER COON VOLCANO

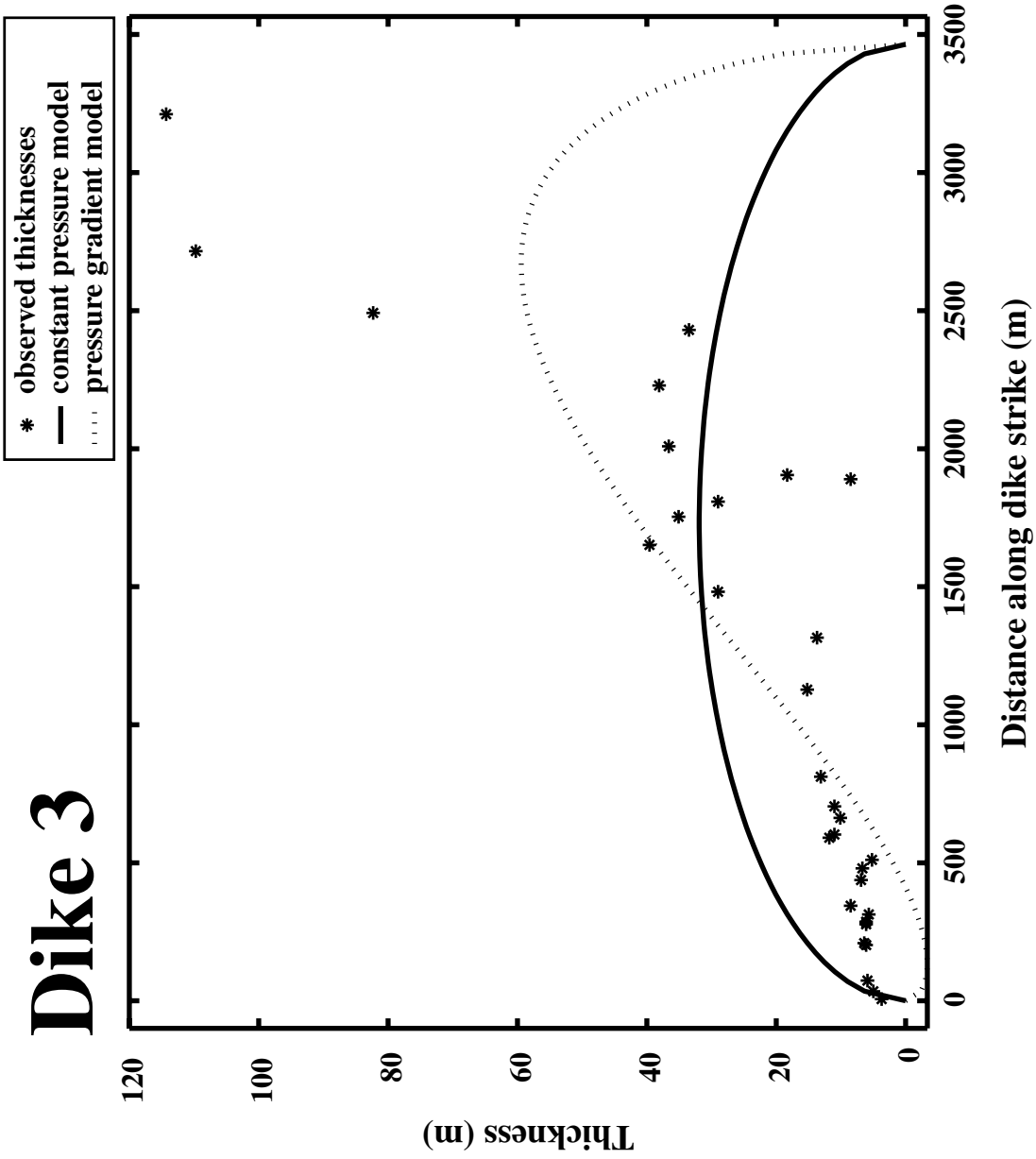
Dike 3
observed thicknesses
constant pressure model
pressure gradient model
Thickness (m)
0
20
40
60
80
100
120
0
500
1000
1500
2000
2500
3000
3500
Distance along dike strike (m)

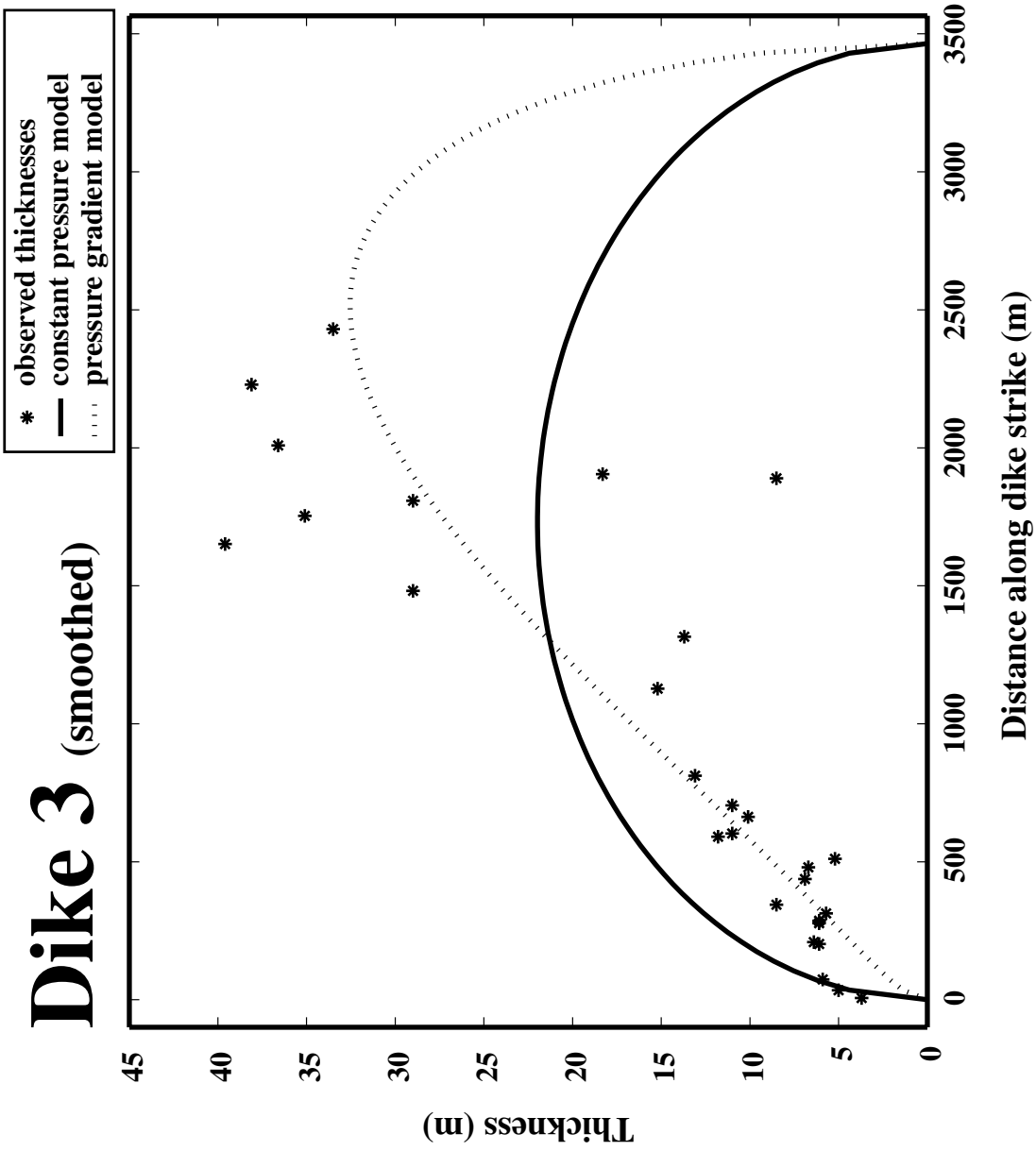
Dike 3 (smoothed)
* observed thicknesses
constant pressure model
pressure gradient model
Thickness (m)
0
5
10
15
20
25
30
35
40
45
0
500
1000
1500
2000
2500
3000
3500
Distance along dike strike (m)

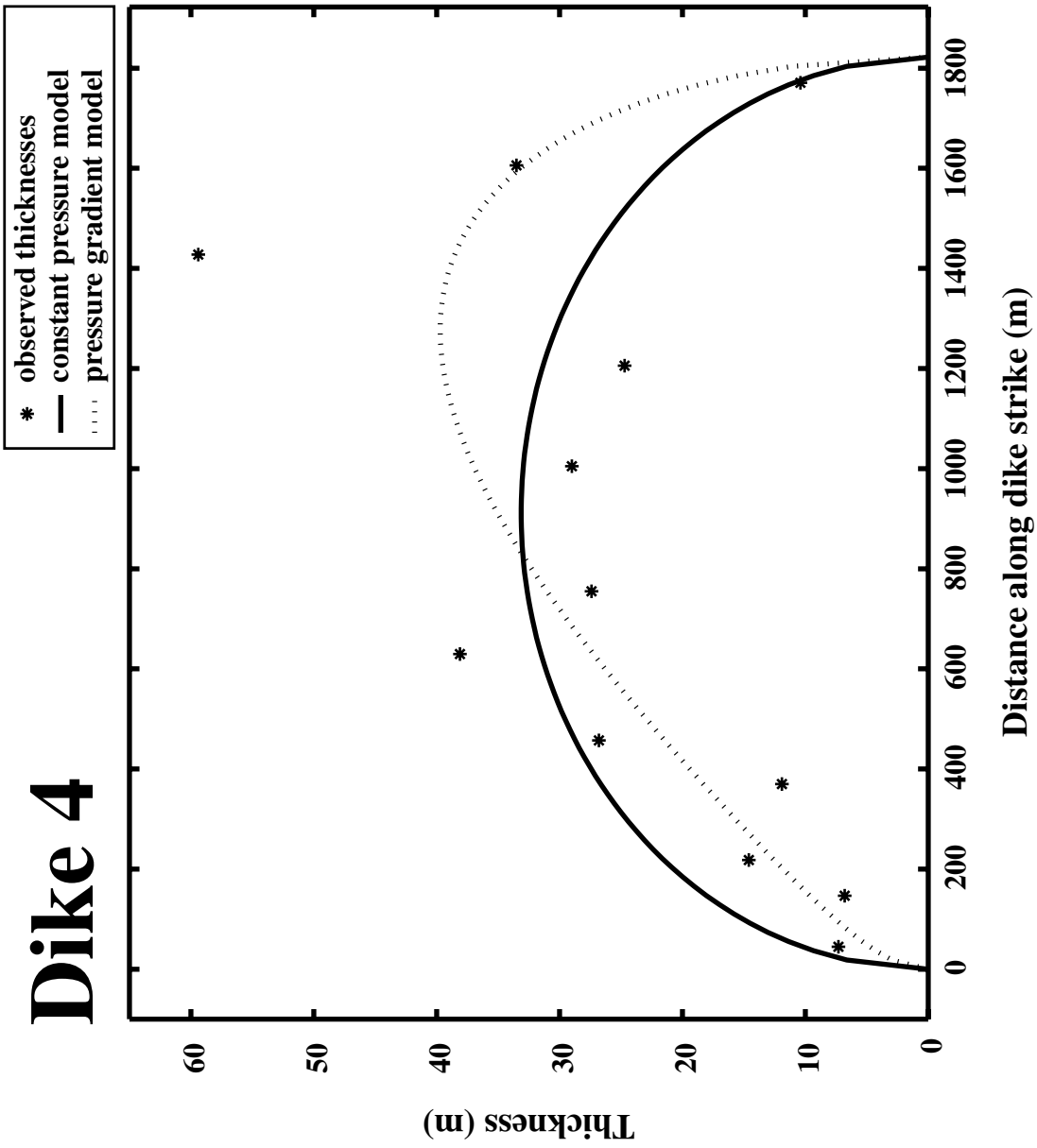
Dike 4
observed thicknesses
constant pressure model
pressure gradient model
Thickness (m)
0
10
20
30
40
50
60
0
200
400
600
800
1000
1200
1400
1600
1800
Distance along dike strike (m)

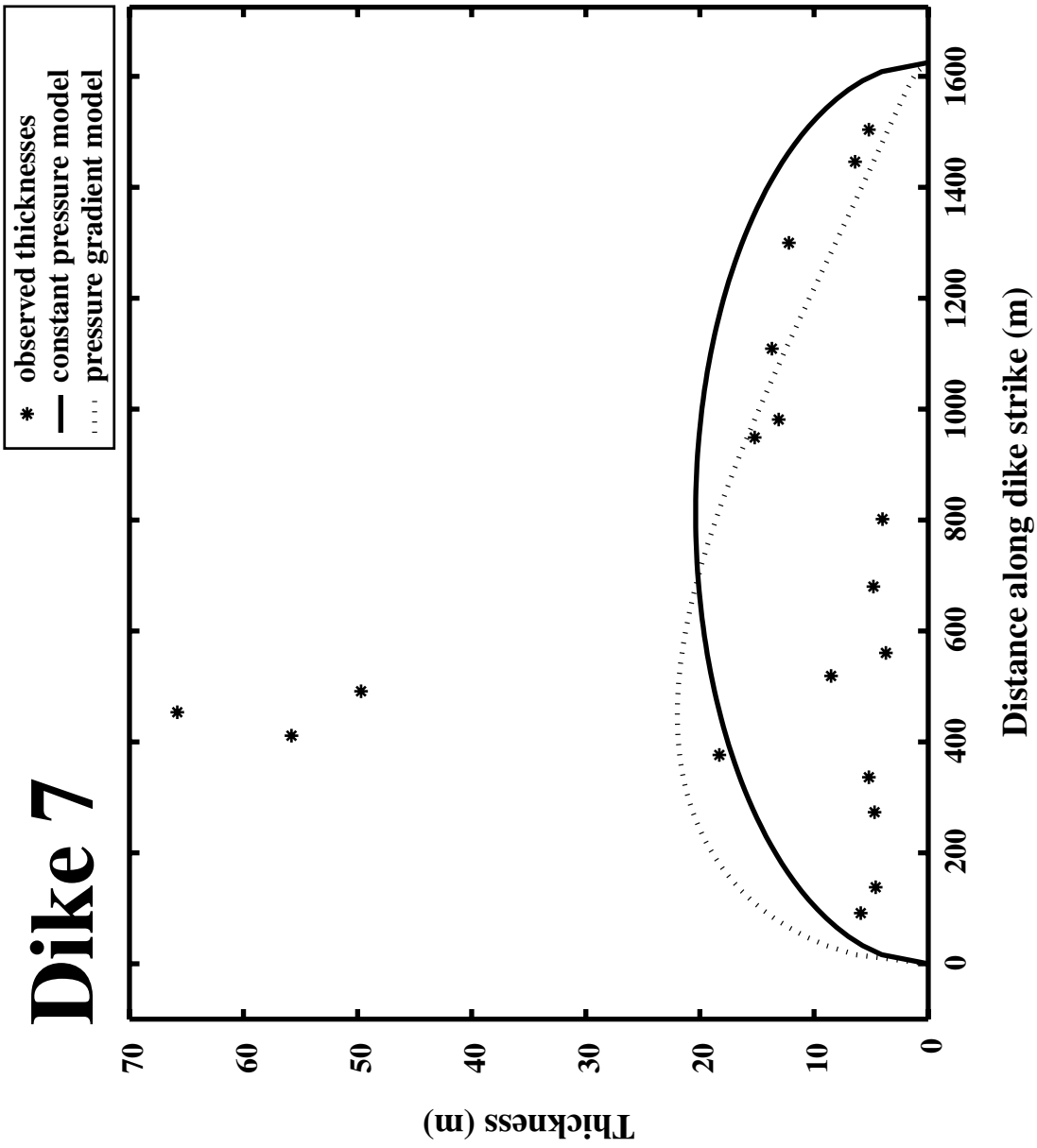
Dike 7
* observed thicknesses
constant pressure model
pressure gradient model
Thickness (m)
0
10
20
30
40
50
60
70
0
200
400
600
800
1000
1200
1400
1600
Distance along dike strike (m)

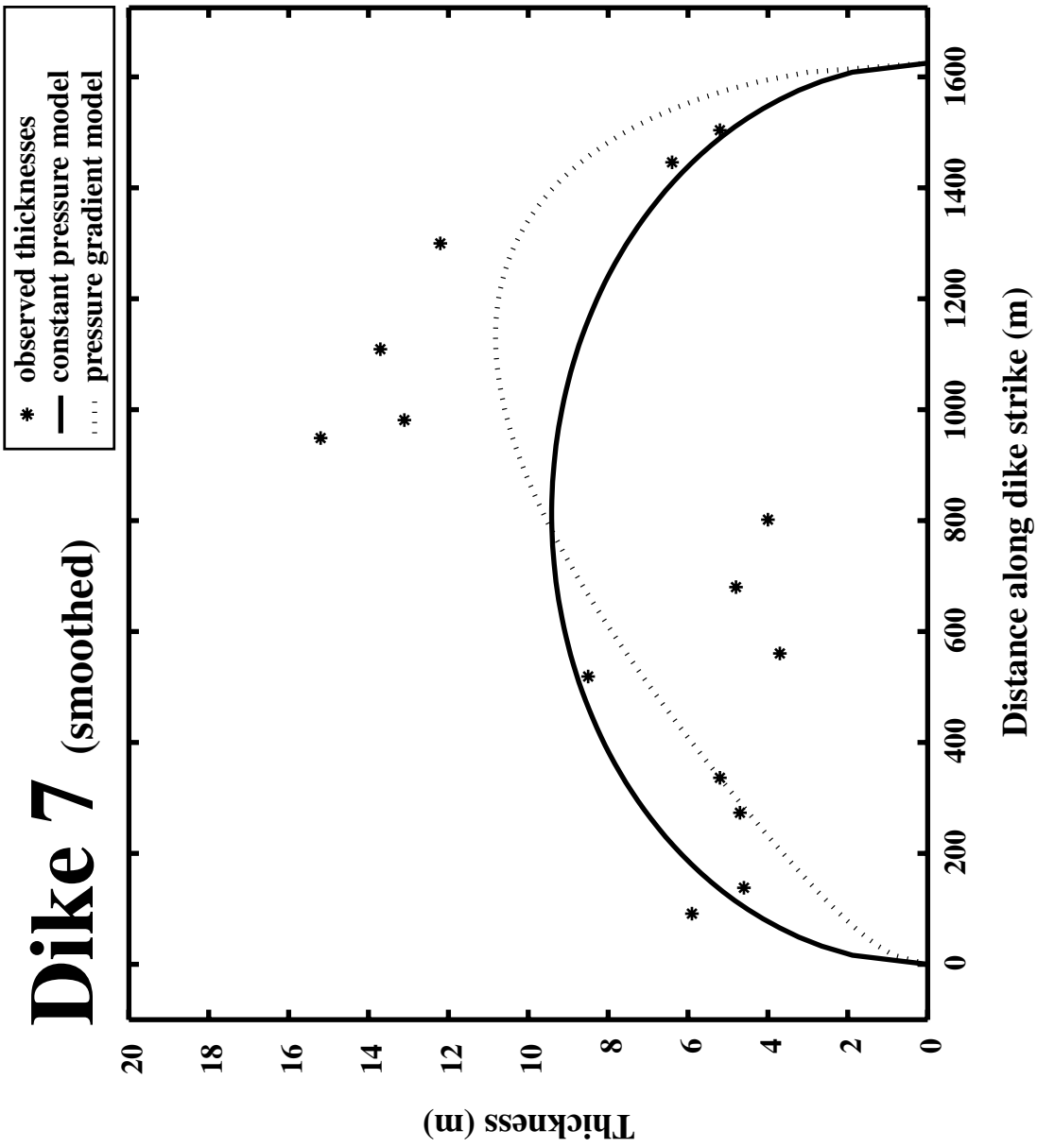
Dike 7 (smoothed)
* observed thicknesses
constant pressure model
pressure gradient model
Thickness (m)
0
2
4
6
8
10
12
14
16
18
20
0
200
400
600
800
1000
1200
1400
1600
Distance along dike strike (m)

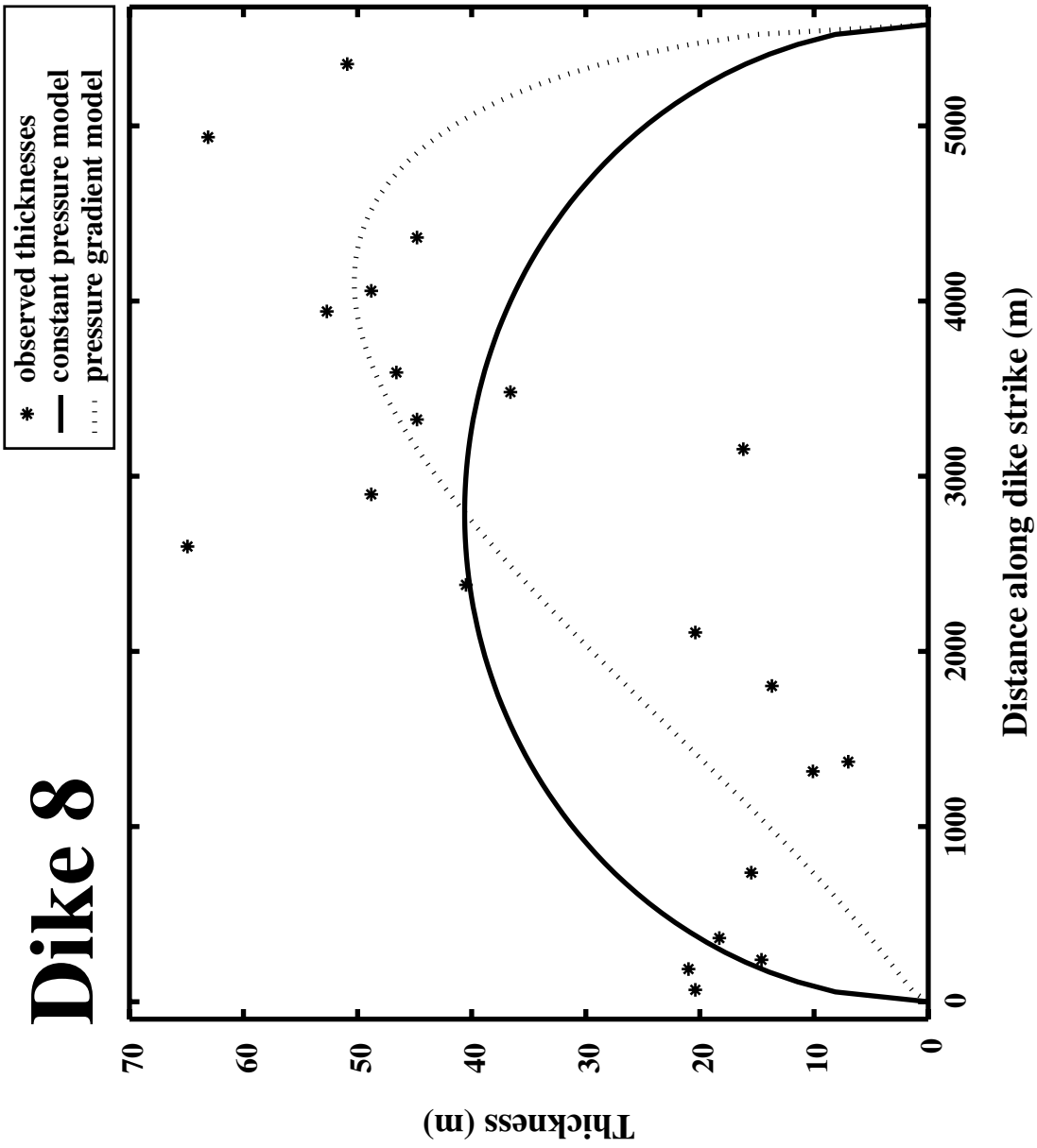
Dike 8
observed thicknesses
constant pressure model
pressure gradient model
Thickness (m)
0
10
20
30
40
50
60
70
0
1000
2000
3000
4000
5000
Distance along dike strike (m)

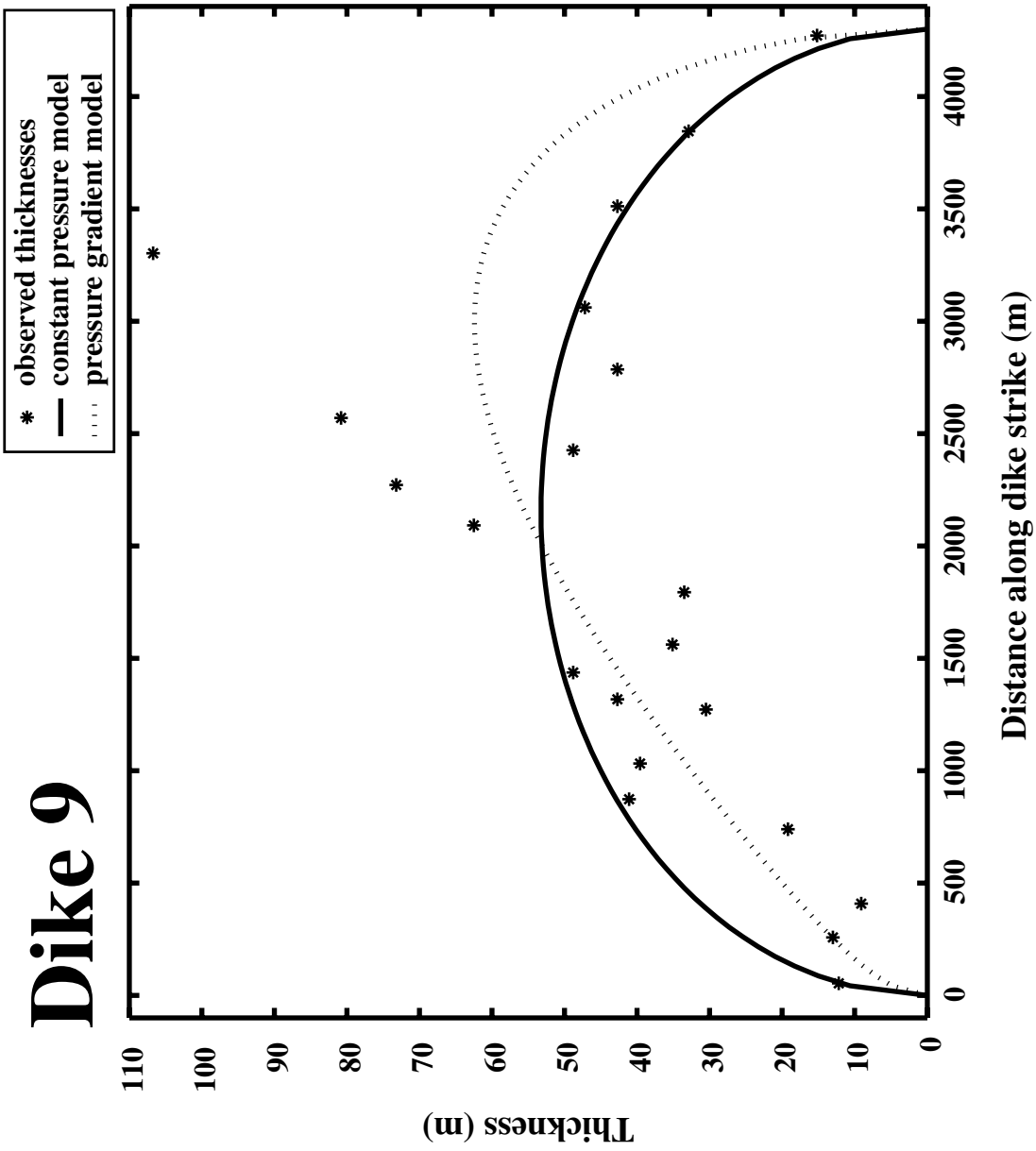
Dike 9
observed thicknesses
constant pressure model
pressure gradient model
Thickness (m)
0
10
20
30
40
50
60
70
80
90
100
110
0
500
1000
1500
2000
2500
3000
3500
4000
Distance along dike strike (m)

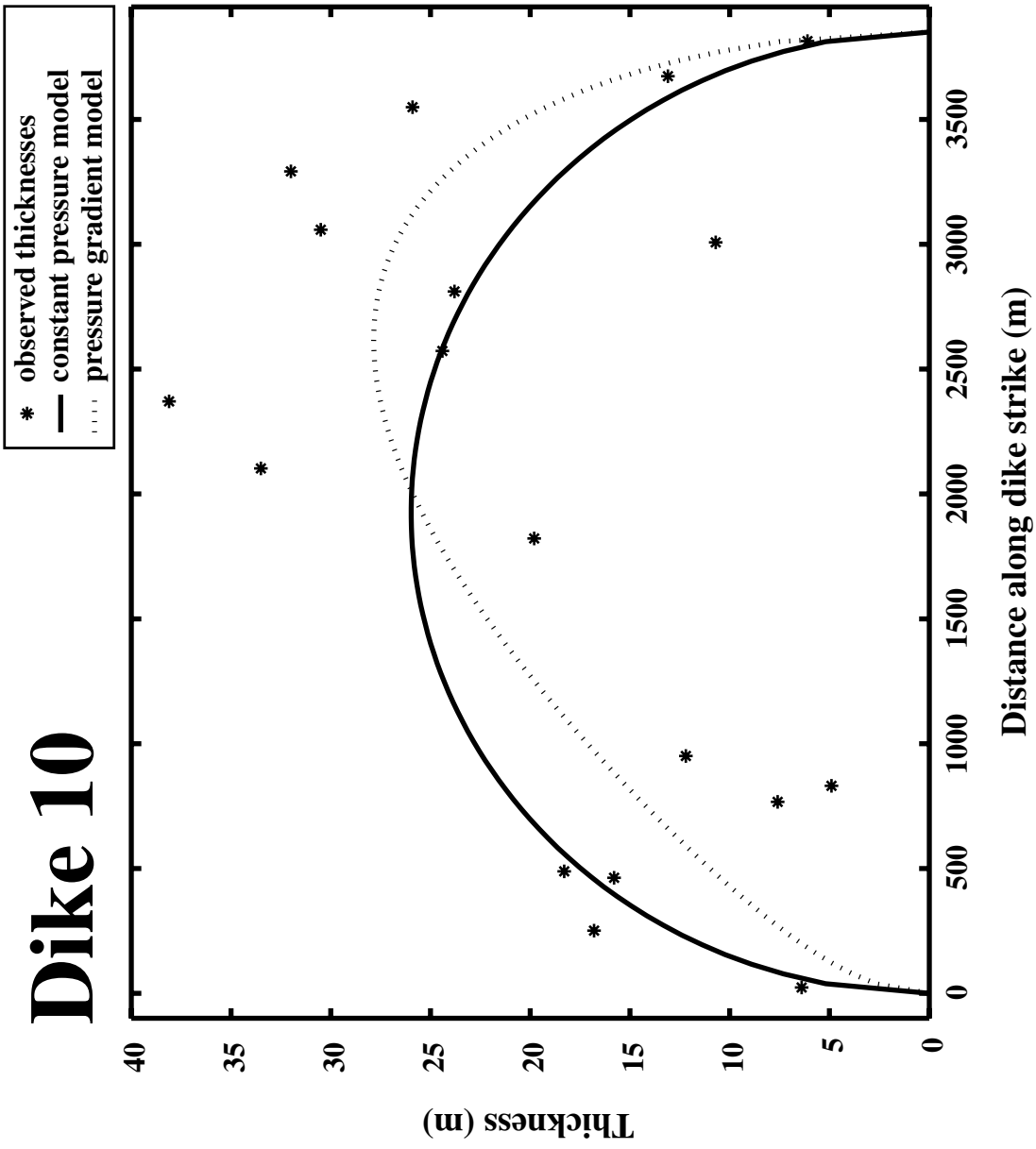
Dike 10
observed thicknesses
constant pressure model
pressure gradient model
Thickness (m)
Distance along dike strike (m)
0
5
10
15
20
25
30
35
40
0
500
1000
1500
2000
2500
3000
3500

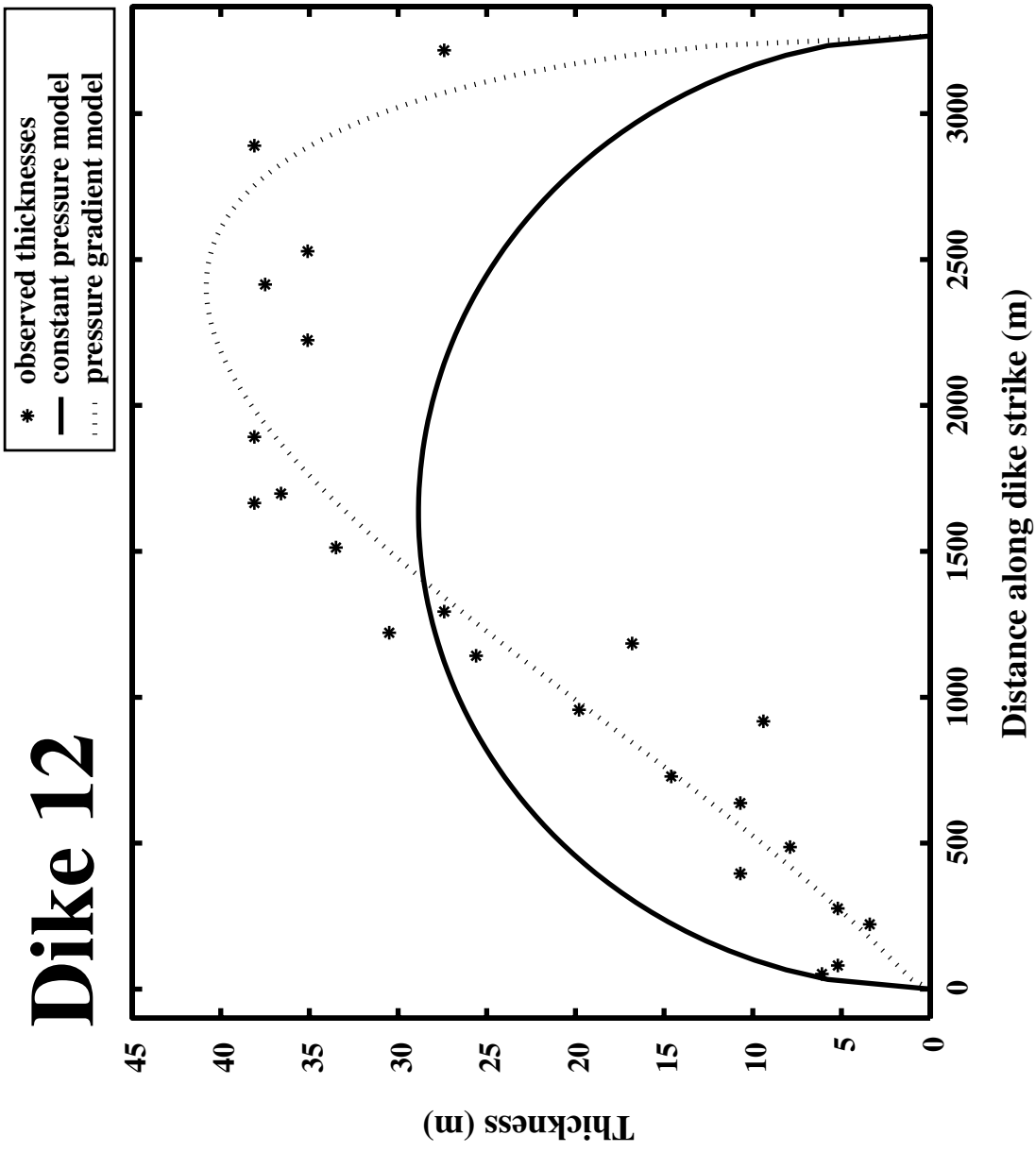
Dike 12
observed thicknesses
constant pressure model
pressure gradient model
Thickness (m)
Distance along dike strike (m)
0
5
10
15
20
25
30
35
40
45
0
500
1000
1500
2000
2500
3000

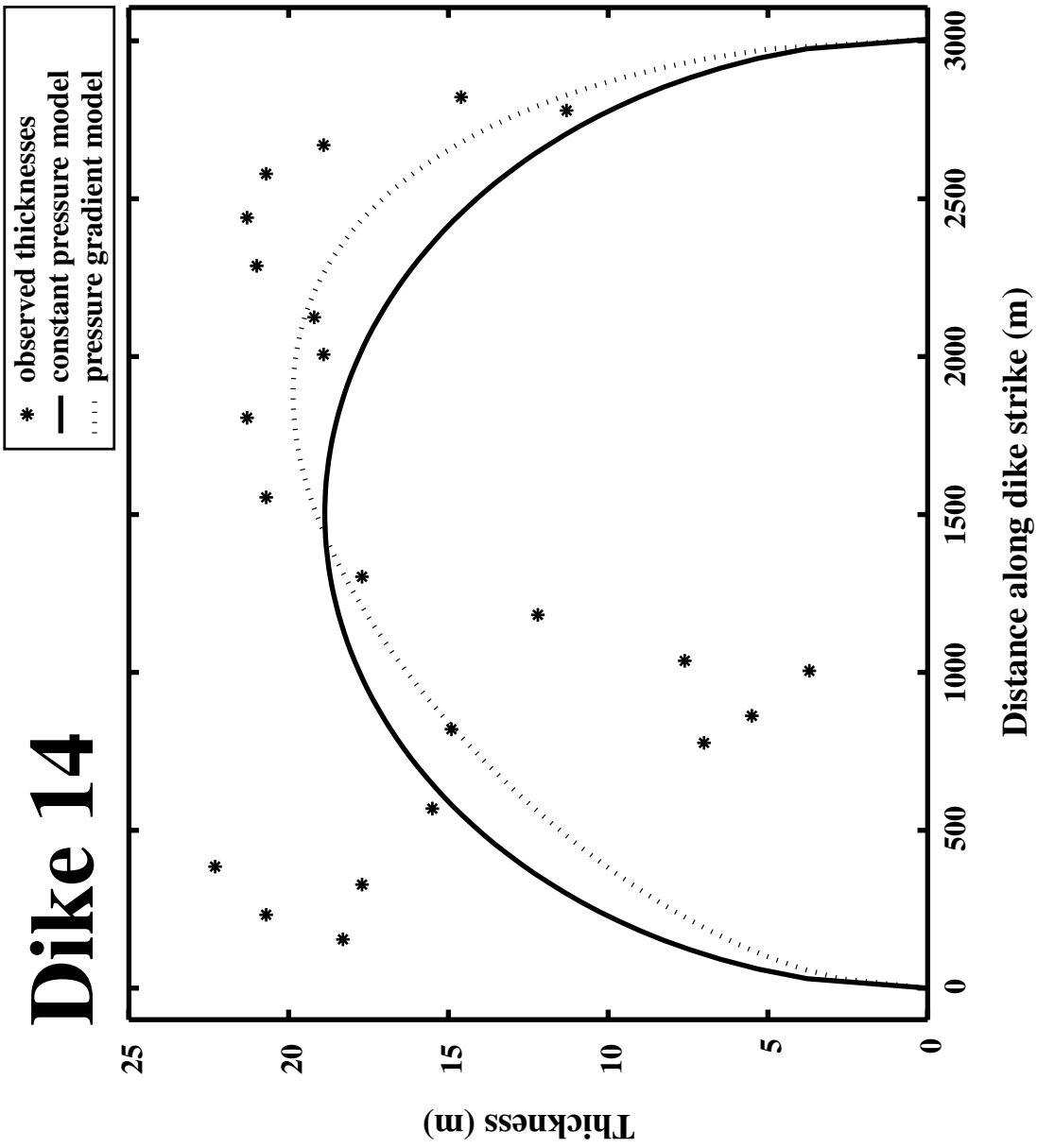
Dike 14
observed thicknesses
constant pressure model
pressure gradient model
Thickness (m)
0
5
10
15
20
25
0
500
1000
1500
2000
2500
3000
Distance along dike strike (m)

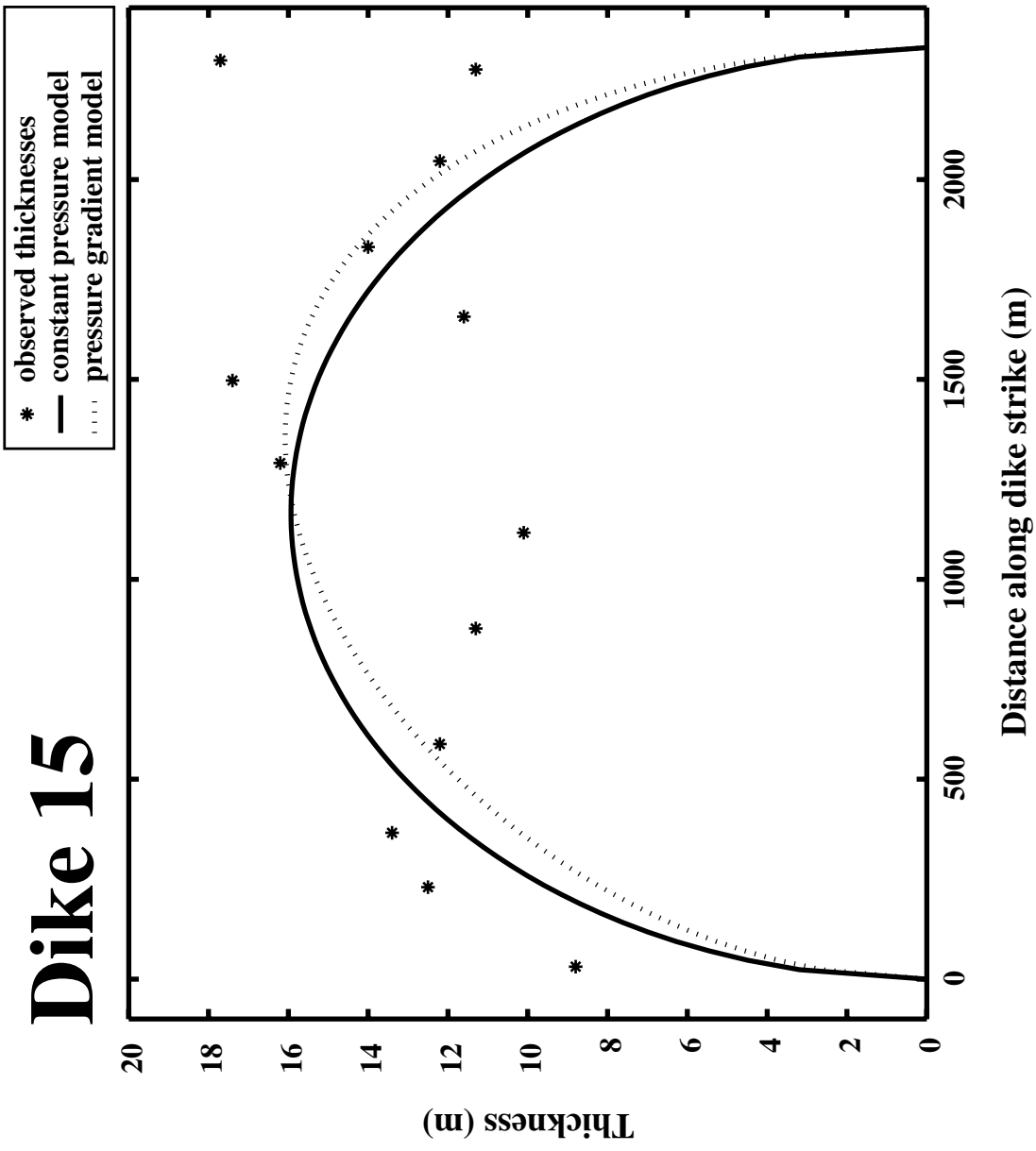
Dike 15
observed thicknesses
constant pressure model
pressure gradient model
Thickness (m)
Distance along dike strike (m)
0
2
4
6
8
10
12
14
16
18
20
0
500
1000
1500
2000

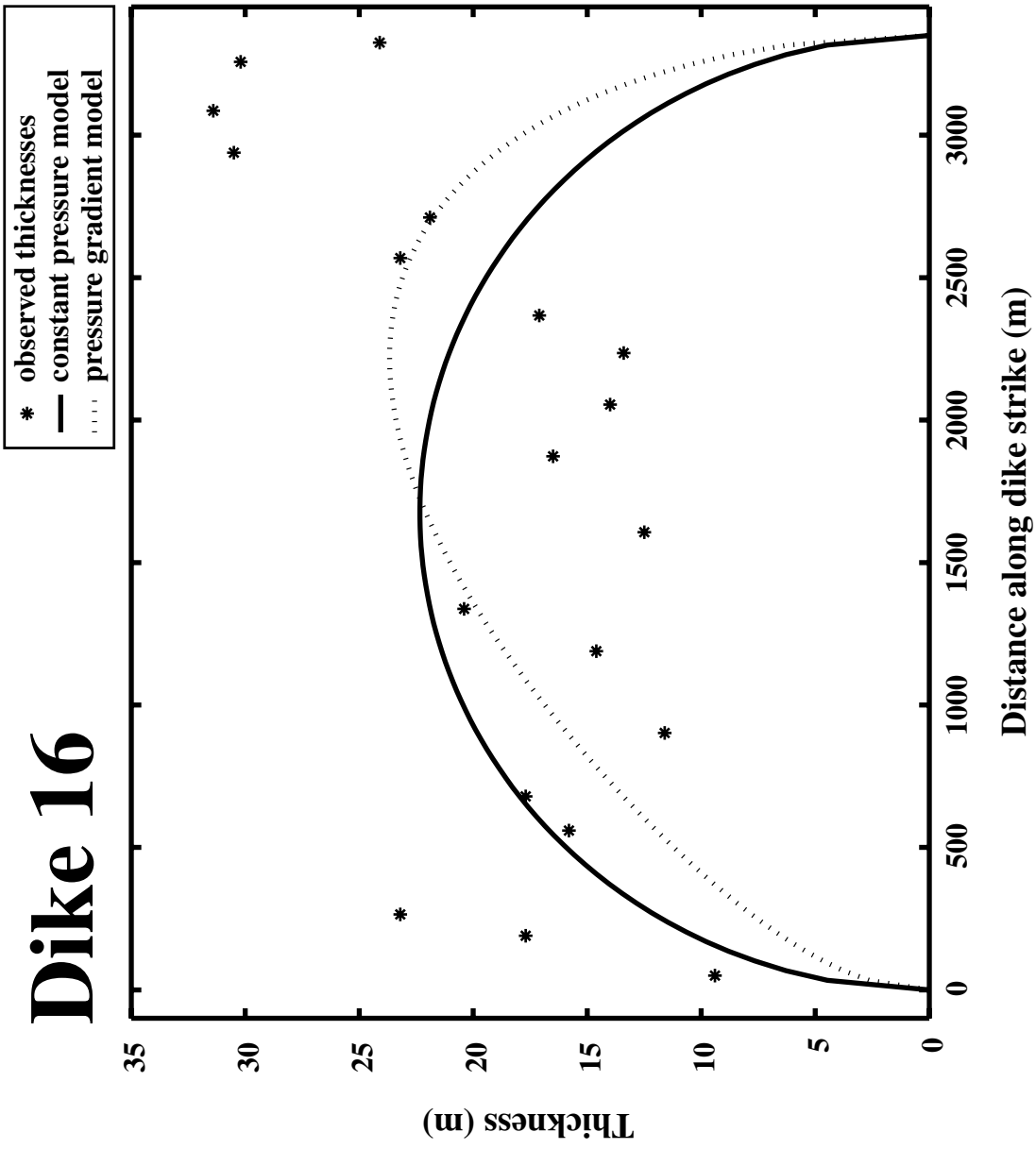
Dike 16
observed thicknesses
constant pressure model
pressure gradient model
Thickness (m)
Distance along dike strike (m)
0
5
10
15
20
25
30
35
0
500
1000
1500
2000
2500
3000

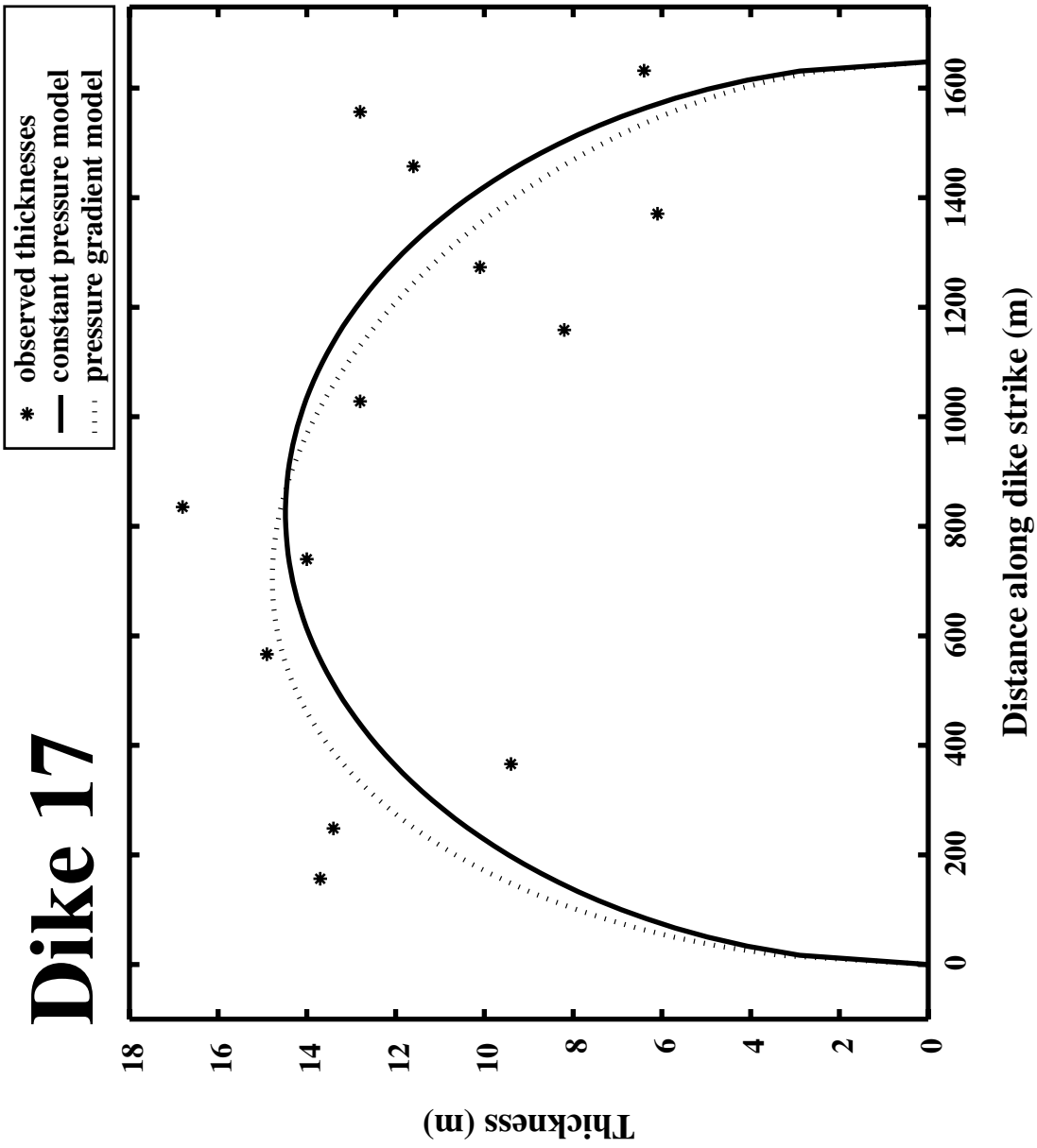
Dike 17
observed thicknesses
constant pressure model
pressure gradient model
Thickness (m)
0
2
4
6
8
10
12
14
16
18
0
200
400
600
800
1000
1200
1400
1600
Distance along dike strike (m)

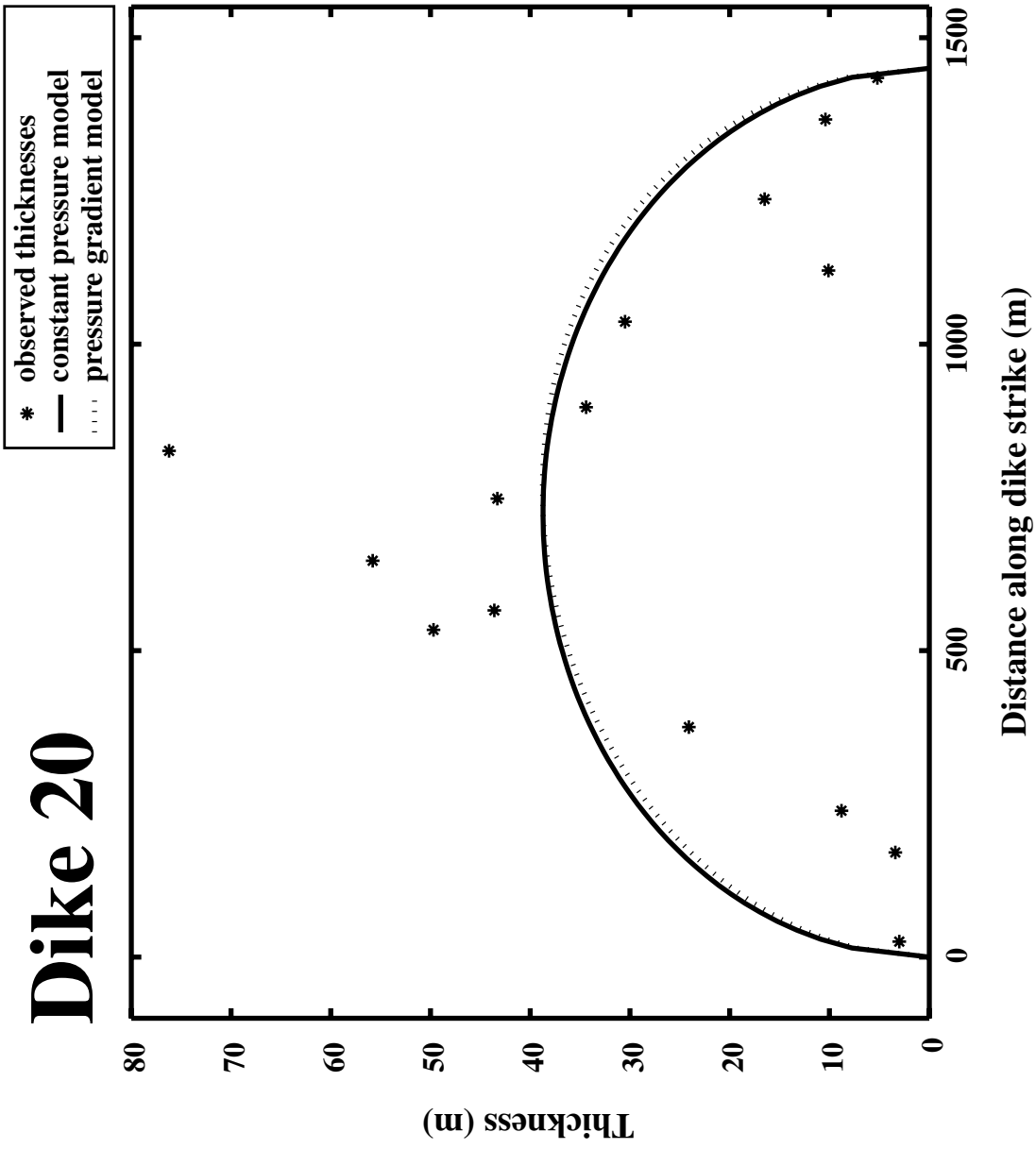
Dike 20
observed thicknesses
constant pressure model
pressure gradient model
Thickness (m)
0
10
20
30
40
50
60
70
80
0
500
1000
1500
Distance along dike strike (m)

APPENDIX C

ANISOTROPY OF MAGNETIC SUSCEPTIBILITY MEASUREMENTS (EIGENVECTORS AND EIGENVALUES) FOR INDIVIDUAL SAMPLES COLLECTED AT SUMMER COON VOLCANO

SITE 3-1

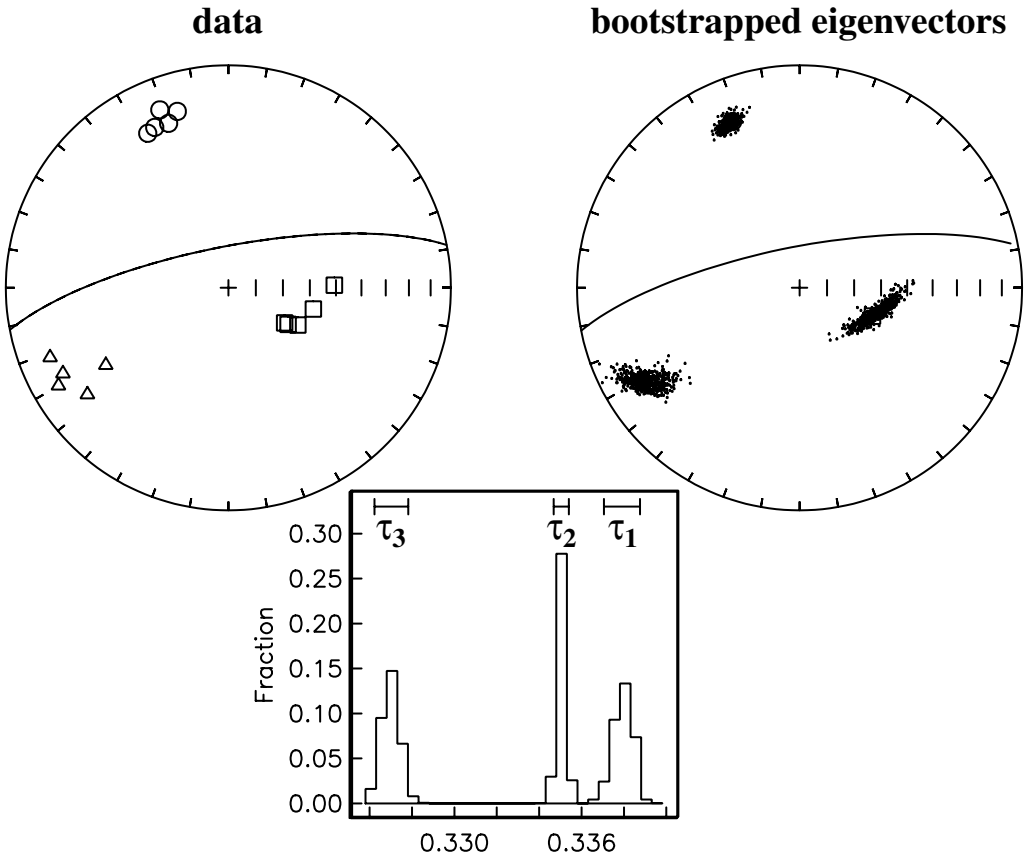

histogram of bootstrapped eigenvalues

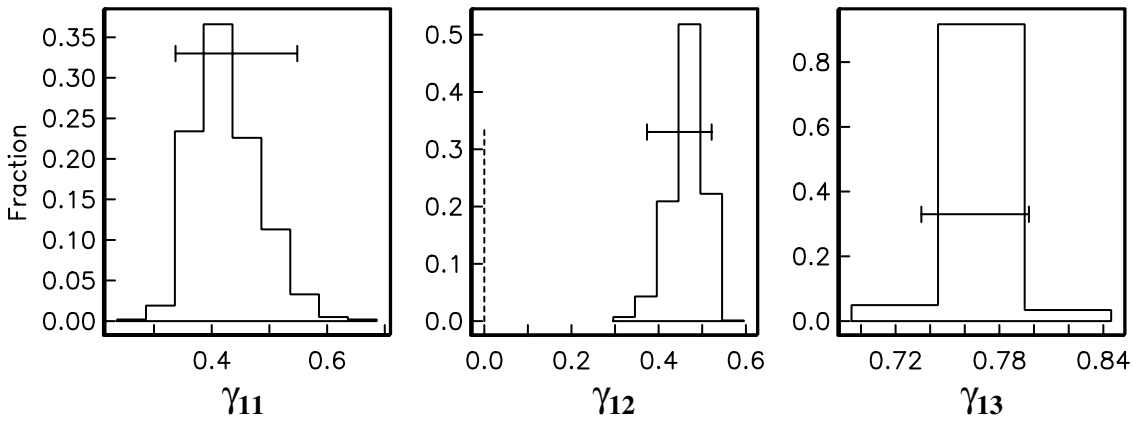

histograms of bootstrapped eigenvectors rotated into dike coordinates (γ_{12} = 0 is dike plane)

SITE 3-2

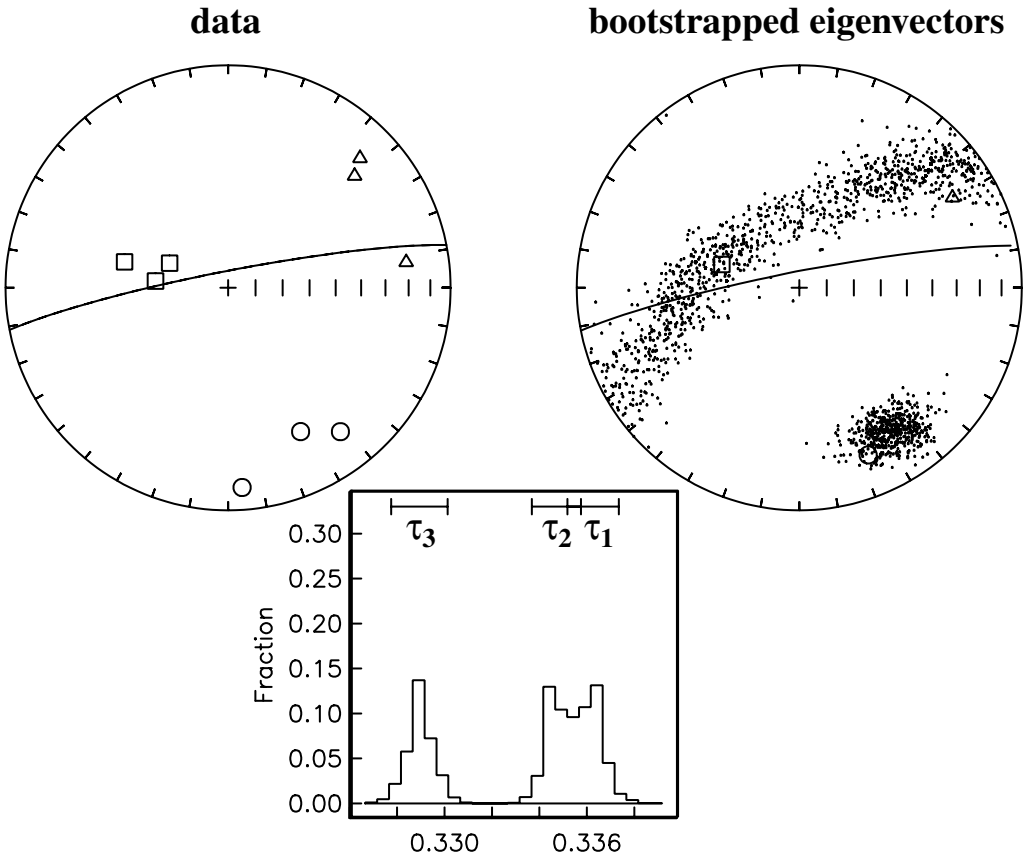

histogram of bootstrapped eigenvalues

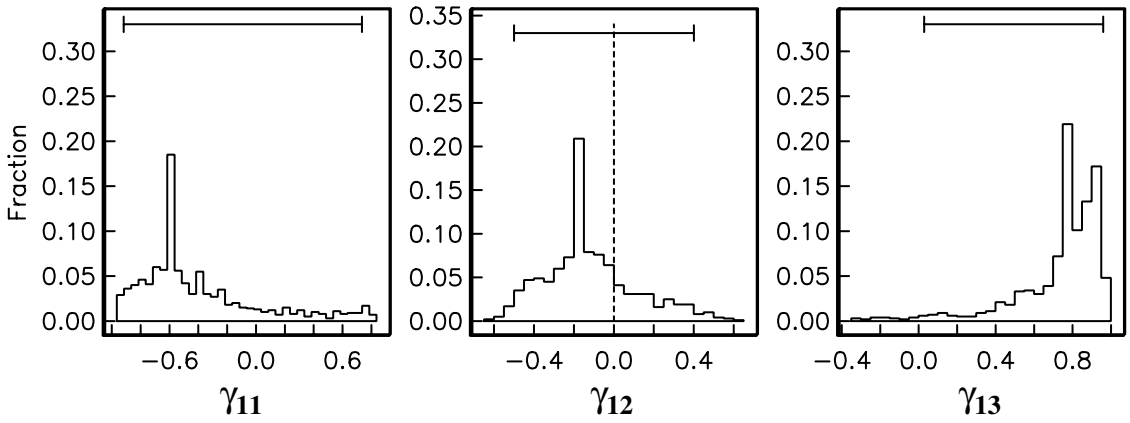

histograms of bootstrapped eigenvectors rotated into dike coordinates (γ_{12} = 0 is dike plane)

SITE 3-3

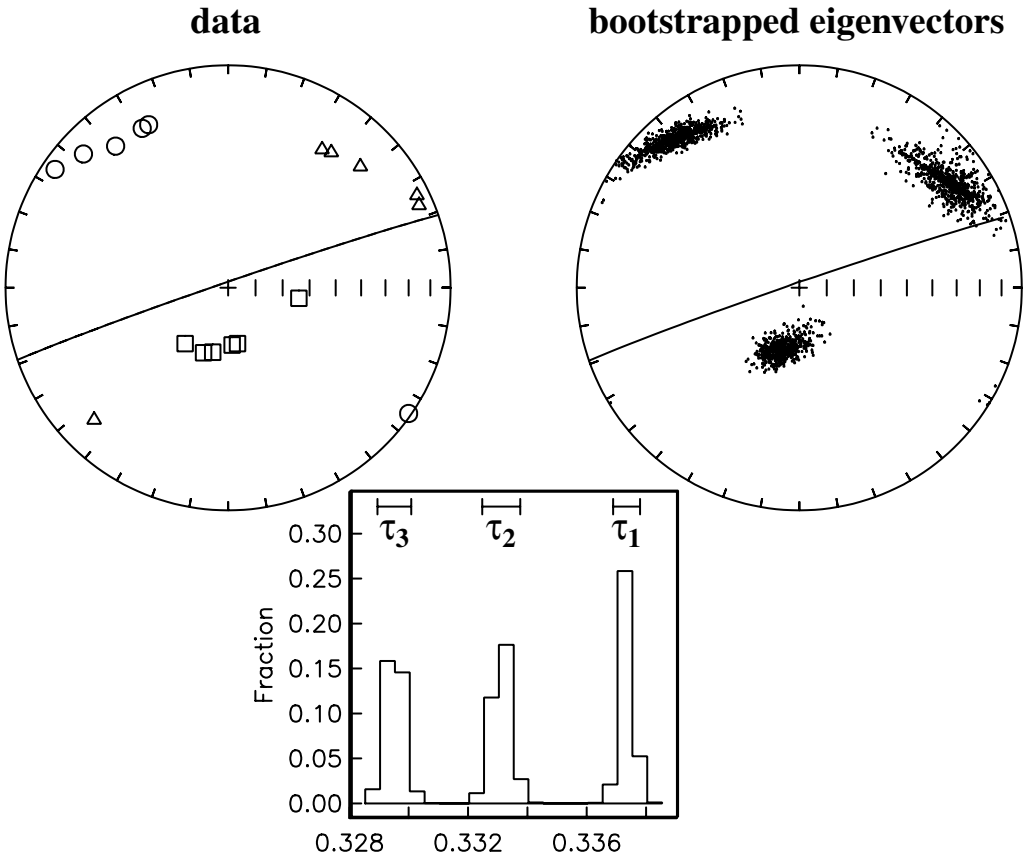

histogram of bootstrapped eigenvalues

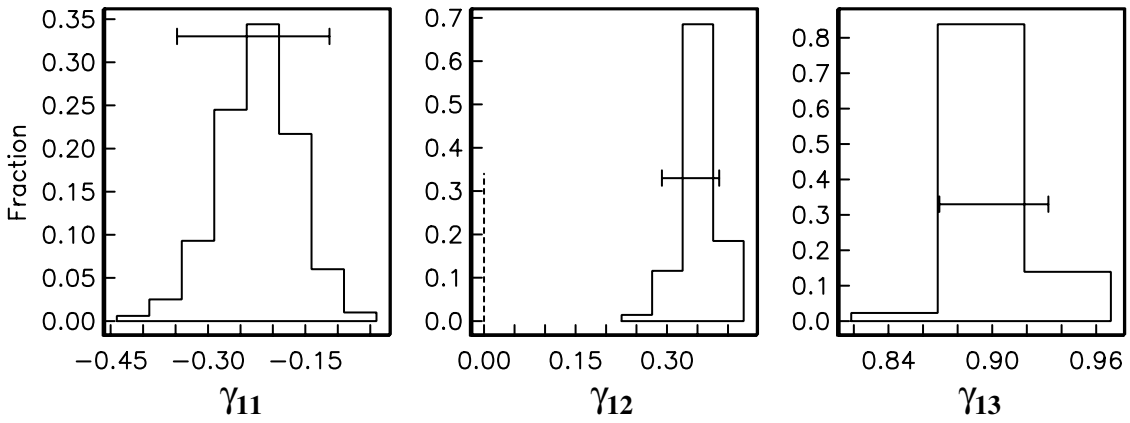

histograms of bootstrapped eigenvectors rotated into dike coordinates (γ_{12} = 0 is dike plane)

SITE 3-4

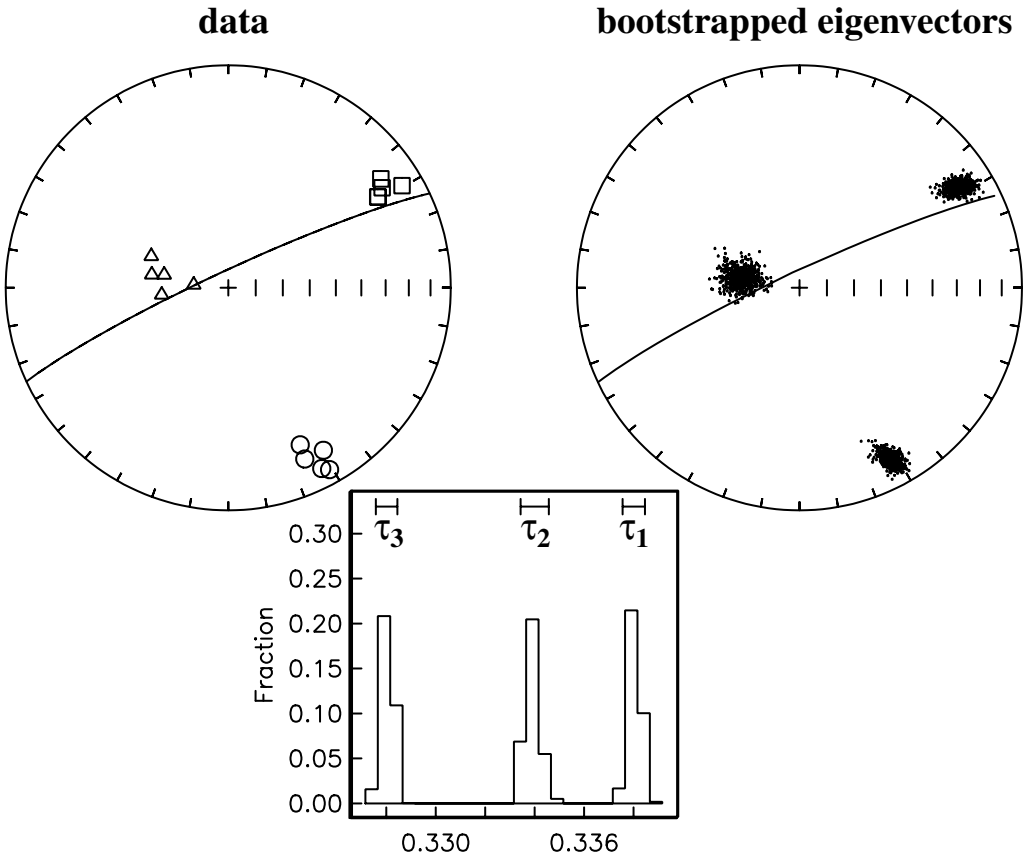

histogram of bootstrapped eigenvalues

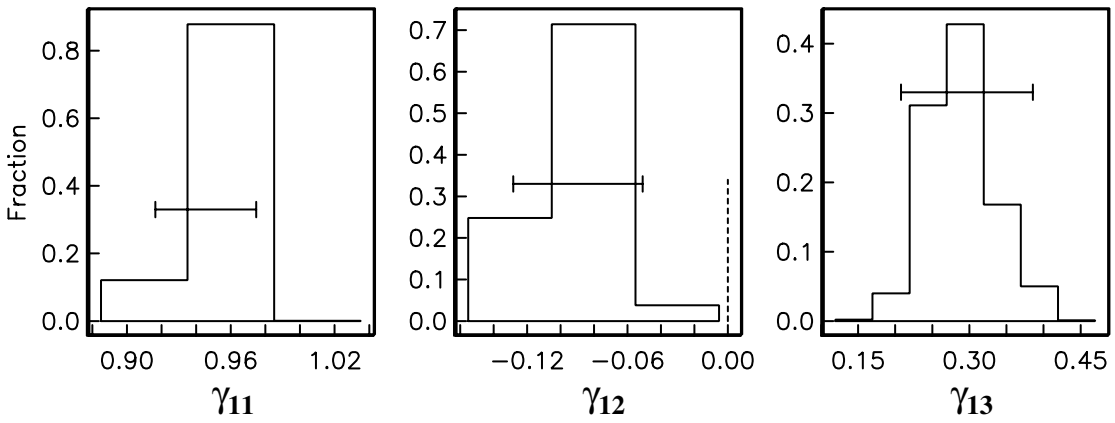

histograms of bootstrapped eigenvectors rotated into dike coordinates (γ_{12} = 0 is dike plane)

SITE 3-5

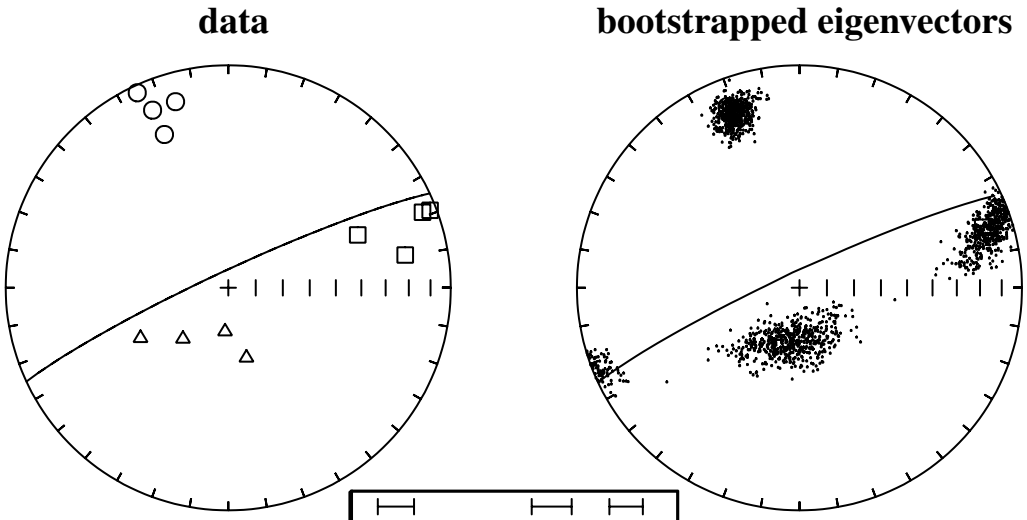

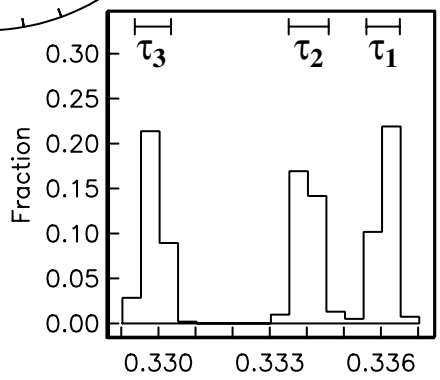

histogram of bootstrapped eigenvalues

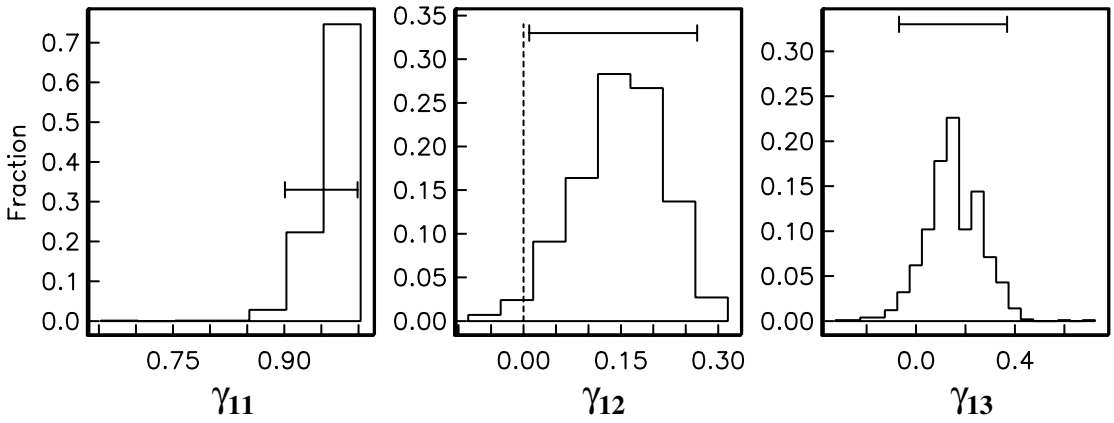

histograms of bootstrapped eigenvectors rotated into dike coordinates (γ_{12} = 0 is dike plane)

SITE 3-6

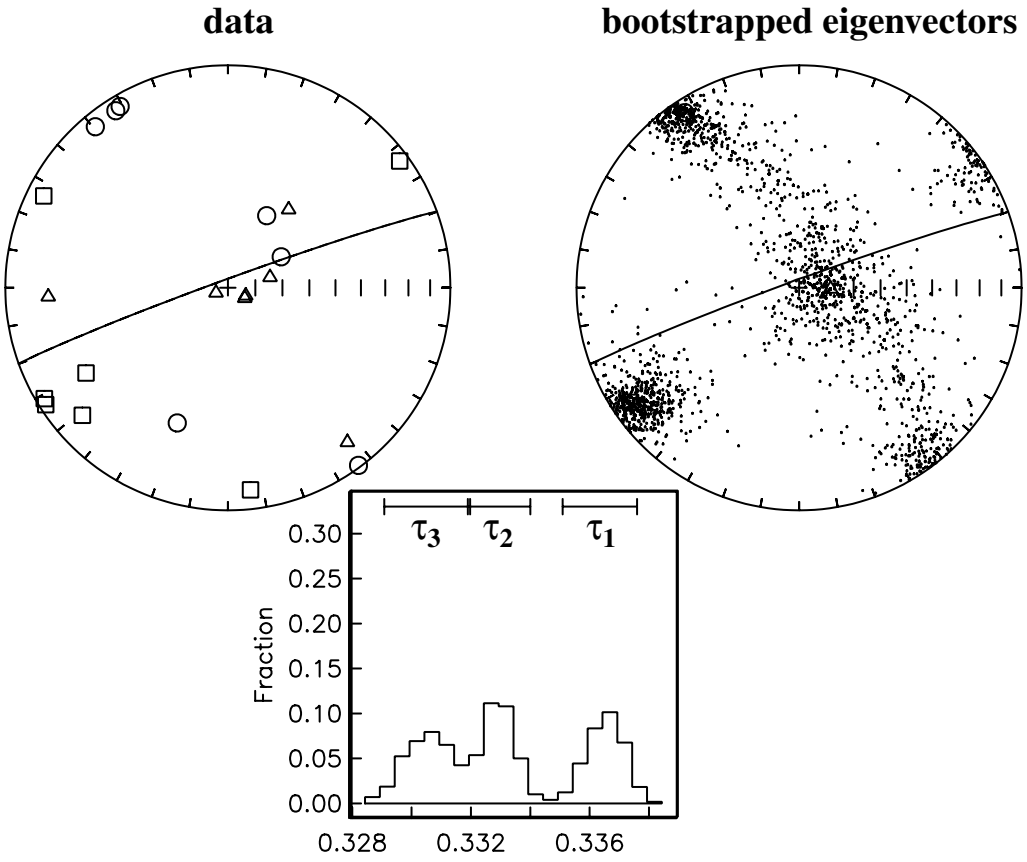

histogram of bootstrapped eigenvalues

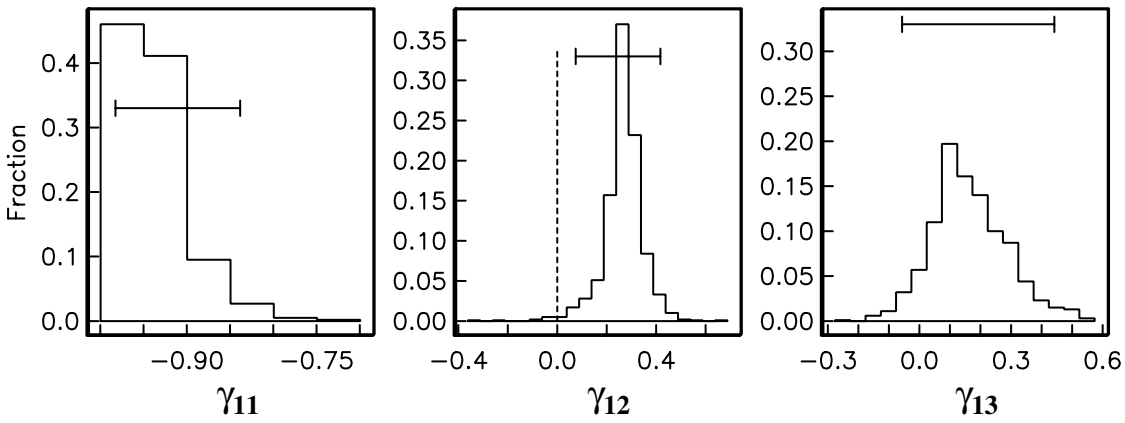

histograms of bootstrapped eigenvectors rotated into dike coordinates (γ_{12} = 0 is dike plane)

SITE 3-7

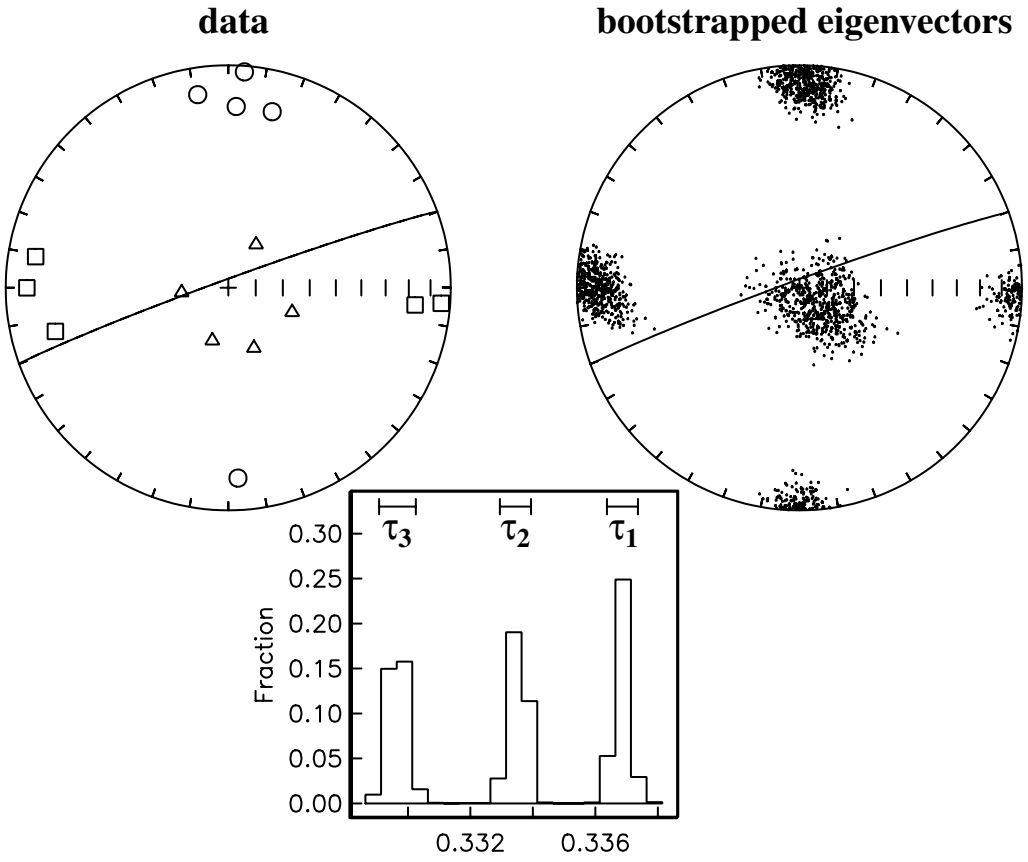

histogram of bootstrapped eigenvalues

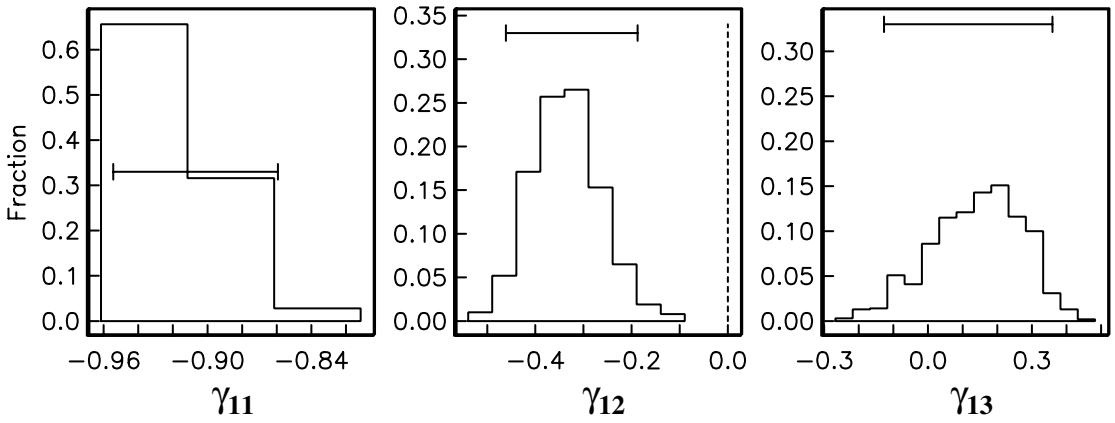

histograms of bootstrapped eigenvectors rotated into dike coordinates (γ_{12} = 0 is dike plane)

SITE 3-8

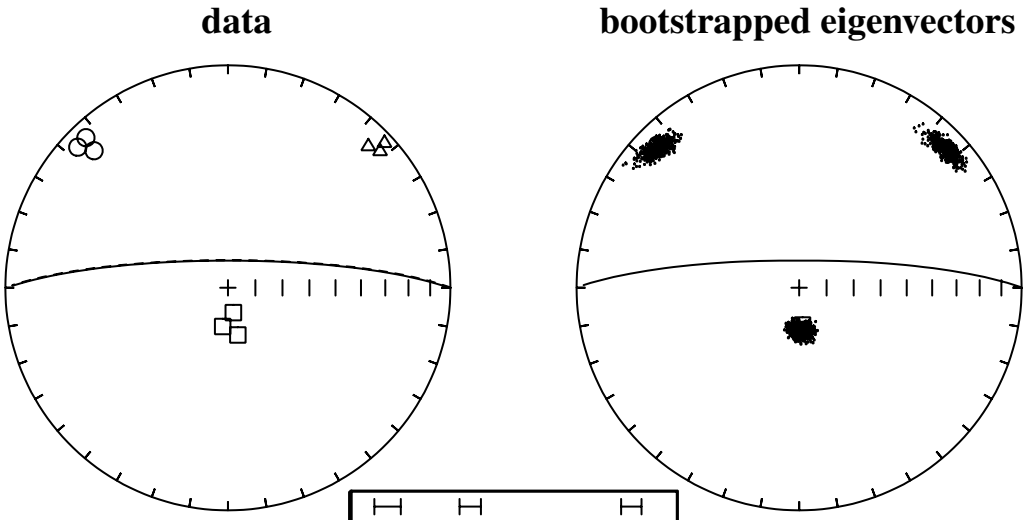

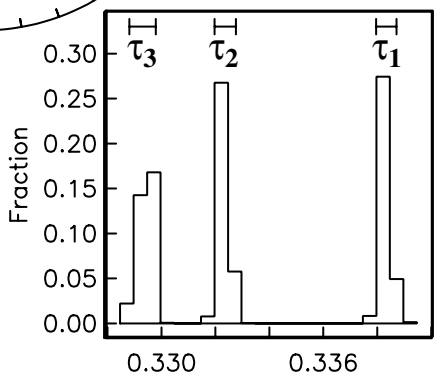

histogram of bootstrapped eigenvalues

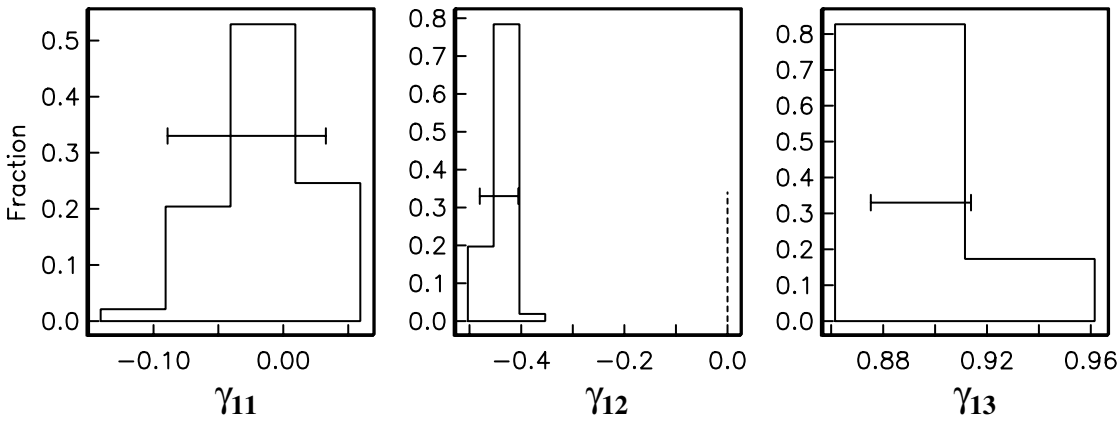

histograms of bootstrapped eigenvectors rotated into dike coordinates (γ_{12} = 0 is dike plane)

SITE 3-9

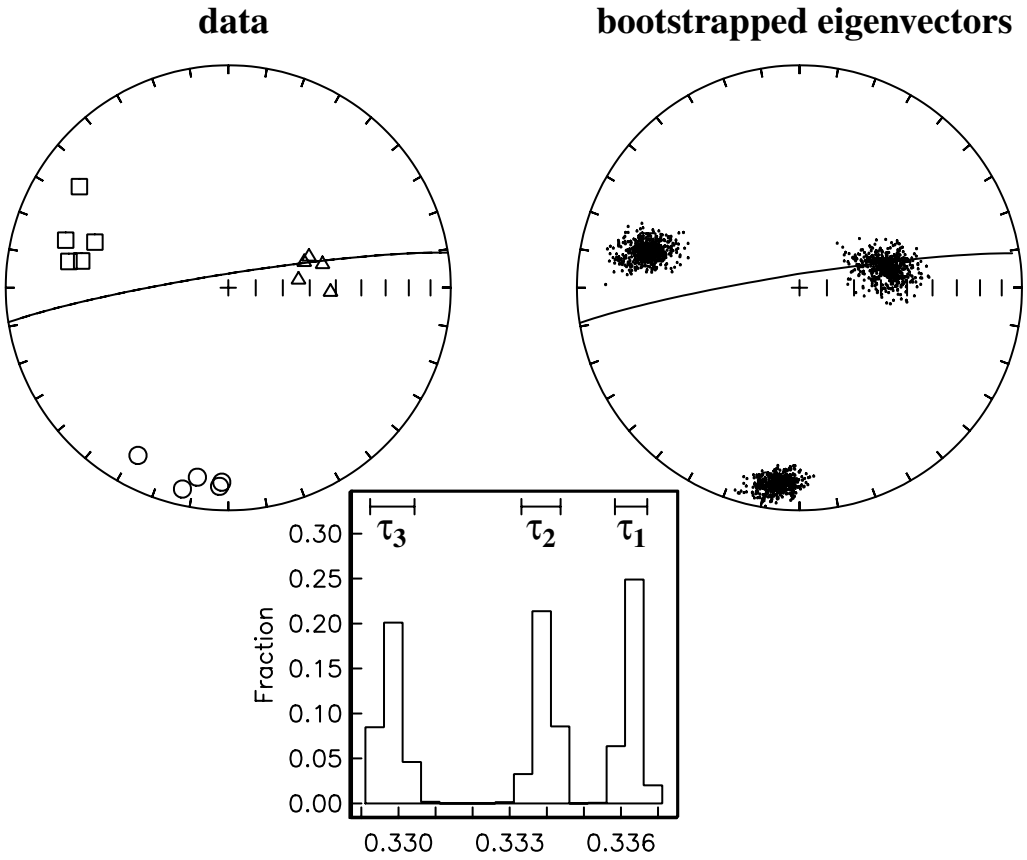

histogram of bootstrapped eigenvalues

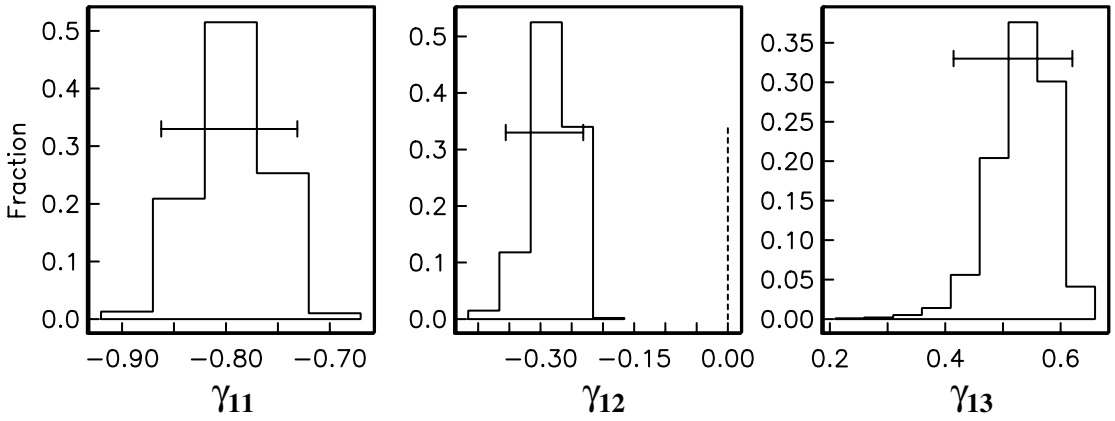

histograms of bootstrapped eigenvectors rotated into dike coordinates (γ_{12} = 0 is dike plane)

SITE 3-10

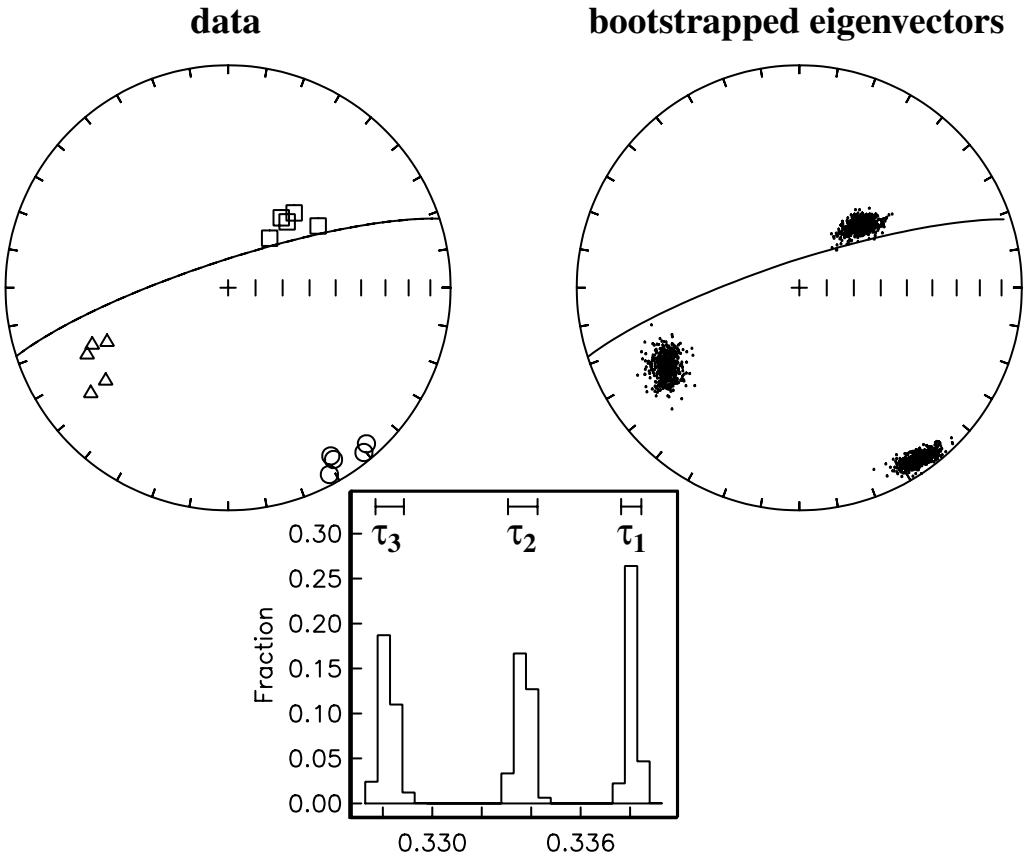

histogram of bootstrapped eigenvalues

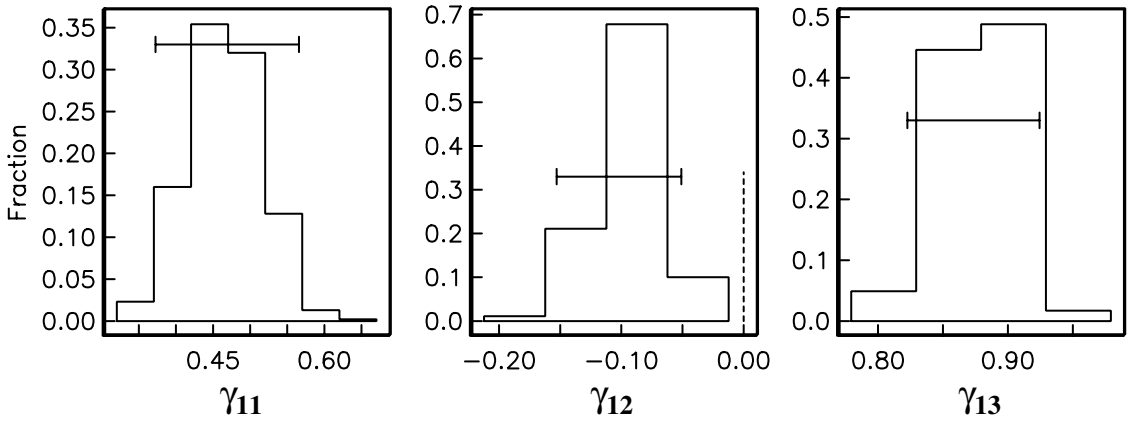

histograms of bootstrapped eigenvectors rotated into dike coordinates (γ_{12} = 0 is dike plane)

SITE 3-11

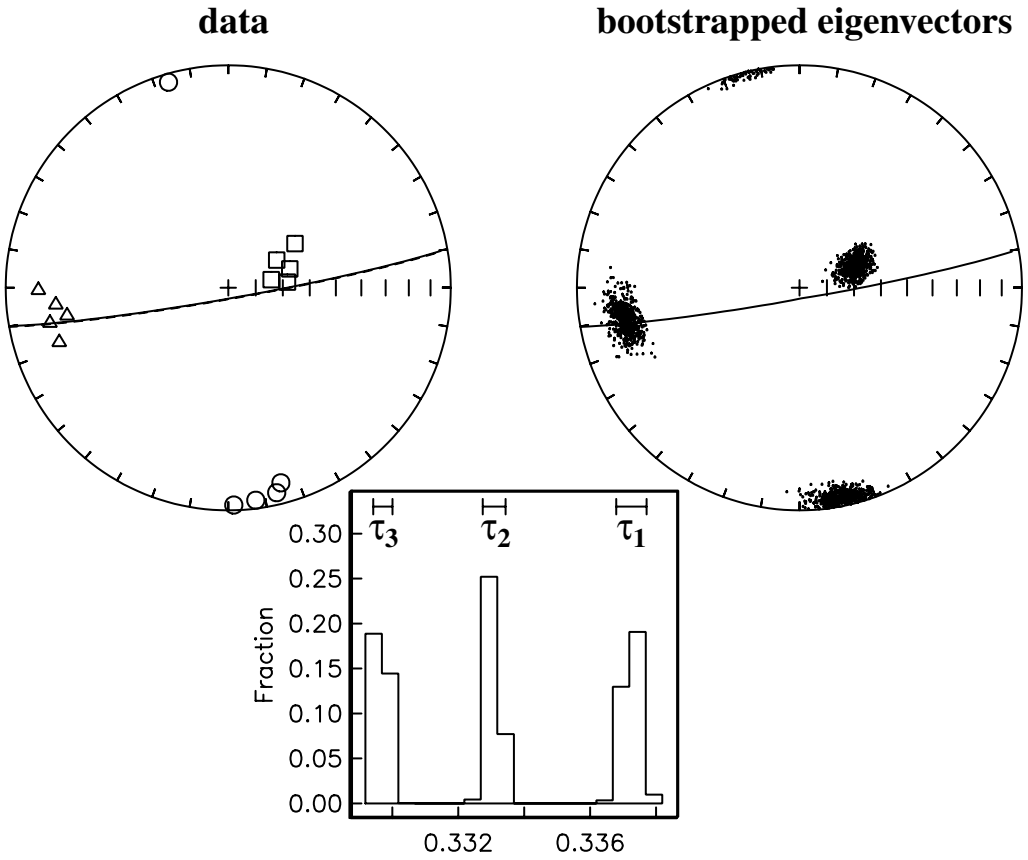

histogram of bootstrapped eigenvalues

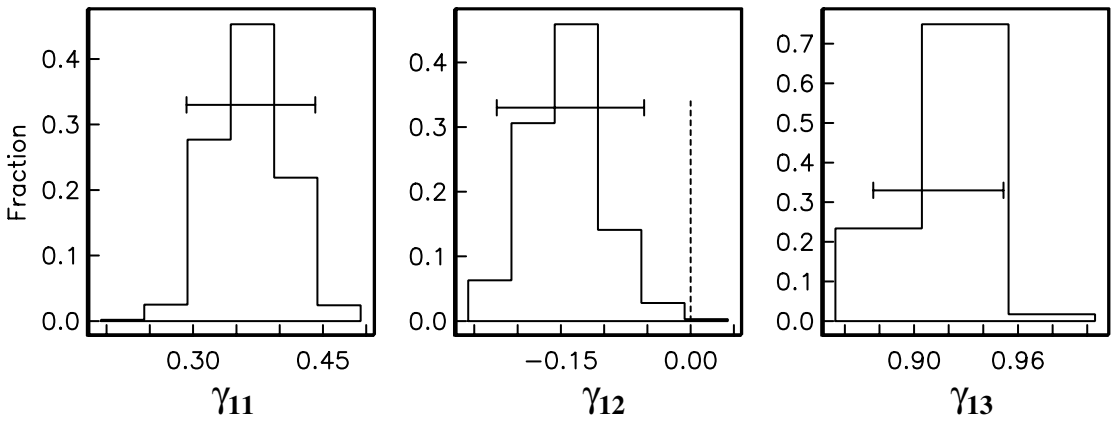

histograms of bootstrapped eigenvectors rotated into dike coordinates (γ_{12} = 0 is dike plane)

SITE 3-12

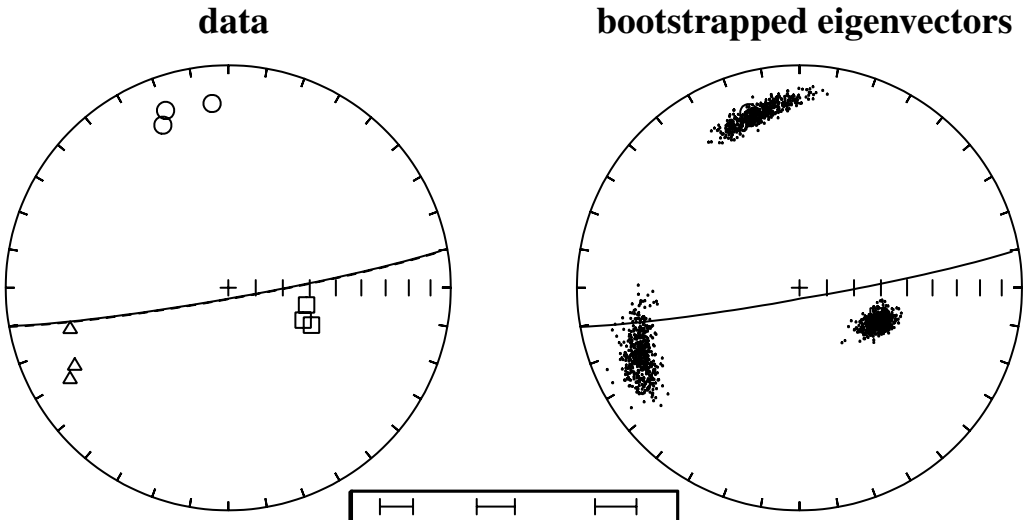

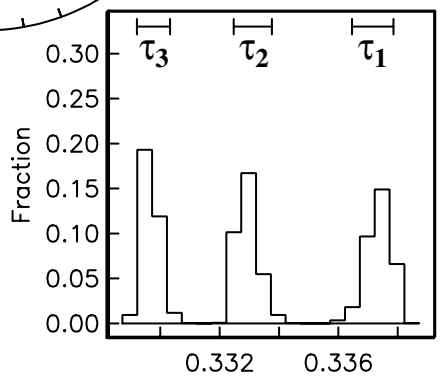

histogram of bootstrapped eigenvalues

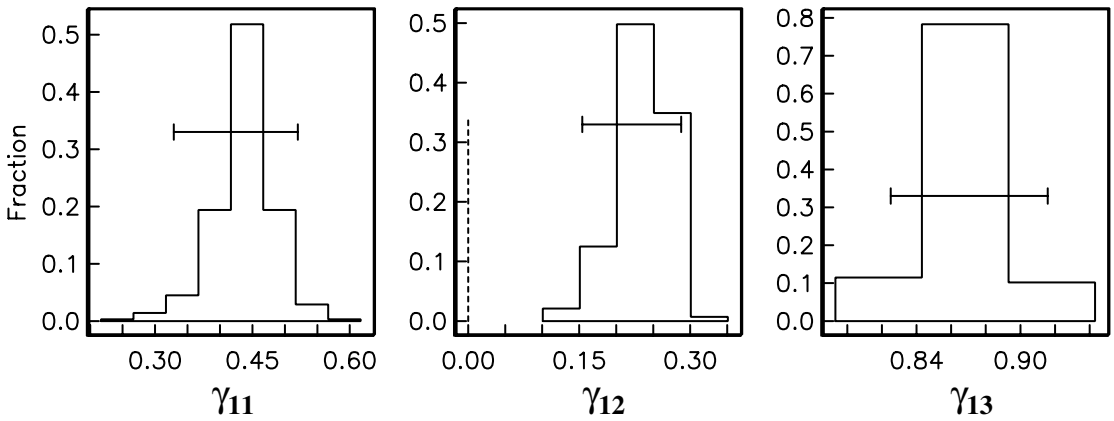

histograms of bootstrapped eigenvectors rotated into dike coordinates (γ_{12} = 0 is dike plane)

SITE 3-13

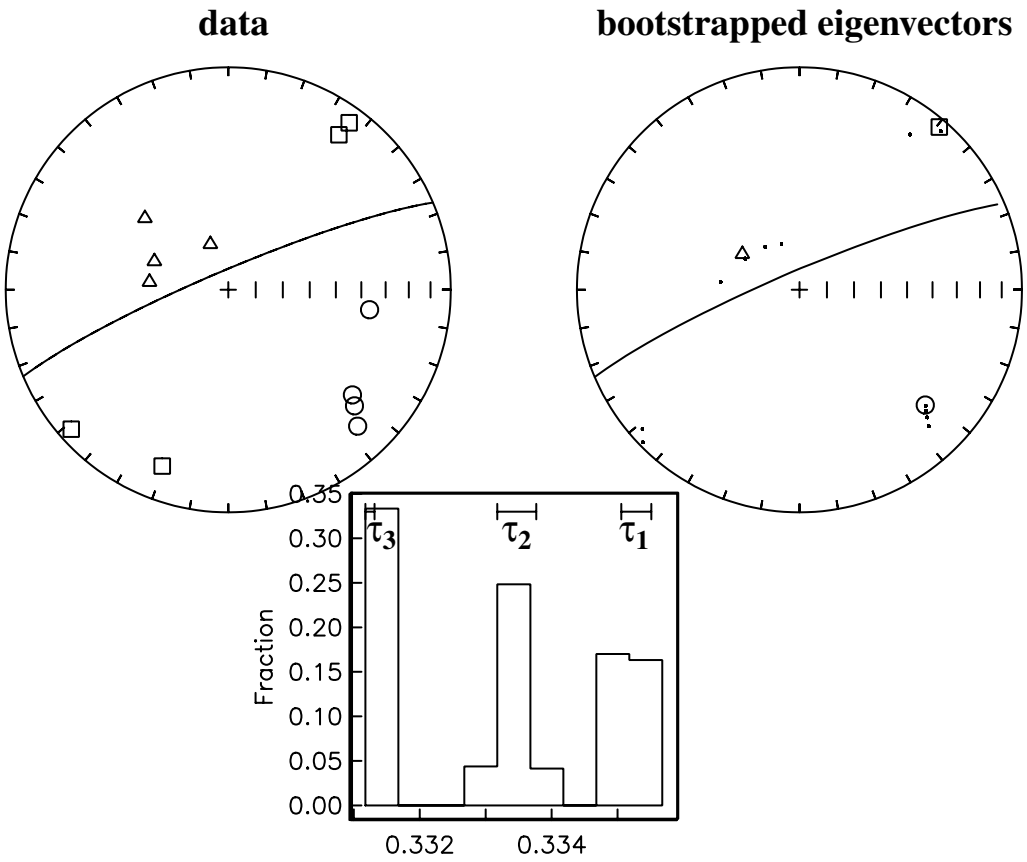

histogram of bootstrapped eigenvalues

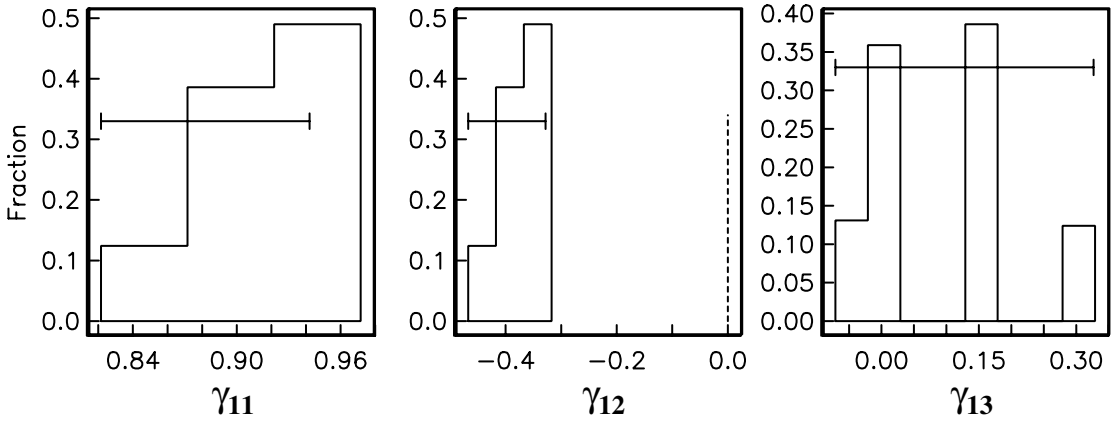

histograms of bootstrapped eigenvectors rotated into dike coordinates (γ_{12} = 0 is dike plane)

SITE 3-14

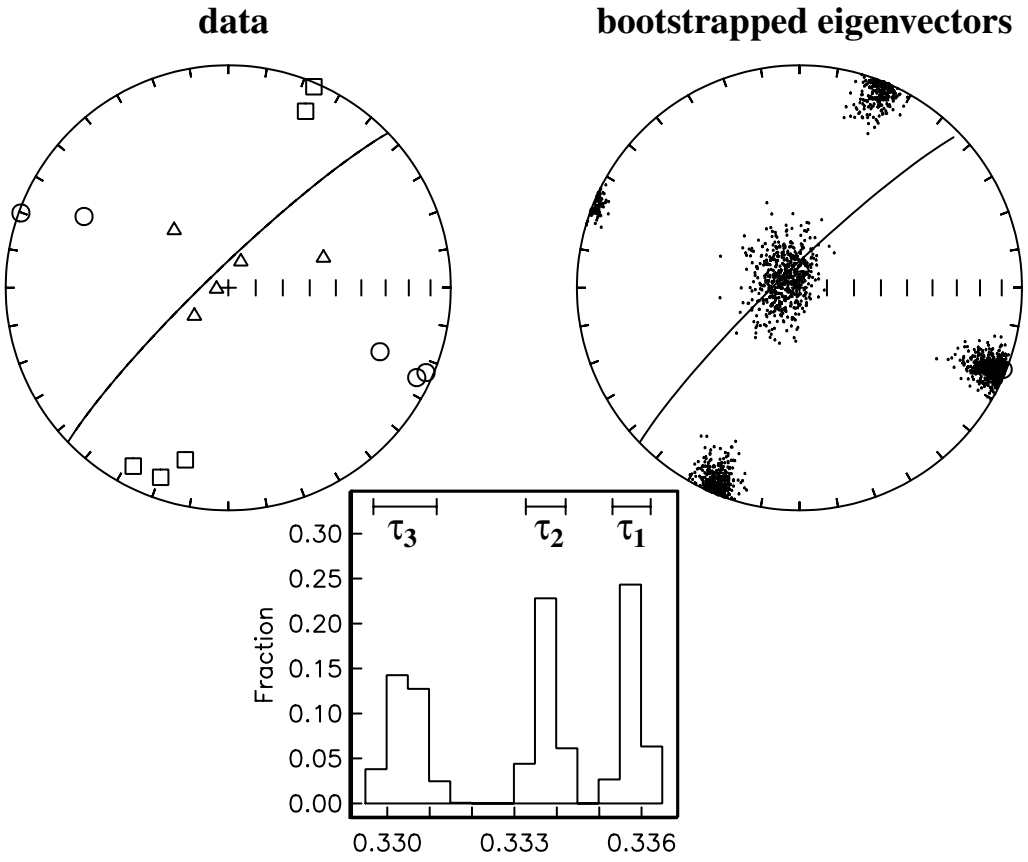

histogram of bootstrapped eigenvalues

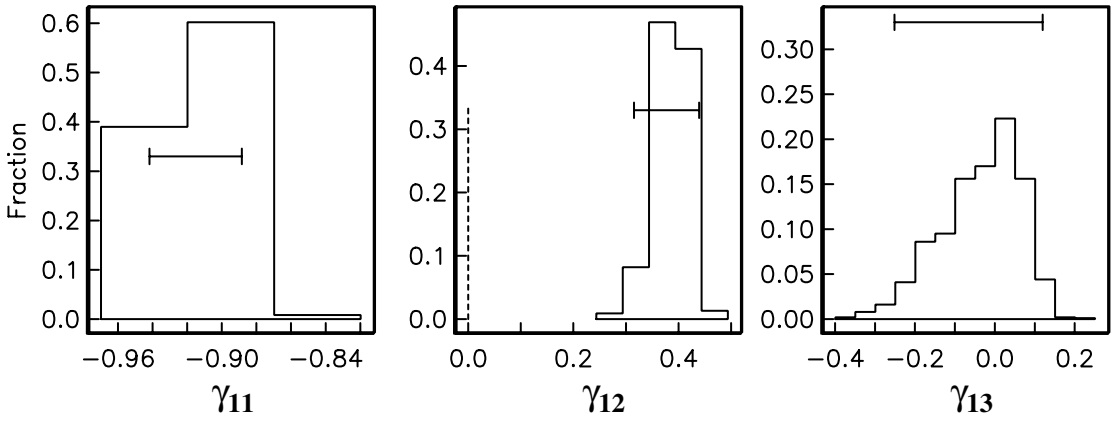

histograms of bootstrapped eigenvectors rotated into dike coordinates (γ_{12} = 0 is dike plane)

SITE 3-15

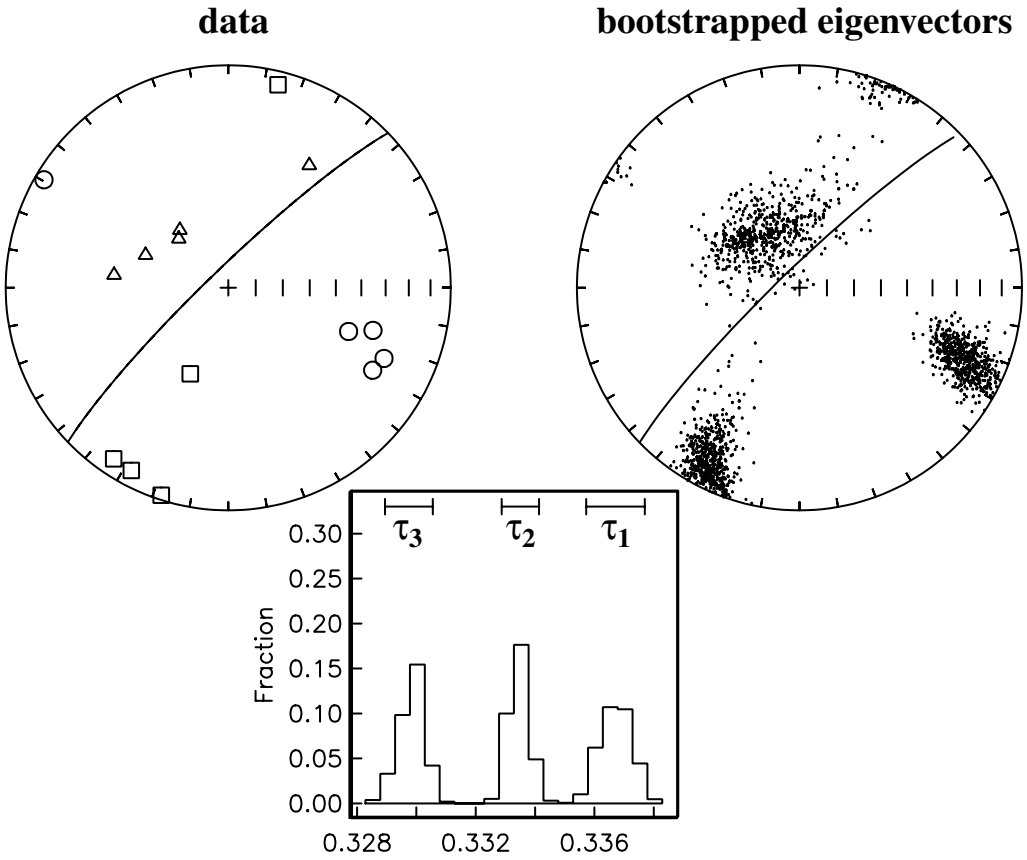

histogram of bootstrapped eigenvalues

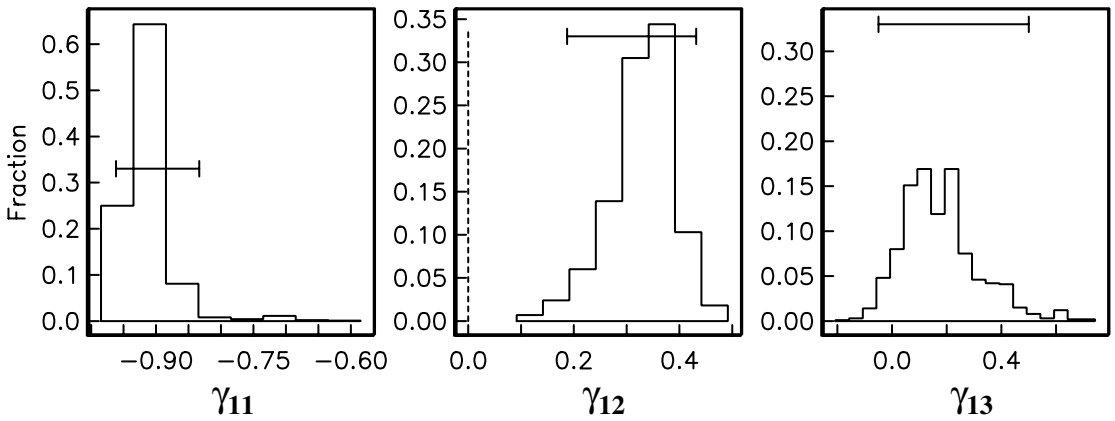

histograms of bootstrapped eigenvectors rotated into dike coordinates (γ_{12} = 0 is dike plane)

SITE 3-16

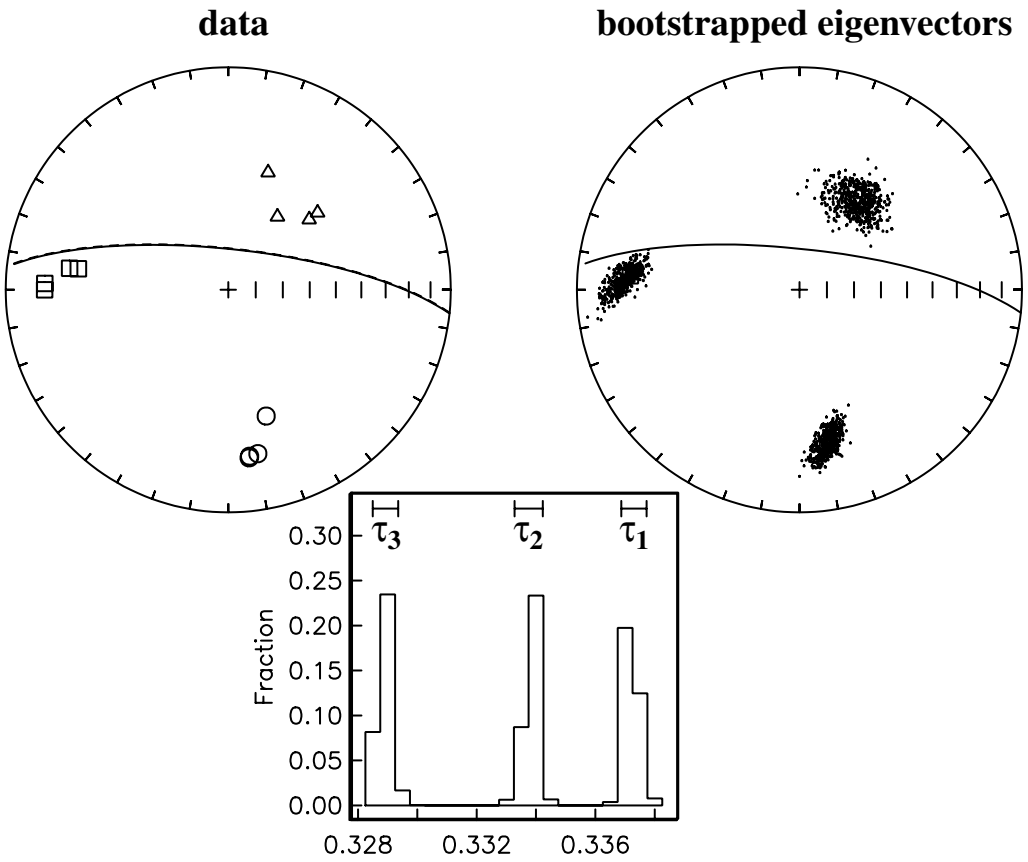

histogram of bootstrapped eigenvalues

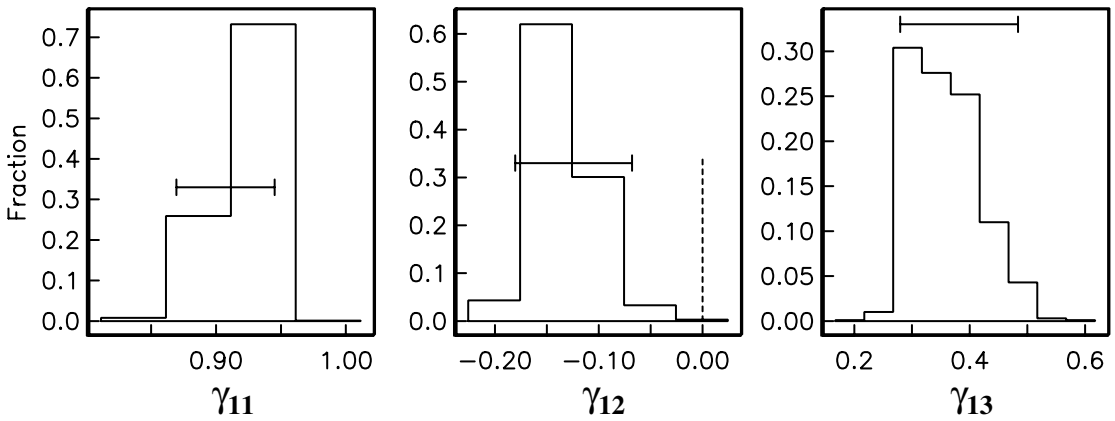

histograms of bootstrapped eigenvectors rotated into dike coordinates (γ_{12} = 0 is dike plane)

SITE 3-17

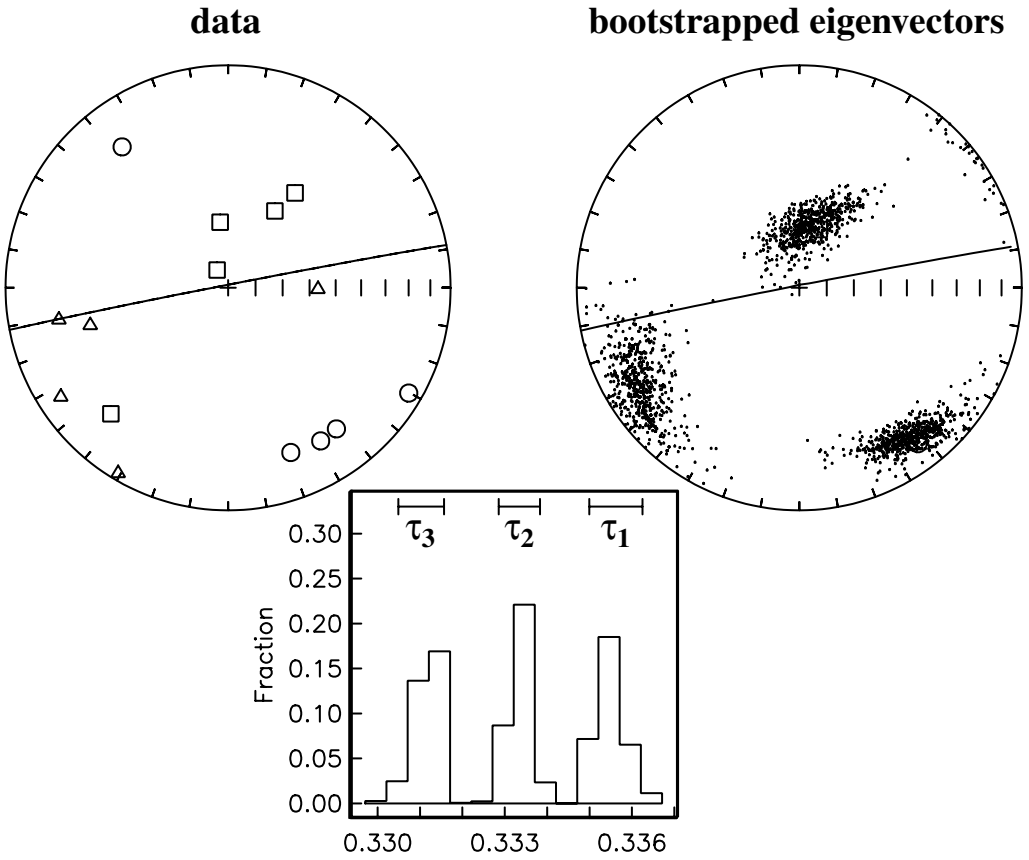

histogram of bootstrapped eigenvalues

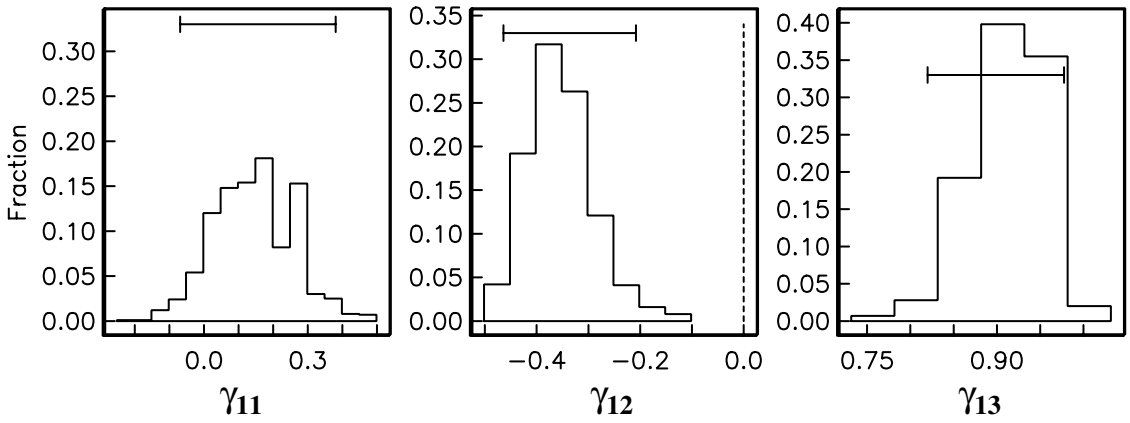

histograms of bootstrapped eigenvectors rotated into dike coordinates (γ_{12} = 0 is dike plane)

SITE 3-18

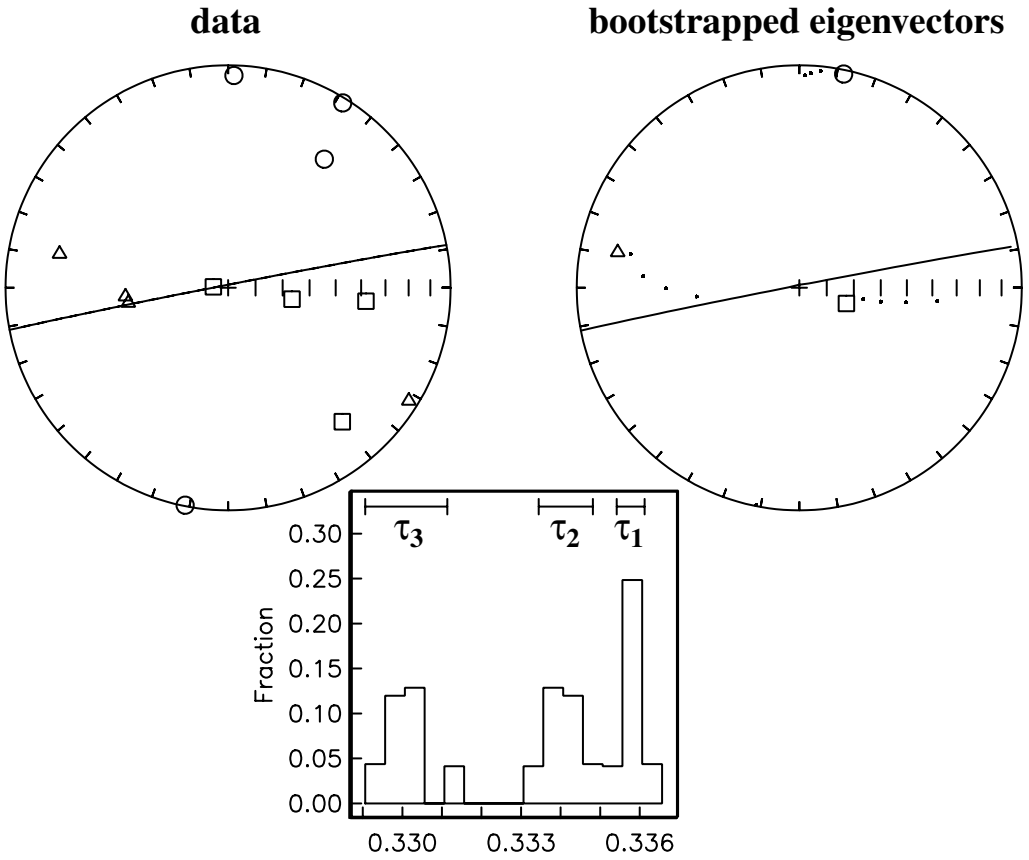

histogram of bootstrapped eigenvalues

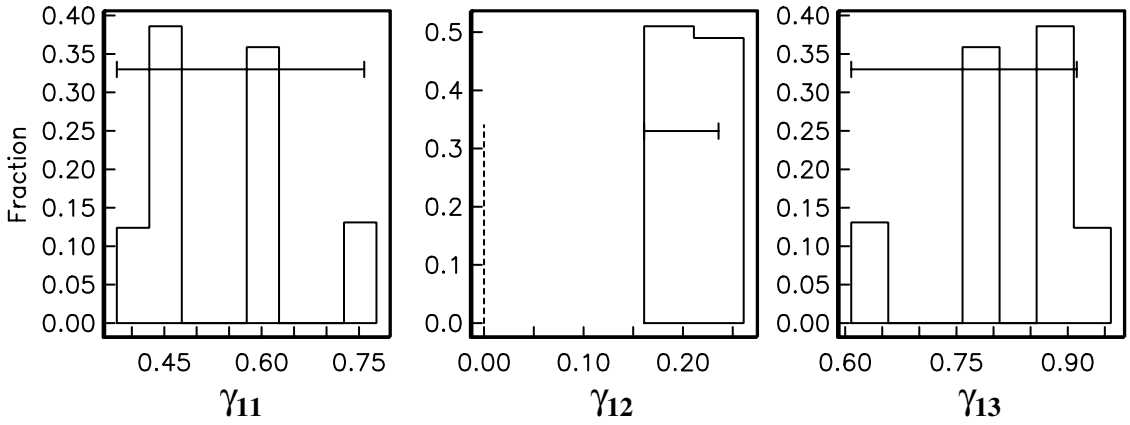

histograms of bootstrapped eigenvectors rotated into dike coordinates (γ_{12} = 0 is dike plane)

SITE 8-1

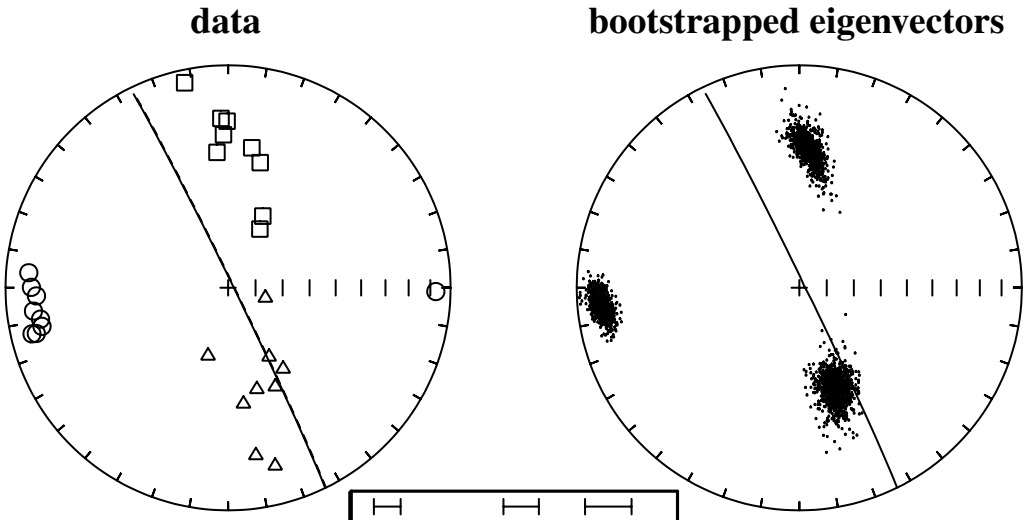

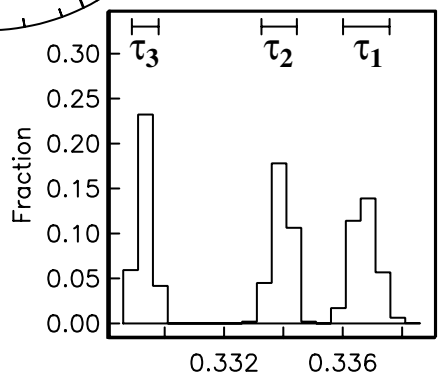

histogram of bootstrapped eigenvalues

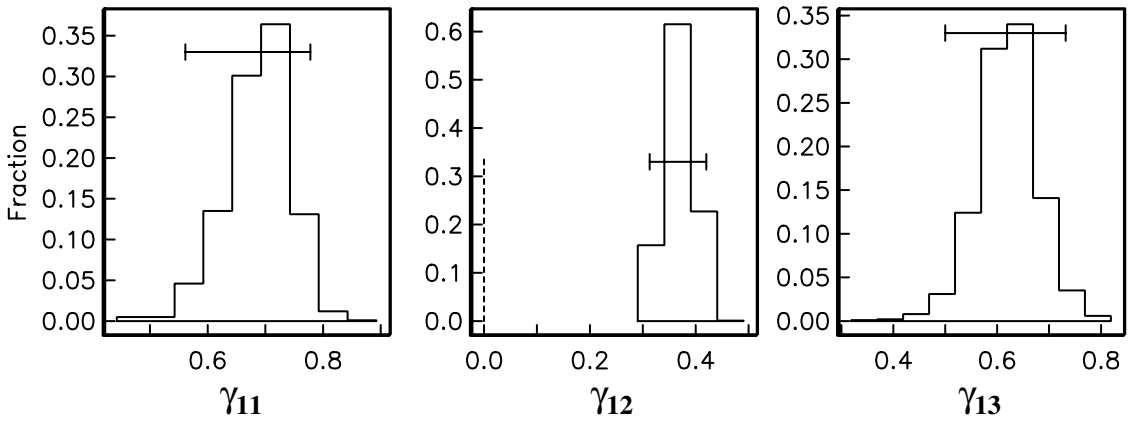

histograms of bootstrapped eigenvectors rotated into dike coordinates (γ_{12} = 0 is dike plane)

SITE 8-2

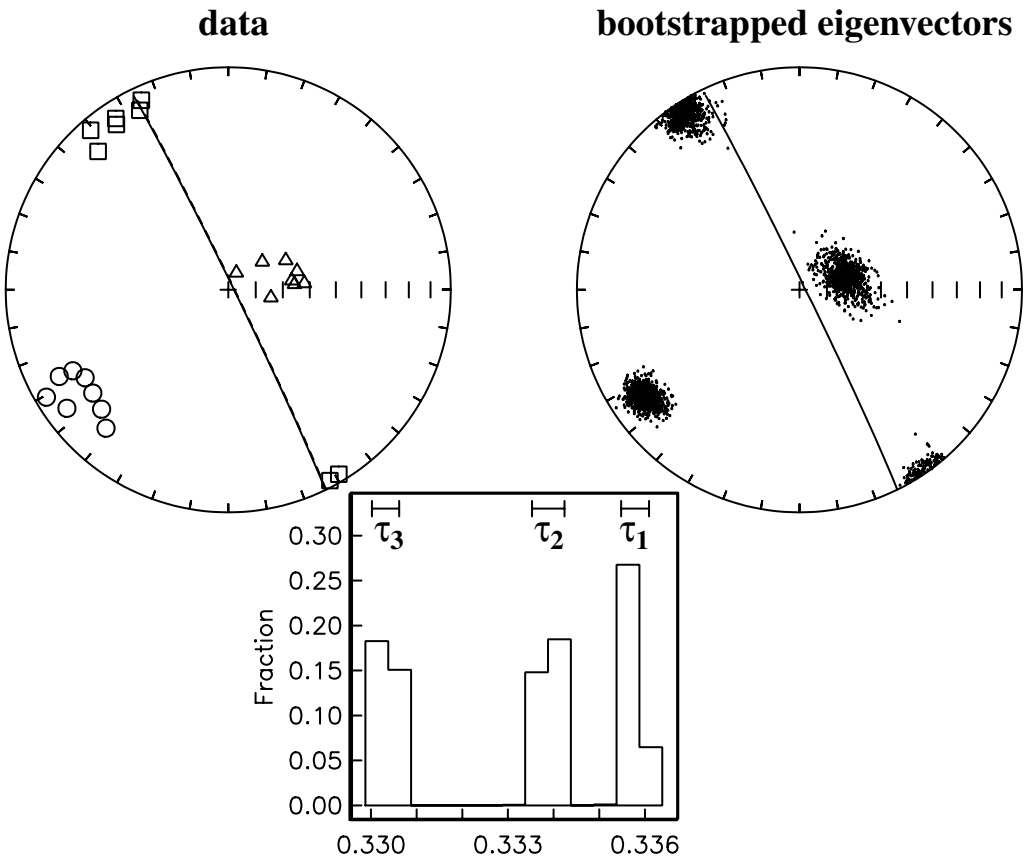

histogram of bootstrapped eigenvalues

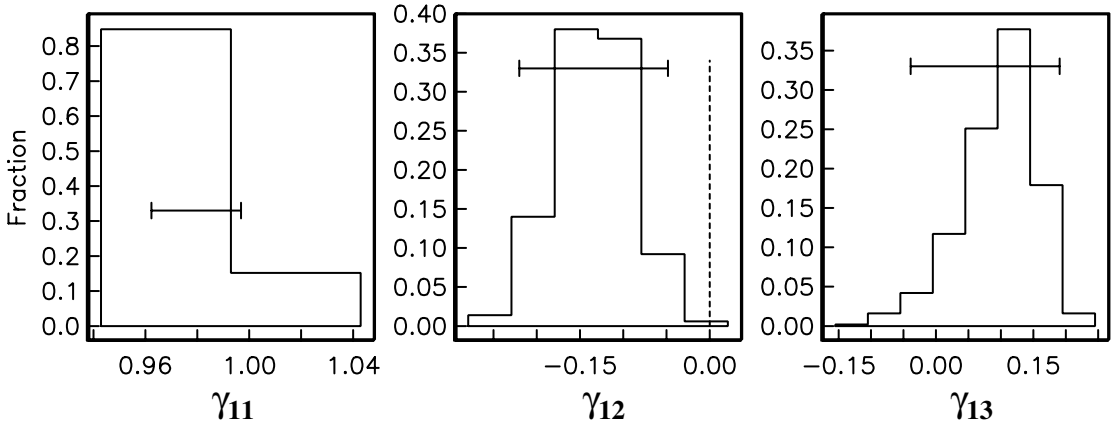

histograms of bootstrapped eigenvectors rotated into dike coordinates (γ_{12} = 0 is dike plane)

SITE 8-3

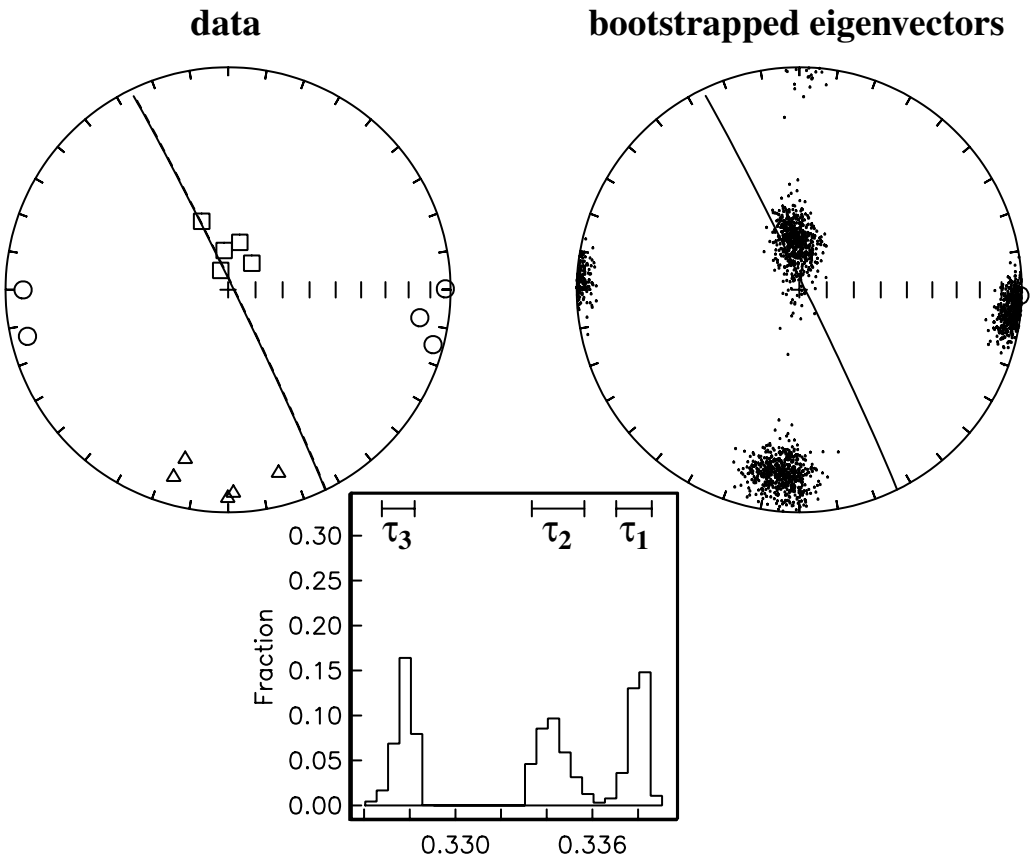

histogram of bootstrapped eigenvalues

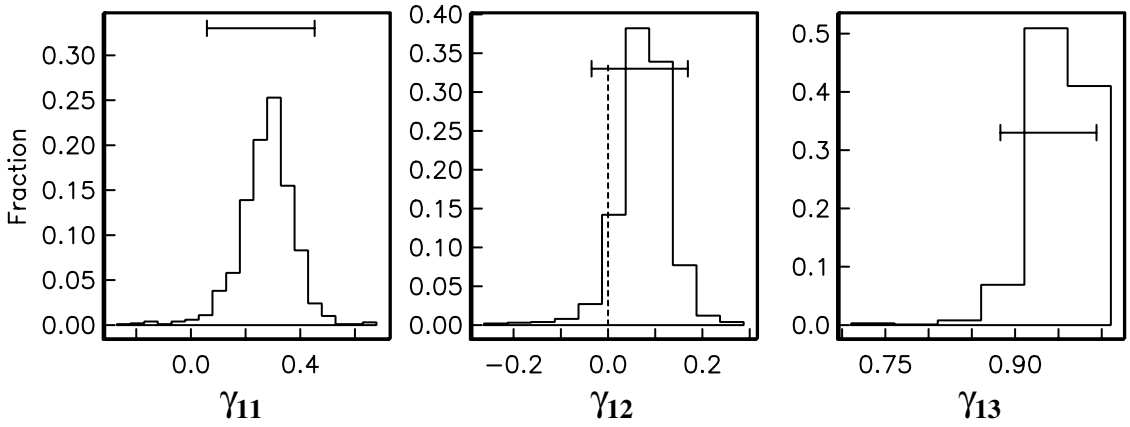

histograms of bootstrapped eigenvectors rotated into dike coordinates (γ_{12} = 0 is dike plane)

SITE 8-4

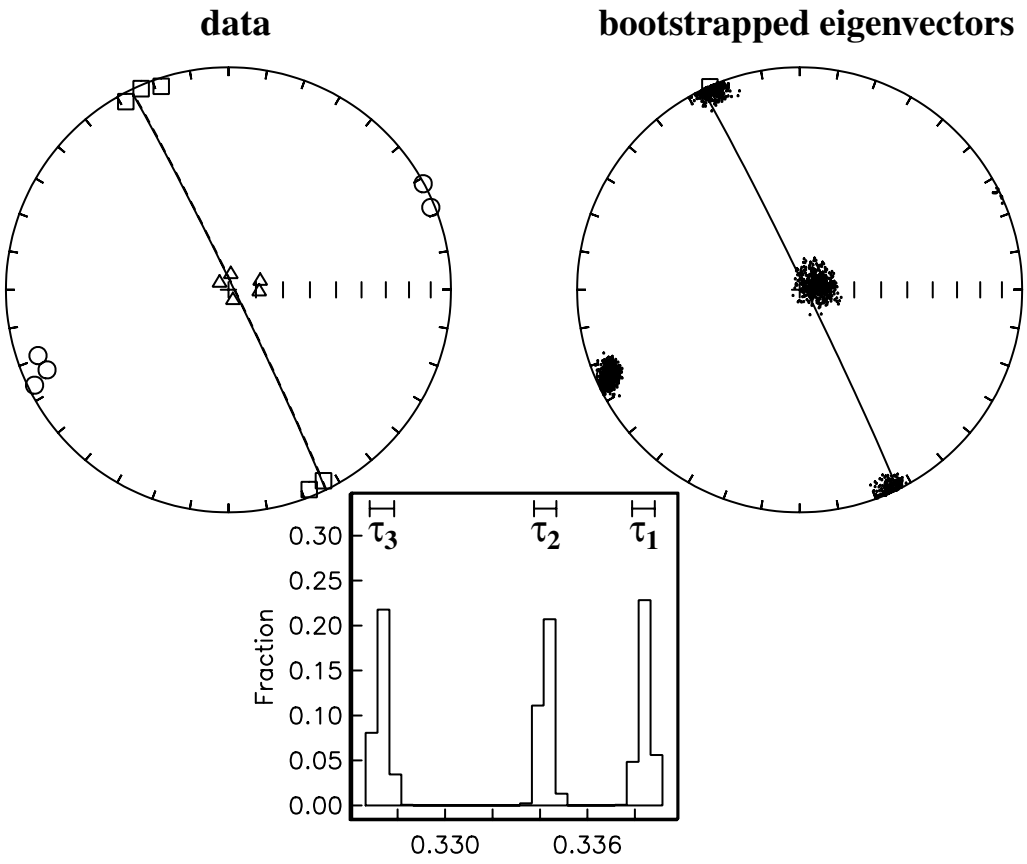

histogram of bootstrapped eigenvalues

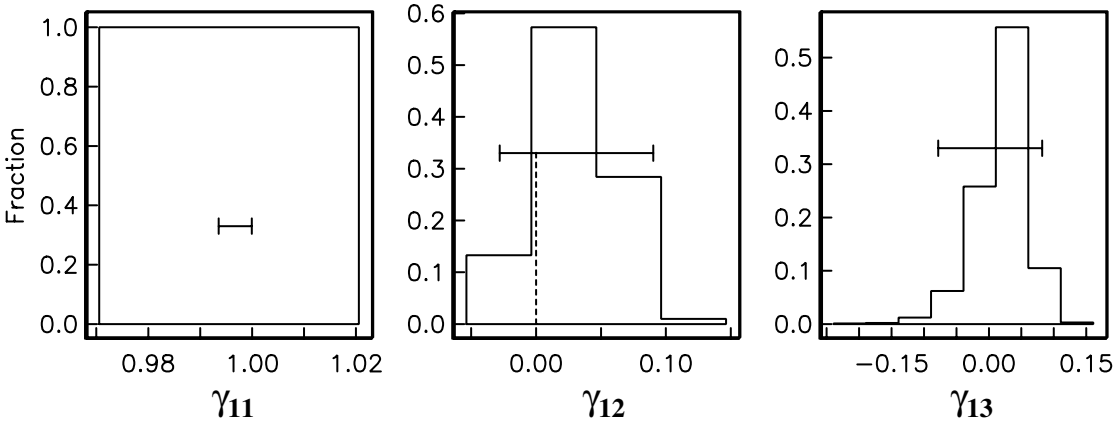

histograms of bootstrapped eigenvectors rotated into dike coordinates (γ_{12} = 0 is dike plane)

SITE 8-5

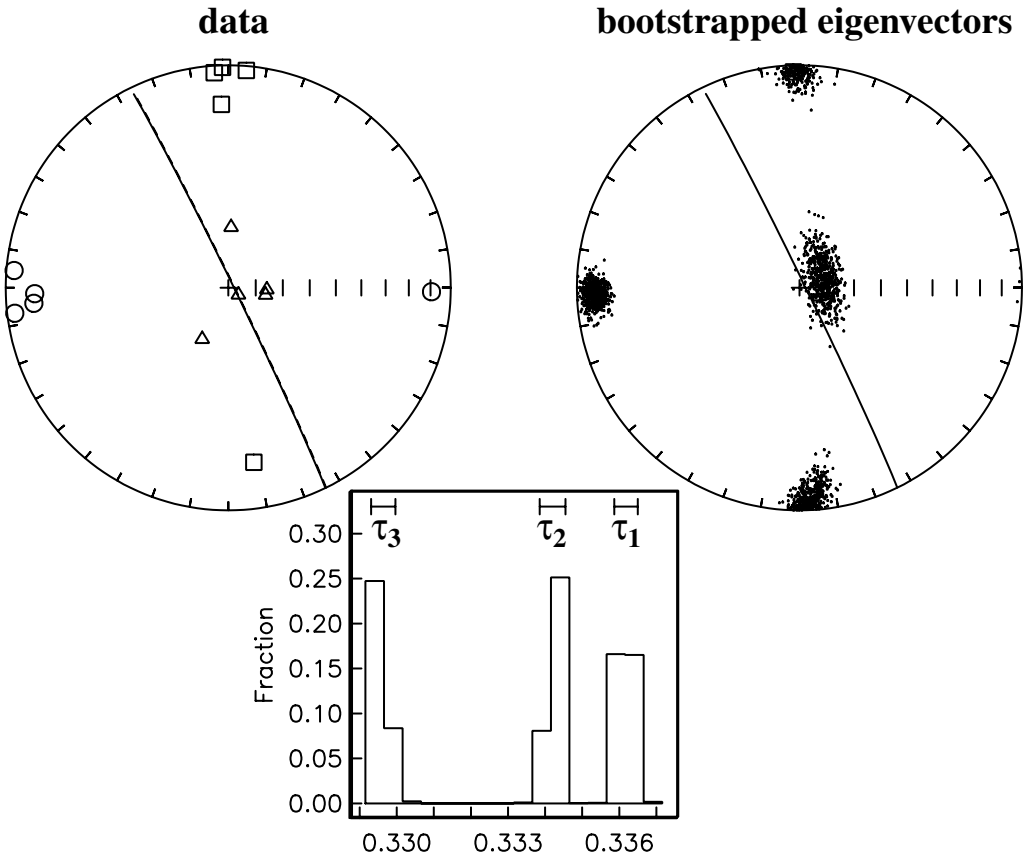

histogram of bootstrapped eigenvalues

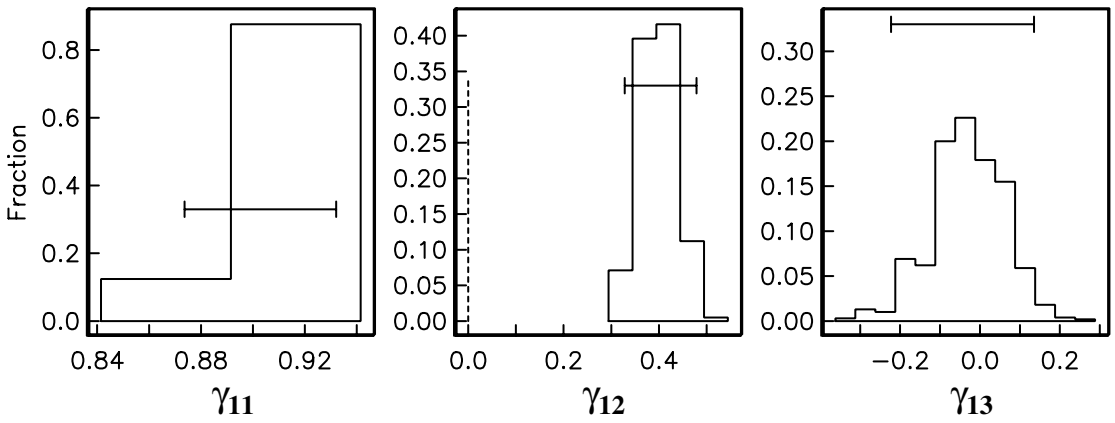

histograms of bootstrapped eigenvectors rotated into dike coordinates (γ_{12} = 0 is dike plane)

SITE 8-6

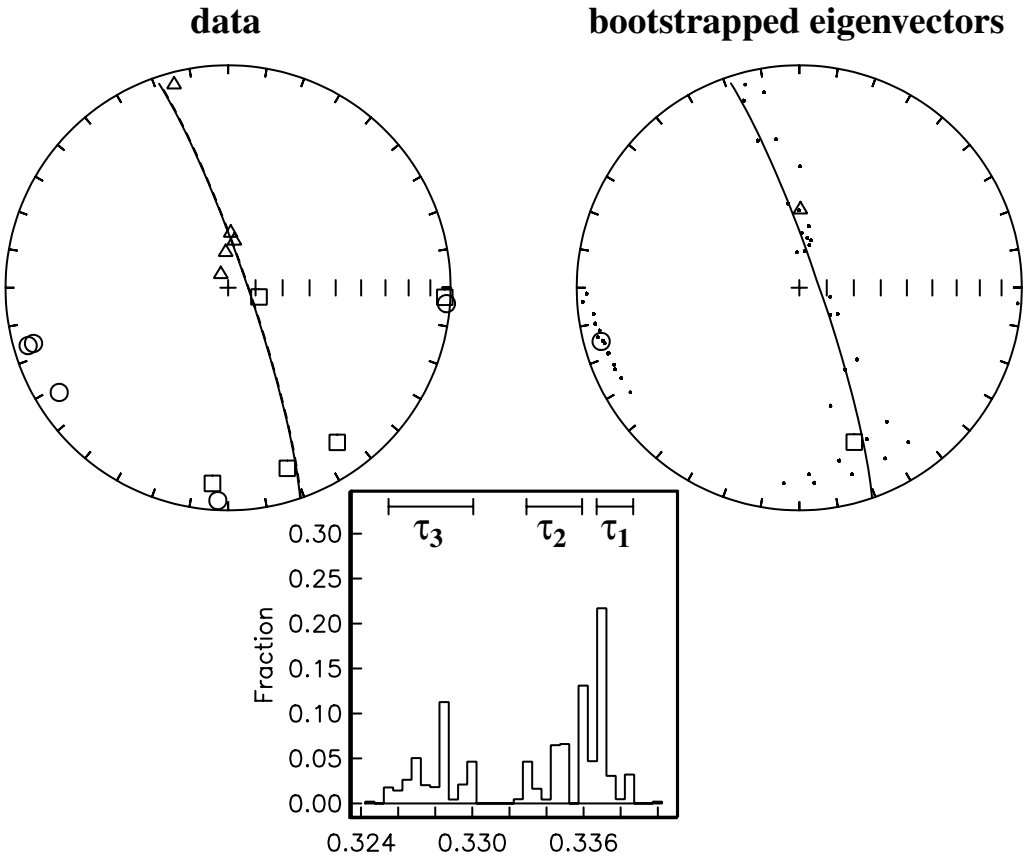

histogram of bootstrapped eigenvalues

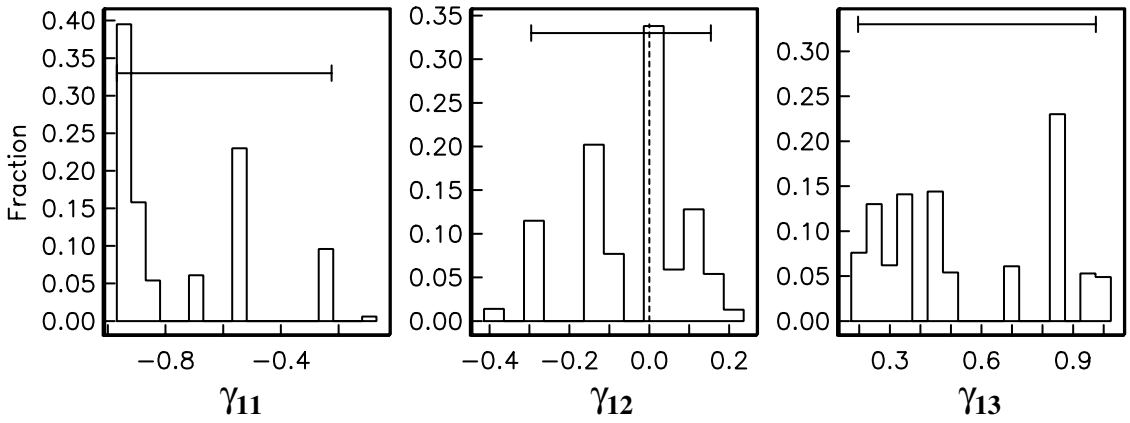

histograms of bootstrapped eigenvectors rotated into dike coordinates (γ_{12} = 0 is dike plane)

SITE 8-7

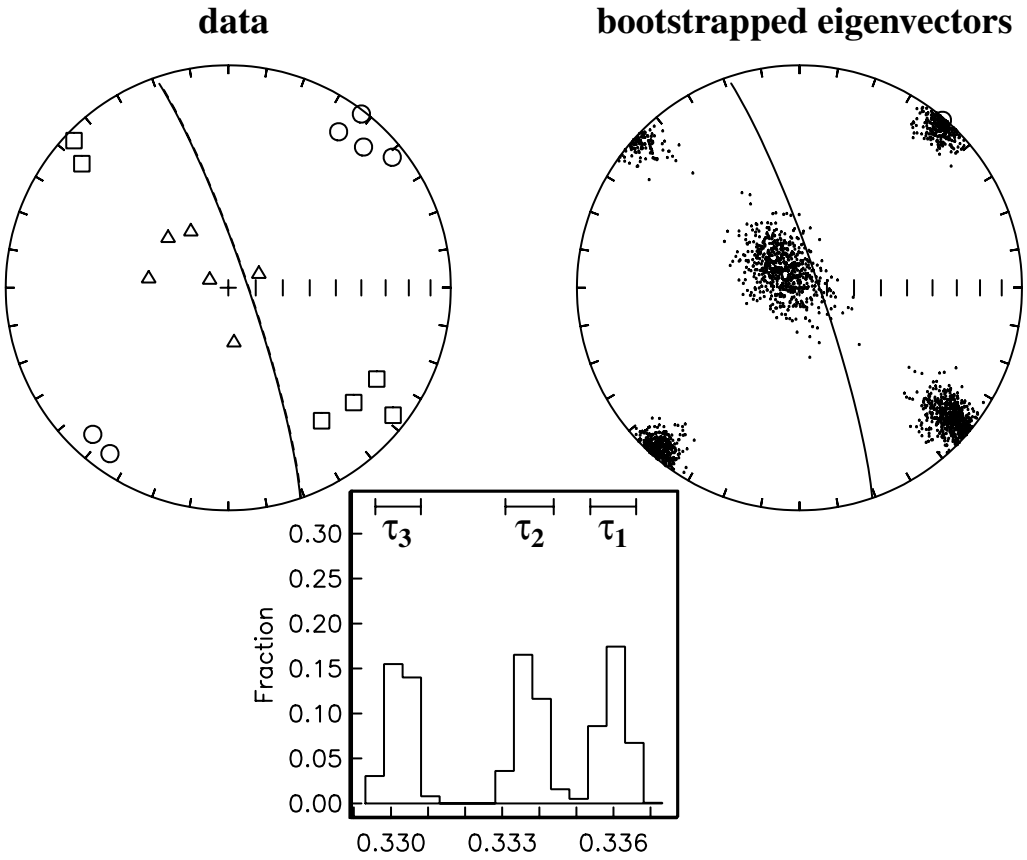

histogram of bootstrapped eigenvalues

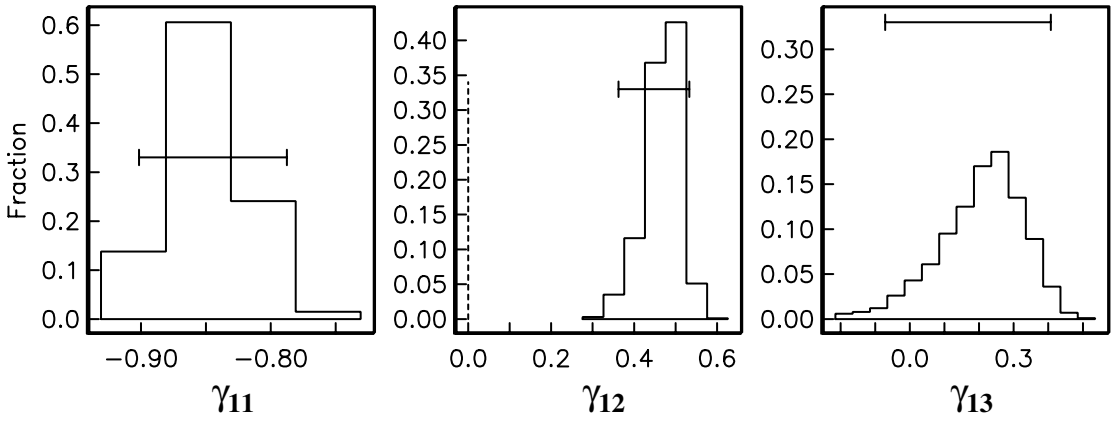

histograms of bootstrapped eigenvectors rotated into dike coordinates (γ_{12} = 0 is dike plane)

SITE 8-8

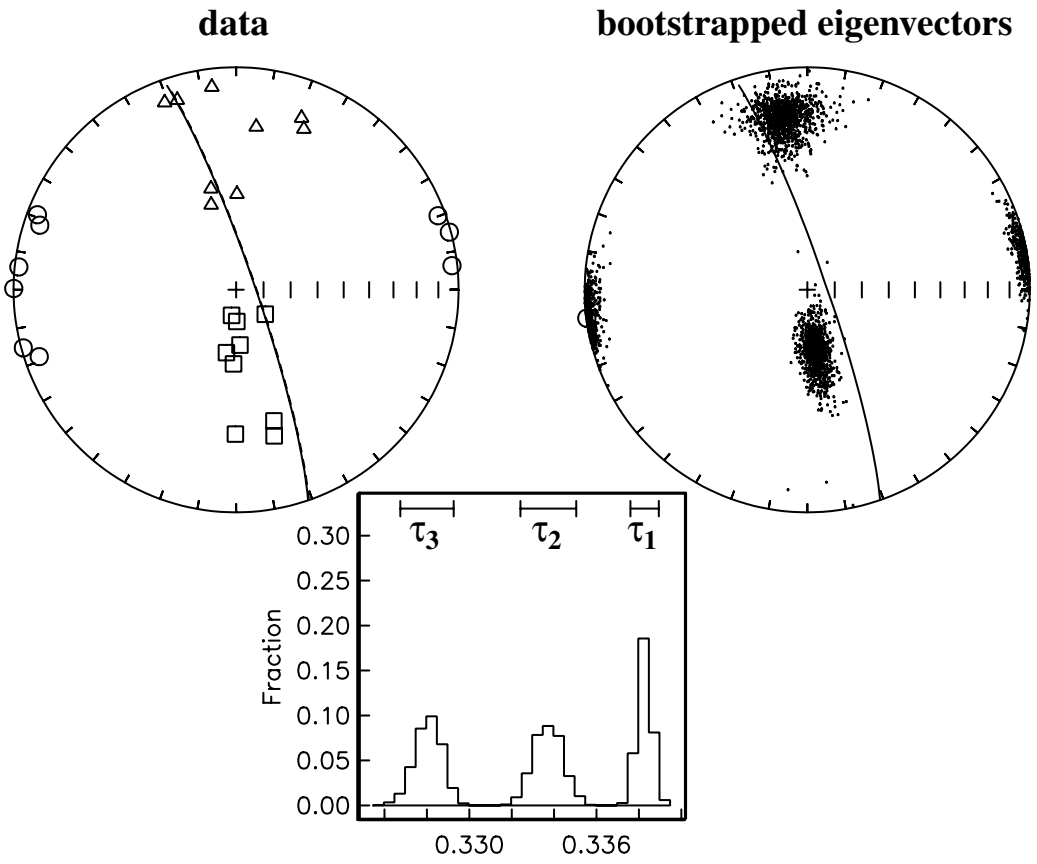

histogram of bootstrapped eigenvalues

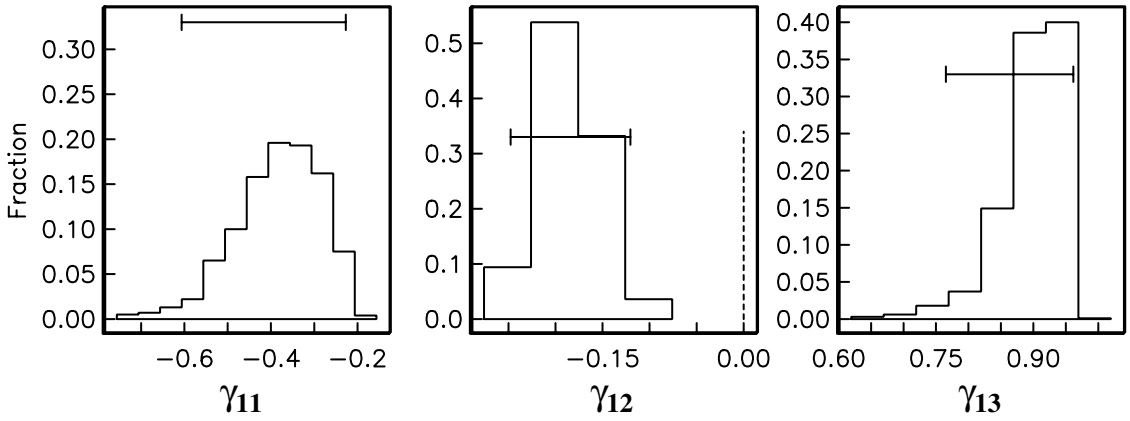

histograms of bootstrapped eigenvectors rotated into dike coordinates (γ_{12} = 0 is dike plane)

SITE 8-9

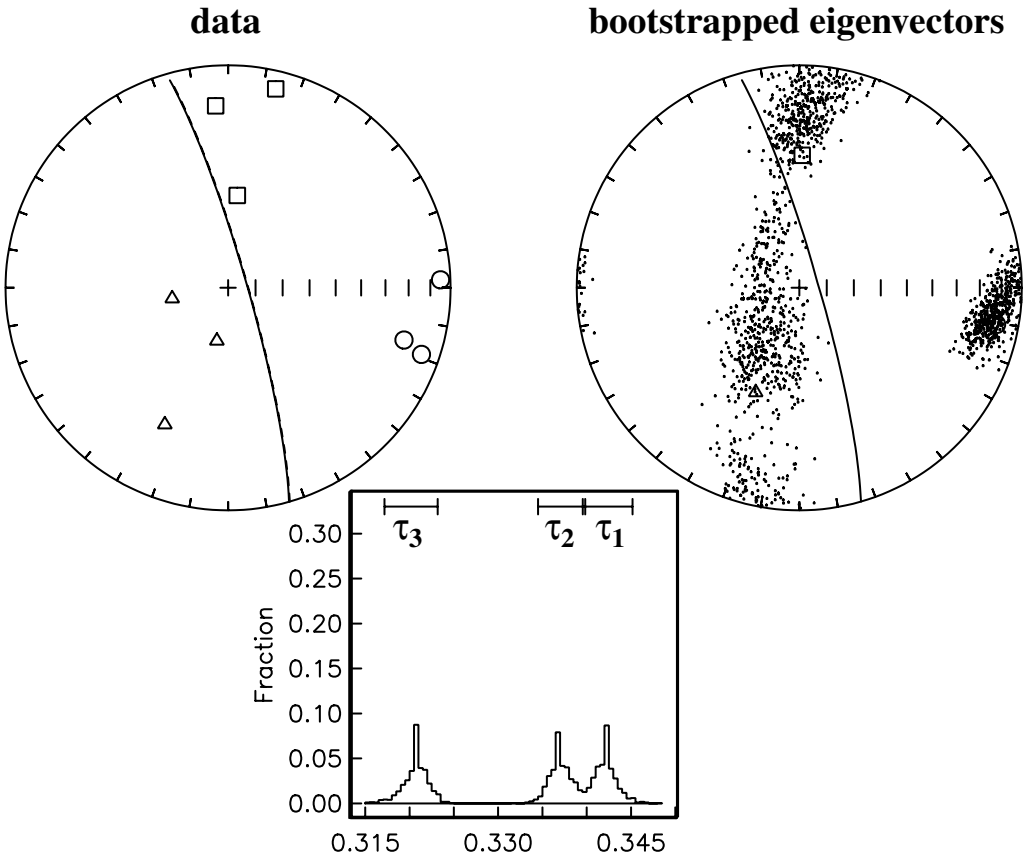

histogram of bootstrapped eigenvalues

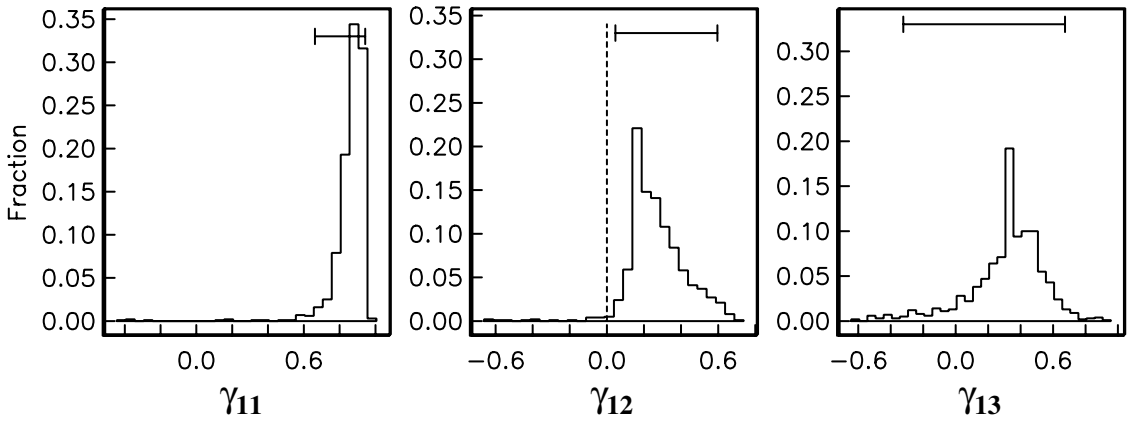

histograms of bootstrapped eigenvectors rotated into dike coordinates (γ_{12} = 0 is dike plane)

SITE 8-10a

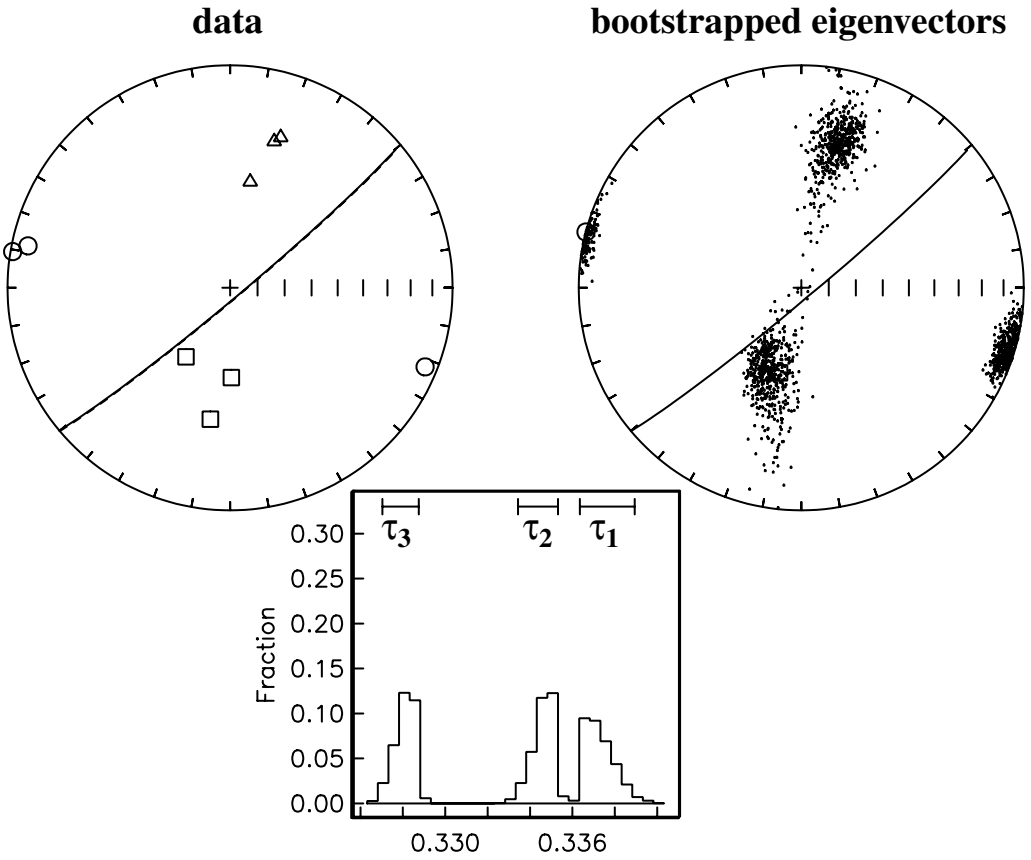

histogram of bootstrapped eigenvalues

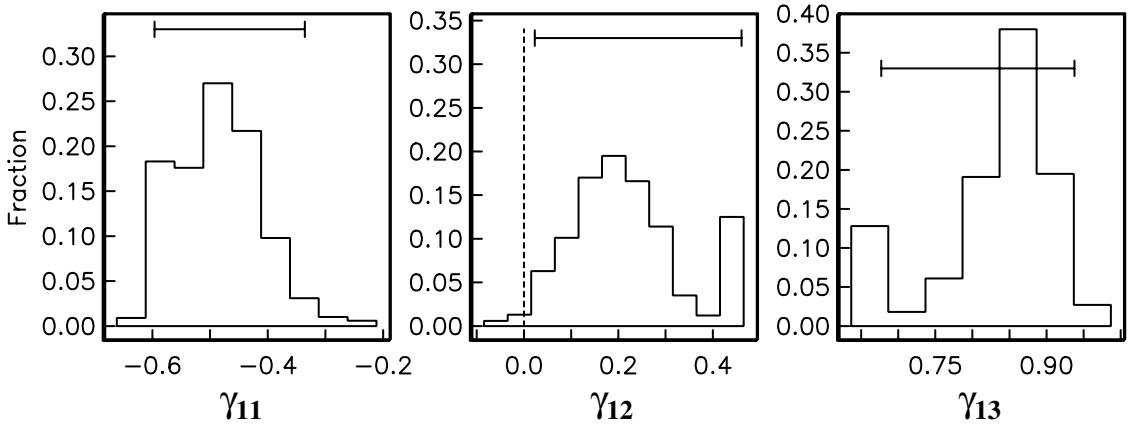

histograms of bootstrapped eigenvectors rotated into dike coordinates (γ_{12} = 0 is dike plane)

SITE 8-10b

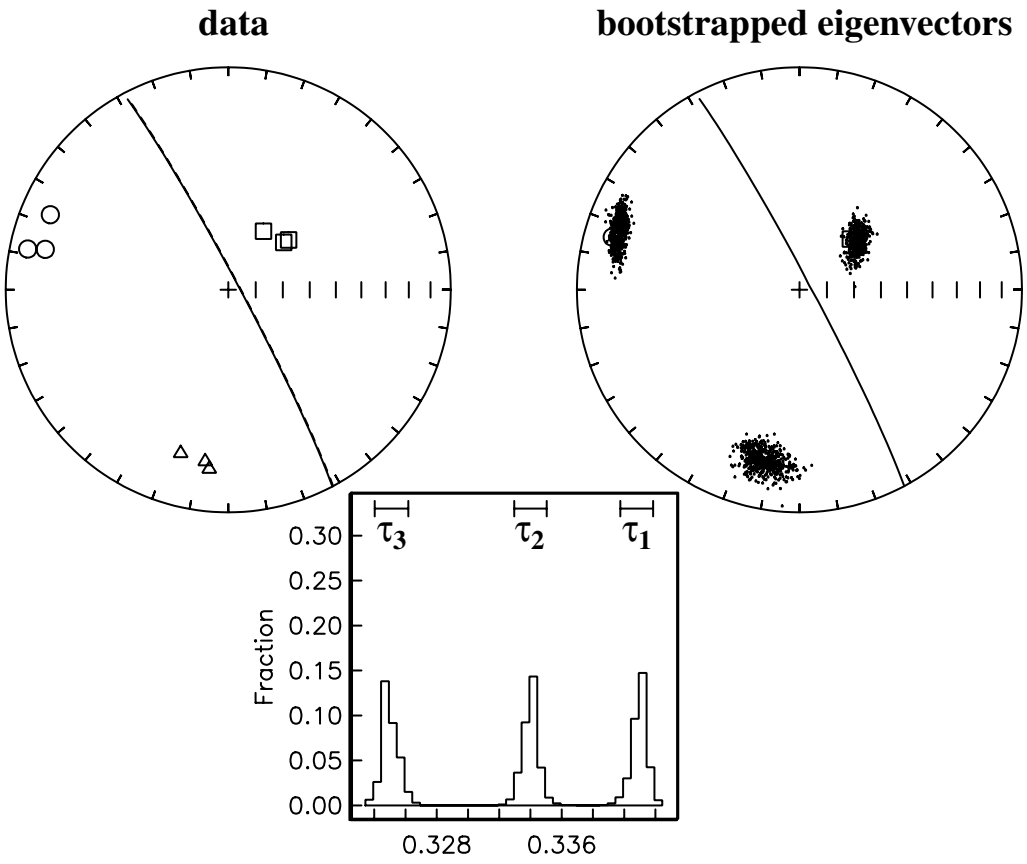

histogram of bootstrapped eigenvalues

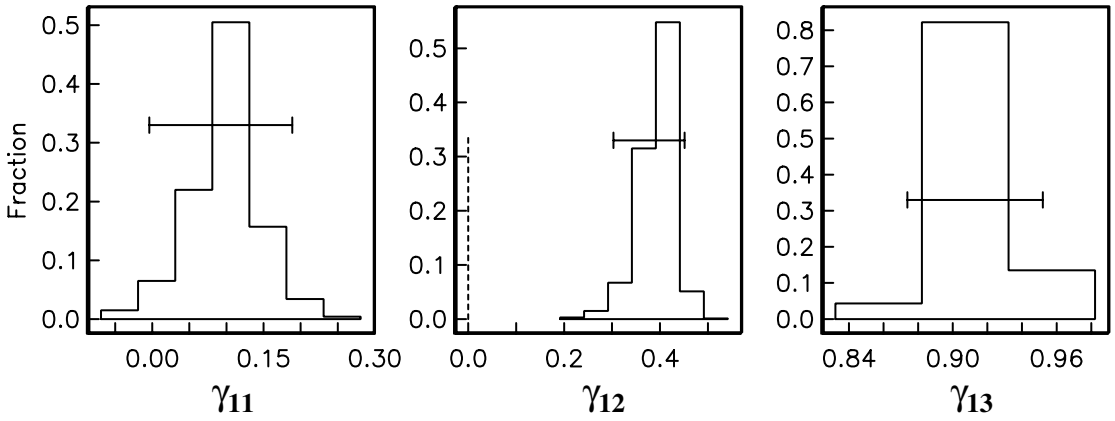

histograms of bootstrapped eigenvectors rotated into dike coordinates (γ_{12} = 0 is dike plane)

SITE 8-11

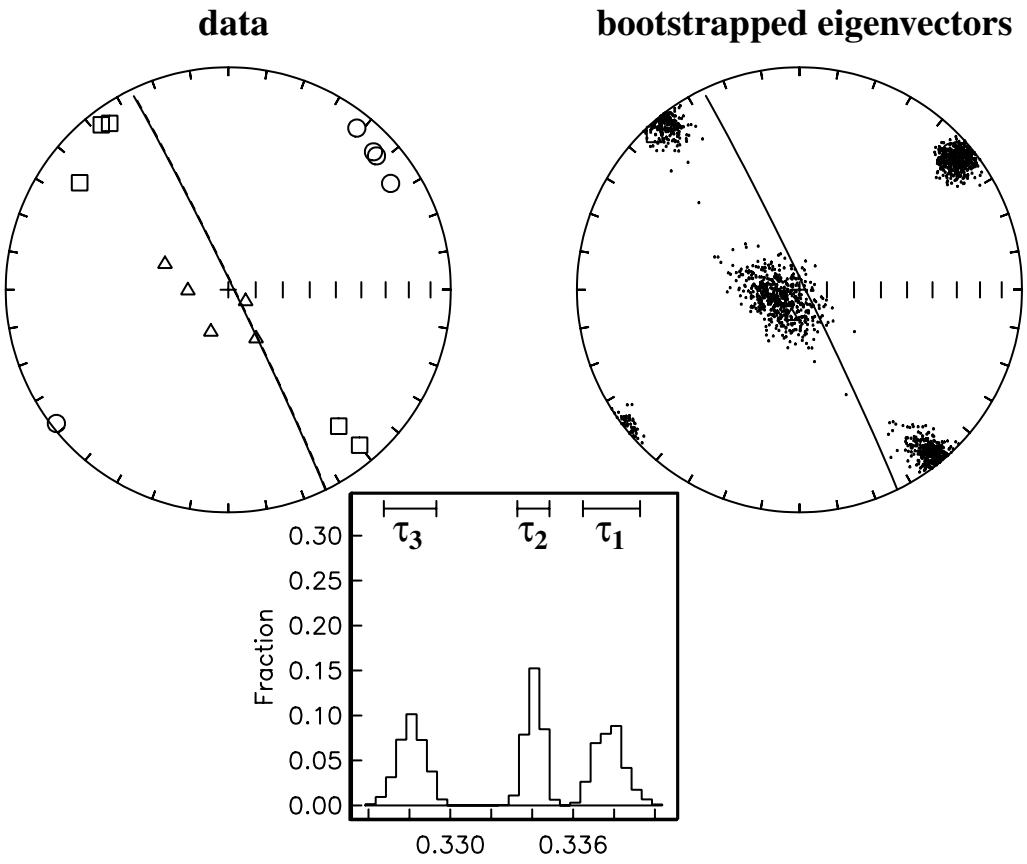

histogram of bootstrapped eigenvalues

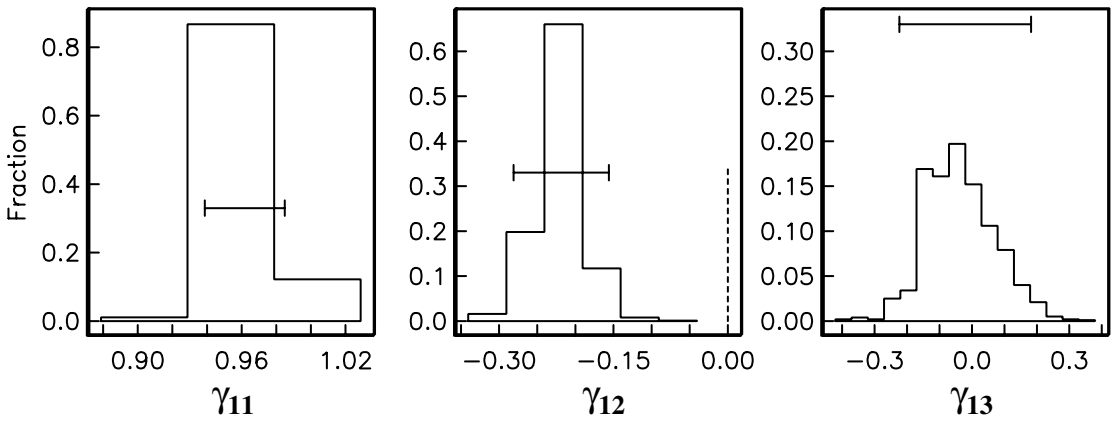

histograms of bootstrapped eigenvectors rotated into dike coordinates (γ_{12} = 0 is dike plane)

SITE 8-12

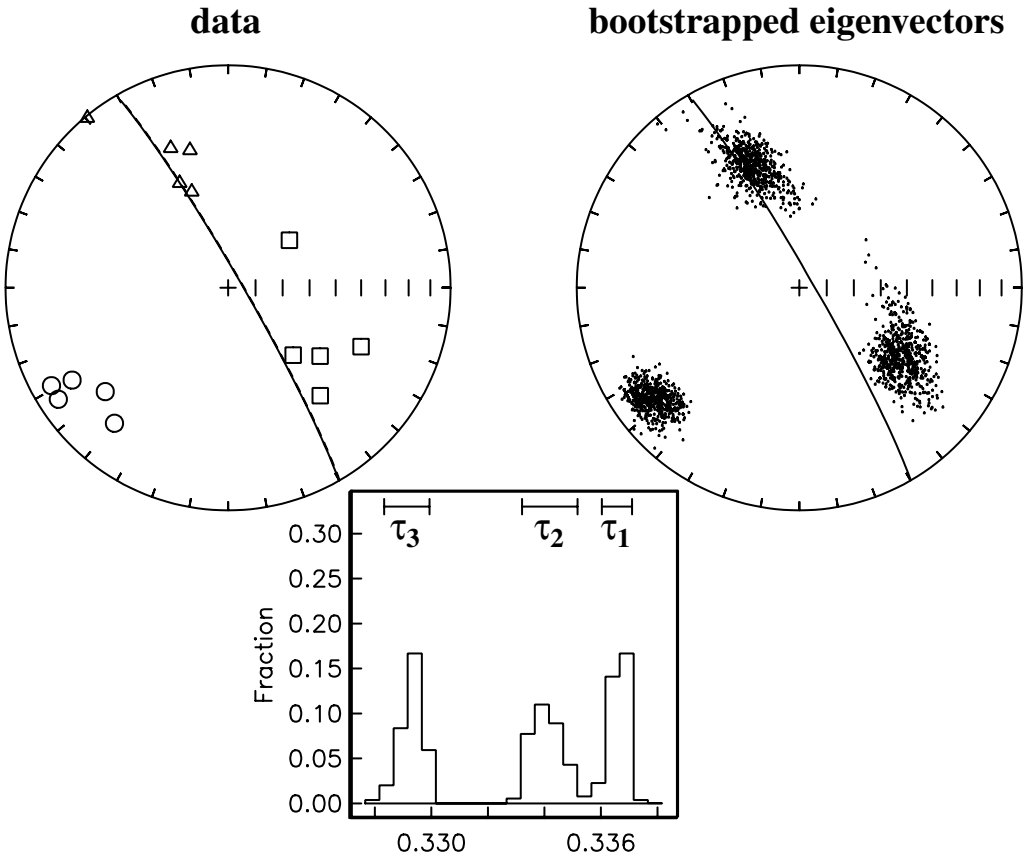

histogram of bootstrapped eigenvalues

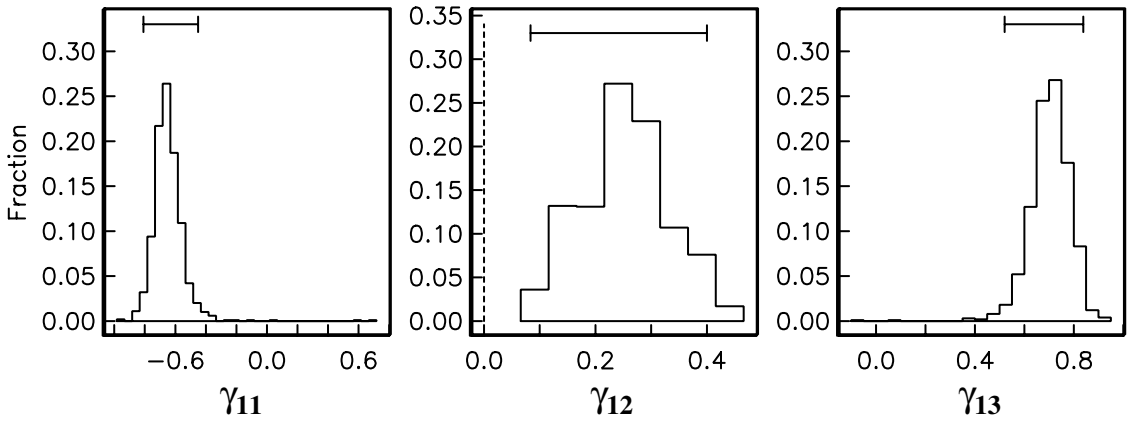

histograms of bootstrapped eigenvectors rotated into dike coordinates (γ_{12} = 0 is dike plane)

SITE 8-13

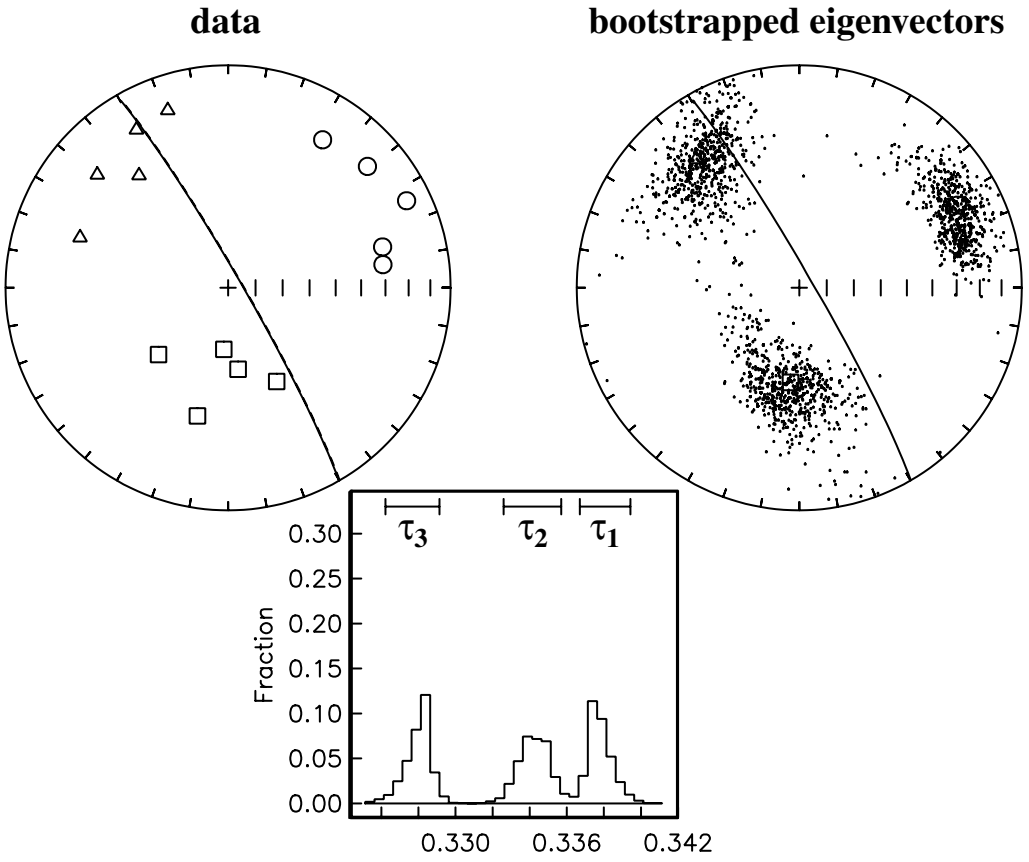

histogram of bootstrapped eigenvalues

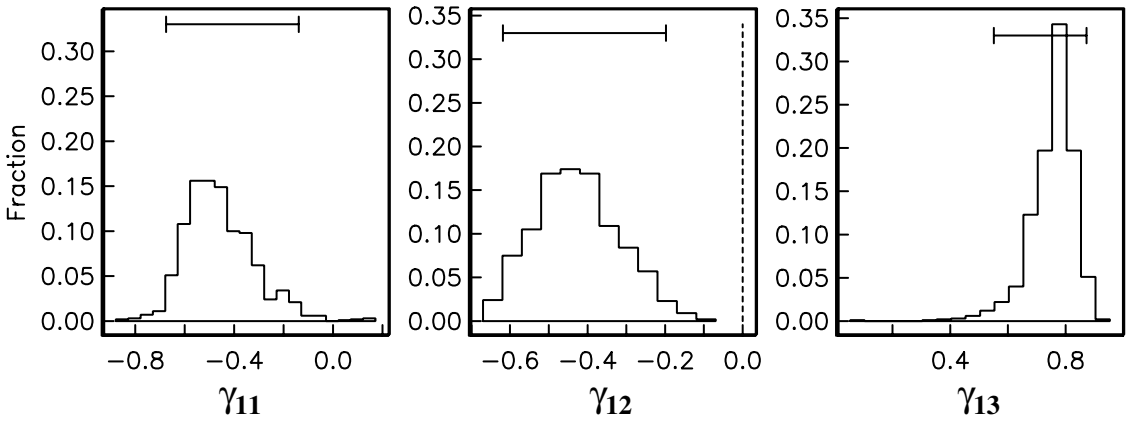

histograms of bootstrapped eigenvectors rotated into dike coordinates (γ_{12} = 0 is dike plane)

SITE 8-14

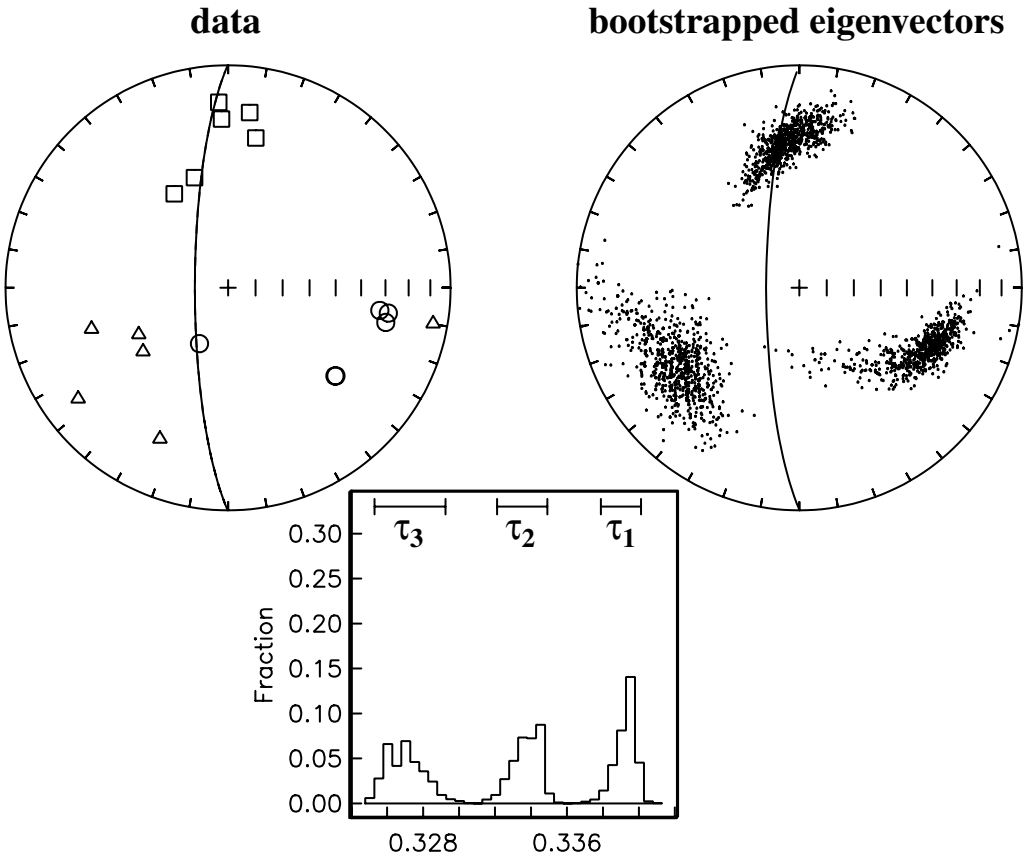

histogram of bootstrapped eigenvalues

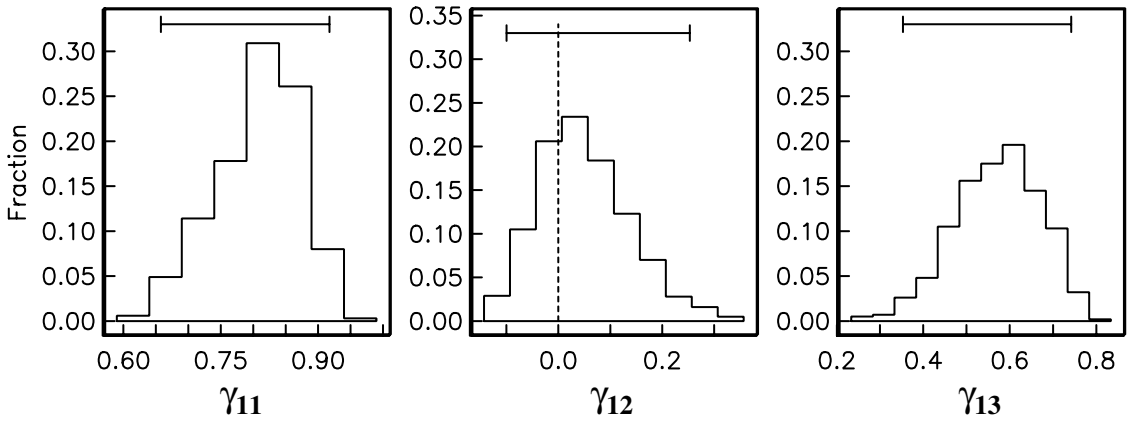

histograms of bootstrapped eigenvectors rotated into dike coordinates (γ_{12} = 0 is dike plane)

APPENDIX D

PLOTS OF BOOTSTRAPPED EIGENVECTORS AND EIGENVALUES FOR ANISOTROPY OF MAGNETIC SUSCEPTIBILITY DATA FROM 33 SAMPLE SITES AT SUMMER COON VOLCANO

SITES 3-4 (north - closed) and 3-5 (south - open)

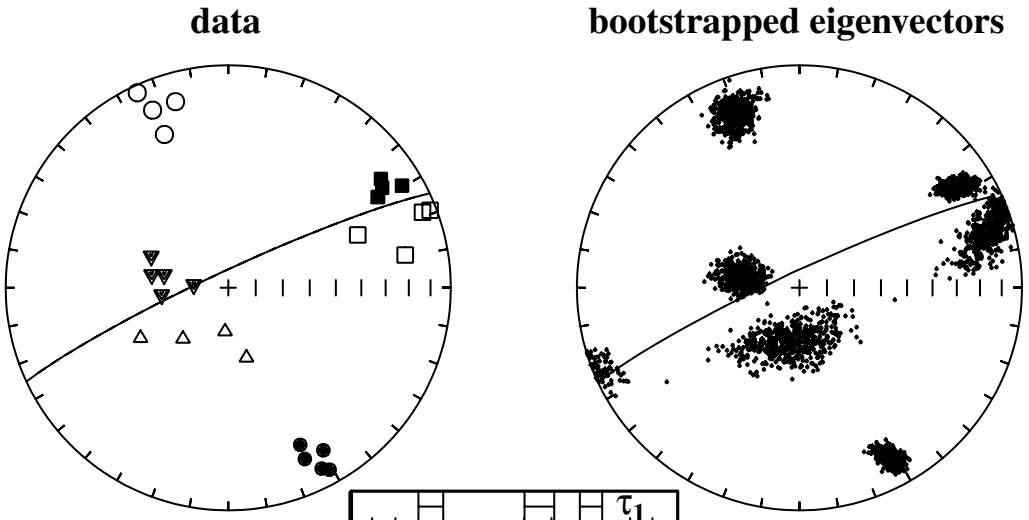

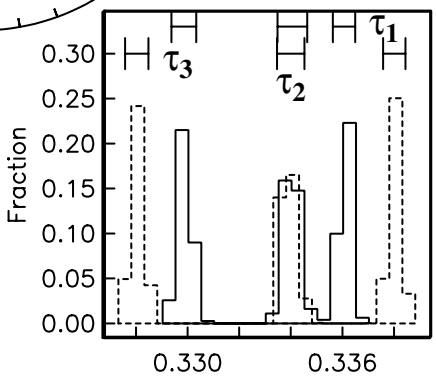

histogram of bootstrapped eigenvalues

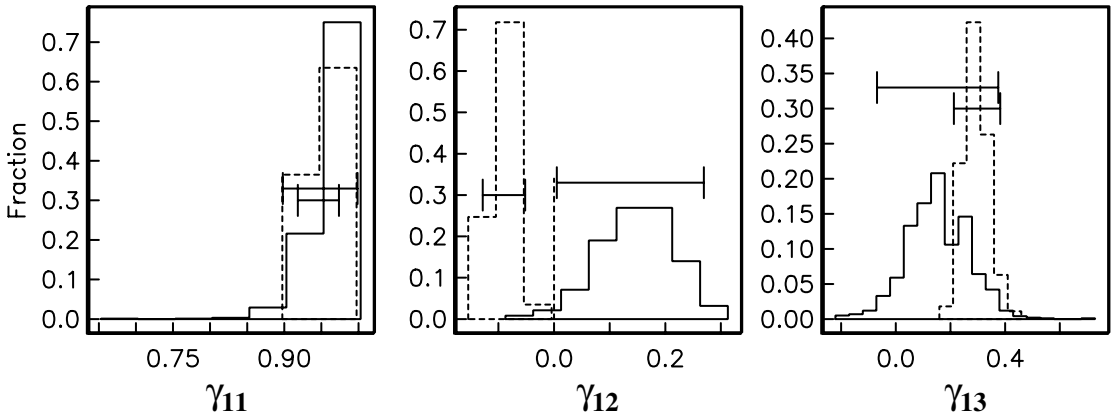

histograms of bootstrapped eigenvectors rotated into dike coordinates (γ_{12} = 0 is dike plane)

SITES 3-6 (north - closed) and 3-7 (south - open)

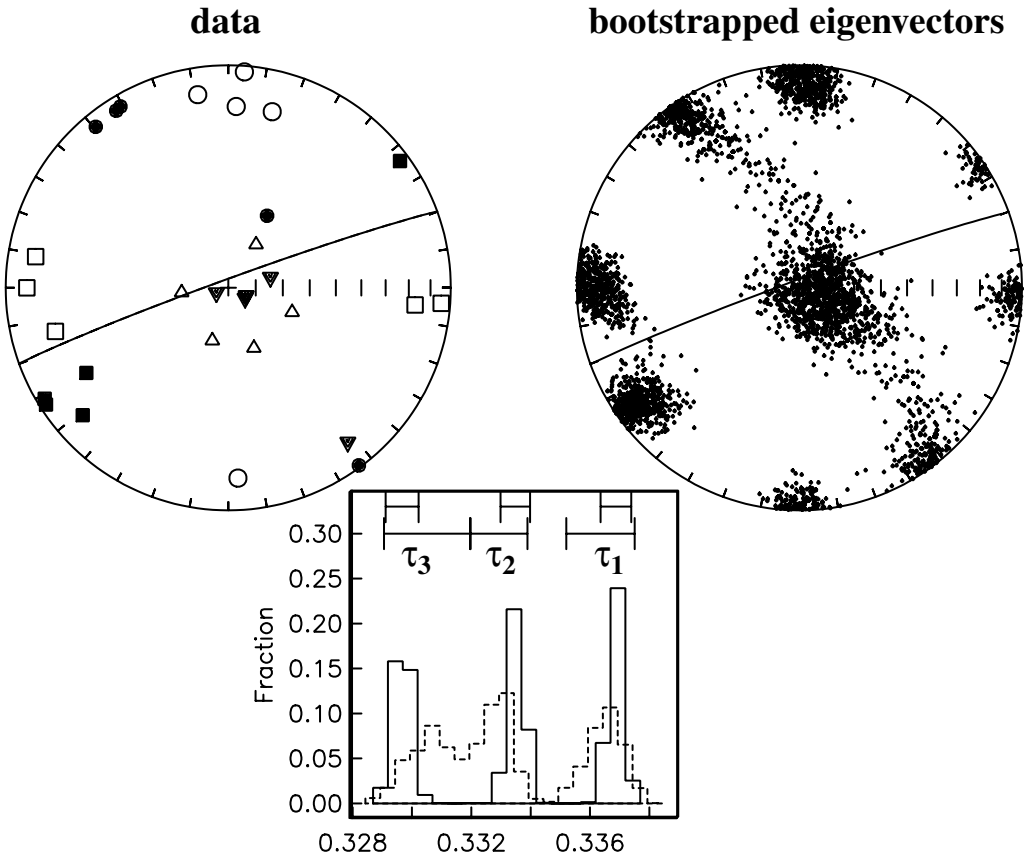

histogram of bootstrapped eigenvalues

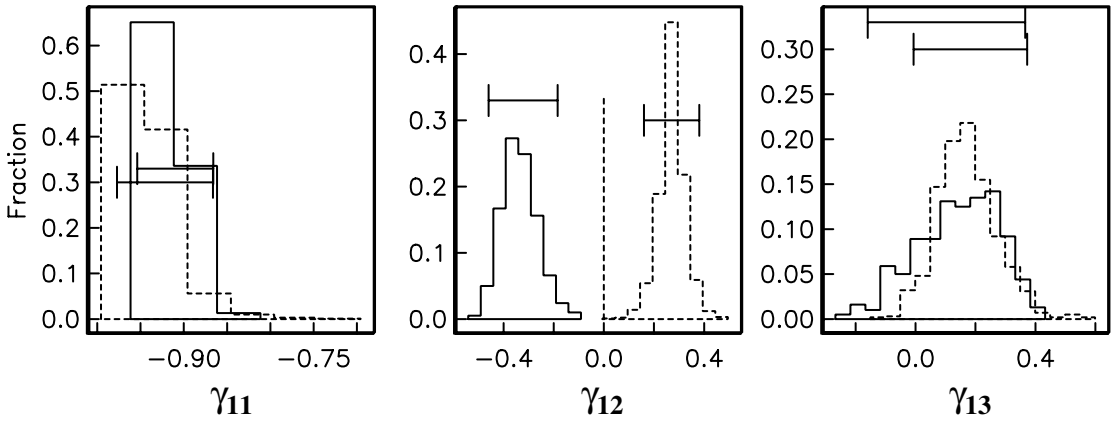

histograms of bootstrapped eigenvectors rotated into dike coordinates (γ_{12} = 0 is dike plane)

SITES 3-11 (north - closed) and 3-12 (south - open)

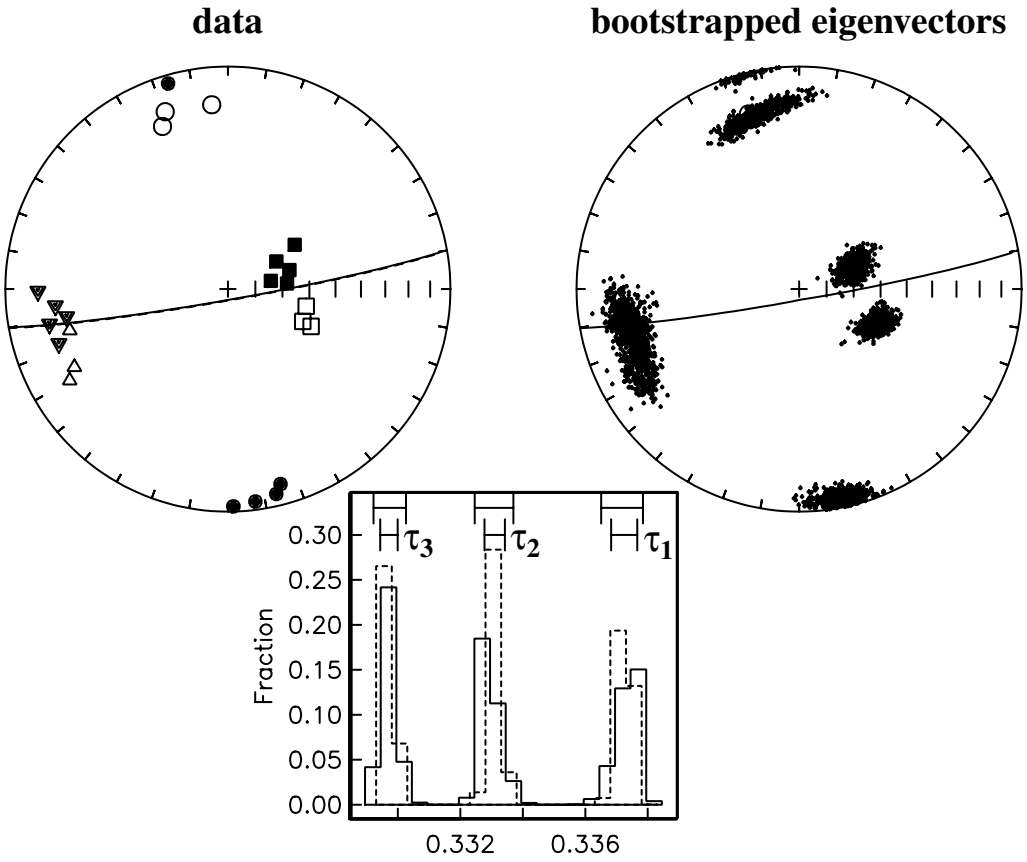

histogram of bootstrapped eigenvalues

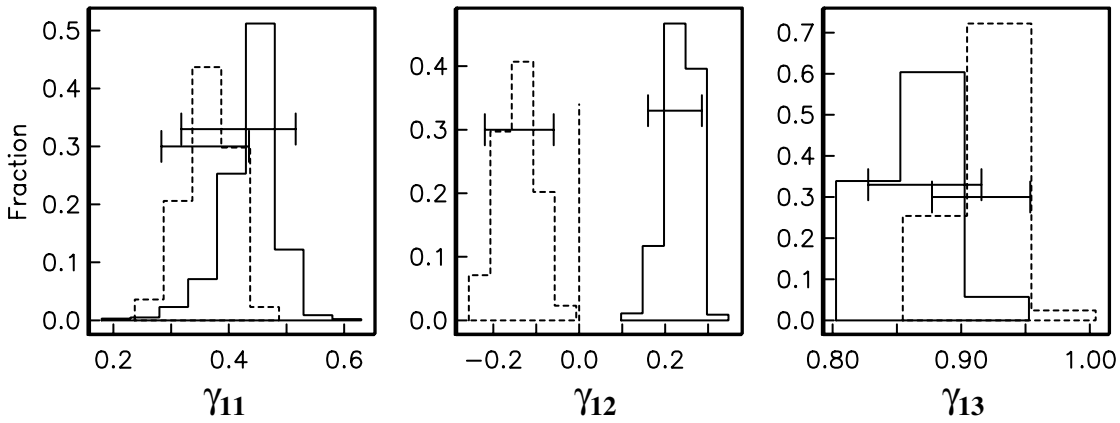

histograms of bootstrapped eigenvectors rotated into dike coordinates (γ_{12} = 0 is dike plane)

SITES 3-17 (north - closed) and 3-18 (south - open)

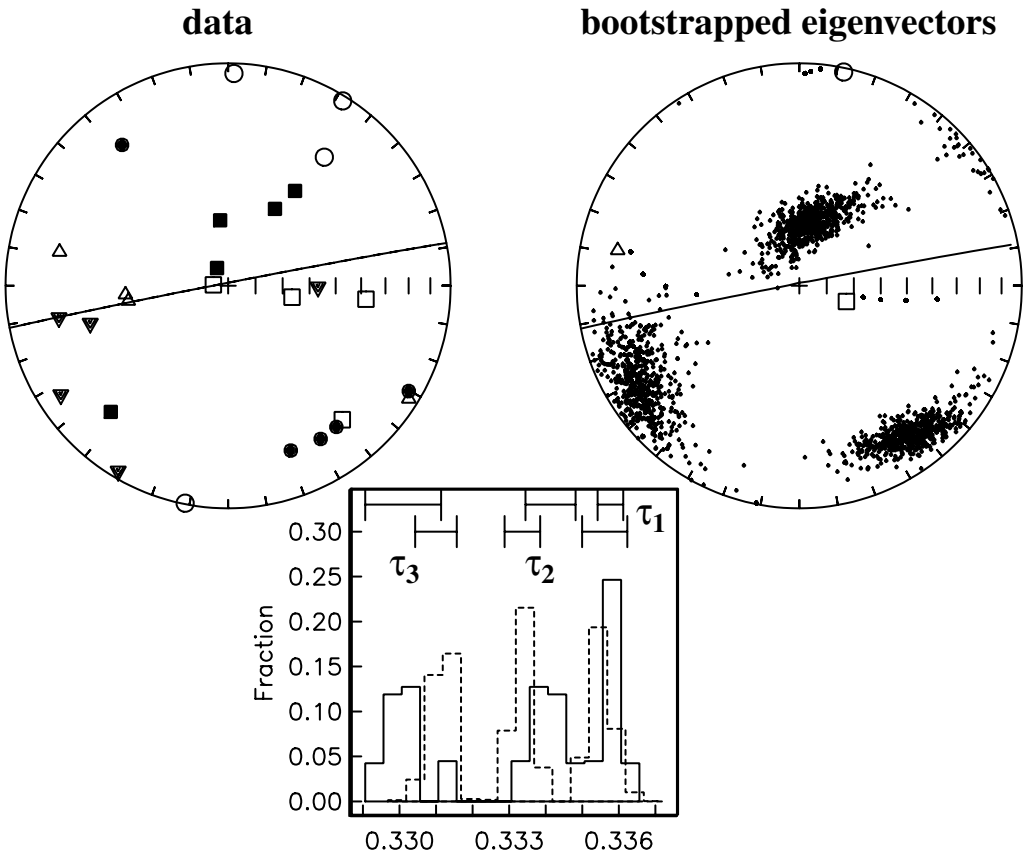

histogram of bootstrapped eigenvalues

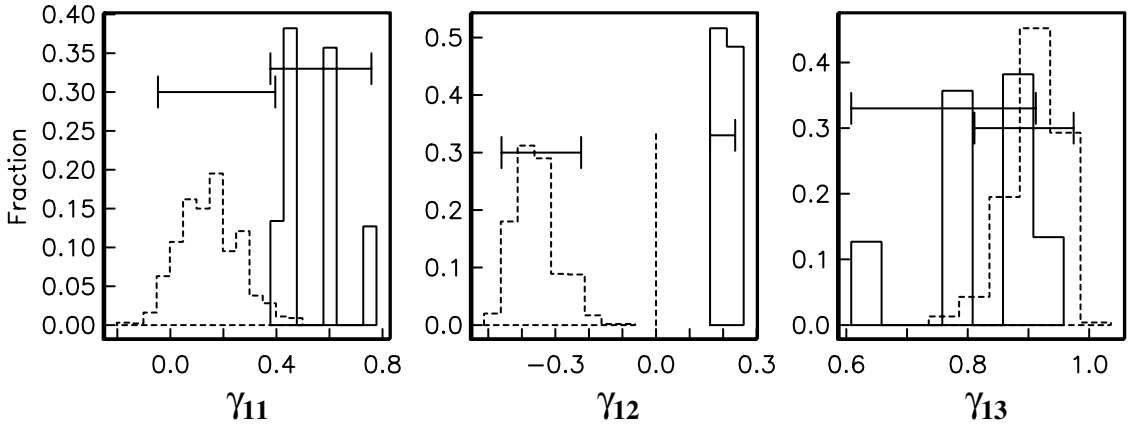

histograms of bootstrapped eigenvectors rotated into dike coordinates (γ_{12} = 0 is dike plane)

SITES 8-5 (west - closed) and 8-11(east - open)

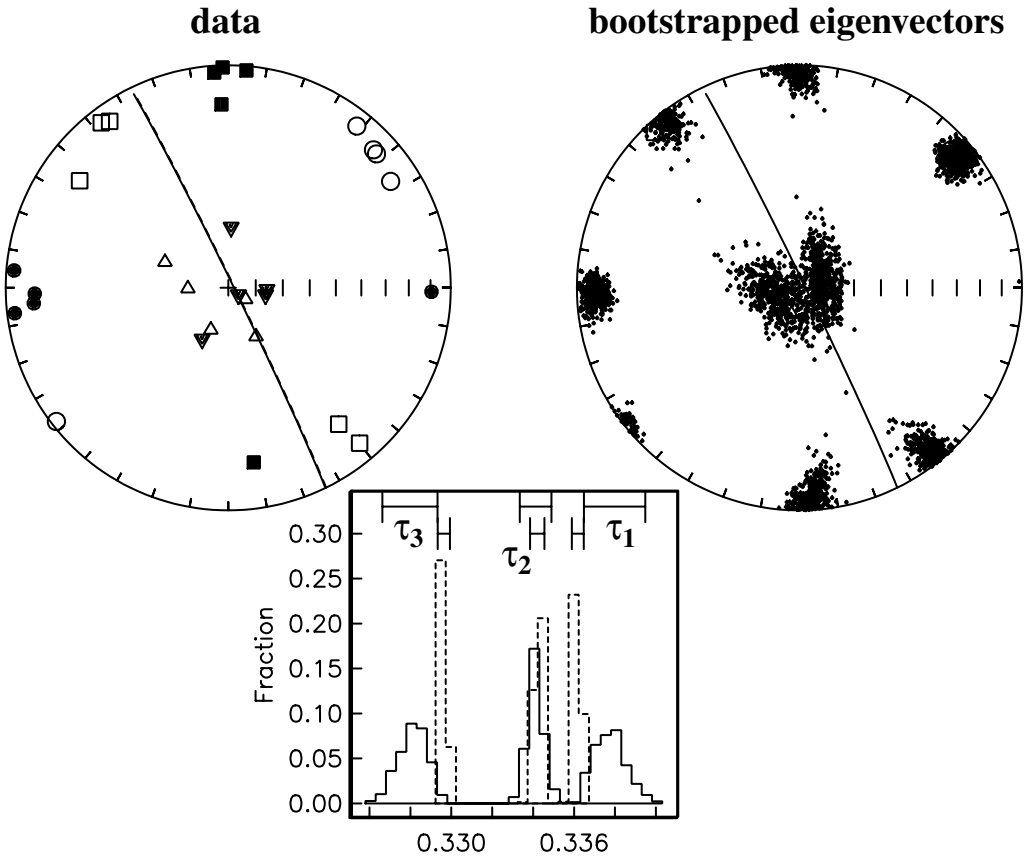

histogram of bootstrapped eigenvalues

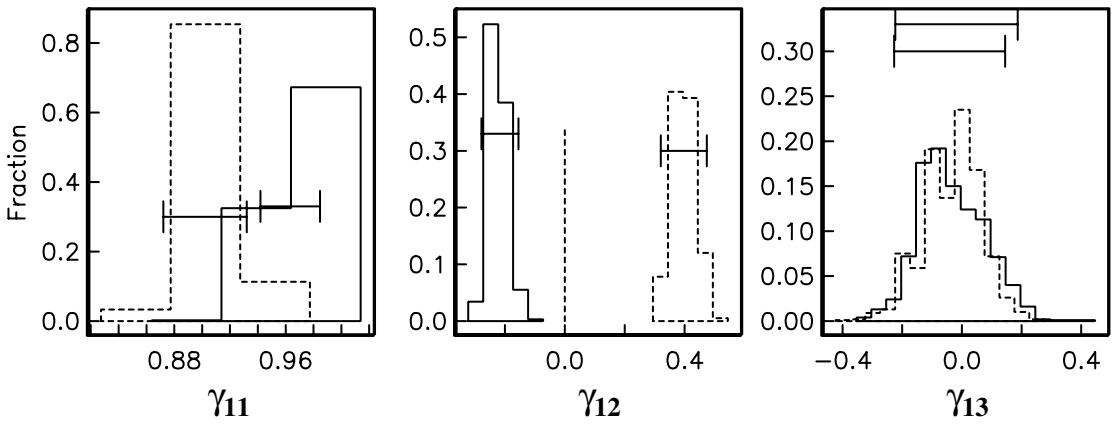

histograms of bootstrapped eigenvectors rotated into dike coordinates (γ_{12} = 0 is dike plane)

SITES 8-13 (west - closed) and 8-12 (east - open)

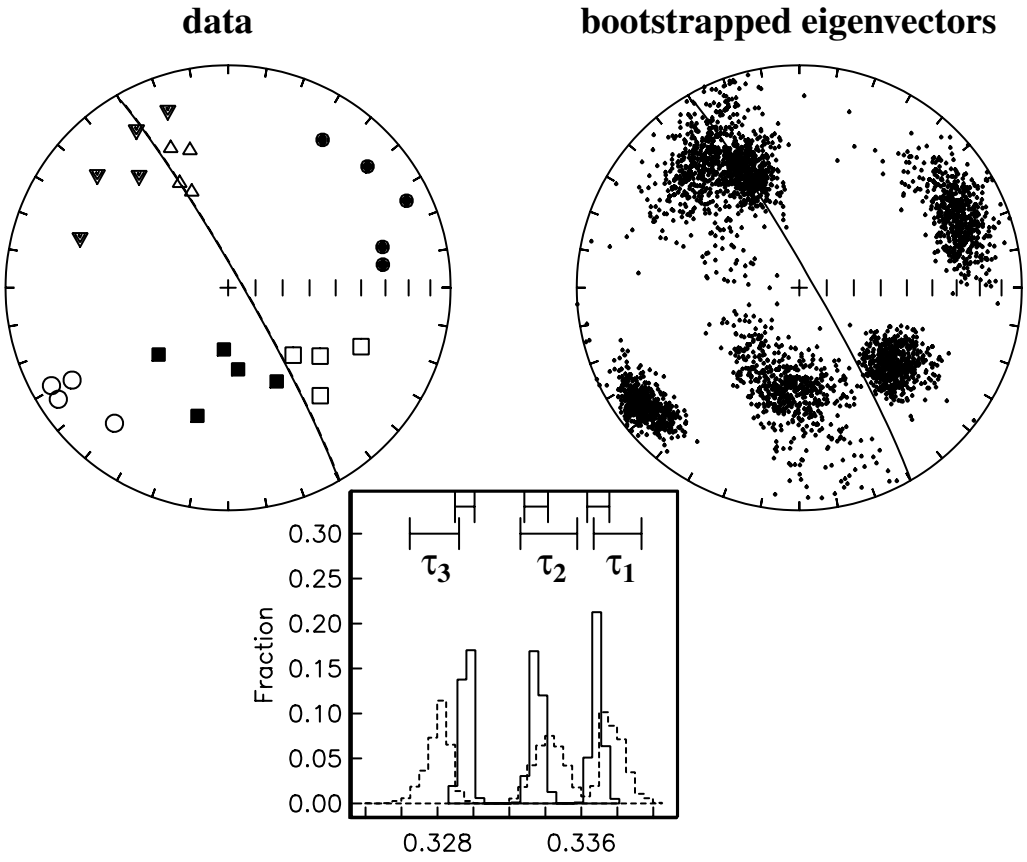

histogram of bootstrapped eigenvalues

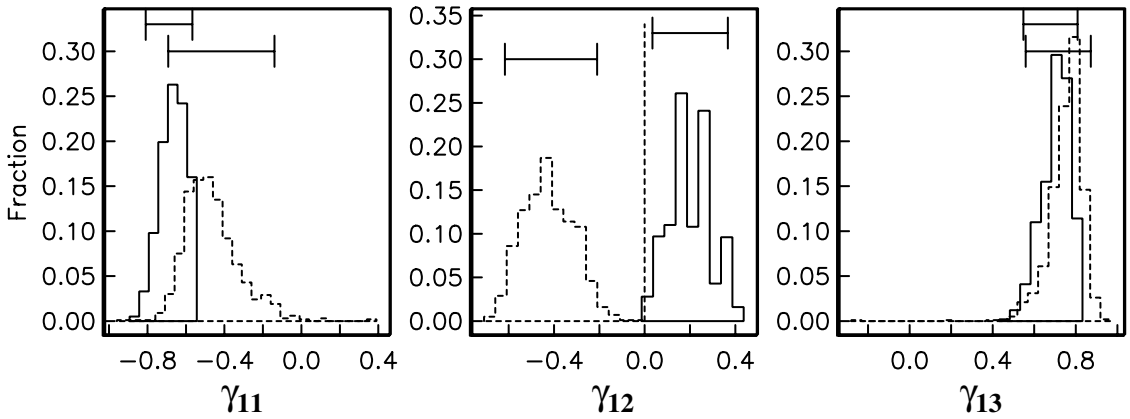

histograms of bootstrapped eigenvectors rotated into dike coordinates (γ_{12} = 0 is dike plane)

APPENDIX E

BOOTSTRAPPED EIGENVECTORS AND EIGENVALUES FOR ANISOTROPY OF MAGNETIC SUSCEPTIBILITY DATA FROM 6 PAIRED SAMPLE SITES (ON OPPOSITE SIDES OF THE SAME DIKE) AT SUMMER COON VOLCANO

Site	Core	Minimum (tau 1)			Intermediate (tau 2)			Maximum (tau 3)			Bulk	% Anisotropy
		eigenvalue	declination	inclination	eigenvalue	declination	inclination	eigenvalue	declination	inclination	Susceptibility	Tauxe et al., 1990
3-1	A	0.32633287	332.46	22.76	0.33493641	232.86	21.67	0.33873066	103.98	57.67	24641	1.24
	B	0.32631254	340.03	22.44	0.33544609	242.59	17.42	0.33824137	118.14	60.98	24751	1.19
	C	0.32661906	335.35	21.79	0.33476707	240.07	12.96	0.33861387	121.52	64.3	24411	1.20
	D	0.32848877	338.95	15.41	0.33510861	237.75	35.17	0.3364026	88.58	50.63	25497	0.79
	E	0.32743666	343.87	18.61	0.33536187	248.66	15.11	0.33720148	121.99	65.67	26039	0.98
3-2	A	0.32893646	142.01	19.09	0.33537444	45.54	18.04	0.3356891	275.33	63.23	21743	0.68
	B	0.32903799	153.23	28.43	0.33459449	48.53	25.1	0.33636755	284.07	50.38	20981	0.73
	C	**ORIENTING MARK LOST**										
	D	**ORIENTING MARK LOST**										
	E	0.3283847	175.97	11.01	0.3349109	81.86	20.23	0.3367044	292.88	66.73	19543	0.83
3-3	A	0.32969818	124.85	1.29	0.33288604	34.22	25.82	0.33741587	217.51	64.14	15598	0.77
	B	0.32957602	304.39	6.47	0.33286282	37.35	24.54	0.33756122	200.63	64.52	16128	0.80
	C	0.32973742	312.78	12.49	0.33272055	47.52	20.47	0.33754209	193.37	65.72	16087	0.78
	D	0.32844689	334.05	19.6	0.33412135	66.63	7.22	0.33743179	175.91	69.01	14470	0.90
	E	0.32897973	331.71	19.74	0.33387196	63.91	6.12	0.33714843	170.37	69.25	14422	0.82
	F	0.32917416	321.57	19.83	0.3344028	225.4	16.58	0.33642301	98.38	63.69	13928	0.72
3-4	A	0.327582	152.65	9.44	0.33480391	263.98	65.44	0.33761415	58.71	22.46	13581	1.00
	B	0.3278726	149.64	16.51	0.33397546	281.49	66.04	0.33815199	54.49	16.86	13414	1.03
	C	0.32788736	150.87	7.18	0.33343026	275.07	77.38	0.33868241	59.55	10.33	8361	1.08
	D	0.32860702	155.38	23.42	0.33363175	292.32	59.33	0.33776128	56.98	18.64	11272	0.92
	E	0.32860616	155.91	16.85	0.33435029	279.74	61.45	0.33704352	58.76	22.33	10739	0.84
3-5	A	0.32982126	336.93	14.32	0.33437774	184.16	73.98	0.33580104	68.74	7.03	9910	0.60
	B	0.33011886	337.41	26.31	0.33345041	165.43	63.47	0.3364307	68.99	3.2	11371	0.63
	C	0.32959583	344.18	14.15	0.33420685	221.55	64.94	0.33619732	79.52	20.23	10537	0.66
	D	0.32954562	335	3.7	0.33432484	240.16	52.53	0.33612952	67.81	37.23	11335	0.66
	E	**CORE BROKE DURING EXTRACTION**										
3-6	A	0.33144194	28.32	59.83	0.3336798	142.25	13.27	0.3348783	239.02	26.56	480	0.34
	B	0.32992986	59.81	67.39	0.3344993	267.15	20.31	0.33557087	173.59	9.53	349	0.56
	C	0.33149084	320.56	6.99	0.33157	76.12	74.13	0.33693916	228.78	14.17	14802	0.54
	D	0.32953158	143.66	1.08	0.33423826	247	85.31	0.33623013	53.57	4.56	8742	0.67
	E	0.32720008	200.54	35.4	0.33450836	37.87	53.33	0.33829159	296.52	8.34	12913	1.11
	F	0.32843339	327.69	6.5	0.33339402	121.78	82.79	0.33817267	237.33	3.13	13792	0.97
	G	0.32888636	329.29	5.82	0.33298177	113.75	82.87	0.33813184	238.87	4.12	14576	0.92
3-7	A	0.32948029	14.03	19.56	0.3335062	156.95	65.99	0.33701363	279.18	13.36	13073	0.75
	B	0.32938716	351.01	13.17	0.33336478	110.96	64.88	0.33724809	255.86	20.99	12348	0.79
	C	0.32963935	177.08	15.48	0.33364123	32.75	71.17	0.33671954	270	10.45	14082	0.71
	D	0.32900688	4.3	3.09	0.33350351	264.21	72.89	0.33748958	95.23	16.81	11372	0.85
	E	0.3285929	2.52	19.59	0.33435944	196.74	69.84	0.3370477	94.15	4.58	11626	0.85
3-8	A	**SAMPLES LOCATED IN DIKE INTERIOR**										
	B	**SAMPLES LOCATED IN DIKE INTERIOR**										
	C	0.32905081	315.69	15	0.3324863	48.12	9.02	0.33846292	168.14	72.39	21071	0.94
	D	0.32978779	313.11	8.37	0.33210129	44.81	11.43	0.33811089	187.66	75.77	21702	0.83
	E	0.32922059	316.6	7.95	0.33248609	47.26	4.7	0.33829334	167.59	80.75	20902	0.91

Site	Core	Minimum (tau 1)			Intermediate (tau 2)			Maximum (tau 3)			Bulk	% Anisotropy
		eigenvalue	declination	inclination	eigenvalue	declination	inclination	eigenvalue	declination	inclination	Susceptibility	Tauxe et al., 1990
3-9	A	0.33051169	189.26	14.85	0.33335671	71.34	60.47	0.33613163	286.33	24.89	16472	0.56
	B	0.32911721	182.51	11.69	0.3346248	75.95	54.01	0.33625805	280.37	33.47	16192	0.71
	C	0.32931671	181.9	13.66	0.33398157	68.93	58.07	0.33670184	279.4	28.24	15646	0.74
	D	0.33016467	192.82	8.08	0.33377764	92.34	52.05	0.33605775	288.91	36.78	14704	0.59
	E	0.33055335	208.3	15.55	0.3333402	83.43	64.04	0.33610642	304.19	20.25	14103	0.56
3-10	A	0.32888225	138.41	7.04	0.3331916	232.76	31.51	0.33792621	37.23	57.53	14281	0.90
	B	0.32830206	148.44	10.35	0.33325168	244.64	30.6	0.33844641	41.88	57.33	14140	1.01
	C	0.32817513	140.49	4.56	0.33382398	232.45	23.26	0.33800101	40.05	66.25	13155	0.98
	D	0.3272894	151.5	5.12	0.33445376	245.84	40.18	0.3382569	55.52	49.36	12886	1.10
	E	0.3273989	148.57	12.51	0.33469877	247.23	34.17	0.3379024	41.45	52.99	13144	1.05
3-11	A	0.3298077	343.79	4.26	0.33327782	252.12	21.31	0.33691454	84.52	68.23	13656	0.71
	B	0.32945755	166.71	6.03	0.33301431	258.85	19.45	0.33752811	60.23	69.56	15380	0.81
	C	0.32945076	164.9	10.15	0.33265671	260.22	27.37	0.33789253	56.44	60.5	13136	0.84
	D	0.32969975	178.54	2.67	0.33342046	269.29	15.75	0.33687982	79.19	74.01	15126	0.72
	E	0.3285256	172.61	4.22	0.33367571	264.42	23.18	0.33779868	72.88	66.39	12808	0.93
3-12	A	0.32980466	338.11	22.32	0.33333477	239.97	19.04	0.33686063	113.33	59.96	19916	0.71
	B	**ORIENTING MARK LOST**										
	C	0.32952145	355.01	17.99	0.33267105	255.3	27.45	0.33780745	114.14	56.3	20425	0.83
	D	0.32850149	340.55	16.6	0.33335701	243.04	23.65	0.33814165	102.34	60.49	22587	0.96
3-13	A	0.33187246	98.03	36.08	0.33374545	310.63	49.14	0.33438215	200.53	16.55	7208	0.25
	B	**CORE BROKE DURING EXTRACTION**										
	C	0.33131415	136.51	16.67	0.33317512	338.54	72.1	0.33551082	228.41	6.34	5929	0.42
	D	0.33117676	132.58	23.98	0.33376795	275.62	60.9	0.33505529	35.5	15.5	4466	0.39
	E	0.33000422	130.22	27.76	0.33373564	291.07	60.87	0.33626017	35.91	8.12	4832	0.63
3-14	A	0.33084428	115.45	6.9	0.33343583	230.26	73.93	0.33571988	23.66	14.45	5229	0.49
	B	0.3313123	112.83	26.92	0.33332637	316.81	60.94	0.33536136	208.04	10.13	7082	0.40
	C	0.32954031	113.2	3.74	0.33430091	264.37	85.73	0.33615884	23.07	2.05	6395	0.66
	D	0.32984319	289.84	1.09	0.33399224	25.66	79.41	0.33616459	199.64	10.53	6273	0.63
	E	0.33078417	296.32	28.52	0.33260852	72.54	53.04	0.33660734	194	21.44	5587	0.58
3-15	A	0.32948196	119.71	26.2	0.33371571	319.98	62.33	0.33680233	213.83	8.3	18045	0.73
	B	0.33039889	300.38	4.55	0.33353356	33.5	34.38	0.33606759	203.79	55.24	8656	0.57
	C	0.32971433	114.39	24.17	0.33298805	314.77	64.42	0.33729765	207.96	7.88	15789	0.76
	D	0.32888627	106.39	32.72	0.33327416	291.54	57.18	0.33783954	197.9	2.35	16223	0.90
	E	0.32947084	109.93	42	0.33399734	276.38	47.2	0.33653182	13.77	6.79	17065	0.71
3-16	A	0.32901165	172.91	24.91	0.3335515	49.06	50.18	0.33743688	277.73	28.84	10578	0.84
	B	**ORIENTING MARK LOST**										
	C	0.32857069	163.27	40.47	0.33428627	18.76	43.66	0.33714303	269.99	18.64	10618	0.86
	D	0.32884005	172.69	25.58	0.33397463	33.98	57.5	0.33718532	271.99	18.65	14146	0.83
	E	0.32963163	169.75	26.14	0.33364323	49.23	45.97	0.33672512	277.98	32.51	12852	0.71
3-17	A	0.33034095	142.48	21.16	0.33313701	236.89	11.24	0.33652207	353.1	65.78	5385	0.62
	B	0.33117405	148.83	20.7	0.33392003	254.78	36.02	0.33490592	35.22	46.68	6732	0.37
	C	0.33139831	120.22	6.73	0.33308491	210.64	3.55	0.33551672	328.28	82.39	4927	0.41
	D	0.33124587	159.15	21.89	0.33331299	259.31	23.71	0.33544123	31.36	56.75	5815	0.42
	E	0.33153522	323.06	21.86	0.3340517	90.86	56.79	0.33441308	222.92	23.68	4146	0.29

Site	Core	Minimum (tau 1)			Intermediate (tau 2)			Maximum (tau 3)			Bulk	% Anisotropy
		eigenvalue	declination	inclination	eigenvalue	declination	inclination	eigenvalue	declination	inclination	Susceptibility	Tauxe et al., 1990
3-18	A	0.32760304	36.8	28.6	0.33524883	261.37	52.58	0.33714813	139.52	21.99	1305	0.95
	B	0.32906297	1.59	5.09	0.33481556	265.1	51.79	0.33612144	95.54	37.75	1026	0.71
	C	0.33113736	191.16	0.49	0.33344609	281.37	23.81	0.33541659	100.05	66.18	1056	0.43
	D	0.33032164	31.8	2.53	0.33393088	122.01	4.71	0.33574745	273.64	84.66	1346	0.54
8-1	A	0.32980123	91.03	7.37	0.33273351	196.39	63.98	0.33746532	357.61	24.81	15954	0.77
	B-A	0.32956296	274.33	11.16	0.33423117	172.4	46.33	0.33620584	14.39	41.52	15522	0.66
	B-B	0.32986799	263.19	12.96	0.33404726	149.25	60.45	0.33608478	359.65	26.06	18706	0.62
	C-A	0.32901052	267.58	14.89	0.33423343	170.57	24.65	0.33675605	25.83	60.67	17929	0.77
	C-B	0.32916903	258.29	15.7	0.33457509	145.77	53.72	0.33625585	358.31	31.75	17428	0.71
	D	0.3296763	260.51	15.66	0.33483413	165.17	18.35	0.33548963	28.46	65.5	19829	0.58
	E-A	0.32878008	270.13	12.64	0.33369303	164.15	50.82	0.33752689	9.63	36.34	18228	0.87
	E-B	0.32797691	256.79	10.42	0.33276388	154.47	49.24	0.33925918	355.3	38.85	18932	1.13
	F	0.32797951	256.61	12.45	0.33507729	104.99	75.91	0.33694321	348.05	6.49	18942	0.90
8-2	A	0.32999876	242.86	15.77	0.3334994	50.6	73.88	0.33650187	151.94	3.25	23812	0.65
	B	0.32961366	239.44	5.71	0.33460957	25.66	83.14	0.33577681	149.06	3.79	24932	0.62
	C-A	0.33033973	242.48	22.33	0.33362985	81.77	66.48	0.33603045	335.37	7	25724	0.57
	C-B	0.33040726	233.71	11.02	0.33397564	100.42	74.15	0.33561713	325.93	11.25	23656	0.52
	D	0.33042672	232.69	24.48	0.33439928	74.92	63.81	0.33517402	326.7	8.74	24216	0.47
	E-A	0.33086014	226.7	22.84	0.33309197	62.99	66.31	0.33604789	319.23	5.96	25313	0.52
	E-B	0.33004159	221.45	18.14	0.33430007	85.19	65.61	0.33565837	316.75	15.74	27145	0.56
	F	0.32956964	238.43	25.49	0.33435741	85.16	61.91	0.33607298	333.76	11.02	25414	0.65
8-3	A	0.32660294	89.75	2.67	0.33659977	180.08	7.07	0.33679727	339.15	82.44	21858	1.02
	B	0.32797357	98.27	13.98	0.33302692	194.21	22.57	0.33899948	338.97	63.03	20260	1.10
	C	0.32777321	104.97	5.19	0.33382297	196.21	13.43	0.33840385	354.29	75.57	21533	1.06
	D	0.32773992	269.98	8.75	0.33403358	178.49	9.56	0.33822647	41.71	76.99	22054	1.05
	E	0.32862765	256.94	8.3	0.33388937	164.59	15.71	0.33748296	13.84	72.13	19894	0.89
8-4	A	0.32787901	243.8	3.29	0.33431846	8.72	84.27	0.33780253	153.53	4.69	25585	0.99
	B	0.32694679	250.93	10.4	0.33478376	93.25	78.78	0.3382695	341.7	4.17	29804	1.13
	C	0.3266564	246.19	11.91	0.33444434	74.4	77.97	0.33889928	336.54	1.67	26176	1.22
	D	0.32758877	61.42	0.39	0.33360243	156.75	85.85	0.33880877	331.39	4.13	24897	1.12
	E	0.32736886	67.86	2.06	0.33417413	307.93	85.88	0.33845717	157.99	3.56	25785	1.11
8-5	A	0.32981452	274.62	3.91	0.33391097	124.63	85.48	0.3362745	4.78	2.25	19882	0.65
	B	0.32944071	268.27	14.07	0.33408648	92.65	75.89	0.33647281	358.53	1.04	19178	0.70
	C	0.32953325	265.45	13.41	0.33446214	100.72	76.12	0.33600461	356.29	3.52	18958	0.65
	D	0.32930398	263.21	3.86	0.33454394	2.72	67.79	0.33615196	171.66	21.84	20358	0.68
	E	0.33100113	91.12	9.53	0.33311808	206.92	68.9	0.33588076	357.87	18.64	17177	0.49
8-6	A	0.32943106	182.75	4.81	0.33342263	331.8	84.4	0.33714643	92.51	2.87	27602	0.77
	B	0.32956326	94.13	1.83	0.3326382	356.16	77	0.33779863	184.55	12.87	22130	0.82
	C	0.32422894	254.05	9.97	0.33573747	345.14	6.17	0.34003362	106.43	78.25	24313	1.58
	D	0.32873842	238.21	11.74	0.33376005	2.73	69.87	0.33750156	144.76	16.12	22705	0.88
	E	0.32710537	253.87	7.2	0.33553496	7.67	72.62	0.33735961	161.83	15.73	19854	1.03

Site	Core	Minimum (tau 1)			Intermediate (tau 2)			Maximum (tau 3)			Bulk	% Anisotropy
		eigenvalue	declination	inclination	eigenvalue	declination	inclination	eigenvalue	declination	inclination	Susceptibility	Tauxe et al., 1990
8-7	A	0.33038136	43.88	13.3	0.33379889	174.02	69.87	0.33581972	310.29	14.84	20748	0.54
	B	0.33037201	215.5	9.35	0.33288142	326.39	65.22	0.33674657	121.55	22.73	19861	0.64
	C	0.32881561	222.73	11.31	0.3349494	65.81	77.74	0.33623502	313.67	4.68	20374	0.74
	D	0.3307986	51.48	6.46	0.33392751	309.54	61.29	0.33527389	144.91	27.84	17090	0.45
	E	0.33016384	37.46	1.86	0.33285624	292.86	82.64	0.33697996	127.7	7.11	17317	0.68
	F	0.32997176	35.29	15.21	0.33343637	276.57	60.5	0.33659184	132.45	24.63	18800	0.66
8-8	A	0.32594439	254.74	1.04	0.33489543	346.04	51.34	0.33916026	163.9	38.64	26704	1.32
	B	0.32742497	270.34	0.14	0.33499044	0.54	54.57	0.33758464	180.24	35.43	26096	1.02
	C	0.32509324	74.87	0.79	0.33608866	343.64	57.31	0.33881813	165.37	32.68	26328	1.37
	D	0.32716504	276	2.08	0.33361751	7.07	27.14	0.33921757	181.96	62.76	23178	1.21
	E	0.32767382	69.87	3.77	0.33329412	339.14	10.91	0.33903208	178.65	78.45	16910	1.14
	F	0.33028388	251.24	7.34	0.33142295	342.77	11.74	0.33829319	129.86	76.1	23214	0.80
	G	0.3286294	83.61	2.69	0.33161736	353.18	9.06	0.33975321	189.98	80.54	19382	1.11
	H	0.33009744	290.71	5.13	0.33207268	22.86	22.68	0.33782995	188.68	66.69	24760	0.77
	I	0.32960123	288.22	7.94	0.3318212	20.9	18.51	0.33857769	176.01	69.74	22720	0.90
8-9	A	**CORE BROKE DURING EXTRACTION**										
	B	**ORIENTING MARK LOST**										
	C	0.31966585	106.51	18.65	0.33829015	259.06	69.18	0.34204409	13.47	8.93	31605	2.24
	D	0.32099533	87.83	5.02	0.33695194	191.92	70.16	0.34205267	356.09	19.14	17900	2.11
	E	0.32312655	109	8.91	0.33249879	204.81	32.81	0.34437463	5.71	55.7	35382	2.12
8-10	A	0.32755572	112.06	6.06	0.33401033	18.63	29.42	0.33843398	212.59	59.84	32889	1.09
	B	0.32844689	279.45	1.12	0.3352007	10.79	49.93	0.33635253	188.51	40.04	31472	0.79
	C	0.32878143	281.72	8.06	0.33398464	16.77	31.89	0.33723396	179.19	56.87	23512	0.85
b	D	0.32529601	282.47	16.93	0.33401409	186.05	20.15	0.34068993	49.5	63.18	23157	1.54
b	E	0.32465848	292.89	14.3	0.33407968	196.23	24.47	0.34126183	50.47	61.17	27169	1.66
b	F	0.32517445	281.49	8.89	0.33552009	187.64	23.24	0.33930549	31.02	64.93	25051	1.41
8-11	A	0.32798192	232.11	2.46	0.33424798	123.36	82.4	0.33777013	322.42	7.19	26885	0.98
	B	0.32860386	46.47	10.93	0.3350651	292.04	64.97	0.33633113	141	22.23	27945	0.77
	C	0.32959238	56.78	13.83	0.33323124	202.45	73.4	0.33717641	324.54	9	28449	0.76
	D	0.32585341	47.91	11.2	0.33386013	269.01	75.27	0.34028643	139.8	9.43	27682	1.44
	E	0.32736814	38.49	7.95	0.33258876	150.33	69.44	0.3400431	305.76	18.84	28662	1.27
8-12	A	0.32782206	229.78	28.54	0.33584666	320.33	1.02	0.33633128	52.2	61.43	22816	0.85
	B	0.3292416	236.71	9.66	0.33353388	339.26	51.93	0.33722445	139.5	36.39	26895	0.80
	C	0.32998404	241.01	10.19	0.33283103	337.64	32.7	0.33718494	135.93	55.36	27188	0.72
	D	0.32918063	219.97	21.65	0.33399445	335.2	47.04	0.33682498	113.86	34.95	28362	0.76
	E	0.32889026	239.38	19.7	0.33357984	344.5	36.07	0.33752996	126.57	47.27	26764	0.86
8-13	A	0.32692513	75.18	28.97	0.33423755	321.61	35.85	0.3388373	193.44	40.54	25539	1.19
	B	0.32663217	81.49	30.33	0.33585986	341.24	16.93	0.33750793	226.14	54.35	26801	1.09
	C	0.3277311	64	11.74	0.33488405	329.89	19.05	0.33738482	183.91	67.38	25658	0.97
	D	0.32812551	32.58	22.16	0.33242357	288.72	30.46	0.33945093	152.55	50.81	29891	1.13
	E	0.32732856	48.96	18.06	0.33214486	310.85	23.38	0.34052658	172.97	59.76	27453	1.32
8-14	A	0.32758984	207.13	67	0.33419538	99.91	7.16	0.33821476	7.04	21.73	29380	1.06
	B	0.32604676	129.5	37.77	0.33419749	233.48	17.32	0.33975571	343.07	47.08	28200	1.37
	C	0.32624075	129.23	37.46	0.33410582	253.22	36.12	0.3396534	10.48	32.12	24541	1.34
	D	0.324779	102.39	28.25	0.33507285	233.11	50.52	0.34014818	357.8	25.12	21017	1.54
	E	0.32479593	98.98	27.91	0.334598	204.25	26.43	0.340606	330.22	49.76	29705	1.58
	F	0.3268024	98.48	31.66	0.3338474	242.43	52.67	0.33935019	357.14	17.68	21797	1.25